ATLAS DETECTOR AND PHYSICS PERFORMANCE

Technical Design Report

Volume I

ii

For this edition typing and typograhical errors have been corrected. Layout and pagination may therefore differ slightly with respect to the first, limited edition.

ATLAS Collaboration

Armenia
Yerevan Physics Institute, Yerevan

Australia
Research Centre for High Energy Physics, Melbourne University, Melbourne
University of Sydney, Sydney

Austria
Institut für Experimentalphysik der Leopold-Franzens-Universität Innsbruck, Innsbruck

Azerbaijan Republic
Institute of Physics, Azerbaijan Academy of Science, Baku

Republic of Belarus
Institute of Physics of the Academy of Science of Belarus, Minsk
National Centre of Particle and High Energy Physics, Minsk

Brazil
Universidade Federal do Rio de Janeiro, COPPE/EE/IF, Rio de Janeiro

Canada
University of Alberta, Edmonton
Department of Physics, University of British Columbia, Vancouver
University of Carleton/C.R.P.P., Carleton
Group of Particle Physics, University of Montreal, Montreal
Department of Physics, University of Toronto, Toronto
TRIUMF, Vancouver
University of Victoria, Victoria

CERN
European Laboratory for Particle Physics (CERN), Geneva

China
Institute of High Energy Physics, Academia Sinica, Beijing, University of Science and Technology of China, Hefei, University of Nanjing and University of Shandong

Czech Republic
Academy of Sciences of the Czech Republic, Institute of Physics and Institute of Computer Science, Prague
Charles University, Faculty of Mathematics and Physics, Prague
Czech Technical University in Prague, Faculty of Nuclear Sciences and Physical Engineering, Faculty of Mechanical Engineering, Prague

Denmark
Niels Bohr Institute, University of Copenhagen, Copenhagen

Finland
Helsinki Institute of Physics, Helsinki

France
Laboratoire d'Annecy-le-Vieux de Physique des Particules (LAPP), IN2P3-CNRS, Annecy-le-Vieux
Université Blaise Pascal, IN2P3-CNRS, Clermont-Ferrand
Institut des Sciences Nucléaires de Grenoble, IN2P3-CNRS-Université Joseph Fourier, Grenoble
Centre de Physique des Particules de Marseille, IN2P3-CNRS, Marseille
Laboratoire de l'Accélérateur Linéaire, IN2P3-CNRS, Orsay
LPNHE, Universités de Paris VI et VII, IN2P3-CNRS, Paris

CEA, DSM/DAPNIA, Centre d'Etudes de Saclay, Gif-sur-Yvette

Republic of Georgia
Institute of Physics of the Georgian Academy of Sciences and Tbilisi State University, Tbilisi

Germany
Physikalisches Institut, Universität Bonn, Bonn
Institut für Physik, Universität Dortmund, Dortmund
Fakultät für Physik, Albert-Ludwigs-Universität, Freiburg
Institut für Hochenergiephysik der Universität Heidelberg, Heidelberg
Institut für Physik, Johannes-Gutenberg Universität Mainz, Mainz
Lehrstuhl für Informatik V, Universität Mannheim, Mannheim
Sektion Physik, Ludwig-Maximilian-Universität München, München
Max-Planck-Institut für Physik, München
Fachbereich Physik, Universität Siegen, Siegen
Fachbereich Physik, Bergische Universität, Wuppertal

Greece
Athens National Technical University, Athens
Athens University, Athens
High Energy Physics Department and Department of Mechanical Engineering, Aristotle University of Thessaloniki, Thessaloniki

Israel
Department of Physics, Technion, Haifa
Raymond and Beverly Sackler Faculty of Exact Sciences, School of Physics and Astronomy, Tel-Aviv University, Tel-Aviv
Department of Particle Physics, The Weizmann Institute of Science, Rehovot

Italy
Dipartimento di Fisica dell' Università della Calabria e I.N.F.N., Cosenza
Laboratori Nazionali di Frascati dell' I.N.F.N., Frascati
Dipartimento di Fisica dell' Università di Genova e I.N.F.N., Genova
Dipartimento di Fisica dell' Università di Lecce e I.N.F.N., Lecce
Dipartimento di Fisica dell' Università di Milano e I.N.F.N., Milano
Dipartimento di Scienze Fisiche, Università di Napoli 'Federico II' e I.N.F.N., Napoli
Dipartimento di Fisica Nucleare e Teorica dell' Università di Pavia e I.N.F.N., Pavia
Dipartimento di Fisica dell' Università di Pisa e I.N.F.N., Pisa
Dipartimento di Fisica dell' Università di Roma 'La Sapienza' e I.N.F.N., Roma
Dipartimento di Fisica dell' Università di Roma 'Tor Vergata' e I.N.F.N., Roma
Dipartimento di Fisica dell' Università di Roma 'Roma Tre' e I.N.F.N., Roma
Dipartimento di Fisica dell' Università di Udine, Gruppo collegato di Udine I.N.F.N. Trieste, Udine

Japan
Department of Information Science, Fukui University, Fukui
Hiroshima Institute of Technology, Hiroshima
Department of Physics, Hiroshima University, Higashi-Hiroshima
KEK, High Energy Accelerator Research Organisation, Tsukuba
Department of Physics, Faculty of Science, Kobe University, Kobe
Department of Physics, Kyoto University, Kyoto
Kyoto University of Education, Kyoto-shi
Department of Electrical Engineering, Nagasaki Institute of Applied Science, Nagasaki
Naruto University of Education, Naruto-shi
Department of Physics, Faculty of Science, Shinshu University, Matsumoto
International Center for Elementary Particle Physics, University of Tokyo, Tokyo
Physics Department, Tokyo Metropolitan University, Tokyo
Department of Applied Physics, Tokyo University of Agriculture and Technology, Tokyo

Morocco

Faculté des Sciences Aïn Chock, Université Hassan II, Casablanca, and Université Mohamed V, Rabat

Netherlands

FOM - Institute SAF NIKHEF and University of Amsterdam/NIKHEF, Amsterdam
University of Nijmegen/NIKHEF, Nijmegen

Norway

University of Bergen, Bergen
University of Oslo, Oslo

Poland

Henryk Niewodniczanski Institute of Nuclear Physics, Cracow
Faculty of Physics and Nuclear Techniques of the University of Mining and Metallurgy, Cracow

Portugal

Laboratorio de Instrumentação e Física Experimental de Partículas (University of Lisboa, University of Coimbra, University Católica-Figueira da Foz and University Nova de Lisboa), Lisbon

Romania

Institute of Atomic Physics, National Institute of Physics and Nuclear Engineering, Bucharest

Russia

Institute for Theoretical and Experimental Physics (ITEP), Moscow
P.N. Lebedev Institute of Physics, Moscow
Moscow Engineering and Physics Institute (MEPhI), Moscow
Moscow State University, Institute of Nuclear Physics, Moscow
Budker Institute of Nuclear Physics (BINP), Novosibirsk
Institute for High Energy Physics (IHEP), Protvino
Petersburg Nuclear Physics Institute (PNPI), Gatchina, St. Petersburg

JINR

Joint Institute for Nuclear Research, Dubna

Slovak Republic

Bratislava University, Bratislava, and Institute of Experimental Physics of the Slovak Academy of Sciences, Kosice

Slovenia

Jozef Stefan Institute and Department of Physics, University of Ljubljana, Ljubljana

Spain

Institut de Física d'Altes Energies (IFAE), Universidad Autónoma de Barcelona, Bellaterra, Barcelona
Physics Department, Universidad Autónoma de Madrid, Madrid
Instituto de Física Corpuscular (IFIC), Centro Mixto Universidad de Valencia - CSIC, Valencia

Sweden

Fysiska institutionen, Lunds universitet, Lund
Royal Institute of Technology (KTH), Stockholm
University of Stockholm, Stockholm
Uppsala University, Department of Radiation Sciences, Uppsala

Switzerland

Laboratory for High Energy Physics, University of Bern, Bern
Section de Physique, Université de Genève, Geneva

Turkey

Department of Physics, Ankara University, Ankara
Department of Physics, Bogaziçi University, Istanbul

United Kingdom

School of Physics and Astronomy, The University of Birmingham, Birmingham
Cavendish Laboratory, Cambridge University, Cambridge
Department of Physics and Astronomy, University of Edinburgh, Edinburgh
Department of Physics and Astronomy, University of Glasgow, Glasgow
Department of Physics, Lancaster University, Lancaster
Department of Physics, Oliver Lodge Laboratory, University of Liverpool, Liverpool
Department of Physics, Queen Mary and Westfield College, University of London, London
Department of Physics, Royal Holloway and Bedford New College, University of London, Egham
Department of Physics and Astronomy, University College London, London
Department of Physics and Astronomy, University of Manchester, Manchester
Department of Physics, Oxford University, Oxford
Rutherford Appleton Laboratory, Chilton, Didcot
Department of Physics, University of Sheffield, Sheffield

United States of America

State University of New York at Albany, New York
Argonne National Laboratory, Argonne, Illinois
University of Arizona, Tucson, Arizona
Department of Physics, The University of Texas at Arlington, Arlington, Texas
Lawrence Berkeley Laboratory and University of California, Berkeley, California
Department of Physics, Boston University, Boston, Massachusetts
Brandeis University, Department of Physics, Waltham, Massachusetts
Brookhaven National Laboratory (BNL), Upton, New York
University of Chicago, Enrico Fermi Institute, Chicago, Illinois
Nevis Laboratory, Columbia University, Irvington, New York
Department of Physics, Duke University, Durham, North Carolina
Department of Physics, Hampton University, Virginia
Department of Physics, Harvard University, Cambridge, Massachusetts
Indiana University, Bloomington, Indiana
University of California, Irvine, California
Massachusetts Institute of Technology, Department of Physics, Cambridge, Massachusetts
University of Michigan, Department of Physics, Ann Arbor, Michigan
Michigan State University, Department of Physics and Astronomy, East Lansing, Michigan
University of New Mexico, New Mexico Center for Particle Physics, Albuquerque
Physics Department, Northern Illinois University, DeKalb, Illinois
Ohio State University, Columbus, Ohio
Department of Physics and Astronomy, University of Oklahoma
Department of Physics, University of Pennsylvania, Philadelphia, Pennsylvania
University of Pittsburgh, Pittsburgh, Pennsylvania
Department of Physics and Astronomy, University of Rochester, Rochester, New York
Institute for Particle Physics, University of California, Santa Cruz, California
Department of Physics, Southern Methodist University, Dallas, Texas
State University of New York at Stony Brook, Stony Brook, New York
Tufts University, Medford, Massachusetts
High Energy Physics, University of Illinois, Urbana, Illinois
Department of Physics, Department of Mechanical Engineering, University of Washington, Seattle, Washington
Department of Physics, University of Wisconsin, Madison, Wisconsin

Acknowledgements

Table Of Contents

Preface

The Large Hadron Collider opens a new frontier in particle physics due to its higher collision energy and luminosity compared to the existing accelerators. The guiding principle in optimising the ATLAS experiment has been maximising the discovery potential for new physics such as Higgs bosons and supersymmetric particles, while keeping the capability of high-accuracy measurements of known objects such as heavy quarks and gauge bosons.

The ATLAS subdetectors have been described in separate Technical Design Reports (TDRs), and the construction of the detector has begun. The purpose of this Detector and Physics Performance TDR is to document the expected overall physics performance of ATLAS. This TDR will serve both as a reference for the collaboration members and as an introduction to the ATLAS experiment and its rich physics potential for other physicists.

Volume I is dedicated to describing the detector performance. After a general overview in Chapter 1, and description of the simulation and reconstruction software in Chapter 2, each subsystem is described in a separate chapter with an emphasis on recent results: Inner Detector (Chapter 3), Electromagnetic Calorimeter (Chapter 4), Hadron Calorimeter (Chapter 5) and the Muon system (Chapter 6). Since physics analyses deal with objects reconstructed across many subdetectors, combined reconstruction is described in the following chapters: Electron/photon measurements (Chapter 7), Muon measurements (Chapter 8), Jet/hadron/E_T^{miss} measurements (Chapter 9), and b tagging (Chapter 10). Finally, common issues vital for physics measurements are addressed: the ATLAS triggers are summarised in Chapter 11, the mass scale measurements in Chapter 12, and luminosity measurements in Chapter 13.

Volume II describes the physics potential of ATLAS. The theoretical and experimental framework is set in the Introduction in Chapter 14, after which the physics studies themselves are presented: QCD (Chapter 15), gauge bosons (Chapter 16), B final states (Chapter 17), top and other heavy quarks and leptons (Chapter 18), Higgs bosons (Chapter 19), Supersymmetry (Chapter 20), and other extensions of the Standard Model (Chapter 21).

1 Experiment overview

1.1 Introduction

The Large Hadron Collider (LHC) is a proton-proton collider with 14 TeV centre of mass energy and design luminosity of 10^{34} cm^{-2}s^{-1}. Beam crossings are 25 ns apart and at design luminosity there are 23 interactions per crossing [1-1].

The ATLAS experiment has now entered the construction phase for many of its detector components, with a strict schedule to meet the first collisions at LHC in summer 2005. The detector concept and its physics potential have been presented in the Technical Proposal [1-2] about four years ago. Over the last two years detailed descriptions of the detector systems and their performance have been presented in the various Technical Design Reports (TDR) [1-3 to 1-13]; the complex task of their integration into the overall ATLAS detector has been recently described in the Technical Coordination TDR [1-15]. The purpose of this Detector and Physics Performance TDR is to document the expected overall performance of ATLAS as well as its rich physics potential at the LHC. The main features of the detector are briefly recalled in this chapter, however the real thrust of the present document is on performance and physics.

1.1.1 Nomenclature

The beam direction defines the z-axis, and the x-y plane is the plane transverse to the beam direction. The positive x-axis is defined as pointing from the interaction point to the centre of the LHC ring, and the positive y-axis is pointing upwards. The azimuthal angle ϕ is measured around the beam axis, and the polar angle θ is the angle from the beam axis. The pseudorapidity is defined as $\eta = -\ln\tan(\theta \div 2)$. The transverse momentum p_T and the transverse energy E_T, as well as the missing transverse energy E_T^{miss} and other transverse variables, are defined in the x-y plane unless stated otherwise. The distance ΔR in the pseudorapidity-azimuthal angle space is defined as $\Delta R = \sqrt{\Delta^2\eta + \Delta^2\phi}$.

Trajectories of charged particles can be described by five helix parameters in an ideal uniform magnetic field. The following helix parametrisation is used in ATLAS, with all quantities measured at the point of closest approach to the nominal beam axis $x = 0$, $y = 0$. Parameters in x-y plane are:

1/p_T	Reciprocal of the transverse momentum with respect to the beam-axis.
ϕ	Azimuthal angle, where $\tan\phi \equiv p_y/p_x$.
d_0	Transverse impact parameter, defined as the transverse distance to the beam axis at the point of closest approach; signed according to the reconstructed angular momentum of the track about the axis.

Parameters in the R-z plane are:

cot θ	Cotangent of the polar angle, where $\cot\theta \equiv p_z/p_T$;
z_0	Longitudinal impact parameter, defined as the z position of the track at the point of closest approach.

The side A of the detector is defined as the side with positive z, and the side C is the side with *z < 0.* Side B is the plane with *z = 0.*

1.2 Overall detector concept

A broad spectrum of detailed physics studies led to the overall detector concept presented in the ATLAS Technical Proposal [1-2]. The basic design criteria of the detector include the following.

- Very good electromagnetic calorimetry for electron and photon identification and measurements, complemented by full-coverage hadronic calorimetry for accurate jet and missing transverse energy (E_T^{miss}) measurements;

- High-precision muon momentum measurements, with the capability to guarantee accurate measurements at the highest luminosity using the external muon spectrometer alone;

- Efficient tracking at high luminosity for high-p_T lepton-momentum measurements, electron and photon identification, τ-lepton and heavy-flavour identification, and full event reconstruction capability at lower luminosity;

- Large acceptance in pseudorapidity (η) with almost full azimuthal angle (ϕ) coverage everywhere. The azimuthal angle is measured around the beam axis, whereas pseudorapidity relates to the polar angle (θ) where θ is the angle from the *z* direction.

- Triggering and measurements of particles at low-p_T thresholds, providing high efficiencies for most physics processes of interest at LHC.

The overall detector layout is shown in Figure 1-i. The magnet configuration is based on an inner thin superconducting solenoid surrounding the inner detector cavity, and large superconducting air-core toroids consisting of independent coils arranged with an eight-fold symmetry outside the calorimeters.

The Inner Detector (ID) is contained within a cylinder of length 7 m and a radius of 1.15 m, in a solenoidal magnetic field of 2 T. Pattern recognition, momentum and vertex measurements, and electron identification are achieved with a combination of discrete high-resolution semiconductor pixel and strip detectors in the inner part of the tracking volume, and continuous straw-tube tracking detectors with transition radiation capability in its outer part.

Highly granular liquid-argon (LAr) electromagnetic (EM) sampling calorimetry, with excellent performance in terms of energy and position resolution, covers the pseudorapidity range $|\eta| < 3.2$. In the end-caps, the LAr technology is also used for the hadronic calorimeters, which share the cryostats with the EM end-caps. The same cryostats also house the special LAr forward calorimeters which extend the pseudorapidity coverage to $|\eta| = 4.9$. The bulk of the hadronic calorimetry is provided by a novel scintillator-tile calorimeter, which is separated into a large barrel and two smaller extended barrel cylinders, one on each side of the barrel. The overall calorimeter system provides the very good jet and E_T^{miss} performance of the detector.

The LAr calorimetry is contained in a cylinder with an outer radius of 2.25 m and extends longitudinally to ±6.65 m along the beam axis. The outer radius of the scintillator-tile calorimeter is 4.25 m and its half length is 6.10 m. The total weight of the calorimeter system, including the solenoid flux-return iron yoke which is integrated into the tile calorimeter support structure, is about 4 000 Tons.

The calorimeter is surrounded by the muon spectrometer. The air-core toroid system, with a long barrel and two inserted end-cap magnets, generates a large magnetic field volume with strong bending power within a light and open structure. Multiple-scattering effects are thereby minimised, and excellent muon momentum resolution is achieved with three stations of high-precision tracking chambers. The muon instrumentation also includes as a key component trigger chambers with very fast time response.

The muon spectrometer defines the overall dimensions of the ATLAS detector. The outer chambers of the barrel are at a radius of about 11 m. The half-length of the barrel toroid coils is 12.5 m, and the third layer of the forward muon chambers, mounted on the cavern wall, is located about 23 m from the interaction point. The overall weight of the ATLAS detector is about 7 000 Tons.

The primary goal of the experiment is to operate at high luminosity (10^{34} cm^{-2}s^{-1}) with a detector that provides as many signatures as possible. The variety of signatures is considered to be important in the harsh environment of the LHC in order to achieve robust and redundant physics measurements with the ability of internal cross-check. The measurement of the luminosity itself will be a challenge. Precision measurements employing the total and elastic cross-sections require specialised detectors. A measurement with a precision of 5% to 10% may be obtained from the machine parameters. Alternative methods involving the production of electron and muon pairs are being considered in Chapter 13.

1.3 Magnet system

The ATLAS superconducting magnet system [1-3] can be seen in Figure 1-i, and the main parameters of its components are listed in Table 1-1. It is an arrangement of a central solenoid (CS) [1-4] providing the Inner Detector with magnetic field, surrounded by a system of three large air-core toroids generating the magnetic field for the muon spectrometer. The overall dimensions of the magnet system are 26 m in length and 20 m in diameter. The two end-cap toroids (ECT) [1-5] are inserted in the barrel toroid (BT) [1-6] at each end and line up with the CS. They have a length of 5 m, an outer diameter of 10.7 m and an inner bore of 1.65 m. The CS extends over a length of 5.3 m and has a bore of 2.4 m. The unusual configuration and large size make the magnet system a considerable challenge requiring careful engineering.

The CS provides a central field of 2 T with a peak magnetic field of 2.6 T at the superconductor itself. The peak magnetic fields on the superconductors in the BT and ECT are 3.9 and 4.1 T respectively. The performance in terms of bending power is characterised by the field integral $\int Bdl$, where B is the azimuthal field component and the integral is taken on a straight line trajectory between the inner and outer radius of the toroids. The BT provides 2 to 6 Tm and the ECT contributes with 4 to 8 Tm in the 0.0-1.3 and 1.6-2.7 pseudorapidity ranges respectively. The bending power is lower in the transition regions where the two magnets overlap ($1.3 < |\eta| < 1.6$).

The position of the CS in front of the EM calorimeter demands a careful minimisation of the material in order to achieve the desired calorimeter performance. As a consequence, the CS and the LAr calorimeter share one common vacuum vessel, thereby eliminating two vacuum walls.

Table 1-1 Main parameters of the toroidal and solenoid magnets in the ATLAS magnet system

	Property	Unit	Barrel Toroid	End-Cap Toroid (one)	Central Solenoid
Overall dimensions:					
	Inner diameter	m	9.4	1.65	2.44
	Outer diameter	m	20.1	10.7	2.63
	Axial length	m	25.3	5	5.3
	Number of coils	-	8	8	1
Weight:					
	Conductor	Tons	118	20.5	3.8
	Cold mass	Tons	370	160	5.4
	Total assembly	Tons	830	239	5.7
Coils:					
	Number of turns per coil	-	120	116	1173
	Operating current	kA	20.5	20	7.6
	Stored energy	MJ	1080	206	38
	Peak field	T	3.9	4.1	2.6
Conductor (NbTi/Cu/Aluminium):					
	Overall size (width x height)	mm^2	57 x 12	41 x 12	30 x 4.25
	Ratio Al : Cu : NbTi	-	28 : 1.3 : 1	19 : 1.3 : 1	15.6 : 0.9 : 1
	Number of strands in Rutherford cable	-	33	40	12
	Strand diameter	mm	1.3	1.3	1.22
	Critical current at 5T, 4.2 K	kA	58	60	20.4
	Total length	km	56	12.8	9.1
	Cooling requirements:				
	at 4.5 K	W	1130	260	100
	at 60-80 K	kW	7.0	2.4	0.50

The CS coil is designed to be as thin as possible without sacrificing the operational safety and reliability. Minimum coil material and an adequate safety margin for operation are obtained by distributing the stress uniformly between the coil components, while keeping the maximum strain due to the magnetic forces below 0.1% in the principal stress components.

Each of the three toroids consists of eight coils assembled radially and symmetrically around the beam axis. The ECT coil system is rotated by 22.5° with respect to the BT coil system in order to provide radial overlap and to optimise the bending power in the interface regions of both coil systems. The BT coils are of a flat racetrack type with two double-pancake windings made of

20.5 kA aluminium-stabilised NbTi superconductor. The windings are housed in an aluminium alloy casing. The magnetic forces are transferred to the warm structure. The coils are housed in individual cryostats taking up the forces between the coils. The toroidal structure consists of eight cryostats and the linking elements between them, called voussoirs and struts, that provide mechanical stability. Services are brought to the coils through a cryogenic ring linking the eight cryostats to a separate service cryostat, which provides connections to the power supply, the helium refrigerator, the vacuum systems and the control system.

Each ECT also consists of eight racetrack, double-pancake coils in an aluminium alloy housing. They are cold-linked and assembled as a single cold mass, housed in one large cryostat. Therefore the internal forces in the toroids are taken by the cold supporting structure between the coils, a different design solution than in the BT. Due to the magnetic forces, the ECT magnets are pulled into the BT and the corresponding axial forces are transferred to the BT cryostats via axial transfer points linking both magnet systems. The ECT cryostats have a classical turret for services. The cryostats rest on a rail system facilitating the movement and parking of the ECT magnets for access to the detector centre.

The magnets are indirectly cooled by forced flow of helium at 4.5 K through tubes welded on the casing of the windings. The CS is cooled via a dewar coupled to the refrigerator, whereas the BT and ECT in addition have cold helium pumps to guarantee appropriate cooling by a forced helium flow. The cooling power is supplied by a central refrigeration plant located in the side cavern and the services are distributed among the four magnets.

Electrically the eight coils of the BT are connected in series, as are the 16 coils in the two ECTs. The toroid coil systems have a 21 kA power supply and are equipped with control systems for fast and slow energy dumps. The CS is energised by an 8 kA power supply. An adequate and proven quench protection system has been designed to safely dissipate the stored energies without overheating the coil windings.

The conductor used in all the coils is a composite that consists of a flat superconducting cable located in the centre of an aluminium stabiliser with rectangular cross section. For the BT and ECT, the stabiliser is made of high-purity aluminium, while in the case of the CS doped aluminium is used to provide increased mechanical strength.

1.4 Inner Detector

The layout of the Inner Detector (ID) [1-7] is shown in Figure 1-ii. It combines high-resolution detectors at the inner radii with continuous tracking elements at the outer radii, all contained in the CS which provides a nominal magnetic field of 2 T.

The momentum and vertex resolution requirements from physics call for high-precision measurements to be made with fine-granularity detectors, given the very large track density expected at the LHC. Semiconductor tracking detectors, using silicon microstrip (SCT) [1-8] and pixel [1-9] technologies offer these features. The highest granularity is achieved around the vertex region using semi-conductor pixel detectors. The total number of precision layers must be limited because of the material they introduce, and because of their high cost. Typically, three pixel layers and eight strip layers (four space points) are crossed by each track. A large number of tracking points (typically 36 per track) is provided by the straw tube tracker (TRT) [1-8], which provides continuous track-following with much less material per point and a lower cost. The combination of the two techniques gives very robust pattern recognition and high precision in

Table 1-2 Parameters of the Inner Detector. The resolutions quoted are typical values (the actual resolution in each detector depends on the impact angle).

System	Position	Area (m²)	Resolution σ (μm)	Channels (10⁶)	η coverage
Pixels	1 removable barrel layer (B-layer)	0.2	$R\phi = 12, z = 66$	16	± 2.5
	2 barrel layers	1.4	$R\phi = 12, z = 66$	81	± 1.7
	5 end-cap disks on each side	0.7	$R\phi = 12, R = 77$	43	1.7-2.5
Silicon strips	4 barrel layers	34.4	$R\phi = 16, z = 580$	3.2	± 1.4
	9 end-cap wheels on each side	26.7	$R\phi = 16, R = 580$	3.0	1.4–2.5
TRT	Axial barrel straws		170 (per straw)	0.1	± 0.7
	Radial end-cap straws		170 (per straw)	0.32	0.7–2.5
	36 straws per track				

both ϕ and z coordinates. The straw hits at the outer radius contribute significantly to the momentum measurement, since the lower precision per point compared to the silicon is compensated by the large number of measurements and the higher average radius. The relative precision of the different measurements is well matched, so that no single measurement dominates the momentum resolution. This implies that the overall performance is robust. The high density of measurements in the outer part of the tracker is also valuable for the detection of photon conversions and of V^0 decays. The latter are an important element in the signature of *CP* violation in the *B* system. In addition, the electron identification capabilities of the whole experiment are enhanced by the detection of transition-radiation photons in the xenon-based gas mixture of the straw tubes.

The outer radius of the ID cavity is 115 cm, fixed by the inner dimension of the cryostat containing the LAr EM calorimeter, and the total length is 7 m, limited by the position of the end-cap calorimeters. Mechanically, the ID consists of three units: a barrel part extending over ± 80 cm, and two identical end-caps covering the rest of the cylindrical cavity. The precision tracking elements are contained within a radius of 56 cm, followed by the continuous tracking, and finally the general support and service region at the outermost radius. In order to give uniform η-coverage over the full acceptance, the final TRT wheels at high z extend inwards to a lower radius than the other TRT end-cap wheels.

In the barrel region, the high-precision detector layers are arranged on concentric cylinders around the beam axis, while the end-cap detectors are mounted on disks perpendicular to the beam axis. The pixel layers are segmented in Rφ and z, while the SCT detector uses small angle (40 mrad) stereo strips to measure both coordinates, with one set of strips in each layer measuring φ. The barrel TRT straws are parallel to the beam direction. All the end-cap tracking elements are located in planes perpendicular to the beam axis. The strip detectors have one set of strips running radially and a set of stereo strips at an angle of 40 mrad. The continuous tracking consists of radial straws arranged into wheels.

The basic layout parameters and the expected measurement resolutions are summarised in Table 1-2. The layout provides full tracking coverage over $|\eta| \leq 2.5$, including impact parameter measurements and vertexing for heavy-flavour and τ tagging. The secondary vertex measurement performance is enhanced by the innermost layer of pixels, at a radius of about 4 cm, as close as is practical to the beam pipe. The lifetime of such a detector will be limited by radiation damage, and may need replacement after a few years, the exact time depending on the luminosity profile. A large amount of interesting physics can be done with this detector during the initial lower-luminosity running, especially in the *B* sector, but physics studies have demonstrated the value of good *b*-tagging performance during all phases of the LHC operation, for example in the case of Higgs and supersymmetry searches. It is therefore considered very important that this innermost pixel layer (or *B*-layer) can be replaced to maintain the highest possible performance throughout the experiment's lifetime. The mechanical design of the pixel system allows the possibility of replacing the *B*-layer.

1.4.1 Pixel detector

The pixel detector [1-9] is designed to provide a very high-granularity, high-precision set of measurements as close to the interaction point as possible. The system provides three precision measurements over the full acceptance, and mostly determines the impact parameter resolution and the ability of the Inner Detector to find short-lived particles such as *B* hadrons and τ leptons. The two-dimensional segmentation of the sensors gives space points without any of the ambiguities associated with crossed strip geometries, but requires the use of advanced electronic techniques and interconnections for the readout. The readout chips are of large area, with individual circuits for each pixel element, including buffering to store the data while awaiting the level-1 trigger decision. Each chip must be bump-bonded to the detector substrate in order to achieve the required density of connections. In addition, the chips must be radiation hardened to withstand over 300 kGy of ionising radiation and over 5×10^{14} neutrons per cm^2 over ten years of operation. The system contains a total of 140 million detector elements, each 50 μm in the $R\phi$ direction and 300 μm in z, which are invaluable for the task of pattern recognition in the crowded environment of the LHC.

The system consists of three barrels at average radii of ~4 cm, 10 cm, and 13 cm, and five disks on each side, between radii of 11 and 20 cm, which complete the angular coverage. The system is designed to be highly modular, containing approximately 1 500 barrel modules and 700 disk modules, and uses only one type of support structure in the barrel and two types in the disks.

The pixel modules are designed to be identical in the barrel and the disks. Each module is 62.4 mm long and 21.4 mm wide, with 61 440 pixel elements read out by 16 chips, each serving an array of 24 by 160 pixels. The output signals are routed on the sensor surface to a hybrid on top of the chips, and from there to a separate clock-and-control integrated circuit. The modules are overlapped on the support structure in order to give hermetic coverage. The thickness of each layer is expected to be about 1.7% of a radiation length at normal incidence.

1.4.2 Semiconductor tracker

The SCT system [1-8] is designed to provide eight precision measurements per track in the intermediate radial range, contributing to the measurement of momentum, impact parameter and vertex position, as well as providing good pattern recognition by the use of high granularity.

The system is an order of magnitude larger in surface area than previous generations of silicon microstrip detectors, and in addition must face radiation levels which will alter the fundamental characteristics of the silicon wafers themselves.

The barrel SCT uses eight layers of silicon microstrip detectors to provide precision points in the $R\phi$ and z coordinates, using small angle stereo to obtain the z measurement. Each silicon detector is 6.36×6.40 cm^2 with 768 readout strips of 80 μm pitch. Each module consists of four single-sided p-on-n silicon detectors. On each side of the module, two detectors are wire-bonded together to form 12.8 cm long strips. Two such detector pairs are then glued together back-to-back at a 40 mrad angle, separated by a heat transport plate, and the electronics is mounted above the detectors on a hybrid. The readout chain consists of a front-end amplifier and discriminator, followed by a binary pipeline which stores the hits above threshold until the level-1 trigger decision. The end-cap modules are very similar in construction but use tapered strips, with one set aligned radially. To obtain optimal η-coverage across all end-cap wheels, end-cap modules consist of strips of either ~12 cm length (at the outer radii) or 6-7 cm length (at the innermost radius).

The detector contains 61 m^2 of silicon detectors, with 6.2 million readout channels. The spatial resolution is 16 μm in $R\phi$ and 580 μm in z, per module containing one Rϕ and one stereo measurement. Tracks can be distinguished if separated by more than ~200 μm.

The barrel modules are mounted on carbon-fibre cylinders which carry the cooling system; the four complete barrels at radii of 30.0, 37.3, 44.7 and 52.0 cm are then linked together. The end-cap modules are mounted in up to three rings onto nine wheels, which are interconnected by a space-frame. The radial range of each disk is adapted to limit the coverage to $|\eta| \leq 2.5$ by equipping each one with the minimum number of rings and by using the appropriate set of modules.

Solutions have been found to the critical issues in the system, and prototype modules have been successfully tested with beams in a magnetic field, demonstrating the required performance in resolution, signal-to-noise and speed. Modules containing both detectors and front-end electronics, irradiated to the level expected for ten years of LHC operation, have also been shown to function within specifications.

Both the pixel and the SCT systems require a very high dimensional stability, cold operation of the detectors, and the removal of the heat generated by the electronics and the detector leakage current. The structures are therefore designed with materials with as low a coefficient of thermal expansion as possible.

1.4.3 Transition radiation tracker

The TRT [1-8] is based on the use of straw detectors, which can operate at the very high rates expected at the LHC by virtue of their small diameter and the isolation of the sense wires within individual gas volumes. Electron identification capability is added by employing xenon gas to detect transition-radiation photons created in a radiator between the straws. This technique is intrinsically radiation hard, and allows a large number of measurements, typically 36, to be made on every track at modest cost. However, the detector must cope with a large occupancy and high counting rates at the LHC design luminosity.

Each straw is 4 mm in diameter and equipped with a 30 μm diameter gold-plated W-Re wire, giving a fast response and good mechanical and electrical properties for a maximum straw length of 144 cm in the barrel. The barrel contains about 50 000 straws, each divided in two at the centre, in order to reduce the occupancy, and read out at each end. The end-caps contain 320 000 radial straws, with the readout at the outer radius. The total number of electronic channels is 420 000. Each channel provides a drift-time measurement, giving a spatial resolution of 170 μm per straw, and two independent thresholds. These allow the detector to discriminate between tracking hits, which pass the lower threshold, and transition-radiation (TR) hits, which pass the higher one. The TRT is operated with a non-flammable gas mixture of 70% Xe, 20% CO_2 and 10% CF_4, with a total volume of 3 m^3.

The barrel section is built of individual modules with between 329 and 793 axial straws each, covering the radial range from 56 to 107 cm. The first six radial layers are inactive over the central 80 cm of their length, in order to reduce their occupancy, while providing extra coverage of the crack between the barrel and end-cap sections.

The two end-caps each consist of 18 wheels. The 14 wheels nearest the interaction point cover the radial range from 64 to 103 cm, while the last four wheels extend to an inner radius of 48 cm in order to maintain a constant number of crossed straws over the full acceptance. To avoid an unnecessary increase in the number of crossed straws and material at medium rapidity, wheels 7 to 14 have half as many straws per cm in z as the other wheels.

A primary concern in the design of this sub-system has been to obtain good performance at high occupancy and counting rate. In the barrel, the rate of hits above the lower threshold varies with radius from 6 to 18 MHz, while in the end-caps the rate varies with z from 7 to 19 MHz. The maximum rate of hits above the higher TR-threshold is 1 MHz. Within a single drift-time bin, the occupancy is about one third of that in the entire active time window. Position accuracies of about 170 μm have been achieved in tests at average straw counting rates of about 12 MHz. At these rates, only about 70% of the straws give correct drift-time measurements because of shadowing effects, but the large number of straws per track guarantees a combined measurement accuracy of better than 50 μm at the LHC design luminosity, averaged over all straws and including a systematic error of ~30 μm from alignment.

A good pattern recognition performance is also assured by the continuous tracking. Within the radial space available, the straw spacing has been optimised for tracking at the expense of electron identification, which would be improved by a greater path length through the radiator material and fewer straw detectors. The distribution of the straws over the maximum possible path length enhances the pattern recognition performance, by reducing the effect of loopers and interactions which can saturate small regions of the detector. The TRT provides additional discrimination between electrons and hadrons, with *e.g.* a pion rejection factor at $p_T = 20$ GeV varying with η between 20 and 100 at 90 % electron efficiency.

1.5 Calorimeters

A view of the ATLAS calorimeters [1-10] is presented in Figure 1-iii. The calorimetry consists of an electromagnetic (EM) calorimeter covering the pseudorapidity region $|\eta| < 3.2$, a hadronic barrel calorimeter covering $|\eta| < 1.7$, hadronic end-cap calorimeters covering $1.5 < |\eta| < 3.2$, and forward calorimeters covering $3.1 < |\eta| < 4.9$.

The EM calorimeter is a lead/liquid-argon (LAr) detector with accordion geometry [1-11]. Over the pseudorapidity range $|\eta| < 1.8$, it is preceded by a presampler detector, installed immediately behind the cryostat cold wall, and used to correct for the energy lost in the material (ID, cryostats, coil) upstream of the calorimeter.

The hadronic barrel calorimeter is a cylinder divided into three sections: the central barrel and two identical extended barrels. It is based on a sampling technique with plastic scintillator plates (tiles) embedded in an iron absorber [1-12]. At larger pseudorapidities, where higher radiation resistance is needed, the intrinsically radiation-hard LAr technology is used for all the calorimeters [1-11]: the hadronic end-cap calorimeter, a copper LAr detector with parallel-plate geometry, and the forward calorimeter, a dense LAr calorimeter with rod-shaped electrodes in a tungsten matrix.

The barrel EM calorimeter is contained in a barrel cryostat, which surrounds the Inner Detector cavity. The solenoid which supplies the 2 T magnetic field to the Inner Detector is integrated into the vacuum of the barrel cryostat and is placed in front of the EM calorimeter. Two end-cap cryostats house the end-cap EM and hadronic calorimeters, as well as the integrated forward calorimeter. The barrel and extended barrel tile calorimeters support the LAr cryostats and also act as the main solenoid flux return.

The pseudorapidity coverage, granularity and longitudinal segmentation of the ATLAS calorimeters are summarised in Table 1-3.

The approximately 200 000 signals from the LAr calorimeters leave the cryostats through cold-to-warm feedthroughs located between the barrel and the extended barrel tile calorimeters, and at the back of each end-cap. The electronics up to the digitisation stage will be contained in radial boxes attached to each feedthrough and located in the vertical gaps between the barrel and extended barrel tile calorimeters.

1.5.1 Electromagnetic calorimeter

The EM calorimeter [1-11] is divided into a barrel part ($|\eta| < 1.475$) and two end-caps ($1.375 < |\eta| < 3.2$). The barrel calorimeter consists of two identical half-barrels, separated by a small gap (6 mm) at $z = 0$. Each end-cap calorimeter is mechanically divided into two coaxial wheels: an outer wheel covering the region $1.375 < |\eta| < 2.5$, and an inner wheel covering the region $2.5 < |\eta| < 3.2$.

The EM calorimeter is a lead LAr detector with accordion-shaped Kapton electrodes and lead absorber plates over its full coverage. The accordion geometry provides complete ϕ symmetry without azimuthal cracks. The lead thickness in the absorber plates has been optimised as a function of η in terms of EM calorimeter performance in energy resolution. The LAr gap has a constant thickness of 2.1 mm in the barrel. In the end-cap, the shape of the Kapton electrodes and lead converter plates is more complicated, because the amplitude of the accordion waves increases with radius. The absorbers have constant thickness, and therefore the LAr gap also increases with radius. The total thickness of the EM calorimeter is > 24 radiation lengths (X_0) in the barrel and > 26 X_0 in the end-caps.

Over the region devoted to precision physics ($|\eta| < 2.5$), the EM calorimeter is segmented into three longitudinal sections. The strip section, which has a constant thickness of ~6 X_0 (upstream material included) as a function of η, is equipped with narrow strips with a pitch of ~4 mm in the η direction. This section acts as a 'preshower' detector, enhancing particle identification

Table 1-3 Pseudorapidity coverage, granularity and longitudinal segmentation of the ATLAS calorimeters.

EM CALORIMETER	Barrel	End-cap	
Coverage	|η| < 1.475	1.375 < |η| < 3.2	
Longitudinal segmentation	3 samplings	3 samplings	1.5 < |η| < 2.5
		2 samplings	1.375 < |η| < 1.5
			2.5 < |η| < 3.2
Granularity (Δη×Δφ)			
Sampling 1	0.003×0.1	0.025×0.1	1.375 < |η| < 1.5
		0.003×0.1	1.5 < |η| < 1.8
		0.004×0.1	1.8 < |η| < 2.0
		0.006×0.1	2.0 < |η| < 2.5
		0.1×0.1	2.5 < |η| < 3.2
Sampling 2	0.025×0.025	0.025×0.025	1.375 < |η| < 2.5
		0.1×0.1	2.5 < |η| < 3.2
Sampling 3	0.05×0.025	0.05×0.025	1.5 < |η| < 2.5
PRESAMPLER	**Barrel**	**End-cap**	
Coverage	|η| < 1.52	1.5 < |η| < 1.8	
Longitudinal segmentation	1 sampling	1 sampling	
Granularity (Δη×Δφ)	0.025×0.1	0.025×0.1	
HADRONIC TILE	**Barrel**	**Extended barrel**	
Coverage	|η| < 1.0	0.8 < |η| < 1.7	
Longitudinal segmentation	3 samplings	3 samplings	
Granularity (Δη×Δφ)			
Samplings 1 and 2	0.1×0.1	0.1×0.1	
Sampling 3	0.2×0.1	0.2×0.1	
HADRONIC LAr		**End-cap**	
Coverage		1.5 < |η| < 3.2	
Longitudinal segmentation		4 samplings	
Granularity (Δη×Δφ)		0.1×0.1	1.5 < |η| < 2.5
		0.2×0.2	2.5 < |η| < 3.2
FORWARD CALORIMETER		**Forward**	
Coverage		3.1 < |η| < 4.9	
Longitudinal segmentation		3 samplings	
Granularity (Δη×Δφ)		$\sim 0.2 \times 0.2$	

(γ/π^0, e/π separation, *etc.*) and providing a precise position measurement in η. The middle section is transversely segmented into square towers of size $\Delta\eta \times \Delta\phi = 0.025 \times 0.025$ (~4×4 cm^2 at $\eta = 0$). The total calorimeter thickness up to the end of the second section is ~24 X_0, tapered with increasing rapidity (this includes also the upstream material). The back section has a granularity of 0.05 in η and a thickness varying between 2 X_0 and 12 X_0. For $|\eta| > 2.5$, i.e. for the end-cap inner wheel, the calorimeter is segmented in two longitudinal sections and has a coarser lateral

granularity than for the rest of the acceptance. This is sufficient to satisfy the physics require-
ments (reconstruction of jets and measurement of E_T^{miss}). The calorimeter cells point towards
the interaction region over the complete η-coverage. The total number of channels is ~190 000.

The total material seen by an incident particle before the calorimeter front face is about 2.3 X_0 at
η = 0, and increases with pseudorapidity in the barrel because of the particle angle. In the re-
gion where the amount of material exceeds ~ 2 X_0 (as is the case for $|η| < 1.8$), a presampler is
used to correct for the energy lost by electrons and photons upstream of the calorimeter. The
presampler consists of an active LAr layer of thickness 1.1 cm (0.5 cm) in the barrel (end-cap) re-
gion. At the transition between the barrel and the end-cap calorimeters, *i.e.* at the boundary be-
tween the two cryostats, the amount of material in front of the calorimeter reaches a localised
maximum of about 7 X_0. In this region, the presampler is complemented by a scintillator slab in-
serted in the crack between the barrel and end-cap cryostats and covering the region
$1.0 < |η| < 1.6$. The region $1.37 < |η| < 1.52$ is not used for precision physics measurements in-
volving photons because of the large amount of material situated in front of the EM calorimeter.

The signals from the EM calorimeters are extracted at the detector inner and outer faces and
sent to preamplifiers located outside the cryostats close to the feedthroughs. Cables of 25 Ω are
used for cells belonging to the second and third samplings, while 50 Ω cables are used for the
strips in the first sampling and for the presampler pads, which have lower capacitance, in order
to optimise the electronic noise performance.

The preamplifier output is formed by bipolar shapers, sampled every 25 ns, and stored in ana-
logue memories using Switching Capacitor Arrays (SCA) during the level-1 trigger latency. If
the level-1 trigger is validated, the corresponding samples (typically five) are extracted from the
SCA, digitised and read out to the data acquisition system.

1.5.2 Hadronic calorimeters

The ATLAS hadronic calorimeters cover the range $|η| < 4.9$ using different techniques best suit-
ed for the widely varying requirements and radiation environment over the large η-range. Over
the range $|η| < 1.7$, the iron scintillating-tile technique is used for the barrel and extended bar-
rel tile calorimeters and for partially instrumenting the gap between them with the intermediate
tile calorimeter (ITC). This gap provides space for cables and services from the innermost detec-
tors. Over the range ~ $1.5 < |η| < 4.9$, LAr calorimeters were chosen: the hadronic end-cap calo-
rimeter (HEC) extends to $|η| < 3.2$, while the range $3.1 < |η| < 4.9$ is covered by the high-
density forward calorimeter (FCAL). Both the HEC and the FCAL are integrated in the same
cryostat as that housing the EM end-caps. Table 1-3 shows the granularity of the hadronic calor-
imetry over the full η-range.

An important parameter in the design of the hadronic calorimeter is its thickness: it has to pro-
vide good containment for hadronic showers and reduce punch-through into the muon system
to a minimum. The total thickness is 11 interaction lengths (λ) at η = 0, including about 1.5 λ
from the outer support, which has been shown both by measurements and simulation to be suf-
ficient to reduce the punch-through well below the irreducible level of prompt or decay muons.
Close to 10 λ of active calorimeter are adequate to provide good resolution for high energy jets.
Together with the large η-coverage, this will also guarantee a good E_T^{miss} measurement, which
is important for many physics signatures and in particular for SUSY particle searches.

1.5.2.1 Tile calorimeter

The large hadronic barrel calorimeter [1-12] is a sampling calorimeter using iron as the absorber and scintillating tiles as the active material. The tiles are placed radially and staggered in depth. The structure is periodic along *z*. The tiles are 3 mm thick and the total thickness of the iron plates in one period is 14 mm. Two sides of the scintillating tiles are read out by wavelength shifting (WLS) fibres into two separate photomultipliers (PMTs).

The tile calorimeter is composed of one barrel and two extended barrels. Radially the tile calorimeter extends from an inner radius of 2.28 m to an outer radius of 4.25 m. It is longitudinally segmented in three layers, approximately 1.4, 4.0 and 1.8 interaction lengths thick at $\eta = 0$. Azimuthally, the barrel and extended barrels are divided into 64 modules. In η, the readout cells, built by grouping fibres into PMTs, are 'pseudo-projective' towards the interaction region. The resulting granularity is $\Delta\eta\times\Delta\phi = 0.1\times0.1$ (0.2×0.1 in the last layer), as shown in Table 1-3. The total number of channels is about 10 000. The calorimeter is placed behind the EM calorimeter ($\approx 1.2\ \lambda$) and the solenoid coil. The total thickness at the outer edge of the tile-instrumented region is 9.2 λ at $\eta=0$.

The barrel cylinder covers the region $|\eta| < 1.0$. A vertical gap of 68 cm width provides space for cables from the ID, feedthroughs, and service pipes for the EM calorimeter and the CS; it also houses front-end electronics for the EM calorimeter. The extended barrel covers the region $0.8 < |\eta| < 1.7$. The azimuthal segmentation is as for the barrel, but the radial segmentation differs for the second and third layers. The thickness of the calorimeter in the gap is improved by the ITC, which has the same segmentation as the rest of the tile calorimeter. It is composed of two radial sections attached on the face of the extended barrel. The outer section, 31 cm thick, starts at the outer radius and covers 45 cm in radius. It is followed by the inner section which is 9 cm thick and extends over 45 cm to lower radii. The ITC is extended further inwards by a scintillator sheet, covering the inner part of the extended barrel and extending to the region between the LAr barrel and end-cap cryostats over $1.0 < |\eta| < 1.6$. This scintillator samples the energy lost in the cryostat walls and dead material. It is segmented in three sections of $\Delta\eta \sim 0.2$.

The signals produced by the scintillating tiles and collected by the WLS fibres are fast. The PMTs have low dark current and are also fast (rise time and transit time of a few ns). The shaper transforms the current pulse from the PMT into a unipolar pulse of FWHM of 50 ns.

1.5.2.2 Liquid-argon hadronic end-cap calorimeters

Each HEC [1-11] consists of two independent wheels, of outer radius 2.03 m. The upstream wheel is built out of 25 mm copper plates, while the cheaper other one, farther from the interaction point, uses 50 mm plates. In both wheels, the 8.5 mm gap between consecutive copper plates is equipped with three parallel electrodes, splitting the gap into four drift spaces of about 1.8 mm. The readout electrode is the central one, which is a three layer printed circuit, as in the EM calorimeter. The two layer printed circuits on either side serve only as high-voltage carriers. This electrode structure forms an 'electrostatic transformer' (EST) with an EST ratio of two. Such a scheme has the same behaviour as a double gap of 4 mm, but without the drawbacks associated with very high voltage (typically 4 kV instead of 2 kV), and ion build up in larger gaps.

Each wheel is built out of 32 identical modules, assembled with fixtures at the periphery, and a central ring. The central (buried) layer of the readout boards features a pad structure which defines the transverse readout granularity. The other layers are made out of a high resistivity coating, with a typical surface resistance of $1\,M\Omega$ per square. Each wheel is divided into two longitudinal segments. The weight of the first (second) wheel is 67 (90) Tons.

Primarily in order to limit the capacitance seen by a single preamplifier, and thus to allow for a fast response, only two gaps are ganged together at the pad level. Miniature coaxial cables running between the sectors carry signals to the preamplifier boards located at the wheel periphery. Output signals from (typically) four preamplifiers are summed together on the same board. A buffer stage drives the output signal up to the cold-to-warm feedthroughs.

Cells defined in this way are fully projective in azimuth, but only 'pseudo-projective' in η. However, the detector envelope is cylindrical, for the sake of mechanical simplicity. To minimise the dip in the material density at the transition between the end-cap and the forward calorimeter (around $|\eta| = 3.1$), the end-cap EM calorimeter reaches $|\eta| = 3.2$, thereby overlapping the forward calorimeter.

1.5.2.3 Liquid-argon forward calorimeter

The FCAL [1-11] is a particularly challenging detector owing to the high level of radiation it has to cope with. In ATLAS, the forward calorimeter is integrated into the end-cap cryostat, with a front face at about 4.7 m from the interaction point. Compared to layouts with a forward calorimeter situated at much larger distances from the interaction point, the survival of such a calorimeter in terms of radiation resistance is clearly more difficult. On the other hand, the integrated FCAL provides clear benefits in terms of uniformity of the calorimetric coverage as well as reduced radiation background levels in the muon spectrometer.

A global view of the FCAL is presented in Figure 1-iii. In order to minimise the amount of neutron albedo in the ID cavity (as an indication, at 47 cm radius and z less than 1 m, the albedo from the forward calorimeter contributes less than 5% of the total neutron fluence), the front face of the FCAL is recessed by about 1.2 m with respect to the EM calorimeter front face. This severely limits longitudinal space for installing about 9.5 active interaction lengths, and therefore calls for a high-density design, which also avoids energy leakage from the FCAL to its neighbours.

The FCAL consists of three sections: the first one is made of copper, while the other two are made out of tungsten. In each section the calorimeter consists of a metal matrix with regularly spaced longitudinal channels filled with concentric rods and tubes. The rods are at positive high voltage while the tubes and matrix are grounded. The LAr in the gap between is the sensitive medium. This geometry allows for an excellent control of the gaps which are as small as $250\,\mu m$ in the first section.

While the construction of the copper section does not present special difficulties, the construction of a tungsten calorimeter is a rather new and challenging task. After successful assembly of several prototypes, a technique has been chosen based on the assembly of small sintered tungsten alloy pieces. The overall density (including the liquid argon) of a section built in this way, with $375\,\mu m$ gaps, is $14.5\ \mathrm{g/cm^3}$.

Particular care is needed to support the FCAL in the end-cap cryostat such that the sensitive area is extended down to an angle as small as possible. An external structural tube carries the weight of the forward calorimeter, and withstands the pressure on the cryostat end-walls, while the central cryostat tube near the beam pipe has no structural role.

In terms of electronics and readout, four rods are ganged on the detector, and the signal is carried out by polyimide insulated coaxial cables. The number of channels is 3 584 for the total of both sides.

1.6 Muon spectrometer

The conceptual layout of the muon spectrometer [1-13] is visible in Figure 1-i. It is based on the magnetic deflection of muon tracks in the large superconducting air-core toroid magnets, instrumented with separate trigger and high-precision tracking chambers. Over the range $|\eta| \leq 1.0$, magnetic bending is provided by the large barrel toroid. For $1.4 \leq |\eta| \leq 2.7$, muon tracks are bent by two smaller end-cap magnets inserted into both ends of the barrel toroid. Over $1.0 \leq |\eta| \leq 1.4$, usually referred to as the transition region, magnetic deflection is provided by a combination of barrel and end-cap fields. This magnet configuration provides a field that is mostly orthogonal to the muon trajectories, while minimising the degradation of resolution due to multiple scattering.

The anticipated high level of particle fluxes has had a major impact on the choice and design of the spectrometer instrumentation, affecting required performance parameters such as rate capability, granularity, ageing properties and radiation hardness. Trigger and reconstruction algorithms have been optimised to cope with the difficult background conditions resulting from penetrating primary collision products and from radiation backgrounds, mostly neutrons and photons in the 1 MeV range, produced from secondary interactions in the calorimeters, shielding material, beam pipe and LHC machine elements.

In the barrel region, tracks are measured in chambers arranged in three cylindrical layers ('stations') around the beam axis; in the transition and end-cap regions, the chambers are installed vertically, also in three stations. Over most of the η-range, a precision measurement of the track coordinates in the principal bending direction of the magnetic field is provided by Monitored Drift Tubes (MDTs). At large pseudorapidities and close to the interaction point, Cathode Strip Chambers (CSCs) with higher granularity are used in the innermost plane over $2 < |\eta| < 2.7$, to withstand the demanding rate and background conditions. Optical alignment systems have been designed to meet the stringent requirements on the mechanical accuracy and the survey of the precision chambers.

The precision measurement of the muon tracks is made in the *R–z* projection, in a direction parallel to the bending direction of the magnetic field; the axial coordinate (*z*) is measured in the barrel and the radial coordinate (*R*) in the transition and end-cap regions. The MDTs provide a single-wire resolution of ~80 µm when operated at high gas pressure (3 bar) together with robust and reliable operation thanks to the mechanical isolation of each sense wire from its neighbours. The construction of prototypes has demonstrated that the MDTs can be built to the required mechanical accuracy of ~30 µm.

The trigger system covers the pseudorapidity range $|\eta| \leq 2.4$. Resistive Plate Chambers (RPCs) are used in the barrel and Thin Gap Chambers (TGCs) in the end-cap regions. The trigger chambers for the ATLAS muon spectrometer serve a threefold purpose:

- bunch crossing identification, requiring a time resolution better than the LHC bunch spacing of 25 ns;

- a trigger with well-defined p_T cut-offs in moderate magnetic fields, requiring a granularity of the order of 1 cm;

- measurement of the second coordinate in a direction orthogonal to that measured by the precision chambers, with a typical resolution of 5–10 mm.

1.6.1 Muon chamber layout

The overall layout of the muon chambers in the ATLAS detector is shown in Figure 1-1, which indicates the different regions in which the four chamber technologies described above are employed. The chambers are arranged such that particles from the interaction point traverse three stations of chambers. The positions of these stations are optimised for essentially full coverage and momentum resolution. In the barrel, particles are measured near the inner and outer field boundaries, and inside the field volume, in order to determine the momentum from the sagitta of the trajectory. In the end-cap regions, for $|\eta| > 1.4$, the magnet cryostats do not allow the positioning of chambers inside the field volume. Instead, the chambers are arranged to determine the momentum with the best possible resolution from a point-angle measurement (this is also the case in the barrel region in the vicinity of the coils).
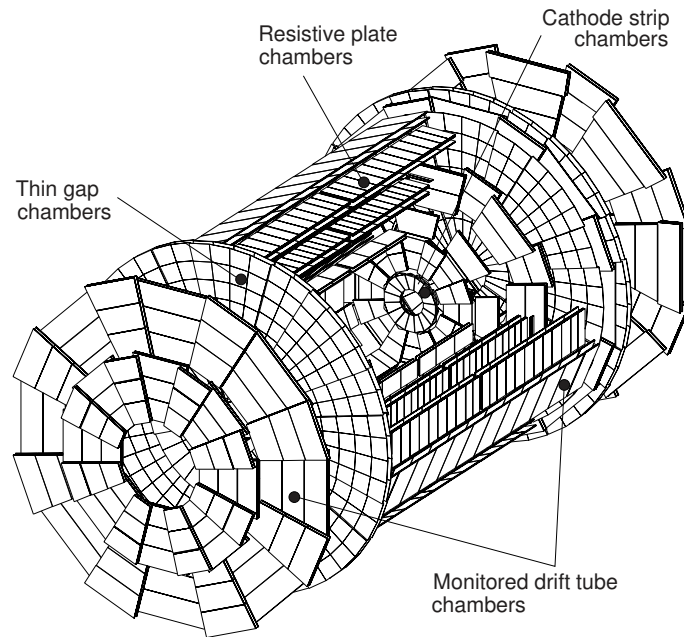
Figure 1-1 Three-dimensional view of the muon spectrometer instrumentation indicating the areas covered by the four different chamber technologies

The barrel chambers form three cylinders concentric with the beam axis, at radii of about 5, 7.5, and 10 m. They cover the pseudorapidity range $|\eta| < 1$. The end-cap chambers cover the range $1 < |\eta| < 2.7$ and are arranged in four disks at distances of 7, 10, 14, and 21–23 m from the inter-

action point, concentric with the beam axis. All chambers combined provide almost complete coverage of the pseudorapidity range $1.0 < |\eta| < 2.7$. There is an opening in the central R–ϕ plane ($\eta = 0$) for the passage of cables and services of the ID, the CS, and the calorimeters.

In the barrel, the chambers are arranged in projective towers. Particles are measured in 2×4 sensitive layers in the inner station and in 2×3 layers each in the middle and outer stations. Within a projective tower, the chambers are optically connected by alignment rays which monitor the relative chamber positions. A different alignment strategy is used in the end-caps, where the positions of complete chamber planes are monitored. No active repositioning of the chambers is foreseen.

Both in the barrel and the end-caps, a 16-fold segmentation in azimuth has been chosen that follows the eightfold azimuthal symmetry of the magnet structure. The chambers are arranged in large and small sectors. The large sectors cover the regions between the BT coils and the small sectors the azimuthal range around the BT coils. In two lower barrel sectors, the rails carrying the calorimeter and their feet require specially shaped chambers to maximise the detector acceptance.

The trigger function in the barrel is provided by three stations of RPCs. They are located on both sides of the middle MDT station, and directly inside the outer MDT station. In the end-caps, the trigger is provided by three stations of TGCs located near the middle MDT station.

Maximum standardisation and the smallest possible number of different chamber sizes have also been important goals of the detector layout. The barrel chambers are of rectangular shape with areas of 2–10 m^2. The end-cap chambers are of trapezoidal shape ('staircase' approximation) with tapering angles of 8.5° and 14° for the small and large chambers, respectively. Their areas range from 1–10 m^2 for individual chamber modules and up to 30 m^2 when several of them are preassembled for installation. Table 1-4 summarises the number of chambers, the area covered, and the number of readout channels for the four chamber technologies.

Table 1-4 Overview of the muon chamber instrumentation. 'Area covered' refers to chamber modules which normally contain several detector layers.

	Precision chambers		Trigger chambers	
	CSC	MDT	RPC	TGC
Number of chambers	32	1194	596	192
Number of readout channels	67 000	370 000	355 000	440 000
Area covered (m^2)	27	5500	3650	2900

All the barrel chambers and a part of the end-cap chambers are supported by the barrel toroid structure. Wherever possible, chambers are installed on rails parallel to the beam axis and connected to the magnet. They will be installed by sliding them in from the two detector ends. The majority of the end-cap chambers are mounted on the service structures at the two extreme ends of the experimental hall, and on special muon chamber support frames.

1.6.2 Monitored drift-tube chambers

The basic detection elements of the MDT chambers [1-13] are aluminium tubes of 30 mm diameter and 400 μm wall thickness, with a 50 μm diameter central W–Re wire. The tubes are operated with a non-flammable mixture of 93% Ar and 7% CO_2 at 3 bar absolute pressure and have a total volume of 800 m^3. The chosen working point provides for a non-linear space–time relation with a maximum drift time of ~700 ns, a small Lorentz angle, and excellent ageing properties. The single-wire resolution is ~80 μm.

The tubes are produced by extrusion from a hard aluminium alloy, and are available commercially. They are closed by endplugs which provide for accurate positioning of the anode wires, wire tension, gas tightness, and electrical and gas connections. The drift tubes can be manufactured to tight mechanical tolerances which are well matched to their intrinsic resolution properties, mostly using automated assembly procedures. The tube lengths vary from 70 cm to 630 cm.

To improve the resolution of a chamber beyond the single-wire limit and to achieve adequate redundancy for pattern recognition, the MDT chambers are constructed from 2×4 monolayers of drift tubes for the inner station and 2×3 monolayers for the middle and outer stations. The tubes are arranged in multilayer pairs of three or four monolayers, respectively, on opposite sides of a rigid support structure. The support structures ('spacer frames') provide for accurate positioning of the drift tubes with respect to each other, and for mechanical integrity under effects of temperature and gravity; for the barrel chambers which are not mounted in a vertical plane, they are designed to bend the drift tubes slightly in order to match them to the gravitational sag of the wires. The spacer frames also support most of the components of the alignment system.

The structural components of the spacer frames are three 'cross-plates', to which the drift-tube multilayers are attached, and two 'long beams' connecting the cross-plates. The frames need to be constructed to a moderate mechanical accuracy of 0.5 mm only; accurate positioning of the drift tubes is provided by the assembly procedure. They will be attached to the rail structures of the spectrometer by three-point kinematic supports. Once a chamber is installed in its final location in the spectrometer, mechanical deformations are monitored by an in-plane optical system; hence the name 'monitored drift-tube chambers'.

Each drift tube is read out at one end by a low-impedance current sensitive preamplifier, with a threshold five times above the noise level. The preamplifier is followed by a differential amplifier, a shaping amplifier and a discriminator. The output of the shaping amplifier is also connected to a simple ADC, to correct the drift-time measurement for time-slewing using the charge-integrated signal.

1.6.3 Cathode strip chambers

The CSCs [1-13] are multiwire proportional chambers with cathode strip readout and with a symmetric cell in which the anode-cathode spacing is equal to the anode wire pitch. The precision coordinate is obtained by measuring the charge induced on the segmented cathode by the avalanche formed on the anode wire. Good spatial resolution is achieved by segmentation of the readout cathode and by charge interpolation between neighbouring strips. The cathode strips for the precision measurement are orthogonal to the anode wires. The anode wire pitch is 2.54 mm and the cathode readout pitch is 5.08 mm; position resolutions of better than 60 μm have been measured in several prototypes. Other important characteristics are small electron

drift times (30ns), good time resolution (7 ns), good two-track resolution, and low neutron sensitivity. A measurement of the transverse coordinate is obtained from orthogonal strips, *i.e.* oriented parallel to the anode wires, which form the second cathode of the chamber.

The spatial resolution of the CSCs is sensitive to the inclination of tracks and the Lorentz angle. To minimise degradations of the resolution due to these effects, they will be installed in a tilted position such that stiff tracks originating from the interaction point are normal to the chamber surface. The CSCs are arranged in 2×4 layers.

The baseline CSC gas is a non-flammable mixture of 30% Ar, 50% CO_2 and 20% CF_4, with a total volume of 1.1 m³. The fact that this gas contains no hydrogen, combined with the small gap width, explains the low sensitivity to neutron backgrounds.

The front-end section of the strip readout electronics consists of a charge-sensitive preamplifier that drives a pulse-shaping amplifier. This is followed by analogue storage of the peak cathode pulse height during the level-1 trigger latency. After a level-1 trigger, the analogue data are multiplexed into a 10-bit ADC. Since the precision coordinate is obtained from charge interpolation, the position resolution depends critically on the relative gain of neighbouring cathode strips and readout channels, which is measured with the help of accurately calibrated test pulses.

1.6.4 Resistive plate chambers

The RPC [1-13] is a gaseous detector providing a typical space–time resolution of $1 \, \text{cm} \times 1 \, \text{ns}$ with digital readout. The basic RPC unit is a narrow gas gap formed by two parallel resistive bakelite plates, separated by insulating spacers. The primary ionisation electrons are multiplied into avalanches by a high, uniform electric field of typically 4.5 kV/mm. Amplification in avalanche mode produces pulses of typically 0.5 pC. The gas mixture is based on tetrafluoroethane ($C_2H_2F_4$) with some small admixture of SF_6, a non-flammable and environmentally safe gas that allows for a relatively low operating voltage. The signal is read out via capacitive coupling by metal strips on both sides of the detector. A trigger chamber is made from two rectangular detector layers, each one read out by two orthogonal series of pick-up strips: the 'η strips' are parallel to the MDT wires and provide the bending view of the trigger detector; the 'ϕ strips', orthogonal to the MDT wires, provide the second-coordinate measurement which is also required for the offline pattern recognition.

The RPCs use no wires and therefore have a simple mechanical structure and are straightforward to manufacture. The 2 mm thick bakelite plates are separated by polycarbonate spacers of 2 mm thickness which define the size of the gas gap. The spacers are glued on both plates at 10 cm intervals. A 7 mm wide frame of the same material and thickness as the spacers is used to seal the gas gap at all four edges. The outside surfaces of the resistive plates are coated with thin layers of graphite paint which are connected to the high voltage supply. These graphite electrodes are separated from the pick-up strips by 200 µm thick insulating films which are glued on both graphite layers. The readout strips are arranged with a pitch varying from 30.0 to 39.5 mm.

Each chamber is made from two detector layers and four readout strip panels. These elements are rigidly held together by two support panels which provide the required mechanical stiffness of the chambers. The panels are made of polystyrene sandwiched between two aluminium sheets. One panel is flat, 50 mm thick, with 0.5 mm thick aluminium sheets; the other panel is

10 mm thick with 0.3 mm sheets and is preloaded with a 1 cm sagitta. The two panels are rigidly connected by 2 mm thick aluminium profiles, such that the preloaded support panel provides uniform pressure over the whole surface of an RPC module.

To preserve the excellent intrinsic time resolution of the RPCs, the readout strips are optimised for good transmission properties and are terminated at both ends to avoid signal reflections. The front-end electronics are based on a three-stage voltage amplifier followed by a variable-threshold comparator. They are mounted on printed circuit boards attached to the edges of the readout panels.

1.6.5 Thin gap chambers

The TGCs [1-13] are similar in design to multiwire proportional chambers, with the difference that the anode wire pitch is larger than the cathode–anode distance. Signals from the anode wires, arranged parallel to the MDT wires, provide the trigger information together with readout strips arranged orthogonal to the wires. These readout strips are also used to measure the second coordinate.

Operated with a highly quenching gas mixture of 55% CO_2 and 45% n-pentane (n-C_5H_{12}), this type of cell geometry permits operation in saturated mode, with a number of advantages:

- small sensitivity to mechanical deformations, which is important to minimise the cost of large-area chambers;

- small dependence of the pulse height on the incident angle, up to angles of 40°;

- nearly Gaussian pulse height distribution with small Landau tails, and no streamer formation.

The total gas volume is 16 m^3. The gas mixture is highly flammable and requires adequate safety precautions.

The main dimensional characteristics of the chambers are a cathode-cathode distance (gas gap) of 2.8 mm, a wire pitch of 1.8 mm, and a wire diameter of 50 μm. The operating high voltage foreseen is 3.1 kV. The electric field configuration and the small wire distance provide for a short drift time and thus a good time resolution. Ageing properties of the chambers have been investigated in detail and were found to be fully adequate for the expected operating conditions at the LHC, including the large safety margin used throughout the muon spectrometer chambers to account for uncertainties in the predicted occupancies from the neutron background.

The TGCs are constructed in doublets and in triplets of chambers. The inner station consists of one doublet and is only used to measure the second coordinate. The seven chamber layers in the middle station are arranged in one triplet and two doublets which provide the trigger and the second coordinate measurements. The anode plane is sandwiched between two cathode planes made of 1.6 mm G-10 plates on which the graphite cathode is deposited. On the backside of the cathode plates facing the centre plane of the chamber, etched copper strips provide the readout of the azimuthal coordinate; no readout strips are foreseen for the central layer of a triplet. The TGC layers are separated by 20 mm thick paper honeycomb panels which provide a rigid mechanical structure for the chambers. On the outside, the gas pressure is sustained by 5 mm thick paper honeycomb panels. These are covered in turn by 0.5 mm G-10 plates.

To form a trigger signal, several anode wires are grouped together and fed to a common readout channel. The number of wires per group varies between 4 and 20, depending on the desired granularity as a function of pseudorapidity. The ganged signals are fed into a low-impedance two-stage amplifier.

1.6.6 Alignment

The requirements on the momentum resolution of the spectrometer call for an accuracy of the relative positioning of chambers traversed by a muon track that matches the intrinsic resolution and the mechanical tolerances of the precision chambers. Over the large global dimensions of the spectrometer, however, it is not possible to stabilise the dimensions and positions of the chambers at the $30\,\mu m$ level. Therefore, chamber deformations and positions are constantly monitored by means of optical alignment systems and displacements up to ~1 cm can readily be corrected for in the offline analysis.

All alignment systems are based on optically monitoring deviations from straight lines. Owing to geometrical constraints, different schemes are used to monitor chamber positions in the barrel, in the end-caps, and the deformations of large chambers ('in-plane alignment'). For reasons of cost, optical monitoring in the barrel is foreseen only for the large sectors of chambers. Chambers in the small sectors are aligned with particle tracks, exploiting the overlap with chambers in the large sectors. Alignment with tracks will also serve to cross-calibrate the optical survey of the large sectors.

The very high accuracy of $30\,\mu m$ is required only for the positioning of chambers within a projective tower. The accuracy required for the relative positioning of different towers to obtain adequate mass resolutions for multimuon final states is in the millimetre range. This accuracy is easily achieved by the initial positioning and survey of chambers at installation time. The relative alignment of muon spectrometer, calorimeters and Inner Detector will rely on high-momentum muon trajectories.

1.7 Trigger and data-acquisition system

The ATLAS trigger and data-acquisition (DAQ) system is based on three levels of online event selection [1-14],[1-16],[1-17]. Each trigger level refines the decisions made at the previous level and, where necessary, applies additional selection criteria. Starting from an initial bunch-crossing rate of 40 MHz (interaction rate of ~10^9 Hz at a luminosity of 10^{34} cm^{-2}s^{-1}), the rate of selected events must be reduced to ~100 Hz for permanent storage. While this requires an overall rejection factor of 10^7 against 'minimum-bias' events, excellent efficiency must be retained for the rare new physics processes, such as Higgs boson decays, which will be searched for in ATLAS. Figure 1-2 shows a simplified functional view of the Trigger/DAQ system. In the following, a brief description is given of some of the key aspects of the event-selection process.

The level-1 (LVL1) trigger [1-14] makes an initial selection based on reduced-granularity information from a subset of detectors. High transverse-momentum (high-p_T) muons are identified using only the trigger chambers, RPCs in the barrel, and TGCs in the end-caps. The calorimeter selections are based on reduced-granularity information from all the calorimeters (EM and hadronic; barrel, end-cap and forward). Objects searched for by the calorimeter trigger are high-p_T electrons and photons, jets, and τ-leptons decaying into hadrons, as well as large missing and total transverse energies. In the case of the electron/photon and hadron/τ triggers, energy iso-
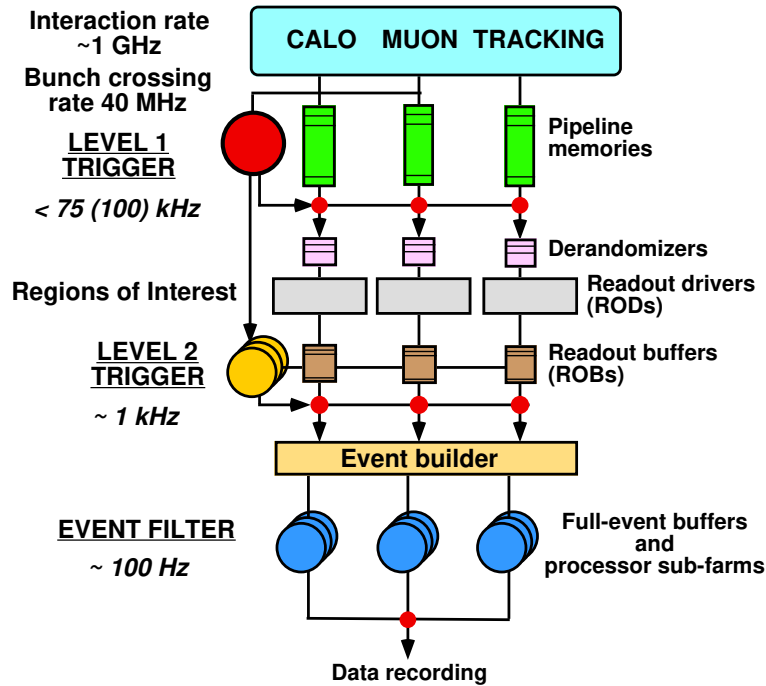
Figure 1-2 Block diagram of the Trigger/DAQ system.

lation cuts can be applied. Trigger information is provided for a number of sets of p_T thresholds (generally 6–8 sets of thresholds per object type). The missing and total scalar transverse energies used in the LVL1 trigger are calculated by summing over trigger towers. In addition, a trigger on the scalar sum of jet transverse energies is also available.

The LVL1 trigger decision is based on combinations of objects required in coincidence or veto. Most of the physics requirements of ATLAS can be met by using, at the LVL1 trigger level, fairly simple selection criteria of a rather inclusive nature. However, the trigger implementation is flexible and it can be programmed to select events using more complicated signatures.

The maximum rate at which the ATLAS front-end systems can accept LVL1 triggers is limited to 75 kHz (upgradable to 100 kHz). The rates estimated in trigger performance studies, using trigger menus that meet the needs of the ATLAS physics programme, are about a factor of two below this limit. Given that there are large intrinsic uncertainties in the calculations, this safety factor is not over-generous. However, if necessary, rates could be significantly reduced without major consequences for the physics programme, for example by increasing the thresholds on some of the inclusive (single-object) triggers when operating at the highest luminosities, and by relying more heavily on multi-object triggers.

An essential requirement on the LVL1 trigger is that it should uniquely identify the bunch-crossing of interest. Given the short (25 ns) bunch-crossing interval, this is a non-trivial consideration. In the case of the muon trigger, the physical size of the muon spectrometer implies times-of-flight comparable to the bunch-crossing period. For the calorimeter trigger, a serious challenge is that the pulse shape of the calorimeter signals extends over many bunch crossings.

It is important to keep the LVL1 latency (time taken to form and distribute the LVL1 trigger decision) to a minimum. During this time, information for all detector channels has to be conserved in 'pipeline' memories. These memories are generally contained in custom integrated

circuits, placed on or close to the detector, usually in inaccessible regions and in a high-radiation environment. The total number of detector channels, excluding the pixel detectors, exceeds 10^7. For reasons of cost and reliability, it is desirable to keep the pipeline lengths as short as possible. The LVL1 latency, measured from the time of the proton–proton collision until the trigger decision is available to the front-end electronics, is required to be less than 2.5 µs. In order to achieve this, the LVL1 trigger is implemented as a system of purpose-built hardware processors. The target latency for the LVL1 trigger is 2.0 µs (leaving 500 ns contingency).

Events selected by LVL1 are read out from the front-end electronics systems of the detectors into readout drivers (RODs) and then into readout buffers (ROBs); present estimates foresee about 1700 ROBs in total. A large number of front-end electronics channels are multiplexed into each ROB. Intermediate buffers, labelled 'derandomisers' in Figure 1-2, average out the high instantaneous data rate at the output of the pipeline memories to match the available input bandwidth of the RODs.

All the detector data for the bunch crossing selected by the LVL1 trigger are held in the ROBs, either until the event is rejected by the level-2 (LVL2) trigger (in which case the data are discarded), or, in case the event is accepted by LVL2, until the data have been successfully transferred by the DAQ system to storage associated with the Event Filter (which makes the third level of event selection) [1-16]. The process of moving data from the ROBs to the Event Filter (EF) is called event building. Whereas before event building each event is composed of many fragments, with one fragment in each ROB, after event building the full event is stored in a single memory accessible by an EF processor.

The LVL2 trigger makes use of 'region-of-interest' (RoI) information provided by the LVL1 trigger. This includes information on the position (η and ϕ) and p_T of candidate objects (high-p_T muons, electrons/γ, hadrons/τ, jets), and energy sums (missing-E_T vector and scalar E_T value). The RoI data are sent by LVL1 to LVL2, for all events selected by the LVL1 trigger, using a dedicated data path. Using the RoI information, the LVL2 trigger selectively accesses data from the ROBs, moving only the data that are required in order to make the LVL2 decision. The LVL2 trigger has access to all of the event data, if necessary with the full precision and granularity. However, typically only data from a small fraction of the detector, corresponding to limited regions centred on the objects indicated by the LVL1 trigger, are needed by the LVL2 trigger. Hence, usually only a few per cent of the full event data are required thanks to this RoI mechanism.

It is expected that LVL2 will reduce the rate to ~1 kHz. In contrast to the 75 kHz (upgradable to 100 kHz) limit for LVL1 that comes from the design of the detector front-end electronics, this is not a hard number. Optimisation of the sharing of the selection task between LVL2 and the EF is currently underway [1-17]. The latency of the LVL2 trigger is variable from event to event and is expected to be in the range 1–10 ms.

In the case of muon triggers, the rejection power at LVL2 comes from sharpening (and, where necessary, raising) the p_T threshold compared to LVL1, and from applying isolation requirements. Sharper p_T thresholds are obtained by using the precision muon chambers and the ID. The isolation requirements use the calorimeter information in a region around the muon candidate.

For isolated electrons, rejection power at LVL2 comes from using the full-granularity calorimeter information and requiring a matching high-p_T charged track in the ID; the transition-radiation signature provides additional rejection power. For photons, less rejection power is possible than in the case of electrons, since the ID cannot be used given the relatively high probability for

photon conversion in the ID material (it is not planned to use a track veto for the photon trigger). However, for the important physics channel $H \rightarrow \gamma\gamma$, the trigger can require a pair of photons, with a further rejection factor for each γ compared to LVL1 due to the use of high-precision, high-granularity calorimeter information.

For the hadron/τ trigger, rejection at LVL2 is achieved using the full-granularity calorimeter information and the ID. A localised, isolated (hadronic) calorimeter cluster with a matching high-p_T track is required.

In the case of jets, much less rejection power is possible. Jets are the dominant high-p_T process at the LHC, and the threshold behaviour of the LVL1 trigger is reasonably sharp. Hence, for jet triggers, LVL2 must either increase the threshold, or make additional requirements in order to significantly reduce the rate. The possibility of identifying b-quark jets at LVL2 using the ID is under study.

Concerning the energy-sum triggers (E_T^{miss}, total scalar E_T), only limited improvement is possible using the RoI mechanism. The energy-sum values from LVL1 are provided to LVL2 and refinements can be made to correct, e.g. for high-p_T muons (the LVL1 E_T^{miss} trigger uses only calorimeter information, so muons contribute to the observed E_T^{miss}) or for saturated trigger-tower signals, a possibility allowed by design to reduce cost. The possibility of performing a full E_T^{miss} recalculation at LVL2 for a small subset of events remaining after other LVL2 selection criteria have already been applied is being investigated.

The LVL1 trigger makes available RoI information for all of the objects that contributed to the event being selected: these are called primary RoIs. In order to allow for additional requirements to be made at LVL2, the LVL1 trigger provides RoI information for objects that did not contribute to the selection of the event. Such RoIs, typically for objects of relatively low p_T, are called secondary RoIs.

After LVL2, the last stage of the online selection is performed by the EF. It will employ offline algorithms and methods, adapted to the online environment, and use the most up to date calibration and alignment information and the magnetic field map. The EF will make the final selection of physics events which will be written to mass storage for subsequent full offline analysis. The output rate from LVL2 should then be reduced by an order of magnitude, giving ~100 Hz, corresponding to an output data rate of ~100 MB/s if the full event data are to be recorded.

It is envisaged that the first task of the EF will be to confirm the results of the LVL2 decision and subsequently use the results of the LVL2 to seed its own analyses. The rejection power of the EF comes from:

- using refined algorithms and, where necessary, tighter p_T thresholds compared to those used in the LVL2;

- the availability of all data relevant to the specific event in calculations and selection criteria;

- the use of complex algorithms and criteria which, due to processing time limits, cannot be performed at LVL2, an example being vertex and track fitting using bremsstrahlung recovery for electrons.

1.8 Computing

Computing is crucial for the success of the ATLAS experiment and the effort to develop and maintain the software will be enormous [1-18]. The software is vitally important to the whole experiment's success, and must be maintained for a lifetime of about 20 years of the project,. Hence, the quality requirements on the software have to be very high. It is estimated that, for the whole ATLAS software-development project, up to 1000 person-years will be required. Effort of such magnitude is only available in the collaboration on a very distributed basis. In order to optimise quality and to assure long-term maintenance, software development has to adhere to accepted international standards, seek common developments with other experiments, and employ commercial solutions wherever possible. It is planned to implement the software following the object-oriented paradigm. Currently, implementation using the C++ language is being pursued.

The anticipated data volume of about 1 PByte (10^{15} Bytes) per year requires new methods for data reduction, data selection, and data access for physics analysis. The basic goal is that every physicist in ATLAS must have the best possible access to the data to be analysed, irrespectively of his or her location. The proposed scheme consists of archiving the 'raw data' (1 PByte/year) selected by the Event Filter system. A first processing step will be performed on all data shortly (a few hours) after data taking. For this step, basic calibration and alignment constants must be available. The purpose is to evaluate basic physics quantities required by most analyses and to classify events into physics channels. The produced data have to be accessible at the event level and, below that, at the reconstruction and physics object level. ATLAS is considering using an object-oriented data-base system for this purpose. One copy of the data will be held at CERN, the replication of some or all of the data at a number of 'regional centres' is also foreseen.

To enable physics analysis to be performed in such a world-wide collaboration, high performance networking is a necessity. Today it is difficult to predict the evolution of the cost and performance of international networks at the time of LHC operation. As these are important parameters for the concrete planning of an analysis scenario, ATLAS is following the ongoing developments and will adjust its plans in these area accordingly.

1.9 References

1-1   'LHC White Book', CERN/AC/93-03; 'LHC Conceptual Design Report, CERN/AC/95-05.

1-2   ATLAS Collaboration, Technical Proposal for a General Purpose pp Experiment at the Large Hadron Collider at CERN, CERN/LHCC/94-43, LHCC/P2, 15 December 1994.

1-3   ATLAS Collaboration, Magnet System Technical Design Report, CERN/LHCC/97-18, 30 April 1997.

1-4   ATLAS Collaboration, Central Solenoid Technical Design Report, CERN/LHCC/97-21, 30 April 1997.

1-5   ATLAS Collaboration, End-Cap Toroids Technical Design Report, CERN/LHCC/97-20, 30 April 1997.

1-6   ATLAS Collaboration, Barrel Toroid Technical Design Report, CERN/LHCC/97-19, 30 April 1997.

1-7   ATLAS Collaboration, Inner Detector Technical Design Report, Volume 1,
        CERN/LHCC/97-16, 30 April 1997.

1-8   ATLAS Collaboration, Inner Detector Technical Design Report, Volume 2,
        CERN/LHCC/97-17, 30 April 1997.

1-9   ATLAS Collaboration, Pixel Detector Technical Design Report, CERN/LHCC/98-13,
        31 May 1998.

1-10   ATLAS Collaboration, Calorimeter Performance Technical Design Report,
        CERN/LHCC/96-40, 15 December 1996.

1-11   ATLAS Collaboration, Liquid Argon Calorimeter Technical Design Report,
        CERN/LHCC/96-41, 15 December 1996.

1-12   ATLAS Collaboration, Tile Calorimeter Technical Design Report, CERN/LHCC/96-42,
        15 December 1996.

1-13   ATLAS Collaboration, Muon Spectrometer Technical Design Report, CERN/LHCC/97-
        22, 31 May 1997.

1-14   ATLAS Collaboration, First-Level Trigger Technical Design Report, CERN/LHCC/98-14,
        30 June 1998.

1-15   ATLAS Collaboration, Technical Coordination Technical Design Report,
        CERN/LHCC/99-01, 31 January 1999.

1-16   ATLAS Collaboration, DAQ, EF, LVL2 and DCS Technical Progress Report,
        CERN/LHCC/98-16, 30 June 1998.

1-17   ATLAS Collaboration, Trigger Performance Status Report, CERN/LHCC/98-15,
        30 June 1998.

1-18   ATLAS Collaboration, Computing Technical Proposal, CERN/LHCC/96-43,
        15 December 1996.

2 Simulation of detector and physics performance

2.1 Introduction

This chapter presents the software tools used throughout this document to evaluate in a consistent way the detailed performance of the various detector systems, both individually (see Chapters 3 to 6) and combined (see Chapters 7 to 13), as well as the corresponding physics performance over a wide variety of different topics (see Chapters 14 to 21).

The requirements from these two aspects of the work (detector performance and physics performance) are sometimes conflicting:

- the detector simulation (Inner Detector, LAr and Tile Calorimeters and Muon System) and combined-performance (b-tagging, electrons/photons, jets/E_T^{miss}/τ-leptons, muons and trigger) working groups have, in most cases, been the promoters of detailed simulations using the GEANT package (version 3.21) [2-1], as described in Section 2.2. These simulations have to be performed in an environment containing many interactions per beam-crossing (in the case of the Inner Detector and calorimeters) and high rates of background noise from low-energy neutrons (in the case of the Muon System), as described in Section 2.3. These groups have also performed detailed studies requiring the full reconstruction of samples of individual particles or of complete physics events, as described in Section 2.4;

- in contrast, the physics-simulation working groups (Higgs bosons, supersymmetry, B-physics and top physics) have concentrated in most cases on fast simulation of high-statistics signal and background samples of complete physics events, as described in Section 2.5. Whenever deemed necessary, *e.g.* when studying invariant masses of reconstructed final-state objects originating from the decay of a narrow resonance, results from full simulation and reconstruction have been used to improve, refine and enrich the fast-simulation program.

The software tools and their technical and performance aspects described below have been developed over the past decade or so, but are now quite complete, from the tools devoted to accurate Monte Carlo generation of complex physics processes, to interactive graphics tools devoted to dynamically display and modify the results of the reconstruction programs, and finally to the tools devoted to interactive physics analysis of very large datasets. They meet in many areas the requirements needed for the final ATLAS software and will have to be maintained active, as a reference, over the next years, while the OO/C++ software for the experiment is designed and produced.

2.2 Full simulation of ATLAS response

2.2.1 General considerations

The complexity of the physics events to be analysed at the LHC and the diversity of the detectors to be integrated into ATLAS make it an absolute necessity to provide an accurate detector simulation program, with which the detector and physics performance can be evaluated in de-

tail. Such a program must be extremely flexible in all its components, in order to meet the wide variety of requirements, which appear throughout the development phase of the experiment. These requirements are very stringent, especially for the detector geometry modules, which must be very powerful and versatile, in order to describe the very complicated experimental setup foreseen for ATLAS, while at the same time maintaining the possibility of changing or replacing parts of the detector in a simple and reproducible way.

The second problem, which the detector simulation program must solve as efficiently and as realistically as possible, is how to reproduce faithfully the harsh experimental conditions to be encountered during operation at the LHC. As is well understood after almost a decade of simulation work, these conditions are the source of phenomena which have in many ways shaped the detector design (event pile-up, radiation background, detector occupancy and background noise). Given the huge complexity of the detector geometry which the simulation program must deal with, one simply cannot afford to simulate complete bunch crossings (which involve 23 inelastic interactions on average at the LHC design luminosity) for different values of the instantaneous luminosity. One must rather find a way to simulate single events and then to add them up (while respecting the time structure of the event) in a sufficient number to reproduce a beam crossing. The same is true for the noise in the detector, which in many cases depends crucially on the luminosity and which must be injected after the GEANT simulation has been performed. Additional requirements are imposed on the event structure passed to the reconstruction program, which must be stable and general enough to allow for an easy and robust interface between the two programs.

The ATLAS simulation program (normally referred to as DICE, Detector Integration for a Collider Experiment) has been developed continuously since 1990, as a tool to cope with the most important deadlines of the collaboration (the Letter of Intent, the Technical Proposal and the Technical Design Reports), for which ever more detailed results concerning the detector performance expected at the LHC have been reported.

The first version of DICE was optimised for conceptual layout studies with all possible options for the various subdetectors ready to be activated and to be assembled into one of the proposed layouts; in this case, the geometrical description was a relatively simple one, with none of the detectors as accurately represented as they are today, in order to save CPU time and to permit different configurations to be studied in parallel.

In the second version of DICE, the geometrical representation of all subdetectors was improved and specialised to include all of the details envisaged as relevant at a certain time. Nevertheless, where two or more options were available for a subdetector, it was still possible to replace complete parts of that particular subdetector.

The third (and current) version of DICE contains an even more specialised version of the geometry representation, where only small adjustments are possible, to take into account detector layout modifications, and to deal with the increased complexity of the geometry description. Utility libraries for building the geometry in a standardised way have been provided, together with a macro-based language which gives definite advantages in terms of description uniformity and bank manipulation.

2.2.2 Infrastructure

The ATLAS simulation program can be logically divided into three separate modules:

- event generation;
- detector simulation;
- digitisation.

These three parts communicate through a set of ZEBRA banks and can be run separately or in sequence. The framework for the simulation program is provided by a package called SLUG (Simulation for LHC Using GEANT). SLUG provides the basic infrastructure for handling ZE-BRA banks. It also provides a set of facilities for dealing with event generation, detector geometry and simulation, event merging for pile-up studies, together with stubs for user-defined routines to gain access to every step in the simulation process and tools for managing histograms and n-tuples. The program flow is controlled via an extensive set of pre-defined command procedures, which the user can control and execute through FFREAD datacards. Although some interactive functionality was initially provided, the program has normally been run in batch mode for production purposes. An interactive facility (ATLSIM), built essentially around the same basic components, has been provided and used for development work using the simulation and reconstruction software.

The DICE package contains general-purpose routines, which control the simulation flow, together with detector geometry modules, digitisation routines, and dedicated routines to model the detector response better than GEANT wherever needed (see Section 2.2.3).

2.2.3 GEANT model and parameters

As stated above, the GEANT package has been used to simulate in detail the detector characteristics and performance: several versions (3.14, 3.15, 3.21) have been run in production during the evolution of the detector simulation software. Version 3.21 is the one best suited for describing some of the very complex aspects of the detector geometry (*e.g.* the Accordion calorimeter), while still providing a reasonable performance in terms of accuracy of the simulation and of CPU time needed to track particles through the complete detector. In addition to describing the detector geometry and tracking particles through it, the GEANT framework is used to describe the materials constituting the detector, to visualise the detector components, and to simulate and record the response of the sensitive elements of the various systems.

When simulating a very complex detector such as ATLAS, the simulation software has to take into account as large a number of physics processes as possible, covering the broadest possible range of energies. Ideally, the program should be able to simulate physics processes with energies as low as 10 eV (*e.g.* ionisation potential in the active gas of various detectors) and as high as a few TeV (*e.g.* catastrophic energy losses of muons traversing the calorimeters). The most challenging task in terms of consumption of CPU time is an accurate simulation of showers in the calorimeters. The critical areas of the GEANT model for each specific detector system are:

- the tracking detectors require ideally a detailed and microscopic simulation of all processes which could affect the track reconstruction efficiency and the momentum measurement. None of the current implementations of *dE/dx* processes nor even of hadronic processes is adequate for the specific requirements of the Inner Detector. In particular, the transition radiation process is not implemented in GEANT and, to understand the electron identification ability of the TRT, careful calculations of the energy deposited by ioni-

sation and transition radiation in the straws have been developed. The ionisation energy is calculated using the Photon Absorption Ionisation (PAI) model, whilst transition radiation photons are generated with the correct energy spectrum (from test beam results) and tracked through the experimental setup by GEANT. All transport cuts have been set at 100 keV for the Inner Detector, whereas the cut for the production of secondaries (mainly bremsstrahlung and δ-rays) has been set at 1 MeV;

- the dominant electromagnetic processes are adequately simulated by GEANT 3.21 over an energy range from 10 keV to 10 TeV. However, a very accurate simulation of electromagnetic showers in the complex geometry of the Accordion calorimeter is not affordable in terms of CPU time. The accuracy of the GEANT electromagnetic physics has been thoroughly confronted with data from test beams and has been found to be acceptable with a cut of 100 keV for electrons and photons, which represents the best compromise between accuracy and performance;

- as far as hadronic processes are concerned, both GEISHA and FLUKA (the implementation of which in GEANT 3.21 has been declared obsolete by the author) fall short of expectations, since the values for the resolution and the constant term of the Hadronic Calorimeters obtained with the simulation are quite different from the experimental results obtained from test-beam measurements. The final choice for the hadronic model was to use the GEANT interface to the CALOR package (which is in fact FLUKA for energies above a few GeV) because, although still far from an optimal fit to the data, it better reproduces the experimental results. A cut set at 1 MeV for most of the hadronic processes has been used for event production, again as a trade-off for performance.

Wherever possible, if the GEANT physics models have proven not to be adequate to the level of accuracy required for the ATLAS detector simulation program, specialised solutions have had to be adopted, as described above.

2.2.4 Geometry

The description of the ATLAS geometry in GEANT is probably the most critical issue for the detector-simulation program, since it must represent the right compromise between accuracy (which is needed to understand the most subtle systematic effects introduced by the detector layout) and performance. To simplify this procedure, a FORTRAN-based macro-language (AGE, Atlas GEant) has been used to set up detector-description banks, to implement the detector geometry, and to define HITS and DIGI structures associated with it. The advantage of this approach for the user is the possibility of having a generic interface to ZEBRA, while still maintaining a high level of flexibility.

Detector-description parameters are stored into ZEBRA banks (DETP, DETector Parameters), which can be overwritten interactively via datacards (*e.g.* for last-minute modifications), before they are used for the construction of the geometry. These banks are stored in the output file, together with the data, and may thus be used as a reference, in particular by the reconstruction program. A set of facilities (the functionality of which is greatly enhanced by parsing the AGE language into FORTRAN) is then used to build the geometry in the most general and efficient way.

All the ATLAS subdetectors have been described to a very high level of detail in DICE. Inactive material (cryostats, support structures, services, *etc*) has been given a great emphasis, and an accurate description of both its layout and material distribution has been introduced wherever possible. These inactive parts of the detector have often been shown to have a direct impact on the physics performance of the experiment and therefore have to be evaluated very carefully.

The numbers of GEANT volumes used to describe the geometry of the various ATLAS systems are shown in Table 2-1, where they can be compared to the total number of active detector elements or equivalently of independent readout channels (recipients in principle of the GEANT DIGI information, as described in Section 2.2.7), and to the total number of modules or chambers. In many systems, essentially each active cell is described explicitly, using sometimes up to ten volumes or more per cell. In contrast, details like the pixel or microstrip structure of the silicon detectors, or the cell structure of the barrel Accordion calorimeter, have not been described in the geometry itself, but only introduced afterwards at the digitisation level (see Section 2.2.7), in order to increase the flexibility and the performance of the simulation chain. Table 2-1 illustrates the complexity of the GEANT description of the ATLAS detector geometry with its 16×10^6 volumes.

Table 2-1 Number of active detector elements, number of modules or chambers, and number of GEANT volumes defined for the detailed simulation of each of the various ATLAS detector systems.

Detector system	Number of active detector elements	Number of modules or chambers	Number of GEANT volumes defined
Pixels	140 000 000	~2 200	26 000
Silicon microstrips	6 280 000	~4100	50 000
Transition radiation tracker	420 000	~240	2 260 000
LAr accordion calorimeters	170 000	48	9 960 000
LAr hadronic end-cap and forward calorimeters	9 000	134	890 000
Tile Calorimeters	10 000	192	900 000
Muon System	1 230 000	~2 000	1 850 000

The magnetic field map used by the detector simulation program has been created through a combination of specific programs (TOSCA package) to evaluate the field in the Inner Detector and the calorimeters and of analytical calculations for the Muon System. The field map is read in during the initialisation phase and stored in a ZEBRA bank, so that it can be also used by the reconstruction program. For the Inner Detector, the deviations of the solenoidal field from a constant field were considered not to be important enough in terms of performance implications (except for the impact on the momentum resolution itself, which is accounted for in most studies reported in this document) to warrant a significant change in the pattern recognition programs, and a constant field map for this part of the detector was used instead (with the exception of the study reported in Section 3.5.4).

2.2.5 Event generation

The event-generation phase is normally run separately in order to have a consistent input stream which can be used many times. Event generation facilities are implemented within SLUG by using the GENZ package, which provides a common interface between the most widely used event generators (PYTHIA, HERWIG, ISAJET) and GEANT via the standard HEP-EVT common block and ZEBRA banks. A separate event generation facility, ATGEN, has also been developed to provide an analysis framework at the event level, by using the same components for booking and manipulating ZEBRA banks, so that the events produced with it can directly be read in by the standard simulation program. *Ad hoc* single-particle generators and test-beam geometries have also been developed for detector-specific studies.

The GENZ output bank can, at this point, be used to fill the GEANT KINE bank and tracking through the detector can begin. During this step, particle filter algorithms can be applied, in order not to track particles outside the geometrical acceptance of the detector or with an energy below a certain threshold, thus achieving a significant gain in CPU time. More sophisticated filter algorithms (for instance on the electromagnetic component of a jet, to see if it can fake an electron) implement a sort of 0-th level trigger, which kills those events which are not interesting for the physics channel under study.

2.2.6 Detector simulation

The detector-simulation part is the most time-consuming and critical; it can be run with different initial conditions (*e.g.* geometrical setup) on the same set of physics events in order to understand the impact of a change in the detector on the physics performance.

The particle four-vectors (stored in the GEANT KINE banks) are tracked through the various detector systems. At any time during this procedure, a snapshot of the current status can be recorded in the detector. This recording process will occur only for those parts of the detector which have been declared sensitive in the simulation program, and this is implemented first and foremost for the detector elements, where information is actually collected (*dE/dx* deposited in silicon sensors or in the active gas of straw tubes or muon chambers, light produced in scintillator tiles, *etc*). However, there exist inactive parts of the detector, *e.g.* the cryostats, for which it is of substantial interest to record the amount of ('invisible') energy deposited. This has often been used as a cross-check, *e.g.* when evaluating tails in the jet energy reconstruction or in the E_T^{miss} distribution.

The information is stored in the GEANT HITS banks through an automated procedure: different types of hits are pre-defined (calorimeter-type hits, tracker-type hits), where the user can store all the information needed to reproduce the detector response at the digitisation step. Hits are produced at tracking time and stored in their respective branch of the HITS bank, to be eventually stored on tape at the end of each event. This procedure is in most cases automatic, since the program, which takes care of retrieving the appropriate information from the GEANT common blocks, stores it with the right format in the relevant HITS bank.

The information collected in the HITS banks, although dependent on the geometry used by GEANT for event tracking, is nevertheless very general and does not contain any assumption on the detector readout structure. It normally consists of hit positions (for tracking detectors) and energy losses (for calorimeters), and it provides the basis for the simulation of the detector response, which takes place at the digitisation step. HITS banks can be added together in order to simulate event superposition or pile-up (see Section 2.3).

The contents of the HITS banks are the most valuable output of the detector simulation program, since most of the CPU time used goes into producing them. The format of these banks (and the geometry description which has been used to produce them and which defines inherently their structure) must be kept as stable as possible. This is especially true for the case of event superposition or pile-up, in which the simulation of the minimum-bias events is particularly demanding in terms of CPU, and where consistency at the level of the HITS banks and of the geometrical description must be guaranteed. Table 2-2 shows a few examples of the CPU time needed to simulate particles or complete events through the ATLAS geometry. The CPU time needed for any physics event is essentially proportional to the amount of energy entering the calorimeters, where most of the CPU time is spent.

Table 2-2 CPU time needed for simulation of the ATLAS detector with GEANT 3.21. The timings, given in SPECint95 seconds for single tracks and for minimum-bias events, were obtained from the CPU time on a Pentium II processor at 400 MHz and scaled by the estimated SPECint95 rating of 10.3.

Event type	Timing in Inner Detector	Timing in Calorimeters
Single track (electron of 10 GeV energy)	6	100
Single track (pion of 10 GeV energy)	4	60
Minimum-bias event ($|\eta| < 3.0$)	190	2500

2.2.7 Digitisation

The digitisation step is a second level of detector simulation, placed just at the interface with the reconstruction program, where the physical information registered within the HITS bank is collected, re-processed in order to simulate the detector output, and eventually written out (in the GEANT DIGI structure) to be then used by the reconstruction programs. The output from the digitisation is obtained in a form similar to that which might be expected from the readout electronics in the actual experiment.

This step was in fact originally conceived to give the user the possibility of changing the readout characteristics (for instance, the strip pitch in the silicon detectors or the cell granularity in the EM Calorimeter) immediately after the detector simulation step, thus gaining considerably in the amount of CPU time needed during the phase of detector optimisation. Detailed signal treatment (for instance, the most accurate possible treatment of dE/dx in the TRT or digital filtering in the calorimeters), simulation of the front-end electronics behaviour, noise injection, *etc.*, can also be performed at this level.

The digitisation step is very fast, except when pile-up at high luminosity is included. It is often therefore rerun as the first step in the reconstruction chain, if noise levels or single-channel efficiencies in some of the detectors are to be varied.

2.3 Simulation of pile-up and radiation backgrounds

2.3.1 General considerations

The cross-section for inelastic, non-diffractive *pp* interactions at the LHC is ~70 mb. At the design luminosity of 10^{34} cm^{-2}s^{-1} and with a bunch spacing of 25 ns, the mean number of minimum-bias events which should be seen by the detector is 18. However, since approximately 20% of the buckets in the LHC will be empty, the average time between filled buckets is increased and the mean number of collisions is about 23 for these non-empty buckets. This implies that, when an interesting event is selected by the trigger, on average there will be 23 single minimum-bias events superimposed: these events are referred to as pile-up.

The bunch structure in LHC is such that there will be many successive filled buckets followed by successive empty buckets. This means that an interesting event will usually follow and be followed by beam-crossings containing pile-up events. Consequently, there is the potential for collisions from previous and following beam-crossings to be recorded by the detector, and this depends critically on the speed of response of the individual subdetectors.

The simulation of pile-up is normally performed just before and during the digitisation step: HITS banks from two different data streams (signal events and minimum-bias events), which have been simulated separately, are brought together, merged and then digitised. The number of minimum-bias events added to one single signal event is generated, beam-crossing per beam-crossing, based on a Poisson probability with a mean defined by the instantaneous luminosity of interest. Several beam-crossings surrounding the triggered beam-crossing can be generated with SLUG, so that the time structure of one complete event recorded by a particular detector can be faithfully reproduced. For those detectors with a signal collection time spanning over several beam-crossings, one can reproduce the time structure of one event; this feature, although very appealing, is not used in the standard pile-up simulation, since, for most of the simulated detectors, the time-of-flight information is not kept in the HITS banks.

A uniform method for simulating pile-up across all the detector systems has been used in general (the one exception is the Muon System, for which, as discussed in Section 2.3.4, the backgrounds are not correlated in time with the beam-crossing of interest). This method adds to each system, depending on its signal-collection speed, an equivalent average number of in-time beam-crossings, which would correctly simulate to first-order the real pile-up in the detector. For the pixel and SCT detectors, with their fast signal-processing speed, the equivalent number of pile-up events added on average is 24 (a multiple of 8 for technical reasons), for the slower TRT detector, with its 40 ns maximum drift-time, the equivalent number is 32 (which increases the straw hit occupancy by 30%) and finally, for all the calorimeter systems, the equivalent number is 48 (*e.g.* the EM Calorimeter has a 400 ns long drift time).

For most studies reported in the following chapters, this standard method for simulating pile-up has been applied by default. There are two notable exceptions to this:

- studies of fake rates in the TRT (see Section 3.5.3.2), using the full time-of-flight information for several beam-crossings around the trigger one, as described in Section 2.3.2;

- studies of pile-up effects in the calorimeter (see Section 4.3.2), using the exact pulse shape (together with optimal filtering at low luminosity) over five beam-crossings, as described in Section 2.3.3.

Since the effects from pile-up are the main concern for the survival and overall performance of the Inner Detector, it is important to note that:

- most of the hits seen in the Inner Detector arise from secondaries and not from the primary particles. In particular, the occupancies in the silicon sensors and the straws contain a significant contribution of 15 to 20% from primary particles produced at $|\eta| > 3.2$ and interacting with the beam pipe. On the other hand, the occupancies due to low-energy neutrons or photons are small with respect to the overall occupancy (see [2-2] for details).

- backsplash from particle showers initiating at or near the front face of the EM Calorimeter produces only a very small contribution to the occupancies in the Inner Detector. The predictions of GEANT 3.21 have been shown to under-estimate backsplash effects by as much as a factor of two [2-3];

- finally, the chosen threshold of 100 keV for most processes results in an under-estimate of the occupancies by about 10-15% (this has been demonstrated in test-beam measurements).

2.3.2 Pile-up in the TRT

In the Inner Detector, low-p_T tracks ($p_T < 400$ MeV) from beam-crossings prior to the one of interest will spiral in the solenoidal magnetic field for extended periods of time (up to 100 ns) and will therefore produce hits in the detectors over that period of time. In the TRT, the maximum drift time is around 40 ns, which is significantly more than the 25 ns bunch spacing, and the requirement to be as efficient as possible for in-time hits necessitates a gate which accepts some hits from fast particles from out-of-time events as well as hits from loopers.

As described above, the standard simulation of pile-up for the TRT superimposes 32 minimum-bias events, to allow for the extra hits which are expected from out-of-time beam-crossings. In reality, when reconstructed with the assumption that they were in time, these hits would be staggered about the true track positions to the left and right, depending on the drift direction in the straws. Instead, the standard simulation superimposes all the tracks in the TRT from a number of additional minimum bias events. These TRT hits are added in-time, hence they are explicitly correlated (*i.e.* they will really look like tracks in the TRT). It has been checked, using the complete simulation described below, that this creates a more difficult environment for pattern recognition than would be seen in reality (see Section 3.5.3).

To understand these issues in detail, a more complete simulation has been performed for the TRT, which does describe correctly the time-structure of beam-crossings, particle and electrical propagation times, and allows parti-
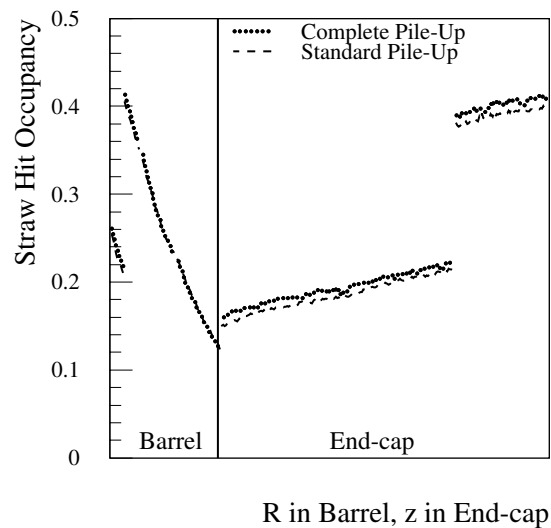

R in Barrel, z in End-cap

Figure 2-1 TRT straw hit occupancy at high luminosity using the complete time-of-flight method (dotted) and the standard method of adding hits from a total of 32 minimum bias events (dashed). The horizontal axis corresponds to layer number: in the barrel, this corresponds to radius; in the end-cap, this corresponds to *z*.

cles to loop in the detector for as long as 250 ns. The results of these detailed simulations are described in [2-2]. It is from such studies that the effective number of events to be superimposed in the TRT for the standard simulation was determined. By design, the number of hits added is intended to ensure that the straw hit occupancy (a measure of the number of hits accepted by the gate associated with the LVL1 trigger and applied to the electronics) is the same as would be seen if the full timing information were used. At high luminosity, a mean of 24 minimum-bias events are expected to be in-time with the signal event. To these, a further eight events are added in the TRT to represent the out-of-time hits.

Figure 2-1 shows the straw hit occupancy using the full time-of-flight information and compares the occupancies with those from the standard method. As intended, the standard method provides a very good description of the occupancy and has the considerable advantage that the simulation code runs an order of magnitude faster.

2.3.3 Pile-up in the calorimeters

As discussed in Section 2.3.1, 23 minimum bias events (around 3500 particles over $|\eta| < 5.0$) are produced on average at each bunch crossing during high-luminosity operation. To cope with this environment, the ATLAS liquid-argon Calorimeters are read out using fast bipolar shapers with a peaking time of ~35 ns.

The standard pile-up simulation [2-4] assumes an average effective number of 48 minimum bias events, computed, for a typical signal shape, so as to obtain the same noise as if all the events were summed with the correct weighting. The advantages of this method are its simplicity and low CPU load, but it does not take into account the bipolar shaping (the pile-up energy distribution is not correct) and it is unable to provide multiple-sampling information.

A complete simulation program [2-5] has been now implemented. It takes into account the exact pulse shape, which depends on three time constants: the drift time, the shaper time constant, and an additional pole given by the gap capacitance and the preamplifier input impedance. Calorimeter data from fully-simulated minimum-bias events are weighted according to the shaper response of each type of cell. At high luminosity, about 700 minimum-bias events are needed to simulate one pile-up event. If required, five consecutive samples are computed in this way and stored separately. In this case, the electronic noise with the correct time correlations may also be superimposed. The digital filtering procedure may also be used. In this way, the electronic shaping is modified (within limits) to reduce the electronic noise when running at low luminosity.

As stated above, this much more accurate method of pile-up simulation will produce the correct spectra of transverse energies per cell from pile-up at high luminosity. In particular, the mean will be centred at zero, which is not the case for the standard simulation. However, as discussed in Section 4.2.4, the rms spreads of the pile-up energies obtained with both methods are very similar, leading to the conclusion that, for most effects, the difference between the two methods is very small.

2.3.4 Backgrounds in the Muon System

The physics performance of the ATLAS Muon System depends strongly on the level of background recorded in the active elements. The main source of this background is from particles produced in the interactions of primary hadrons from proton-proton collisions with the materi-

al of the detector (especially the calorimeters and the toroid structures), and with machine elements such as the collimators and the beam pipe. This background cannot be generated by the standard pile-up method described in Section 2.3.1.

The particles are neutrons, low-energy photons originating from neutron capture, and charged particles. The neutrons mostly have thermal energies, while the photons are concentrated in the 200 keV to 2 MeV energy range. The interaction of these photons with the detector material (aluminium in the case of the precision chambers, bakelite or G10 in the case of the trigger detectors) produces a signal in the sensitive volume of the chamber via the Compton effect with a probability of about 10^{-2}. Neutrons have a much lower probability to produce a direct signal in the muon detectors, but are directly responsible for the photon flux. The charged-particle background consists mainly of muons, charged pions, protons, electrons and positrons. The muons and pions are produced mostly in K^0 decays, while the protons emerge from neutron spallation processes. Hadrons and muons have a typical momentum of 100 MeV.

Detailed studies have been performed and reported in [2-6], using two Monte Carlo packages:

- GCALOR, which designates the CALOR package interfaced to GEANT. This package unfortunately does not contain many of the physics processes necessary to accurately estimate the backgrounds in the Muon System;

- FLUKA [2-7], which is the most developed package in terms of the implemented physics processes of relevance, but which cannot be interfaced readily to the detailed description of the detector geometry.

In practice, the standard ATLAS detector simulation package, based on GEANT, cannot simulate adequately the backgrounds from low-energy neutrons, photons and charged particles expected in the Muon System, because none of the GEANT-based packages provides adequate particle propagation at such low energies. Hence, other specialised programs, such as FLUKA, are used to simulate these backgrounds.

The muon-detector counting rate, as predicted by FLUKA, depends strongly on the muon station position and pseudorapidity. Typically, in the barrel chambers at high luminosity, the nominal rate in the first station is ~10 Hz/cm^2, and increases to 100 Hz/cm^2 around $|\eta| = 0.7$ (where the Tile Calorimeter gaps are located). For the end-cap chambers, the counting rate in the inner stations increases up to ~1 kHz/cm^2. The counting rate in all the other stations is significantly lower, with values in the range between 10 and 30 Hz/cm^2, and depends weakly on pseudorapidity. The dominant contribution to this rate comes from the photon flux, whereas charged particles contribute a rate of only a few Hz/cm^2.

The background studies are performed by conservatively multiplying the nominal Monte Carlo counting rates by a factor of ten, to evaluate the maximum expected counting rates in the Muon System. This large factor is justified by:

- the simplified implementation in FLUKA of the detector and shielding geometry (cracks which will inevitably appear in the real detector have not been taken into account);

- the difference between the effective nuclear composition of the materials which will be used in the experiment and that of the materials considered at present in the simulation;

- the uncertainties on the properties of the minimum-bias events (cross-section, particle composition, particle spectra, *etc.*);

- the uncertainties on particle transport and on the estimates of the sensitivity of the detectors to low-energy photons and neutrons.

The most important consequences of this background are:

1. high occupancy of the muon detectors, especially in the inner stations at large $|\eta|$;

2. space-charge effects;

3. reduced lifetime of the muon detectors;

4. high fake LVL1 muon trigger rate.

The first three effects are determined mainly by the intensity of the photon flux, and therefore indirectly by the intensity of the neutron flux. Muon track reconstruction studies [2-6] have shown that the physics performance of the Muon System begins to be degraded if the background level becomes larger than ten times the one presently estimated. Hence, it is very important to keep under constant control all changes proposed for the shielding system and the detector (*e.g.* the Tile Calorimeter gaps).

In contrast to the above, the most critical background for the LVL1 muon trigger rate is that from charged particles with a momentum around 100 MeV. With the design described in [2-8], the LVL1 muon trigger can only tolerate the nominal background rates, leaving almost no contingency for the uncertainties in the Monte Carlo predictions. Nevertheless, as discussed already to a certain extent in [2-8], improvements have been made to the trigger design to make it more robust against this type of background. The revised design and expected performance are documented in [2-9] (see also Section 11.3.1.6).

In order to allow physics simulation studies accounting for the background in the Muon System, a program that parametrises the particle rates and kinematics, as predicted by FLUKA in the region of the muon detectors, has been implemented. This program operates in the detector-simulation framework to digitise the hits collected in the muon detector in the same way as for physics events. At present, for the charged-particle backgrounds, only muons and pions have been simulated (within a simple model tuned to the FLUKA results). Concerning the simulation of the hits induced by photons (the neutron hit rate is negligible and therefore this source has been ignored), the only practical solution was to 'inject' directly, into the sensitive regions of the Muon System, Compton electrons with an energy close to the one predicted on average by FLUKA.

2.4 Reconstruction

The reconstruction of particles and other physics objects in the ATLAS detector has been developed over many years, and is implemented in a single program named ATRECON, based on the SLUG framework (see Section 2.2.2). ATRECON is mostly written in Fortran77, using ZEBRA as memory manager, although some parts have already been rewritten in C++, but not with a fully object-oriented design. This software will be replaced over the coming years by new OO software [2-10], which will use the existing software and its performance as a reference benchmark and will build from the algorithms and experience gained in developing ATRECON. ATRECON runs on fully simulated GEANT 3.21 data and does not handle raw data nor calibration/alignment constants. However, it is today rather complete, and can reconstruct full events with all detectors included, without using generator-level Monte Carlo information, in an acceptable amount of CPU time (see below).

The reconstruction proceeds in two stages (in addition to initialisation). First, data from each detector is reconstructed in a stand-alone mode. Second, the information from all detectors is combined to get the most accurate measurements and identification of the final objects used in the analysis: photons, electrons, muons, τ-leptons, K_S^0, jets, b-jets, E_T^{miss}, primary vertex, *etc*. This is described in great detail throughout this volume, and only a very brief summary is given below. The output of the various algorithms is stored in standardised ZEBRA banks, but control n-tuples and histograms are also available. The output is also stored in a menu-driven combined n-tuple, which allows rapid checks, analysis in a PAW framework and comparisons between algorithms. A third stage which is not described here, but rather in Chapters 14 to 21, is the analysis-specific part: reconstruction of exclusive B decays, W's, Z's, top quark decays, Higgs bosons, SUSY particles, *etc*. Figures 2-i and 2-ii show two views of a high-p_T reconstructed $H \rightarrow ZZ^* \rightarrow ee\mu\mu$ decay, with reconstructed tracks in the Inner Detector and the Muon System and with the reconstructed energy clusters of the two electrons and the high-p_T jet in the calorimeters.

2.4.1 Initialisation

At the start of reconstruction, the ATLAS geometry is rebuilt either from the event geometry as stored in ZEBRA banks from the simulation program, or from the ATLAS geometry database (AMDB). GEANT or AMDB routines are used during reconstruction to obtain the global coordinates of hits and cells. The magnetic field map is loaded. By default, the field is constant in the Inner Detector and as realistic as possible elsewhere, but some studies have been done with a realistic solenoidal magnetic field in the Inner Detector (see Section 3.5.4). Loading of calibration and alignment constants has not been implemented, except in an *ad hoc* way for some specific studies. The program is driven by datacards which allow a large spectrum of running conditions: switching on/off packages, changing noise levels, thresholds, efficiencies or internal algorithm parameters.

2.4.2 Stand-alone reconstruction

Matrices containing the energies in all calorimeter cells are filled. Jets are built following various algorithms with the cone algorithm used as a default (see Section 9.1). The E_T^{miss} vector is computed from the vector sum of the cell transverse energies (see Section 9.2).

Electromagnetic clusters are reconstructed in the barrel and end-cap EM Calorimeters (see Section 4.2.3). Modulations in the measurement of the positions and the energies, due to the finite cell/cluster sizes or to the detector geometry, are corrected for by using the known correlations between shower position and biases in position and energy. Standalone electron/gamma identification is performed using shower-shape variables.

Muon track segments in the Muon System are found from a combinatorial search of the single-station track segments, followed by a fit using the hits (see Section 6.3.1). The tracking, performed in the highly non-homogeneous magnetic field, takes into account multiple scattering in the material of the apparatus. The output is a list of tracks with parameters extrapolated back to the interaction region, and also a list of track segments in the inner stations, possibly corresponding to low-p_T muons, which cannot be reconstructed with high efficiency in a standalone mode.

Hit coordinates are reconstructed in the precision tracker and in the TRT. Tracks from charged particles are searched for (see Section 3.1.2). Three rather different algorithms with comparable performances have been developed:

- iPatRec starts from a combinatorial search in the precision tracker;

- PixlRec uses a track-following algorithm starting from the pixel *B*-layer outwards;

- xKalman finds tracks in the TRT with a histograming method and follows them inwards using Kalman-filtering techniques.

Track reconstruction can be performed over the full Inner Detector (except for iPatRec), or over a limited $\Delta\eta\times\Delta\phi$ range around 'seeds' found by the other detectors (electromagnetic clusters, jets, muons) and around Monte-Carlo truth information for checks. Seeds cannot be used for events like inclusive *b* production ($b\overline{b} \rightarrow \mu_6 X$, *i.e.* events containing a muon with $p_T > 6$ GeV), where all tracks need to be reconstructed. The use of seeds in the reconstruction algorithm can save a factor of up to 100 in CPU time for events including the pile-up expected at high luminosity.

Trigger algorithms have so far been developed in an independent package (see Chapter 11), but it is possible to run LVL1 and LVL2 trigger algorithms prior to reconstruction.

2.4.3 Combined reconstruction

In a second stage, information from several detectors is combined. Muons reconstructed in the Muon System are refined by matching the track to an Inner Detector track (see Section 8.1). This improves the momentum resolution, especially at moderate p_T, and yields accurate track parameters at the vertex. Lower-p_T (down to 2 GeV) muons are found by matching an Inner Detector track to the Tile Calorimeter cells (see Sections 8.2 and 10.4.2).

Photon conversions (see Section 7.5.1) and K_S^0 decays (see Section 3.6.2.1) are searched for by pairing Inner Detector tracks. The primary vertex is reconstructed using all the tracks in the event (see Section 3.6.1).

High-p_T (above 10 GeV) photon identification requires electromagnetic cluster shower-shape variables and the absence of reconstructed tracks in the Inner Detector, except for identified conversions (see Sections 7.5 and 7.7). High-p_T electron identification requires a track reconstructed in the Inner Detector with transition-radiation hits and a measured momentum matching a calorimeter energy deposition compatible with an electromagnetic shower (see Section 7.4). Softer non-isolated electrons (down to p_T of 1 GeV) are identified by extrapolating Inner Detector tracks to the EM Calorimeter (see Section 7.3.1).

Finally, τ-leptons are identified from narrow jets associated with a small number of charged tracks (see Section 9.1.5). Candidate *b*-jets are tagged by combining the impact parameter of high-quality tracks with soft electrons or muons (see Chapter 10).

2.4.4 Timing

The complete reconstruction is seldom needed for any particular analysis. The various items are split into different packages that can be activated or not to save CPU time. Even though reconstruction speed has always been a concern, the algorithms have been tuned to obtain the best

possible performance (efficiency and resolution) rather than the fastest execution time. Significant improvements are still possible for all packages. Table 2-3 shows, as an illustration, the present average CPU time needed to reconstruct different types of events. There is a significant degradation in speed of all algorithms at high luminosity, although some of it can be recovered in the Inner Detector by using seeds. Even low-luminosity pile-up increases significantly the time needed for track reconstruction. In practice, the CPU time needed depends significantly on parameters like the size of the $\Delta\eta\times\Delta\phi$ window (here 0.1×0.1 for single tracks, 0.5×0.5 for jets), the minimum p_T to be reconstructed (1 GeV in the example shown below), the cell energy thresholds and internal parameters. The timing for muon reconstruction scales with the number of muons and is relatively independent of luminosity. It does however depend on the muon p_T with an optimum around 50 GeV and a degradation of more than a factor of two at low p_T (low-momentum tracking in the highly inhomogeneous field) and at high p_T (handling of electromagnetic showers).

Table 2-3 Timing obtained for the most important reconstruction packages for some typical events in SPECint95 seconds. No minimum-bias events were added for the generic studies, 2.3 were added for low-luminosity operation and 23 for high-luminosity operation. The timings are quoted for PA8000 processors at 180 MHz, scaled by the estimated SPECint95 rating of 7.

Event	Muon	Calorimeter	xKalman (complete events)	xKalman (seed)	iPatRec (seed)
$b\overline{b}\to\mu_6X$	238	9	26	-	-
$b\overline{b}\to\mu_6X$ at low luminosity	238	9	99	-	-
$WH\to\mu\nu b\overline{b}$ with $m_H=100$ GeV	154	12	39	26	9
$WH\to\mu\nu b\overline{b}$ with $m_H=100$ GeV at high luminosity	170	93	2660	366	40
$H\to ZZ^*\to ee\mu\mu$ with $m_H=130$ GeV	242	10	24	7	4

2.5 Fast simulation and reconstruction

Fast particle-level simulation and reconstruction is an intermediate step between simple parton-level analysis of the event topology, which in general yields much too optimistic results for physics processes at hadron colliders, and very sophisticated and CPU-consuming full detector simulation (see Section 2.2) and reconstruction (see Section 2.4). This kind of approach is needed for quick and approximate estimates of signal and background rates for specific channels. In addition, fast simulation and reconstruction is the only practical tool for high-statistics studies of complex background processes.

A complete package for fast detector simulation and physics analysis has been implemented over the past few years and exists in two implementations:

- ATLFAST, the FORTRAN implementation of the algorithm [2-11], interfaced to PAW;

- ATLFAST++, the OO/C++ implementation of the same algorithm [2-12], interfaced to ROOT [2-13].

Both versions have been used for the results presented in this document.

ATLFAST can be used for fast simulation of signal and background processes, including the most crucial detector aspects: jet reconstruction in the calorimeters, momentum/energy smearing for leptons and photons, magnetic field effects and missing transverse energy. It provides, starting from the list of particles in the event, a list of reconstructed jets, isolated leptons and photons, the expected missing transverse energy, and reconstructed charged tracks. Values for the rejections against non-b jets and non-τ jets are also provided as a function of the efficiencies for identifying b-jets and τ-jets. In most cases, the detector-dependent parameters are tuned to what is expected for the performance of the ATLAS detector from full simulation and reconstruction (see below).

The ATLFAST package aims to reproduce as well as possible the expected detector performance in terms of resolution and particle-identification for important physics signals. It does not attempt, at present, to reproduce accurately the expected efficiencies for lepton and photon isolation. In the case of hadronic jets, the jet reconstruction (and veto) efficiency is often dominated by physics effects, which are straightforward to model in the fast simulation. For any specific channel, the predictions from ATLFAST in terms of resolution and reconstruction efficiency, should always be confirmed with full-simulation results. Such detailed comparisons have been done in many cases, *e.g.* for the *WH, H* $\to b\bar{b}$ [2-14], *H/A* $\to \tau\tau$ [2-14] and *H* $\to WW \to l\nu jj$ [2-15] channels, as well as for several Higgs-boson decay channels with multi-b-jet final states [2-16]. The acceptances, jet reconstruction efficiencies, jet-veto efficiencies, and mass resolutions have shown good agreement between fast and full simulations.

Not all the detector effects can be readily parametrised in fast simulation and only the basic information of the detector geometry is used in the package. This basic information is for example: the η-coverage for precision physics and for the calorimetry, the size of the barrel/end-cap transition region for the EM Calorimeter, and the granularity of the hadronic calorimeters. No effects related to the detailed shapes of particle showers in the calorimeters, the charged track multiplicity in jets, *etc.,* are taken into account. In particular, energy isolation of leptons is only simulated in a crude way.

For practical reasons, the package has been divided into two parts: the main ATLFAST package, executed on the generated events, and a supplementary package, ATLFAST-B, which can be executed on the filtered n-tuples during user analysis. In the following, the main features of ATLFAST and their relationship to the full simulation and reconstruction results are described.

2.5.1 Calorimeter clusters

The transverse energies of all undecayed particles, except for neutrinos, muons and the SUSY *LSP*, are summed up in calorimeter cells of granularity 0.1x0.1 over $|\eta| < 3.2$, and 0.2x0.2 (for $|\eta| > 3.2$) in $\eta \times \phi$ coordinates over the full calorimeter coverage. The effect of the solenoidal 2 T magnetic field on the ϕ-position of charged particles with p_T above 0.5 GeV threshold is parametrised. It has been checked that the contribution from charged particles with p_T below this threshold can be neglected. A fixed-cone algorithm is used for the cluster reconstruction (see Table 2-4 for the expected efficiencies of cluster reconstruction); other reconstruction algorithms can be also activated as options.

Table 2-4 Efficiency for cluster reconstruction at low luminosity, for different types of initial partons with $p_T^{parton} > 15$ GeV and $p_T^{jet} > 15$ GeV.

Type of initial parton	Reconstruction efficiency in $\Delta R < 0.4$
u-quark	83%
b-quark	76%
gluon	74%

2.5.2 Isolated electrons and photons

Photon and electron candidates, isolated from any hadronic activity, are searched for in the particle list. The polar angle of the photon and the photon and electron four momenta are smeared with a parametrisation directly derived from the full simulation. Isolation criteria in terms of distance from other clusters and of maximum transverse energy deposition in a cone around the photon/electron candidate, as well as the geometrical acceptance, are verified. As a benchmark, the resolutions expected for $H \rightarrow \gamma\gamma$ and $H \rightarrow ZZ^* \rightarrow 4e$ reconstruction show reasonable agreement between the parametrisation used for the fast simulation and the expected performance from full simulation, as shown in Table 2-5.

Table 2-5 Expected mass resolutions for a few benchmark processes, as obtained from fast and full simulation.

Process	ATLFAST	ATLAS
$H \rightarrow \gamma\gamma$, $m_H = 100$ GeV	$\sigma_m = 1.2$ GeV (high L)	$\sigma_m = 1.3$ GeV (high L)
$H \rightarrow ZZ^* \rightarrow 4e$ $m_H = 130$ GeV	$\sigma_m = 1.6$ GeV (high L)	$\sigma_m = 1.8$ GeV (high L)
$H \rightarrow ZZ^* \rightarrow 4\mu$ $m_H = 130$ GeV	$\sigma_m = 1.3$ GeV (combined ID+ Muon System)	$\sigma_m = 1.4$ GeV (combined ID+ Muon System)

2.5.3 Isolated muons

Isolated muon candidates are searched for in the particle list. Each muon momentum is smeared according to a resolution parametrised as a function of muon p_T, $|\eta|$ and ϕ. Three options depending on which subdetectors are assumed to be used for the muon measurement can be invoked: Muon System stand-alone, Inner Detector stand-alone (parametrisation from [2-17]) and combined Inner Detector plus Muon System. Isolation criteria in terms of distance from other clusters and of maximum transverse energy deposition in a cone around the muon candidate, as well as the fiducial geometrical acceptance, are applied. As a benchmark, the mass resolution expected for the $H \rightarrow ZZ^* \rightarrow 4\mu$ reconstruction shows reasonable agreement between the parametrisation used for the fast simulation and the expected performance from full simulation (see Table 2-5).

ATLFAST does not correct for efficiencies in the reconstruction/identification of muons, electrons nor photons, so the estimated efficiencies (from the full simulation study) should be included by the user in the event analysis. However, the package simulates muon trigger efficiencies if required to, and isolated and non-isolated muons are flagged with an appropriate flag.

2.5.4 Jets and pile-up

Clustered cells are used for the jet reconstruction. As a default, a cone size of 0.4 is used. The energies of clusters, which have not been selected as associated with isolated electrons or photons, are smeared with the energy resolution, parametrised according to results from full simulation of the hadron calorimeters [2-4]. Two options can be invoked: low luminosity and high luminosity. In the latter case, the expected effects from pile-up are included in

Table 2-6 Reconstructed mass peak position and rms width for generated *WH* events with $m_H = 100$ GeV.

Final state	$<m_{jj}>$ (GeV)	σ_m (Gev)	Acceptance in $m_H \pm 20$ GeV
$H \rightarrow b\bar{b}$	103.0	12.5	90%
$H \rightarrow u\bar{u}$	100.7	8.2	86%
$H \rightarrow gg$	101.3	11	79%

the parametrisation of the resolution. The measured momenta from non-isolated muons which fall inside the cluster cone and are within $|\eta| < 2.5$ is added to the smeared cluster energy. Reconstruction with the JetFinder library [2-18] of alternative jet algorithms is also implemented.

2.5.5 Jet energy recalibration

The effect of the energy loss outside the cone is corrected using a p_T^{jet}-dependent calibration factor, calculated as an average p_T^{parton}/p_T^{jet}. The set of calibration factors, separately for *b*-jets and light-quark jets, is provided in the supplementary package ATLFAST-B. Table 2-6 shows the expected mass resolution, acceptance and peak position for the *WH* process. This calibration is process independent, however it might be optimised depending on the average p_T of the initiating partons.

Table 2-7 Mass resolution and acceptance for reconstructed *WH* decays with $H \rightarrow b\bar{b}$, using standard recalibration and clustering algorithm.

$m_H = 400$ GeV	σ_m (GeV)	Acceptance in $m_H \pm 2\sigma_m$
Standard recalibration	52	82%
Clustered jets	45	77%

In some cases, for the reconstruction of high-mass resonances, a better procedure is to collect into a cluster the jets reconstructed inside a larger cone, *e.g.* $\Delta R = 0.8$, and applying recalibration to clustered jets only. Table 2-7 compares the resolutions and acceptances obtained for $H \rightarrow b\bar{b}$ reconstruction with $m_H = 400$ GeV (the intrinsic Higgs width was set to zero for this comparison).

2.5.6 *b*-tagging

Of special interest are jets originating from *b*-quarks (so-called *b*-jets) which can be identified using *b*-tagging techniques (vertex or soft-lepton tags). The package labels a jet as a *b*-jet, if a *b*-quark of $p_T > 5$ GeV (after final-state radiation) is found in a cone of $\Delta R = 0.2$ around the reconstructed jet for jets with $|\eta| < 2.5$. These criteria have been discussed in more detail in [2-2]. Jets originating from *c*-quarks are labelled as *c*-jets if similar criteria are satisfied.

Table 2-8 Assumed nominal performance for *b*-tagging of *b*-labelled jets at low and high luminosity

Efficiency	Low luminosity	High luminosity
ε_b	60%	50%
ε_c	10%	10%
ε_j	1%	1%

ATLFAST does not include efficiencies for *b*-jet tagging or non-*b* jet rejection. In the supplementary package ATLFAST-B, for *b*-labelled jets, efficiencies for tagging and inefficiencies for mistagging *c*-jets and other jets have been parametrised as p_T-dependent functions. These parametrisations can be applied randomly by the user during event analysis (Table 2-8 shows the nominal parametrisation averaged over p_T). Detailed comparisons between these parametrisations and results from *b*-tagging algorithms for the fully simulated events, as presented in Chapter 10, can also be found in [2-11].

2.5.7 τ-tagging and τ-veto

Jets originating from τ-decay (so-called τ-jets), can be identified in the case of hadronic τ–decays. A systematic study of the ATLAS potential for τ identification has been documented in [2-19] (see also Section 9.1.5). In the case of fast simulation, τ-jet candidates are τ-labelled if the hadronic τ-decay product(s) is relatively hard (default: $p_T^{\tau\text{-}had} > 10$ GeV), inside tracking range ($|\eta| < 2.5$), dominates reconstructed jet (default: $p_T^{\tau\text{-}had}/p_T^{jet} > 0.9$) and within jet cone (default: $\Delta R_{jet,\,\tau\text{-}had} < 0.3$). These criteria are consistent with the identification procedure of fully simulated events. The efficiency for τ-labelling is 92% for τ-hadronic decays from $A \rightarrow \tau\tau$ and for $m_A = 300$ GeV.

A τ-veto can be useful for the rejection of backgrounds containing τ-leptons. A more detailed study of the τ-veto was done using $A \rightarrow \tau\tau$ events and a large sample of jet events, as presented in [2-19], using cut-offs on the electromagnetic radius and on the number of associated tracks with $p_T^{track} > 1$ GeV. As an example, for $p_T^{cluster} > 60$ GeV, $\varepsilon^{veto,jet} = 90\%$ with $\varepsilon^{veto,\tau} = 5\%$ can be achieved.

ATLFAST does not correct for efficiencies for τ-jet identification or other jet misidentification. For τ-labelled jets, the efficiencies for τ tagging and mistagging have been parametrised [2-19] and are available in supplementary package ATLFAST-B.

2.5.8 Track reconstruction

The track reconstruction is provided for charged, stable particles inside the Inner Detector coverage. Reconstructed track parameters (d_0, b, ϕ, $\cot(\theta)$, q/p_T) are smeared with parametrisation from [2-17] as derived from the studies for the Inner Detector TDR [2-2]. Parametrisation for

muons, pions (including tails) and electrons (including bremsstrahlung) as well as the respective reconstruction efficiencies, are available. This implementation is dedicated mainly to the *B*-physics studies.

2.5.9 Missing transverse energy

The missing transverse energy, E_T^{miss}, is calculated by summing-up the transverse momenta of identified isolated photons, electrons and muons, jets, *b*-jets and *c*-jets, and of non-isolated muons not added to any jet cluster. Finally, the transverse energies deposited in cells not used for cluster reconstruction are also included in the total sum. Transverse energies deposited in unused cells are smeared with the same energy resolution function as for jets. In case of high luminosity, pile-up is included in the smearing parametrisation for energy deposited in unused cells. From the calculation of this total sum E_T^{obs} the missing transverse energy is obtained, $E_T^{miss} = E_T^{obs}$, as well as its components, $p_x^{miss} = -p_x^{obs}$, $p_y^{miss} = -p_y^{obs}$. The E_T^{miss} resolution given by ATLFAST for di-jet events with $p_T > 17$ GeV at low luminosity, $\sigma_{miss} = 5.7$ GeV, is consistent with what is expected from the full simulation of the ATLAS detector (see Section 9.1.5). Since ATLFAST is not adding pile-up to cells which remain empty after particle energy deposition, the high-luminosity result of $\sigma_{miss} = 11.3$ GeV represents an optimistic estimate.

2.5.10 Trigger selections

A primitive trigger routine to validate selected physics events can be invoked after each event has been analysed by the algorithm. This routine is not meant to cover the complete trigger menus, but rather to eliminate events which have essentially no chance of passing the LVL1 and LVL2 trigger as specified in the trigger menus today [2-20] (see also Section 11.7.3). It is more specifically dedicated to SUSY-particle searches, which will include many complex topologies of the type: n-jets + m-leptons + E_T^{miss}.

The proposed trigger selection is aimed at being compatible with the present LVL1/LVL2 understanding; slightly lower thresholds than in [2-20] are used for some cases where it might turn out to be justified from the physics and where it is not clearly impossible to implement. Three classes of trigger particles are used for low- and high-luminosity performance: isolated electrons and photons, muons and jets. For muons, a parametrised trigger efficiency, as studied in [2-6], is included. For electrons/photons and jets a trigger efficiency of 100% is assumed.

2.5.11 Mass reconstruction in multi-*b*-jet channels

To illustrate the consistency between fast and full simulation and reconstruction (see also Section 9.3) the mass reconstruction of the *WH* with $H \rightarrow b\bar{b}$ process with $m_H = 100$ GeV is presented in Figure 2-2. Jets with $p_T > 15$ GeV before energy recalibration are accepted and the efficiency for reconstruction is about 80% per *b*-jet from fast and full simulation. The mass peak can be reconstructed with an expected resolution of ~15 GeV with full simulation (resp. 12.5 GeV with fast simulation) and a correct position of the peak in the distribution (after jet energy recalibration), nevertheless with a some fraction of the signal appearing as non-Gaussian tails. Most of these effects can be attributed to the final-state radiation and hadronisation, as discussed in detail in [2-11]. More details on the comparison between full and fast simulation and reconstruc-

tion for multi-*b*-jet final states of Higgs-boson decays can be found in [2-16]. Some benchmark numbers, illustrating the good agreement between fast and full simulation, are collected in Table 2-9.

Table 2-9 Acceptances and resolutions for full and fast simulation of several Higgs-boson signatures in multi-*b*-jet channels for low-luminosity operation (the *b*-tagging efficiency is not included). When two resonances are present, the second one is reconstructed after applying a mass constraint on the first one.

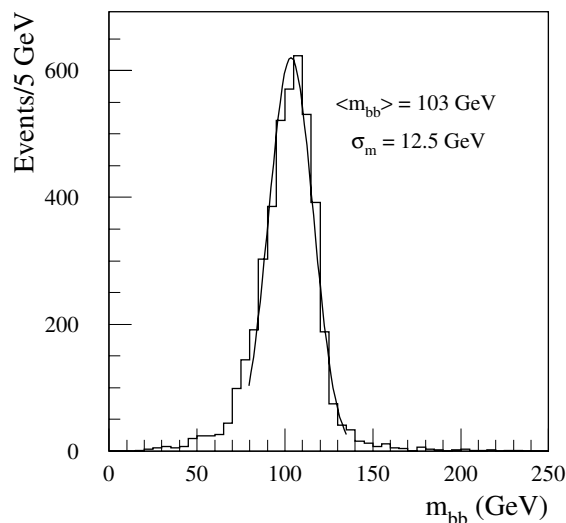| Reconstructed events	*b*-jets	Resonance 1 σ_m (GeV)	Resonance 1 Acceptance in $\pm 2\sigma_m$	Resonance 2 σ_m (GeV)	Resonance 2 Acceptance in $\pm 2\sigma_m$
WH with $H \to b\bar{b}$ (see Section 19.2.4.2) ($m_H = 100$ GeV and $p_T^{\text{jet}} > 15$ GeV)	2 *b*-jets	$H \to b\bar{b}$	$H \to b\bar{b}$		
Full simulation	65%	14.7	89%		
Fast simulation	65%	12.5	90%		
WH with $H \to b\bar{b}$ (see Section 19.2.4.2) ($m_H = 400$ GeV and $p_T^{\text{jet}} > 75$ GeV)	2 *b*-jets	$H \to b\bar{b}$	$H \to b\bar{b}$		
Full simulation	72%	45	84%		
Fast simulation	71%	40	73%		
$A \to Zh \to llb\bar{b}$ (see Section 19.3.2.10) (with $m_A = 300$ GeV)	2 *b*-jets	$h \to b\bar{b}$	$h \to b\bar{b}$	$A \to Zh$	$A \to Zh$
Full simulation	61%	11.2	80%	8.6	71%
Fast simulation	64%	10.1	82%	7.8	75%
$H \to hh \to b\bar{b}b\bar{b}$; ($m_H = 300$ GeV and $p_T^{\text{jet}} > 15$ GeV)	4 *b*-jets	$h \to b\bar{b}$	$h \to b\bar{b}$	$H \to hh$	$H \to hh$
Full simulation	40%	9.2	89%	13.1	82%
Fast simulation	45%	8.7	87%	12.8	83%
$t\bar{t}H$ with $H \to b\bar{b}$ (see Section 19.2.4.3) ($m_H = 100$ GeV)	4 *b*-jets	$t \to jjb$	$t \to jjb$	$H \to b\bar{b}$	$H \to b\bar{b}$
Full simulation	25%	11.7	75%	20.0	66%
Fast simulation	32%	10.0	80%	19.0	65%
$t\bar{t}$ with single top reconstruction ($p_T^{\text{jet}} > 40$ GeV)	2 *b*-jets	$W \to jj$	$W \to jj$	$t \to jjb$	$t \to jjb$
Full simulation	37%	8.1	87%	13.4	83%
Fast simulation	43%	7.3	82%	11.4	78%

Figure 2-2 Distribution of reconstructed invariant mass, $m_{b\bar{b}}$, as obtained using fast simulation of *WH* production with $m_H = 100$ GeV and $H \rightarrow b\bar{b}$ decay at low-luminosity operation.
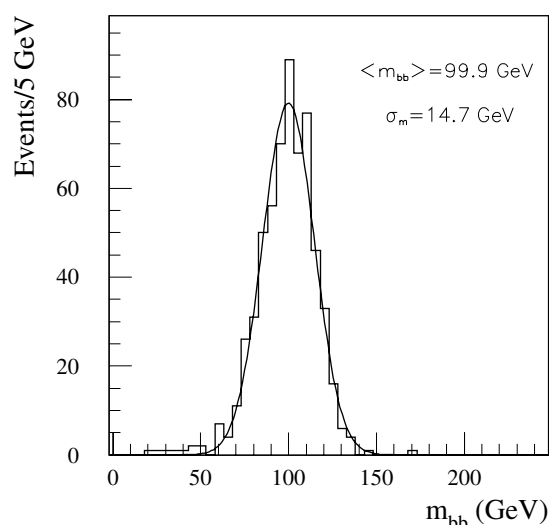
Figure 2-3 Same as Figure 2-2, but using full simulation of the ATLAS detector (see Section 9.3.2).

2.6 References

2-1   R. Brun *et al.*, GEANT3, CERN/DD/EE/84-1 (1996).

2-2   ATLAS Collaboration, Inner Detector Technical Design Report Vol. I, ATLAS TDR 4, CERN/LHCC 97-16 (1997).

2-3   W. Funk, 'Study of backsplash effects in the TRD tracker', ATLAS Internal Note ATL-INDET-93-032 (1993).

2-4   ATLAS Collaboration, Calorimeter Performance Technical Design Report, ATLAS TDR 1 CERN/LHCC 96-40 (1996).

2-5   S. Simion, 'Pile-up simulation for ATLAS Calorimeters', ATLAS Internal Note ATL-SOFT-99-001 (1999).

2-6   ATLAS Collaboration, Muon Spectrometer Technical Design Report, ATLAS TDR 10, CERN/LHCC/97-22 (1997).

2-7   A. Ferrari *et al.*, Z. Phys. **C70** (1996) 413; and FLUKA manual http://www.cern.ch/alice/Projects/offline/Simulation/fluka.

2-8   ATLAS Collaboration, First-Level Trigger Technical Design Report, ATLAS TDR 12, CERN/LHCC/98-14 (1998).

2-9   Level-1 muon trigger group, 'Improvements to the level-1 muon trigger giving increased robustness against backgrounds', ATLAS Communication ATL-COM-DAQ-99-011 (1999).

2-10   ATLAS Collaboration Computing Technical Proposal, CERN/LHCC/96-43 (1996).

2-11   E. Richter-Was, D. Froidevaux and L. Poggioli, 'ATLFAST 1.0 A package for particle-level analysis', ATLAS Internal Notes ATL-PHYS-96-079 (1996) and ATL-PHYS-98-131 (1998).

2-12   R. Brun and E. Richter-Was, 'Getting started with ATLFAST++',
        http://atlasinfo.cern.ch/Atlas/GROUPS/PHYSICS/HIGGS/ATLFAST-
        www/OOimplementation.html.

2-13   R. Brun et al., http://root.cern.ch.

2-14   D. Cavalli and S. Resconi, 'Comparison between full and fast simulation of ATLAS
        detector', ATLAS Internal Note ATL-PHYS-97-100 (1997).

2-15   P. Savard and G. Azuelos, 'The discovery potential of a Heavy Higgs (m_H = 800 GeV)
        using full GEANT simulation of ATLAS', ATLAS Communication
        ATL-COM-PHYS-98-007 (1998).

2-16   D. Cavalli and M. Sapinski, 'Full and fast simulation and reconstruction of Higgs decay
        channels with multi-b-jet final states', ATLAS Communication ATL-COM-PHYS-99-033
        (1999).

2-17   E. J. Buis *et al.*, 'Parametrisation of the Inner Detector Performance', ATLAS Internal Note
        ATL-INDET-97-195 (1997); 'Update of Inner Detector Performance Parametrisation',
        ATLAS Internal Note ATL-INDET-98-215 (1998).

2-18   M. Bosman *et al.*, 'Jet Finder Library: version 1.0', ATLAS Internal Note ATL-SOFT-98-038
        (1998).

2-19   D. Cavalli and S. Resconi, 'Tau-jet separation in ATLAS detector', ATLAS Internal Note
        ATL-PHYS-98-118 (1998).

2-20   ATLAS Collaboration, Trigger Performance Status Report, CERN/LHCC/98-15 (1998).

3 Inner Detector

3.1 Introduction

The ATLAS Inner Detector (ID) and its performance were described extensively in the ID TDR [3-1][3-2]. In this chapter, a summary of the results which are of most interest to physics analyses is given. In addition, updates arising from changes in the layout and further study are included. Despite various layout changes, the resolutions of the subdetectors and the number of hits on tracks have changed very little, hence the overall performance expected of the ID is very similar to that presented in the ID TDR.

The current baseline layout of the ID is described in Chapter 1. The ID consists of three subdetectors covering the range $|\eta| \leq 2.5$. The inner subdetector consists of three layers of pixel detectors, with a layer at a radius of 4 cm, called the *B*-layer, which is vital for good vertexing. Each pixel is 50 μm wide in $R\phi$ and 300 μm long. The SemiConductor Tracker (SCT) consists of four double layers of silicon strips. Each double layer consists of strips aligned in the azimuthal direction and strips rotated by a 40 mrad stereo angle with respect to the first set. The strips have an 80 μm pitch and are 12 cm long. The Pixel and SCT subdetectors are jointly referred to as the Precision Tracker. The outer subdetector, the Transition Radiation Tracker (TRT), consists of ~36 layers of 4 mm diameter straw tubes with resolutions ~200 μm, interspersed with a radiator to stimulate transition radiation (TR) from electrons. There are two thresholds for recording hits, the high threshold being used to detect TR photons.

In Chapter 1, the 98_2 layout, as described by the GEANT simulation and which was used extensively for the studies of this report, is shown. The differences between this layout and the current baseline layout are explained in a subsequent section.

Figure 3-i shows an example of the decay $B_d^0 \rightarrow J/\psi \; K_s^0$ in the Inner Detector.

3.1.1 Test-beam results

Pre-production modules are not yet available for the ID subdetectors. Nevertheless, there have been extensive tests of prototypes in test-beams. The hit resolution of the silicon detectors (pixels and strips) is well described by the pitch divided by $\sqrt{12}$: for the Pixels, see Chapter 8 of [3-3]; for the SCT see Chapter 3 of [3-1]. Because of the long pulse-lengths in the TRT, the readout of the TRT straws is sensitive to overlapping hits and consequently deteriorates at higher luminosities. A comparison between test-beam and the simulation for single straws as well as the luminosity dependence of the drift-time resolution can be found in Chapter 3 of [3-1].

Test-beam results for the TRT prototypes to study the transition radiation (TR) performance are discussed in more detail in Section 3.4.2.

3.1.2 Pattern recognition programs

Three pattern recognition programs (iPatRec, PixlRec and xKalman) have been used extensively to study the ID performance. These programs were described in some detail in Section 2.5.2 of the ID TDR and only a brief summary is given in this report. iPatRec searches for tracks using

space-points formed in the Pixels and SCT. Candidates are extrapolated to the TRT and drift-time hits added. This code is partially written in C++. PixlRec searches for tracks in the Pixels. Candidates are then extrapolated to the SCT. The Kalman Filter is used at the end of the pattern recognition phase to improve the track, add TRT hits and produce the final fit. xKalman searches for tracks in the TRT using fast histogramming of straw hits. Candidates are extrapolated to the SCT and Pixels to provide confirmation. The improved tracks are then extrapolated back into the TRT and drift-time hits added. Kalman Filtering techniques are used to extrapolate the tracks and remove wrong hits. At the time of writing, a new version of the code has been prepared in C++.

In addition, a program called ASTRA [3-4] has been used recently. ASTRA is an OO pattern recognition program designed and written in C++. It relies on iPatRec to provide space-points as input and returns track candidates which are fitted by iPatRec. The performance both in results and CPU-time consumption is very similar to that found by iPatRec.

The various programs have different advantages, for example xKalman is fast because it benefits from the histogramming in the TRT; iPatRec is less sensitive to interactions or bremsstrahlung. Nevertheless, the different programs have similar performance since they use the Precision Tracker to resolve ambiguities. In the future, effort will be made to consolidate the good features of the different programs.

3.1.3 Standard track quality cuts

Track quality cuts have been developed in the context of *b*-tagging (see Section 5.2 of the ID TDR). These cuts prove very useful in general, especially when it is important to ensure that a track comes from the primary vertex or a short-lived particle, such as a *b*-hadron. These cuts are particularly valuable in rejecting conversion electrons and they help to reduce the background to prompt muons from π/K decays. The basic track quality requirements are as follows.

- Number of precision hits ≥ 9 (out of a maximum of ~11, ignoring overlaps).
- Number of pixel hits ≥ 2 (out of a maximum of 3, ignoring overlaps).
- At least one associated hit in the *B*-layer.
- Transverse impact parameter < 1 mm.

Where it is important to ensure high track quality or the TRT transition radiation information is required, an additional cut on the TRT has been found to be useful. The extended track quality cuts have in addition.

- Number of TRT straw hits ≥ 20.

3.2 Detector layout

The detector layout was described in detail in the ID TDR [3-1][3-2]. There has been some evolution since then and summary of the design is given in Chapter 1.

3.2.1 Evolution since the ID TDR

A number of simulated layouts have been used for recent studies. These are:

ID TDR (96_12)   This layout was used for the ID Performance TDR, Vol I. It did not completely correspond to the hardware description in Vol. II, because of time delays.

97_6   This layout corresponds to the hardware description in ID TDR, Vol. II [3-2].

98_2   This layout is identical to 97_6 for the ID description.

Pixel TDR   This layout was updated from 97_6 to describe the layout in the Pixel TDR [3-3].

Material Report   This layout was updated from Pixel TDR layout. It provides the best existing description of the ID material [3-5].

Current   This is the current baseline layout, as described in Chapter 1.

The majority of studies undertaken for this report have used the 98_2 (97_6) layout. The principle differences of the various layouts are described below. For the studies described in this chapter, the differences in the layout are highlighted if the effects are significant.

Following the ID TDR layout, the 97_6 (equivalent to 98_2) layout was developed to include a change in the sign of the tilt angle of all pixel detectors to reduce cluster sizes, and an improved description of the ID services and the ID material. For the Pixel TDR, the layout was updated to include a new module design with thicker detectors, the change from four to five pixel disks in each end-cap, and small modifications to the barrel radii, number of ladders and detector tilt angles.

The design of the ID is now very close to being finalised. The 4th and 5th pixel disks have been moved to $|z| < 78$ cm to ensure that the Pixel system is contained within the ID barrel to avoid the beam pipe supports having to penetrate the Pixel end-caps. This only affects $|\eta| > 2.0$. Possible changes which are being evaluated include: extending the length of the pixel diodes to ensure that the electronics can be fitted into the design (see Section 3.2.1.2), fine-tuning of the SCT wheel positions to ensure hermeticity, and moving the non-emission getter (NEG) pumps into smaller $|z|$ (see Section 3.2.1.1).

3.2.1.1 TRT rates

The performance of the TRT depends critically on the hit rates in the straws. Figure 3-1 shows a comparison of the rates from the current best description of the ID material (corresponding to the so-called Material Report Layout) with the rates from the time of the ID TDR. Additional material in the ID volume increases the rate of secondaries, but this has been compensated by small reductions in the straw lengths. The net result is that the rates are little changed.

A further development which could affect the TRT rates is modifications to the beam pipe and the associated vacuum equipment. The non-emission getter (NEG) pumps consist of a thin layer of zirconium alloy sputtered on constantan strips placed on the inner surface of the beam pipe [3-7]. The main material components are the vacuum jacket and heaters. These pumps are designed to remove gas from inside the beam pipe. If they could be moved to smaller $|z|$, it may

be possible to avoid a bake-out of the beam pipe, which would necessitate the removal of the *B*-layer or the addition of unwanted insulation. Apart from significant mechanical considerations, this would have consequences for the backgrounds in the detector.

The beam pipe is modelled as 1 mm of beryllium. In one model, the NEG pumps can be represented as an additional 1 mm of beryllium at the radius of the beam pipe and with $|z| \geq 70$ cm. The increase in the TRT hit rate from secondaries at high luminosity is shown in Figure 3-2. The increases are 10-15% of the expected rates. Although not being catastrophic, increased hit rates will result in some degradation of performance.
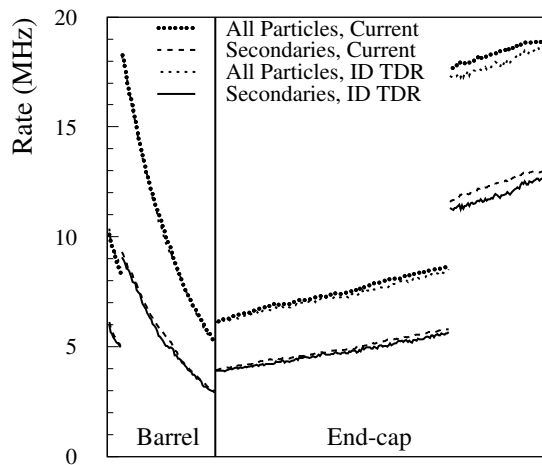
Figure 3-1 TRT hit rates at high luminosity. Comparison is made between the layout using the current best estimate of the material in the ID volume and the layout used for the ID TDR. The horizontal axis corresponds to layer number: in the barrel this corresponds to radius; in the end-cap this corresponds to *z*.
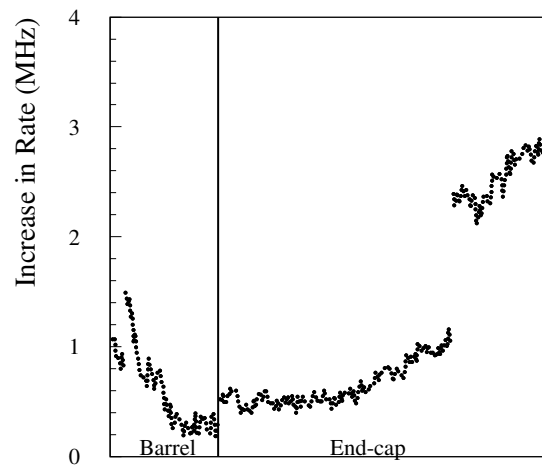
Figure 3-2 Increase in TRT hit rate arising from extended NEG pumps at high luminosity. The horizontal axis corresponds to layer number: in the barrel this corresponds to radius; in the end-cap this corresponds to *z*.

Changes to the beam pipe would also affect the impact parameter resolution. If the thickness of the pipe were doubled, then at $|\eta| = 0$, the multiple scattering term in the transverse impact parameter resolution would increase by 2.2%. A similar change would be expected if the radius of the beam pipe were increased from 25 mm to 35 mm.

3.2.1.2 Changes to the Pixels

It may prove necessary to increase the length of the pixel diodes. To study this in the simulation, the pixel dimensions were changed from 50×300 μm^2 to 50×400 μm^2. The changes in the transverse resolutions are fairly small, although not negligible due to charge sharing effects. Larger effects are seen in the longitudinal resolution, although the effects are less than might be expected, again due to charge sharing. Figures 3-3 and 3-4 show the comparison between the shorter pixels (used for all studies to date) and the longer pixels. While it may be necessary to lengthen the pixels, subsequent advances in technology may allow the detectors used for the *B*-layer to be constructed with 50×300 μm^2 diodes at a later date. This would maintain the better impact parameter performance, since the resolutions are dominated by the design of the *B*-layer.
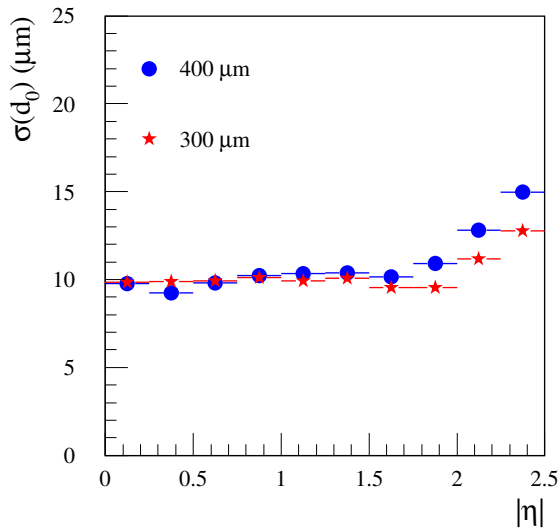
Figure 3-3 Transverse impact parameter resolution for high-p_T tracks. Comparison is made between 300 and 400 µm long pixels.
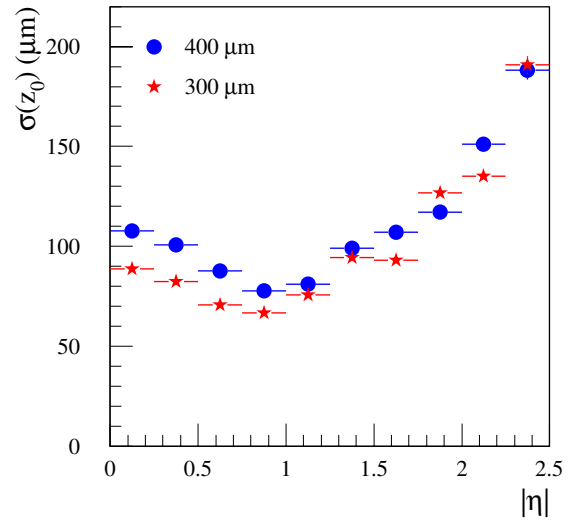

Figure 3-4 Longitudinal impact parameter resolution for high-p_T tracks. Comparison is made between 300 and 400 µm long pixels.

3.2.2 Material distributions

Since the ID TDR, there have been two studies of the material in the ID. The first was in Autumn 1997 where the possibility of reducing the number of precision layers [3-6] was considered. At that time, the description of the material was improved to bring the simulation in line with the engineering design presented in the ID TDR [3-2], resulting in layout 97_6 (equivalent to 98_2). The net increase in the Precision Tracker was small, but there was an increase of ~9% X_0 for $0.8 < |\eta| < 1.9$ in the TRT. The second study in Spring 1998 produced the Material Report Layout [3-5] where there was an increase ~5% X_0 for $|\eta| > 1.9$ in the Precision Tracker, with little net change in the TRT. Changes in the ID services outside the TRT have a relatively small effect on the performance of the ID and EM Calorimeter. The greatest sensitivity is to material within the volume of the silicon detectors, where the net increase from the ID TDR averaged over $|\eta| < 2.5$ is ~2% X_0 giving ~27% X_0; the corresponding numbers including the TRT are ~5% X_0 and ~48% X_0 respectively.
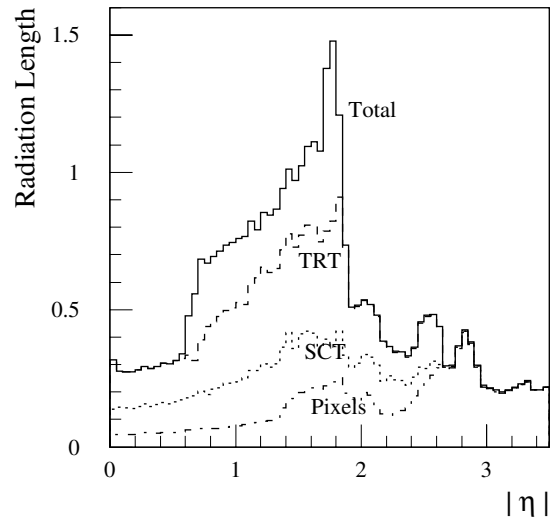

Figure 3-5 Material distribution of the ID vs |η| for the 98_2 layout, used in this report. The various bands include all services and supports within the corresponding fiducial volumes. The pixel band also includes the beam pipe. The total includes the ID services outside the TRT.

Figure 3-5 shows the material distribution for the ID corresponding to the 98_2 layout. This layout has been used for much of the simulation described in this report and provides a reasonable estimate of the material to be expected in the final design.

3.2.3 Magnetic field

The ATLAS solenoid [3-8] is 5.3 m long, compared with the 6.7 m length of the tracking volume of the Inner Detector. Consequently, the field deviates significantly from uniformity. Maps of the field are shown in Figures 3-6 and 3-7. The maximum value of the field depends on the current in the solenoid. The current proposed for the solenoid is that which would be required to produce a uniform 2 T field in an infinite solenoid in the absence of magnetic materials. With the same current, the maximum field in ATLAS will be about 2.09 T – this is enhanced by the iron in the Hadronic Calorimeter. It can be seen that B_z falls to about 1.0 T at the end of the solenoid and 0.5 T at the end of the detector. B_R becomes important for $|z| > 2$ m, with a maximum of ~0.8 T at the coil aperture.
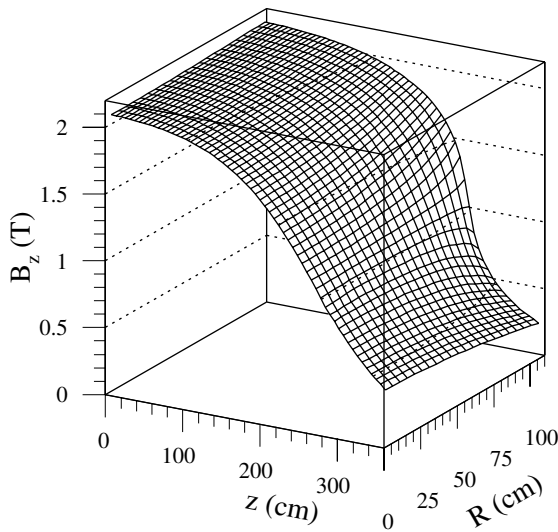

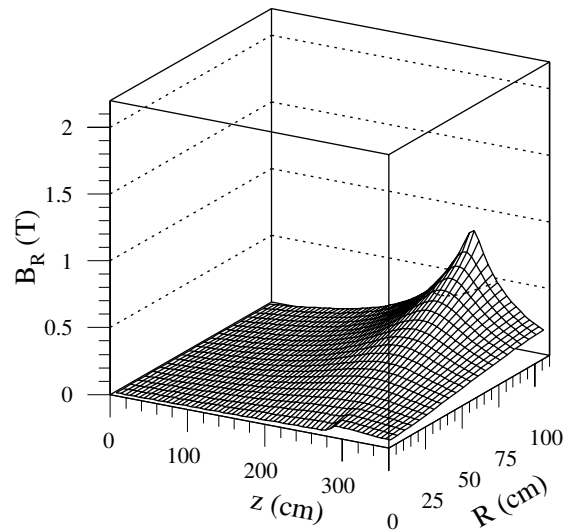**Figure 3-6** B_z as a function of z and R.

Figure 3-7 B_R as a function of z and R.

The consequences for the performance of the deviation of the field from uniformity are not major – the main effect is the need for more complex tracking algorithms which are consequently slower (this is a concern for the LVL2 trigger [3-9]). Most of the simulations discussed in this report has been performed with a uniform 2 T field. However, the track parameter resolutions presented in Section 3.3.1 explicitly show the effects of the solenoidal field, while the consequences for pattern recognition are examined in Section 3.5.4.

3.3 Reconstructed track parameters

The resolutions of the fitted track parameters are considered in this section. All results are shown for low luminosity. At high luminosity, there should be little effect on the hit resolutions of the silicon detectors. However, the spatial resolution of the TRT straws will be degraded (see Chapter 3 of [3-1]). The effects will be greatest at lower radii although these straws are less critical in the determination of the track parameters. Hence the net degradations expected at high luminosity are not great, as was shown in Chapter 4 of [3-1].

3.3.1 Muons

The track parameter resolutions have been estimated using the analytic calculations which were outlined in Chapter 4 of [3-1]. These calculations were shown to be in good agreement with a full simulation. Any small discrepancies between the full simulation and the analytic calculation are probably no bigger than the uncertainties of the real detector performance.

The calculations were updated to allow for an improved understanding of the material distributions and for the modifications to the Pixel layout. The net result of all changes relative to the ID TDR [3-1] is small. The largest changes are in the impact parameter resolutions caused by modifications to the Pixel layout. The transverse resolution at high p_T has improved slightly while the longitudinal resolution is slightly deteriorated. At low p_T, the resolutions are degraded by increases in the material in the Pixels. Detailed comparisons can be found in the Pixel TDR [3-3].

In the ID TDR, the parameter resolutions were shown for a uniform 2 T magnetic field. In the plots which follow, the baseline configuration is with the solenoidal field which will exist in AT-LAS. For this simulation, the field was scaled to a maximum value of 2 T. Where appropriate, a transverse beam constraint has been included in the calculations.

3.3.1.1 Resolution in 1/p_T

Figure 3-8 shows the resolution in 1/p_T. The degradation in resolution caused by the solenoidal field compared to the uniform field is clearly visible for $|\eta| > 1.5$. The use of the beam constraint improves the resolutions by a few percent.

3.3.1.2 Resolution in ϕ

Figure 3-9 shows the resolution in ϕ. The degradation in resolution caused by the solenoidal field is only apparent at high p_T. The improvement obtained from the beam constraint is significant at lower p_T.

3.3.1.3 Resolution in cot θ

Figure 3-10 shows the resolution in cot θ. Measurements in the R-z plane are fairly insensitive to the distortions in the B-field and the use of a transverse beam constraint.

3.3.1.4 Resolution in d_0

Figure 3-11 shows the resolution in d_0. Since the determination of d_0 is dominated by measurements near the primary vertex, a region where the B-field is fairly uniform, there is a relatively small dependence on the field distortions. The performance seen at high p_T and high pseudorapidity is slightly different from that found in the full simulation (see Figure 3-3) because of the analytic calculation represents the B-layer $R\phi$ resolution as a constant, whereas in the full simulation, there is a small degradation associated with charge sharing.
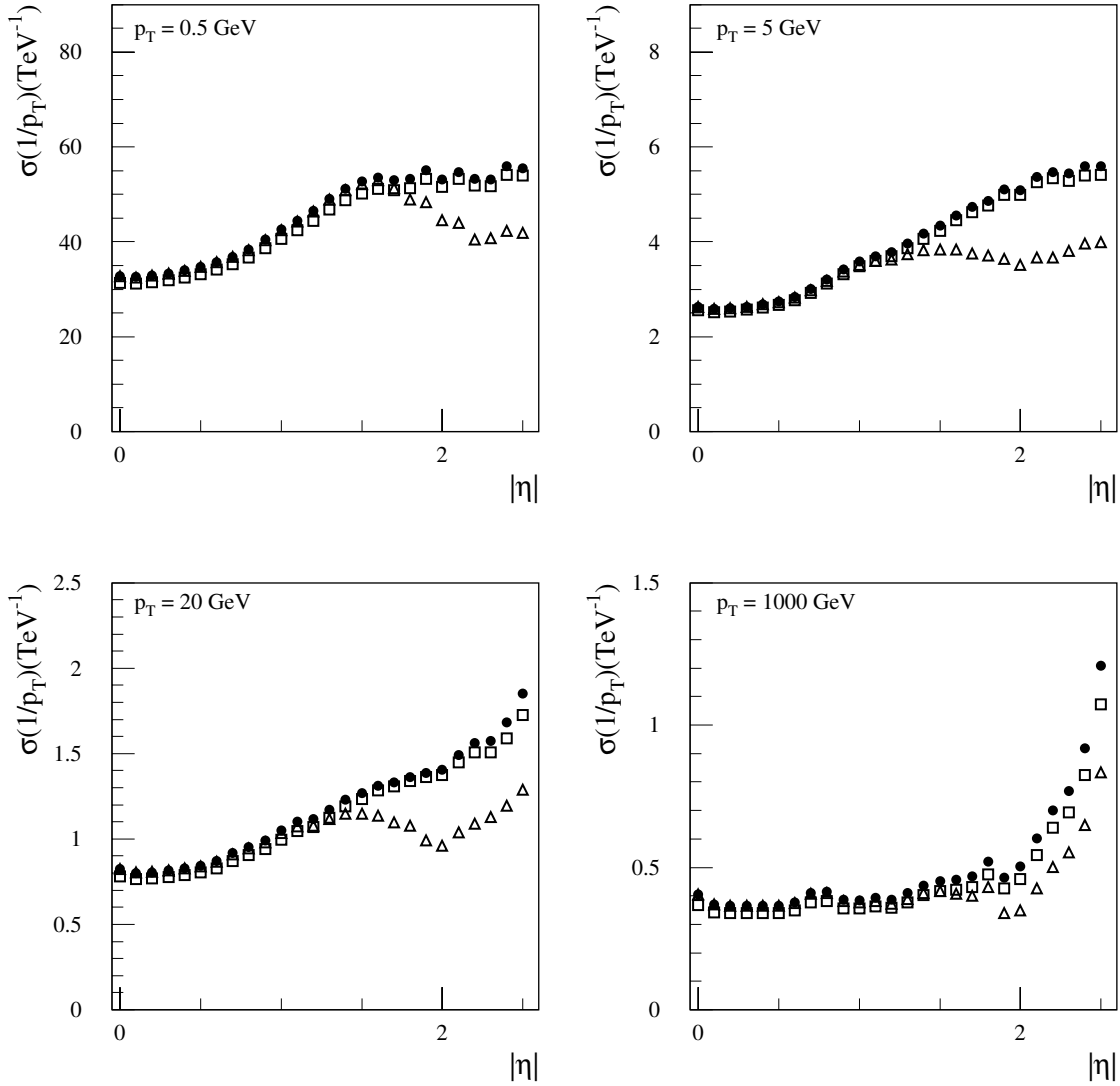
Figure 3-8 p_T resolution as a function of $|\eta|$ for muons of various momenta. Results are shown for a solenoidal field without (circles) and with (squares) a beam constraint, and for a uniform field without a beam constraint (triangles).

3.3.1.5 Resolution in $\sin\theta \times z_0$

Figure 3-12 shows the resolution in z_0. What is generally of most interest is the projection of z_0 on to the plane transverse to the track direction – this is achieved by multiplying by $\sin\theta$. This corresponds to the measurement which is of most interest for vertexing and b-tagging and can be compared more directly with the transverse impact parameter d_0.

3.3.1.6 Simple parametrisations

If the features of the tracking system (the position and resolution of measurements, the location of material and the B-field) are uniform as a function of the transverse radius R, the resolutions can be expressed approximately in a simple form $A \oplus B/p_T$ [3-10]. This uniformity is achieved by design to a good approximation; however it deviates from this due to a reduced radial lever-
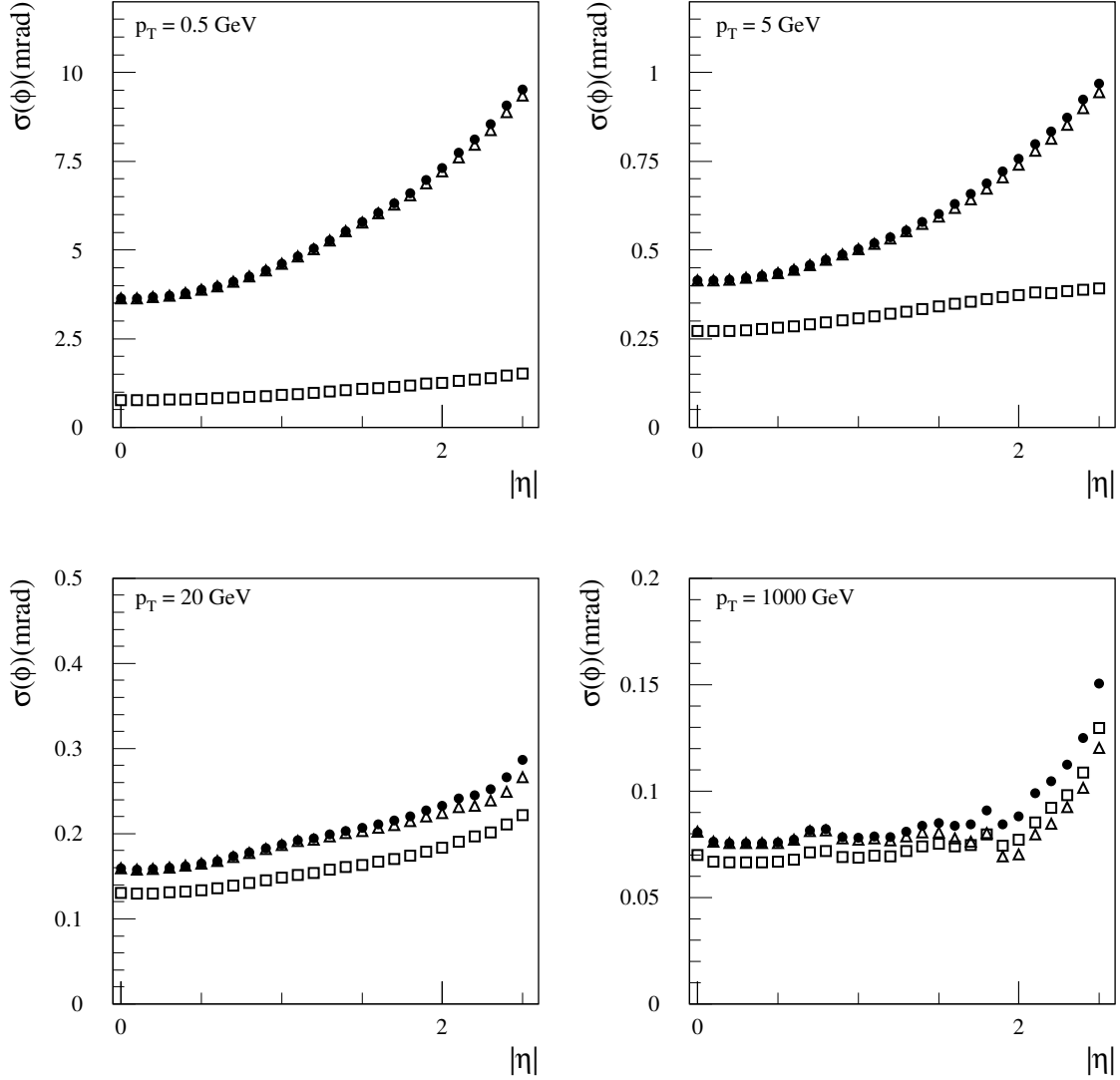
Figure 3-9 Azimuthal resolution as a function of |η| for muons of various momenta. Results are shown for a solenoidal field without (circles) and with (squares) a beam constraint, and for a uniform field without a beam constraint (triangles).

arm at high $|\eta|$, variations in detector spatial resolution as a function of $|\eta|$, a complex material distribution aimed at minimising material and including services, and a non-uniform field. Approximate forms for the resolutions as a function of p_{T} (in GeV) and θ for a solenoidal field without a beam constraint are:

$$\sigma\!\left(\frac{1}{p_{\mathrm{T}}}\right) \approx 0.36 \oplus \frac{13}{p_{\mathrm{T}}\sqrt{\sin\theta}} \quad (\mathrm{TeV}^{-1})$$

$$\sigma(\phi) \approx 0.075 \oplus \frac{1.8}{p_{\mathrm{T}}\sqrt{\sin\theta}} \quad (\mathrm{mrad})$$

$$\sigma(\cot\theta) \approx 0.70 \times 10^{-3} \oplus \frac{2.0 \times 10^{-3}}{p_{\mathrm{T}}\sqrt{\sin^{3}\theta}}$$

Figure 3-10 cot θ resolution as a function of |η| for muons of various momenta. Results are shown for a solenoidal field (circles) and for a uniform field (triangles) without a beam constraint.

$$\sigma(d_0) \approx 11 \oplus \frac{73}{p_T \sqrt{\sin\theta}} \quad (\mu m)$$

$$\sigma(z_0) \approx 87 \oplus \frac{115}{p_T \sqrt{\sin^3\theta}} \quad (\mu m)$$

The coefficients have been determined from tracks in the barrel with p_T = 1 and 1000 GeV.

Without the above approximations, the complete resolutions obtained for muons from the analytic calculation have been parametrised as a function of p_T and |η| for various configurations [3-11][3-12] so that they can be used for fast simulation with the ATLFAST package (see Section 2.5). The p_T-dependence of the impact parameter resolutions is shown in Figures 3-13 and 3-14.

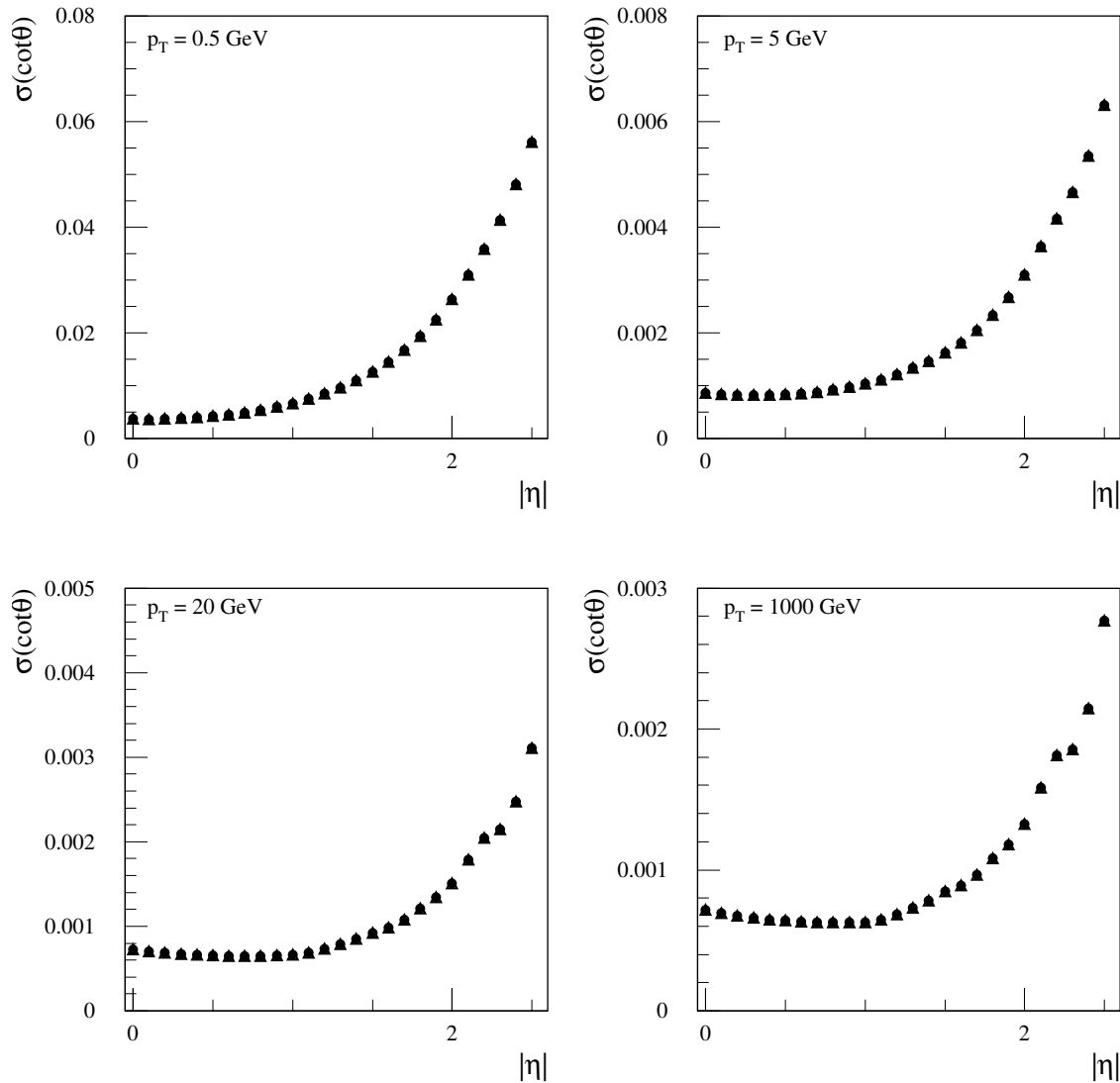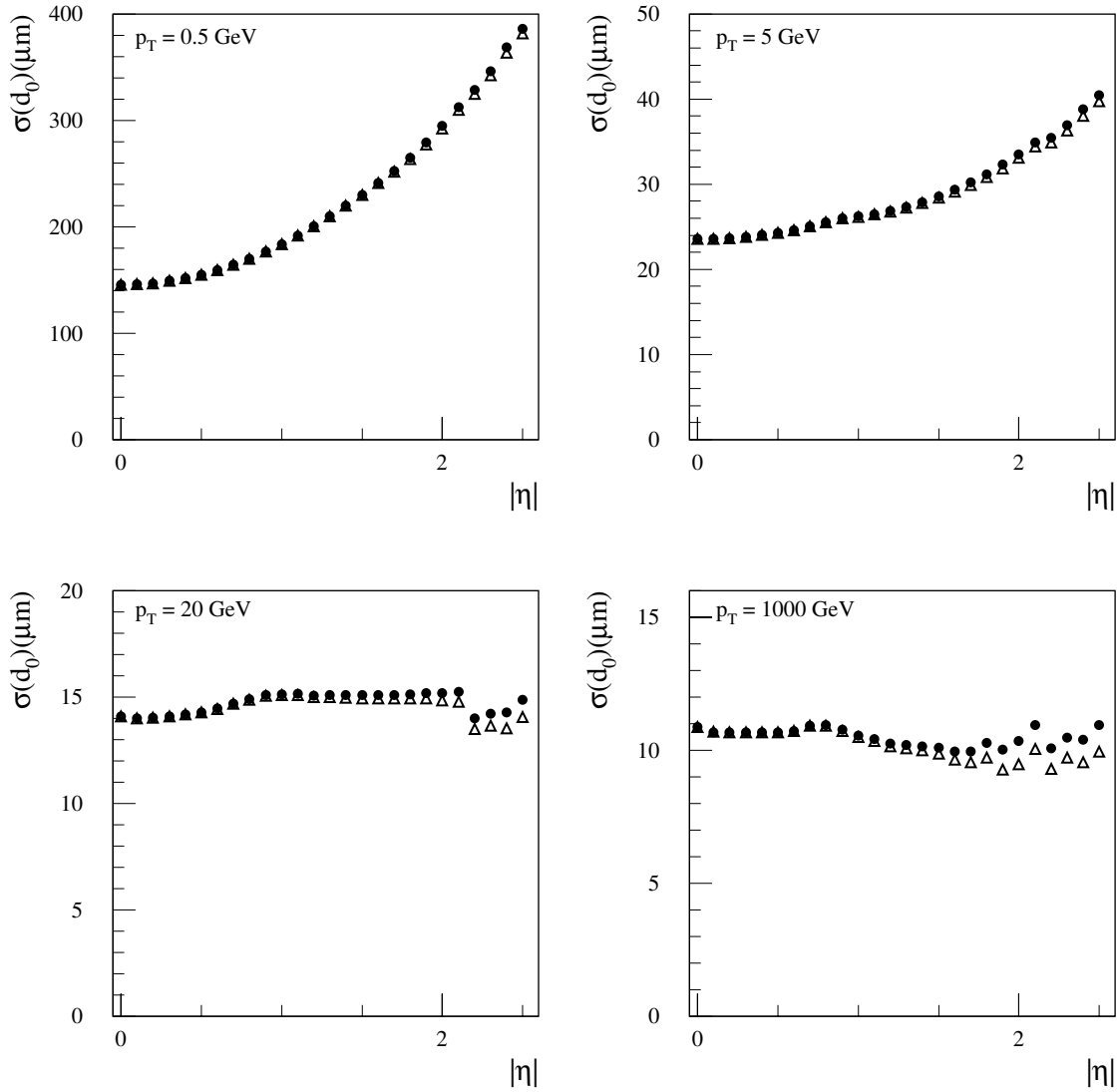**Figure 3-11** Transverse impact parameter (d_0) resolution as function of $|\eta|$ for muons of various momenta. Results are shown for a solenoidal field (circles) and for a uniform field (triangles) without a beam constraint.

3.3.1.7 Correlations

The most important correlations occur between parameters in the transverse x-y plane ($1/p_T$, ϕ, d_0) and between those in the R-z plane ($\cot\theta$, z_0); however the two sets of measurements are largely decoupled. Figure 3-15 shows the normalised correlation coefficients for very low and very high p_T. At low p_T, the fitted angles and impact parameters are strongly correlated since they are dominated by the scattering in the material at the lowest radius (in particular in the B-layer).
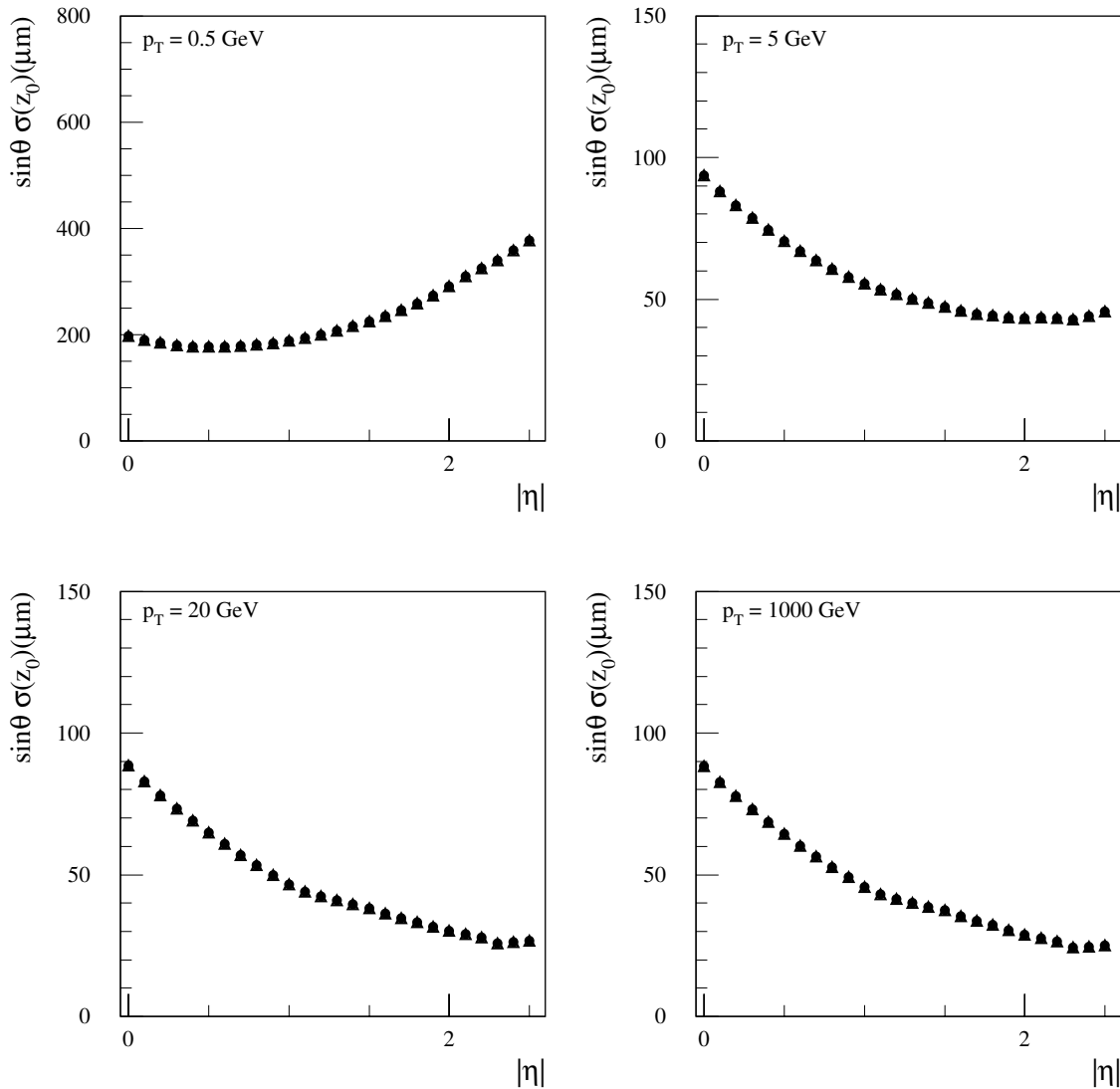
Figure 3-12 Longitudinal impact parameter (z_0) resolution projected transversely to the track direction as function of $|\eta|$ for muons of various momenta. Results are shown for a solenoidal field (circles) and for a uniform field (triangles) without a beam constraint.

3.3.2 Other particles

The resolutions shown in the previous sections correspond to muons. These represent charged particles in the idealisation that there are no interactions other than multiple scattering. The distributions of reconstructed muon track parameters are very close to Gaussian, and in the absence of pattern recognition problems, do not have any significant tails (see Figures 3-19 and 3-20). In the ID TDR, it was shown that the fractions of tracks beyond 3σ in $1/p_T$ or d_0 are typically ~2% (see Section 5.1.2.1 of [3-1]). Small deviations from true Gaussian distributions arise from non-Gaussian components in the simulation of multiple scattering and from an incomplete description of the simulated material in the track fitting.
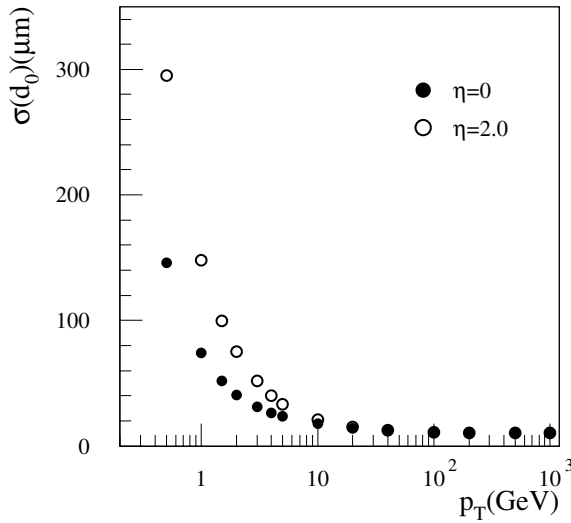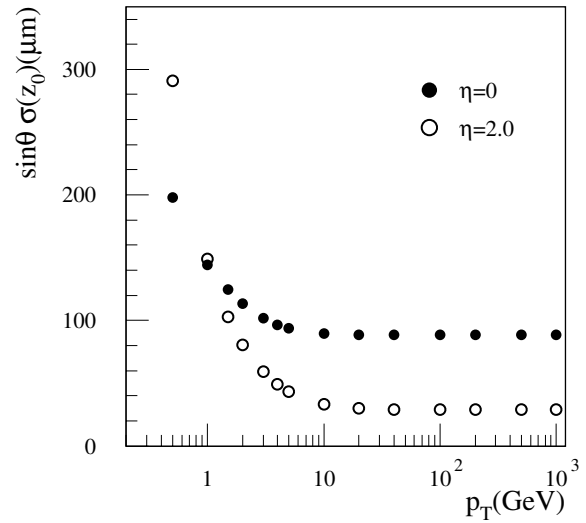
Figure 3-13 d_0 resolution as a function of p_T.

Figure 3-14 z_0 resolution as a function of p_T.

3.3.2.1 Pions

The probability for a pion to have a nuclear interaction is between 10 and 20% (see Chapter 3 of [3-1]). Interactions can cause tracks to be lost or produce tails in the reconstructed parameters. When track quality cuts (see Section 3.1.3) are applied, there is a reduction in track finding efficiency compared to muons (see Section 3.5.1.1) and the tails are greatly reduced. Consequently, the reconstructed pion track parameter distributions are very similar to those of muons (see Section 3.3.2.3).

For *B* physics studies using the fast simulation with the ATLFAST package, it is important to have a parametrised description of the pion track parameters for pions produced at or close to the primary vertex as well as for those which may be produced in the volume of the ID (arising from K_s^0 decays for example). Hence the distributions of track parameters for single pions and pions from K_s^0 decays were studied, using looser cuts to retain the decay pions. The track parameters were parametrised by the sum of two Gaussians as a function of p_T, $|\eta|$ and the production radius [3-12][3-13]. Nominally, the Gaussians describe separately the core and tail of the distributions, although, in practice, there is a significant correlation between the two and hence the interpretation of the parameters is not straightforward. Both Gaussians describe the five fitted track parameters and their correlations and the relative amplitude is determined by a fit to the impact parameter distributions. Further examples showing the comparison between full and fast simulation related to pions can be found in Section 17.2.2.2.

3.3.2.2 Electrons

An electron traversing the ID will emit bremsstrahlung as it crosses the material (see Figures 7-1 and 7-2 in Chapter 7). This introduces distortions to the track which cause the resolutions of the fitted parameters to be degraded and the reconstructed parameters to be biased. By using the so-called 'bremsstrahlung recovery' procedures (discussed in Section 7.2.1.1), it is possible to improve on average the reconstructed electron track parameters compared to the results which would be obtained using the same fitting procedure adopted for minimum ionising (non-radiating) particles. In what follows, electron track parameters have been obtained using bremsstrahlung recovery in the ID alone, as implemented in xKalman.
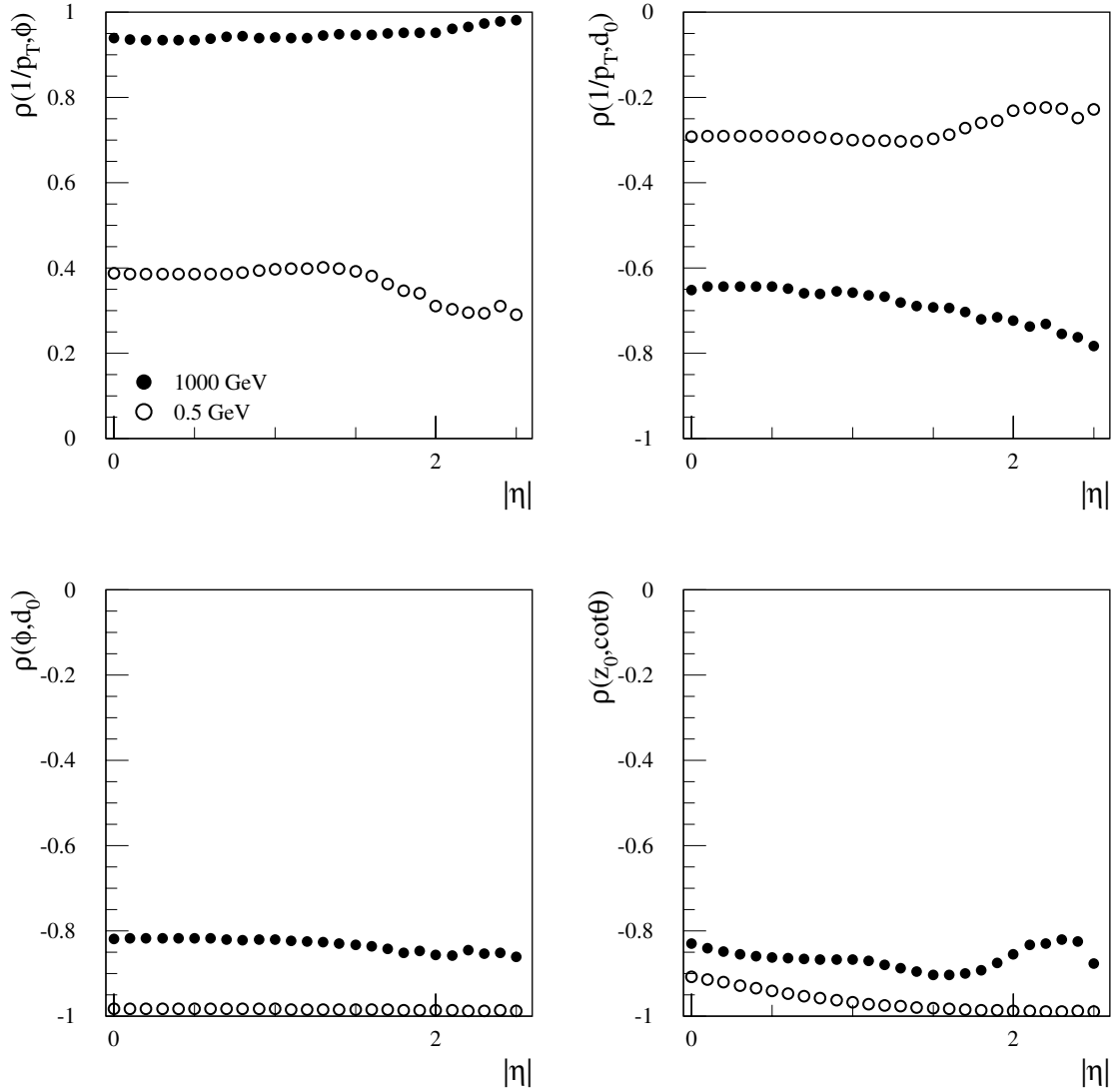
Figure 3-15 Correlations between track parameters for muons with p_T = 1000 GeV (filled circles) and 0.5 GeV (empty circles) in a solenoidal field without a beam constraint.

Figure 3-16 shows distributions for the reconstructed electron p_T. The distributions are significantly non-Gaussian (even for $1/p_T$) due to the bremsstrahlung which increases the track curvature causing the electrons to be reconstructed with a lower p_T. Since the radiation is almost collinear with the electron, it significantly affects all of the reconstructed track parameters in the bending plane ($1/p_T$, ϕ, d_0), but hardly affects those in the non-bending plane (cot θ, z_0). The correlation between the reconstructed transverse impact parameter and the reconstructed p_T is shown in Figure 3-17. The scatter plot exhibits structure (bands running top-left to bottom-right, at different angles) which corresponds to hard bremsstrahlung from different planes of material in the Precision Tracker.

Using distributions like those above for a variety of generated p_T's, parametrisations of the reconstructed electron track parameters were derived as a function of p_T and $|\eta|$ [3-12] so that they could be used for fast simulation with the ATLFAST package. For a given electron track, the parametrisation is derived from the location of a single hard bremsstrahlung chosen ran-
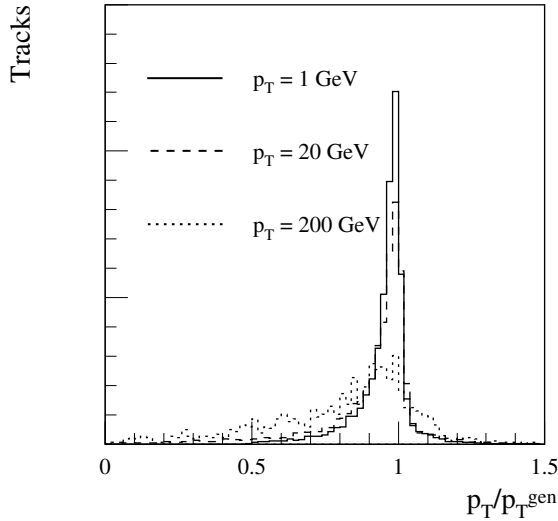
Figure 3-16 Ratio of reconstructed p_T to true p_T for electrons of various p_T's, averaged over $|\eta|$. The distributions are normalised to the same area.
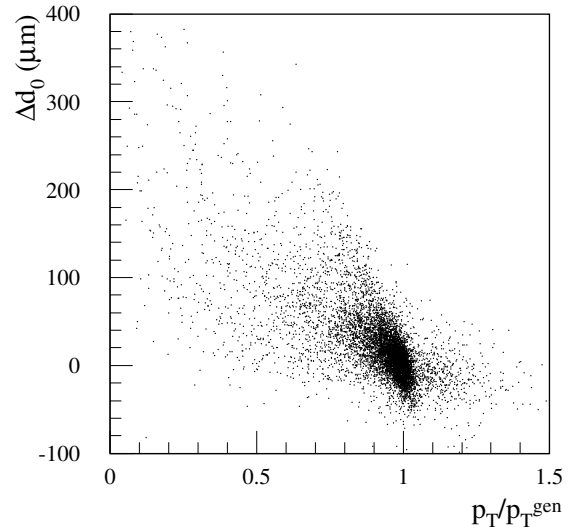
Figure 3-17 Difference between the reconstructed and true transverse impact parameter vs the ratio between the reconstructed and true p_T for 20 GeV electrons.

domly from the appropriate distribution. Plots showing the agreement between the full and fast simulation are shown in Figure 3-18. Further examples showing the comparison between full and fast simulation related to electrons can be found in Section 17.2.2.1.

3.3.2.3 Comparison between muons, pions and electrons

Figures 3-19 and 3-20 compare the reconstructed $1/p_T$ and d_0 distributions for muons, pions and electrons. The muon distributions are very Gaussian, the pion distributions have small tails while the electron distributions are significantly distorted. To compare the distributions, Gaussian fits were made to the cores of the distributions in exactly the same way for muons, pions and electrons. Since the electron distributions are significantly skewed, it was not simple to choose the range for the fit: for the $\Delta 1/p_T$ (Δd_0) distribution, the fit was made in the range ± 1 (± 2) times the rms centred on the peak. The fitted quantities were: the position of the peak, the rms and the tail fraction. The tail fraction was calculated as the fraction of the area of the distribution not contained in the Gaussian fit when extended over the complete range.

In Figure 3-21, these quantities are shown for 20 GeV p_T particles. The distributions for cot θ and z_0 are very similar for all particles. It can be seen that the peaks of the distributions are well centred for muons and pions, but there are significant biases for electrons. The resolutions for muons and pions are similar, but significantly worse for electron tracks. While the muons and pions have tails which are at the level of a few percent (these tails are sensitive to the fit range and are measures of the deviation from a perfect Gaussian; the actual number of muon 'outliers' is very small), the electron tails are very significant. Similar effects are seen at $p_T = 1$ GeV, although the electron tails are reduced by about a third.
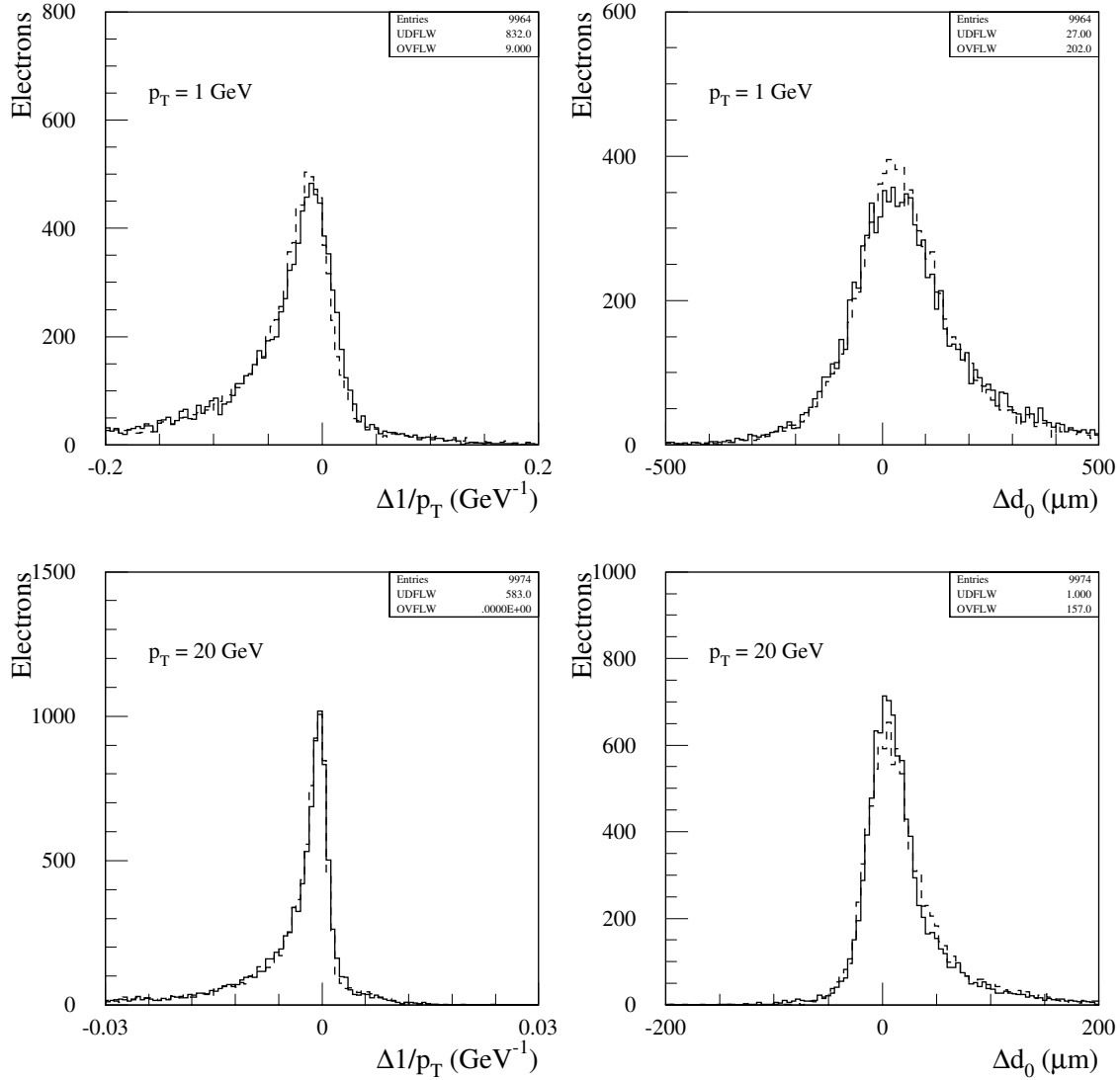
Figure 3-18 Differences between the reconstructed and true values of $1/p_T$ and transverse impact parameter for p_T = 1 and 20 GeV electrons. Comparison is made between fully simulated electrons (solid lines) and the fast simulation as used in ATLFAST (dashed lines). The fully simulated histograms are normalised to the same area as the fast simulation.

3.3.3 Charge determination

The specification on the p_T resolution (at high p_T) is set by the desire to be able to investigate the charge asymmetries in the decays of possible heavy gauge bosons W' and Z'. It is required that at p_T = 0.5 TeV, the sign of an electron should be determined to better than three standard deviations, corresponding to a misidentification probability of 0.13%. This means that the intrinsic resolution $\sigma(1/p_T)$ should be at least as good as 0.6 TeV^{-1}. From Figure 3-8 (p_T = 1000 GeV), it can be seen that this is satisfied for muons up to $|\eta| \sim 2.2$, beyond which the resolution degrades like $1/R^2$ due to the reduced lever-arm as tracks fail to cross the full radial extent of the ID.

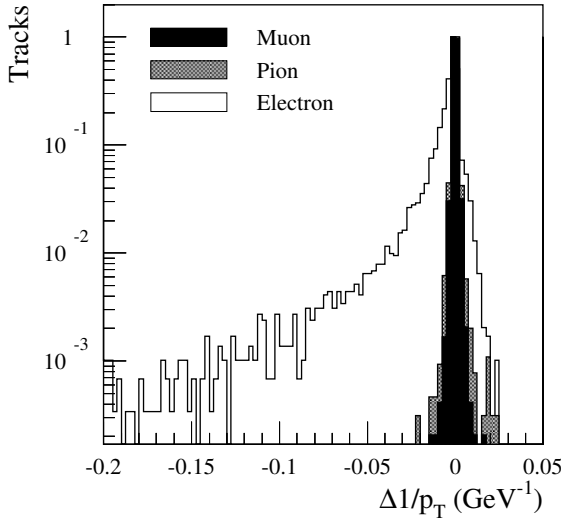**Figure 3-19** Difference between the reconstructed and generated $1/p_T$ for single 20 GeV negatively charged particles.
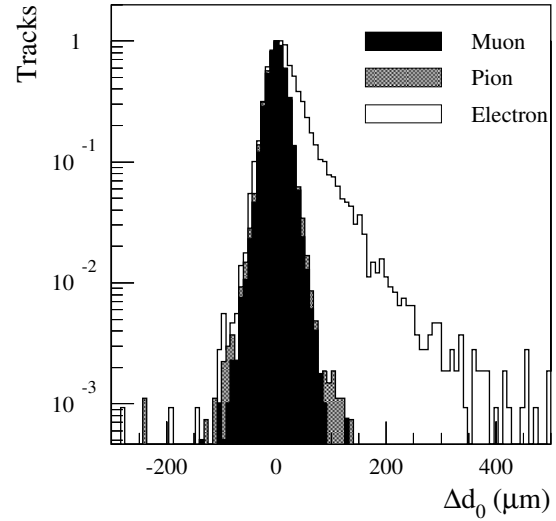
Figure 3-20 Difference between the reconstructed and generated transverse impact parameter for single 20 GeV negatively charged particles.

For electrons, the reconstruction of tracks is complicated by bremsstrahlung and subsequent conversions. In reducing the electron's momentum, the bremsstrahlung can also improve an electron's charge determination. Pileup does not affect the charge measurement significantly. More details can be found in Section 4.2 of [3-1].

Using full simulation with additional smearing on $1/p_T$ to allow for the solenoidal field, the wrong sign fraction for electrons and muons (after a beam constrained fit) has been found as a function of p_T. The results, averaged over $|\eta| \leq 2.5$, are shown in Figure 3-22 and summarised in Table 3-1. The muons are well described by the intrinsic resolution; for electrons, this is only true at very high p_T. The effect of the B-field distortions is not great. Although the specification is not actually met for electrons, mainly because of tails arising from bremsstrahlung, the determination of the electron charge appears to be perfectly satisfactory up to ~1 TeV. The muon charge will be determined by the Muon System.

Figure 3-22 Wrong sign fraction as a function of p_T for muons and electrons, averaged over pseudorapidity in the presence of either a solenoidal or uniform magnetic field.

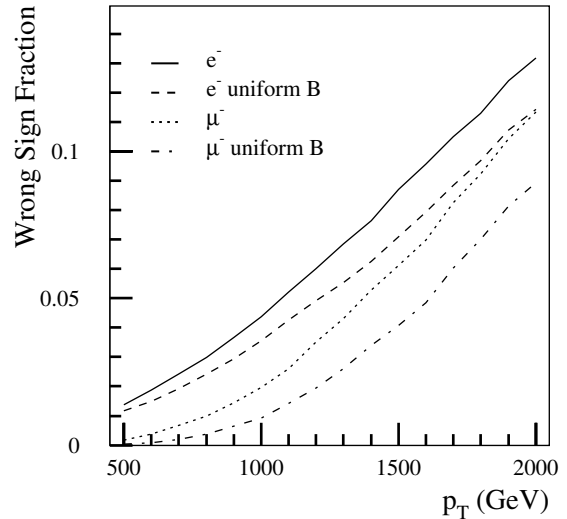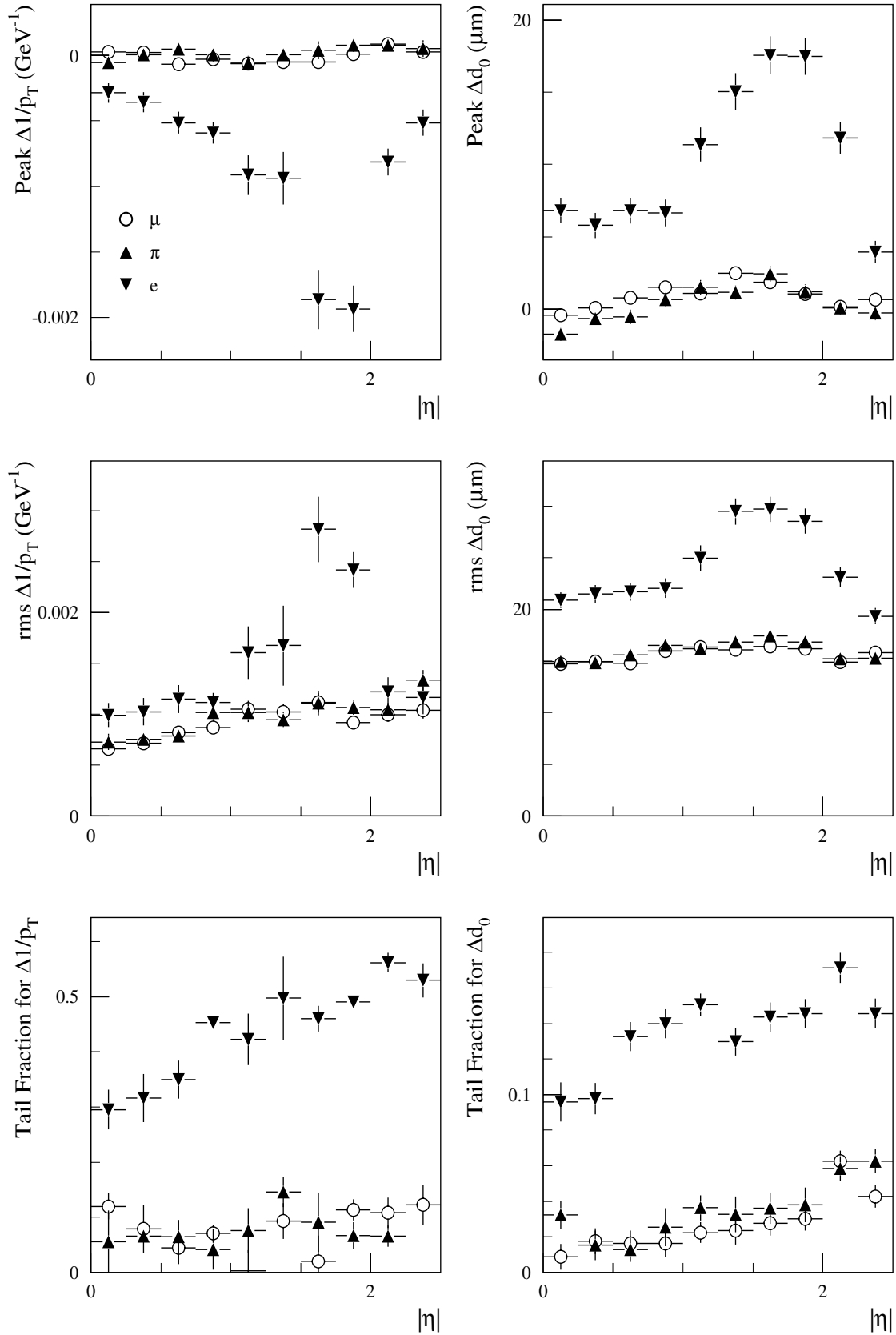**Figure 3-21** Comparison of fitted parameters for distributions of the reconstructed $1/p_T$ and d_0 for muons (circles), pions (up-triangles) and electrons (down-triangles) all with $p_T = 20$ GeV. See text for more details.

Table 3-1 Wrong sign fraction for high-p_T muons and electrons. Numbers in brackets are what would be expected from a Gaussian distribution with the nominal resolution.

p_T (GeV)	Wrong sign fraction (%)			
	Uniform *B* field		Solenoidal *B* field	
	Muons	Electrons	Muons	Electrons
500	0.04 (0.02)	1.2 (0.03)	0.2	1.4
1000	0.9 (0.9)	3.6 (1.2)	1.9	4.4
2000	9.2 (9.1)	11.5 (10.1)	11.6	13.3

3.4 Particle identification in the TRT

3.4.1 Use of transition radiation

The measurement of transition radiation (TR) in the TRT provides separation between hadrons and electrons. The emission of TR photons is a threshold effect which depends on the relativistic velocity p/m (and not p_T/m) and which turns on for $\beta\gamma > \sim 1000$ (see [3-14] for more details of the mechanism). Nevertheless, since p_T is the quantity of interest for many physics studies, the TR performance is examined as a function of p_T rather than p. The TR performance was discussed in Section 4.6 of the ID TDR [3-1]. In this section, a summary of the pion rejection is given.

Rejection against charged pions is achieved by counting the fraction of TRT straws which have a high-threshold (TR) hit. This has been studied for tracks which pass the extended ID track quality cuts described in Section 3.1.3, however, the results are not sensitive to the details of these cuts. Cuts on the fraction of TR hits as a function of p_T and pseudorapidity have been developed so as to maintain a specified electron efficiency for those electrons accepted by the quality cuts. The results shown in this section come from the description of the TRT used for the simulation at the time of the ID TDR and correspond to the physics studies presented in this report. Improvements in the understanding of the TR performance are discussed in Section 3.4.3.

Figures 3-23 and 3-24 show the pion efficiency for $p_T = 2$ GeV and 20 GeV, respectively, for 90% and 80% electron efficiencies. All the efficiencies are relative to the track quality cuts; to derive the total efficiencies, the numbers must be multiplied by the efficiencies to pass the quality cuts. The rejection, defined as the reciprocal of the efficiency, is best in the TRT end-cap where there is more TR radiator and a longer path length. Some of the variation with $|\eta|$ for fixed p_T arises from the fact that the TR rejection is more properly a function of p rather than p_T. For $|\eta| > 1.9$, particles leave the TRT through the last wheel and as pseudorapidity increases, the path length decreases causing a reduction in the pion rejection.

Figure 3-25 shows how the pion rejection varies as a function of p_T. As the electron p_T increases from 0.5 GeV, the electron radiation increases causing improved π/e separation. This is maximal for p_T around 2–5 GeV. At higher energies, the relativistic rise in dE/dx causes the pions to deposit more energy resulting in reduced separation. At high energies, $p > 100$ GeV, the pions emit TR photons at a comparable rate to electrons causing the separation to vanish. The plots shown so far correspond to single particles with no pile-up; the effect of pile-up can be seen in Figure 3-26. At high luminosity, other particles, including electrons from conversions, deposit energy in
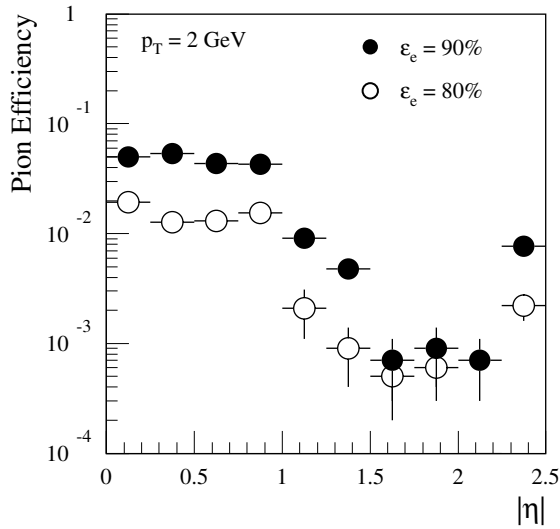
Figure 3-23 Pion efficiency as a function of $|\eta|$ for p_T = 2 GeV for two different electron efficiencies. The efficiencies are relative; to get the total efficiency, the values must be multiplied by the efficiencies to pass the extended track quality cuts.
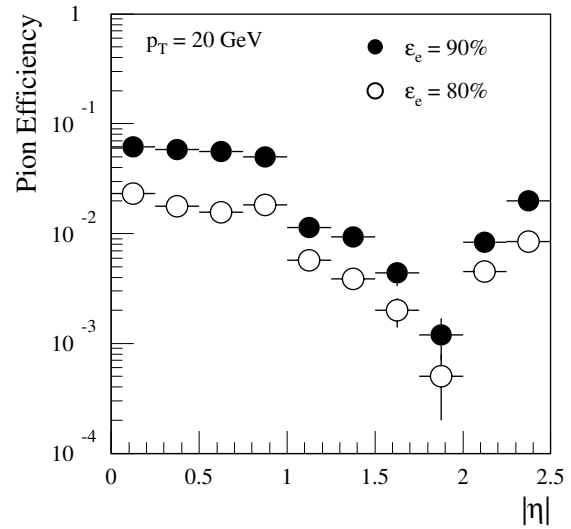
Figure 3-24 Pion efficiency as a function of $|\eta|$ for p_T = 20 GeV for two different electron efficiencies.

the straws crossed by the particles of interest. This causes an increase in the number of high threshold hits for both pions and electrons, but the net effect is a degradation in the π/e separation.
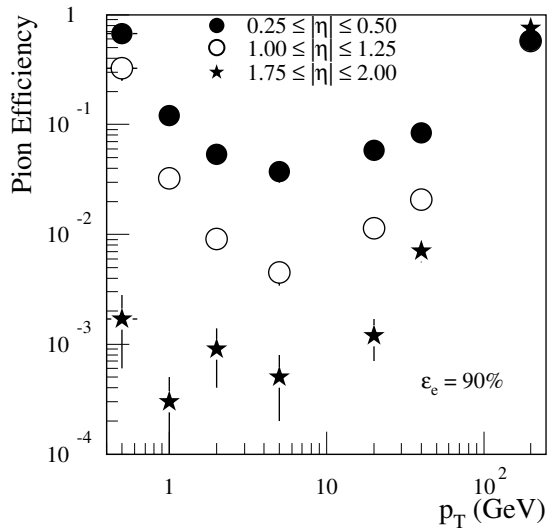
Figure 3-25 Pion efficiency as a function of p_T in various pseudorapidity intervals for 90% electron efficiency.
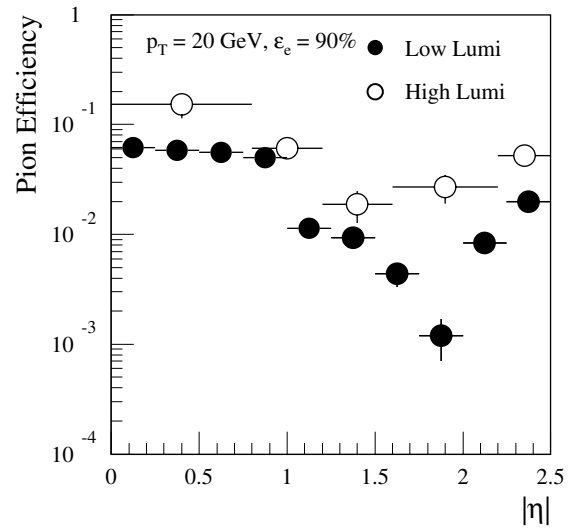
Figure 3-26 Pion efficiency as a function of $|\eta|$ for low and high luminosity for p_T = 20 GeV for 90% electron efficiency.

3.4.2 Test-beam comparisons

The set-up used to make the test-beam measurements consisted of ten straws arranged one after another along the test-beam axis so that a single track could pass through all ten straws. There was a 2 cm gap between each straw into which samples of different radiator material could be placed. Each straw was read out by an ADC which was calibrated to the energy deposition in the straw. The set-up was studied with pions and electrons of 20 GeV in the H8 test-beam area.

Samples of 20 GeV pions and electrons were generated and tracked through a GEANT simulation of the test-beam apparatus. TR photons were generated and hits created by them were recorded during the tracking procedure. The response of each straw to the charged tracks and the TR photons impinging on it was calculated using a modified version of the TRT digitisation procedure. The simulation routines were tuned empirically to match the measured test-beam results. The comparison of data with Monte Carlo results is shown in Figures 3-27 (differential energy deposition spectrum) and 3-28 (the integrated probability that the energy deposition exceeds a certain threshold). The overflows, which are not visible in Figure 3-27, are 0.015 and 0.115 for the pions and electrons respectively, to be compared with the values of 0.015 and 0.123 respectively from the simulation. The rise in the differential distribution at very low energies is caused by the tracks which graze the straws very near the straw walls.
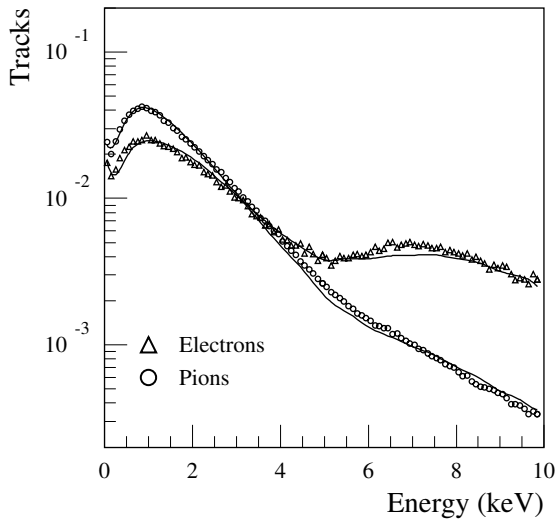
Figure 3-27 Energy deposition in TRT straws in the test-beam set-up for electrons and pions. The areas under the curves are normalised to unity. The associated lines come from the GEANT simulation.
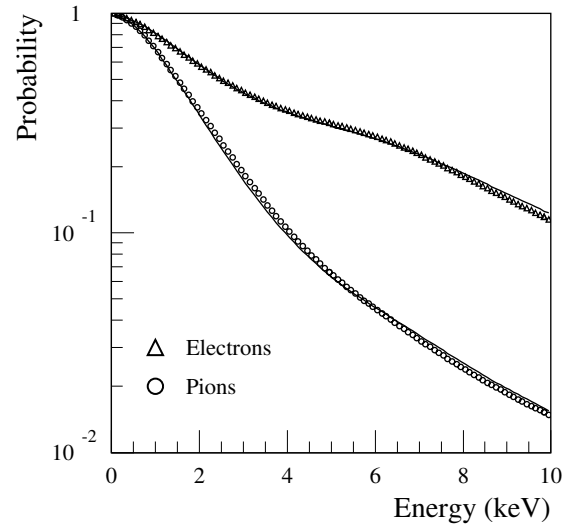
Figure 3-28 Probability that the energy deposition in TRT straws in the test-beam set-up exceeds the threshold (indicated by the horizontal axis) for electrons and pions. The associated lines come from the GEANT simulation.

3.4.3 Improved simulation

Figures 3-29 and 3-30 show the expected TR performance after improvements in the TR simulation, some of which are stimulated by the comparison of test-beam data with its simulation. Compared with the performance shown in Section 3.4.1, the expected performance for $p_T = 2$ GeV (Figure 3-29) has improved by a factor of ~2 in the barrel region and degraded by a factor of between 3 and 30 depending on pseudorapidity in the end-cap, although the best performance, which is achieved around $|\eta| = 1.7$, is little changed. At $p_T = 20$ GeV (Figure 3-30),

the performance has improved by a factor of ~2 in the barrel region and degraded by a factor of ~4 in the end-cap. The degradation in the end-cap is mostly due to the inclusion of the exact geometry foreseen for the radiator stacks, normalised to the recent test-beam measurements (in the ID TDR, the end-cap radiators were simulated as foam filling all the volume not occupied by straws). Also included in the improved simulation was a detailed description of the modular barrel TRT design including the carbon fibre module walls and inter-module gaps (in the ID TDR, the barrel geometry was simulated in a simplified way without explicit modules but with an equivalent amount of material) – this degrades the performance by ~20%. The other effects are linked to the better description of the *dE/dx* for pions and electrons as obtained from the recent test-beam measurements – this leads to a factor two improvement in rejection. A 5 keV simulated discriminator threshold was selected for identifying high threshold hits by systematically varying the threshold so as to obtain the optimal pion rejection. It was found that the rejection changes slowly as a function of this threshold.
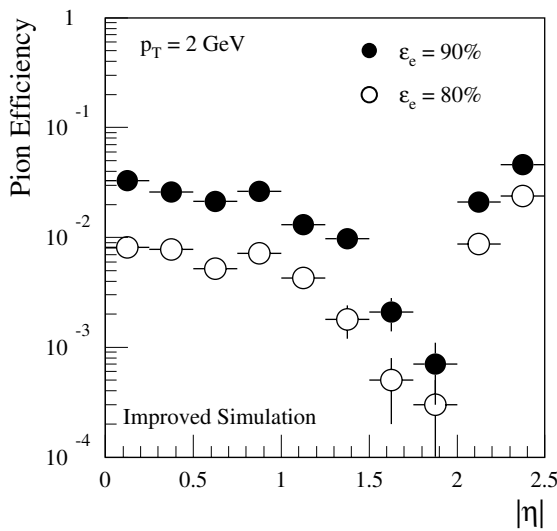
Figure 3-29 Pion efficiency as a function of $|\eta|$ for p_T = 2 GeV for two different electron efficiencies using the improved TR simulation.
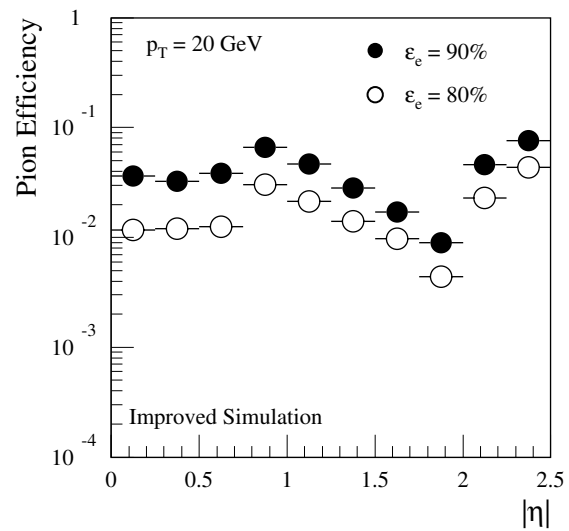
Figure 3-30 Pion efficiency as a function of $|\eta|$ for p_T = 20 GeV for two different electron efficiencies using the improved TR simulation.

3.4.4 Particle identification by *dE/dx*

No charged hadron identification has been foreseen in the Inner Detector, because it is not necessary to fulfil the major physics goals of ATLAS. However, the absence of K-π separation is a clear handicap for some *B* physics studies such as the measurement of $\sin(2\alpha)$, where the signal $B_d^0 \rightarrow \pi^+\pi^-$ channel is plagued by other two-body *B* decays involving kaons and protons (see Section 17.2.3). Even a modest (~1σ) K-π separation in the momentum range 4–50 GeV would help to separate statistically the signal contribution. Furthermore, the identification of highly ionising massive particles would be useful in the search for new particles in Gauge Mediated SUSY Breaking scenarios (see Section 20.3).

The design of the TRT allows for some K-π separation due to the significant relativistic rise of the ionisation loss (a factor of ~1.7) and to the high number of straws crossed, even though no pulse-height is measured. Three measurements can be used to estimate the specific ionisation:

the fraction of 'holes' (*i.e.* the absence of low-threshold hits) on a track, the fraction of high-threshold (TR) hits, and the measured drift-distance (both the shift and resolution of the drift-distance depend on the amount of charge deposited in a straw).

In this section, the results of a preliminary study [3-15] are presented. Figure 3-31 shows the probability to observe holes and high-threshold hits; Figure 3-32 shows the shift (and resolution) in the reconstructed drift-distance compared with the true value. Since the reconstruction of hits assumes that the corresponding particle travelled from the collision point at the speed of light, particles which travel more slowly will also give rise to reconstructed hits which are displaced. The ionisation in a given straw depends critically on the distance of closest approach of the particle to the wire and to the crossing angle with respect to the straw axis. Hence the measurements which are made must be parametrised in terms of these two variables in order to extract the specific ionisation.
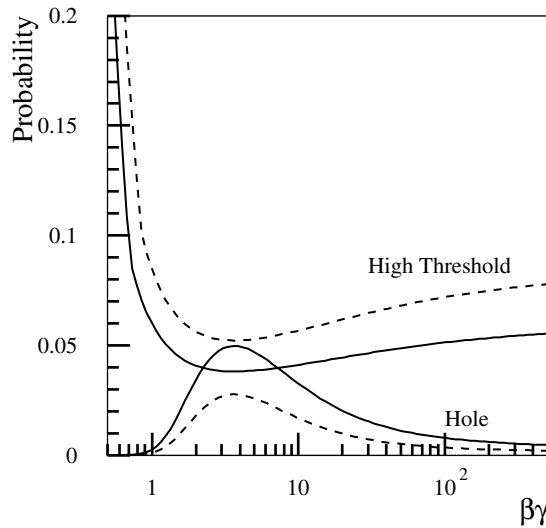
Figure 3-31 Hole and high-threshold hit probability as a function of $\beta\gamma$, for a straw (radius 2 mm) crossed at normal incidence at 1.5 mm (solid line) and 0.5 mm (dashed line) from the wire.
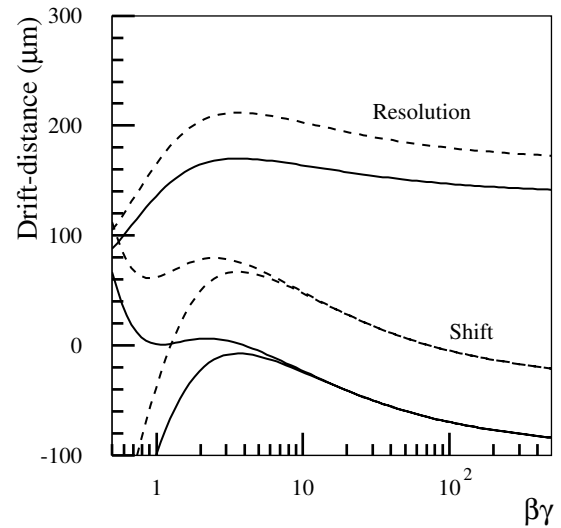
Figure 3-32 Drift-distance shift and resolution as a function of $\beta\gamma$, with the same conditions as in Figure 3-31. For the curves showing the 'shifts', the lower branches make no allowance for time-of-flight, while the upper branches allow for an average flight distance of 150 cm.

To obtain the shift of the measured drift-distance for each straw, the reconstructed drift-distance was compared to that estimated from the track fit where the hit on that straw was excluded from the fit. The resolution on the extrapolation is of the order of 100 µm (for a 5 GeV track), to be compared with the 180 µm drift-distance resolution. The track fit itself is not affected by the $\beta\gamma$ dependence of the drift-distance as it is averaged with the left-right ambiguities. The track crossing angle and closest distance to the wire, the residual on the drift-distance, and the presence of a hole or high-threshold hit for each TRT straw were combined in an unbinned maximum likelihood fit for a given track (more details can be found in [3-15]). The fitted parameter is the logarithm of the 60% truncated-average energy deposit.

The performance of the algorithm was studied using full simulation for single particles with no pile-up, with the straw and electronic response tuned on test-beam data. The resolution for the logarithm of the energy deposit was found to be Gaussian (Figure 3-33) and independent of the momentum. The p-K-π separation depends of the position on the Bethe-Bloch curve (Figure 3-

34) and is best around a momentum (p not p_T) of ~5 GeV. At this momentum, the K-π separation is 0.9σ, while the p-π separation is 1.4σ and the p-K separation 0.5σ. The K-π separation drops to 0.5σ at 30 GeV momentum – this corresponds to a p_T = 5 GeV particle at $|\eta|$ = 2.5. If the drift-distance information alone were used, the separation power would drop by only 10%, indicating that it is the most important single discriminant. Verification of this approach with test-beam data remains to be done, as does the study of the identification of massive slowly-moving particles.
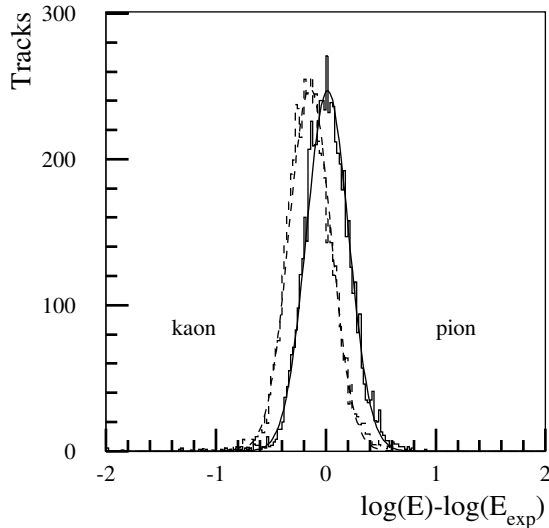
Figure 3-33 Comparison between energy actually deposited by a charged particle and the expected energy corresponding to a pion mass hypothesis, for p_T = 5 GeV pions (dashed line) and kaons (solid line).
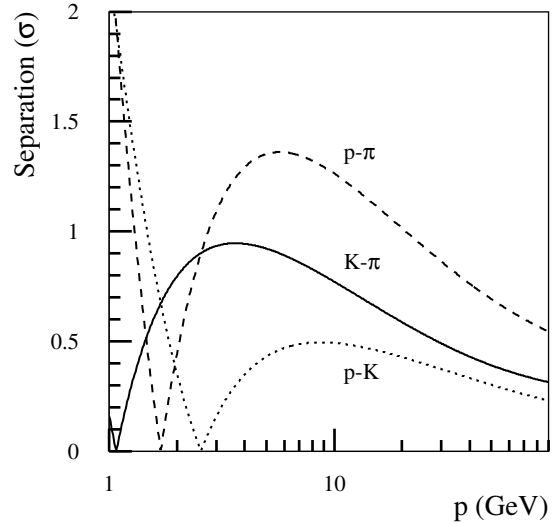
Figure 3-34 K-π, p-π and p-K separation as a function of momentum.

3.5 Pattern recognition

The performance of the pattern recognition programs was extensively analysed in Chapter 5 of the ID TDR [3-1] and [3-6]. To a large extent it has been found that iPatRec and xKalman give similar performance, implying that what was being studied arises from the design of the detector, the interactions of particles with the detector and the topology of the events being considered. More recently, tests were made with ASTRA (see Section 3.1.2), which gives results which are strongly correlated with those of iPatRec.

3.5.1 Isolated tracks

3.5.1.1 Basic results

The reconstruction efficiency for muons is determined mainly by the quality cuts (see Section 3.1.3), while for pions and electrons, it depends strongly on the interactions which the particles have with the detector and the magnetic field. It is important to contrast the efficiencies for track finding with some measure of the number of bad tracks found. Fake tracks are defined as those where ≤50% of the hits come from a single particle or which are associated with a

particle to which another reconstructed track is already associated. Even at high luminosity, the rate at which the pattern recognition programs reconstruct fake tracks which pass the quality cuts is very low: typically three orders of magnitude less than the rate of pile-up tracks and this can be reduced further by cutting on the TRT information. In addition to fake tracks, spoilt tracks are defined as those tracks whose reconstructed parameters are distorted by the inclusion of incorrect hits. For isolated tracks, these effects are generally less than those arising from interactions or bremsstrahlung (see Section 3.3.2).

Figure 3-35 shows the track reconstruction efficiency at low luminosity for isolated muons, pions and electrons of various p_T's (the efficiencies, averaged over $|\eta|$, are summarised in Table 3-2). The first three plots are shown for the basic track quality cuts. The muons and pions are not strongly affected by the requirement of TRT hits for the extended track quality cuts; by contrast, the electrons are strongly affected due to the effects of bremsstrahlung – their efficiency after the TRT cut can be seen from the last plot. The efficiencies are derived from xKalman. Since iPatRec does not start from the TRT, it is less susceptible to interactions in the Precision Tracker, and tends to result in somewhat higher efficiencies. Nevertheless, after the application of a TRT cut, the two programs give comparable results. The results presented in Figure 3-35, should be taken as indicative, since only in the case of decays of massive objects to leptons would one expect to find well isolated tracks and further, the efficiencies depend strongly on the algorithms used and the cuts applied. The single particle efficiencies have been parametrised as a function of p_T and $|\eta|$ [3-12] so that they can be used for fast simulation with the ATLFAST package.

Table 3-2 Summary of reconstruction efficiencies (xKalman) corresponding to Figure 3-35, averaged over $|\eta|$.

p_T (GeV)	Reconstruction Efficiency (%)			
	Basic Cuts			Extended Cuts
	Muon	Pion	Electron	Electron
200	98.6	94.9	95.9	94.8
5	98.2	89.5	90.4	84.4
1	96.8	84.0	76.4	69.4

3.5.1.2 Effect of pile-up

It was shown in Chapter 5 of the ID TDR that the pattern recognition performance depends little on the presence of pile-up at high luminosity. Despite high occupancies at high luminosity (10–40%), the TRT continues to function well for pattern recognition even in stand-alone mode, due to the large number of straws (this is illustrated in Figure 12-2 of [3-2]).

3.5.1.3 Effect of detector noise

Figure 3-36 shows the fake rate at high luminosity and the reconstruction efficiency for single tracks as a function of the fraction of noisy strips in an SCT module. The fake rates are shown for relaxed cuts in order to have an observable number of fakes. If the cut on the number of precision hits is tightened from 7 to 9, then the fake rate falls by an order of magnitude. The rates are shown for $p_T > 5$ GeV; they are a factor of ~3 higher for $p_T > 2$ GeV. The fake rate rises dramatically with the fraction of noisy strips, and for ~1% noisy strips (albeit with the relaxed cuts of ≥ 7 precision hits)), approaches the rate of real pile-up tracks with $p_T > 2$ GeV (2×10^{-2} in
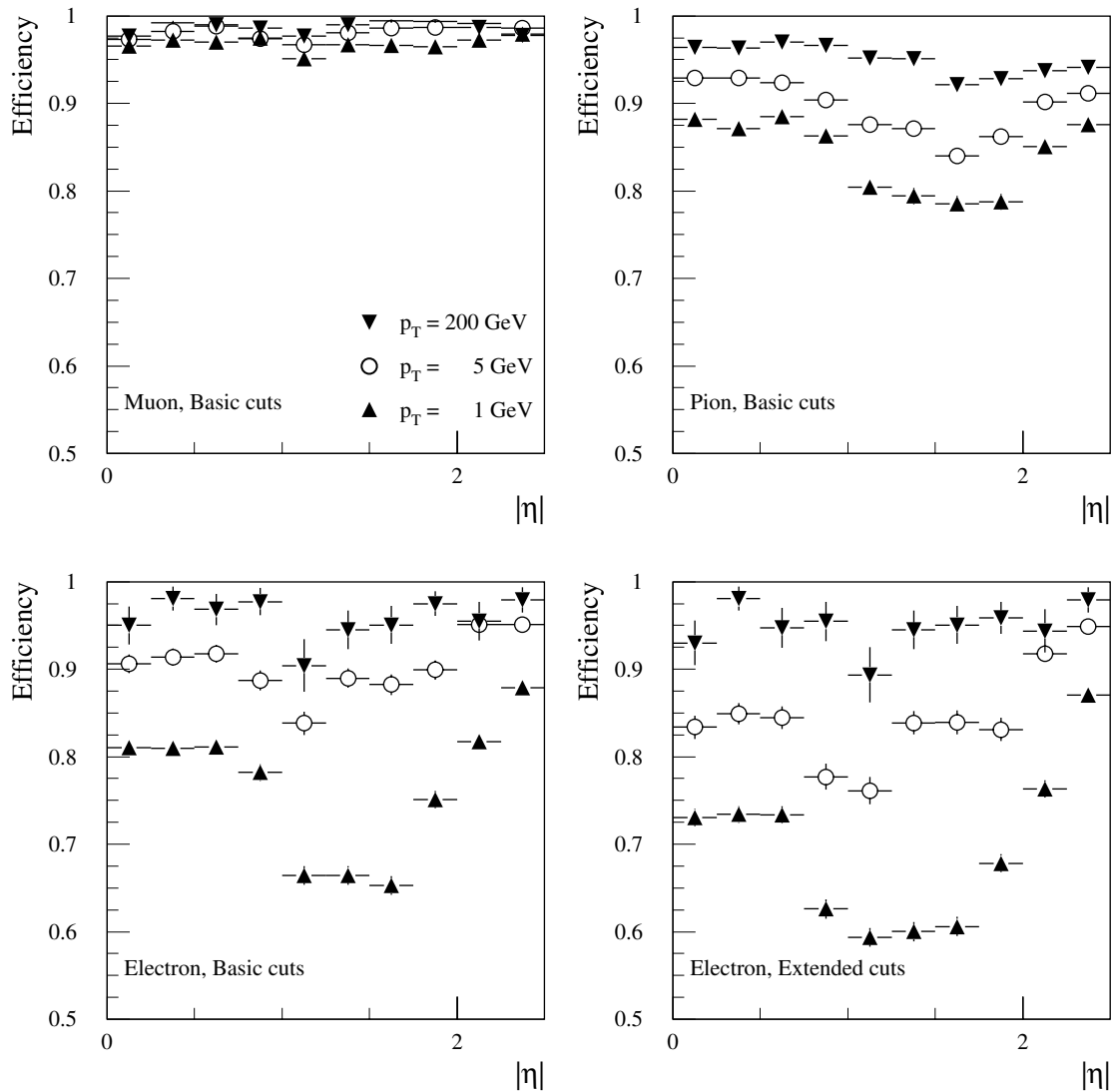
Figure 3-35 Track reconstruction efficiencies as a function of |η| for muons, pions and electrons with basic cuts and for electrons with extended cuts (see Section 3.1.3). Efficiencies are shown for tracks of p_T = 1, 5 and 200 GeV (xKalman).

$\Delta\eta \times \Delta\phi = 0.2 \times 0.2$). In practice the noise occupancy is expected to be $O(10^{-4})$ (see Figure 11-67 of [3-2]). However, should the noise increase, the thresholds will be raised to restore the low occupancy. Figure 3-37 shows the consequences of increased noise where the thresholds are set to four times the rms of the noise. It is clear from the figure, that by adjusting the threshold, the fake rate can be kept at an acceptable level without significant loss of efficiency. In the case that the detectors suffer significant radiation damage, the output signals will be reduced and the signal-to-noise ratio will need to be optimised more carefully. More details on the effect of noise in the SCT can be found in [3-16].

Figure 3-36   Fake   rate   in $\Delta\eta\times\Delta\phi = 0.2\times0.2$
($p_T > 5$ GeV)   and   reconstruction   efficiency
($p_T = 20$ GeV muons) as a function of the fraction of
noisy strips in an SCT module (iPatRec).

Figure 3-37   Fake   rate   in $\Delta\eta\times\Delta\phi = 0.2\times0.2$
($p_T > 5$ GeV)   and   reconstruction   efficiency
($p_T = 20$ GeV muons) as a function of the noise in the
SCT strips (with a variable threshold) (iPatRec).

3.5.1.4 Effect of detector inefficiencies

Figure 3-38 shows the effect of reduced efficiency of the SCT strips, allowing for intrinsic efficiency, bonding faults, faults in the electronics *etc*. The pixel efficiency is held constant at 97%. The design SCT strip efficiency is ≥97%. It can be seen that the pattern recognition is fairly insensitive to variations in the SCT strip efficiency, although if the pixel efficiency is varied at the same time, it is found that there are significant losses arising from the insistence on a *B*-layer hit. In practice, should the efficiency of a module fall below ~90%, it may be replaced or removed from analysis by fiducial cuts. More details on the effect of inefficiencies in the SCT can be found in [3-16].

Figure 3-38   Fake   rate   in $\Delta\eta\times\Delta\phi = 0.2\times0.2$
($p_T > 5$ GeV)   and   reconstruction   efficiency
($p_T = 20$ GeV muons) as a function of the efficiency of
SCT strips (iPatRec).

3.5.1.5 Effect of removal of layers

In an effort to reduce material in the ID, layouts with one less layer of silicon were examined [3-6]. These studies also served to highlight the consequences of large regions of the precision tracker becoming inefficient. Most of the emphasis was on *b*-tagging, as is discussed in Section 10.5.2. In a study of the electron efficiency after the LVL2 trigger, it was found that if one layer of silicon was removed, the efficiency resulting from the use of just the silicon could be maintained by adjusting the track cuts. However there was a ~40% increase in the background

rate from jets. If the TRT was included, then there was little degradation in the trigger performance. In a second study of K_s^0 reconstruction, it was estimated that if one SCT layer were removed, the acceptance would fall by ~5%.

3.5.1.6 Effect of misalignment

The targets for the alignment uncertainties of the ID detector elements are typically less than half of the intrinsic resolution of the devices (see Chapter 9 of [3-1]). To a large extent these should be achieved by surveying techniques and *in situ* monitoring. The alignment will be verified and improved by using tracks from *pp* collisions (see Section 3.7). To ensure that tracks can be found in the first place, the internal cuts used by the pattern recognition programs will need to be loosened. However, after an initial alignment has been completed, the remaining misalignments should be sufficiently small so as not to perturb the pattern recognition.

3.5.1.7 Recent changes to the pattern recognition programs

The ID pattern recognition programs have been undergoing continuous revision. Since the writing of the ID TDR and the studies reported above, the changes which have occurred have had the largest effects on the fake rates. In particular, xKalman was modified to give increased efficiency for conversion electrons and daughters of V^0's. This led to an increased fake rate when applying loose cuts on the number of precision hits. To compensate for this, additional quality cuts were applied for some recent studies. These cuts are: there should be no shared hits in the Precision Tracker, and the fit χ^2 should be less than 2 per degree of freedom.

Figure 3-39 shows the fake rates and track finding efficiency as a function of the number of precision hits required on a track using the latest version of xKalman. The shape of the efficiency curve is similar to that shown in the
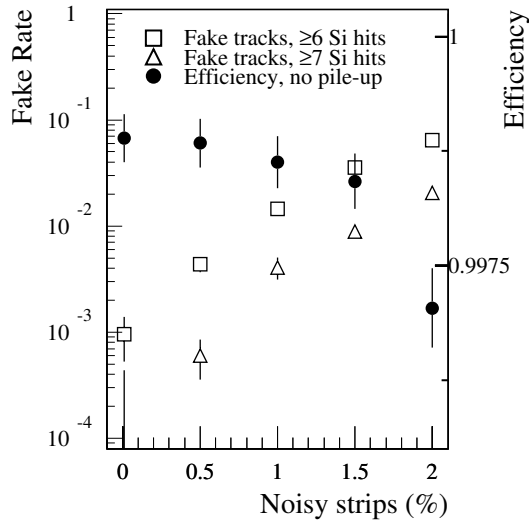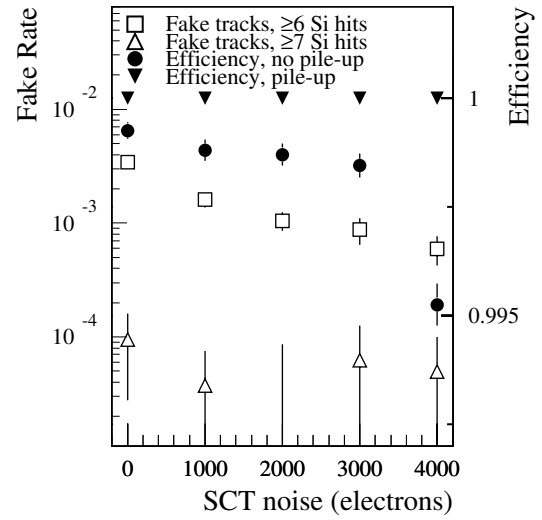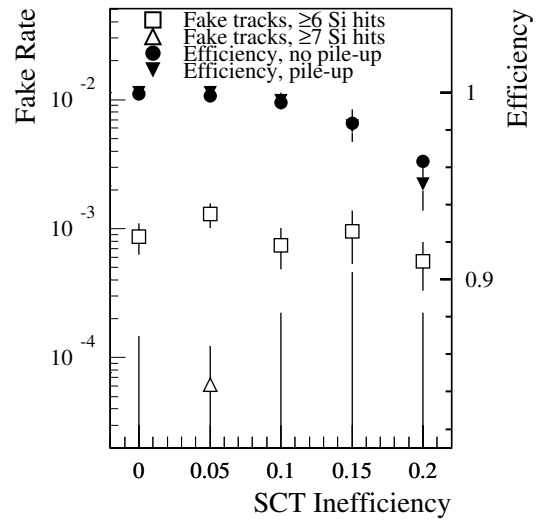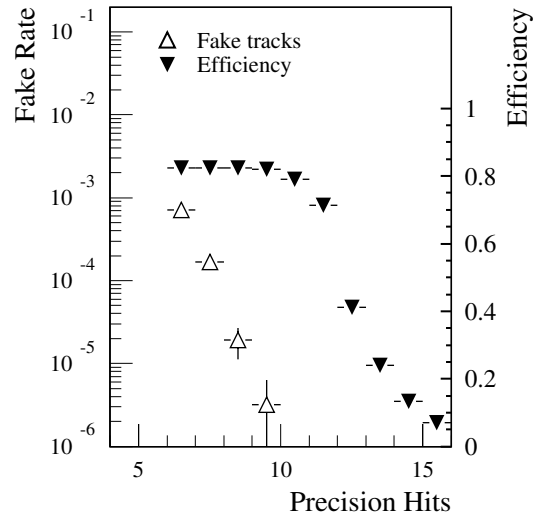

Figure 3-39 Fake rate in $\Delta\eta\times\Delta\phi = 0.2\times0.2$ ($p_T > 2$ GeV) and reconstruction efficiency ($p_T > 3$ GeV) as a function of the number of precision hits (6 to 15) (xKalman).

ID TDR. However, the fake rate in a cone $\Delta\eta\times\Delta\phi = 0.2\times0.2$ falls more rapidly. Requiring at least six hits on a track leads to a fake rate of 7×10^{-4} compared to 3×10^{-4} reported in the ID TDR. However, requiring at least nine hits on a track leads to a fake rate of 3×10^{-6} compared to a rate of 3×10^{-5} reported in the ID TDR. Similar effects are seen for both xKalman and iPatRec in the *b*-tagging studies (see Section 10.2.2), where it is shown for the *b*-tagging cuts (at least nine precision hits), that the rate of fakes and secondaries is reduced using the latest programs, compared to the versions of the programs which were used for the ID TDR.

3.5.2 Tracks in jets

3.5.2.1 Basic results

Obviously the performance of the pattern recognition depends critically on the density of tracks in a jet, which in turn depends on the energy of the jet. Throughout the studies carried out recently, jets from 400 GeV Higgs bosons forced to decay to $q\bar{q}$ have been used to provide benchmarks. All tracks with $p_T > 1$ GeV and within a cone of $\Delta R < 0.4$ around the jet axis were analysed.

Figures 3-40 and 3-41 show respectively the reconstruction efficiency and the probability of fake tracks as a function of $|\eta|$ obtained by ASTRA (see Section 3.1.2). The effects of the material distribution are clear in these figures. The average track reconstruction efficiency over all $|\eta|$ is 87–90% and the average fraction of fakes is 0.1–0.4% – the ranges come from the comparison of different pattern recognition programs (see [3-6]). Figure 3-42 shows the reconstruction efficiency as a function of the distance from the jet-axis. The axis is determined from the initial *b*-quark direction – due to gluon radiation, this choice of axis causes the distribution to be smeared with respect to what would be seen with respect to the final quark direction. Figure 3-43 shows the efficiency as a function of the track p_T.
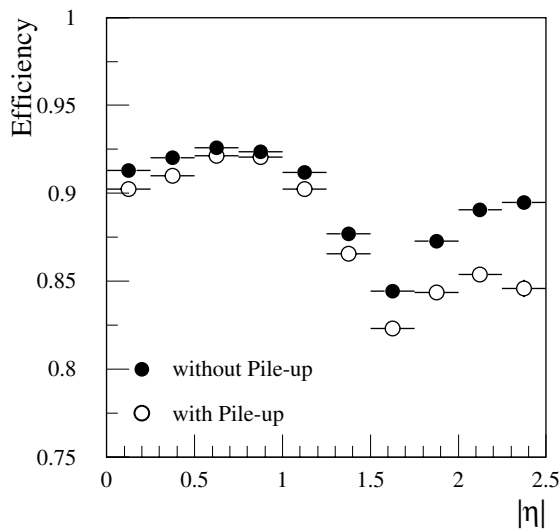
Figure 3-40 Track reconstruction efficiency as a function of pseudorapidity without and with pile-up at high luminosity for tracks in a jet (ASTRA).
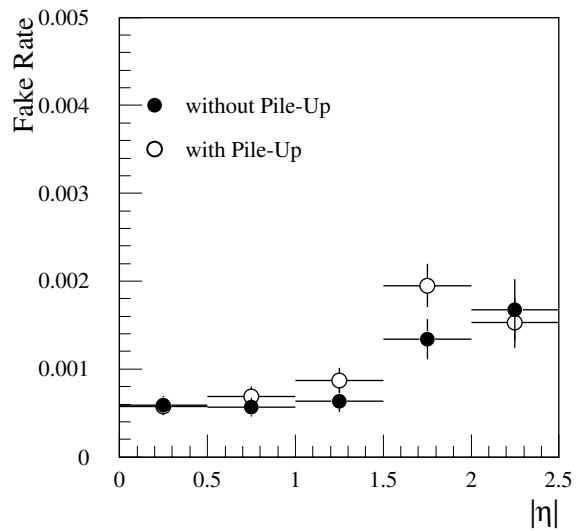
Figure 3-41 Fake rate as a function of pseudorapidity without and with pile-up at high luminosity for tracks in a jet (ASTRA).

3.5.2.2 Effect of pile-up and detector degradation

Table 3-3 shows a summary from [3-6] of the effect of various degradations on the pattern recognition performance. The consequences for *b*-tagging are discussed more extensively in Section 10.5. As well as basic efficiencies and rates, the fraction of tracks with bad hits (see [3-6] for definition) and the fraction in the tails (beyond ±3σ) are given. Those tracks in the d_0 tails can have a significant effect on the *b*-tagging performance. Along with the default conditions at low
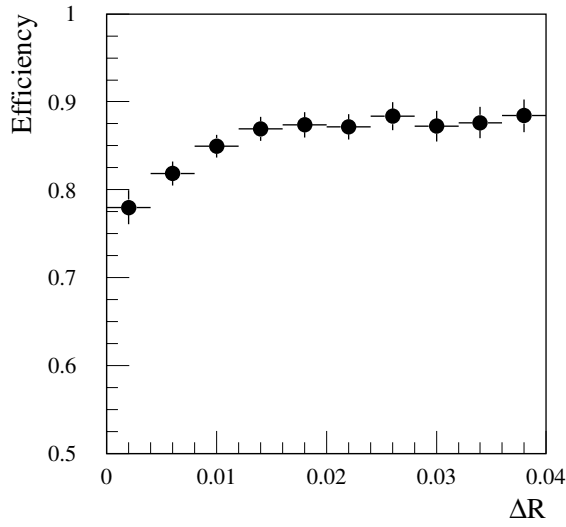
Figure 3-42 Track reconstruction efficiency as a function of distance from jet-axis for tracks in a jet (xKalman).
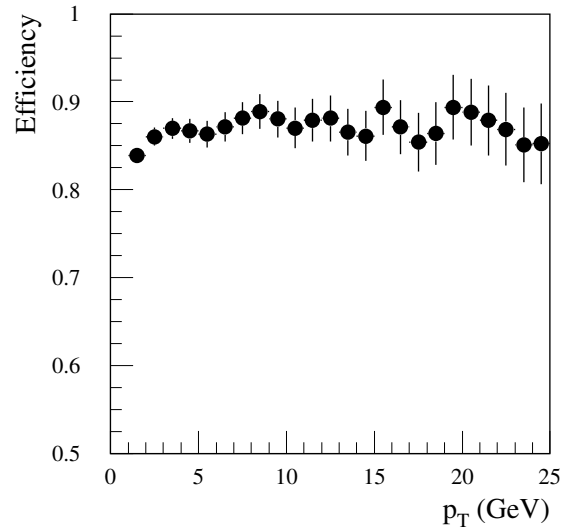
Figure 3-43 Track reconstruction efficiency as a function of track p_T for tracks in a jet (xKalman).

luminosity, the effects of pile-up at 10^{34} cm^{-2}s^{-1}, reduced silicon detector efficiency of 90% (default is 97%) and the effects of removing a middle layer of Pixels or the SCT have been considered.

It is not surprising that the effect of pile-up is not great, since the local occupancy arising from the tracks in jets of $p_T \sim 200$ GeV is typically three times that arising from pile-up tracks (see Tables 3-14 and 3-15 in [3-1]). Likewise, occupancy from noise hits is unlikely to be a problem since the pattern recognition problems are dominated by the proximity of tracks from the jet itself.

Table 3-3 Summary of the pattern recognition performance for tracks with $p_T > 1$ GeV in u-jets of $p_T \sim 200$ GeV (xKalman). The primary efficiency is the efficiency to reconstruct tracks belonging to the jet; the secondary rate is the fraction of reconstructed tracks coming from secondary interactions; the fake rate is the fraction of reconstructed tracks not associated with real particles. Results are shown for the default layout, with pile-up added at a luminosity of 10^{34} cm^{-2}s^{-1}, with reduced silicon efficiency and with silicon layers removed. More details can be found in [3-6].

	Default	With pile-up	$\varepsilon_{Si} = 90\%$	Remove Pixel layer	Remove SCT layer
Primary efficiency (%)	89.5	87.7	83.9	89.3	89.0
Secondary rate (%)	3.3	3.5	3.1	3.6	3.7
Fake rate (%)	0.24	0.31	0.27	0.36	0.46
Tracks with bad Pixel hits (%)	4.7	5.1	4.9	8.2	4.9
Tracks with >20% bad Si hits (%)	2.3	3.8	3.6	5.9	4.6
Tracks in $1/p_T$ tails (%)	1.9	2.2	2.2	2.3	2.1
Tracks in d_0 tails (%)	1.9	2.1	2.4	3.2	2.0

Degrading the silicon efficiency to 90% has a significant effect on the reconstruction efficiency and on the d_0 tails. The ID is fairly robust to the loss of large regions of a single SCT layer, but the performance degrades significantly if a Pixel layer is lost. Of course, significant losses of modules in the *B*-layer would have dramatic effects for all physics related to displaced vertices.

3.5.3 Effect of improved TRT simulation

For all of the studies performed to date, including all those shown in this report, TRT hits from out-of-time beam-crossings have been treated as if they originated from in-time collisions (the standard simulation). In this section, the validity of this approximation is compared with what would be expected using the complete time-of-flight information.

3.5.3.1 Changes to the TRT digitisation

Details of the complete simulation can be found in Section 3.7.2 of the ID TDR. Since the time of the ID TDR, two improvements were made to the simulation of the TRT digitisation. Firstly, the energy dependence of the signal shape was included. Secondly, the TRT low threshold was modified to match the hit efficiency found in test-beam.

A new algorithm was implemented for the complete simulation, corresponding to what will be used in the TRT read-out electronics. The new algorithm is based on the fact that all tracks passing through a straw deposit some ionisation near the straw wall which causes the trailing edges of the output pulse to have a very narrow distribution in time (relative to the beam-crossing). The algorithm uses a gate which is 3 TDC bins (9 ns) wide to select this edge. This gate has the effect of considerably reducing the number of hits from out-of-time bunch-crossings which are seen by the pattern recognition programs when the time-of-flight information is used. The consequences for the complete method are that there is a larger chance of drift-time measurements being 'shadowed' by earlier pulses leading to bad or no drift-time information being recorded for a track.

3.5.3.2 Fake track study

A study of the fake track rate was undertaken to compare the standard pile-up method with the complete method using time-of-flight information (see Section 2.3.2). To examine the effect of the improved TRT simulation, xKalman was used because it is sensitive to the TRT digitisation by virtue of starting from the TRT hits using a fast histogramming method. A recent version of xKalman was used in the way described in Section 3.5.1.7. The fake rate was estimated in a cone $\Delta\eta\times\Delta\phi = 0.2\times0.2$ for tracks with $p_T > 2\,\text{GeV}$. A corresponding track efficiency was found for 'good' tracks, *i.e.* tracks which were in-time, with $p_T > 3\,\text{GeV}$ and came from the minimum bias collisions.

Figures 3-44 and 3-45 show the fraction of drift-time hits found on good and fake tracks using the standard pile-up simulation and using the complete simulation respectively. To be considered, drift-time hits were required to be within $\pm2.5\sigma$ of the position expected from the fit to the complete track. There is a large difference between the distributions for good tracks compared to those for fakes. Comparing the different pile-up simulations, it can be seen that the mean number of drift-time hits is about 15% less using the complete simulation, since it provides a
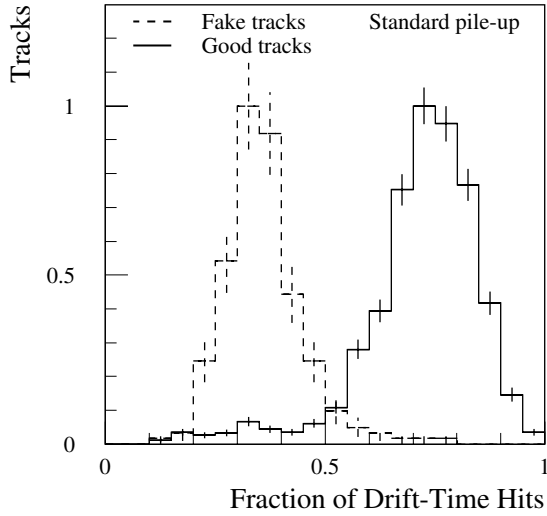
Figure 3-44 Fraction of drift-time hits for good tracks with $p_T > 3$ GeV and fake tracks with $p_T > 2$ GeV using the standard pile-up method. All tracks are required to have ≥6 precision hits. The normalisation is arbitrary.
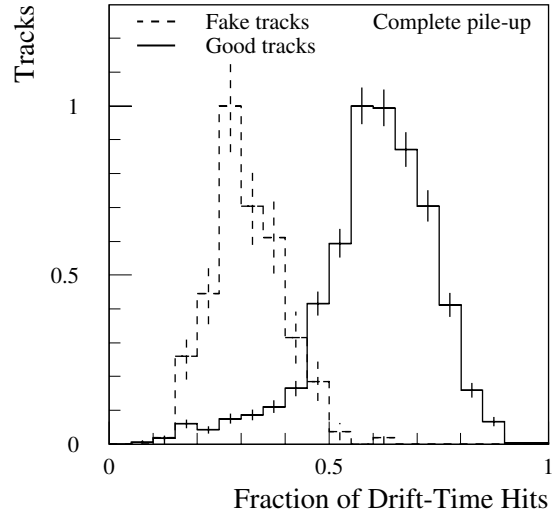
Figure 3-45 Fraction of drift-time hits for good tracks with $p_T > 3$ GeV and fake tracks with $p_T > 2$ GeV using the complete pile-up method, incorporating time-of-flight information. All tracks are required to have ≥6 precision hits. The normalisation is arbitrary.
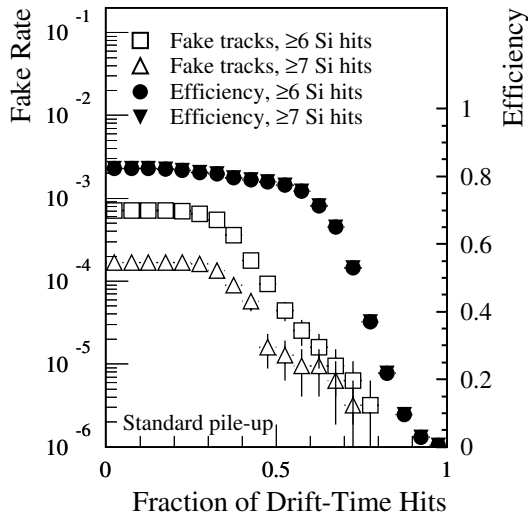
Figure 3-46 Fake rate in $\Delta\eta \times \Delta\phi = 0.2 \times 0.2$ ($p_T > 2$ GeV) and reconstruction efficiency ($p_T > 3$ GeV) as a function of the fraction of drift-time hits (xKalman). Distributions correspond to standard pile-up simulation.
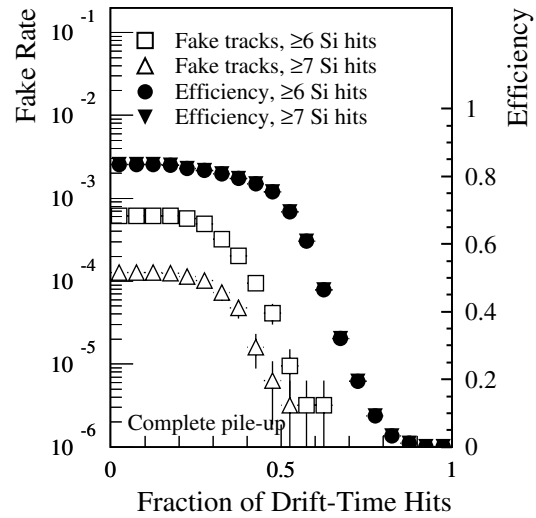
Figure 3-47 Fake rate in $\Delta\eta \times \Delta\phi = 0.2 \times 0.2$ ($p_T > 2$ GeV) and reconstruction efficiency ($p_T > 3$ GeV) as a function of the fraction of drift-time hits (xKalman). Distributions correspond to complete pile-up simulation using time-of-flight information.

better description of the shadowing of the hits of interest by earlier pulses. Nevertheless, the total number of straw hits found on a track (regardless of whether a leading edge can be identified or not) changes by only about 3%.

Figures 3-46 and 3-47 show the track finding efficiencies and fake rates using the standard pile-up simulation and using the complete simulation respectively. Tracks are found with a slightly higher efficiency (1.5%) in the complete pile-up sample because it is possible to use the narrow gate level gate to exclude out-of-time hits. The fake rates generated by the complete pile-up

method are ~20% lower than using the standard method. Some of the reduction in fake rate may be partially as a result of the reduced number of valid drift-time hits. Using the complete method, both the fake rate and efficiency fall off more rapidly as a function of fraction of drift-time hits than they do using the standard pile-up method.

3.5.4 The effect of the solenoidal field

The analytic calculations of Section 3.3.1 indicate that the reduced magnetic field in the outer regions of the ID will lead to reduced track parameter resolution, especially in the case of the transverse momentum. However, to first order, no degradation in the performance of the pattern recognition is expected since the hit density will be little changed.

xKalman has been upgraded from Fortran to C++ and allowance has been made for the non-uniform B-field which is created by the solenoid. The improved program uses Runge-Kutta extrapolation techniques and, despite the added complexity, is only a factor of 1.5 slower than the Fortran version for a uniform field.

3.5.4.1 Track reconstruction

It is essential to allow for the field non-uniformities when reconstructing tracks, otherwise momenta will be overestimated. If a particle is tracked through the solenoidal field, but reconstructed as if the field were uniform, the shift in $1/p_T$ is a strong function of pseudorapidity, varying between +5% ($|\eta| < 1$) and −10% ($|\eta| > 2$) for p_T's in the range 1 to 20 GeV. Figure 3-48 shows the fractional difference between the reconstructed and true values of $1/p_T$ as a function of $|\eta|$ when allowance is made correctly for the solenoidal field. The means are systematically displaced from zero with an average over $|\eta| \leq 2.5$ of (0.14 ± 0.02)%. However, this is much less than if the field were assumed incorrectly to be uniform in the reconstruction. Similar effects to those seen in Figure 3-48 are seen with simulations made with a uniform field. Furthermore, the shape as a function of $|\eta|$ is similar to that of the material distribution (see Figure 3-5), suggesting that their may still be some effects related to the material and dE/dx. Work is continuing in this area in order to remove the remaining biases.

Figure 3-49 shows the comparison of the resolutions obtained with the solenoidal and uniform field. The superimposed line is derived from the ratio of the corresponding curves taken from Figure 3-8. It can be seen that the analytic calculation provides a reasonable description of the effects of the non-uniform field. Allowance has been made for the fact that inside the ID cavity, the field will be enhanced by ~5% due to the presence of the iron of the Hadronic Calorimeter.

3.5.4.2 Pattern recognition

If no allowance is made for the fact that particle trajectories in the solenoidal field are different from helices (even allowing for multiple scattering), then there is the likelihood of missing hits on a track and hence of a reduced track efficiency. For p_T = 20 (1) GeV muons tracked through a solenoidal field, but reconstructed as if the field were uniform, the reconstruction efficiency is 95 (82)% to be compared with 98 (97)%, as seen from Table 3-2 corresponding to simulation with a uniform field. However, if allowance is made correctly for the field, there is no difference between the efficiency found in the case of the solenoidal field compared to the case of a uniform field. This confirms that the pattern recognition in the non-uniform field can be undertaken with no loss of performance.
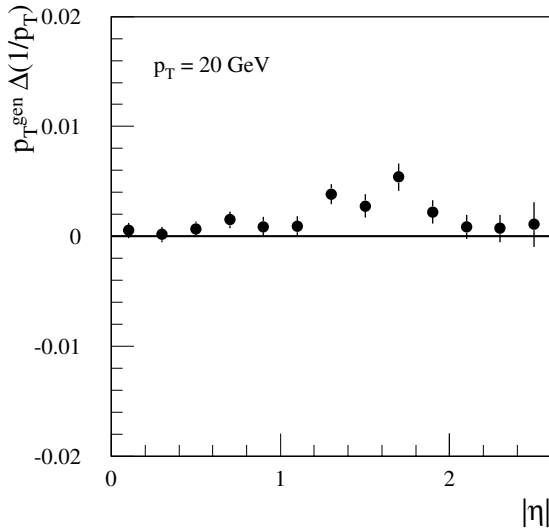
Figure 3-48 Fractional difference between reconstructed and true $1/p_T$ for single 20 GeV muons in a solenoidal *B*-field as a function of pseudorapidity.
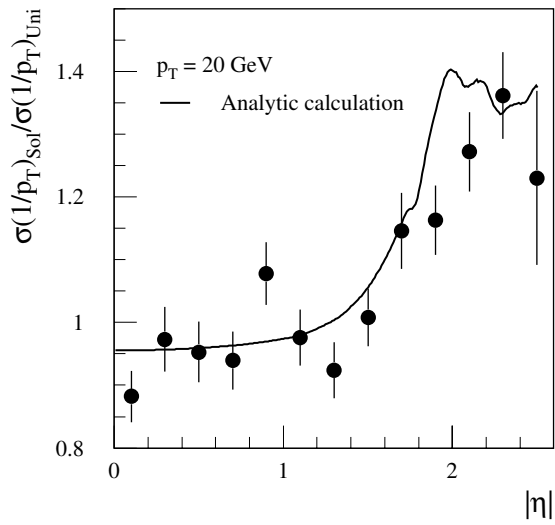
Figure 3-49 Ratio of resolution obtained with a solenoidal field to that with a uniform field for 20 GeV muons. Superimposed is the analytic calculation.

Reconstructing electron tracks is more difficult than muons since the field causes an electron after bremsstrahlung to deviate from the original trajectory. This effect will be reduced in a weaker field. Hence, electron reconstruction should be no more difficult with the solenoidal field than with a uniform one. Further, the difference between the associated calorimeter cluster and the electron impact point in the calorimeter will be less, which will be advantageous for the calorimetric energy measurement.

3.6 Vertex reconstruction

3.6.1 Primary vertex reconstruction

At the LHC, the beam-spot will be described by Gaussian parameters: $\sigma_x = \sigma_y = 15\ \mu m$ and $\sigma_z = 5.6$ cm. For most analyses, this information (especially that in the transverse plane) is already sufficient, but for some analyses, a better knowledge of the position of the primary vertex is desirable.

In Section 6.4 of the ID TDR [3-1], it was shown how, at low luminosity, it is possible to determine the position of the primary vertex on an event-by-event basis by an iterative procedure which tries to fit all the reconstructed tracks to a common vertex, removing at each step those tracks which look inconsistent with the hypothesis that they come from the primary vertex (secondaries from interactions, particles with a lifetime and mismeasured tracks). With this procedure, the primary vertex position resolution becomes basically a function of the total number of tracks (and of their quality) which can be successfully attached to the same vertex. The fitting procedure was found to improve the transverse resolution only for high track-multiplicity events (more than 30 tracks in the primary vertex fit, as in $H \rightarrow b\bar{b}$ events with $m_H = 400$ GeV). Additional improvements can be obtained by combining this method with some other inde-

pendent estimate of the transverse position of the primary vertex, such as the beam-spot position determined on a run-by-run basis (as done in some of the LEP experiments and in CDF [3-17]), by using the d_0-ϕ correlation of the tracks in the event.

Significant improvements in the z-position measurement can be achieved: a resolution in the range 22–50 µm (although with some non-negligible tails) for track multiplicities ranging between 10 and 36. These figures are well inside the ATLAS physics requirements of 1 mm for the resolution of the z-coordinate of the primary vertex [3-18]. A summary of the results for low luminosity is shown in Table 3-4.

Table 3-4 Widths of residual distributions for position measurements of the primary vertex (transverse and longitudinal) for various samples of physics events at low luminosity. The Gaussian widths of the core and the rms's are given.

Sample	σ (µm)		rms (µm)	
	x or *y*	*z*	*x* or *y*	*z*
Minimum bias	31	49	59	72
$H \rightarrow \gamma\gamma$, $m_H = 100$	22	41	32	49
$H \rightarrow b\bar{b}$, $m_H = 400$	10	22	14	27
$B_d \rightarrow J/\psi K_s$	23	35	38	50
$B_s \rightarrow D_s\pi$	23	38	39	51

At high luminosity, the problem of multiple interactions in the same bunch-crossing needs to be addressed. An average of 24 minimum bias pile-up events are expected to be superimposed on a signal event in the Inner Detector. In principle, it is necessary to reconstruct only the signal event, and in some cases, this could be identified easily because minimum bias events will have a smaller charged track multiplicity and a smaller total transverse momentum. Unfortunately this is not always true and in some analyses, the selection of the signal event based on these selection criteria might introduce dangerous biases. Therefore, it would be preferable to reconstruct as many as possible of the primary vertices in an event and leave the identification of the primary vertex of the signal event for later in the analysis chain when more sophisticated information is available (including the presence of leptons, photons, jets, b-jets, τ's, *etc.*).

A generalisation of the algorithm used in the low luminosity case has been developed [3-14]. In a first step the algorithm assumes that all tracks are coming from the beam-line in the transverse plane (this is a good approximation due to the small transverse beam-spot size) and determines the z-coordinate of each track. Each of these values constitutes an entry in a histogram with a 500 µm bin size. This histogram is then scanned to look for locations where the tracks cluster as they should do if they are coming from the same vertex. A minimum of four tracks is required to define a cluster. For each cluster, the corresponding tracks constitute the input to the same algorithm used at low luminosity. If the fit is successful, the vertex is retained.

The algorithm was applied to a sample of H $\rightarrow \gamma\gamma$ events with $m_H = 100$ GeV. Reconstructed charged tracks were selected using the same quality cuts described in Section 6.4 of the ID TDR; the only difference was that a higher track p_T threshold (1 GeV instead of 0.5 GeV) was applied.

In Figure 3-50, an example of the histogram of the *z*-coordinate of the tracks for one beam-crossing is shown. The *z*-coordinate of the reconstructed tracks (bottom) is compared to the distribution of the *z*-coordinate of particles (top). The arrow on the upper histogram indicates the signal event. In this example, it can be seen that the signal event is associated with the cluster which has the highest track multiplicity, however, this is not always true.
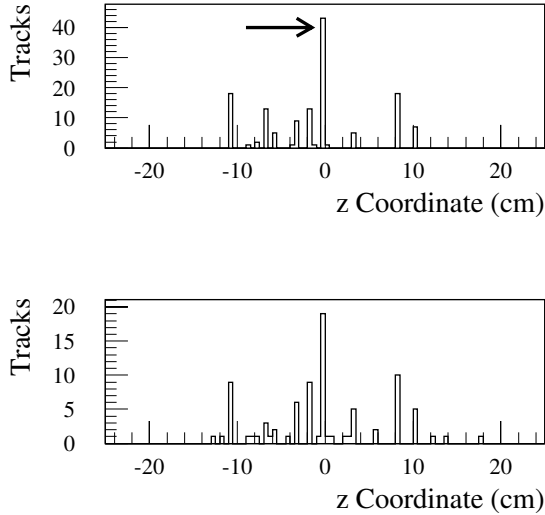
Figure 3-50 Distribution of the intersection of the tracks with the *z*-axis for one particular beam-crossing at high luminosity at particle level (top) and after reconstruction (bottom). The arrow indicates the $H \to \gamma\gamma$ vertex.
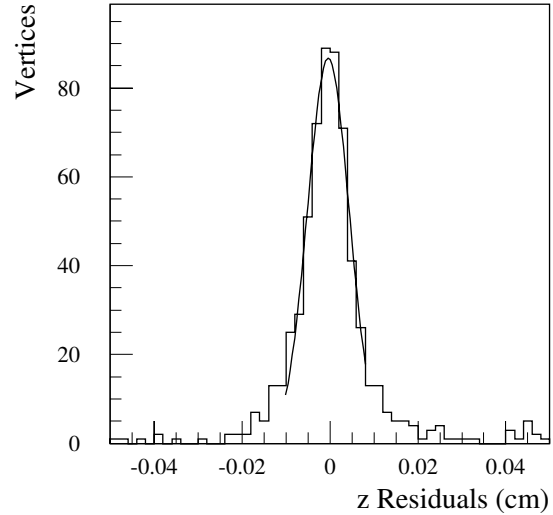
Figure 3-51 Residuals on the *z*-measurement of the primary vertex for $H \to \gamma\gamma$ with pile-up. Superimposed is a Gaussian fit to the core of the distribution.

On average, the algorithm reconstructs five primary vertices at high luminosity. This number is considerably lower than the ~25 vertices present in one beam-crossing. This difference is due to track losses resulting from the 1 GeV p_T cut as well as the fact that some of the vertices merge. With a requirement of a minimum of two tracks to define the primary vertex, the primary vertex of the signal event is found in the list of reconstructed vertices 72% of the time. The *z*-resolution is about 48 µm with an rms of 106 µm, compared to values of 41 µm and 49 µm, respectively, observed on the same sample at low luminosity. The residual distribution for the *z*-coordinate of the reconstructed primary vertices is shown in Figure 3-51.

3.6.2 Secondary vertices

3.6.2.1 *V⁰* reconstruction

The reconstruction of the decay $K_s^0 \to \pi^+\pi^-$ was studied in Section 6.5 of [3-1]. The reconstruction of such decays is difficult due to the long lifetime of the K_s^0, which leads to tracks with reduced numbers of silicon hits and large impact parameters.

The previous studies were performed using single K_s^0's of fixed p_T (3, 5 and 7 GeV), distributed uniformly in the interval $|\eta| \leq 2.5$. Due to the importance of K_s^0 reconstruction for *B* physics and, in particular, for the decay $B_d^0 \to J/\psi \, K_s^0$ (see Section 17.2.2), the reconstruction has now been studied in the context of B_d^0 decays (in the absence of pile-up).

The analysis was performed using 15,000 $B_d^0 \to J/\psi \, K_s^0$ events generated with PYTHIA and fully simulated using GEANT. The average p_T of the K_s^0's was 4.7 GeV. Charged tracks were reconstructed using xKalman, down to a minimum p_T of 0.5 GeV for $|\eta| \leq 2.5$. The analysis was similar to that performed previously, except that a minimum of six precision hits was required. This choice allowed the reconstruction of K_s^0's up to a decay radius of 37 cm in the barrel region. The algorithm for finding K_s^0's looped on all pairs of oppositely charged tracks in the event and fitted them in 3D to a common vertex. It was required that the χ^2 per degree of freedom be less than six. Pion masses were assigned to both tracks and the invariant mass calculated. Track pairs were retained if the invariant mass was within $\pm 3\sigma$ of the nominal K_s^0 mass. Finally, to reduce the prompt track background, the reconstructed transverse decay radius of the K_s^0 candidate was required to be greater than 1 cm.

To be compatible with the sin(2β) analysis, all events were subjected to all trigger and selection cuts used in the B_d^0 analysis to reconstruct a J/ψ. The cuts used to select K_s^0 candidates effectively defined a fiducial region inside the ID in which decays could be reconstructed: $1 < R < 37$ cm and $|z| < 210$ cm. The K_s^0 reconstruction efficiency was defined as the fraction of events with a reconstructed J/ψ where the true K_s^0 from the B_d^0 decay was correctly reconstructed and satisfied the various selection cuts. The total efficiency is 41.1% which includes: the acceptance for K_s^0's with a decay inside the fiducial region of 68.6%, the xKalman reconstruction efficiency for the two pion tracks of 76.9% and the effect of cuts on reconstructed K_s^0 candidates of 77.8%. If the cut on the number of precision hits is relaxed to four, then the corresponding efficiencies are: 41.4% (total) and 73.4%, 74.9% and 75.3% respectively – the acceptance is increased but the quality of the reconstruction is decreased. This definition of efficiency is different from that used in [3-1] but more useful for the studies of Section 17.2.2, since in the ID TDR, the efficiencies were normalised to decays with $1 < R < 44$ cm for which the tracks were reconstructed. The total reconstruction efficiency is shown as a function of the K_s^0 decay radius and of the K_s^0 pseudorapidity in Figures 3-52 and 3-53, respectively. The reconstruction efficiency falls from a maximum of 70% where the decay is in the Pixel volume to close to zero at the outer radius of the fiducial volume where pions, even if they can be reconstructed, fail the selection cuts. It can be seen that there is a dip in the efficiency as a function of the K_s^0 pseudorapidity in the overlap region between the barrel and the end-cap.

Figures 3-54 and 3-55 show the mass and decay radius resolution as a function of the decay radius. The mass resolution varies between 4.5 and 7 MeV in the fiducial volume. It is affected mainly by the reconstruction of momenta and angles which are well determined by the tracking layers beyond the decay vertex and hence are less sensitive to the position of the decay. As expected, the decay radius resolution depends strongly on the radius of the decay and is much better for decays just in front of the Pixel layers, but is worse for decays inside the SCT, which has poorer $R\phi$ resolution, especially in the absence of R-z measurements from the Pixels.

3.6.2.2 Lifetime measurements

Measurements of vertices displaced by O(1) mm from the primary vertex will be essential for *B* physics (see Chapter 17), *b*-tagging (for example $H \to b\bar{b}$) (see Chapter 10) and lifetime measurements. In the Pixel TDR [3-3], it was shown that a resolution of the proper time of 0.073 ps could be obtained – this is discussed more in Section 17.3. It may be possible for ATLAS to make
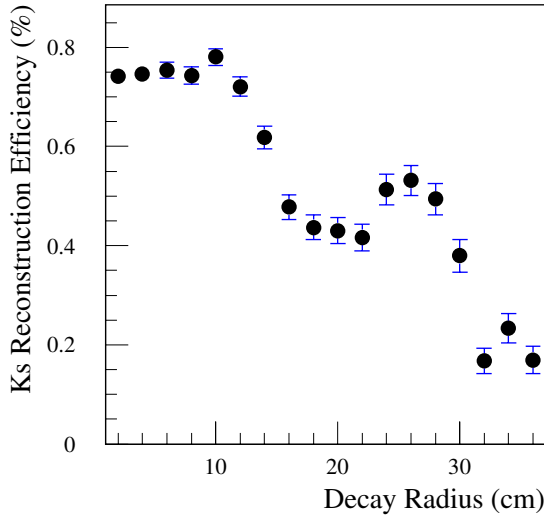
Figure 3-52 K_s^0 reconstruction efficiency as a function of decay radius.
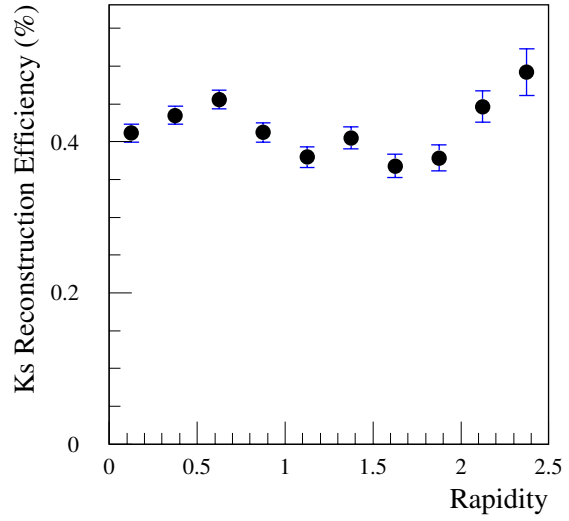
Figure 3-53 K_s^0 reconstruction efficiency as a function of $|\eta|$.
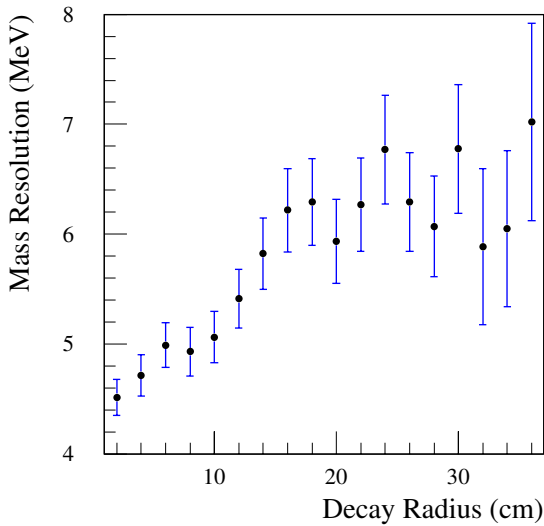
Figure 3-54 K_s^0 mass resolution as a function of decay radius.
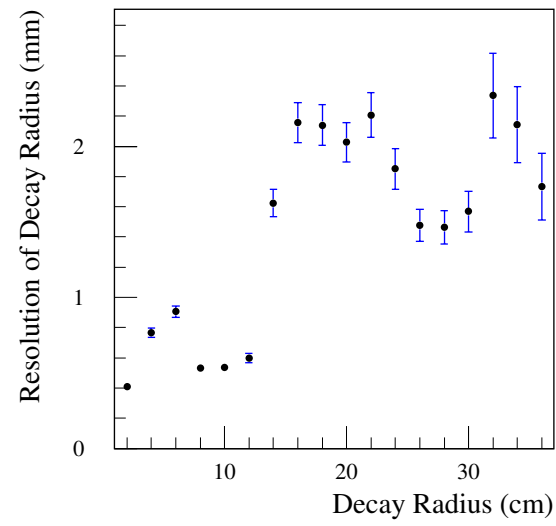
Figure 3-55 Resolution of K_s^0 decay radius as a function of decay radius.

useful measurements of the τ lifetime. Although the ID will be essential for this, the use of the calorimetry to determine the τ momentum will be critical in order to obtain the proper lifetime distributions. This is discussed more in Section 9.3.3.3.

3.7 Alignment

In the ID TDR, the targets for the alignment were such that misalignments should degrade the track parameter resolutions by no more than 20%. This led to requirements that in $R\phi$, the Pixel detectors should be aligned to ~7 μm, while the SCT detectors should be aligned to ~12 μm. The desire to measure the W mass to 20 MeV (see Chapter 16) will necessitate knowing the momentum scale measured by the Inner Detector to ~0.02%. This level of precision will be attained by

calibrating with the Z mass (see Chapter 12). Nevertheless, to be able to control the systematics sufficiently well will require a very good understanding of the alignment. It is plausible that this may require understanding the alignment of detectors in $R\phi$ at the level 1 µm, although this value is very difficult to justify. Achieving this accuracy may seem unrealistic, however it may be sufficient to consider averages in intervals of space and time. Further requirements on the ID motivated by a W mass measurement are discussed in Section 12 and in more detail in [3-19].

Information on alignment of the Inner Detector will come from: the metrology of individual modules at the time of construction, the system tests of sets of modules, surveys of the completed barrels and wheels (in particular, from the X-ray survey), and the Frequency Scan Interferometry (FSI) which measures a network of lengths *in situ* on the SCT. This information will be used to provide a starting point for the offline alignment using physics events. More details can be found in Chapter 9 of [3-1].

3.7.1 Strategy

The alignment of the ID will inevitably start in the Precision Tracker (Pixels and SCT). After an initial alignment to ensure that tracks can be reconstructed with reasonable efficiency, the alignment between neighbouring modules within single barrels and wheels will be performed using tracks of modest momentum passing through the overlaps. To correct more complex misalignments such as the translation and rotation in 3D of modules and global distortions such as rotations of complete units and radial distortions (*e.g.* elliptical ones), stiffer tracks crossing the complete ID will be needed. In principle, all alignment constants might be determined in a single pass by solving a very large matrix equation, as has been done by ALEPH [3-20] and SLD [3-21]. However, because the ID is so complicated, a great deal of iteration will be needed to accommodate related information. Some effects, such as thermal distortions, have the potential to mask smaller systematics. These will need to be understood by combining data from different runs so that such effects can then be parametrised, for example, as a function of measured temperature or luminosity. This would then allow some systematics to be factorised out of the alignment problem at some level. Having understood the Precision Tracker, the TRT can then be investigated.

3.7.2 Study of alignment in the Precision Tracker

Specialised triggers for alignment are foreseen in the trigger menus (see Section 11.2.6), however these are not considered here. To start to understand the potential for aligning the ID, a study [3-22] was made using single muons of different p_T (45, 6 and 2 GeV), distributed uniformly in $|\eta| < 2.5$. The momenta were chosen to be characteristic of muons from $W \rightarrow \mu\nu$, 6 GeV muons which provide triggers for *B* physics and lower energy particles in triggered events. It is important to allow for multiple scattering when fitting a track in the ID, however, in fitting the scattering angles at each silicon plane, there is a tendency for the fitted track to be pulled strongly by each hit and to minimise the residuals unrealistically, especially at low p_T. Therefore, the residuals between the track fit and the reconstructed hit position on each silicon plane were found by fitting the tracks in the rest of the Precision Tracker with iPatRec, but excluding that plane.

Figure 3-56 shows the width of the $R\phi$ residuals in the middle Pixel barrel. At high momentum, these are a bit larger than the intrinsic resolution (16 µm vs 11 µm). At lower momenta, the residuals are inflated by multiple scattering which increases with $|z|$. The jump around $|z| = 30$ cm comes from falling off the outer pixel barrel and picking up hits on the first pixel

disk. Figure 3-57 shows the width of the $R\phi$ residuals in the middle pixel barrel using the $R\phi$ overlaps. The residuals in the overlaps were found from the difference in the residuals of one module and the overlapping module and are much less sensitive to multiple scattering. The widths should be close to $\sqrt{2}$ times the intrinsic resolution, *i.e.* about 15 μm. It can be seen that there is an oscillatory behaviour as a function of z. This arises since the distributions of the differences of the residuals are not Gaussian but show some signs of the discrete nature of the pixel measurements.
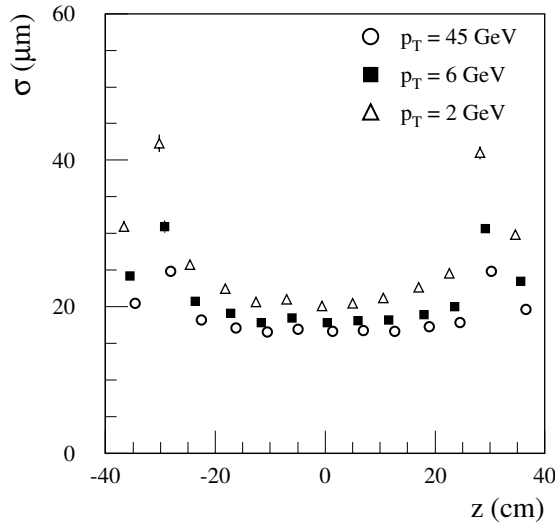
Figure 3-56 Width of $R\phi$ residual distributions in modules of the middle pixel barrel layer as a function of the position of the module. (Points are offset horizontally to avoid overlapping.)
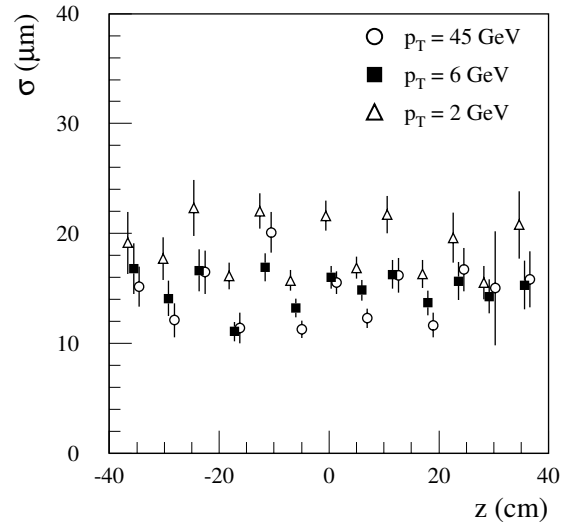
Figure 3-57 Width of $R\phi$ residual distributions using R-ϕ overlaps in the middle pixel barrel layer as a function of the position of the module. (Points are offset horizontally to avoid overlapping.)

Figures 3-58 (barrels) and 3-59 (end-cap disk and wheels) show the widths of the $R\phi$ residuals in the various pixel and SCT layers. The widths were found from the residual distributions for all hits in a given layer. The residuals in the SCT are typically twice as large as those in the Pixels, reflecting the difference in the intrinsic resolutions: 11 μm vs 22 μm. The averaged residuals in the B-layer are much larger than in the other pixel layers because there are no constraints at lower radii (the same effect is seen in outer SCT barrel) and the modules at large $|z|$ are hit at small angles of incidence leading to large multiple scattering at lower p_T. The residuals seen in the end-caps are comparable to those in the barrel.

The alignment precision which can be achieved after one day of running at low luminosity was derived from the widths of the residual distributions shown in Figures 3-58 and 3-59 and the expected rates. Alignment between layers was studied assuming muons from $W \to \mu\nu$ and $p_T \geq 6\,\text{GeV}$ muons (from the B physics sample) can be used. Alignment within layers requires tracks crossing the overlaps with higher rates to compensate for the smaller solid angle. Since multiple scattering is less important, it was assumed that $p_T \geq 6\,\text{GeV}$ muons and all particles (predominantly pions) with $p_T \geq 2\,\text{GeV}$ in triggered events could be used. Assuming events triggered by $p_T \geq 6\,\text{GeV}$ muons for B physics will be reasonably characteristic of any triggered events, it was found that each event had 10 particles with $p_T \geq 2\,\text{GeV}$ in the absence of pile-up. For the three types of tracks ($W \to \mu\nu$, $p_T \geq 6\,\text{GeV}$ muons and all particles with $p_T \geq 2\,\text{GeV}$) the residuals from the three muon samples ($p_T = 45$, 6 and 2 GeV) were assumed. The corresponding rates at peak luminosity were assumed to be 3 Hz (after triggering and all cuts), 50 Hz (where the $p_T \geq 6\,\text{GeV}$ muon trigger is assumed to take half of the available DAQ bandwidth)
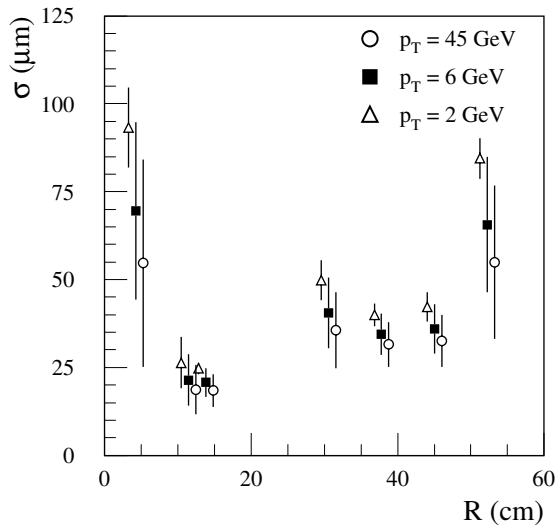
Figure 3-58 Width of $R\phi$ residual distributions in barrels layers, averaged over the complete layer, as a function of the position of the layer. The 'error bars' indicate the spread of measurements from different modules in the same layer. (Points are offset horizontally to avoid overlapping.)
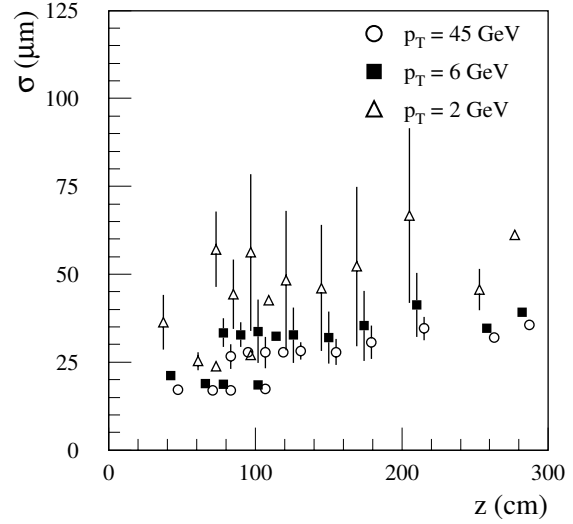
Figure 3-59 Width of $R\phi$ residual distributions in endcap layers, averaged over the complete layer, as a function of the position of the layer. Note that the last pixel disks are at similar positions in z to the first SCT wheels. The 'error bars' indicate the spread of measurements from different modules in the same layer. (Points are offset horizontally to avoid overlapping.)

and 10×100 Hz (allowing for 10 tracks in every event). It was assumed that the running time in one day would be 2×8 hours and that for $W \rightarrow \mu\nu$, the rate of which is limited by the luminosity, a 60% efficiency should be used to allow for the luminosity lifetime. These two effects were accounted for by a scale factor. To make the calculations transparent, a 1% $R\phi$ overlap of the sensitive area for all modules has been assumed (that is 1% on each edge of each module).

The calculations are illustrated for the middle Pixel barrel in Table 3-5, which shows the precision which can be obtained for the $R\phi$ alignment after one day of low luminosity running – more details can be found in [3-22]. A summary of the precisions which can be obtained for the different barrel layers using all the hits in a module is shown in Figure 3-60. The 'error bars' show the spread of the values for the different modules of a given layer arising from different rates and residual distributions. Figure 3-61 shows the precision which can be obtained in the Pixel barrel layers using the overlaps. The results are summarised in Table 3-6. For the averages in the first column (precision for Pixel barrels using complete modules), the B-layer was excluded because of the large variations in the precision arising from modules at large $|\eta|$.

Table 3-5 Components of the calculation of the alignment precision in $R\phi$ which can be obtained in the middle Pixel barrel after one day of low luminosity running. See text for more details.

Type of track	Rate (Hz)	Scale fact	Width of resid. (μm)		Precision (μm)	
			Module	Overlap	Module	Overlap
$W \rightarrow \mu\nu$	3	0.4	19	17	0.9	
Single muons, $p_T \geq 6$ GeV	50	0.66	21	19	0.3	2
Low-p_T tracks, $p_T \geq 2$ GeV	10×100	0.66	26	27		0.8
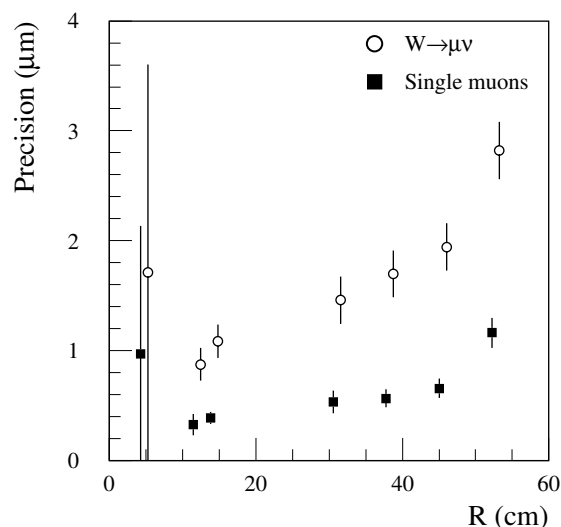
Figure 3-60 Precision which can be achieved after one day of low luminosity running for the $R\phi$ alignment of barrel modules as a function of the position of the layer. Results are shown for different types of tracks — see text for more details. The 'error bars' indicate the spread of measurements from different modules in the same layer. (Points are offset horizontally to avoid overlapping.)
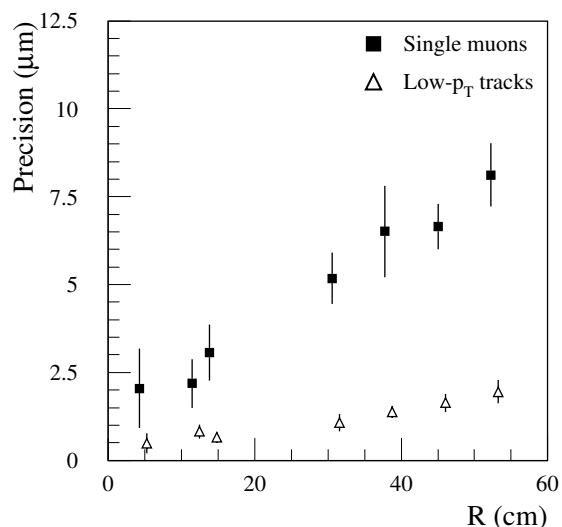
Figure 3-61 Precision which can be achieved after one day of low luminosity running for the $R\phi$ alignment of barrel modules using the $R\phi$ overlaps as a function of the position of the layer. Results are shown for different types of tracks — see text for more details. The 'error bars' indicate the spread of measurements from different modules in the same layer. (Points are offset horizontally to avoid overlapping.)

**Table 3-6** $R\phi$ alignment precisions (μm) which can be obtained after one day of low luminosity running. Results are given for different types of tracks, using both complete modules and the $R\phi$ overlaps.

| Type of Track | Pixels | | | | SCT | | | |
| | Barrel | | End-cap | | Barrel | | End-cap | |
	Module	Overlap	Module	Overlap	Module	Overlap	Module	Overlap
$W \rightarrow \mu\nu$	1.0		1.2		2		1.3	
Single muons	0.4	2.4	0.4	4	0.7	7	0.5	5
Low-p_T tracks		0.7		0.9		1.5		1.0

From Table 3-6, it would seem that at low luminosity it should be possible to align the Precision Tracker to O(1) μm in one day using tracks crossing the complete detector (anywhere in a module) or using the overlaps (assumed to be 1%). The information provided by the overlaps is complementary to that provided by the complete detector and will be sensitive to different systematics. These conclusions must be qualified by several effects which are potentially more significant than some of the steps made in these calculations. There are uncertainties in the cross-sections and efficiencies (trigger and reconstruction) for the different types of tracks which have been considered and in the actual luminosities which will be delivered. The alignment needs to be done in 3D (each module having six degrees of freedom), which may degrade the results of the naive calculations. In addition, there will be other sources of systematics which will need to be understood and these may be greater than 1 μm. The $p_T \geq 6$ GeV muons used to trigger B physics events may be contaminated by π/K decays and such tracks may not be good for alignment. Nevertheless, at the LHC, it is certain that there will be many low-p_T tracks which

will be valuable for alignment with the overlaps and sufficient high-p_T tracks for more global alignment. It would seem that the statistical precision which can be obtained using track-based alignment will allow the more complex systematics in the ID to be studied and corrected.

3.8 Conclusions

Since the ID TDR, the largest changes to the layout have occurred in the Pixel System. Nevertheless, because the intrinsic detector resolutions have not changed significantly and the philosophy of providing at least three pixel measurements on tracks ($|\eta| \leq 2.5$) has been maintained, to a large extent, the expected performance presented in this report is similar to that found at the time of the ID TDR. After two years of refining the engineering design, the material in the active region of the ID has increased by about 5% X_0 to ~48% X_0.

The track resolutions for muons can be described approximately by:

$$\sigma\left(\frac{1}{p_T}\right) \approx 3.6 \times 10^{-4} \oplus \frac{1.3 \times 10^{-2}}{p_T\sqrt{\sin\theta}} \quad (\text{GeV}^{-1})$$

$$\sigma(d_0) \approx 11 \oplus \frac{73}{p_T\sqrt{\sin\theta}} \quad (\mu\text{m})$$

where p_T is in GeV. The effects expected for a solenoidal field have been confirmed using full simulation: there is little change in the $1/p_T$ resolution in the barrel, but at higher pseudorapidity, the resolution degrades, becoming 40% worse at $|\eta| = 2.5$. Nevertheless, good charge determination is maintained up to $p_T = 1$ TeV where the misidentification probabilities are <2% and <5% for muons and electrons respectively.

Systematic comparisons have been made between muons, pions and electrons. While the distributions of reconstructed track parameters of pions are similar to those of muons, electrons suffer from bremsstrahlung. At high momenta, muons can be reconstructed with 99% efficiency, which is limited by the track quality cuts; pions and electrons can be found with efficiencies around 95%. For $p_T = 1$ GeV, the efficiencies to find and reconstruct isolated muons, pions and electrons are 97%, 84% and 76% respectively. These efficiencies are fairly robust to the effects of detector inefficiency and noise as well as pile-up at 10^{34} cm^{-2}s^{-1}. The single particle track parameter resolutions and reconstruction efficiencies have been parametrised for use in the fast simulation, ATLFAST.

The TR performance of the TRT for π/e separation has been re-evaluated in the light of test-beam data. Compared to the performance reported in the ID TDR, the pion rejection has improved in the barrel by a factor of ~2, but has degraded in the end-cap by a factor of approximately 4 which depends critically on pseudorapidity. For a 90% electron efficiency, the pion rejection is typically around 40. A new result is that the TRT may be able to provide a statistical separation between pions and kaons of >0.5σ up to a momentum of ~30 GeV – this is still being studied.

Algorithms have been developed which allow the primary vertices of hard-scattering collisions to be reconstructed at high luminosity. For $H \rightarrow \gamma\gamma$ (a difficult case since there are no primary tracks associated with the Higgs boson decay), an efficiency of ~70% can be achieved with a

background of around four vertices from pile-up events. In decays $B_d^0 \rightarrow J/\psi \, K_s^0$, the K_s^0 decays can be reconstructed with an efficiency of ~40%. The vertex b-tagging, discussed in Chapter 10, has improved significantly since the time of the ID TDR.

The alignment and calibration of the ID has been considered in more detail than before. To make a useful precision measurement of the W mass will require an understanding of the systematics on the momentum scale of better than 0.02%. This will be very challenging, but looks as if it may be possible.

To summarise: the Inner Detector will have a direct role in the physics of ATLAS, for example in B physics. In combination with the calorimeters, it will prove essential in identifying crucial physics signatures such as electrons and b-jets. Lastly, it will be valuable in calibrating other parts of ATLAS, in particular the EM Calorimeter.

3.9 References

3-1   ATLAS Collaboration, Inner Detector Technical Design Report Vol. I, CERN/LHCC 97-16 (1997).

3-2   ATLAS Collaboration, Inner Detector Technical Design Report Vol. II, CERN/LHCC 97-17 (1997).

3-3   ATLAS Collaboration, Pixel Technical Design Report, CERN/LHCC 98-13 (1998).

3-4   P. Luthaus, Ph.D. Thesis, University of Dortmund (1998)

3-5   A. Parker *et al.*, 'The Material Budget of the ATLAS Inner Detector', ATLAS Internal Note INDET-NO-207 (1998).

3-6   D. Barberis *et al.*, 'A Comparative Study of Reduced Layouts of the ATLAS Inner Detector', ATLAS Internal Note INDET-NO-188 (1997).

3-7   ATLAS Collaboration, Technical Coordination Technical Design Report, CERN/LHCC 99-01.

3-8   ATLAS Collaboration, Central Solenoid Technical Design Report, CERN/LHCC 97-21.

3-9   S. Sivoklokov, 'TRT Trigger Performance in the Solenoidal Magnetic Field', ATLAS Internal Note ATL-DAQ-004, INDET-99-005 (1999).

3-10   S. Haywood, 'Impact Parameter Resolution in the Presence of Multiple Scattering', ATLAS Internal Note INDET-NO-91 (1995).

3-11   E. Buis *et al.*, 'Parametrisation of the Inner Detector Performance', ATLAS Internal Note INDET-NO-197 (1997).

3-12   E. Buis *et al.*, 'Update of the Inner Detector Performance Parametrisations', ATLAS Internal Note INDET-NO-215 (1998).

3-13   N. Labanca, Ph.D. Thesis, University of Milano (1998).

3-14   U. Egede, Ph.D. Thesis, Lund University LUNFD6/(NFFL-7150) (1997).

3-15   D. Rousseau, 'Hadron Identification in the TRT', ATLAS Internal Note ATL-COM-INDET-99-002 (1999).

3-16   L. Drage and A. Parker, 'An Investigation into the Effects of Increased SCT Noise and Inefficiency', ATLAS Internal Note, INDET-NO-181.

3-17   See for example: CDF Collaboration, Phys. Rev. **D52** (1995) 4784.

3-18   D. Froidevaux and M. Parker, 'The Performance Specifications of the ATLAS Inner Detector', ATLAS Internal Note, INDET-NO-046 (1994).

3-19   S. Haywood, 'Offline Alignment and Calibration of the Inner Detector', ATLAS Internal Note ATL-COM-INDET-99-001 (1999).

3-20   A. Bonissent *et al.*, 'Alignment of the Upgraded VDET at LEP2', ALEPH Internal Note ALEPH-97-116 (1997).

3-21   K. Abe *et al.*, Nucl. Instrum. Methods **A40** (1997) 287.

3-22   S. Peeters, 'Alignment of the ATLAS Precision Tracker using Tracks', ATLAS Internal Note ATL-COM-INDET-99-007 (1999).

4 Electromagnetic calorimetry

The Calorimeter Performance TDR [4-1] and the Liquid Argon Calorimeter TDR [4-2], submitted two years ago, gave a rather detailed description of the Electromagnetic (EM) Calorimetry of ATLAS and of its performance.

This chapter reviews the main issues related to the EM Calorimeter performance, obtained with the present (final) layout of the ATLAS detector. Emphasis will be put on progress and changes with respect to the Calorimeter TDR.

After a description of the present calorimeter layout, and in particular of the evolution since the Calorimeter TDR, the main progress in the simulation and reconstruction (more realistic description of the charge collection in liquid argon, improved simulation of the pile-up) are illustrated. The most important performance issues, and their impact on physics at the LHC, are then discussed: energy measurement, position and angular resolution, γ/π^0 separation, *etc*. The calorimeter performance was also evaluated by using complete physics events, namely $Z \rightarrow ee$ decays, which in addition represent a powerful tool for the *in situ* calibration of the calorimeter. The main outcomes of these studies are described. Finally, preliminary results obtained from the beam tests of the EM Calorimeter 'module zero' are presented.

4.1 Present detector layout

An overall view of the EM Calorimetry is shown in Figure 4-i and a brief description can be found in Chapter 1. Since the Calorimeter TDR, nothing has changed in design concept. However, due to various constraints, such as cost and engineering issues, or as a result of additional studies, a few elements have changed or evolved. The main changes are described briefly in this section.

Module zero's of the barrel presampler (PS), barrel EM calorimeter and end-cap EM calorimeter have been built and partially tested with beam. Experience from the assembly of the modules has also been used to simplify the construction and define Quality Control procedures. A few selected measurements made on some parts of the calorimeter already delivered are presented in Section 4.3.6, since they have an impact on the uniformity of the calorimeter response.

4.1.1 Changes in the barrel cryostat

4.1.1.1 Inner cold wall and bulkheads

In the Liquid Argon Calorimeter TDR, the barrel cryostat had an inner cold wall with a so-called 'isogrid' structure. The same structure was also proposed for the smaller radius part of both the cold bulkhead and the warm bulkhead, in order to reduce dead material in the transition region between barrel and end-caps. While isogrid is a technique mastered by a few companies, it was realised that large size tests would have been necessary in order to validate the most critical parts, namely the cylinder to bulkhead transitions. It appeared also that those transitions areas would have had to be rather massive, thus partly reducing the advantages of the technique. An alternative study was therefore undertaken, based on a much simpler plain tapered cold wall. By adding a reinforcement ring in the symmetry plane, a cold wall with a thick-

ness between 28 mm (η=0.2) and 14 mm (η=1.2) was found to meet the safety requirements (the main constraint is given by buckling). As shown in Table 4-1, this solution increases the amount of material in front of the EM Calorimeter by 0.25 X_0 with respect to the isogrid at small pseudorapidity, where the overall material budget is not critical, and by only 0.1 X_0 at large pseudorapidity, where the total material in front of the calorimeter is more critical. Furthermore a solid cold wall has the advantage of a more uniform material distribution than the isogrid structure. The impact of this wall change on the EM Calorimeter performance is marginal, as discussed in more detail in Section 4.3. The cold bulkhead and the flange connecting the bulkhead and the cold wall have also been studied in detail, and their thickness minimised. This flange is now located on 'side C' of the detector ($z < 0$). Furthermore, in order to reduce the material in front of the end-cap calorimeter, the bolts connecting the inner warm cylinder to the warm bulkhead are now made of aluminium.

4.1.1.2 Supporting structure

In the design presented in the Liquid Argon Calorimeter TDR, the cold vessel (which contains the calorimeter and the liquid argon) was supported by two steel slings at each end. It was realised that, due to the difference in expansion coefficients between aluminium and steel, some extra space would have been necessary to accommodate a small vertical excursion between the solenoid (attached to the warm vessel) and the cold vessel. Fitting the sling ends in the warm bulkhead while preserving the symmetric distribution of feedthroughs around the circumference turned out to be quite difficult as well. In order to circumvent these difficulties, a different system of supporting, based on feet, has been implemented.

4.1.1.3 Cooling

The heat brought in at the feedthrough level by conduction in the cables is about 500 W per side. While this is a sizeable fraction (about 50%) of the total heat input, the heat exchangers were laid on the inner surface of the outer cold vessel, far from the feedthroughs. Such a layout was not optimal for limiting temperature variations in the calorimeter to a fraction of a degree, which is needed for a response uniform to a fraction of a percent. Therefore it has been decided to add, at each end of the cold vessel, a cooling loop near the feedthroughs. It is laid against the cold bulkhead, at the largest possible radius. Calculations of temperature uniformity, incorporating this new feature, have been recently started using a 3D model.

Table 4-1 Thickness of the old isogrid wall and of the new tapered wall, as a function of pseudorapidity, as seen by a particle coming from the interaction vertex.

Pseudorapidity	Thickness of isogrid wall (X_0)	Thickness of tapered wall (X_0)
0.24	0.12	0.37
0.64	0.14	0.37
1.0	0.17	0.37
1.2	0.21	0.36
1.3	0.23	0.37
1.4	0.25	0.35

4.1.2 Changes in the end-cap cryostat

A few changes have taken place in the end-cap cryostat design, mainly in order to improve the reliability and to reduce the cost of fabrication. Among the main points are an improved design of the feet, and the choice of double cold seals. None of these changes affect the performance of the EM Calorimeter. It should also be noted that the space reserved for the beam-pipe pumps in front of the FCAL is now likely to stay empty. This will improve the background situation in the FCAL, but has almost no visible effect on the performance of the EM Calorimeter. Furthermore, due to a different ganging scheme of rod-shaped electrodes in the FCAL (see Chapter 5), the number of feedthroughs per end-cap was reduced from 28 to 25. Finally the cold door in the back (in aluminium) is now somewhat thicker (+50 mm), at the expense of space for cables and of the copper plug which is now thinner (-30 mm). The induced change in background in the chambers of the Muon System is negligible.

4.1.3 Improvements in the optimal filtering

In the course of the development of the front-end readout boards, and using measurements made in test beams, it was found that the merits and limitations of the 'optimal filtering' technique needed to be reanalysed. This study [4-3] was started because, by using five samples and optimising the signal to noise ratio for test-beam data, it was not possible to obtain the gain factor on electronic noise which was anticipated. The analysis showed that the main limitation comes from an 'aliasing effect': with a sampling period of 25 ns, components of the noise frequency spectrum around 40 MHz, 80 MHz, *etc.* are fully transmitted, and contribute sizably to the noise after sampling. As a result of this work, which included the full description of the preamplifiers and shapers already prototyped for ATLAS, the electronic and pile-up noise as a function of luminosity as well as the time constant of the shaper have been reanalysed. Figure 4-1 shows that, with a time constant of 15 ns (instead of 13 ns as in the Liquid-Argon Calorimeter TDR), optimal filtering allows minimisation of the total noise for luminosities between 10^{33} cm^{-2}s^{-1} and 5×10^{34} cm^{-2} s^{-1} as efficiently as changing by hardware the time constant (15 ns) selected for the nominal high luminosity of 10^{34} cm^{-2}s^{-1}. Going beyond this luminosity range in an optimised way would require changing the shaper time constant. The feasibility of such a scheme for the very low luminosity case (LHC start-up, heavy-ion running) is under study. More details on pile-up and electronic noise are given in Section 4.2.4.
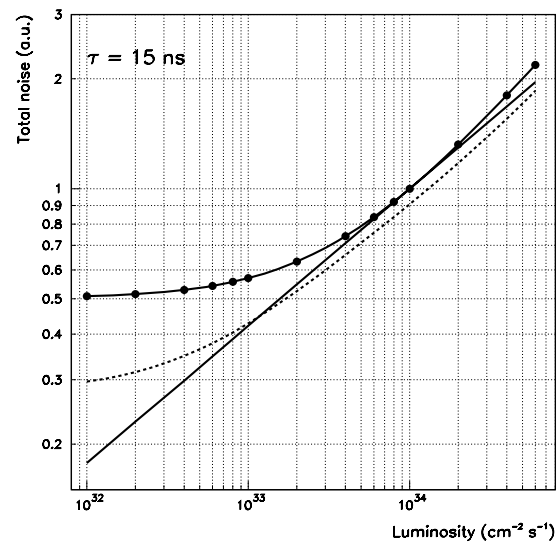

Figure 4-1 Total noise as a function of luminosity for a shaping constant of 15 ns. The dots and the dashed line show the performance without and with optimal filtering respectively. The full line indicates the total noise which could be obtained with the best possible (hardware) time constant for each luminosity.

4.2 Simulation and reconstruction environment

The ATLAS simulation and reconstruction environment is described in Chapter 2. Therefore only aspects related to the EM Calorimeter are discussed here.

The GEANT simulation of the EM Calorimeter did not change significantly since the Calorimeter TDR. It includes all details of the accordion geometry and of the cryostats, as well as a faithful description of the inactive material (cables, services, inactive liquid, *etc.*), as shown in Figure 4-i. The recent changes in the cryostat design mentioned in Sections 4.1.1 and 4.1.2 have been implemented in the simulation.

Very recently, a better simulation of the charge collection in the liquid-argon gaps based on realistic field maps has been developed. This is discussed in Sections 4.2.1 and 4.2.2. This detailed simulation has allowed evaluation of the impact of a realistic charge collection mechanism on several performance issues. It was found that the impact is negligible in most cases (see Section 4.3), therefore most of the results shown here were obtained without the full charge collection mechanism.

4.2.1 Signal simulation in the barrel

In the simulation used for the Calorimeter TDR, the signal collection in the barrel used the energy deposited in the liquid argon. This ignores the drifting of the ionisation charges in an electric field with large non-uniformities in the accordion folds. The total current induced by a charge q drifting in the gap is expressed by:

$$i = q\bar{v}(\bar{E}/V)$$

where $\bar{E}$ is the local electric field, $\bar{v}$ is the drift velocity depending on E as $\sim E^{0.3}$ and V is the voltage applied between electrodes.

In the straight parts, *i.e.* regions with plane and parallel electrodes, the electric field is uniform ($E \sim 10$ kV/cm). In the folds, which represent about one third of the barrel active volume, the two-dimensional electric field is determined by a numerical solution of Poisson's equation (PRIAM package [4-4]).

To get the resulting induced current, each hit in the liquid argon (from GEANT) is divided into n quasi-punctual charges (<n> ~ 7) of 200 µm length (below this value no change in results was observed). Each elementary charge drifts in the local electric field. The resulting current (see equation above) is then folded with the specific electronic functions (impulse response of the preamplifier-shaper chain), which depend on both the longitudinal compartment and the η coordinate of the hit. In the straight parts, the uniform field yields a constant current during the drift time and the convolution with the electronic function is straightforward. In the folds, on the other hand, the drifting of an elementary charge has to be followed step by step in time (typical time step: ~2 ns) up to about 100 ns. The resulting current $i(t)$ is then folded with the corresponding electronic function. The increase in the event processing time using this method (including the response of the electronic chain) instead of deposited energies is about 10%.

Improvements have also been made in the description of the signal sharing between adjacent strips. Due to the fine granularity in η of the first compartment of the EM Calorimeter, an elementary charge induces a signal on more than one strip (typically three strips are involved). To take this sharing into account, in the Calorimeter TDR simulation the total charge (not the total

current) induced on a semi-infinite conducting plane bounded by a straight line had been used. Because of the non-uniformity of the electric field in the folds, the total current induced by an elementary charge in the first compartment is obtained as explained above, then sharing functions between the hit strip (under the charge) and the two neighbour strips are used. These functions depend on two variables: the distance from the charge to the electrode (divided by the local gap width), and the distance from the charge to the strip middle (divided by the local strip width). Pile-up (if any) due to multiple elementary charges is taken into account.

4.2.2 Signal simulation in the end-cap

In the end-cap calorimeter the gap geometry varies with radius. Therefore a simulation based on the energy deposited in the liquid argon is not fully realistic, because the electric field varies significantly with radius even in the straight parts of the electrodes. Charge collection effects in the end-cap are important, and are now simulated in two steps.

In the straight parts of the electrodes, the signal (*S*) is calculated using the expression

$$S = (E/g(R))R^{1.3}$$

where *E* is the deposited energy and *g(R)* the gap thickness as a function of radius. It is obtained from the current expression given in the previous Section, by taking into account the fact that the electric field is $E=V/g$ and that the drift velocity v is proportional to $E^{0.3}$. The gap thickness at each radius is obtained from a linear interpolation based on a precalculated table. The high-voltage variation with pseudorapidity is taken into account during analysis.

On the other hand in the folds, where the electric field is not uniform, electric field maps are calculated using the PRIAM package. As in the barrel, each GEANT hit is divided into several punctual charges and for each of them the contribution to the current is calculated. Since the geometry of the end-cap is more complicated, the procedure for calculation of the current has been simplified with respect to that in the barrel: the current is assumed to be proportional to the electric field at the position of the elementary charge, without convoluting with the exact shaping function. For small shaping time this simplification has no significant impact.

4.2.3 Reconstruction in the EM Calorimeter

The reconstruction in the EM Calorimeter is divided into four steps.

The deposited energies (DIGI's from GEANT) are stored into cell matrices, with one matrix per region of uniform granularity. Electronic noise and pile-up can be added at this level by using the method described in Section 4.2.4. Five samples can be made available and digital filtering can be applied. The energies in all matrices are then calibrated, on a cell-by-cell basis, by asking that the total energy reconstructed in the calorimeter for photons of $E_T = 50$ GeV be equal, on average, to the incident energy.

The energies are then mapped onto a matrix of granularity $\Delta\eta \times \Delta\phi = 0.025 \times 0.025$ and summed in depth. A sliding window algorithm with a 5x5 cell window is applied on this matrix. The threshold on the cluster energy can be chosen as a function of luminosity, and may depend on the physics channel. Figure 4-2 shows the number of fake clusters, in the 5x5 window, due to electronic noise and pile-up at high luminosity for various cluster thresholds.

Around the direction of each cluster, the energies are measured in each compartment in windows of various sizes. The energies are corrected for the η and φ modulations (see Section 4.3.3) and the calibration is adjusted to take into account the finite cluster size. The φ position is measured in the middle compartment and corrected for an offset due to the accordion shape of the cells. The η positions are measured in the first two longitudinal compartments. They are corrected for the 'S-shapes' (see Section 4.4.2), and they are then used to determine the shower direction and the position of the primary vertex in *z*.

Finally, an efficient electromagnetic shower identification algorithm, based only on the information from the Hadronic and Electromagnetic calorimeters, is used. It provides an efficiency for electrons and photons of $E_T = 20$ GeV, integrated over $|\eta| < 2.4$ but excluding the barrel/end-cap transition region, of larger than 96%, while keeping less than 2% of single charged pions. More powerful electron and photon identification requires the use of the Inner Detector and is described in Chapter 7.
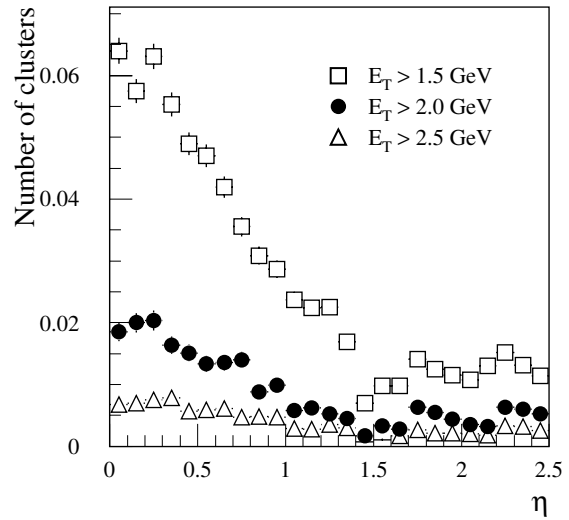
Figure 4-2 Number of fake clusters due to pile-up and electronic noise in a window of size $\Delta\eta \times \Delta\phi = 0.125 \times 0.125$, as a function of pseudorapidity for different cluster thresholds.

4.2.4 Simulation of pile-up and electronic noise

As discussed in Section 2.3.1, 24 minimum-bias events (around 3500 particles inside $|\eta| < 5.0$) are produced on average for each bunch crossing when running at high luminosity. To cope with this environment, the EM Calorimeter is read out using fast bipolar shapers with a peaking time of ~35 ns. The simulation of the pile-up in the EM Calorimeter is described in some detail in Section 2.3.3. The electronic noise with the correct time correlations is superimposed to the energies stored in the individual cells just before reconstruction. The digital filtering procedure may also be used in this more refined simulation procedure. In this way, the electronic shaping can be modified (within limits) to reduce the electronic noise for operation at low luminosity.

Figure 4-3 shows the energy spectrum of the pile-up expected at high luminosity in the middle compartment of the EM Calorimeter for a typical cluster size of 3×7 cells in η×φ. The correlation between the pile-up noise and the bunch-crossing number is illustrated in Figure 4-4: large positive fluctuations are always caused by the so-called 'in-time pile-up', *i.e.* events sampled at the peak of the shaper response.

4.2.4.1 Pile–up levels in the EM Calorimeter

The results presented here are based on 5000 fully-simulated minimum-bias events. The rms of the pile-up transverse energy distribution is shown in Figure 4-5 for different cluster sizes and separately for the presampler, the strip section and the middle compartment of the EM Calorimeter. The presampler energy was weighted as described in Section 4.3.2. The increase (decrease) of the pile-up in the presampler (calorimeter) at the transition between the barrel and the end-
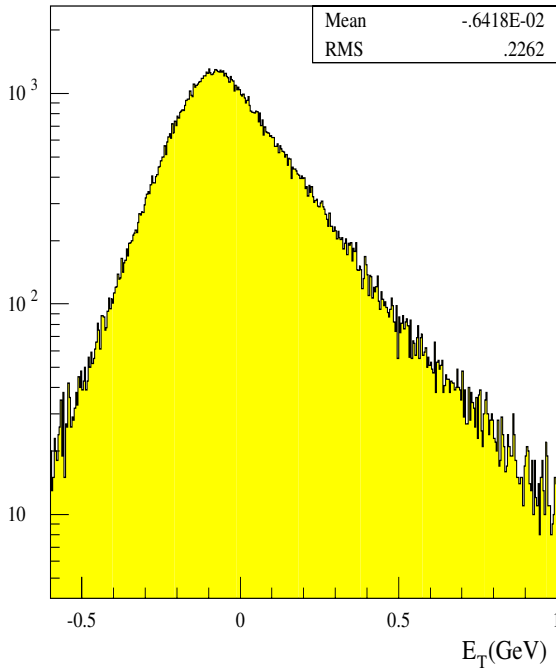
Figure 4-3 Distribution of the pile-up transverse energy in a 3×7 cell cluster in the middle compartment of the EM Calorimeter at η = 0.3.
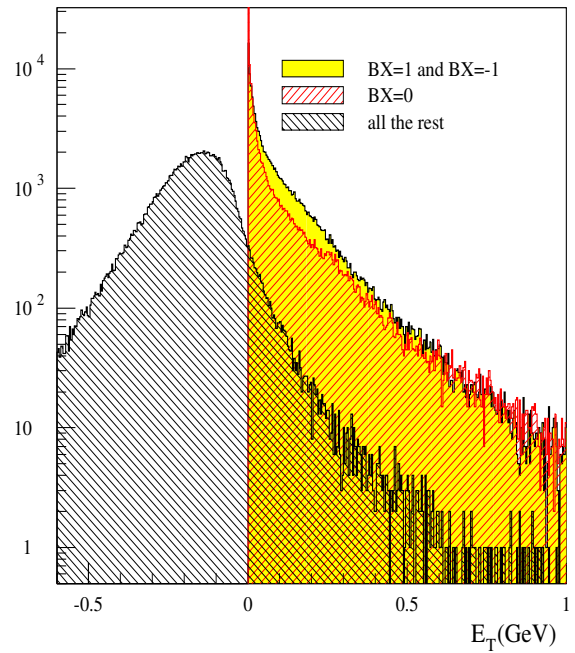
Figure 4-4 Different contributions to the pile-up transverse energy in a 3×7 cell cluster in the middle compartment. BX=0 denotes the pile-up at bunch crossing zero, that is the in-time pile-up; BX = 1 and BX = -1 refer to events delayed by ±25 ns with respect to the peak, *i.e.* belonging to the previous and next bunch crossing.

cap calorimeter is due to the large amount of upstream material, which absorbs soft particles traversing these regions, so that they reach the presampler but not the calorimeter. Figure 4-6 shows the total noise (electronic plus pile-up) summed over the presampler and the first two longitudinal compartments of the calorimeter, as well as the electronic noise alone. The cluster sizes are 3x5, 3x7, and 5x5 cells (units of Δη×Δφ = 0.025×0.025) in the middle compartment, and respectively 1×1, 1×2, and 2×2 in the strips and in the presampler (units of Δη×Δφ = 0.025×0.1). The pile-up levels obtained with the present more realistic simulation are similar to those reported in the Calorimeter Performance TDR.

The occupancy of the EM Calorimeter is presented in Figure 4-7, which shows the fraction of cells where the pile–up energy exceeds a given threshold expressed in units of electronic noise at high luminosity. At high luminosity the fraction of cells with a pile-up energy exceeding two standard deviations of the electronic noise is about 1% in the barrel and less than 10% in the end-cap.

4.2.4.2 Coherent noise

Since the EM Calorimeter has almost 200 000 channels, the presence of coherent noise, which scales linearly with the number of channels, could have a serious impact on measurements involving many cells, such as the measurement of the event missing transverse energy. According
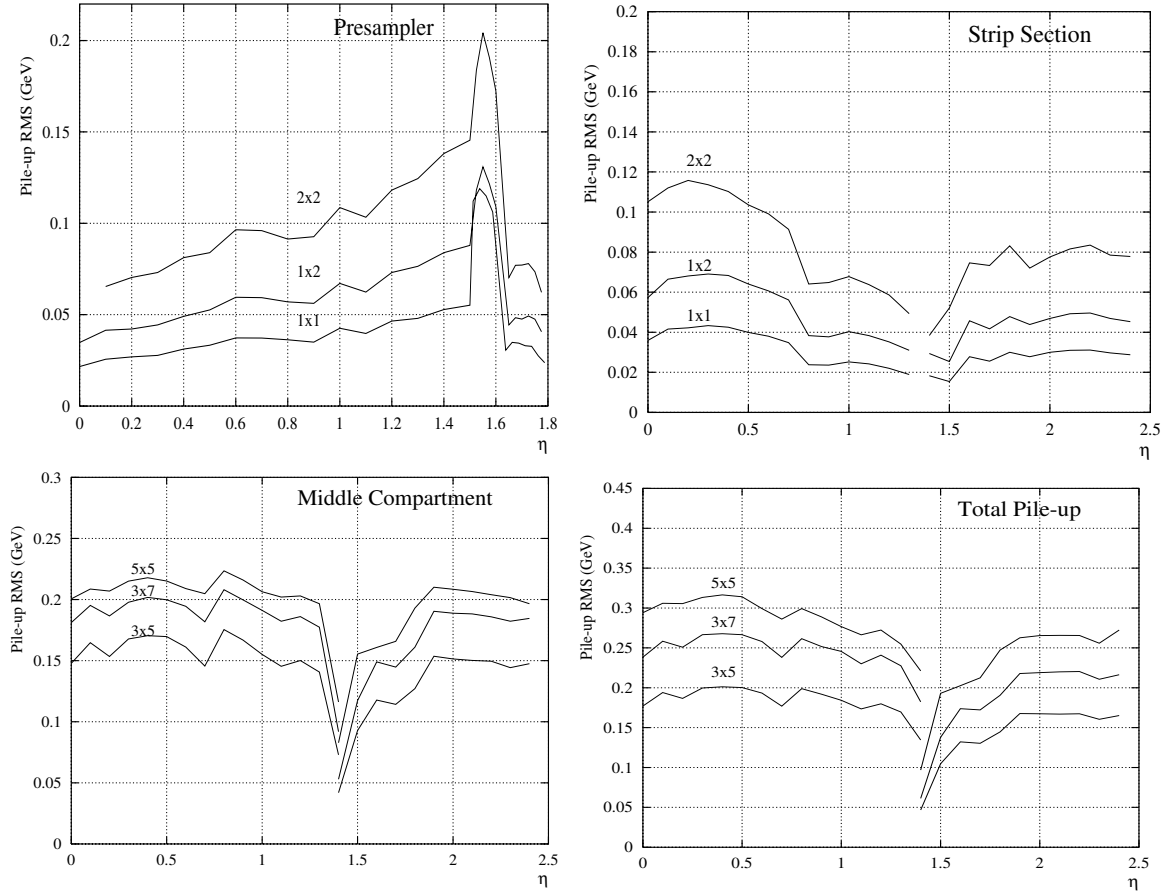
Figure 4-5 The rms of the pile-up transverse energy distribution as a function of pseudorapidity in the presampler, the strip section, the middle compartment and the total. Three different cluster sizes are shown: 3x5, 3x7 and 5x5 for the middle compartment (units of $\Delta\eta \times \Delta\phi$ = 0.025x0.025), and 1x1, 1x2 and 2x2 for the strip section and the presampler (units of $\Delta\eta \times \Delta\phi$ = 0.025x0.1) respectively. In the top left plot, the contribution of the scintillator has been included in the region $1.5 < \eta < 1.6$.

to studies reported in [4-1], the coherent noise in the middle compartment of the EM Calorimeter should not exceed 3 MeV per channel, which is about 5% of the white noise, in order not to spoil the E_T^{miss} measurement.

The coherent noise can be controlled by a careful design of the grounding and shielding on the input stages. Thus, the preamplifiers are located very close to the feedthroughs, inside a Faraday cage which comprises the cryostat, the feedthroughs and the crates. This minimises the sensitivity to external electromagnetic interferences. The ground currents are minimised by an optical coupling of the readout boards to the external world for fast digital input/output, by avoiding large ground loops and by providing low-impedance connection to the crates. Application of these criteria, except for the optical coupling, to the module-zero tests of '98, reduced the coherent noise to the level of 10% of the white noise over 128 channels. Furthermore, bench tests with optical coupling has decreased this value to 5%, which is within the specifications mentioned above.
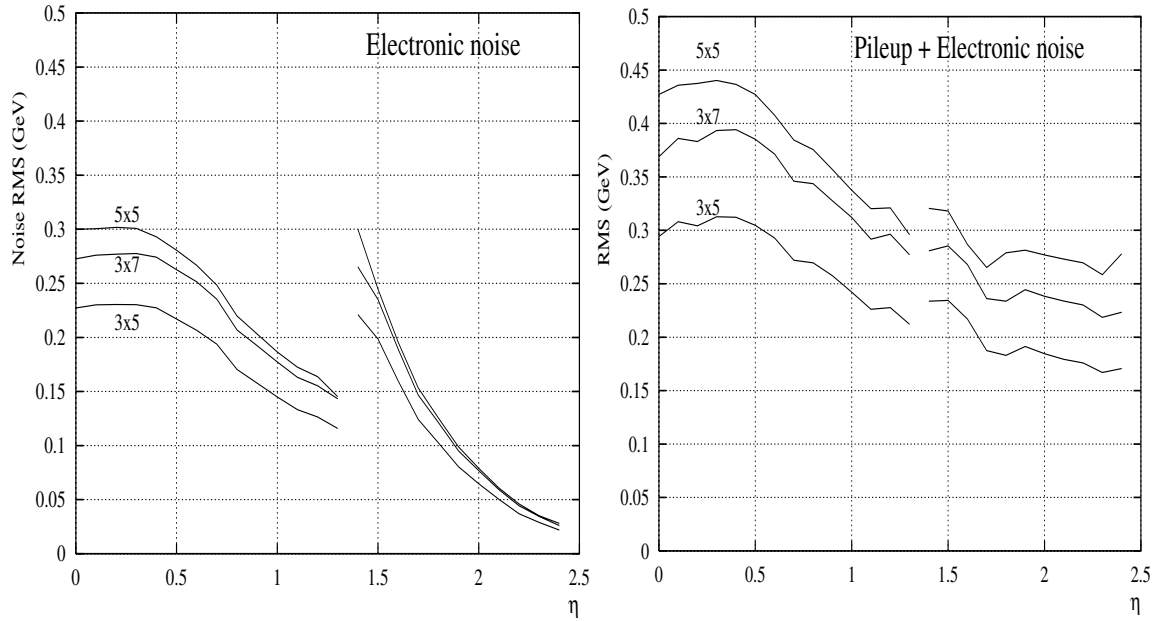
Figure 4-6 The rms of the electronic noise (left) and total noise (right) transverse energy distributions, as a function of pseudorapidity, for three different clusters (see text).
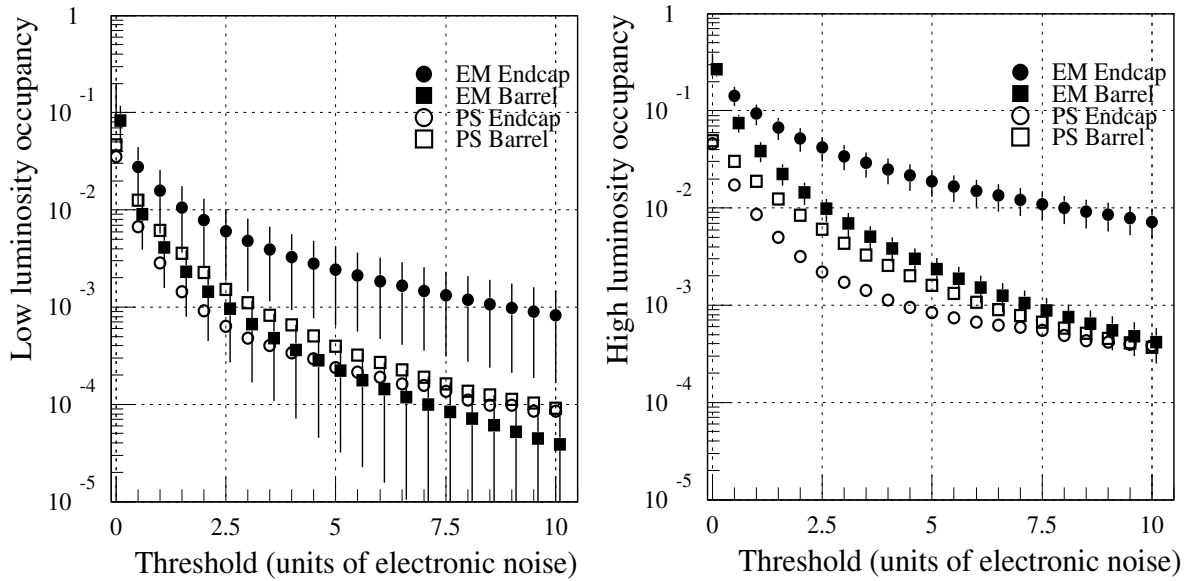
Figure 4-7 The average fraction of cells with a pile-up energy larger than a given energy threshold (in units of electronic noise), as a function of the threshold, at low (left) and high (right) luminosity.

4.3 Energy measurement

The procedure to reconstruct the energy of an incident particle in the EM Calorimeter has been described in detail in [4-1]. Therefore only the main features will be recalled here.

In general, the reconstructed energy can be written as:

$$E_{tot} = w_{glob}(w_{ps}E_{ps} + E_{str} + E_{mid} + E_{back}) \qquad\qquad 4\text{-}1$$

where w_{glob} is a global calibration factor, and E_{ps}, E_{str}, E_{mid} and E_{back} are the energies measured in a given cluster of cells in the presampler, strip section, middle and back compartments of the calorimeter respectively. The presampler weight w_{ps} is chosen to optimise the energy resolution. The energy response of the calorimeter is potentially affected by several factors which are described one by one in the following sections, after a discussion of the cluster size.

4.3.1 Optimisation of the cluster size

The optimum cluster size is the result of a compromise between two competing effects. A relatively large cluster is needed to fully contain the shower and therefore to limit the impact of lateral fluctuations on the energy resolution. On the other hand, the smallest possible cluster is needed to reduce the contribution of the pile-up and electronic noise to the energy resolution. The cluster size depends on the particle type, energy and pseudorapidity. Electron reconstruction needs larger clusters than photons because of their larger interaction probability in the upstream material and the presence of a magnetic field.

The results presented in the Calorimeter Performance TDR, which were obtained with a pile-up approximately simulated by a simple Gaussian smearing of the energy deposited in each cell, were checked using the complete simulation of the electronic and pile-up noise described in Section 4.2.4.

In the strip section, the optimal cluster size was obtained by looking at the rms of the energy measured inside a cluster of increasing width in η divided, event by event, by the total energy in the first compartment. In azimuth, an average size of 1.5 strips was used, that is one or two strips were chosen according to the shower position with respect to the strip centre. As an example, Figure 4-8 shows the results obtained for electrons of $E_T = 20$ GeV at η = 0.9. In the presence of electronic and pile-up noise, a shallow minimum can be seen around ±8 strips (with respect to the shower impact point), in agreement with the result presented in [4-1].
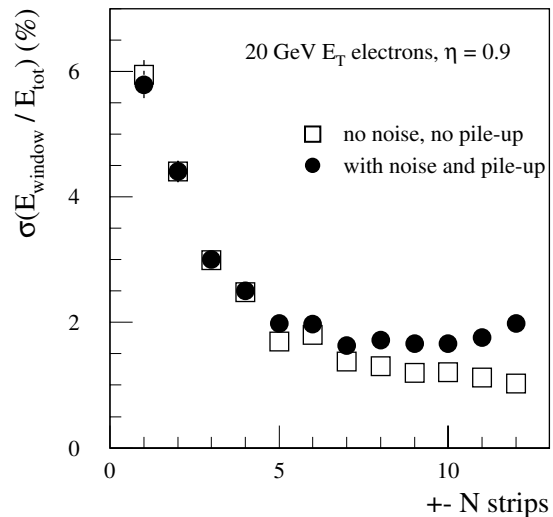
Figure 4-8 Rms of the energy deposited in ±*N* strips around the electron impact point, divided by the total energy in the strip section without noise and pile-up, for electrons of $E_T = 20$ GeV at η = 0.9, as a function of the number of strips used.

The optimal cluster sizes in the middle compartment of the barrel calorimeter were found to be the same as in [4-1], *i.e.* 3x5 cells in ηxφ for unconverted photons and 3x7 cells for electrons and converted photons. In the end-caps, where the cell size in η is smaller with respect to the shower size than in the barrel, and where the effect of the magnetic field in φ is also smaller, a window of 5x5 cells gives the best performance. For example, for unconverted photons of $E_T = 50$ GeV at η = 1.8, the rms of the energy deposited in windows of 3x5, 3x7 and 5x5 cells, divided by the total energy in the middle compartment, is (0.738 ± 0.018)%, 0.670% and 0.585% respectively.

For low-energy particles, the fraction of the shower energy deposited in the back compartment of the calorimeter is small: on average 2.7% of the particle energy for electrons of 50 GeV at $\eta = 0.3$. Therefore, because of the contribution of the electronic noise, it is better not to use the energy measured in this compartment at low energy. Table 4-2 shows the calorimeter energy resolution obtained with and without including the energy measured in the back compartment, when the electronic noise and the pile-up are added. It can be seen that the energy resolution for particles with energy smaller than 50 GeV is slightly better if the back compartment is not used. At higher energies, on the other hand, the energy deposited in the back compartment must be included (see Section 4.3.4).

Table 4-2 Energy resolution of the EM Calorimeter for electrons of various energies at $\eta = 0.3$, obtained by using or not using the energy measured in the back compartment.

	E = 10 GeV	E = 50 GeV	E = 200 GeV
With back compartment	$(6.33 \pm 0.09)\%$	$(1.39 \pm 0.02)\%$	$(0.795 \pm 0.018)\%$
Without back compartment	$(6.24 \pm 0.09)\%$	$(1.38 \pm 0.02)\%$	$(0.847 \pm 0.021)\%$

The optimal cluster size in the presampler was chosen by looking at the variation of the calorimeter energy resolution as a function of the number of presampler cells used. As a result, a window of size 2x1.5 presampler cells (1.5 means that one or two cells are used in ϕ, according to the shower position with respect to the cell centre) was used for converted photons and electrons, and a window of size 2x1 cells was used for unconverted photons.

At low luminosity, somewhat larger cluster sizes could be used, since the total noise is a factor of two smaller than at high luminosity (see Figure 4-1). However, for the study presented here the cluster sizes determined at high luminosity as described above were used in all cases. Therefore the low-luminosity results are slightly conservative.

4.3.2 Impact of dead material

The material in front of the EM Calorimeter is shown in Figure 4-ii, and a comparison with the layout described in [4-1] is presented in Figure 4-9. The total amount has increased since the Calorimeter Performance TDR due to:

- The use of a solid cold wall for the barrel cryostat. The increase in material is significant only at small pseudorapidity thanks to the tapered shape.

- A 10% increase in the thickness of the Pixel and SCT layers (see Chapter 3). Since these layers are at small radii, they have a significant impact on the energy reconstructed in the calorimeter, in particular on the appearance of low-energy tails.

- A more realistic description of the Inner Detector services, which contribute for $0.7 < |\eta| < 1.8$ and in front of the end-cap inner wheel (Figure 4-9). The services, however, are located at relatively large radii and therefore their impact on the calorimeter performance is small in most cases.
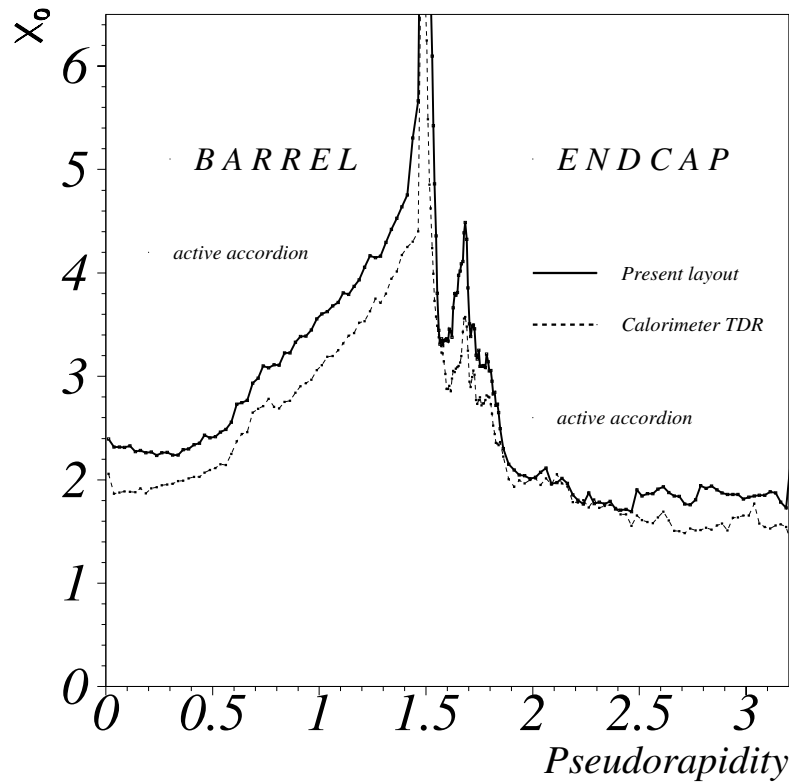
Figure 4-9 Amount of material in front of the EM Calorimeter, as a function of pseudorapidity, with the layout described in [4-1] and with the present layout.

On the other hand, the increase in the region $|\eta| \sim 1.7$ is due to the fact that, in the detector simulation used for the studies presented here, the bolts of the warm flange were in titanium instead of aluminium. No significant material increase is expected with aluminium bolts.

As already discussed in [4-1], the material in the Inner Detector, at large distance from the EM Calorimeter and inside a magnetic field, mainly contributes to the formation of low-energy tails in the energy spectra reconstructed in the calorimeter, whereas the material close to the calorimeter (cryostat, coil) broadens the width of the Gaussian part of the spectra. In both cases the effect is more serious for lower energies and for electrons rather than for photons. The low-energy tails are discussed in Section 4.3.7.
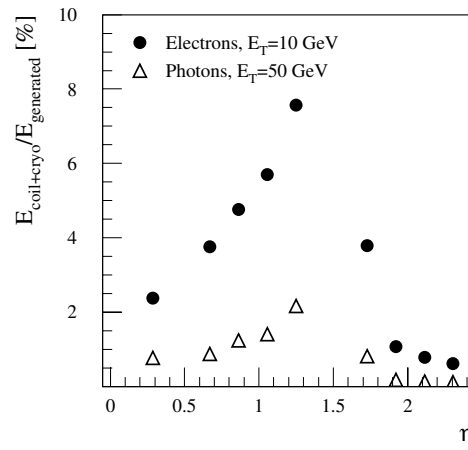
Figure 4-10 Fraction of energy lost by electrons and photons in the cryostats and coil as a function of pseudorapidity.

The transition between the barrel and the end-cap calorimeter represents a special case, because there the amount of material in front of the calorimeter reaches several radiation lengths. Dedicated devices (end-cap presampler, scintillator slab) are used in order to limit the impact of this material on the calorimeter energy measurement. Details about the layout and the calorimeter response in this region are discussed in Section 4.3.8.1.

The fraction of energy lost by electrons of E_T = 10 GeV and photons of E_T = 50 GeV in the cryostat and coil is shown in Figure 4-10 as a function of pseudorapidity. As already mentioned, the losses are larger for low-energy electrons than for high-energy photons. The shape of the distribution in Figure 4-10 reflects the material profile in front of the calorimeter (see Figure 4-ii).

The energy losses can be recovered, and thus the resolution improved, by weighting the energy deposited in the presampler. The optimisation of the weight (w_{ps} in Equation 4-1) was performed for electrons and for converted and unconverted photons of various transverse energies and at different incidence points. The calorimeter energy resolution was studied for several presampler weights, and the weight which minimises the resolution was determined. An example is shown in Figure 4-13, which demonstrates that the use of the presampler improves the calorimeter energy resolution significantly. The optimum weight was found to be $w_{ps} \sim 3.5$ in the barrel. The linearity of the calorimeter response, which is better than 1%, is not affected by the presampler weighting .
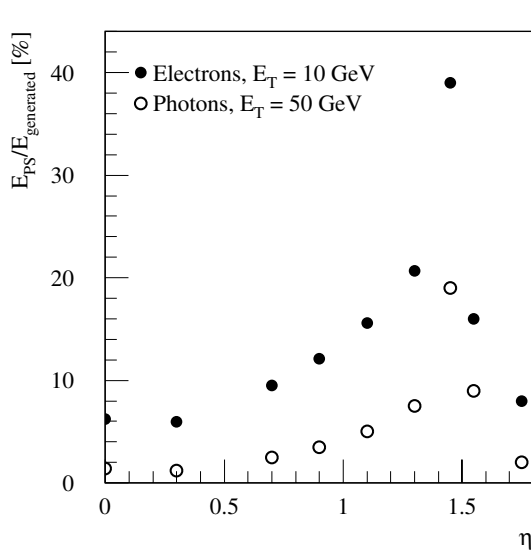
Figure 4-11 Fraction of energy in the presampler (after weighting) for electrons of E_T = 10 GeV and photons of E_T = 50 GeV, as a function of pseudorapidity.
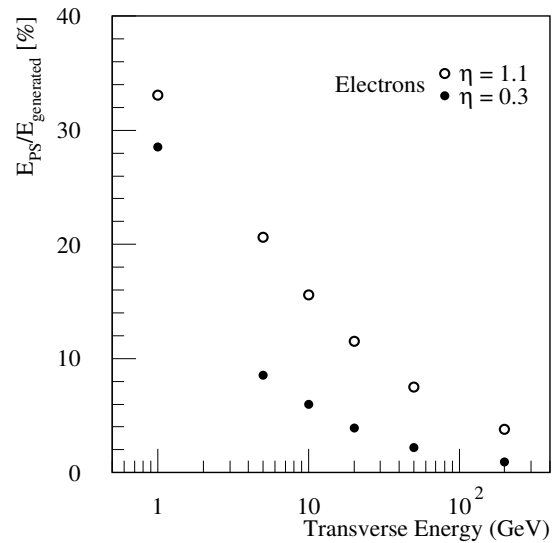
Figure 4-12 Fraction of (weighted) energy in the presampler for electrons incident at two pseudorapidities, as a function of the electron energy.

The impact of the presampler on the calorimeter energy measurement is also illustrated in Figure 4-14, which shows the energy spectra for electrons of E_T = 10 GeV at η = 1.3 obtained using and without using the presampler information.

The role of the presampler [4-5], *i.e.* to ensure robustness against possible increases in the amount of material in front of the calorimeter, has been recently demonstrated with the increase in the thickness of the barrel cold wall: essentially no degradation is observed in the energy res-

olution with respect to the isogrid solution, as discussed in Section 4.3.5. The weighted energy in the presampler is shown in Figures 4-11 and 4-12 as a function of pseudorapidity and energy and for electrons and photons.
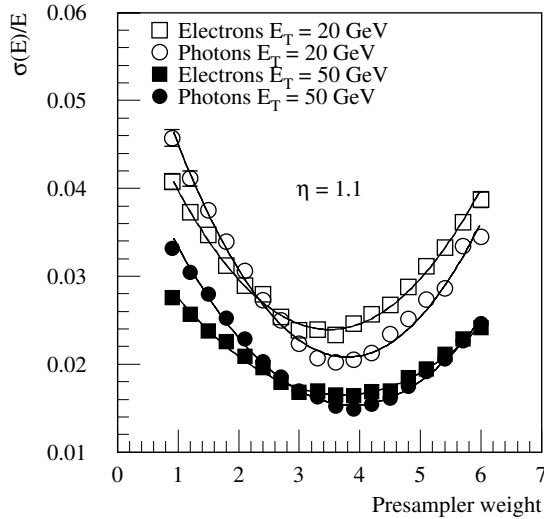
Figure 4-13 Energy resolution of the EM Calorimeter (a large cluster size is used) as a function of the presampler weight for electrons and photons of E_T = 20 GeV and 50 GeV at η = 1.1.
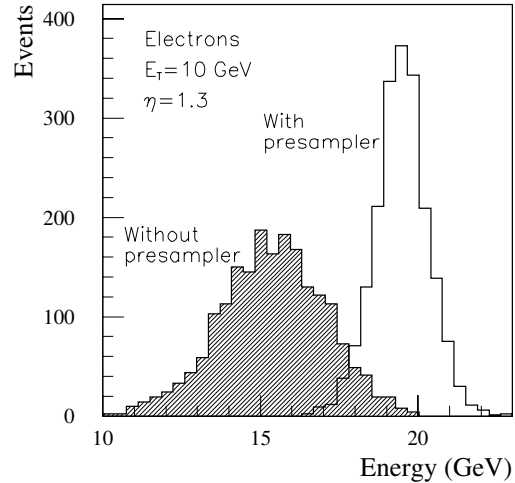
Figure 4-14 Energy spectra reconstructed in the EM Calorimeter with (white histogram) and without (black histogram) using the presampler information for electrons of energy 19 GeV at η = 1.3. Both histograms are normalised to the same number of entries.

4.3.3 Variation of response with ϕ and η

Due to the accordion geometry (imperfect overlap among absorbers due to the finite bending radius), the amount of passive material crossed by an incident particle varies as a function of the position in ϕ. This gives rise to a response modulation, called 'ϕ-modulation'. The geometrical parameters of the accordion, such as the length of the folds and the bend angle, have been optimised, as a function of the calorimeter depth, so as to minimise this response variation.

The energy reconstructed in the calorimeter as a function of ϕ is shown in Figure 4-15 at several pseudorapidity points in the barrel and end-cap.

In the barrel, the response variation has an rms of 0.35% before correction. In the end-cap, due to the more complicated geometry, the absorber overlap is less good, and the response rms is 0.6%. The ϕ-modulation can be corrected for with a function (superimposed to the calorimeter response in Figure 4-15), consisting of the sum of four sigmoids. The parameters of the sigmoids depend on the pseudorapidity. After correction, the residual rms is 0.2-0.3%.
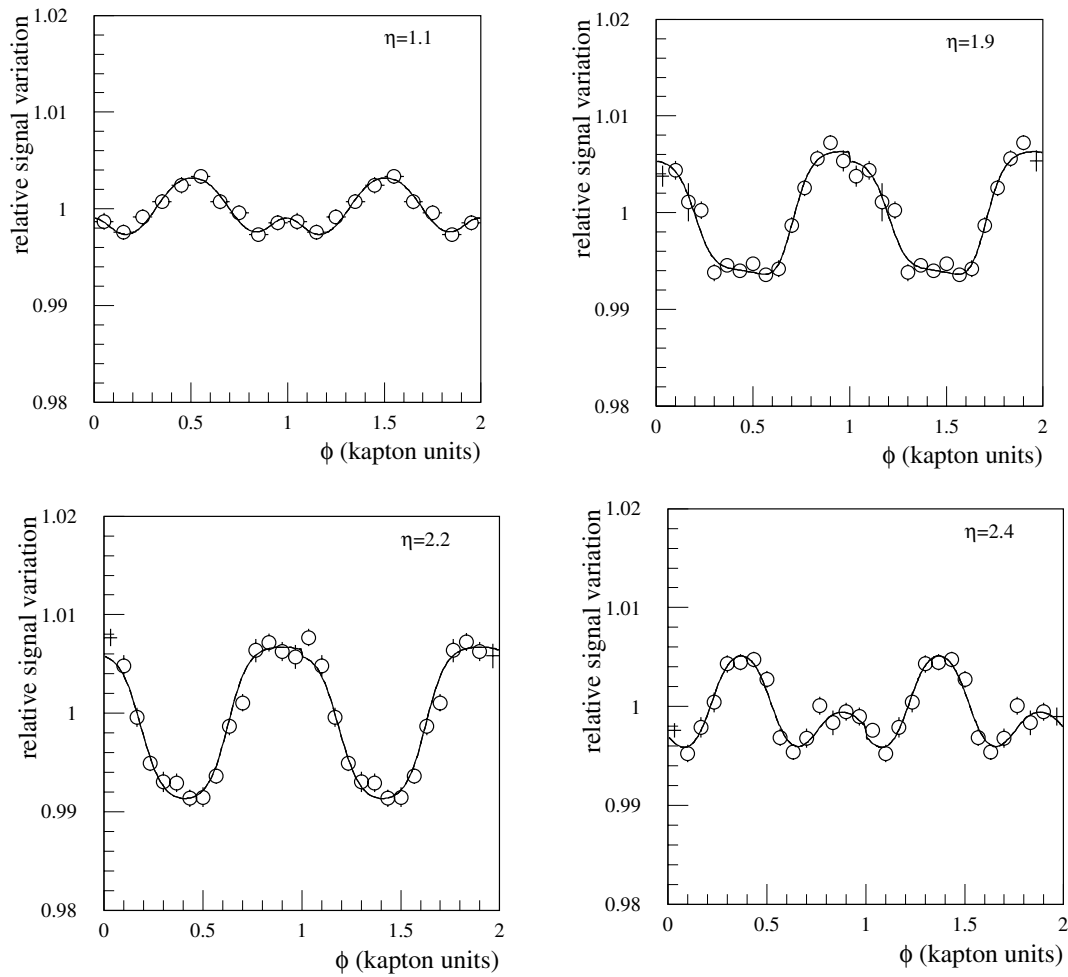
Figure 4-15 Calorimeter response to photons of E_T = 50 GeV, normalised to the generated energy, as a function of ϕ inside one cell, as obtained at various pseudorapidity points: η = 1.1 (top left), η = 1.9 (top right), η = 2.2. (bottom left), η = 2.4 (bottom right). The correction function is superimposed. One Kapton unit corresponds to 1/4 of a cell in the barrel and 1/3 in the end-cap.

The response modulation in ϕ is affected by the non-uniformity of the electric field in the accordion folds. Figure 4-16 shows the calorimeter response in the end-cap, as a function of ϕ, as obtained when the realistic field map described in Section 4.2.2 is used. It is compared to the response obtained with a uniform electric field, as used in the baseline simulation code. With a realistic field, the modulation is less regular and has a smaller amplitude. This is because the peaks in the response, which are due to the excess of liquid in the accordion folds, are to some extent compensated by the lower electric field in the folds.

The cluster size used for the energy measurement is relatively small in η (three cells in most cases). Therefore, the shower energy is not fully contained, and the calorimeter response depends on the particle impact point inside a cell: the response is maximum for particles hitting the cell centre, and drops (by typically 5%) at the cell edges. This response variation is corrected for with a second-order polynomial function, by using the shower position reconstructed by the calorimeter itself. The parameters of the η–correction depends on the pseudorapidity, since the physical size of the cells changes with η.

4.3.4 Longitudinal leakage

The total thickness of the EM Calorimeter (active plus upstream material) is at least 26 X_0 over the full pseudorapidity coverage, except in the region $|\eta| < 0.4$ and in the transition between the barrel and the end-cap. This depth is sufficient to ensure that the longitudinal shower leakage does not significantly degrade the energy resolution, in particular the constant term, up to the highest energies (TeV range). Furthermore, for showers of a few hundred GeV or more, the energy resolution can be preserved by weighting the energy deposited in the back compartment of the EM Calorimeter (see Section 4.3.5).

Figure 4-16   Calorimeter response to photons of $E_T = 50$ GeV at $\eta = 2$, normalised to the generated energy, as a function of ϕ inside one cell, when a uniform electric field (open circles) or a realistic field (solid squares) are used.

4.3.5 Energy resolution: sampling term

The results presented in this section were obtained by using the nominal cluster sizes for the different particles (electrons, unconverted photons, converted photons) described in Section 4.3.1. Furthermore, the various corrections discussed above (presampler weight, η and ϕ-modulation) were applied.
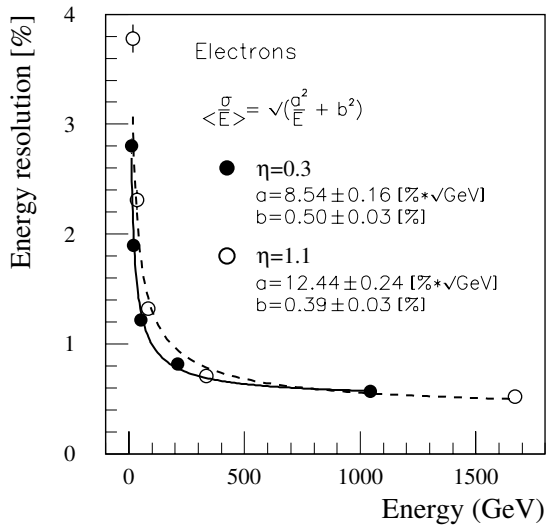
Figure 4-17 Energy resolution for electrons at $\eta = 0.3$ and $\eta = 1.1$, as a function of the incident energy.
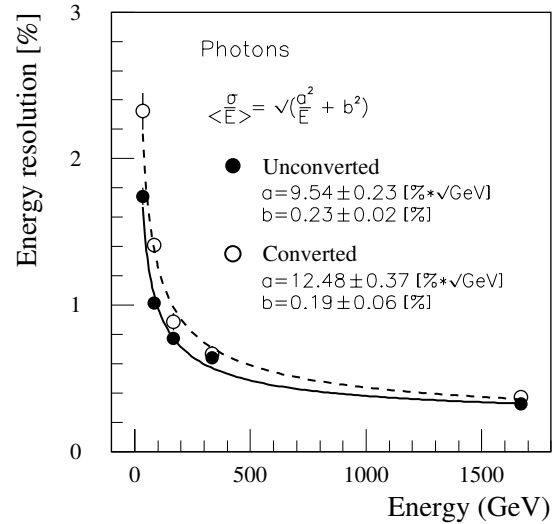
Figure 4-18   Energy resolution for converted and unconverted photons at $\eta = 1.1$, as a function of the photon energy. The fraction of converted photons is about 40% at $\eta = 1.1$.

Figures 4-17, 4-18 and 4-19 show the energy resolution, as a function of the incident energy, at various pseudorapidities. The points follow a scaling law of the type $1/\sqrt{E(GeV)}$, apart from a small local constant term (hereafter called 'cell constant term'). The latter originates mainly from residual longitudinal leakage and response modulation after correction. The sampling term is of order $10\%/\sqrt{E(GeV)}$ or smaller, except for converted photons and electrons at the end of the barrel, where the material in front of the calorimeter is large.

For very energetic showers, the longitudinal leakage behind the calorimeter would lead to an increase of the constant term if not compensated. By weighting the energy deposited in the back compartment (the optimum weight is ~1.3 for showers of $E = 1$ TeV in the barrel), an energy resolution of 0.5% or better can be achieved in the TeV range. For instance, for photons at $\eta = 2.0$, the cell constant term decreases from 0.4% to 0.28% when the energy deposited in the back compartment is weighted.
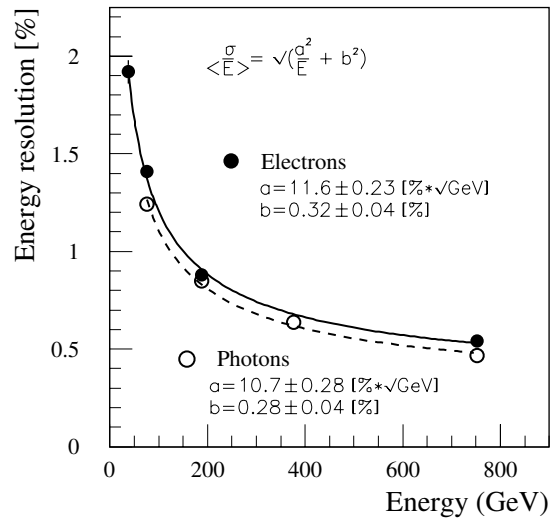
Figure 4-19 Energy resolution for electrons and photons at $\eta = 2.0$, as a function of the incident energy.
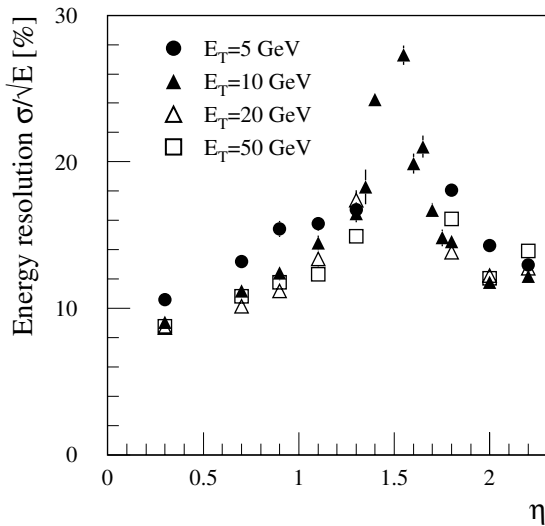
Figure 4-20 Energy resolution for electrons of various transverse energies, as a function of pseudorapidity.
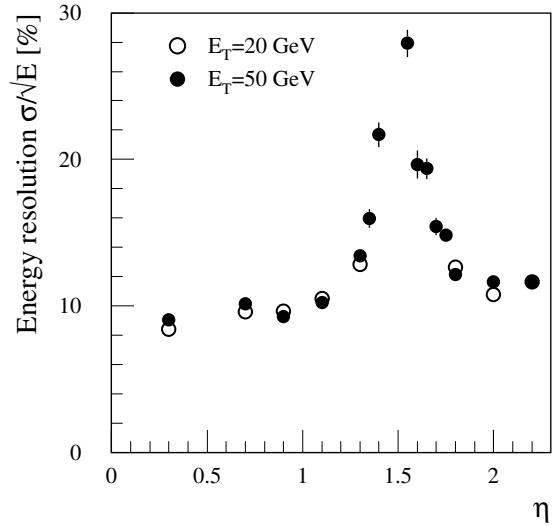
Figure 4-21 Energy resolution for photons of $E_T = 20$, 50 GeV as a function of pseudorapidity.

The calorimeter resolutions, as obtained over the full pseudorapidity coverage and for particles of various energies, are presented in Figures 4-20 (electrons) and 4-21 (photons). The cell constant term has not been unfolded. For this reason, these results are slightly worse than the sampling terms obtained from the fits to the points in Figures 4-17 - 4-19, especially in the end-cap region. With the exception of the crack region at $|\eta| \sim 1.5$, the dependence of the resolution on pseudorapidity follows the changes in the amount of upstream dead material and in the sampling frequency. The crack regions are discussed in more detail in Section 4.3.8.

One modification of the layout, which may have an impact at low energy, is the above-mentioned use of a tapered cold wall instead of an isogrid for the barrel cryostat. The sampling terms for electrons of $E_T = 10$ GeV, as obtained with the old isogrid wall and the

Figure 4-22 Energy resolution for electrons of $E_T = 10$ GeV, as function of pseudorapidity, as obtained with the old isogrid wall (dots) and the new tapered wall (open triangles) of the barrel cryostat.

new solid wall, are compared in Figure 4-22 . No significant difference is observed. This is because at small pseudorapidity, where the increase in material is largest, the total amount of material is relatively small (~2 X_0). On the other hand, at large pseudorapidity, where the amount of material is critical, the new tapered wall has an equivalent thickness similar to the isogrid wall.

Figure 4-23 shows the reconstructed energy spectra for photons of $E_T = 50$ GeV at $\eta = 2.0$, obtained with a realistic electric field map or with a uniform field. The calibration coefficients (Equation 4-1) determined with a uniform field have been used in both cases. The distribution obtained with a realistic field peaks at lower values, as a consequence of the lower electric field in the folds. On the other hand, there is no significant difference in the resolution and in the tails of the spectra.

4.3.6 Energy resolution: constant term

To meet the LHC physics requirements [4-1], the global constant term of the energy resolution, over the full calorimeter coverage relevant for precision physics, must be equal to or smaller than 0.7%. The strategy to achieve this goal is to have a small constant term, by con-

Figure 4-23 Ratio between the reconstructed and the generated energy for photons of $E_T = 50$ GeV at $\eta = 2.0$, as obtained when a uniform electric field (dashed line) or a realistic field (full line) are simulated. Both distributions are normalised to the same number of events.

struction, over a limited region of the calorimeter coverage (the so-called 'local' constant term), and then calibrate out long-range non-uniformities *in situ* by using physics samples (*e.g.* $Z \rightarrow ee$ events).

In this section, the main sources of non-uniformities contributing to the local and overall constant term of the calorimeter resolution are discussed, and first measurements obtained with the calorimeter parts under construction are presented.

A summary of the expected contributions to the constant term is given in Table 4-3. These numbers are based on the experience gained in the construction and test of various prototypes [4-6].

4.3.6.1 The local constant term

Table 4-3 Expected short-range and long-range contributions to the overall constant term of the energy resolution.

Source	Contribution to the constant term (%)
Detector geometry (short range):	
Residual ϕ modulation, leakage, *etc.*	0.25
Variation of sampling fraction (end-cap only)	0.35
Mechanics (short range):	
Absorber and gap thickness	<0.25
Calibration (short range):	
Amplitude accuracy and stability	0.25
Difference between calibration and physics signal	0.3
Long range:	
Signal dependence on LAr impurities	< 0.1
Signal dependence on temperature	0.2
HV variations	<0.1
Others (*e.g.* upstream material, mechanical deformations, cable lengths.)	<0.1

The goal is to achieve a local constant term over a calorimeter region of size $\Delta\eta \times \Delta\phi = 0.2 \times 0.4$, which corresponds to the size of a motherboard in the middle compartment, of 0.5%. There are 440 such regions in the whole EM Calorimeter.

In the absence of imperfections in the detector mechanics and electronics, a constant term of about 0.25% is obtained for particles incident in a given cell of the barrel (see Section 4.3.5). The main contribution to this cell constant term is the residual ϕ modulation after correction. Additional contributions to the local constant term come from mechanical and calibration non-uniformities. Adding quadratically the short-range contributions listed in Table 4-3, a local constant term of about 0.5% (0.6%) is obtained in the barrel (end-cap), which is slightly larger than the values presented in [4-1]. This is mainly due to a more conservative estimate of the last short-range contribution in Table 4-3, which comes from possible differences between the calibration and the physics signals and which is discussed in Section 4.3.6.3. Due to the limited knowledge of these effects, their sizes can only be assessed from the measurements performed with the module zero.

4.3.6.2 The overall constant term

In order to fully benefit from the good expected local constant term, it is necessary to guarantee the calorimeter long-range uniformity over the 440 regions. Several potential sources of long-range non-uniformities can be envisaged.

The liquid-argon pollution can produce non-uniform signal losses as a function of time. Although the use of fast shaping reduces the sensitivity of the response to the pollution, extensive measurements of all the materials which will be inside the cryostat have been performed, also under irradiation [4-7]. Furthermore, the calorimeter will be equipped with several probes, which will monitor the liquid-argon purity as a function of time.

The calorimeter response depends on the temperature of the liquid Argon. The signal drops by about 2% per degree, which is due to both the variation of the LAr density and the variation of the electron drift velocity. Detailed calculations of the temperature uniformity inside the barrel cryostat have started. In addition, temperature probes installed inside the cryostat will monitor the temperature variation with time [4-8], with a precision of better than 0.1 K.

The material distribution in front of the EM Calorimeter, possible small deformations of the calorimeter, the different lengths of the calibration cables, chosen to compensate for the particle time of flight in physics events, could give rise to additional response non-uniformities. However, these non-uniformities do not vary with time, and therefore corrections should be more straightforward.

In addition to the monitoring system based on probes, the long-range non-uniformities can be monitored and corrected *in situ* by using control physics samples such as $Z \rightarrow ee$ events. This is discussed in Section 4.6.2.

4.3.6.3 Detector uniformity measurements

Parts of the EM Calorimeter have already been built and prototypes of the electronics, operational in test beams, exist. Preliminary measurements have been performed in order to check whether the requirements for the constant term are satisfied. A selection of these measurements is discussed below.

Lead thickness. The lead plates for the whole EM Calorimeter have been delivered. The thicknesses have been measured with two methods: a fast on-line method during the rolling process based on X-ray absorption, and a more careful off-line method based on ultrasound [4-9]. The distribution of the average plate thickness, as obtained from the on-line measurements, is shown in Figure 4-24 for the full set of 2048 plates equipping the barrel region $|\eta| > 0.8$ (nominal Pb thickness is 1.13 mm). If the plates were assembled randomly, the dispersion (~7 μm) would already
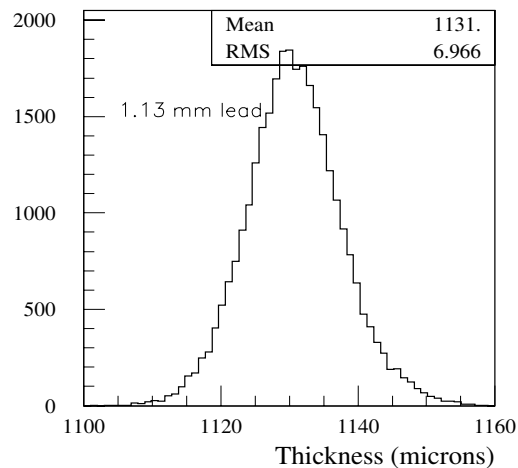
Figure 4-24 Distribution of the thickness of the 2048 lead plates for the half-barrel region $|\eta| > 0.8$, as measured at several positions inside the plates.

result in a contribution to the constant term of less than 0.2%, which is within the requirements mentioned above. In order to further minimise the response variation due non-uniformities in the absorber thickness, an algorithm has been developed to sort and pair the absorber plates [4-10]. It minimises the thickness dispersion computed over five plates, by considering several combinations of plates. The contribution of the fluctuations in the plate thicknesses to the constant term is about $0.6 \times \sigma^{(5)}/e_n$, where $\sigma^{(5)}$ is the rms of the mean thickness of the five plates and e_n the nominal thickness of the plates. Table 4-4 shows the improvement due the pairing procedure for the absorbers of the barrel module zero. For the 1.13 mm plates the dispersion decreases by almost a factor of two, whereas no improvement is observed for the 1.53 mm plates since the original distribution is already very good.

Table 4-4 For the plates of the barrel module zero, the overall dispersion in the thicknesses, and the normalised dispersion over five absorber plates as obtained without and with pairing.

Lead plates thickness	Rms dispersion	$\sigma^{(5)}/e_n$ without pairing	$\sigma^{(5)}/e_n$ with pairing
1.13 mm	8.5 µm	7.4×10^{-3}	4.1×10^{-3}
1.53 mm	6.8 µm	2.3×10^{-3}	2.2×10^{-3}

Calibration system. To correct the gain dispersion of the electronic channels, which is of order a few percent, a precise calibration system is required.

A calibration pulse which simulates the triangular signal from the calorimeter, with a fast rise-time and a very precise amplitude, is required. Calibration boards, with 128 channels, have been designed and built for the beam tests. The measurements demonstrate good linearity over a 16-bit dynamic range and good uniformity. Figure 4-25 shows the pulse amplitude, as a function of the channel number, for a few boards already characterised. The dispersion of 0.11% is compatible with the intrinsic limitation of the injection resistors [4-2].

The signal is sent through cables to the motherboards and then distributed to the calorimeter. Since the calibration cables are terminated at both ends, the amplitude is not very sensitive to the characteristic impedance of the cables. However, production tolerances on the impedance dispersion from cable to cable at the level of 4% rms are needed to achieve the required uniformity of the calibration system. Such precision has been obtained for the cables built for the module zero's [4-11]. The uniformity of the calibration signal has been measured including cables and pin carrier, in order to simulate the ATLAS set-up, and no sizeable deterioration of the amplitude dispersion has been observed.

Physics and calibration signals do not follow exactly the same path, which can give rise to differences between them. In particular, any inductance in parallel with the calibration signal but in series with the physics signal introduces amplitude differences. Such inductances exist by construction in the electrodes and have to be corrected for. Moreover, cross-talk affecting differently the physics and the calibration signals would also introduce non-uniformities. A careful design of the motherboards is being developed, in order to minimise additional sources and to ensure small cross-talk. Measurements of these effects with module zero's are foreseen in the near future.
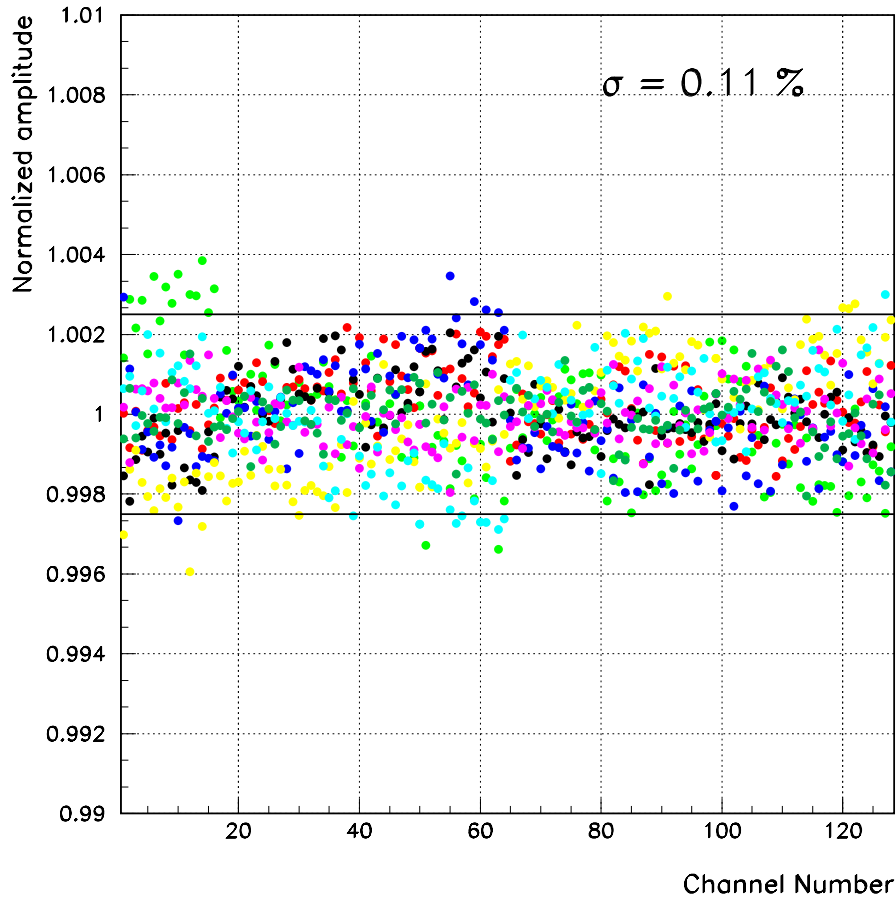
Figure 4-25 Normalised output signals from eight calibration boards, as a function of the channel number.

4.3.7 Low-energy tails

Most of the low-energy tails in the energy spectra reconstructed in the EM Calorimeter are caused by the material in the Inner Detector. A photon/electron shower which starts in the Inner Detector is opened in ϕ by the magnetic field, the effect being larger for smaller particle energies and interaction radii. As a consequence, the shower energy is not completely contained in the calorimeter cluster, and low-energy tails appear in the calorimeter energy distributions. For this reason, asymmetric clusters (larger in ϕ than in η) are used, which are bigger for electrons (3x7 cells) than for photons (3x5 cells).

The material distribution in the Inner Detector is shown in Figure 3-5, and the evolution since the detector TDR's is discussed in Section 3.2.1.

The dependence of the low-energy tails on the particle interaction radius is illustrated in Figure 4-26, which shows the distribution of the radius at which the electron has radiated the hardest bremsstrahlung photon, for electrons of $E_T = 10$ GeV at $\eta = 1.2$. At this pseudorapidity, the material in the Inner Detector reaches $0.8\ X_0$. Clear peaks are visible at the positions of the Pixel and Silicon layers (at this pseudorapidity the electron track crosses only three SCT layers before entering the end-cap region), as well as a continuous distribution in the TRT region. The open histogram is for all electrons and the shape and height of the peaks simply reflect the dis-

tribution and amount of material in the various parts of the Inner Detector. The black histogram is for electrons in the low-energy tails of the calorimeter energy measurement, *i.e.* electrons for which the reconstructed energy is smaller than 92% of the true energy. At this pseudorapidity, the fraction of events in the tails is (19.2 ± 0.6)%. It can be seen that the tails are populated mainly by electrons which have interacted in the internal layers of the Inner Detector. A more quantitative estimate of the contribution of the various parts of the Inner Detector to the tails is given in Table 4-5. Each of the pixel and SCT layers produces about 2% of the tail. A similar contribution comes from the ensemble of the TRT and the services running at the outer radius, despite the fact that the total material in this region is much larger than in a single precision layer. Some decrease of the tail with radius is visible also in the three SCT layers.
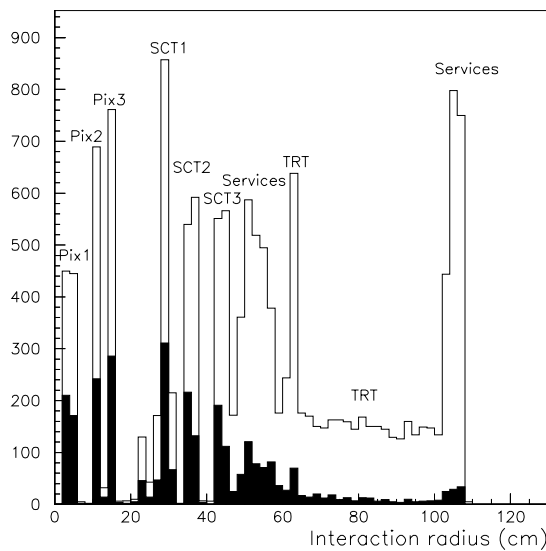
Figure 4-26 Distribution of the radius at which the electron has emitted the hardest Bremsstrahlung photon for electrons of E_T = 10 GeV at η = 1.2. The white histogram is for all electrons, the black histogram is for electrons in the low-energy tail of the calorimeter spectrum.
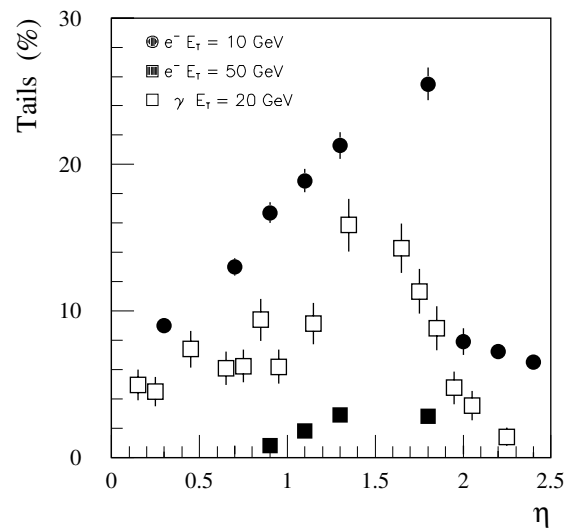
Figure 4-27 Fraction of events for which the energy reconstructed in the EM Calorimeter is smaller than 92% of the true energy, as a function of pseudorapidity and for electrons and photons of various transverse energies.

Figure 4-27 shows the tails for electrons and photons of various transverse energies, as a function of pseudorapidity. The distribution of the points in Figure 4-27 reflects mainly the material profile in the Inner Detector shown in Figure 3-5. By combining the information of the Inner Detector and of the calorimeter, it is possible to reduce the tails by 20%. This is discussed in Chapter 7.

4.3.8 Crack regions

There are regions in the EM Calorimeter acceptance where the detector performance is degraded. These regions, which correspond to the transitions in η between mechanically independent detector modules, are:

- A 6 mm wide liquid-argon gap between the two half barrels at η = 0. As already mentioned in Section 4.1.1, since the time of the Calorimeter TDR the cold flange, which was

Table 4-5 Contributions to the calorimeter low-energy tails coming from the various layers of the Inner Detector. The errors are ~0.2%.

	Contributions to tails (%)
Beam pipe	0.5
Pixel barrel 1	2.2
Pixel barrel 2	2.3
Pixel barrel 3	2.2
Pixel support	0.4
SCT barrel 1	2.5
SCT barrel 2	2.2
SCT barrel 3	1.9
SCT services	2.4
TRT	2.4
TOTAL	19.2 ± 0.6

located at $\eta \sim 0$, has been moved to the end of the barrel, thus reducing the amount of material in this region. As a consequence, the detector response is degraded over a region of size $|\Delta\eta| < 0.01$, which is narrower than in [4-1]. No further discussion of this region is presented here.

- A 3 mm wide liquid-argon gap at $|\eta| \sim 2.5$ between the outer and the inner wheel of the end-cap calorimeter, which is preceded by the end-cap intermediate support ring. Since the detector response is deteriorated over a very small region of size $|\Delta\eta| < 0.01$, and since nothing has changed with respect to the results reported in [4-1], no further discussion of this region is presented here.

- The transition between the barrel and the end-cap calorimeters at $|\eta| \sim 1.5$. Since a few changes have been made to the layout of this region after the Calorimeter TDR, and since this transition gives rise to the largest crack in the calorimeter acceptance, an update of the detector response around $|\eta| \sim 1.5$ is presented below (Section 4.3.8.1).

- Gaps between presampler sectors. A detailed study has been performed of the energy losses in the small inactive gaps between the barrel presampler modules [4-12]. The results are presented in Section 4.3.8.2.

The absence of cracks in azimuth is an intrinsic feature of the accordion geometry.

4.3.8.1 Barrel/end-cap transition region

A detailed description of the detector response in this region is given in [4-1], therefore only an update is presented here.

The layout of the transition between the barrel and the end-cap calorimeter is shown in Figure 4-i and the material in front of it in Figure 4-iii. The barrel and end-cap calorimeters are housed in two different cryostats, separated by 9.5 cm of space used to route services and cables of the Inner Detector. Particles incident at $|\eta| \sim 1.5$, that is at the end of the barrel calorimeter,

where the dead material in front of the end-cap calorimeter reaches a maximum of 7 X_0, cross six cryostat walls, the edge of the coil, cables and services and several layers of dead liquid before reaching the end-cap calorimeter. For larger pseudorapidities, the material is smaller because the coil and the cold wall of the barrel cryostat do not contribute.

Since the time of Calorimeter TDR, the amount of material in this region has slightly increased (see Figure 4-9). The new tapered wall has a marginal impact on the material at the end of the barrel, whereas the cold flange of the barrel cryostat adds about 1.5 X_0 at $\eta \sim -1.5$ and the Inner Detector services add 0.4 X_0 at the end of the barrel, with respect to the layout in [4-1]. It is stressed again that the increase by about 0.8 X_0 at $|\eta| \sim 1.7$ in Figure 4-9 is due to the fact that in the detector simulation used for the studies presented here the warm flange had titanium (instead of aluminium) bolts. Therefore these results are somewhat conservative.

Energy losses in this region can be, to a large extent, recovered by using two dedicated devices: the end-cap presampler, which covers the region $1.5 < |\eta| < 1.8$, and a scintillator slab, which covers the region $1.0 < |\eta| < 1.6$.

The energy response at the barrel/end-cap transition is shown in Figure 4-28 for low-energy electrons, which are most sensitive to the dead material. The uncorrected response drops by more than a factor of two at the end of the barrel calorimeter. By using the energy deposited in the presampler and in the scintillator, suitably weighted, the average response can be recovered.
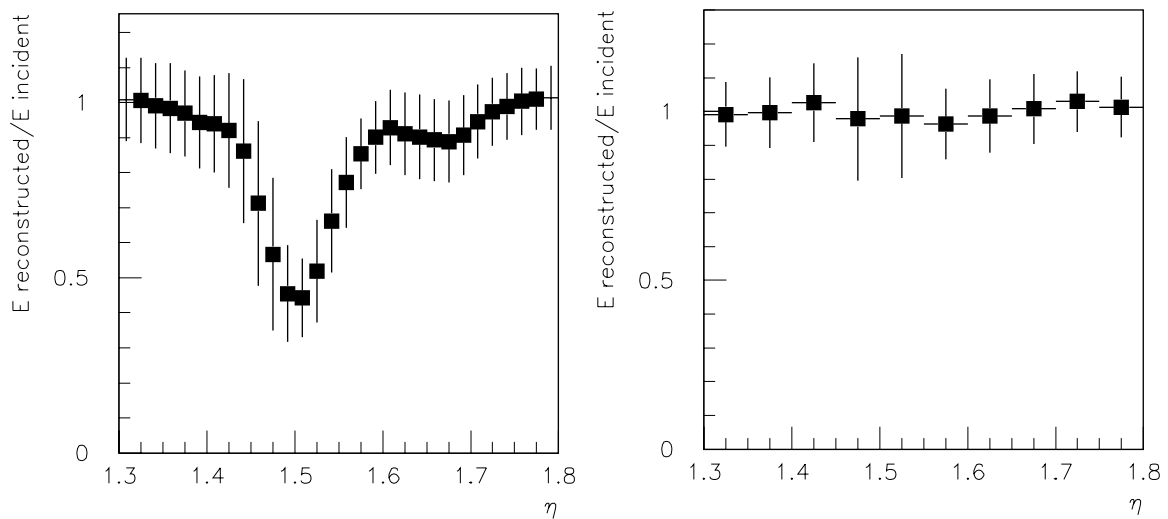
Figure 4-28 Ratio between the energy reconstructed in the calorimeter (3x7 cell cluster) and the incident energy, as a function of pseudorapidity in the barrel/end-cap transition region, for electrons of $E_T = 10$ GeV, before (left) and after (right) adding the (weighted) energy in the presampler and in the scintillator. The error bars give the rms spread on the reconstructed energy.

The correlation between the energy deposited in the presampler and in the calorimeter, which is exploited to compensate for the energy lost upstream of the calorimeter, is depicted in Figure 4-29. Figure 4-30 shows the energy resolution in the transition region for electrons of $E_T = 10$ GeV and photons of $E_T = 50$ GeV. It can be seen that adding the presampler and the scintillator weighted energies improves the energy resolution by up to a factor of three. The resolution at $|\eta| \sim 1.5$ is a factor of two worse than in [4-1], as a consequence of the larger material in the transition region with the present layout. For precision physics, fiducial cuts are applied in this region over a rapidity range of size $|\Delta\eta| \sim 0.15$.
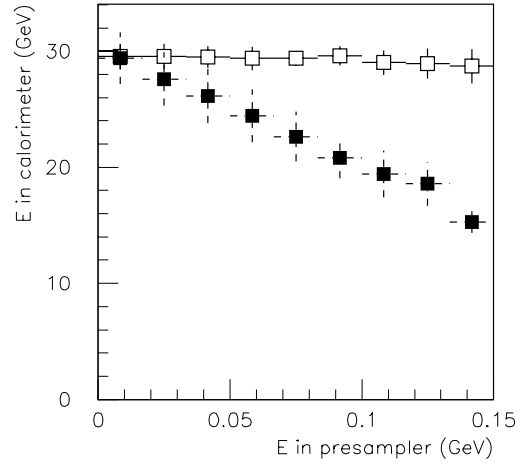
Figure 4-29 Calibrated energy reconstructed in the calorimeter, as a function of the energy deposited in the presampler, for electrons of $E = 30$ GeV at $\eta \sim 1.7$, before (closed symbols) and after (open symbols) adding the (weighted) presampler energy.
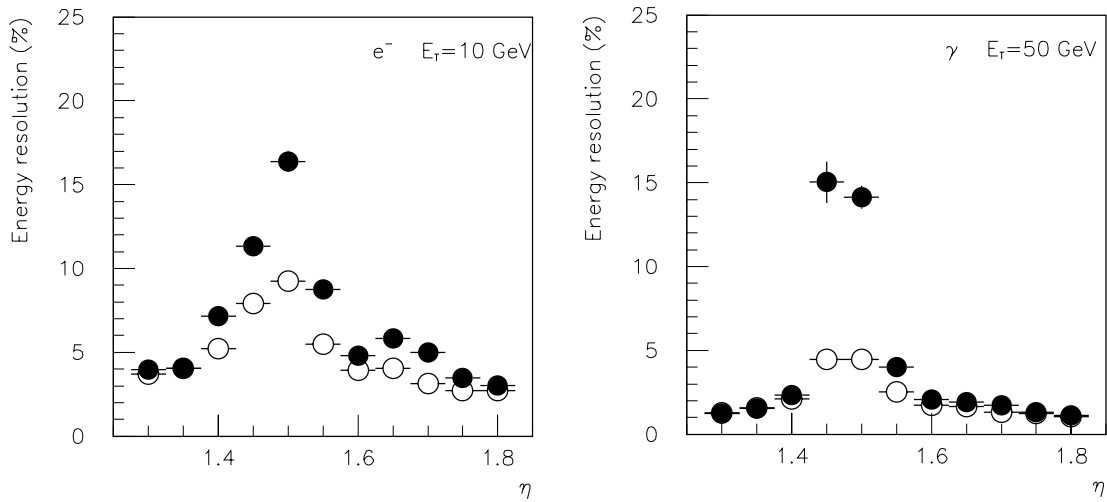
Figure 4-30 Energy resolutions for electrons of $E_T = 10$ GeV (left) and photons of $E_T = 50$ GeV (right), as a function of pseudorapidity in the transition region, before (closed symbols) and after (open symbols) adding the weighted energy deposited in the presampler and in the scintillator. Electronic and pile-up noise are not included. A 3x7 cell cluster has been used.

4.3.8.2 Gaps between presampler sectors

There is a gap between the barrel presampler sectors in the ϕ direction. At the temperature of liquid argon, this gap is about 1.8 mm wide: the clearance between the skirts is around 1 mm while the skirt thickness is 0.4 mm. Furthermore, the distance between the skirt inner conductive surface and the copper edge of the anode is 2 mm. The fraction of energy ρ which is not measured because of these gaps was determined by using a two-dimensional map of the electric field and full charge collection. The probability that a fraction ρ of the presampler energy is lost because of the gaps is shown in Figure 4-31. For electrons of $E_T = 10$ GeV at $\eta = 0.9$, on average 1.3% of the energy deposited in the presampler is lost in the gaps, which corresponds to 0.1% of the total shower energy. The influence of the presampler gaps on the energy measured in the presampler and in the calorimeter is therefore small.
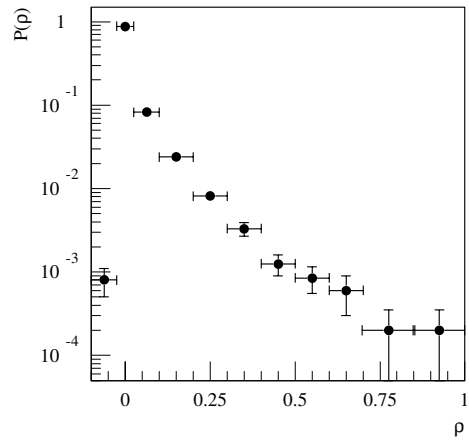
Figure 4-31 Probability that a fraction ρ of the presampler energy is lost due to the gaps between sectors for electrons of $E_T = 10$ GeV at $\eta = 0.9$.

4.3.9 Total energy resolution

The total energy resolution of the calorimeter includes the contributions of the sampling term, of the constant term (0.7%) and of the electronic and pile-up noise expected at low or high luminosity, individually discussed in the previous sections.
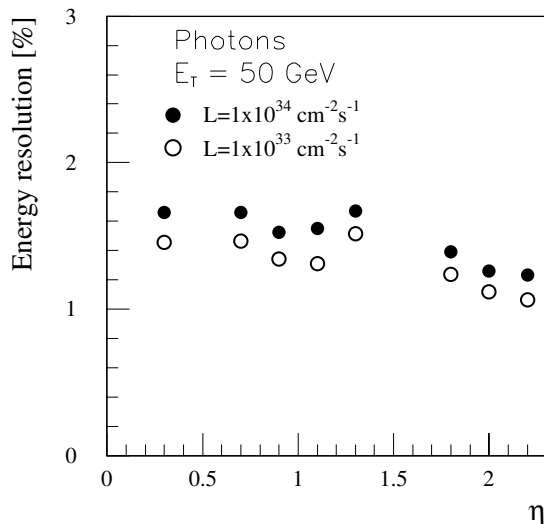
Figure 4-32 Total energy resolution for photons of $E_T = 50$ GeV, as a function of pseudorapidity, as obtained at low (open symbols) and high (closed symbols) luminosity.
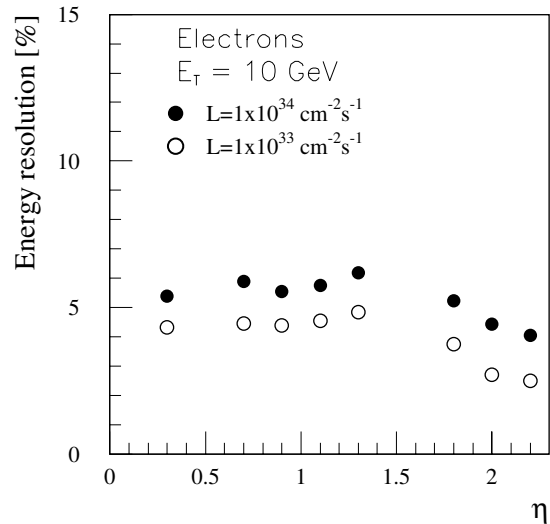
Figure 4-33 Total energy resolution for electrons of $E_T = 10$ GeV, as a function of pseudorapidity, as obtained at low (open symbols) and high (closed symbols) luminosity.

For photons of moderate E_T (Figure 4-32) the total resolution is of order 1.6% or better at all luminosities over most of the pseudorapidity coverage. For low-energy electrons (Figure 4-33) the total resolution is about 5% (3%) in the barrel (end-cap). This performance ensures mass resolutions of order 1.5 GeV for $H \rightarrow \gamma\gamma$ and $H \rightarrow eeee$ decays with $m_H \sim 100$ GeV (Chapter 7), and therefore good sensitivity to both these channels (see Chapter 19).

The impact of the electronic noise and pile-up on the reconstructed energy spectra for low-energy electrons is further illustrated in Figure 4-34. Distributions are shown for the case of no noise and no pile-up, for the noise and pile-up expected at low luminosity, and for the noise and pile-up expected at high luminosity. The smearing of the energy spectrum with increasing noise is evident.
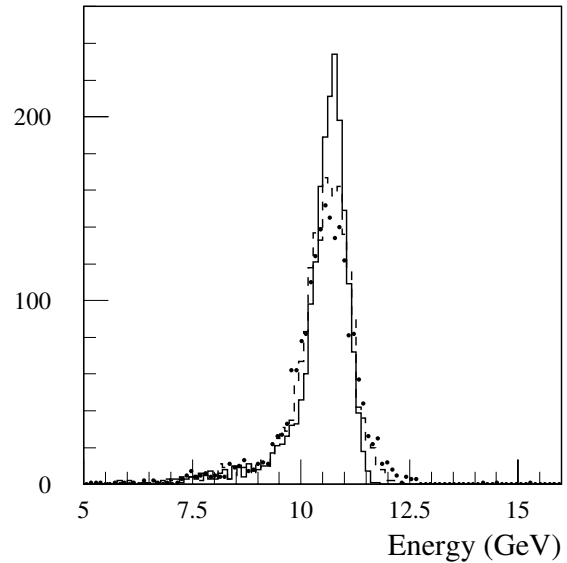
Figure 4-34 Energy spectra for electrons of $E_T = 10$ GeV at $\eta = 0.3$, as obtained without pile-up and noise (full line) and with the pile-up and noise expected at low luminosity (dashed line) and high luminosity (dotted line). The three distributions are normalised to the same number of events.

4.4 Position and angular measurements

The excellent longitudinal and lateral granularity of the EM Calorimeter, in particular of the strip section, allow several measurements of the shower position to be performed with high precision. The position in ϕ can be measured in the middle compartment and the position in η can be measured in the strip section and in the middle compartment. By combining the measurements of the shower η–position obtained in the first two compartments, it is possible to determine the shower direction in θ, and therefore to measure the position of the primary vertex along the z axis ('pointing'). Indeed, the z-position of the primary vertex is not known unambiguously at high luminosity in events with a $H \rightarrow \gamma\gamma$ decay, and therefore the angular information from the calorimeter is needed to obtain a precise reconstruction of the Higgs mass. By using the same method it is also possible to tag photons which do not come from the primary vertex. Such photons are predicted by Gauge-Mediated-Supersymmetry-Breaking theories (see Chapter 20).

The various position and angular measurements provided by the EM Calorimeter are discussed below.

4.4.1 Measurement of the position in ϕ

The ϕ position of a cluster is measured in the middle compartment. Because of the accordion shape of the cells, the measured position is affected by an offset, which depends on the shower depth and which is corrected for as described in [4-1]. Figure 4-35 shows the ϕ-resolution obtained for unconverted photons of $E_T = 20$ and $E_T = 50$ GeV without pile-up and electronic
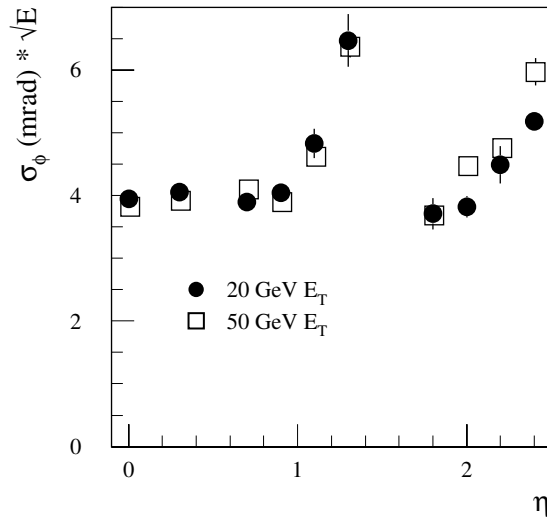
Figure 4-35 Calorimeter resolution in ϕ, as a function of pseudorapidity, for unconverted photons of E_T = 20 GeV and E_T = 50 GeV.
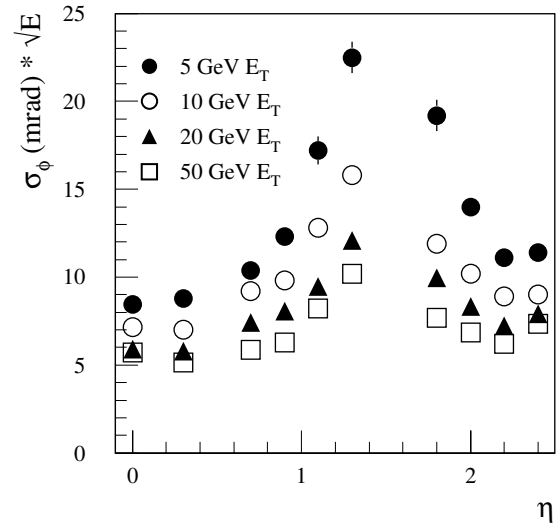
Figure 4-36 Calorimeter resolution in ϕ, as a function of pseudorapidity, for electrons of various transverse energies.

noise. The calorimeter resolution scales as 4-6 mrad/$\sqrt{E}$, corresponding to 6.5-10.5 mm/$\sqrt{E}$ in the barrel and to 4-5 mm/$\sqrt{E}$ in the end-caps. The scaling law $1/\sqrt{E}$ is not valid for electrons, which emit bremsstrahlung in the Inner Detector. Figure 4-36 shows that the ϕ-resolution for electrons degrades faster at low energies.

Electronic noise and pile-up at high luminosity deteriorate the position resolution for E_T = 5 GeV electrons by up to a factor of two if the standard cluster of 3x7 cell is used. A smaller window (3x5 cells) is therefore more suitable to measure the shower position for low-energy particles at high luminosity.

The use of the calorimeter ϕ-position measurement for many physics applications is illustrated in Chapter 7.

4.4.2 Measurement of the position and direction in η

4.4.2.1 Photons coming from the vertex

In order to reconstruct the $H \rightarrow \gamma\gamma$ invariant mass at high luminosity, the calorimeter must be able to measure the direction of both photons in η with high precision. This measurement makes use of the reconstructed shower positions and shower depths in the strip and middle compartments. Corrections for the modulation of the reconstructed position with the particle impact point ('S-shapes') have to be made to achieve a good resolution.

The shower depths in the calorimeter and the S-shape corrections in the first compartment were determined in the same way as in [4-1]. As the dominant contribution to the final resolution in the photon direction comes from the S-shape corrections in the middle compartment, an attempt has been made to improve these corrections.

The S-shapes depend on:

- The position $\eta^* = \text{mod}(\eta, 0.025)$ of the shower in the cell, relative to the cell boundaries.

- The shower depth, which depends on the material in front of the calorimeter and on the particle energy. This depth fluctuates event by event and is strongly correlated with the fraction of energy *F1* measured in the first compartment.

- The shower pseudorapidity, especially in the end-caps, because the physical cell size decreases with respect to the shower size as η increases.

Two feed-forward multilayer neural networks (NN) have been used to fit the S-shape corrections as a function of (η^*, η, F_1) in the barrel and in the end-caps. More details about this method are given in [4-13].

The resolutions of the measurements of the shower η–positions in the first two compartments of the calorimeter are presented in Figure 4-37. From these two measurements one can obtain the photon direction in θ, after dividing by the lever arm, and thus a measurement of the position of the primary vertex in *z*. The calorimeter angular resolution obtained in this way is shown in Figure 4-38. It is of the order of 60 mrad$/\sqrt{E}$, where *E* is measured in GeV. The resulting resolution on the reconstructed *z*-position of the vertex is shown in Figure 4-39. The use of a better correction in the middle compartment improved the *z*-resolution by 10% to 20% at all pseudorapidities with respect to the results presented in [4-1]. If the electronic and pile-up noise expected at high luminosity are included, the vertex resolution degrades by about 20%.

In $H \rightarrow \gamma\gamma$ events, two photons are available in the final state, and the primary vertex can be reconstructed as the weighted average of the two vertices provided by both photons plus the constraint that the nominal vertex position is at $z = 0$ and has a dispersion of $\sigma = 5.6$ cm. The vertex obtained in this way is compared to the true vertex in Figure 4-40. The precision of the vertex measurement provided by the calorimeter alone, averaged over the full pseudorapidity coverage, is 1.3 cm. Tails are small, given that about 87% of the events are contained within $\pm2\sigma$, where $\sigma = 1.3$ cm, from the peak of the distribution.

It is expected that the readout electrodes of the EM Calorimeter will be mutually aligned in z with a dispersion of about ±400 μm. The impact of this non-perfect alignment on the position and angular measurements has been evaluated, and the results have been used to define the mechanical tolerances. In the simulation each of the 1024 electrodes was displaced by an amount randomly chosen in the range ±400 μm or ±1000 μm around the nominal position. The shower position was reconstructed using corrections determined with perfect alignment. The results are summarised in Table 4-6.

Table 4-6 Resolution in the position, angle and vertex measurements, as obtained from the calorimeter for photons of $E_T = 50$ GeV at $\eta = 0.3$ and for three dispersions in the electrode alignment.

Dispersion	0 μm	±400 μm	±1000 μm
σ_η strip section	$(0.217 \pm 0.005) \times 10^{-3}$	$(0.215 \pm 0.008) \times 10^{-3}$	$(0.274 \pm 0.009) \times 10^{-3}$
σ_η middle compartment	$(0.695 \pm 0.013) \times 10^{-3}$	$(0.652 \pm 0.021) \times 10^{-3}$	$(0.657 \pm 0.021) \times 10^{-3}$
σ_θ (mrad)	8.270 ± 0.180	7.180 ± 0.260	7.540 ± 0.250
σ_z (cm)	1.380 ± 0.030	1.268 ± 0.043	1.260 ± 0.042
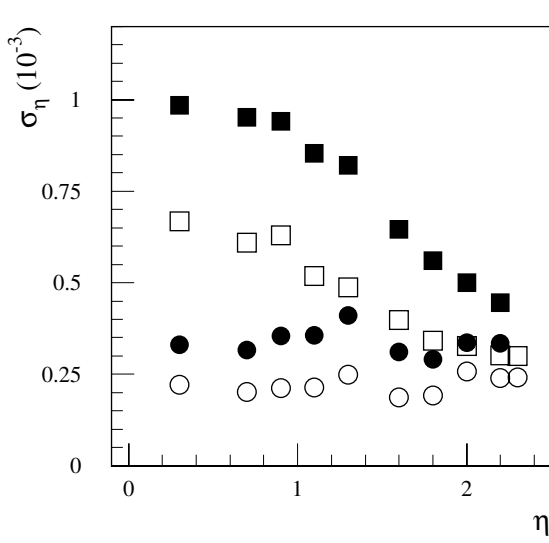
Figure 4-37 Position resolution in the η–direction, as measured in the strips (dots) and in the middle compartment (squares), as a function of pseudorapidity, for photons of $E_T = 20$ GeV (closed symbols) and $E_T = 50$ GeV (open symbols).
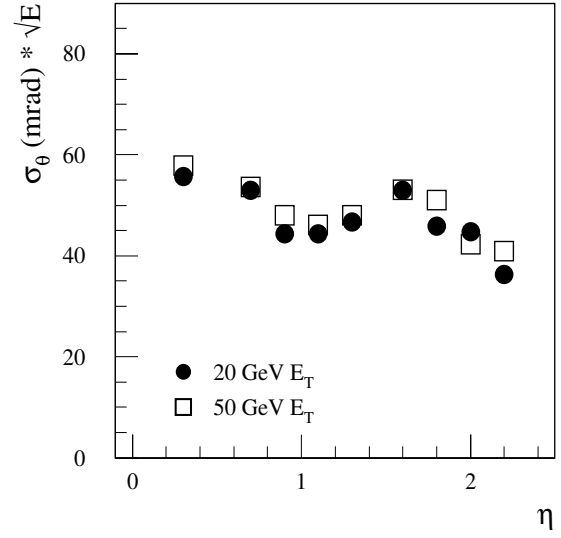
Figure 4-38 Calorimeter angular resolution in θ, as a function of pseudorapidity, for photons of $E_T = 20$ GeV and $E_T = 50$ GeV.

The position resolution in the strip section degrades with the increasing dispersion, as expected since the considered dispersions are comparable to, or larger than, the intrinsic resolution of the strips. On the other hand, the angular and vertex resolutions are not affected by the misalignment, at least up to ±1000 μm, because when the electrode position is displaced, both compartments are displaced in the same direction and by the same amount.

4.4.2.2 Non-pointing photons

As discussed in more detail in Chapter 20, Gauge-Mediated-Supersymmetry-Breaking (GMSB) models can give rise to a long-lived lightest neutralino (χ_1^0), which could decay via $\chi_1^0 \rightarrow \tilde{G}\gamma$ inside the volume of the Inner Detector. With typical χ_1^0 masses of order 100 GeV, the decay into a massless photon and a very light Gravitino (mass $\approx$ keV) often produces a finite opening angle. Since both the χ_1^0 and the Gravitino escape detection, the photon would provide the only evidence of the decay, and the signature would be that of an isolated photon which does not point back to the main event vertex.

As described previously, the segmentation of the EM Calorimeter has been designed to allow measurement of photon direction by using the lateral and the longitudinal positions of the shower in the strip section and in the middle compartment. While the geometry of the EM Calorimeter has been optimised for the case of photons which point back to the interaction point, the fine segmentation allows reasonable angular precision to be achieved over a wide range of photon impact angles.
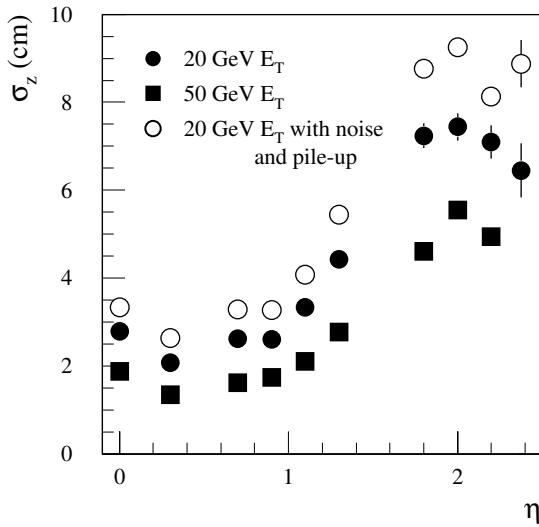
Figure 4-39 Resolution in the position of the primary vertex along the z axis, as obtained from the calorimeter pointing with single photons of E_T = 20 GeV (with and without pile-up and noise) and E_T = 50 GeV.
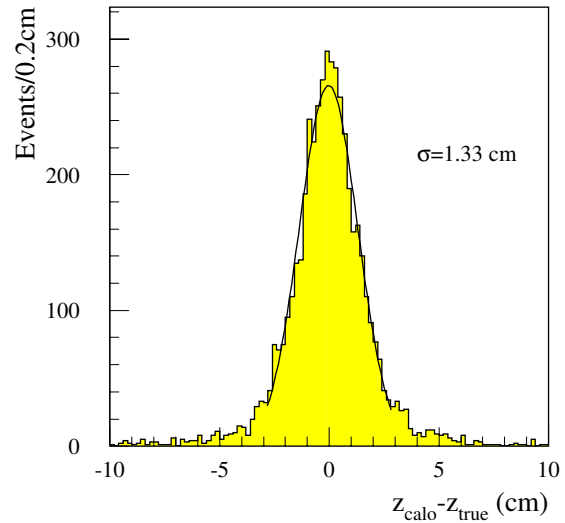
Figure 4-40 The difference between the reconstructed vertex, provided by the EM Calorimeter alone, and the generated vertex, as obtained for $H \rightarrow \gamma\gamma$ events with m_H = 100 GeV.

To study quantitatively the angular resolution for 'non-pointing' photons, two different samples of single photons were used. The first sample consisted of 20000 single photons, as produced from χ_1^0 decays in GMSB events with the GMSB parameters set to the values discussed in Section 20.3.2.4. Of these, over 7500 photons were fully simulated in the detector. In addition, the full sample of 20000 events was studied using parametrisations of the resolution function. The mean E_T of these photons, for which several distributions are presented in Section 20.3.2.4, is 84.4 GeV. The GMSB simulation shows that over 75% of the photons of interest impact the EM barrel calorimeter. For this reason, only photons hitting the barrel were considered. The second sample comprised several sets of fully-simulated 50 GeV photons, impacting the calorimeter at a given value of pseudorapidity and from a given direction. The sets were generated at

Figure 4-41 Angular resolution as a function of $\Delta\theta$, the deviation from pointing, for GMSB photons with $0 < \eta < 1.4$, as obtained with the standard reconstruction (open symbols) and with a neural network (closed symbols).

pseudorapidity values of 0.3, 0.7 and 1.2, and with angular deviations from pointing of 0°, ±15°, and ±30° in θ, as well as 0°, 7° and 19° in azimuthal angle. The electronic noise was not included in the analysis discussed here, but should have a small impact on the results because of the large photon energies.

For both samples of photons, the reconstruction of the photon direction was studied as a function of the impact point and the angular deviation from pointing. Although the φ measurement would slightly increase the ability to separate pointing from non-pointing photons, only the θ

measurement was used in the study presented here.The angular resolution obtained with the standard reconstruction algorithm (using a 7x7 cell cluster) is shown, as a function of the angular deviation from pointing ($\Delta\theta$), in Figure 4-41 for the GMSB photon sample and in Figure 4-43 for the sample of 50 GeV photons with fixed η, $\Delta\theta$ and $\Delta\phi$. Here $\Delta\theta$ and $\Delta\phi$ indicate the difference between the direction of the photon trajectory in θ and ϕ and the direction which goes from the vertex to the calorimeter impact point. The resolution from the standard reconstruction is seen to degrade significantly for large absolute values of $\Delta\theta$ and differently for different signs of $\Delta\theta$. This is due to the fact that the S-shape corrections used (see Section 4.4.2.1) are tuned for pointing events. For large deviations from pointing, these corrections are no longer valid and actually deteriorate the angular resolution. Also, for severely non-pointing showers, the cluster window considered by the standard reconstruction (which assumes pointing) is no longer centred properly on the actual cluster, and starts to lose energy leaking outside the cluster. Finally, the mean longitudinal positions of the shower in the first and second compartments have been determined by using the barycentres obtained for pointing showers, and again, for large deviations from pointing, these values are no longer valid. This effect gives rise to systematic shifts of the mean value θ reconstructed for non-pointing showers (Figure 4-42).
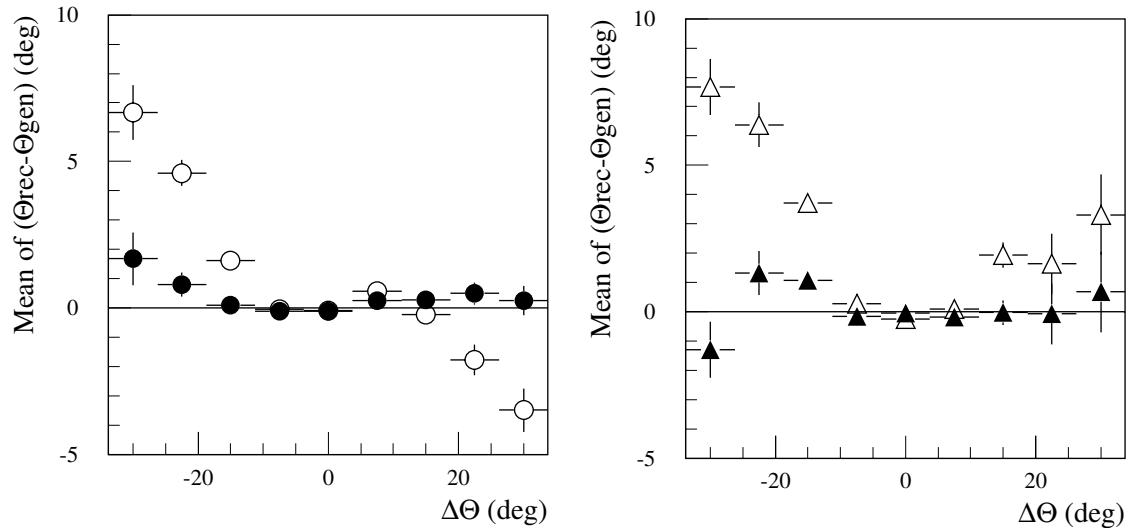
Figure 4-42 Mean of the deviation of the reconstructed value of θ from the generated value, as a function of $\Delta\theta$, for GMSB photons with $0 < \eta < 0.6$ (left) and $0.6 < \eta < 1.2$ (right), as obtained with the standard reconstruction (open symbols) and with a neural network (closed symbols).

Given this non-optimal performance of the standard reconstruction, two different algorithms have been investigated to take better into account the feature of non-pointing showers. These approaches and their performance are discussed briefly below. Details can be found in [4-14].

One approach uses a feed-forward multilayer neural network (NN) with three layers of nodes. The NN inputs were the uncorrected shower positions in the first and middle compartment, the position $\eta^* = \text{mod}(\eta, 0.025)$ of the shower in the cell for the first and middle compartment, the total reconstructed energy of the shower, the energy deposited in the strip section compared to the sum of the energies in the strip section and in the middle compartment ($E_1/(E_1+E_2)$), and the value of θ from the standard reconstruction. The generated θ for each event was used as the target to train the NN on half of the GMSB photon sample. The results were then tested on the second half of the sample. The NN resolution is shown in Figure 4-41 and the mean value of the difference between the reconstructed and generated values of θ is shown in Figure 4-42. The

NN improves the resolution and also gives a smaller systematic shift compared to the standard reconstruction. The same NN reconstruction was applied to the sample of photons generated at constant values of $\Delta\theta$ and $\Delta\phi$. It was seen that the θ reconstruction was not significantly affected by deviations from pointing in ϕ. Therefore, the results for the θ resolution can be applied independently of deviations in ϕ.

The NN was trained on a sample of photons with a wide range of deviations from pointing. Not surprisingly, the resolution for pointing photons as obtained with the NN is inferior to that of the standard reconstruction, which has been tuned to the case of pointing photons.

A second algorithm, called 'the nearest neighbour clustering', does not restrict itself to a specific cluster size. The algorithm begins with the highest energy cell in the middle compartment of the EM Calorimeter and compares the energy deposited in the adjacent cells to that in the most energetic cell. If the fractional energy deposited in an adjacent cell exceeds a preset threshold (1.5% of the most energetic cell), the cell is accepted as a part of the cluster. This procedure is repeated until no more cells in the immediate neighbourhood of cells which form the cluster exceed the fractional energy threshold. The threshold was chosen by optimising the energy resolution using a sample of 50 GeV single pointing photons. The same principle was employed to deter-

Figure 4-43 Angular resolution as a function of $\Delta\theta$, the deviation from pointing, for three different impact points in the EM Calorimeter. The open symbols show the results from the standard reconstruction, and the closed symbols show the results from the nearest neighbour clustering algorithm.

mine the energy weighted position of the shower in the first and back compartment, and a constraint was applied requiring that the position of the most energetic cell in the first and back compartment be near the vicinity of the most energetic cell in the middle compartment.

The angular measurement was made using the position information in the first and middle compartment only. The angular resolution obtained with this algorithm is shown superimposed to the standard reconstruction results in Figure 4-43. The performance of the nearest neighbour algorithm is much better than the standard reconstruction for the case of photons with large deviations from pointing. If S-shape corrections are included, the nearest neighbour algorithm provides results similar to the standard reconstruction for pointing photons and slightly better for non-pointing photons. This behaviour is expected, since the out-of-cluster showering is important for non-pointing objects in the case of fixed-cluster algorithms, whilst the nearest neighbour algorithm accounts for this effect.

In conclusion, the EM Calorimeter has a good capability to recognise and measure non-pointing photons. While the angular resolution with the standard reconstruction degrades for large deviations from pointing, preliminary investigations using neural networks and alternative clustering methods provide superior performance for non-pointing photons. As discussed in Section 20.3.2.4, the angular precision obtained so far is already sufficient to efficiently distinguish between non-pointing photons and pointing photons, providing excellent sensitivity to GMSB models. Further optimisation of the reconstruction techniques for non-pointing photons is in progress.
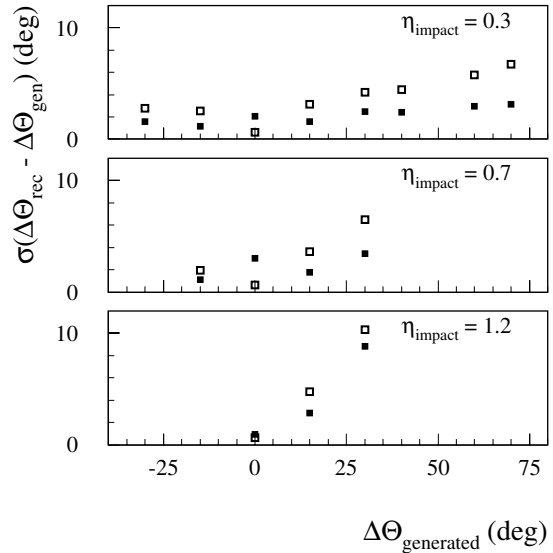
4.5 γ / π^0 separation

The EM Calorimeter must be able to efficiently reject isolated π^0, in order to extract a possible $H \to \gamma\gamma$ signal over the background. A π^0 rejection factor of about three, for a single-photon efficiency of 90%, is needed. The calorimeter performance and the algorithms used for γ/π^0 separation have been described in detail in [4-1]. Since the recent changes to the calorimeter design do not have a significant impact on this aspect of the performance, only a few additional studies and results are reported here. The effect of the electronic noise and pile-up at high luminosity has been checked with the complete simulation procedure described in Section 4.2.4. The results are summarised in Figure 4-44. For a fixed photon efficiency of 90%, the electronic noise and pile-up expected at high luminosity reduce the π^0 rejection by less than 10%.
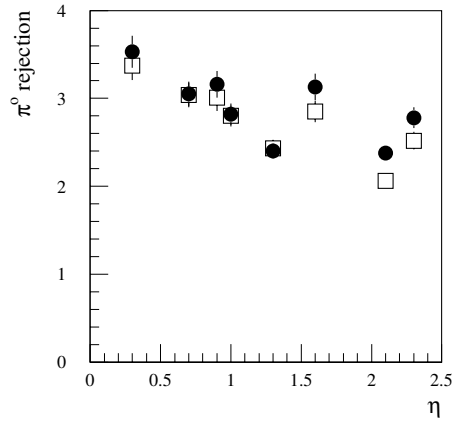
Figure 4-44 Rejection of π^0 of $E_T = 50$ GeV for 90% photon efficiency, as a function of pseudorapidity, with (open squares) and without (dots) including the electronic and pile-up noise expected at high luminosity.

Table 4-7 Rejection factors of π^0 of $E_T = 50$ GeV, as a function of the dispersion in the electrode alignment. Results are given at two pseudorapidity points and for 90% photon efficiency.

Dispersion	0 μm	± 400 μm	± 1000 μm
$\eta = 0.3$	3.53 ± 0.18	3.50 ± 0.17	3.35 ± 0.18
$\eta = 1.0$	2.89 ± 0.13	2.86 ± 0.12	2.77 ± 0.08

The impact of a possible cross-talk between adjacent strips in η has been evaluated. The results are shown in Figure 4-45. For a cross-talk of 10%, the π^0 rejection is degraded by about 10%. Recent results obtained from the beam test of module zero's indicate that the cross-talk between strips expected in ATLAS is of order 5%.

The impact of a non-perfect alignment of the kapton electrodes along the z direction (see Sections 4.4.2) has been studied, since a dispersion in the electrode position may affect the shower shape. The results are presented in Table 4-7. The rejection deteriorates by a few percent for very large misalignments (± 1000 µm), because the shower appears to be broader, but is not affected for the expected dispersion of ± 400 µm.
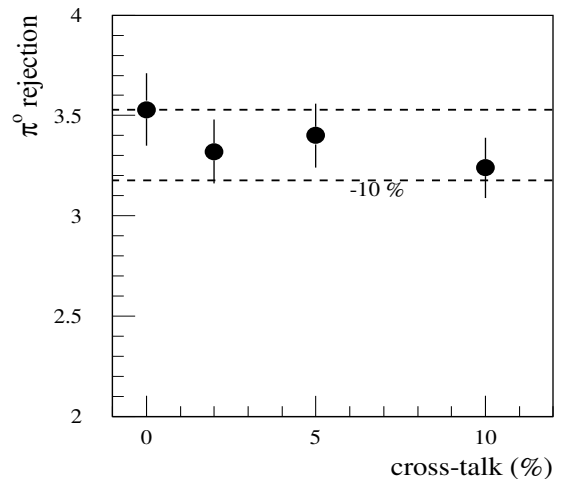
Figure 4-45 Rejection against π^0 of $E_T = 50$ GeV at $\eta = 0.3$, for 90% photon efficiency, as a function of the amount of cross-talk between adjacent strips.

4.6 Calorimeter performance and calibration with *Z → ee* events

The calorimeter performance, which has been illustrated in the previous sections using single particles, has also been studied with complete fully-simulated physics events, namely $Z \to ee$ decays. This channel has the advantage of being a simple, background-free, well-known process, and therefore ideal for benchmark performance studies in the LHC environment. Moreover, $Z \to ee$ decays are expected to be used to understand several aspects of the detector response, *e.g.* calibration of the absolute calorimeter scale, intercalibration of the calorimeter cells.

A sample of 50000 inclusive $Z \to ee$ events, which corresponds to an integrated luminosity of $0.07 \ \text{fb}^{-1}$, has been generated by using PYTHIA interfaced to PHOTOS [4-15], in order to simulate single-photon emission and radiative decays. At the generation level, both electrons were required to have transverse momenta larger than 15 GeV and to be emitted at pseudorapidities $|\eta| < 2.5$. The generated sample was then processed with the ATLAS full simulation.

Several performance results obtained with these events are presented in Section 4.6.1, whereas the determination of the global constant term of the energy resolution is discussed in Section 4.6.2. At the LHC, $Z \to ee$ decays will also be used to determine the calorimeter absolute energy scale, as described in Chapter 12.

4.6.1 Calorimeter performance with *Z → ee* events

The main calorimeter performance issues have been studied with $Z \to ee$ events. These events are characterised by a realistic p_T spectrum of the electrons in the final state, by angular distributions covering more or less uniformly the full pseudorapidity acceptance of the calorimeter, and by the presence of an underlying activity from the spectator partons.

Electrons were required to have $E_T > 20$ GeV. Events containing a hard photon from internal bremsstrahlung were removed. Electronic noise and pile-up were not included.

The energy reconstructed in the calorimeter is shown in Figure 4-46 as a function of pseudorapidity, over the full calorimeter coverage. The calorimeter was calibrated in this simulation with single photons of $E_T = 50$ GeV incident at fixed pseudorapidity points. The energy of both electrons was then scaled up by 0.5%, in order to correct for the slightly different response to photons and electrons, arising from the material in front of the calorimeter.

The reconstructed energy spectrum is shown in Figure 4-47. The overall resolution is $11.4\%/\sqrt{E}$ and includes the contribution of the sampling term (averaged over pseudorapidity), of the constant term due to the calorimeter geometry (residual non-uniformities such as the ϕ-modulation) and of the underlying event. Electrons in the crack region $1.37 < |\eta| < 1.52$ were not considered. This result is in agreement with the single-particle resolution presented in Section 4.3.5.

About 80% of the events are contained inside a window of ±2σ around the peak, where σ is the resolution shown in Figure 4-47. Additional information about the (mostly low-energy) tails is presented in Figure 4-48, which shows the pseudorapidity distribution for electrons outside the ±2σ window. Excesses of events are visible in the regions of the cracks at $\eta \sim 0$, $|\eta| \sim 1.5$ and $|\eta| \sim 2.5$, where the resolution is degraded.
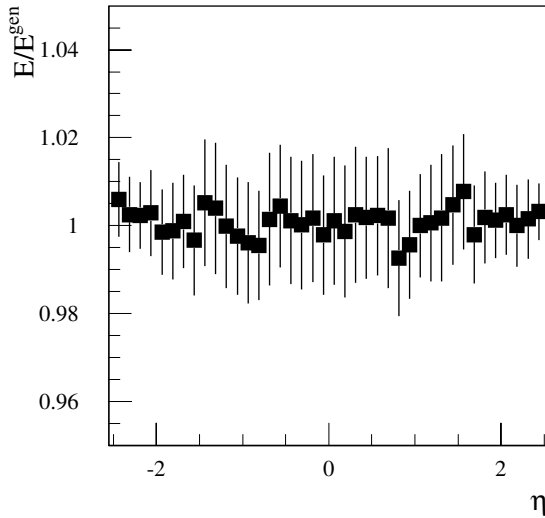
Figure 4-46 Reconstructed energy in the calorimeter, divided by the true energy, for electrons from Z decays as a function of pseudorapidity. The error bars give the rms spread on the reconstructed energy.
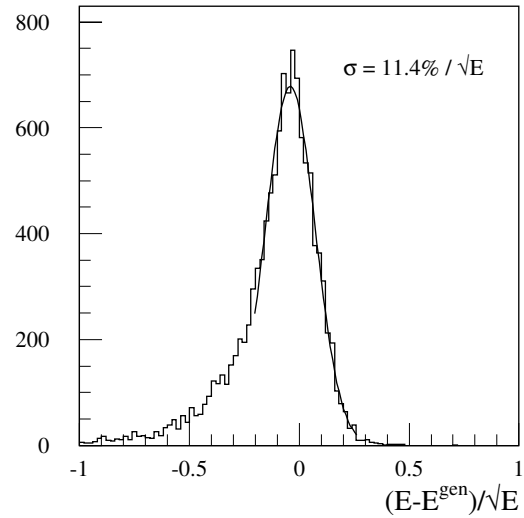
Figure 4-47 Difference between the reconstructed energy in the calorimeter and the true energy, divided by the square root of the true energy, as obtained for electrons from Z decays. The best fit is superimposed.

The position resolutions in ϕ and η are shown in Figures 4-49 and 4-50 respectively. The ϕ-resolution of the middle compartment is about $9.5 \text{ mrad}/\sqrt{E}$, the η-resolution of the strip section is about $2.7\times10^{-3}/\sqrt{E}$, and the η-resolution of the middle compartment is about $5.3\times10^{-3}/\sqrt{E}$. These results are in agreement with those obtained for single particles, presented in Section 4.4.1 and Section 4.4.2.

In conclusion, no deterioration of the performance is observed for complete physics event, as compared to single particles incident at fixed pseudorapidity points.
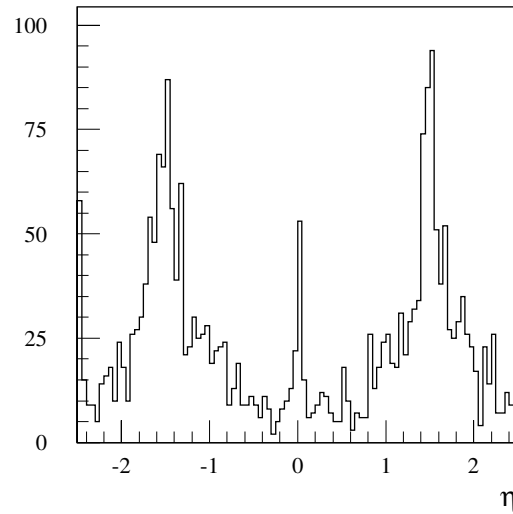
Figure 4-48 Distribution of the electron pseudorapidity for events which are at more than $\pm2\sigma$ from the peak of the distribution in Figure 4-47.

4.6.2 Calorimeter calibration and the global constant term

As discussed in Section 4.3.6, good uniformity of response of the EM Calorimeter will be provided, inside regions of size $\Delta\eta\times\Delta\phi = 0.2\times0.4$, by the electronic calibration system and by construction tolerances, which should guarantee a local constant term of 0.5% or smaller. Electron pairs from Z decays can then be used to intercalibrate the 440 regions of which the calorimeter is composed.
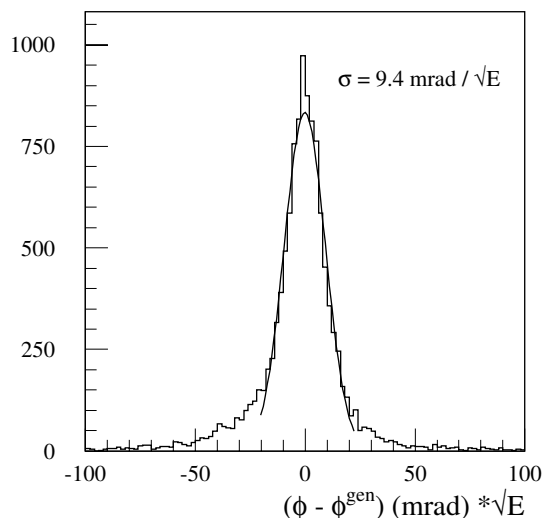
Figure 4-49 Difference between the reconstructed φ-position in the calorimeter and the true position, divided by the square root of the true energy, as obtained for electrons from Z decays. The best fit is superimposed.
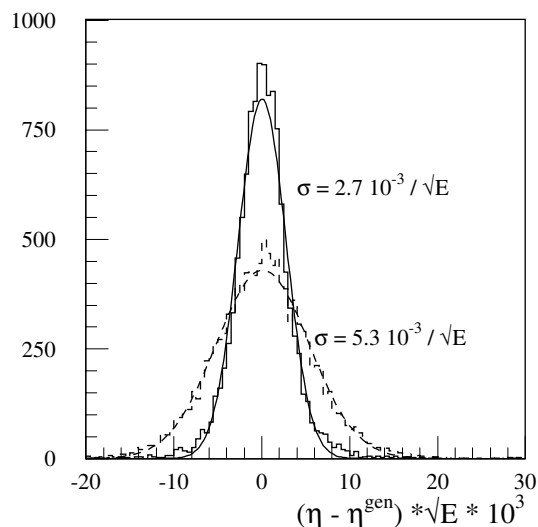
Figure 4-50 Difference between the reconstructed η-position in the calorimeter and the true position, divided by the square root of the true energy, as obtained for electrons from Z decays in the strip section (full histogram) and in the middle compartment (dashed histogram). The best fits are superimposed.

The advantages of using this process are:

- $Z \rightarrow ee$ decays occur at a very high rate, approximately 1 Hz at low luminosity.

- It is a clean channel, almost background free.

- Since the calibration is performed by imposing the Z-mass constraint, no information from other subdetectors is needed. Therefore $Z \rightarrow ee$ decays provide a mean of calibrating the EM Calorimeter in a standalone way. In this respect this method is complementary to measuring E/p for isolated electrons (Chapter 7), which is based on the momentum measurement in the Inner Detector.

- The Z resonance is close in mass to several particles which will be precisely measured or looked for, such as W bosons (see Chapter 16) and the low-mass Higgs boson (see Chapter 19).

The calibration is done by constraining the two-electron invariant mass to the Z mass.

The long–range non–uniformity of the calorimeter has been simulated by injecting random miscalibration coefficients (with an rms of 1.5%) in the 440 regions of size $\Delta\eta \times \Delta\phi = 0.2 \times 0.4$. These coefficients were then recovered by a log–likelihood fit of the reconstructed Z mass to the expected Z lineshape, which is shown in Figure 4-51.

Depending on whether the different compartments of the EM Calorimeter, *i.e.* the strip section and the middle compartment, are considered separately or not, there are 880 or 440 correction coefficients entering the fit (the back compartment is always added to the middle compartment). Simulations done at the particle level, with the correct energy smearing and energy fraction deposited in the strip section, show that for small Z samples (up to 50K events), it is better to use a 440-coefficient correction set, that is to calibrate by towers rather than by cells, even if the responses of the strip section and of the middle compartment fluctuate independently. Therefore the two compartments have not been distinguished in the study done with full simulation.
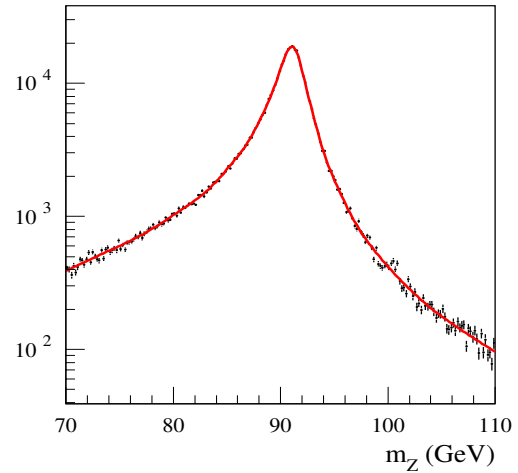
Figure 4-51 The Z lineshape as obtained from PYTHIA and PHOTOS.

Due to the fiducial cut $|\eta| < 2.5$ for both electrons, a few regions located close to the boundary had less than 25 electrons. Miscalibration (input) coefficients were injected also in these regions as in the rest of the calorimeter, but no fit was attempted. The calibration procedure was repeated ten times, each time with a different set of input coefficients. Figure 4-52 shows the correlation between the miscalibration (input) coefficients and the correction (output) coefficients.
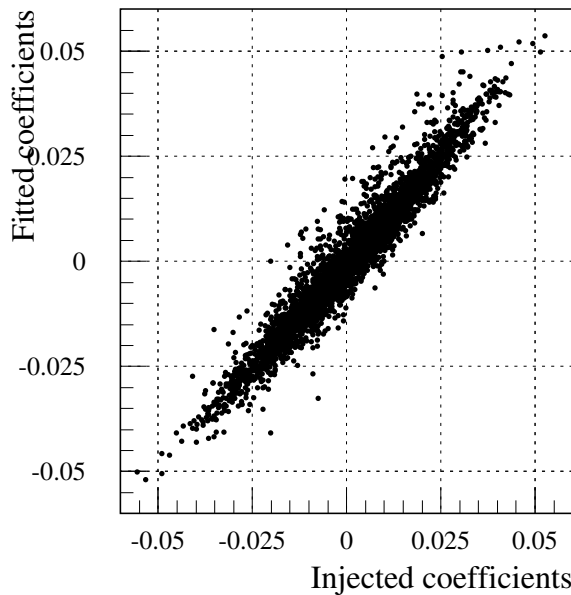
Figure 4-52 The fitted correction coefficients versus the injected coefficients, as obtained for $Z \rightarrow ee$ events.
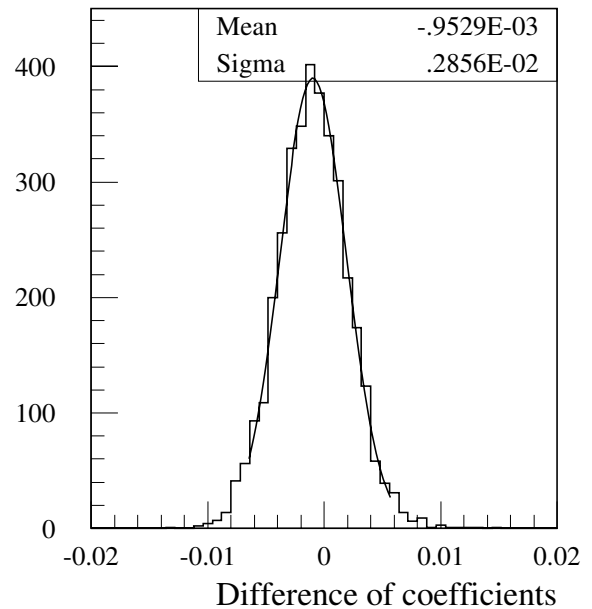
Figure 4-53 The difference between the injected coefficients and the correction coefficients after the fit.

The resulting uniformity after the calibration procedure is shown in Figure 4-53 for regions with at least 60 incident electrons. Regions located near the crack at $\eta = 1.5$ are excluded. After the fit, the rms non-uniformity (*i.e.* the global constant term) has been reduced from 1.5% to less than 0.3%. The Z sample used in this example will be collected in less than 48 hours of data taking at low luminosity. Therefore, by summing the local constant term of 0.5% (Section 4.3.6) with the global constant term of 0.3% obtained as described here, a total constant term of about 0.6% should be achieved in a few days of data taking. This is well within the goal of 0.7%.

Several checks have been made of the stability of this procedure, given the large number of unknowns and possible strong correlations between coefficients. For instance, the reconstructed Z mass can be corrected by using only one of the two regions involved. In this respect, the transverse momentum of the Z is essential to stabilise the system of equations. Without some acoplanar e^+e^- pairs, only regions which are back-to-back in ϕ would be involved, leading to non-unique solutions of the system. However, only a small fraction (~1%) of events with acoplanar electron pairs is sufficient to remove such ambiguities. A test was also made, which consisted in injecting a large offset of 6% over the whole upper half of the calorimeter ($0° < \phi < 180°$) in addition to the 1.5% non-uniformity. The fit converged without problems.

4.7 Performance of module zero's

After a rather long period of prototype activities (1990 to 1996), which addressed the detector's mechanical structure, the choice between a presampler and a preshower, and the development of the front-end electronics, the construction of module zero's was launched in 1996-1997.

Module zero's have exactly the same dimensions and structure as the detector modules. Their construction is intended to be a final qualification of all fabrication processes, and a last assessment of the performance. In order to be as close as possible to the ATLAS conditions, motherboards, cold cables, feedthroughs, crates and back-planes, which connect a given calorimeter cell to its electronic circuit on the front-end boards, and the electronic circuit itself, were built according to the final design (radiation hardness of the various circuits was the only exception). The absorbers and support fixtures were built with the final tooling and Quality Control procedure. Detailed mechanical measurements have shown that all tolerances meet the specifications [4-16].

On the other hand, the construction of the readout electrodes presented some difficulties, which resulted in significant delays. Therefore, in order to be ready for the beam tests in 1998, the endcap module contained only 15 electrodes instead of the foreseen 128, and the barrel module 23 electrodes instead of 128. This allowed studies of the local performance to be made, but did not permit a test of the uniformity of the calorimeter response over a large area.

The module zero of the barrel presampler, which consisted of two sectors, was complete.

The electronic calibration of both the calorimeter and the presampler modules was made using prototypes of the 128-channel calibration boards designed for ATLAS. The uniformity of the delivered signals, shown in Figure 4-25, is 0.2% rms, which meets the requirement of 0.25%. Checks are going on to ensure that this uniformity is preserved at the level of the current pulses generated close to the calorimeter cell.

The front-end readout boards (128 channels) used in the test of the module zero's have all the final functionalities. Each channel consists of a preamplifier, a three-gain shaper, and for each gain a 144 cell-deep analog memory (SCA) in which samples of the signals taken every 25 ns are stored. Digitisation is performed using 12 bits. Calibration and test-beam data were processed using five samples around the maximum. Using these five samples and the optimal-filtering technique, all beam events could be used, irrespective of their exact arrival time with respect to the 40 MHz clock of the SCA. The set-up also allowed to record continuous waveforms of both beam and calibration events, which proved extremely useful for the detailed understanding of the signal behaviour (presence of inductive effects, cross-talk, *etc.*).

The system-aspect information and the data gathered during the beam tests and their preparation are very valuable and allow the last details to be frozen before the detector production starts. Preliminary results from the beam tests are discussed in the next sections.

Figure 4-54 Energy spectrum reconstructed in the barrel module zero for 20 GeV electrons at η = 0.3. A 5x4 cell cluster in η×φ has been used.

4.7.1 The barrel module zero

The barrel module was tested with 20 GeV electrons, obtained from a lead-ion beam. The energy reconstructed in the calorimeter at one of the beam impact positions, which corresponds to η = 0.3, is shown in Figure 4-54. Despite that cuts were applied to suppress pions in the beam, a small fraction of them remain in the low-energy tail. The energy resolution measured after the subtraction of the electronic noise is $10.0\%/\sqrt{E}$. This is somewhat worse than the performance expected at this pseudorapidity (see Figure 4-20). Likely explanations are the contribution of the beam spread, which was not subtracted, and the fact that the best possible calibration was not used in obtaining these preliminary results.

The noise levels per cell, 18 MeV in the strip section, 47 MeV in the middle compartment and 35 MeV in the back compartment, are slightly better (15%) than expected. The measured sensitivity is 2.6 μA/GeV, to be compared to the expected 2.74 μA/GeV.

4.7.2 The end-cap module zero

In the past a prototype with a variable thickness of the lead plates had been tested [4-17], therefore this was the first time that an end-cap module with the final geometry (constant thickness of the lead plates) was exposed to beam.

Since the module was only partially equipped with readout electrodes, it was not possible to perform complete azimuthal scans to look at the response uniformity. However, the calorimeter energy resolution could be measured at two pseudorapidity positions (η ~ 1.55 and η ~ 2.2). Electron beams in the energy range 20 to 200 GeV were used for this measurement.

The reconstructed energy spectrum for electrons of energy 150 GeV at $\eta \sim 2.2$ is shown in Figure 4-55. The low-energy tails are due to the poor quality of the beam. The resolution is about 1%.

Figure 4-56 shows the calorimeter energy resolution as a function of the incident beam energy. At each energy point, the beam spread as well as the electronic noise (see below) were subtracted in quadrature. The local constant term of $0.42 \pm 0.05\%$ is somewhat higher than expected (0.3%). It is, however, good enough given that results are preliminary.
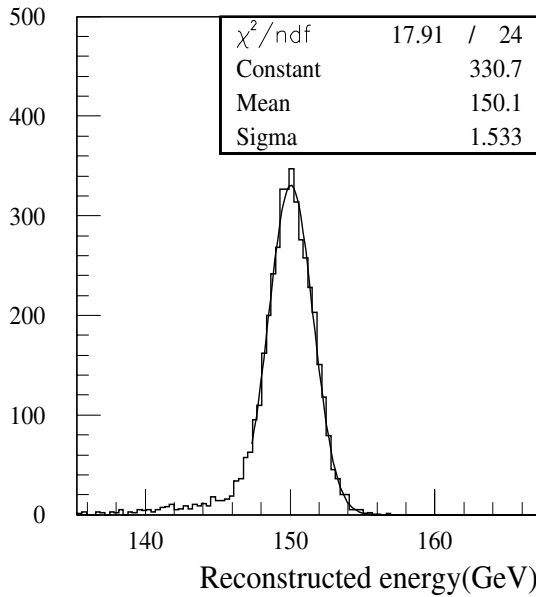
Figure 4-55 Energy spectrum reconstructed in the end-cap module zero for electrons of energy 150 GeV at $\eta \sim 2.2$.
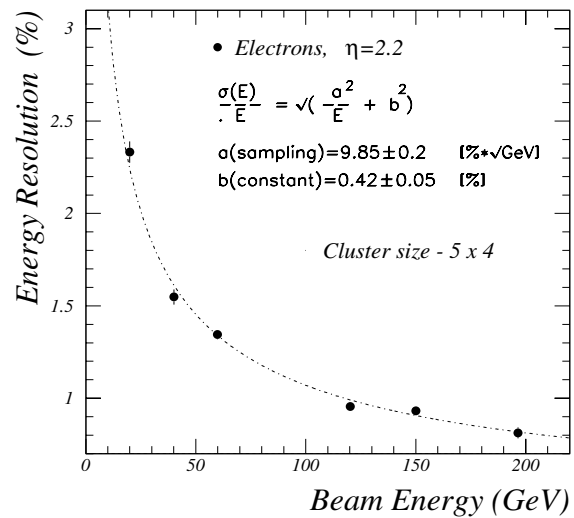
Figure 4-56 Energy resolution of the end-cap module zero as a function of energy at $\eta \sim 2.2$. The best fit (see text) is superimposed.

These measurements were done with two different gains of the electronic chain: high gain up to 60 GeV and medium gain above 60 GeV. This results in different values of the electronic noise for the two groups of runs. Since the number of energy points was limited, instead of obtaining the electronic noise in a given cluster from the fit to the energy resolution curve, the noise levels were directly measured in random-trigger events. The observed noise per channel is of the order of 20 MeV in the strip section and 50 MeV in the middle compartment, in agreement with the expectation. The cross-talk observed between the middle and back compartment of the calorimeter (~3%) is larger than expected, and has been attributed to the motherboard design. The linearity of the calorimeter energy response, shown in Figure 4-57, is well within 1%.
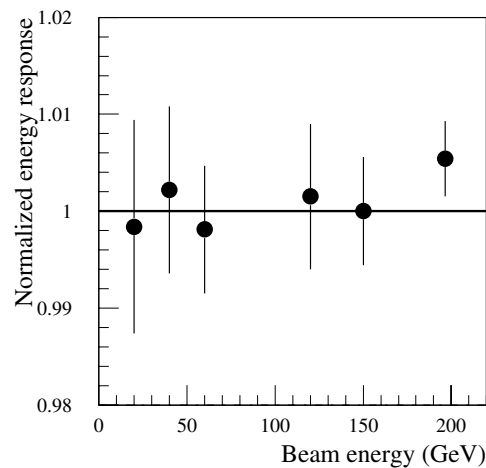
Figure 4-57 Mean energy response of the end-cap module zero as a function of the beam energy at $\eta = 2.2$.

In conclusion, apart from the overall uniformity of the calorimeter, which will be measured in the future with modules fully equipped with readout electrodes, and apart from some problems (noise, cross-talk) which have been understood and will be cured, the results obtained so far from the beam tests of the EM module zero's indicated that the detector performance meets the requirements.

4.8 Conclusions

An extensive optimisation work over the past years has led to the design of an electromagnetic calorimeter which offers good energy resolution, excellent response uniformity and angular resolution, and powerful particle identification capability.

The main performance issues presented in this chapter, which are based on a full detailed simulation of the accordion geometry within the rest of the ATLAS detector, can be summarised as follows. The sampling term of the energy resolution is at the level of $10\%/\sqrt{E}$. Owing to the intrinsic uniformity of the liquid-argon technique, and to strict construction tolerances, a global constant term of less than 0.7% should be achieved in a few days of data taking at low luminosity using $Z \to ee$ events. At high luminosity, the total energy resolution for photons of $E_T = 50$ GeV is 1.6% or better.

By using the fine longitudinal and lateral segmentation, several precision measurements of the shower position and angle can be performed. In particular, the primary vertex in $H \to \gamma\gamma$ events can be measured with an accuracy of 1.3 cm by using the calorimeter information alone, and high sensitivity should be achieved for new physics characterised by the presence of photons not coming from the primary vertex.

An average rejection factor of three against π^0 should be obtained for a photon efficiency of 90%. More examples of particle identification issues, involving the use of the EM Calorimeter, the Inner Detector and the Hadronic Calorimeters, can be found in Chapters 7 and 9.

With respect to the studies reported in the Calorimeter Performance TDR, the results presented here are based on a more realistic simulation and deeper understanding of several effects. In particular, the impact on the performance coming from a more correct treatment of the pile-up and from several imperfections in the mechanics and electronics (cross-talk, electrode alignment, non-uniformity of the electric field, *etc.*) was evaluated.

Finally, preliminary results from the beam tests of module zero's indicate that the performance of the detector which is being built is in agreement with the physics requirements and the expectations from the simulation.

4.9 References

4-1   ATLAS Collaboration, Calorimeter Performance Technical Design Report, CERN/LHCC 96-40 (1996).

4-2   ATLAS Collaboration, Liquid Argon Calorimeter Technical Design Report, CERN/LHCC 96-41 (1996).

4-3   Y. Jacquier *et al.*, 'Strengths and weaknesses of digital filtering', ATLAS Internal Note ATL-LARG-97- 80 (1997).

4-4   G. Le Meur and F. Touze, 'PRIAM/ANTIGONE: a 2D/3D package for accelerator design', in Proceedings of the 2nd European Particle Accelerator Conference, London 1993, p1321-1323.

4-5   ATLAS Collaboration, Technical Proposal, CERN/LHCC 94-43 (1994).

4-6   RD3 Collaboration, Nucl. Instr. Meth. **A364** (1995) 290.

4-7   M.-L. Andrieux *et al.*, 'Pollution of liquid argon after neutron irradiation measured at SARA: summary of raw data', ATLAS Internal Note ATL-LARG-98-105 (1998).

4-8   L. Poggioli, 'The LARG Slow Control. Status Report', ATLAS Internal Note ATL-LARG-98-110 (1998).

4-9   B. Canton *et al.*, 'Analysis and results of the measurements of the plate thickness, done at the factory, during the production of the lead for the module zero of the barrel and end-cap ATLAS Electromagnetic Calorimeter', ATLAS Internal Note ATL-LARG-97-76 (1997).

4-10   B. Mansoulie, 'Non-uniformity of lead plates and gaps: analytical estimates of the shower averaging effect', ATLAS Internal Note ATL-LARG-98-99 (1998).

4-11   W. Bonivento *et al.*, 'Cold cables for the EM Calorimeters: specifications and measurements of the electrical properties', ATLAS Internal Note ATL-LARG-98-106 (1998).

4-12   A. Ferrari and J. Soderqvist, 'A study of the presampler intersector crack', ATLAS Internal Note ATL-LARG-97-084 (1997).

4-13   J. Schwindling, 'S-shape correction using a neural network', ATLAS Internal Note ATL-LARG-98-104 (1998).

4-14   L. Borissov *et al.*, 'Study of non-pointing photon signatures of Gauge-Mediated SUSY-Breaking models', ATLAS Internal Note ATL-PHYS-99-37 (1999).

4-15   Z. Was *et al.*, Comput. Phys. Commun. **79** (1994) 291.

4-16   L. Labarga and P. Romero, 'Analysis of the quality control measurements performed on the absorbers produced for the module zero of the ATLAS Electromagnetic end-cap Calorimeter', ATLAS Internal Note ATL-LARG-99-004 (1999).

4-17   RD3 Collaboration, Nucl. Instr. Meth. **A389** (1997) 398.

5 Hadronic calorimetry

The hadronic calorimetry of ATLAS (a view of which is presented in Figure 1-iii) consists of three main devices. In the barrel region ($|\eta| < 1.7$) there is the scintillating Tile Calorimeter. The Hadronic End-cap LAr Calorimeter (HEC) extends up to $|\eta| = 3.2$. The range $3.1 < |\eta| < 4.9$ is covered by the high density Forward Calorimeter (FCAL). Up to $|\eta| = 2.5$ the basic granularity of the hadron calorimeters is $\Delta\eta \times \Delta\phi = 0.1 \times 0.1$. This region is to be used for precise measurements of the energy and angles of jets and, at low luminosity, of single charged particles. In the region $|\eta| > 2.5$, the basic granularity is approximately $\Delta\eta \times \Delta\phi = 0.2 \times 0.2$. A more detailed description of all ATLAS calorimeters is given in the Calorimeter TDRs ([5-1], [5-2], [5-3]) and in Section 1.5 of this document.

Recent test beam results from prototypes and module zero's of these detectors are presented in Section 5.1 to illustrate their basic performance. They are compared with predictions of the hadronic shower simulation package used for the studies presented in this report. In Section 5.2 the changes in the overall design of the ATLAS calorimetry since the Calorimeter TDRs are reviewed. The performance of the calorimetry for single particle detection for the full pseudorapidity range is described in Section 5.3 (performance for jets and for missing E_T measurements is described in Chapter 9). In Section 5.4 the possibility of calibrating the calorimeters with single charged hadrons is discussed.

5.1 Test beam results for pions, muons and electrons

The performance for single particle detection, obtained from recent test beam results, is reviewed in this section. Results are presented for the three main sections of the calorimetry: the barrel, end-cap and forward calorimeters.

5.1.1 Combined tests of the EM LAr and Hadronic Tile Calorimeters

Combined tests of the EM LAr and Tile barrel calorimeter prototypes have been performed in 1994 [5-4] and 1996 [5-5] with a set-up representative of the final configuration. The LAr and Tile prototype modules used in the test beam have performances similar to the final modules. The cryostat dead material and the distance between the two prototypes were close to the actual set-up. One difference was that the Tile prototypes were 1.80 m long and segmented in four longitudinal compartments, while the final modules are 1.60 m thick and have three compartments in depth. A presampler in front of the LAr barrel prototype was used to select minimum ionising particles and thus to remove particles with early interactions which could take place in the material in front of the calorimeter.

The simplest method to reconstruct the pion energy, denoted as the 'Benchmark Method', consists of introducing a set of energy independent corrections. Both prototypes were first calibrated at the electromagnetic scale. The total reconstructed energy is then expressed as:

$$E_{rec} = a \cdot E_{had} + E_{em} + b \cdot E_{em}^2 + c \cdot \sqrt{a \cdot E_{had1} \cdot E_{em3}} \ . \qquad \text{5-1}$$

Both calorimeter sections are non-compensating and the coefficient a takes into account their different responses to the pion energy. The quadratic term bE_{em}^2 provides a first order correction for the non-compensation (the coefficient is negative, it suppresses the signal for events with a
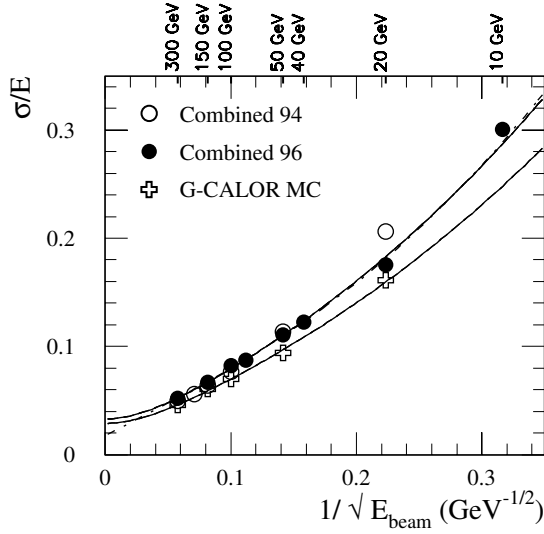
Figure 5-1 Energy resolution for pions as obtained with the Benchmark Method. The solid dots (open circles) give the results for the 1996 (1994) test beam data, the crosses show the G-CALOR predictions. The solid lines give fits with Equation 5-3, the dashed-dotted line gives a fit with Equation 5-2.
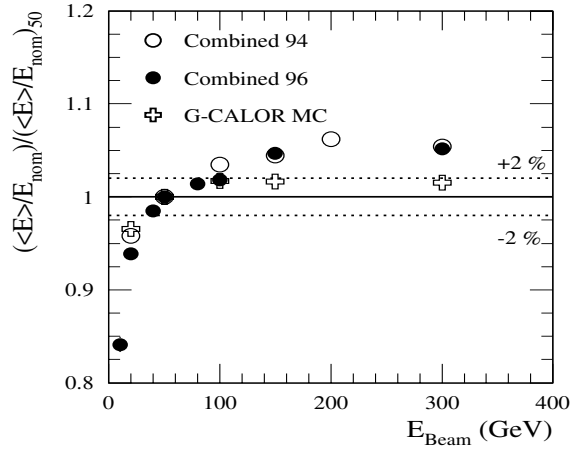
Figure 5-2 Relative non-linearity as a function of the beam energy for the Benchmark Method. The solid dots (open circles) give the results for the 1996 (1994) test beam data, the crosses show the G-CALOR predictions. The points are normalised to the 50 GeV case.

large fraction of electromagnetic energy). The last term estimates the energy loss in the cryostat wall separating the two calorimeters. The validity of using the geometric mean of the last LAr compartment energy (E_{em3}) and the first Tile Calorimeter compartment energy (E_{had1}) has been tested with the insertion of a mid-sampler between the calorimeters. The values of the coefficients are obtained by minimising the energy resolution for 300 GeV pions. The resolution for pions obtained with the Benchmark Method is shown in Figure 5-1. The energy dependence of the resolution can be parametrised by one of the following formulae:

$$\sigma/E = (A/\sqrt{E} + B) \oplus C/E , \qquad 5\text{-}2$$

$$\sigma/E = A/\sqrt{E} \oplus B \oplus C/E , \qquad 5\text{-}3$$

where the resolution σ/E is usually in percent, the sampling term A is in % GeV$^{1/2}$, the constant term B is in percent and the noise term C is in GeV. Results of the fit with these expressions are given in Table 5-1. The results are compared to the prediction of the G-CALOR hadronic shower simulation package [5-6].

Table 5-1 Terms of the pion energy resolution as obtained with the Benchmark Method.

	A (% GeV$^{1/2}$)	*B* (%)	*C* (GeV)
Experimental data: Equation 5-2 fit	59.5 ± 0.3	1.8 ± 0.2	2.0 ± 0.1
Experimental data: Equation 5-3 fit	69.8 ± 0.2	3.3 ± 0.2	1.8 ± 0.1
G-CALOR prediction: Equation 5-3 fit	61.7 ± 0.1	2.9 ± 0.3	fixed at 1.5

With the simple Benchmark Method, the effect of non-compensation is not fully corrected for and the pion response shows some non-linearity (see Figure 5-2), of the order of 5% in the range between 50 and 300 GeV. G-CALOR predicts only 2% of non-linearity of the response in the same energy range.

The degree of non-compensation of the calorimeter e/h, that is the ratio of the calorimeter response to the electromagnetic and non-electromagnetic (purely hadronic) component of the hadron showers, can be determined from the energy dependence of the e/π ratio. This ratio depends on e/h and on the electromagnetic fraction $F(\pi^0)$ produced in the interaction:

$$e/\pi = \frac{e/h}{1 + (e/h - 1) \cdot F(\pi^0)} . \qquad 5\text{-}4$$

To extract the value of e/h, the pion response has to be calculated using the electromagnetic scale only, hence Equation 5-1 becomes simply

$$E_{rec} = E_{em} + E_{had} + E_{cryo}$$

and the fraction of π^0's is taken as $F(\pi^0) = 0.11 \cdot \ln E$ [5-7]. The fit results in a value of e/h of the order of 1.35-1.37 (see Figure 5-3). G-CALOR again predicts a lower level of non-compensation.

Figure 5-3 Energy dependence of the e/π ratio, fitted with Equation 5-4. The solid dots (open circles) give the results for the 1996 (1994) test beam data, the crosses show the G-CALOR predictions.

A second method to correct for the effect of non-compensation was applied to the data. This weighting technique, inspired on a method developed for the LAr calorimeters of the H1 experiment at HERA [5-8], consists of correcting upwards the response of individual cells with relatively small signals, to equalise their response to that of cells with large (typically electromagnetic) deposited energies. The reconstructed energy is expressed as

$$E_{rec} = \sum_{em-cells} (W_{em}(E_{cell}) \cdot E_{cell}) + \sum_{had-cells} (W_{had}(E_{cell}) \cdot E_{cell}) + E_c.$$

The weights are characteristic parameters of the calorimeter type, the electromagnetic (*em*) or hadronic (*had*) compartments, and they vary smoothly with the energy of the incident particle. The energy resolution obtained with this method is shown in Figure 5-4 (see also Table 5-2) and the relative response as a function of the energy is shown in Figure 5-5. The resolution is improved and the linearity restored to better than 2%.

5.1.2 Tile Calorimeter module zero test beam results

An extensive test beam programme of the Tile Calorimeter barrel and extended barrel module zero's has been carried out starting in 1996. The response to charged pions, electrons and muons has been studied.

Figure 5-4 Energy dependence of the energy resolution for pions as obtained with the H1 cell-weighting method. The solid line is a fit with Equation 5-3, the dashed-dotted line is a fit with Equation 5-2.
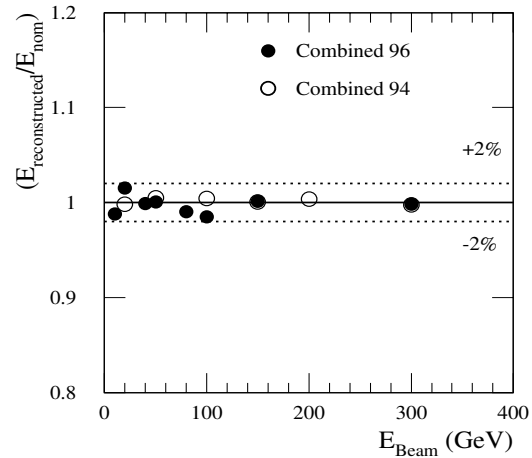
Figure 5-5 Energy dependence of the relative non-linearity for pions as obtained with the H1 cell-weighting method.

Table 5-2 Terms of the pion energy resolution as obtained with the H1 cell-weighting method.

	A (% GeV$^{1/2}$)	B (%)	C (GeV)
Experimental data: Equation 5-2 fit	41.9 ± 0.2	1.8 ± 0.1	1.8 ± 0.1
Experimental data: Equation 5-3 fit	52.1 ± 0.1	3.0 ± 0.1	1.6 ± 0.1

Table 5-3 Terms of the pion energy resolution for the module zero of the Tile Calorimeter.

	A (% GeV$^{1/2}$)	B (%)
Experimental data: Equation 5-2 fit	43.6 ± 0.8	2.4 ± 0.1
G-CALOR prediction: Equation 5-2 fit	42.6 ± 0.2	1.7 ± 0.2
Experimental data: Equation 5-3 fit	52.0 ± 0.6	4.1 ± 0.1
G-CALOR prediction: Equation 5-3 fit	48.0 ± 1.2	3.3 ± 0.2

5.1.2.1 Response to pions

The response of the detector to pions has been measured in the energy range from 10 to 400 GeV. Figure 5-6 shows the energy resolution obtained in the barrel module zero for pions, when summing the total energy deposited in the calorimeter without any correction for non-compensation. The hadronic shower was required to start in the first compartment to avoid longitudinal leakage, since the thickness of the module (1.60 m) was adapted to the final configuration, *i.e.* with the additional 1.2 λ of the LAr calorimeter in front. The data are in good agreement with the results obtained with the 1.80 m thick Tile Calorimeter prototype. The resolution is well fitted with the formulae in Equation 5-2 and Equation 5-3 with the term $C = 0$, since the noise contribution is negligible (see Table 5-3). The e/π ratio is shown in Figure 5-7. The fitted level of non-compensation of the calorimeter is $e/h = 1.30 \pm 0.01$. The G-CALOR Monte Carlo predicts (see Table 5-3) a similar sampling term, as for the experimental data, but a small-
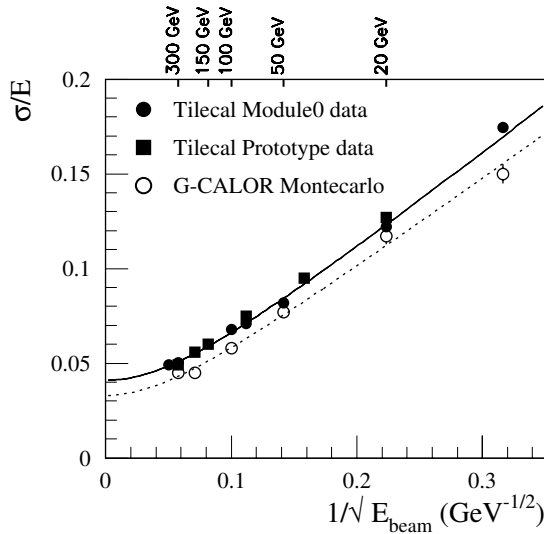
Figure 5-6 Energy resolution for pions, measured in the Tile Calorimeter barrel modules for incident pion energies between 10 and 400 GeV. The lines give fits with Equation 5-3.
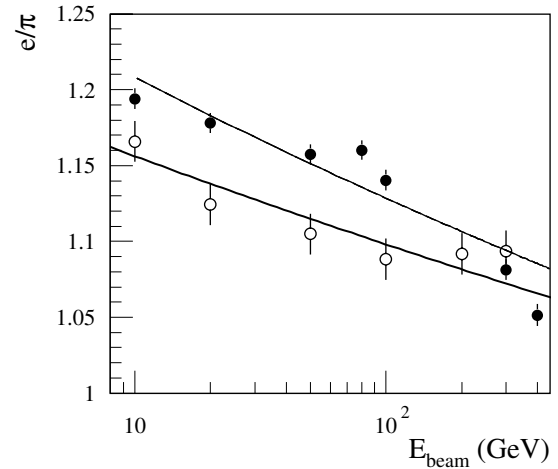
Figure 5-7 e/π ratio measured in the Tile Calorimeter barrel module zero for incident pion energies between 10 and 400 GeV. The solid dots show experimental data, the open circles show G-CALOR prediction. The dependencies are fitted with Equation 5-4.

er constant term and a lower level of non-compensation of $e/h = 1.22 \pm 0.02$ [5-9]. A good uniformity of the response of the module as a function of pseudorapidity and azimuthal angle was observed [5-3].

5.1.2.2 Response to electrons

The electron response for the module zero of the Tile Calorimeter was measured in the energy range from 10 to 300 GeV [5-10]. The electrons were sent at 90° with respect to the planes of scintillator tiles. The energy dependence of the resolution is shown in Figure 5-8. The energy resolution is well fitted with the modified square sum formula without the noise term:

$$\sigma/E = A/\sqrt{E} \oplus B . \qquad \text{5-5}$$

The sampling term A of the energy resolution is $(25.6 \pm 0.4)\%$ GeV$^{1/2}$ and the constant term B is $(0.67 \pm 0.04)\%$.

5.1.2.3 Response to muons

The response to muons was extensively studied in the Tile Calorimeter test beam programme. In particular, the response in the
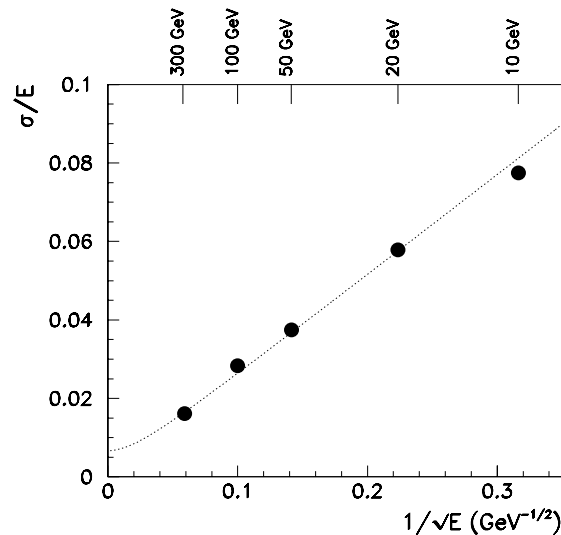
Figure 5-8 Energy dependence of the energy resolution for electrons, measured in the Tile Calorimeter barrel module zero. The line is a fit with Equation 5-5.
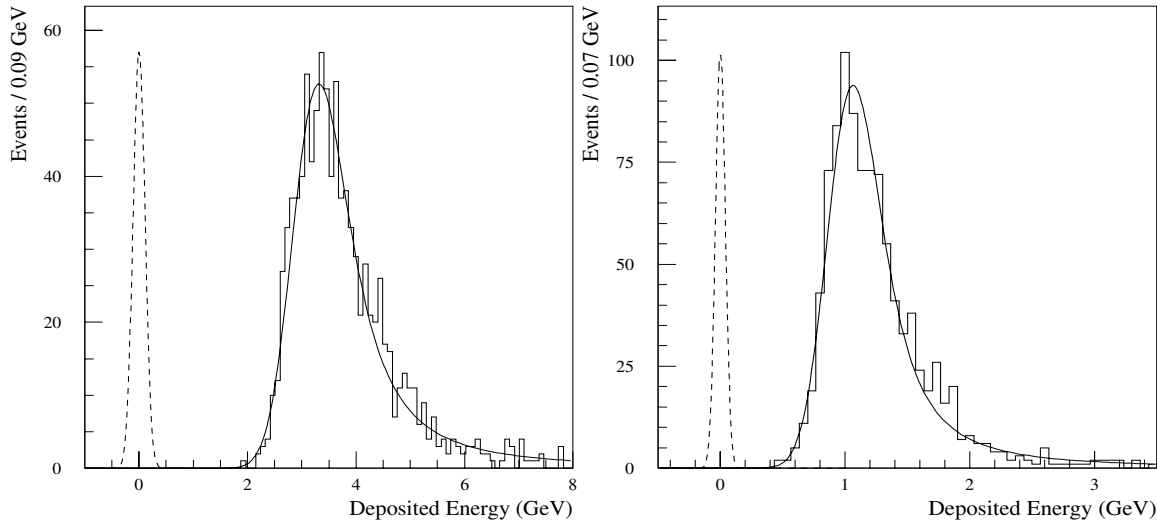
Figure 5-9 Total deposited energy (left-hand plot) and energy deposited in the third compartment (right-hand plot) by 100 GeV muons in the Tile Calorimeter extended barrel module zero at a pseudorapidity of 1.3. The signal is fitted with a Landau distribution convoluted with a Gaussian. The peaks around zero (dashed) are the electronic noise distributions.

three compartments of the calorimeter as a function of pseudorapidity was measured. The ability to measure a clean signal above noise allows the Tile Calorimeter to contribute to the muon identification at the trigger and analysis levels. An example of the total signal deposited by 100 GeV muons in the full Tile Calorimeter is given in Figure 5-9 (left-hand plot). The signal is fitted with the convolution of a Landau distribution with a Gaussian [5-11]. The peak, or most probable value, is at 3.32 GeV. The FWHM is 1.3 GeV. The signal is asymmetric; the left-hand side of the peak is essentially a Gaussian with $\sigma = 0.48$ GeV. Typically the signal has to be summed over three to four cells, or six to eight photomultiplier tubes (PMT). The expected level of electronic noise is about 20 MeV per PMT, hence about 55 MeV for eight PMTs. In the test beam, some channels were equipped with different electronics. The actual noise level (see dashed distribution in the left-hand plot of Figure 5-9) was 100 MeV, dominated by the contribution of the two PMTs of the first compartment. The signal is separated by more than six standard deviations from the noise.

Since in physics events muons may overlap with other particles and, at high luminosity, minimum bias events may deposit a non-negligible amount of energy in the innermost layers of the calorimeter, the ability to see a clean muon signal in the outermost compartment is an important asset. The right-hand plot of Figure 5-9 shows the signal deposited by muons in the third compartment. The peak is at 1.06 GeV and the FWHM is 0.55 GeV. The left-hand side of the peak is essentially a Gaussian with $\sigma = 0.20$ GeV. The electronic noise contribution from summing the signal of two PMTs (shown as a dashed distribution on the right-hand plot) is 40 MeV. The signal is separated from the noise by five standard deviations. More experimental information about the response of the muons in the Tile Calorimeter (barrel and extended barrel) modules can be found in Section 5.3.3.

5.1.3 Hadronic end-cap calorimeter module zero test beam results

5.1.3.1 The test beam set-up

Beam tests of Hadronic End-cap Calorimeter (HEC) module zero's have been performed in the H6 beam line of the CERN SPS. Four modules, two of the front wheel and two of the rear wheel, have been exposed in 1998 to electron, pion and muon beams at energies in the range 10-200 GeV.

In contrast to the final detector configuration, the impact angle of the beam with respect to the calorimeter front face was chosen to be 90°, irrespective of the impact position. Thus lateral energy leakage could be minimised - an important issue given the limited lateral coverage of the two ϕ-wedges of the total wheel used. Impact positions were typically within ±25 cm of the centre of the modules in the vertical and horizontal directions. This allowed detailed measurements to be made of the homogeneity of the response for electrons, pions and muons. In particular, the response when crossing the inactive regions (*e.g.* the crack between the modules) was studied in detail. In addition, energy scans in up to 16 different impact positions were carried out and yielded detailed information on the expected performance of the calorimeter. The data were analysed using the standard digital filtering technique and signal reconstruction [5-12].

5.1.3.2 Noise performance

The noise measured for an individual channel was typically 290 (400, 800) MeV for the first (second, third) longitudinal compartment. These results were obtained using a digital filtering technique with five time samplings [5-13]. Digital filtering reduced the noise by a factor of order 1.5. As expected, the noise per channel was correlated with the related read-out cell capacitance. In addition, some coherent noise was present, typically at the level of 20%. The source of this coherent noise was traced back to the shaper and preshaper card. This part of the read-out electronics is being redesigned.

5.1.3.3 Results for electrons

The electron signal was reconstructed from a cluster of the most active read-out cells. The clusters use typically from three to seven cells, all located in the first two longitudinal compartments, *i.e.* in the first wheel only ([5-14], [5-15]). Using all data sets, an overall calibration constant (from nA to GeV) was determined from a χ^2-minimisation of the energy resolution. The energy resolution was parametrised using Equation 5-3, where the term *C* reflects the electronic noise. The noise was determined from the read-out cells of the related cluster for the given impact point using randomly triggered events or from a three parameter fit to the energy resolution.

The parameters *A*, *B* and *C* were obtained from a fit to the data of each individual impact point. For four different impact positions, the results are shown in Figure 5-10. In this figure, the energy resolution as a function of the electron energy is shown along with the result of the fit (solid line). Typical values obtained for the sampling and constant terms were $A = (21.0 \pm 0.5)\%\ \mathrm{GeV}^{1/2}$ and $B = (0.2 \pm 0.2)\%$. These results agree well with Monte Carlo expectations. The noise term was determined to be 0.7-1.0 GeV. Reducing the cluster size to three cells changed the noise to the level of 0.5 GeV with an energy resolution only marginally worse. The linearity of the calorimeter response with respect to the electron energy is another important issue. The linearity was measured to be within ±0.5%, in good agreement with Monte Carlo predictions. The lateral and vertical scans showed a constant response within ±1% over the active regions of the module.
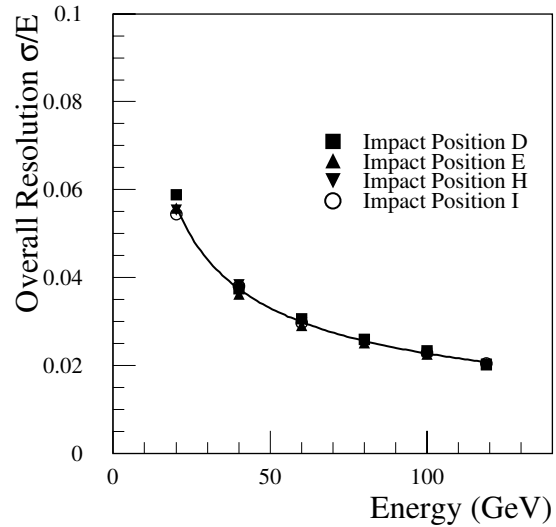
Figure 5-10 Energy dependence of the energy resolution for electrons at four different impact positions. The line shows a fit with Equation 5-5.

5.1.3.4 Results for pions

Strongly interacting particles initiate hadronic showers which cover larger regions of the calorimeter. Some of the secondary particles may exit the calorimeter, giving rise to a lateral leakage of energy. This has to be taken into consideration when comparing to simulations, before final conclusions on the energy resolution, linearity and homogeneity of the calorimeter can be made. The most active read-out cells were selected for each impact position, when reconstructing the energy. A typical cluster contained from 39 to 45 channels (see [5-14], [5-15]). Increasing the signal threshold reduced the number of read-out cells considered and therefore the noise, while giving additional signal losses which worsened the energy resolution. As for the electrons, an overall calibration constant was determined from a χ^2-minimisation of the energy resolution of all data sets. In addition, at each impact point, weight factors for the individual longitudinal compartments were determined. They mostly reflect the different sampling ratio for the modules of the rear wheel.
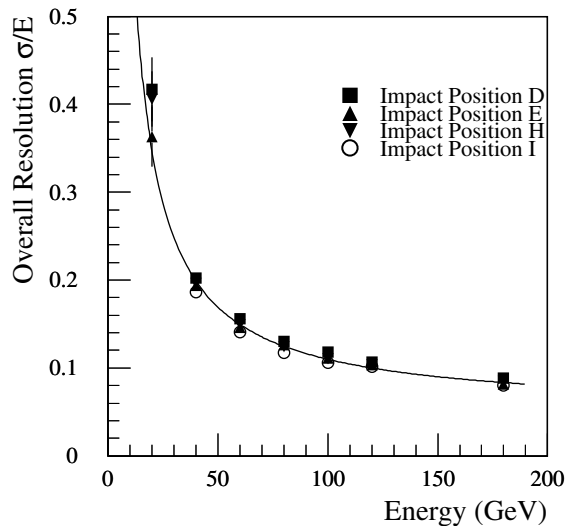
Figure 5-11 Energy dependence of the energy resolution for pions at four different impact points. These data include a contribution from electronic noise which is different for each impact beam position. The solid line, included to guide the eye, is drawn using the parameters obtained from a fit to the noise-subtracted resolution, summed in quadrature with the average electronic noise measured over the four impact positions.

For example, Figure 5-11 shows the energy resolution as a function of the pion energy for four different impact points. The electronic noise was obtained from the related cluster of read-out cells using randomly triggered events. The correlation between individual read-out cells was implicitly taken into account in the fit as well. Concerning the energy resolution, typical results are the following: for the sampling term $A = (75 \pm 2)\%\,\mathrm{GeV}^{1/2}$ and for the constant term $B = (5.0 \pm 0.3)\%$, the corresponding noise term is typically $C = 5\text{-}6\,\mathrm{GeV}$ (as fitted with Equation 5-3).

5.1.3.5 Comparison of the pion response with Monte Carlo simulation

Monte Carlo simulations modelling the test beam set-up as well as the case of full lateral coverage (see Figures 5-12 and 5-13) were performed for comparison. The signals of all read-out cells were summed in the simulation. This differs from the method employed for test beam data where the signal is reconstructed by summing read-out cells with signals above a given threshold. Effects caused by the binning in ADC units were ignored in the simulation as well. Nevertheless, the results for the energy resolution, $A = 63\%\,\mathrm{GeV}^{1/2}$ for the sampling term and $B = 5.4\%$ for the constant term, are not far from the measured values. The energy dependence of the pion response, which reflects the energy dependence of the e/h ratio of this non-compensating calorimeter, shows good agreement between experimental and simulated data.
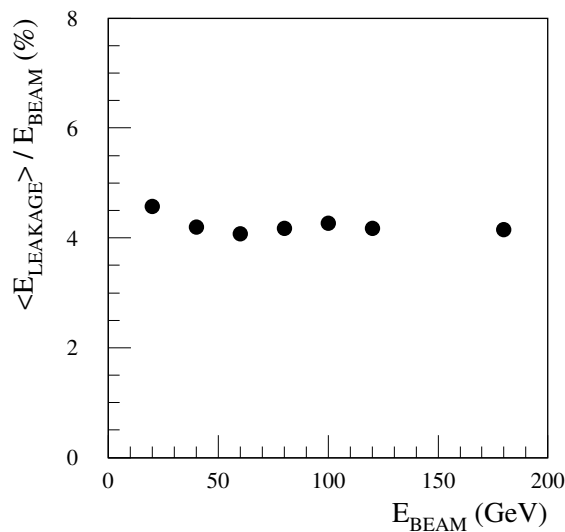
Figure 5-12 G-CALOR prediction for pions: energy dependence of the relative energy leakage as expected for the test beam set-up.
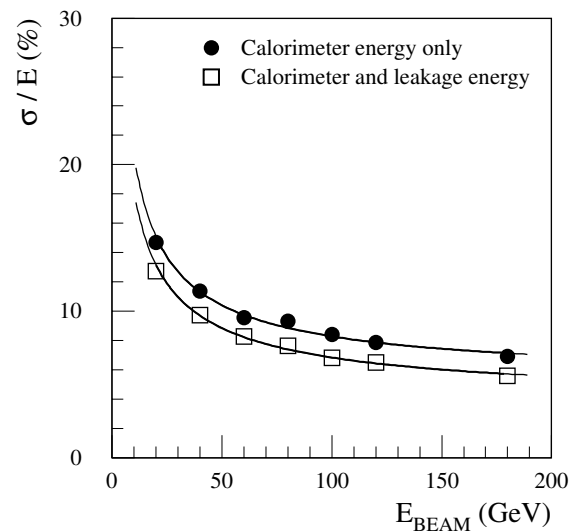
Figure 5-13 G-CALOR prediction for pions: energy resolution for the test beam set-up (solid dots) and the corresponding values for full lateral coverage (open squares). Energy dependence of the resolution is parametrised by Equation 5-5 with $A = (63 \pm 1)\%\,\mathrm{GeV}^{1/2}$, $B = (5.4 \pm 0.2)\%$ for the first set and with $A = (56.1 \pm 0.9)\%\,\mathrm{GeV}^{1/2}$, $B = (3.9 \pm 0.2)\%$ for the second one.

G-CALOR [5-6] was employed for detailed simulations. Noise was added using the response measured in randomly triggered events. To study the lateral distribution of hadronic showers, the size of the tower, used to reconstruct the pion response, was varied: a large tower, medium tower and small tower were used. The corresponding number of read-out cells was 44, 22 and 14 respectively. Figure 5-14 shows the energy resolution of the data in comparison with the predictions of G-CALOR. The noise was subtracted quadratically for both beam test and simulated data. One overall energy independent calibration constant was determined from a fit over all the energy points. In general, G-CALOR describes the data fairly well, particularly the shower core.
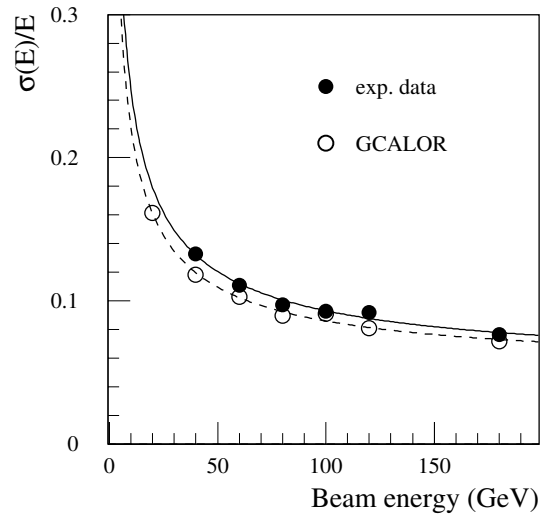
Figure 5-14 Energy resolution for pions as obtained using a large tower for the energy reconstruction. The solid dots show the data, the open circles show the predictions from G-CALOR. The lines give fits with Equation 5-5.

5.1.3.6 Results for muons

Module zero's of the HEC were also tested with a 120 GeV muon beam. Muon data are essential to provide information on the calorimeter response in the region of low energy. In addition, lateral and vertical scans allow testing the homogeneity of the calorimeter over the full depth.

Given the horizontal positioning of the calorimeter modules, the beam particles do not enter the module parallel to the read-out structure, in contrast to the actual configuration of the ATLAS detector. Therefore, twice as many read-out cells as in the final detector have to be summed to reconstruct the deposited energy of a traversing muon [5-16]. As a consequence, the noise contribution is increased and the signal to noise ratio is poorer. Nevertheless, the muon signal is well reconstructed. Figure 5-15 shows the reconstructed muon signal compared to the electronic noise obtained from identical towers of read-out cells for a few impact positions. The impact points covered both φ-wedges, employed with different high voltage technologies: (a) Canadian and (b) European ones. The ratio of signal to noise is about three in good agreement with Monte Carlo expectations. Figure 5-16 shows the relative muon response (response in a given cell as a fraction of the muon response in this longitudinal compartment) when scanning vertically across a few read-out cells. The read-out cell boundaries can be clearly identified and the transition to the neighbouring cell is as expected. Figure 5-17 shows the total response to 120 GeV muons. The mean value as well as the most probable (maximum) value are plotted for individual runs at different horizontal and vertical positions. The regions of increased inactive material (tie rods), where the signal is reduced, are clearly visible. The data are from the April 1998 run for both φ-wedges of the beam test set-up: (a) for the Canadian part and (b) for the European one. The data from the August run (c) are also shown for the Canadian φ-wedge. The deposited energy in the two different φ-wedges agrees within 1%. The ratio between the August data and the April data deviates only by 2% from unity, demonstrating the stability of the absolute calibration between the two run periods.
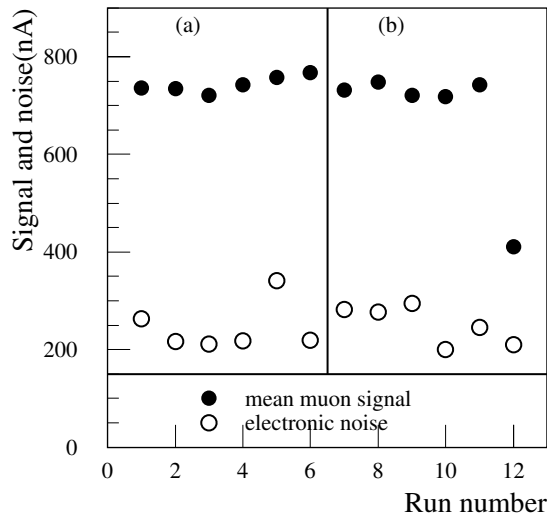
Figure 5-15 Reconstructed muon signal and electronic noise at different impact positions. The scan extends over both ϕ-wedges of module pairs.
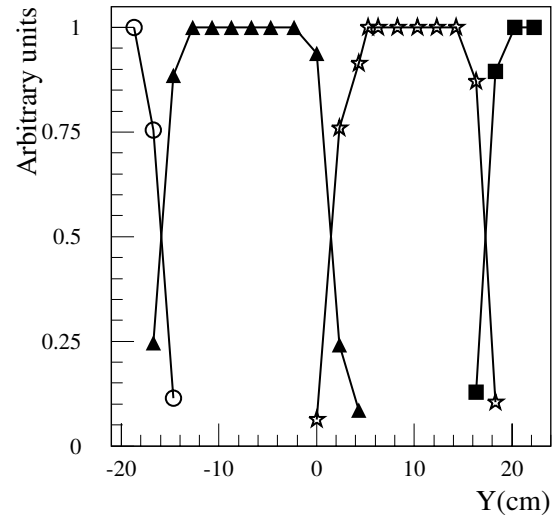
Figure 5-16 Relative muon signal in read-out cell 1 (open circles), 3 (solid triangles), 5 (stars) and 7 (solid squares) with respect to the total signal in the first longitudinal compartment as a function of impact position.

Finally, Figure 5-18 shows the distribution of the total deposited energy together with Monte Carlo expectation. The distributions agree fairly well. This holds also for the absolute value. An electron-to-muon ratio of 0.96 was obtained for data; the corresponding Monte Carlo prediction is 0.94. This corresponds to an electron to MIP (Minimum Ionising Particle) ratio of 0.83 for the data and 0.82 for the Monte Carlo.

5.1.4 Forward Calorimeter module zero test beam results

5.1.4.1 The test beam set-up

Beam tests of module zero's of the copper FCAL1 modules and the tungsten FCAL2 modules were performed in the H6 beam line at CERN. The modules were not cylindrical, but consisted of 45° sectors. These sectors are identical in construction to the final modules. The FCAL1 module contained 2350 electrodes grouped in 256 read-out channels, and the FCAL2 module contained 2550 electrodes grouped in 160 channels. Monte Carlo studies indicate that these sector modules provide 99% lateral containment for 100 GeV pions.

The modules were tested in the H1 cryostat using a beam line arrangement similar to the HEC tests. The set-up was modified mainly by adding a crude iron/scintillator 'tail catcher' calorimeter behind the cryostat. This was done in order to detect longitudinal leakage energy from the FCAL modules, as the combined length of the FCAL1 and FCAL2 modules is only 6 λ. The total length of the two modules was considerably less than the diameter of the cryostat, so liquid argon excluders made of low-density foam were positioned in front and behind the modules under test. The modules were oriented in the cryostat such that with the beam impinging on the central tile of the sector, the angle corresponded to $\eta = 3.7$ in the final detector.
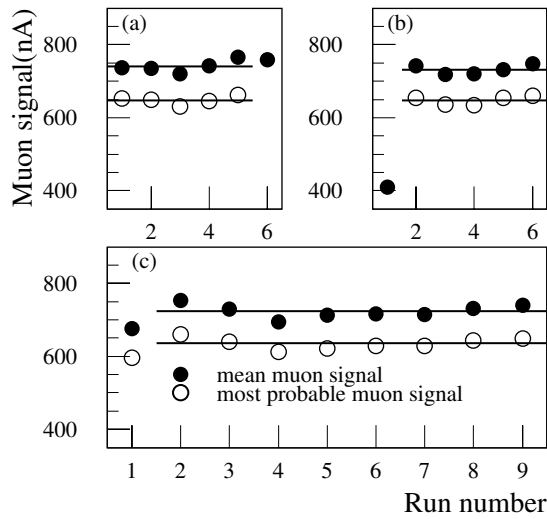
Figure 5-17 Total response to 120 GeV muons, plotted as the mean value and as the most probable (maximum) value, for individual runs at different horizontal and vertical positions. Shown are the data for (a) the Canadian and (b) the European ϕ-wedges for the April 98 run, and for the Canadian ϕ-wedge for the August 98 run (c).
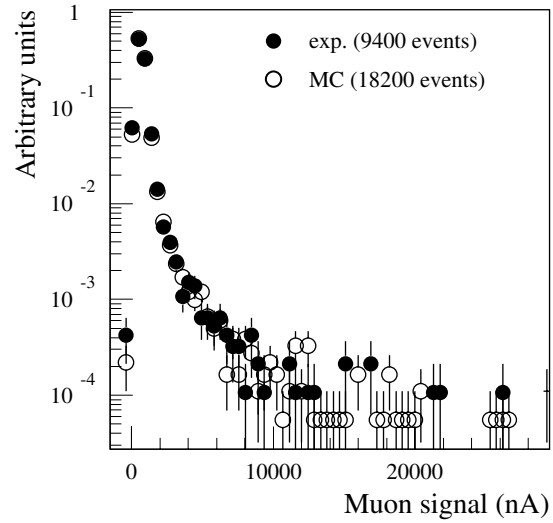
Figure 5-18 Distributions of the total response to muons of $E = 120$ GeV for the data (solid dots) and for the simulation (open circles).

The electronic read-out chain used prototypes of the signal cables, the cold transformer summing boards, and the warm feedthrough flange. So, the configuration in the cold was close to the expected final set-up. In the warm, the front-end boards and the cables between them and the feedthrough were also prototypes of the final design. This allowed meaningful measurements of the electronic noise levels to be performed.

The FCAL beam test was divided into two periods. In the first period, only the tungsten FCAL2 module was in the cryostat. This allowed measurements of the response of the FCAL2 to electrons, which gave the inter-calibration between FCAL1 and FCAL2. In the second running period, the FCAL1 module was inserted in the cryostat in front of FCAL2. This corresponded to the final configuration in the detector, and allowed measurements of the behaviour of the combined system. In both run periods data were collected with electrons and pions of energy between 20 and 200 GeV. Horizontal scans with electrons were also performed over a 16 cm range. The response at $\eta = 3.8$ was measured for muons with energy 80 and 120 GeV. These data should allow deep understanding of the FCAL performance. Here, preliminary results on the response of FCAL1 to electrons and the response of FCAL1+FCAL2 to pions are presented.

5.1.4.2 Noise performance

The major source of 'noise' in the FCAL will come from pile-up of minimum bias events, whereas the electronic noise should not play a significant role in the performance of the device. The test beam energies are small compared with the energies expected in the experiment, so the electronic noise does play a role in characterising the device from test beam data. The noise performance was determined using random-trigger events. For FCAL1 the rms noise, summed over the whole sector, corresponds to 6.8 GeV. Within a cylinder of radius 15 cm, centered on the beam direction, the noise is 4.0 GeV. The total rms noise in FCAL1+FCAL2 is 17 GeV. These are close to the expected values, and correspond to 10% of the expected pile-up at high luminosity.
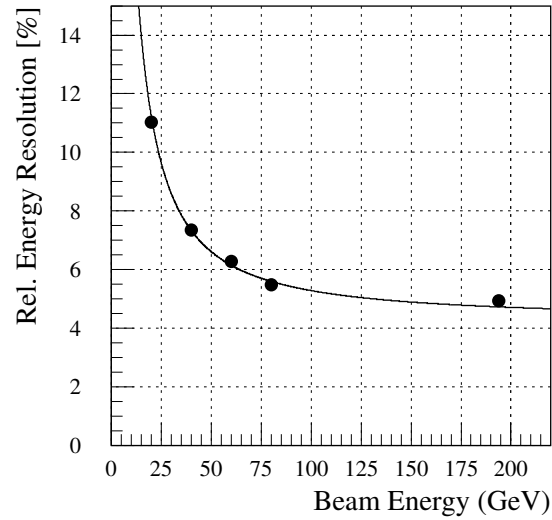
Figure 5-19 The energy dependence of the FCAL1 energy resolution for electrons. The fitted curve corresponds to the parametrisation from Equation 5-3.

5.1.4.3 Response of FCAL1 to electrons

The electron signal was studied using the energy collected over cylinders of various radii, centered on the beam impact point. This allowed the noise contribution to be minimised. In order to avoid signal saturation, the central portion of each module was instrumented with bi-gain ADC channels, and this bi-gain feature was used in the analysis. The energy resolution was parametrised using Equation 5-3. It was found that the optimum energy resolution resulted for a cylinder of radius 6 cm, the resulting fit is shown in Figure 5-19. The sampling term is better than 30% GeV$^{1/2}$ as expected, and the constant term is an acceptable 4%. The fitted values from a three-parameter fit to the resolution are given in Table 5-4. The deviation from linearity of the response was found to be smaller than 1% (see Figures 5-20 and 5-21).

5.1.4.4 Response of combined FCAL1 and FCAL2 to hadrons

In studying the response of the combined FCAL1+FCAL2 to pions, the energies in two modules were weighted with the relative response to electrons, which was determined to be

$$E = E_{FCAL1} + 2.1 \times E_{FCAL2}.$$

The small size of the hadron signals in FCAL2 resulted in electronic noise having a more sig-

Table 5-4 Terms of the electron energy resolution for FCAL1, obtained with the parametrisation from Equation 5-3.

Parameter	Fitted Value
Sampling term, A (% GeV$^{1/2}$)	26.63 ± 2.06
Constant term, B (%)	4.23 ± 0.12
Electronic noise, C (GeV)	1.70 ± 0.08

nificant contribution than in the electron runs. There are two possible approaches to allowing for the effect of electronic noise on the energy resolution. Only summing channels above some noise cut considerably reduces the level of noise per event. This results in the energy scale being non-linear, due to the effect of the noise cut varying with beam energy. Therefore results ob-

Figure 5-20 The response of the FCAL1 module as a function of the electron energy.
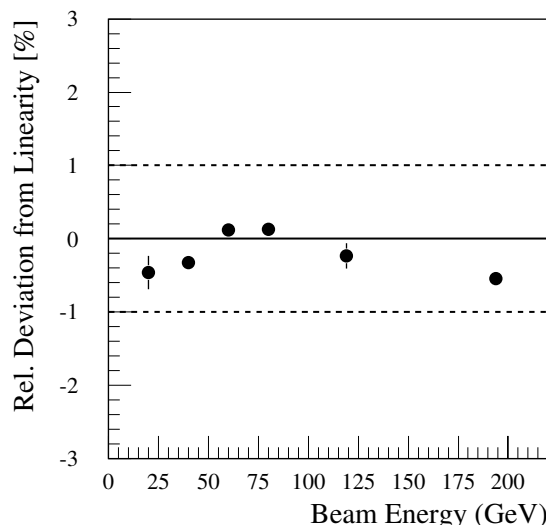
Figure 5-21 Deviation of the response of FCAL1 from linearity.

tained by summing all the energy in the modules are presented here. The noise contribution is then removed, energy by energy, by subtracting in quadrature the noise level determined from random-trigger events.

Due to the length of FCAL1+FCAL2, there is a significant amount of longitudinal energy leakage at the higher beam energies. So, from this beam test it was not possible to determine the energy resolution expected from FCAL1+FCAL2+FCAL3. Nonetheless, the tail catcher allows the study of the resolution for events with full longitudinal containment in FCAL1+FCAL2, and the resolution obtained from an unbiased sample of events with no tail catcher requirement. In fitting these results there is no need to include a noise term, and a two parameter model (see Equation 5-5), with only a sampling term A and a constant term B, is used.

The energy dependence of the energy resolution obtained for events required to have no energy in the tail catcher is shown in Figure 5-22; the fitted parameter values are given in Table 5-5. The tail catcher requirement clearly results in a biased event sample. The events will be those with a shorter shower development due, for example, to a higher than average electromagnetic portion. In general one would expect that the sampling term of $A = (81 \pm 16)\% \, \mathrm{GeV}^{1/2}$ is an optimistic estimate of the sampling term for the full

Table 5-5 Fitted values of the two parameter fit (Equation 5-5) to the FCA1+FCAL2 energy resolution for pions. The column labelled 'Tail Cut' corresponds to the fitted curve in Figure 5-22, and that labelled 'No Tail Cut' to the fitted curve in Figure 5-23.

Parameter	Tail Cut	No Tail Cut
Sampling, A (% $\mathrm{GeV}^{1/2}$)	80.9 ± 15.5	98.4 ± 10.6
Constant, B (%)	7.7 ± 1.2	10.6 ± 0.6

FCAL1+FCAL2+FCAL3 configuration. On the other hand, the constant term of $B = (8 \pm 1)\%$ may be expected to be a good measurement of the effect of inhomogeneities and channel-to-channel variations in response.

The energy resolution dependence with no requirement on the tail catcher energy deposition is shown in Figure 5-23; again the fitted parameter values are in Table 5-5. This is an unbiased sample of events, with incomplete longitudinal containment. One can expect that sampling term of $A = (98 \pm 11)\% \, \mathrm{GeV}^{1/2}$, and the constant term of $B = (10.6 \pm 0.6)\%$, are both overesti-
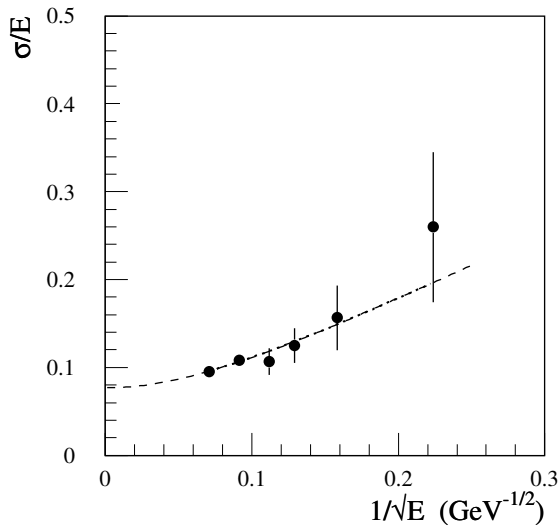
Figure 5-22 The energy dependence of the FCAL1+FCAL2 energy resolution for pions. The events were required to have no energy deposition in the tail catcher. The noise was subtracted. The solid line is a fit with a two-parameter model (Equation 5-5).
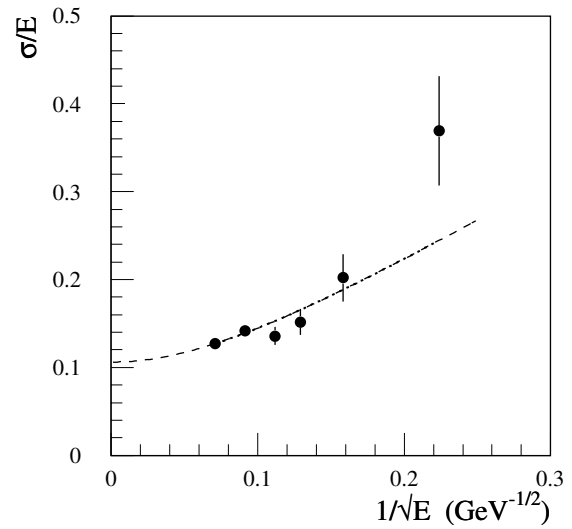
Figure 5-23 The energy dependence of the FCAL1+FCAL2 energy resolution for pions. No requirement was made on the tail catcher energy. Otherwise the treatment of the data is as in Figure 5-22.

mates of what would be expected in FCAL1+FCAL2+FCAL3. These results indicate that a final energy resolution with the sampling term $A = 100\%\,\mathrm{GeV}^{1/2}$ and the constant term $B = 7\%$, which corresponds to the ATLAS requirement, is attainable.

The results presented here are preliminary. For example no electronic calibration has been applied, and the results of studies of cross talk, noise, and deficient channels have not been taken into account.

5.2 Evolution of ATLAS calorimetry since the system TDR

Since the submission of the Calorimeter TDRs, the layout of the calorimetry has evolved towards the final design. Modifications include changes in the cryostat and dead material. The main changes to the cryostats are discussed in Section 4.1. The final read-out granularity of all calorimeters has been chosen. The update of the detector description in the simulation includes as much as possible all elements that contribute significantly to the amount of dead material, in particular rails or feet which support the detector. Here the main changes which affect simulations are summarised.

The Inner Detector rails and supports have been included. These are aluminium pieces of $\Delta\phi{\sim}5°$ and radial thickness of 13 mm located at azimuthal angles of 0° and 180° and fixed on the warm wall of the barrel cryostat. The four 8.5 cm thick iron feet supporting the barrel calorimeter are described. Each one covers partially 12° in azimuth. Barrel and end-cap rails, made mostly from aluminium, have been implemented in the simulation. All these elements introduce azimuthal asymmetry.

Stainless steel support bars of the HEC modules (thickness corresponding to 0.7 interaction lengths) are now simulated, as well as tie-rods which maintain the structural strength of the HEC copper plates. This increases the amount of dead material in front of the extended Tile Cal-

orimeter and inside the Hadronic LAr Calorimeter respectively. The modified read-out structure of the HEC has been implemented: four longitudinal compartments instead of three are now foreseen.

The shape of the cryostat wall in front of the Forward Calorimeter has changed. The outer radius of the FCAL has been reduced by 5 mm: it is now 449.5 mm (in cold) for all modules. The new read-out scheme for the FCAL has been introduced, according to which FCAL read-out channels are non-projective in azimuthal angle and pseudorapidity. The total number of electrodes is now 12 255, 10 200 and 8 532 in FCAL modules 1, 2 and 3, respectively.

5.3 Single particle performance

In this section the performance of the calorimetry for the detection of single charged hadrons and muons is reviewed. The pion energy loss in the dead material is described in Section 5.3.1 and the response to charged pions and muons in Section 5.3.2 and Section 5.3.3 respectively. Studies are based on the full simulation of the calorimeter response, done with GEANT 3.21 [5-17] and the G-CALOR hadronic shower package [5-6].

5.3.1 Energy loss in dead material across pseudorapidity

The total thickness of the ATLAS calorimetry as a function of pseudorapidity is shown in Figure 5-24. The total thickness of the active calorimeters is close to or larger than 10 λ over the full coverage up to $|\eta| = 4.9$. This figure shows also the amount of the dead material in front of the calorimeters and in the regions between the Tile and EM Calorimeters.

The energy lost in the dead material by neutral and charged pions, the two main components of a jet, is shown in Figure 5-25. The average energy lost by neutral pions (mostly in the inner wall of the cryostat and in the coil) increases from about 2% at central pseudorapidity to about 4% at $|\eta| = 1.2$. The profile of the cryostat has been designed to concentrated the dead material in a small window of about 0.2 in pseudorapidity centred at 1.45. The energy loss in this region reaches 30-35%. In the end-cap region, the loss is small, as the particles cross the cryostat walls almost perpendicularly. Significant losses appear in the crack between the end-cap and Forward Calorimeters at $|\eta| = 3.2$.

The profile of the energy lost by charged hadrons is quite different. There are two components contributing to it: the dead material in front of the calorimeter and the dead material between the electromagnetic and the hadronic calorimeters due to the outer cryostat wall. The energy loss of a charged hadron depends on the starting point of the hadronic shower. About 20% of the charged hadrons do not start showering before reaching the hadronic compartment and deposit only the energy of a minimum ionising particle. On the other hand, when the shower develops in the EM Calorimeter, the dead material is close to the shower maximum. The average energy loss is 7% with large fluctuations. In the transition region between the barrel and the end-cap, two peaks appear due to the dead material inside the vertical gap between the Tile central and extended barrel calorimeters (~12%) and due to the barrel and end-cap cryostat corners (~17%), respectively. In the end-cap region, the loss is small, except in the crack between the end-cap and Forward Calorimeters, where it is of order 8%.
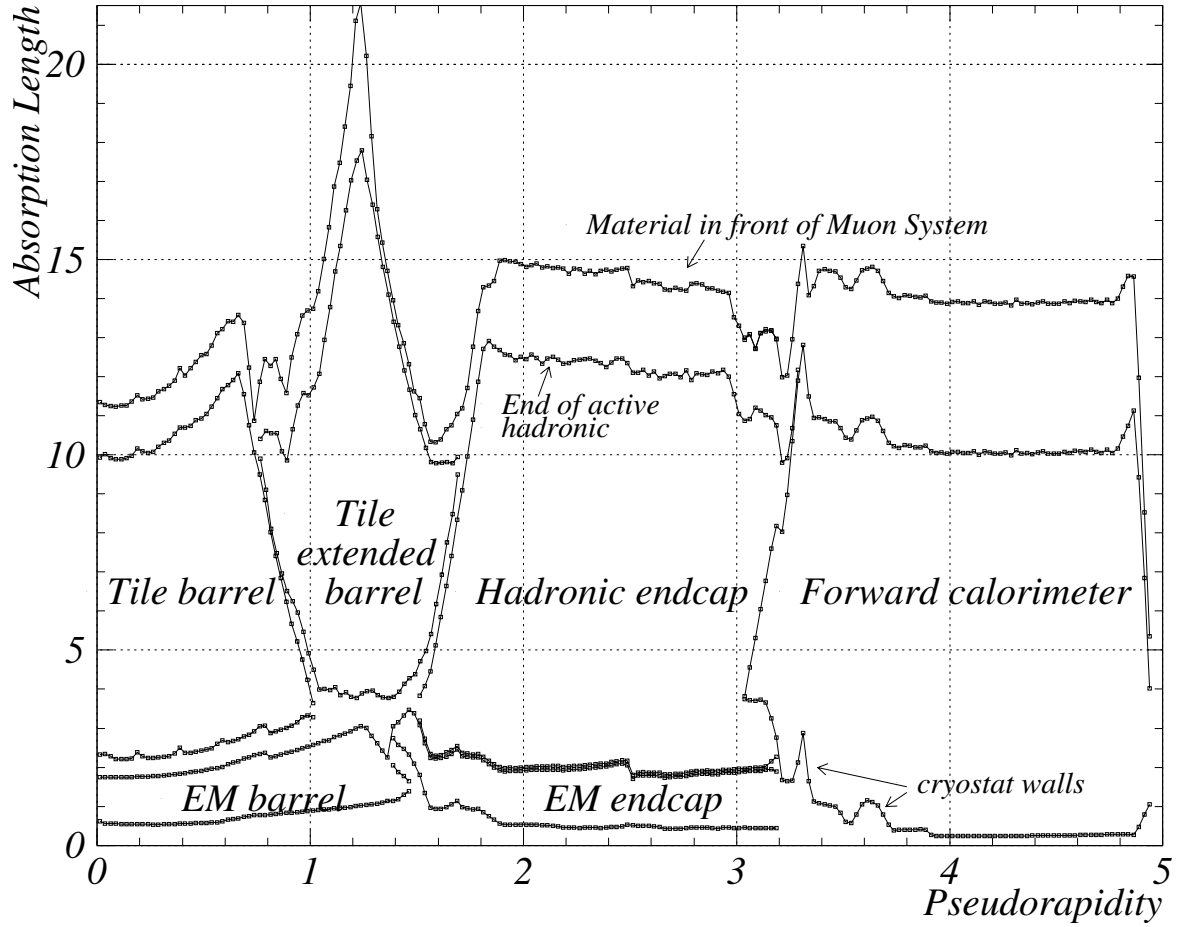
Figure 5-24 Total thickness (in absorption lengths) of the ATLAS calorimetry as a function of pseudorapidity.

5.3.2 Pion response

The performance of the hadronic calorimetry for the measurement of charged pion energy was studied. Firstly, the intrinsic energy resolution is presented in the different regions corresponding to the different calorimeter components. Then the effects of electronic noise and limited cone size are discussed.

5.3.2.1 Energy resolution

In the barrel region, the response of the calorimeter was studied at two pseudorapidity values: $\eta = 0.3$ (central barrel) and $\eta = 1.3$ (extended barrel) [5-18]. Firstly, the energy sampled in the different calorimeter compartments was converted to a total deposited energy using the electromagnetic energy scale (EM scale). Here the energy considered was not restricted to a cone and electronic noise was not added. These effects are discussed in Section 5.3.2.3. To estimate the pion energy, an algorithm similar to the Benchmark Method used to reconstruct the combined LAr-Tile test beam data (see Section 5.1.1 and Equation 5-1) was applied:

$$E_{rec} = \alpha \cdot E_{had} + \beta \cdot E_{em} + \gamma \cdot E_{em}^2 + \delta \cdot \sqrt{E_{had1} \cdot E_{em3}} + \kappa \cdot E_{ITC} + \lambda \cdot E_{scint}. \qquad 5\text{-}6$$
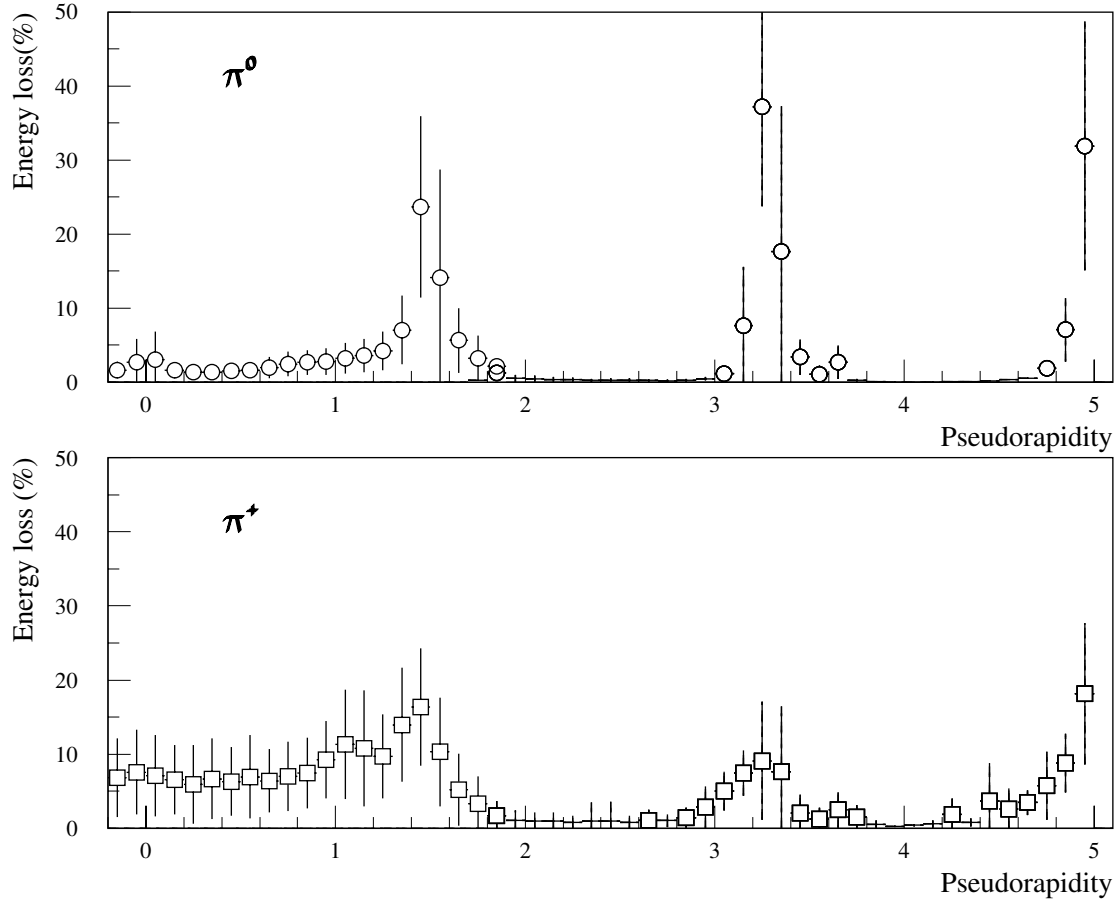
Figure 5-25 Average energy loss in the dead material as a function of pseudorapidity for neutral (top plot) and charged pions (bottom plot). The error bars correspond to the rms of the distributions.

The coefficients α and β take into account the different response of the hadronic and EM calorimeters to the pion energy. The quadratic term γE_{em}^2 provides an additional first order correction for non-compensation. The term $\delta \cdot \sqrt{E_{had1} \cdot E_{em3}}$ estimates the energy loss in the cryostat wall separating the LAr and Tile Calorimeters. In the central barrel, the energy is taken from the geometric mean of the energies in the last compartment of the LAr EM barrel and the first compartment of the Tile barrel calorimeter, whereas in the extended barrel the energy is taken from the geometric mean of the energies in the outer wheel of the EM end-cap and the first compartment of the Tile extended barrel calorimeter. The term $\kappa \cdot E_{ITC}$ corrects for the energy loss in the dead material in the vertical gap between the Tile central and extended barrels. It is sampled by the two Intermediate Tile Calorimeter (ITC) modules (see Figure 5-i). The last term $\lambda \cdot E_{scint}$ corrects for the energy loss in the barrel and end-cap vertical cryostat walls, as sampled by the three scintillators installed in that region.

The response and the energy resolution for pions in the energy range from $E_0 = 20$ GeV to 1 TeV at $\eta = 0.3$ and 1.3 are shown in Figures 5-26 and 5-27. The open crosses show the results when the coefficients of Equation 5-6 are independent of energy. There is a residual non-linearity of the pion response of the order of 4-5% between 20 GeV and 1 TeV, while the test beam data showed 10% non-linearity between 20 and 300 GeV for the Benchmark Method (see Figure 5-2), reflecting the fact that G-CALOR predicts a lower degree of non-compensation. The energy dependence of the resolution is fitted with the two-term formula (Equation 5-5). Although the res-
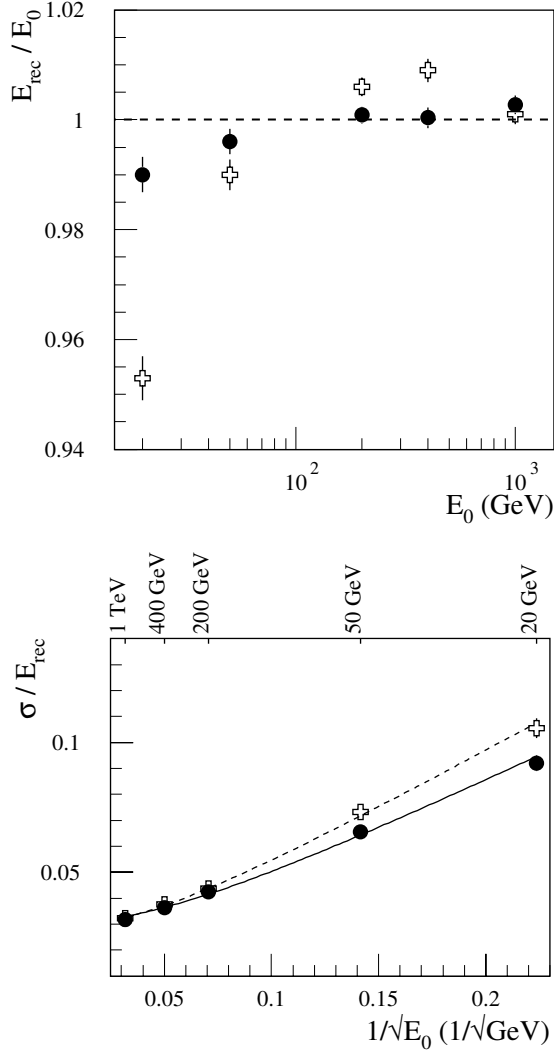
Figure 5-26 Pion energy scan in the central barrel ($\eta = 0.3$). The top plot shows the residual non-linearity, the bottom plot shows the energy resolution with the results of the fit with Equation 5-5. Two sets of parameters for the pion energy reconstruction have been used: open crosses - for energy independent parameters; solid dots - for parameters fitted at each energy and pseudorapidity.
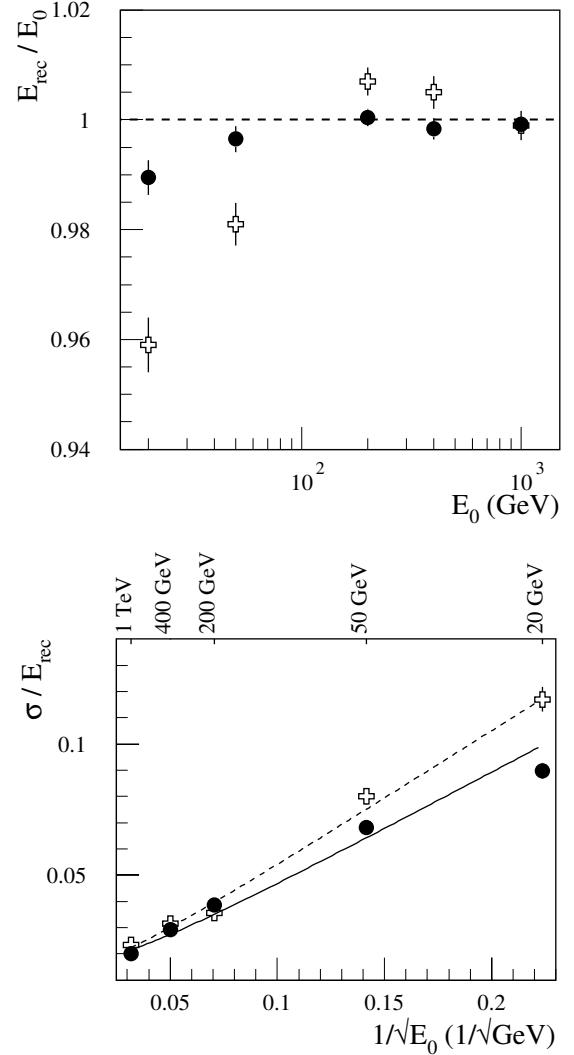
Figure 5-27 Pion energy scan in the extended barrel ($\eta = 1.3$). The top plot shows the residual non-linearity, the bottom plot shows the energy resolution with the results of the fit with Equation 5-5. Two sets of parameters for the pion energy reconstruction have been used: open crosses - for energy independent parameters; solid dots - for parameters fitted at each energy and pseudorapidity.

olutions obtained for low-energy pions are similar in both cases, at high energy there is some longitudinal leakage in the central barrel, yielding a resolution at 1 TeV of 3% instead of 2%, as achieved in the extended barrel. When energy dependent parameters are applied (solid dots), the linearity of the response is restored and the resolution improved. The results are the following: $A = (40 \pm 1)\%\ \mathrm{GeV}^{1/2}$, $B = (3.0 \pm 0.1)\%$ for $\eta = 0.3$ and $A = (44 \pm 3)\%\ \mathrm{GeV}^{1/2}$, $B = (1.6 \pm 0.3)\%$ for $\eta = 1.3$.

The response of the calorimeter in the end-cap region was studied with single charged pions of energies $E_0 = 100, 200, 500$ and 1000 GeV - a range of energies characteristic of the pseudorapidity coverage of the end-cap calorimeter. The pion energy is reconstructed as:

$$E_{rec} = \sum C_i \cdot E_i, \qquad\qquad 5\text{-}7$$

where E_i is the energy deposited in the different calorimeters, *i.e.* the hadronic end-cap, the EM end-cap, the Tile calorimeter with ITCs and scintillators, the EM barrel calorimeter and the Forward Calorimeter. No dead material correction term is needed here because there is no cryostat separating the EM and the hadronic parts. The parameters C_i are determined by minimising $(E_{rec}\text{-}E_0)^2$ at each energy and pseudorapidity.

In Figure 5-28 the parameters for the hadronic and EM end-cap calorimeters are shown as a function of the initial pion energy and pseudorapidity. The parameters vary significantly but smoothly with energy and pseudorapidity.
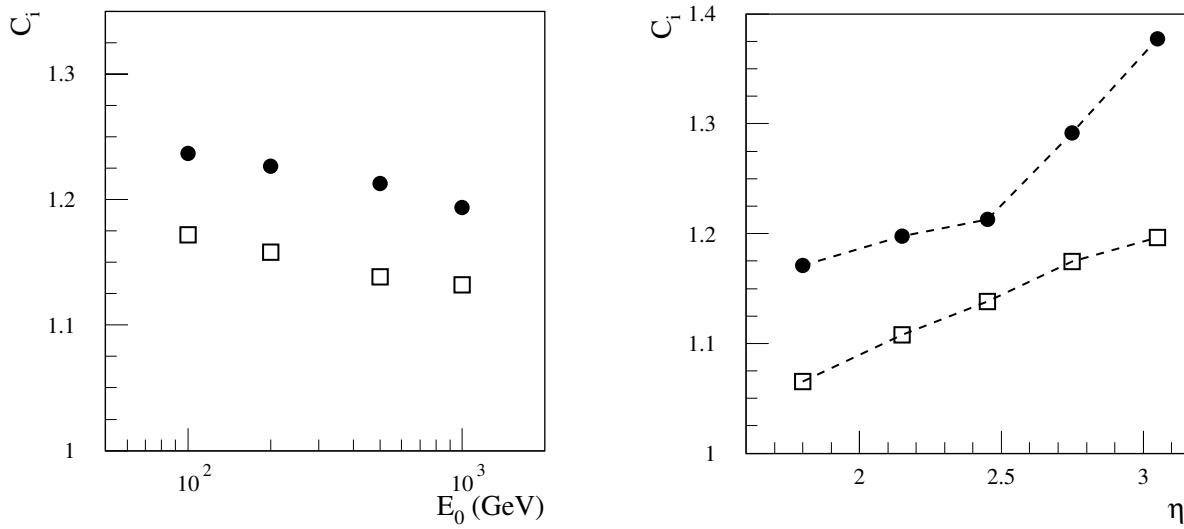
Figure 5-28 Pion energy scale parameters obtained for the hadronic end-cap calorimeter (solid dots) and for the EM end-cap calorimeter (open squares), as a function of the initial pion energy at $\eta = 2.45$ (left-hand plot) and as a function of pseudorapidity for $E_0 = 500$ GeV (right-hand plot).

In Figure 5-29 the sampling and constant terms of the pion energy resolution, obtained by the fit with the two-term formula (Equation 5-5), are plotted (solid dots) as a function of the pion pseudorapidity. In the pseudorapidity range $1.8 < |\eta| < 3.05$, covered by the end-cap calorimeters, these terms are fairly stable: $A = 55\text{-}60\%$ GeV$^{1/2}$, $B = 2.5\text{-}3.0\%$. The effect of restricting the reconstruction to a cone around the pion direction is discussed in Section 5.3.2.3.

5.3.2.2 Pseudorapidity scan

A pseudorapidity scan with pions of constant transverse energy $E_T = 20$ and 50 GeV was carried out to check that the linearity of the response can be maintained and that no significant tail appears in the line shape. In the central and extended barrel region, the algorithm, characterised by Equation 5-6, with energy and pseudorapidity dependent parameters was applied. The resulting distribution of the mean fitted responses was a Gaussian with $\sigma = 2.6\%$ for pions of $E_T = 20$ GeV and $\sigma = 1.5\%$ for pions of $E_T = 50$ GeV. In the end-cap and forward regions, the procedure to reconstruct pion energies was similar to the one described by Equation 5-7. The only difference was that the energy depositions in individual longitudinal compartments of the hadronic and EM end-cap calorimeters and of the Forward Calorimeter were used for the terms E_i.
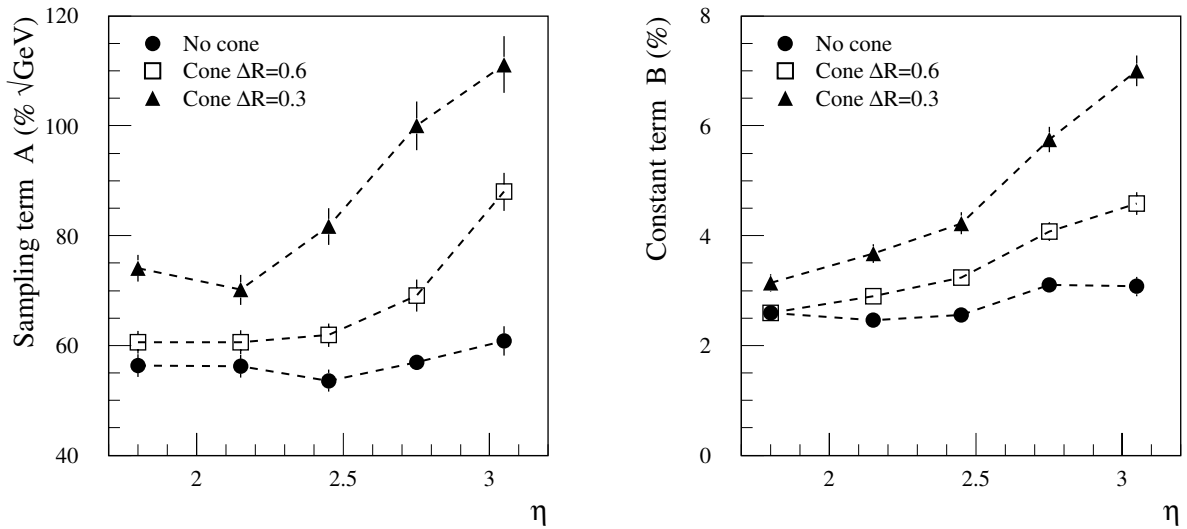
Figure 5-29 Pseudorapidity dependence of the sampling and constant terms of the energy resolution for single charged pions in the end-cap region. The solid dots show the results obtained without restriction on the reconstruction volume; open squares - with a pion reconstruction cone of $\Delta R = 0.6$; triangles - with a pion reconstruction cone of $\Delta R = 0.3$.

The energy resolutions obtained for the two scans are shown in Figure 5-30. The solid lines show the goal for the jet energy resolution of the ATLAS hadronic calorimetry in the region $|\eta| < 3$, set out in [5-1]. The pion energy resolution is close to this line and even better at some pseudorapidities. In the regions of the cracks between the calorimeters (around $|\eta| = 1.5$ and $|\eta| = 3.2$), where the amount of dead material is the largest, the resolution is somewhat worse. At a pseudorapidity of 4.8, close to the edge of the FCAL, the lateral leakage from the calorimeters starts to be important and leads to a significant degradation of the resolution.
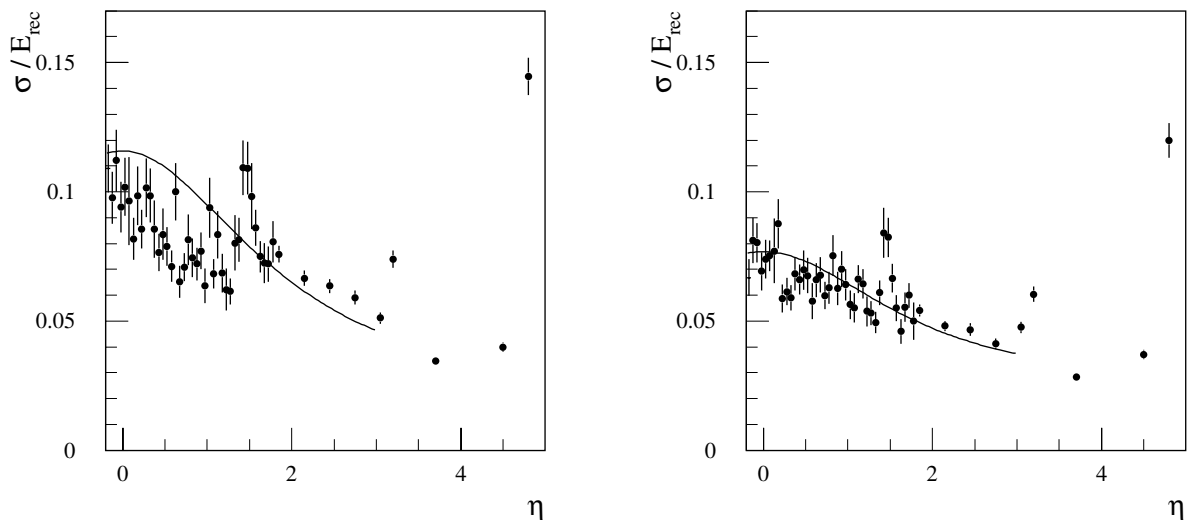
Figure 5-30 The dependence of the energy resolution on pseudorapidity for charged pions of constant transverse energy: $E_T = 20$ GeV (left-hand plot) and $E_T = 50$ GeV (right-hand plot). The lines correspond to the energy resolution parametrised using Equation 5-5 with $A = 50\%$ GeV$^{1/2}$ and $B = 3\%$.

In addition, the tails of the distributions of the reconstructed energy were investigated. Figure 5-31 shows the events with a pion response more than three standard deviations away from the mean. No significant tails are present: the fraction of events in the tails does not exceed 1-2%. A few events out of a total of 5000 events per energy scan, mostly from the sample of pions of $E_T = 20$ GeV, deposit relatively little energy. These correspond to pions decaying to muons before reaching the calorimeter.
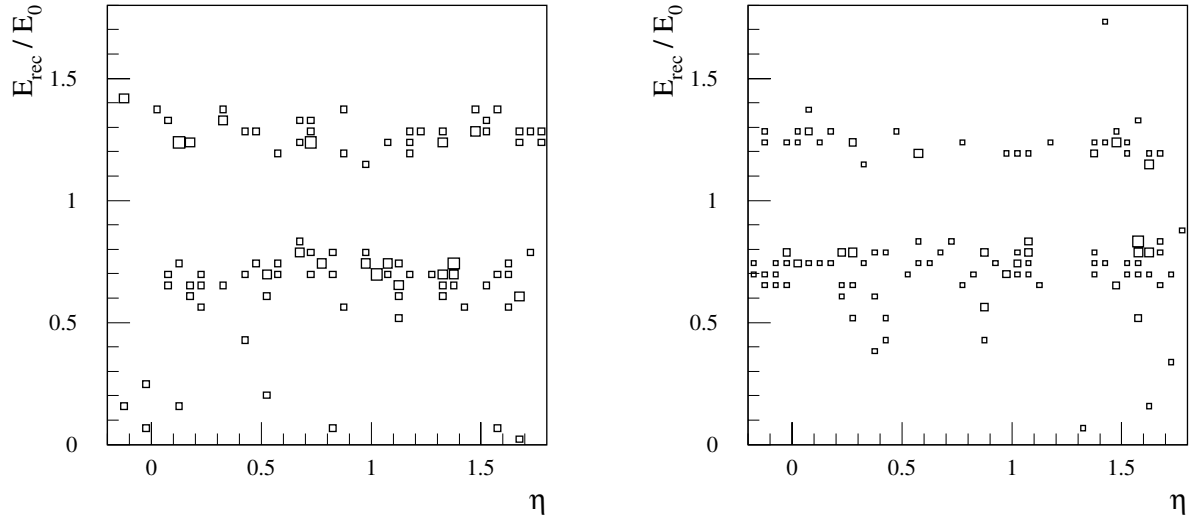
Figure 5-31 Events in the tails of the distribution of the reconstructed energy as a function of pseudorapidity for pions of $E_T = 20$ GeV (left-hand plot) and for pions of $E_T = 50$ GeV (right-hand plot). Tails are defined as events with reconstructed energies more than three standard deviations away from the mean.

5.3.2.3 Effects of electronic noise and cone size

The results presented so far were obtained without any restriction on the pion reconstruction volume. These results characterise the intrinsic performance of the calorimeters. The presence of electronic noise does not allow integration over too wide a region, therefore the measurement of the pion energy must be restricted to a cone $\Delta R = \sqrt{\Delta^2\eta + \Delta^2\phi}$. A compromise has to be found between the pion energy lost outside of this cone and the noise included inside. The optimum varies as a function of pseudorapidity, since the showers have a width which is characterised by the polar angle whereas the calorimeter cells subtend intervals of constant pseudorapidity. Hence, at higher values of pseudorapidity, the showers extend laterally over more cells.

In Figure 5-32 the electronic noise in a cone is shown as a function of pseudorapidity. For a cone of $\Delta R = 0.6$, noise is above 3 GeV even in the barrel region. Digital filtering [5-13] allows noise suppression (approximately by a factor 1.6). But even this level of noise is large and is comparable to the intrinsic resolution of the calorimeters for pions with energy of a few tens of GeV. A smaller cone of $\Delta R = 0.3$ is preferable from this point of view; after digital filtering, noise can be kept around 1 GeV in the barrel region and below 3 GeV in the transition region between the barrel and the endcap. The levels of electronic noise in the different calorimeters in towers of $\Delta\eta\times\Delta\phi = 0.1\times0.1$ are presented in Table 5-6.

The response and the energy resolution in the barrel region are presented in Figures 5-33 and 5-34 as a function of the cone size used for the pion energy reconstruction. Energy losses outside a cone noticeably increase with decreasing cone size, especially for 50 GeV pions. The energy resolution also becomes worse, but it is still acceptable for the cone of $\Delta R = 0.3$.
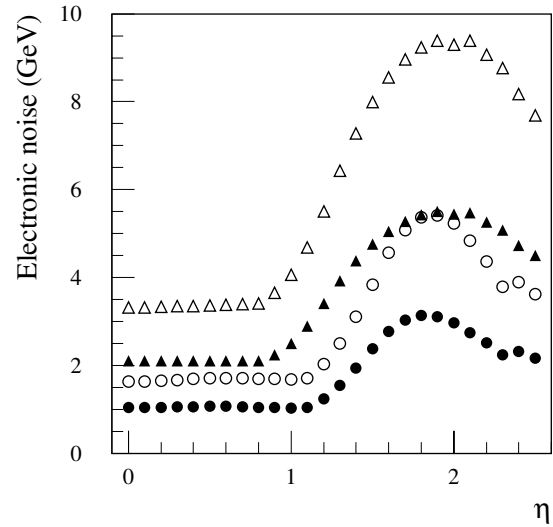
Figure 5-32 Level of electronic noise in the calorimeter (in EM scale) as a function of pseudorapidity. The triangles (dots) show the noise for a cone of $\Delta R = 0.6$ ($\Delta R = 0.3$). Open symbols correspond to the normal electronic noise, solid symbols correspond to the noise after digital filtering.

Table 5-6 Electronic noise (in EM scale) in the calorimeter tower of $\Delta\eta\times\Delta\phi = 0.1\times0.1$, obtained after digital filtering.

Central barrel region $\eta = 0.3$		Extended barrel region $\eta = 1.3$		End-cap region $\eta = 2.45$	
Calorimeter	Noise (GeV)	Calorimeter	Noise (GeV)	Calorimeter	Noise (GeV)
Tile	0.056	Tile	0.047	Hadronic end-cap	0.366
EM barrel	0.164	EM barrel	0.151	EM end-cap	0.113
Presampler	0.098	Presampler	0.107		
Total	0.199	Total	0.191	Total	0.384

In the end-cap region, the worsening of the energy resolution with decreasing cone size is more pronounced, especially in the region $|\eta| > 2.5$. This can be seen in Figure 5-29.

Selecting cells with energy deposition above a certain threshold decreases the noise contribution. Studies made for pions in the barrel region enabled optimisation of the cone size and of the noise cut to obtain the best energy resolution. In Figure 5-35, the energy dependency of the resolution is plotted for two pseudorapidities: $\eta = 0.3$ and $\eta = 1.3$. Results of the fit of these dependencies with the standard formulae are presented in Table 5-7. Using a 2σ-noise cut to select calorimeter cells within the cone of $\Delta R = 0.3$ leads finally to the best energy resolution, when electronic noise is taken into account. However, in comparison to the ideal case, *i.e.* without noise and without a cut on the cone size (see Section 5.3.2.1 or the first row in Table 5-7), the sampling and the constant term (especially in the extended barrel region) become worse.
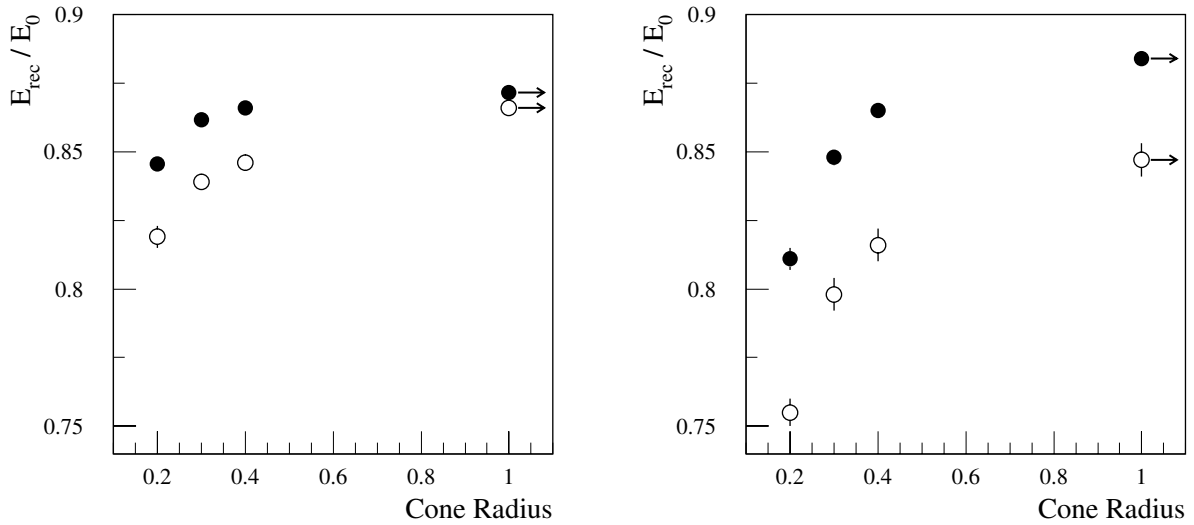
Figure 5-33 Energy response for 50 GeV (open circles) and 200 GeV (solid dots) charged pions at $\eta = 0.3$ (left-hand plot) and at $\eta = 1.3$ (right-hand plot) as a function of the cone size. The points with arrows correspond to the case without a cone restriction. Energy and pseudorapidity independent parameters were used for the energy reconstruction (see Equation 5-6).
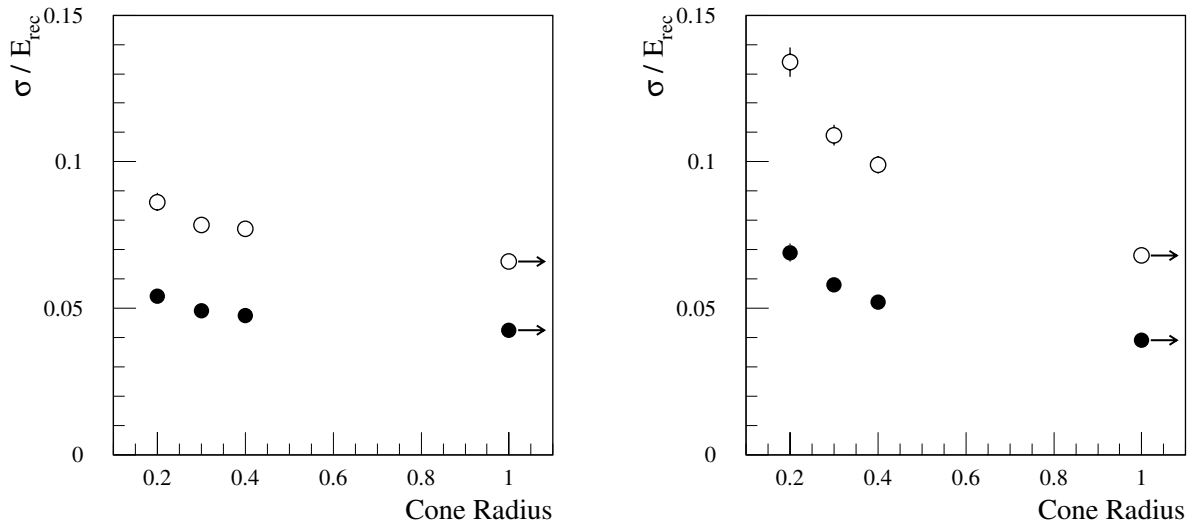
Figure 5-34 Energy resolution for 50 GeV (open circles) and 200 GeV (solid dots) charged pions at $\eta = 0.3$ (left-hand plot) and at $\eta = 1.3$ (right-hand plot) as a function of the cone size. The points with arrows correspond to the case without a cut on the cone size. Energy and pseudorapidity dependent parameters were used for the energy reconstruction (see Equation 5-6).

5.3.3 Muon response

The response of the hadronic compartments to isolated muons was studied. Figure 5-36 (left-hand plot) shows the energy deposited by 100 GeV muons in the Tile Calorimeter as a function of pseudorapidity. The open circles show test beam results. The barrel and extended barrel module zero's have been exposed to muons of 100 GeV at various pseudorapidity values. The most probable value (MOP) resulting from a fit with a Landau distribution convoluted with a Gaussian to the experimental muon spectrum is shown (see Section 5.1.2.3 and Figure 5-9). Typ-
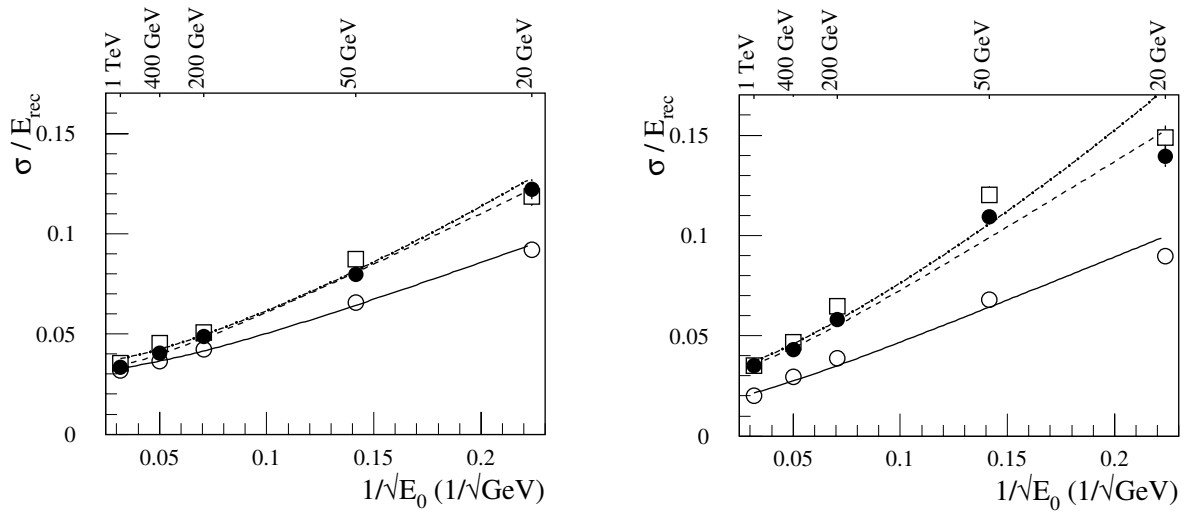
Figure 5-35 Energy dependence of the resolution for pions at $\eta = 0.3$ (left-hand plot) and at $\eta = 1.3$ (right-hand plot). The open circles show results obtained without a cut on the cone size and without electronic noise. The solid dots show results obtained for a cone of $\Delta R = 0.3$ and without electronic noise. The open squares show results obtained for a cone of $\Delta R = 0.3$ with a 2σ-noise cut (when electronic noise was included). Curves show the results of fits with the two-term formula (Equation 5-5) for the first two sets and with the three-term formula (Equation 5-3) for the third set.

Table 5-7 Terms of the pion energy resolution fitted with the two-term (Equation 5-5) and the three-term (Equation 5-3) expressions.

	Central barrel region $\eta = 0.3$			Extended barrel region $\eta = 1.3$		
	A (% GeV$^{1/2}$)	B (%)	C (GeV)	A (% GeV$^{1/2}$)	B (%)	C (GeV)
No cone, no noise	40 ± 1	3.0 ± 0.1	-	44 ± 3	1.6 ± 0.3	-
Cone $\Delta R = 0.3$, no noise	53 ± 2	3.0 ± 0.2	-	67 ± 4	2.9 ± 0.4	-
Cone $\Delta R = 0.3$, noise with a 2σ-cut	50 ± 4	3.4 ± 0.3	fixed at 1.0	68 ± 8	3.0 ± 0.7	fixed at 1.5

ical values in the barrel are 2 GeV for the MOP and 400 MeV for the σ on the left-hand side of the peak. The level of expected electronic noise when summing typically six cells (12 PMTs) is about 70 MeV, hence, the signal is well separated from the noise. In the region of the vertical crack between the barrel and extended barrel section, the thickness of active calorimeter is reduced. Figure 5-36 shows also the Monte Carlo prediction for the muon signal when the energy deposited in the ITCs is added. Full efficiency is then reached.

Inside jets, muons may overlap with other particles. Low-p_T pions tend to be absorbed in the inner part of the calorimeter while muons are much more penetrating. At high luminosity, minimum bias events will deposit more energy in the innermost compartments. The rms of the energy deposition by minimum bias events is about 100-150 MeV in the first two compartments and decreases to only 10-15 MeV in the last compartment [5-3]. Hence an efficient muon detection in the outermost compartment provides a useful muon tagging tool. Figure 5-36 (right-hand plot) shows the response in the last compartment. Experimental data from the barrel and extended barrel are compared to the Monte Carlo prediction when the energy in the ITCs has
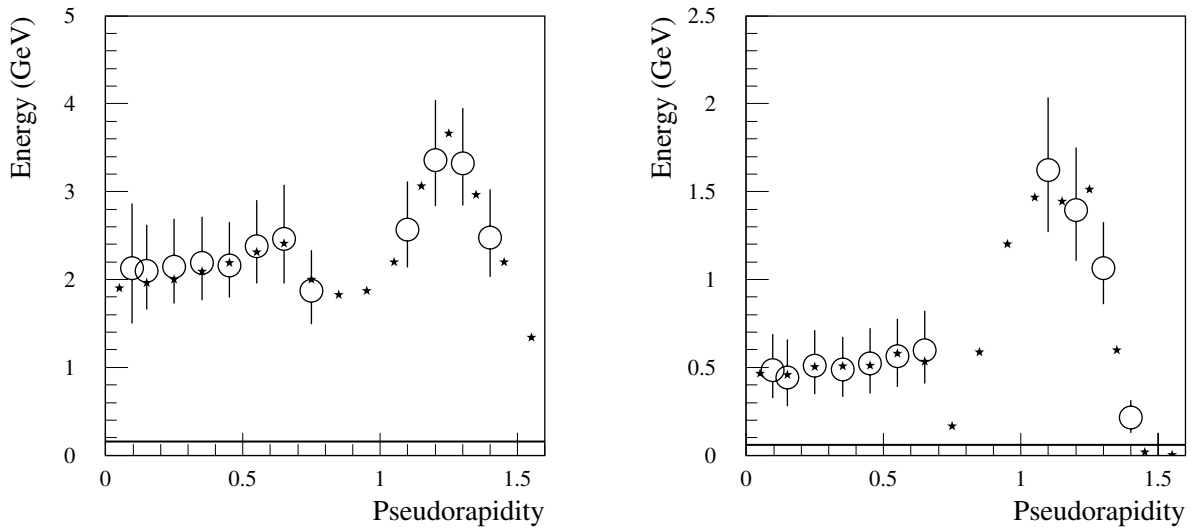
Figure 5-36 Total deposited energy (left-hand plot) and energy deposited in the outermost compartment (right-hand plot) by 100 GeV muons in the pseudorapidity range covered by the Tile Calorimeter. The open circles show results from the test beam. The error bars show the asymmetric contribution to the FWHM. The stars represent the simulated response in the ATLAS set-up, including the signal in the ITCs. The solid lines show the expected level of electronic noise.

been added. Only the pseudorapidity gap between 0.7 and 0.8 is not efficiently covered. For very central pseudorapidity ($|\eta| < 0.075$), the muon trajectories are almost parallel to the staggered iron-scintillator structure and the signal varies strongly as a function of the impact point. The efficiency to detect a muon in the last compartment only with a 3σ significance above the electronic noise is reduced to 80% in that pseudorapidity interval. If the total signal in the calorimeter is used, then full efficiency is restored.

The effect of pile-up on the muon signal has been studied. Figure 5-37 (top left) shows the signal deposited by muons of $E_T = 20$ GeV in the Tile barrel calorimeter ($0.2 < |\eta| < 0.6$) without (solid line) and with (dashed line) minimum bias events included. The effect is small: the minimum bias events deposit in average 150 MeV along the muon track with an rms of 210 MeV. This has to be compared to the average 2.4 GeV deposited by the muon in the calorimeter. Figure 5-37 (top right) shows the signal deposited by muons in the last compartment of the calorimeter. The level of energy deposited by minimum bias events in that case is on average 32 MeV with an rms of 45 MeV, to be compared to the average energy deposited by muons of 0.6 GeV.

The bottom plots in Figure 5-37 show the fraction of events which passed an energy threshold cut for minimum bias events (solid line) and for muons (dashed line). An efficiency of 99% for muons is obtained with a fake rate of the order of 0.5%, both for the full calorimeter and for the third compartment. These are the basic performance numbers, which will be masked by other effects, such as the acceptance, the road in the calorimeter used for muon reconstruction, the overlap with other particles in the event. These effects have to be evaluated in their context: on-line trigger or off-line analysis.

A preliminary study of muon detection in the hadronic end-cap calorimeter was done. The total noise consists of two parts: electronic noise and noise due to pile-up of minimum bias events. The use of multi-sampling read-out and the digital filtering method allows suppression of the total noise. The degree of suppression depends on the relative contributions of electronic and
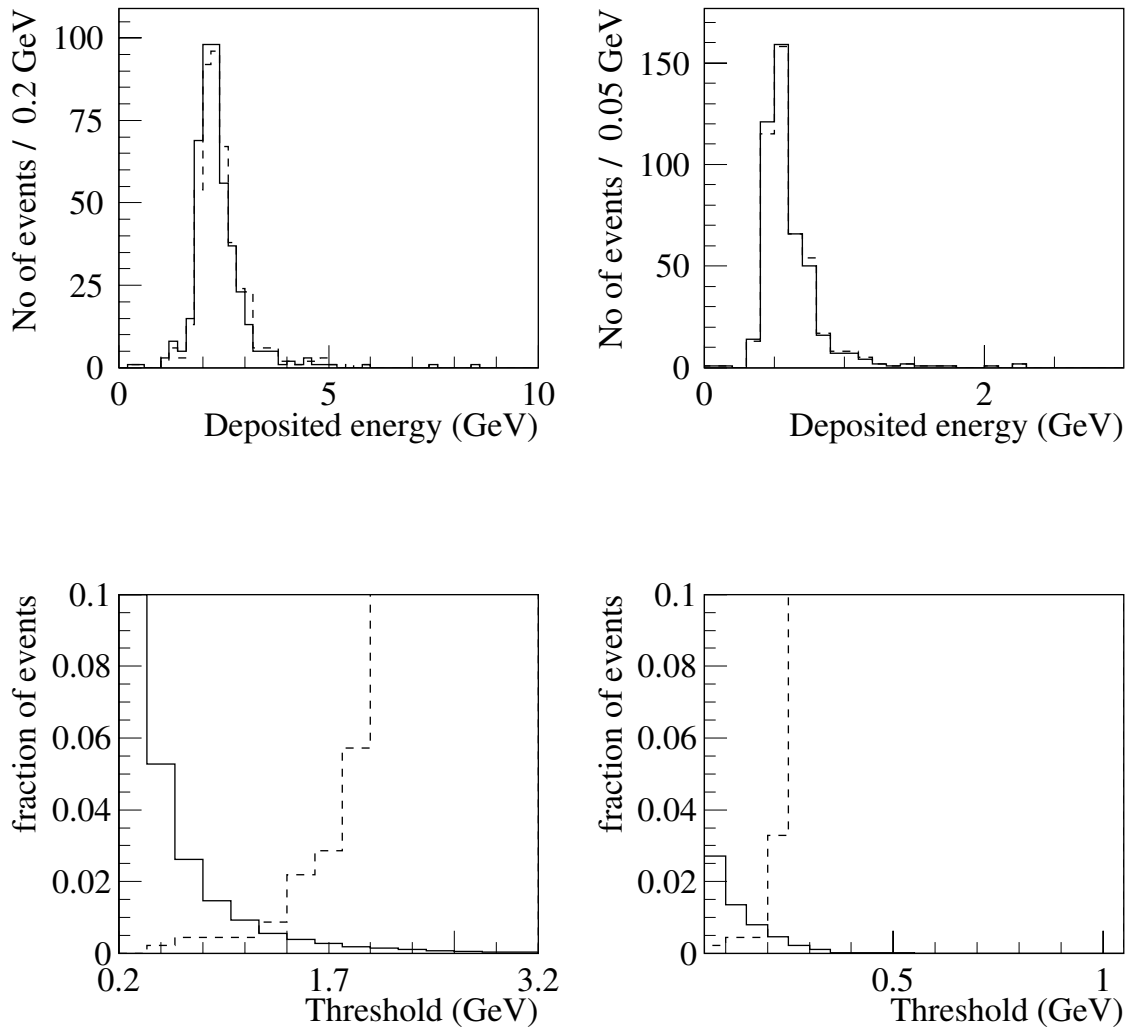
Figure 5-37 Top: energy depositions in the Tile barrel calorimeter by muons of E_T = 20 GeV without (solid line) and with (dashed line) minimum bias events included. Bottom: the fraction of minimum bias events that are kept (solid line) and the fraction of signal events with muons that are lost (dashed line) as a function of the threshold applied. The left-hand plots correspond to the full calorimeter, the right-hand plots correspond to the third compartment only.

pile-up noise and on the parameters of the electronics chain. As an example, in Figure 5-38 the ratio of the signal from a minimum ionising particle (MIP) and the noise in a cell of the hadronic end-cap calorimeter is presented. For optimised values of the parameters of the electronics, even at the highest luminosity, it is possible to keep this ratio above 2.5 in the last longitudinal compartment for $|\eta| < 2.5$.
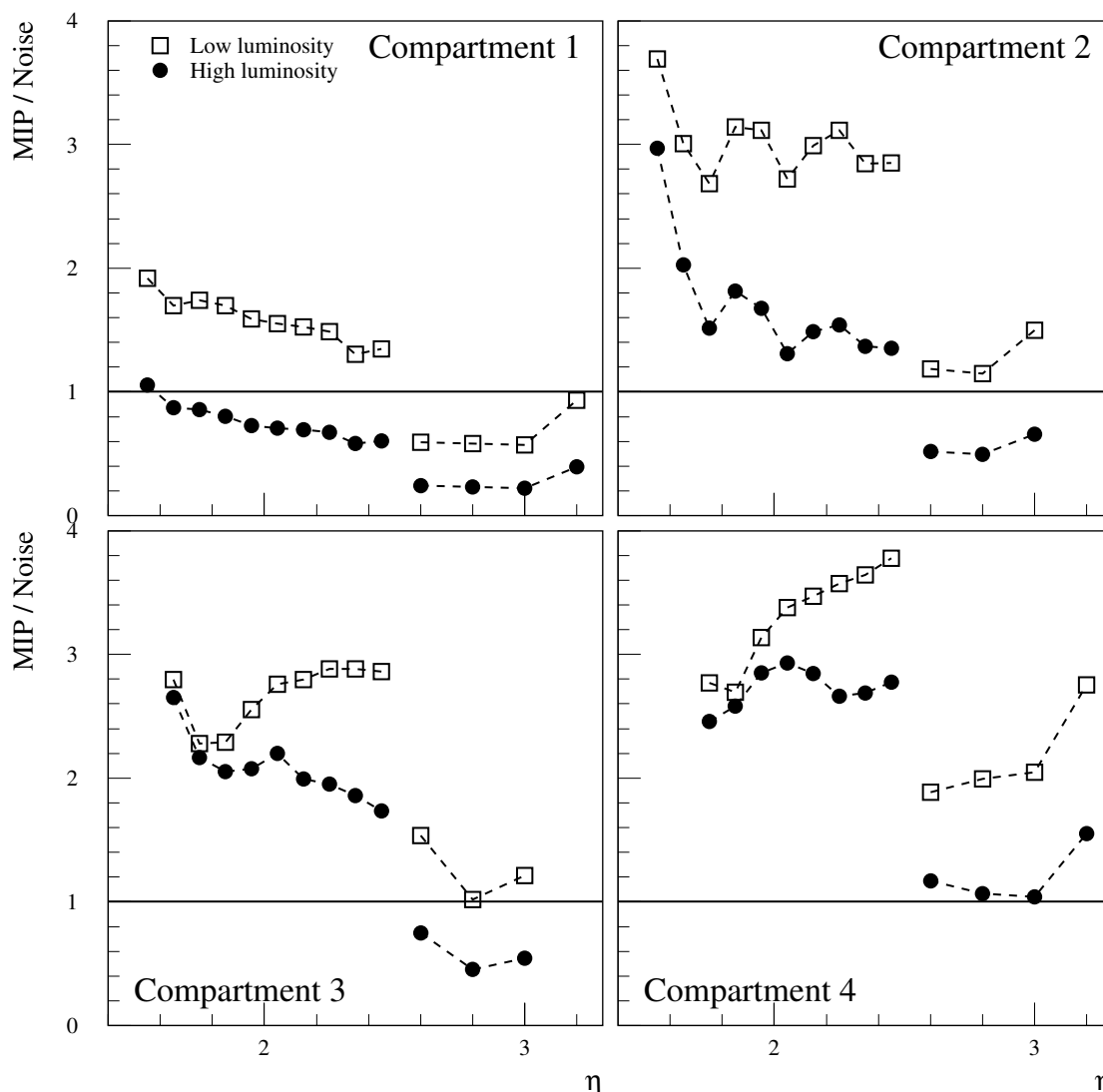
Figure 5-38 Expected ratio of the signal from a minimum ionising particle (MIP) and the noise in a cell of the hadronic end-cap calorimeter. The noise is calculated after digital filtering, applied for two values of luminosity.

5.4 Calibration with *E/p* from single hadrons

5.4.1 Introduction

The detection of single charged isolated hadrons from $\tau \to h\nu$ decays [5-19] where the charged hadron can either be a pion or a kaon can be used to transfer the calibration from the test beam to the actual detector and to inter-calibrate the various regions of the calorimeter. The precise measurement of their momentum p in the tracking detectors, compared to the energy E measured in the calorimeters could, in addition, provide a cross-calibration between these detectors.

All processes generating isolated single charged hadrons are potentially useful. For simplicity, the signal considered here [5-20], containing an isolated charged pion coming from τ decay ($\tau \to \pi\nu$ with a branching ratio of 11.08%), is Drell-Yan *W* production followed by the decay

$W \rightarrow \tau\nu$. The event rate is large and this process could therefore provide a calibration sample over a large energy range. The lower energy range is constrained by the trigger requirements whereas the upper is limited by production kinematics: 60 GeV in the barrel calorimeter, 120 GeV in the extended barrel and 250 GeV in the end-cap calorimeters. The main difficulty with this calibration method arises from background events where the π is accompanied by one or more photons from π^0 decay which could distort the energy measurement. These events must be rejected by isolation and shower shape cuts that do not bias the measurement for the *E/p* matching to be effective. This background is considered below.

Despite the fact that QCD backgrounds are potentially huge, clean signals from $W \rightarrow l\nu$ have been observed at hadron colliders [5-21]. The combination of E_T^{miss} and τ identification using isolation should be sufficient to reduce the QCD background to a level below 10% of the signal. Nevertheless, studies need to be done to demonstrate that the residual QCD background does not distort the *E/p* calibration with isolated charged pions beyond 1% which is the goal of this method.

5.4.2 Signal and backgrounds

W events were generated with PYTHIA 6.122 [5-22] (without pile-up of minimum bias events). The τ decay was performed with TAUOLA 2.6 [5-23]. The fast simulation package ATLFAST 2.20 [5-24] was used to simulate the ATLAS detector response. Table 5-8 summarises the τ decay channels that are studied and their branching ratios.

The distributions of the transverse momentum of charged pions and of E_T^{miss} are shown in Figure 5-39. The charged pions are distributed uniformly in pseudorapidity in the range covered by the Inner Detector.
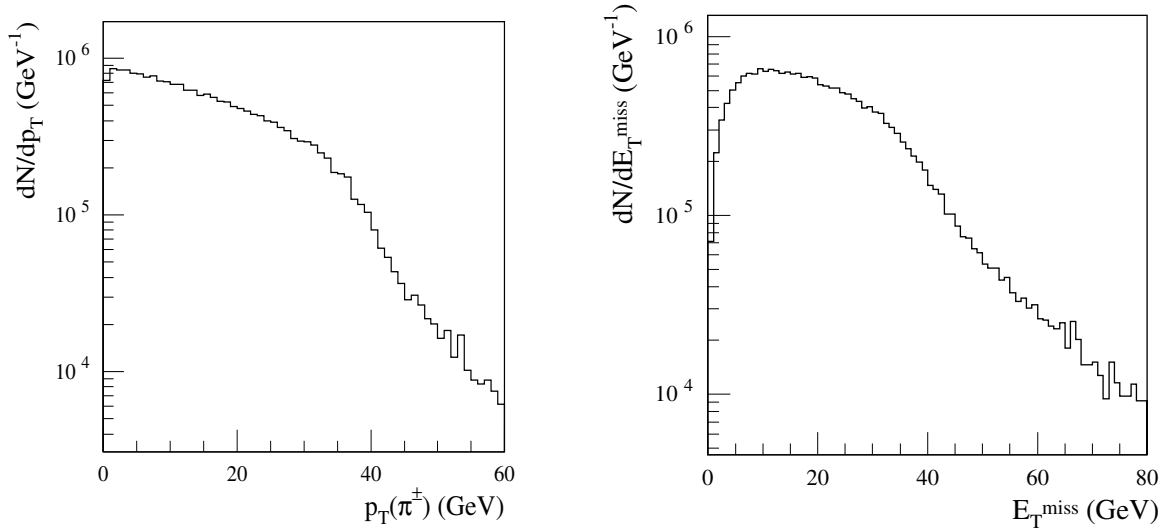
Figure 5-39 Distributions of the transverse momentum of charged pions from $\tau \rightarrow \pi\nu$ decays (left-hand plot) and missing transverse energy (right-hand plot) for the $W \rightarrow \tau\nu$ events, for an integrated luminosity of 10 fb-1.

Since QCD backgrounds are assumed to be small the most dangerous source of background are the τ decays to more than one prong or containing neutral pions which remain undetected in the tracking detectors. The relevant decay modes are those with one charged particle and with at least one neutral pion ($\tau \rightarrow h\nu + n\,\pi^0$ ($n \geq 1$) with the branching ratio of 37.0%) and those with multi-prongs ($\tau \rightarrow hhh\nu + n\,\pi^0$ ($n \geq 0$) with a branching ratio of 14.9%). The most dangerous backgrounds are those coming from τ decay to one charged hadron accompanied by neutral pions, because the additional energy deposited by the π^0 in the calorimeters biases the E/p ratio. Moreover, the exclusive decay channel that has the largest branching ratio has also a topology which is very similar to the one of the signals, namely $\tau \rightarrow \rho\nu$ with $\rho \rightarrow \pi\pi^0$ and branching ratio is 24.2%.

5.4.3 Event selection and results

5.4.3.1 Trigger

The specific trigger available at low luminosity for the signal channel is the τ-jet trigger combined with the missing E_T trigger. At LVL1, the trigger is T20+XE30; the jet has $p_T > 20$ GeV and there is at least 30 GeV of E_T^{miss}, for details see Section 11.2.5.2. The LVL2 trigger is discussed in Section 11.4.4. At level 2 the τ identification cuts are tightened; the rate for the τ20+xE30 LVL2 trigger is estimated to be 400 Hz at low luminosity (Section 11.7.3.3). A simulation of the LVL1 trigger was performed in order to estimate the efficiency for each of the τ decay modes. It gives a total rate from $W \rightarrow \tau\nu$ of 0.16 Hz. Table 5-8 summarises the trigger efficiency for τ decay modes studied in $W \rightarrow \tau\nu$ production. The number of expected signal events, for 10 fb^{-1} is 1.59×10^6 while the number of background events from τ decays with neutral pions is 9.43×10^6.

Table 5-8 Branching ratios, trigger, preselection and selection efficiencies for $W \rightarrow \tau\nu$ events. The number of expected events that pass the selection criteria are given for integrated luminosity of 10 fb^{-1}.

τ decay mode	τ branching ratio	Trigger efficiency (%)	Preselection efficiency (%)	Selection efficiency (%)	Number of events
single pion	11.1	7.4	2.3	1.80	3.9×10^5
$\rho \rightarrow 2\pi$ mode	24.2	11.4	2.2	0.27	1.2×10^5
$a_1 \rightarrow 3\pi$ mode	13.00	15.4	0.9	0.04	9.3×10^4
K^* mode	1.3	10.2	1.8	0.36	8.5×10^3
$3\pi^{\pm}\pi^0$ mode	1.5	17.3	0.1	0.02	1.5×10^2

5.4.3.2 Event Selection

The signal consists of a single isolated charged energetic hadron which is detected in the Inner Detector as a single isolated track and in the calorimeter as a narrow jet. A cone of $\Delta R = 0.15$, centered on the jet direction was constructed and events with one and only one charged track

inside the cone were accepted. Table 5-8 summarises the preselection efficiencies of τ decay modes in the $W \rightarrow \tau\nu$ events. Since the topology of the signal and the $\tau \rightarrow \rho\nu$ background are similar, their preselection efficiencies are similar.

Two additional isolation cuts were used, as these will help to reject QCD background events. The first one characterises the isolation of the track in the tracking detectors and the second one characterises the isolation of the calorimeter cluster in the calorimeters. An additional track is searched for inside a $\Delta R = 0.3$ cone centred on the track direction. Events were rejected if this extra track had transverse momentum larger than 2 GeV. Additional energy measured in the same cone in the calorimeter was required to be less than 3 GeV.

Table 5-8 shows the selection efficiency and the numbers of events expected for the relevant τ decay modes and for 10 fb^{-1} of integrated luminosity: 389 000 signal events and 138 000 background events from τ decays with neutral pions remain.

5.4.3.3 Results

The *E/p* ratio was studied for these events and is shown in Figure 5-40. The ratio is peaked at one for the signal process whereas the background ratio is shifted towards larger values, because of the energy deposited by neutral pions. At this level the residual bias of the global *E/p* distribution is 4%; the mean of the *E/p* is 1.039 for the full sample as can be seen from the figure. This must be reduced further if the calibration goal is to be met.

The fine granularity of the EM Calorimeter can be used to increase the rejection. A study of the distance in ΔR between the charged track and the photons (without any smearing and with E_T larger than 1 GeV) shows that 20% of the photons from π^0 decay are inside a cone, centred on the matching track, of $\Delta R = 0.025$ which is the size of a cell in the EM Calorimeter over the pseudorapidity range $|\eta| < 2.5$. By rejecting events where energy is observed *outside* this cone an additional rejection factor of order five might be obtained, re-

Figure 5-40 The distributions of *E/p* ratio for the signals (the dotted line, the mean value is 1.005, the rms is 0.140), the backgrounds (the dashed line, the mean value is 1.133, the rms is 0.239) and their sum (the solid line, the mean value is 1.039, the rms is 0.181) for integrated luminosity of 10 fb^{-1}.

ducing the residual bias in the *E/p* distribution below 1%. A study using full simulation is needed to assess this possibility as the shower spreading must be included.

5.5 Conclusions

An extensive programme of beam tests of prototypes and module zero's of the hadronic calorimeters was carried out from 1994 to 1998. Beams of charged pions, electrons and muons were used to evaluate the performance of the calorimeters. These tests have been vital for optimising and finalising the design, structure, and read-out of the hadronic calorimeters.

These tests were accompanied by detailed studies, based on Monte Carlo simulation of the response of calorimeter modules to particles. These studies have considerably improved the understanding of the calorimeters. Comparison between experimental data, obtained in beam tests, and Monte Carlo predictions was used to verify the different hadronic shower models, used in simulations.

At the same time, the response of the whole ATLAS calorimeter system to single pions and muons was investigated using full simulation. In contrast to hadronic jets, analysis of the single particle data gives a clearer picture of the calorimeter response and of the energy loss in the dead material and in the crack regions between different calorimeters. Monte Carlo studies of single-particle response can connect the energy region up to 400 GeV (verified by comparison with test beam data) and the TeV region, which will be explored at the LHC.

First results, obtained with fast simulation, have shown that it might be possible to use the precise measurements of the energy and momentum of single isolated charged hadrons to transfer the test beam calibrations to the actual detector and to constrain the absolute energy calibration of the hadronic calorimeters.

5.6 References

5-1   ATLAS Collaboration, Calorimeter Performance Technical Design Report, ATLAS TDR 1, CERN/LHCC 96-40 (1996).

5-2   ATLAS Collaboration, Liquid Argon Calorimeter Technical Design Report, ATLAS TDR 2, CERN/LHCC 96-41 (1996).

5-3   ATLAS Collaboration, Tile Calorimeter Technical Design Report, ATLAS TDR 3, CERN/LHCC 96-42 (1996).

5-4   E. Berger *et al.*, Nucl. Inst. Meth. **A387** (1996) 333.

5-5   M. Cobal e*t al.*, 'Analysis results of the April 1996 combined test of the LArgon and TILECAL barrel calorimeter prototypes', ATLAS Internal Note ATL-TILECAL-98-168 (1998).

5-6   T.A. Gabriel and C. Zeitnitz, Nucl. Inst. Meth. **A349** (1994) 106.

5-7   R. Wigmans, Nucl.Instr. Meth. **A259** (1987) 389.

5-8   M.P. Casado and M. Cavalli-Sforza, 'H1-inspired analysis of the 1994 combined test of the Liquid Argon and Tilecal calorimeter prototypes', ATLAS Internal Note ATL-TILECAL-96-075 (1996).

5-9   I. Efthymiopoulos, 'Comparison between the ATLAS/TileCal hadron barrel calorimeter prototype test beam data and Hadronic Simulation packages', ATLAS Internal Note ATL-TILECAL-96-092 (1996); Frascati Physics Series Vol. VI (pp.497-507), VI Int.Conf. on Calorimetry in HEP, Frascati, June 8-14,1996.

5-10   M. Cobal and S. Nemecek, 'Electron Resolution with Tilecal Module 0', ATLAS Internal Note ATL-COM-TILECAL-99-010 (1999).

5-11   T. Davidek and R. Leitner, 'Parametrisation of the Muon Response in the Tile Calorimeter', ATLAS Internal Note ATL-TILECAL-97-114 (1997).

5-12   M. Lefebvre and D. O'Neil, 'End-cap Hadronic Calorimeter Offline Testbeam Software: The hec_adc Package Version 3.6', ATLAS Internal Note ATL-LARG-99-002 (1999).

5-13   W.E. Cleland and E.G. Stern, Nucl. Inst. Meth. **A338** (1994) 467.

5-14   M. Dobbs, M. Lefebvre, D. O'Neil, 'Hadronic End-cap Modules Zero Pion and Electron Energy Scan Analysis from April 98 Testbeam Data', ATLAS Internal Note ATL-LARG-99-001 (1999).

5-15   A.A. Minaenko, 'Analysis of Test-Beam Data, Obtained with Module Zero of Hadron End-Cap Calorimeter', ATLAS Internal Note ATL-COM-LARG-99-009 (1999).

5-16   M.S. Levitsky, 'Analysis of Muon Test-beam Data, Obtained with the HEC Module Zero in April and August 1998', ATLAS Internal Note ATL-COM-LARG-99-010 (1999).

5-17   R. Brun *et al.*, 'GEANT3', CERN DD/EE/84-1 (1986).

5-18   M. Bosman, Y. Kulchitsky, M. Nessi, 'Charged pion energy reconstruction in the ATLAS Barrel Calorimeter', ATLAS Internal Note ATL-COM-TILECAL-99-011 (1999).

5-19   H. Plothow-Besch, 'First Study on the Absolute Energy Calibration of the ATLAS Hadron Calorimeters using Isolated Single Hadrons', ATLAS Internal Note ATL-PHYS-95-067 (1995).

5-20   C. Biscarat, 'Calibration of the hadronic calorimeter using E/p from single hadrons', ATLAS Internal Note ATL-COM-CAL-99-003 (1999).

5-21   F. Abe *et al.*, Phys. Rev. Lett. **68** (1992) 3398;
J. Alitti *et al.*, Z. Phys. **C52** (1991) 209.

5-22   T. Sjostrand, Computer Phys. Comm. **82** (1994) 74.

5-23   S. Jadach, Z. Was, J.H. Kuehn, Computer Phys. Comm. **64** (1991) 275; 'TAUOLA - A library of Monte Carlo programs to simulate decays of polarized τ leptons', CERN-TH-5856-90 (1990).

5-24   E. Richter-Was, D. Froidevaux, L. Poggioli, 'ATLFAST 2.0 a fast simulation package for ATLAS', ATLAS Internal Note ATL-PHYS-98-131 (1998).

6 Muon System

In this chapter the Muon System is described. The first section is devoted to the changes in the muon spectrometer chamber layout since the muon TDR [6-1]. The geometrical acceptance and the single muon performance are discussed in the two subsequent sections.

6.1 Muon spectrometer layout

The layout of the muon spectrometer has been described in detail in the muon TDR [6-1], based on layout version L. The Muon System simulation described here uses layout version M2, the design as of February 1998. The only significant difference between these layouts concerns the chambers in the middle and outer end-cap stations. All other modifications are small adjustments which either slightly improve the acceptance and performance or result in minor losses due to unavoidable constraints from other parts of the detector. These changes are described below in detail.

The layout described here is likely to be close to the final layout except for regions where services (mainly of the Inner Detector and of the calorimeter) will be routed through the Muon System. This affects mostly the regions around $\eta = 0$ and some of the inner end-cap chambers.

6.1.1 The rearrangement of the end-cap chambers

Following the revision of the overall ATLAS access strategy (see Chapter 14 in Ref. [6-2]), the layout of the middle and outer stations of the end-cap chambers has been modified. The new access scheme allows for a simpler arrangement of the EM and EO chambers since no separation between inner and outer chamber rings is required and all chambers (MDTs and TGCs) within a station can be located in the same plane. With the new layout of the forward region there is no need for holes in the muon chambers for the passage of the detector rails, a major simplification for the construction of the muon chambers and a net gain in acceptance.

A longitudinal view of the new chamber arrangement is shown in Figure 6-1. All end-cap chambers are now separated by 20 mm (instead of 15 mm) radially from their neighbours. This follows the same scheme as applied in the barrel. The influence on acceptance should be minor since there is still full coverage in the transition between two chambers.

In changing the layout of the end-cap chambers, the chamber naming scheme was changed with respect to muon TDR Chapter 3. All chambers are now called E(nd-cap) chambers and the numbering of the chambers inside each plane is unique, running from 1 to n with increasing radius. Thus the names are EMS and EML for the MDT chambers and TM1, TM2, TM3 for the TGCs in the three trigger planes.

6.1.1.1 EM chambers

The layout of the MDTs in the middle station is shown in Figures 6-2 and 6-3. All chambers within a plane are mounted on a common support structure the form of a wheel suspended from two rails connected at a height of about 19 m to the cavern walls [6-3]. On each side of the

detector there are four such support wheels, one for the MDTs and three for the three TGC planes. As before, the MDTs are arranged in small and large chambers; now, however, there is no radial gap between EMx.2 and EMx.3.

The TGC layout is shown in Figures 6-4 and 6-5. It has been considerably simplified by the placing of all chambers of a trigger plane on the same structure. The acceptance of the TGC system remains unchanged, with the exception of a small improvement due to avoidance of an overlap between the movable and fixed chambers of the TDR layout. The layout of the TGCs on the three wheels is shown for the example of the TGC1 plane in Figure 6-4. The layouts of the TGC2 and TGC3 planes follow the same general scheme with the whole structure at higher radius. The outer dimensions of the three TGC planes are indicated in Figure 6-1.

6.1.1.2 EO chambers

Like the EM chambers, the EO chambers have also been arranged in a single plane. The inner ring of chambers (as in the TDR layout) has been moved about 1.1 m closer to the interaction point (IP) and the outer ring moved about 0.5 m away from the IP. The new positions in z are 21 332 mm for the EOL and 21 746 mm for the EOS chambers. In addition, all chambers have the same spacer thickness of 170 mm. The internal layout of the chambers is shown in Figure 6-3. The chambers are mounted on the end-wall scaffolding structure.

6.1.2 The crack region

In the region around $\eta = 0$ a gap of 300 mm in the BIL, BML, BMS, and BOL chambers had been foreseen for the passage of the services of the Inner Detector, the solenoid, and the calorimeters. The exact space requirements for these services are not yet defined and have not been taken into account yet. It is clear that, at least in some sectors, the foreseen space is not sufficient and needs to be increased. Estimates of the required space are difficult to make at this time. It is likely that different openings will be required for each sector. It is hoped that on average the opening will not increase by more than a factor two.

6.1.3 Other changes and changes after version M2

The other main change of the layout is the reduction of the longitudinal gaps between the BMS chambers as the result of decreasing the longitudinal extent of the barrel toroid ribs from 300 mm to 240 mm. This leads to some improved coverage in the barrel, in particular for the trigger.

Changes to the layout since version M2 are small (excluding the necessary future changes with respect to the passage of services). They concern some internal rearrangement of chambers which should have no impact on the acceptance calculations, and some small adjustments in chamber positions in order to avoid interference with other detector parts.
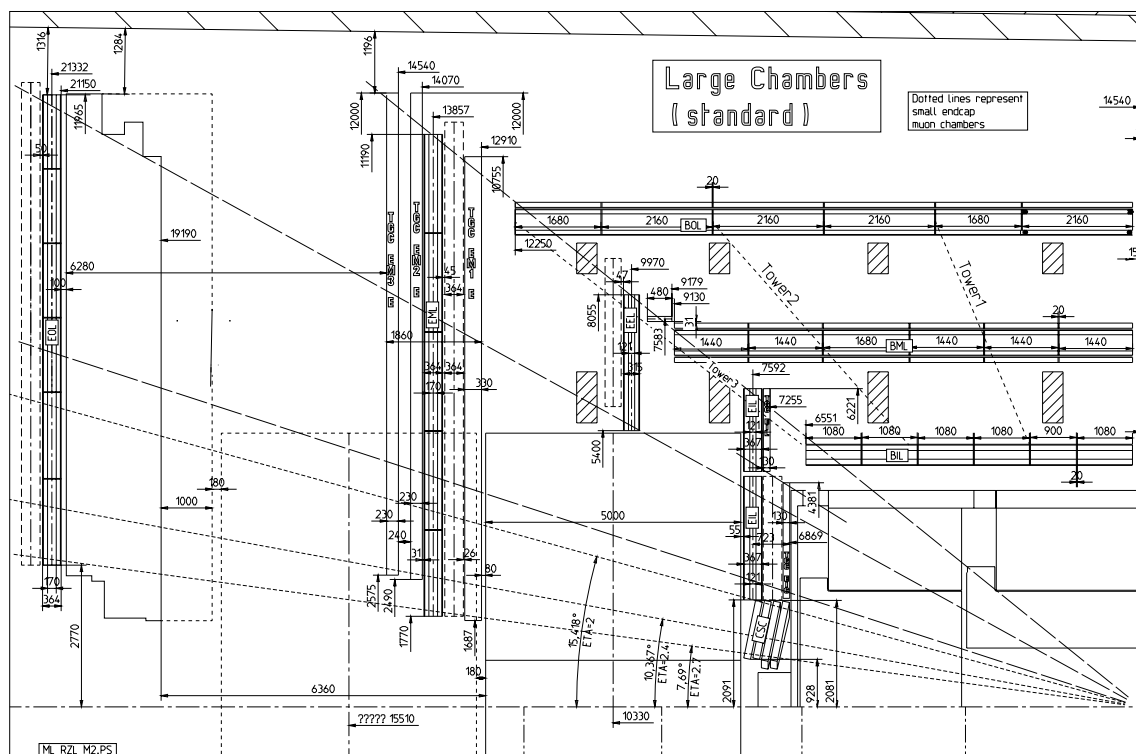
Figure 6-1 Longitudinal view of the muon spectrometer; cut in the *y-z* plane showing the large chambers (solid lines) and the small chambers (dashed lines).
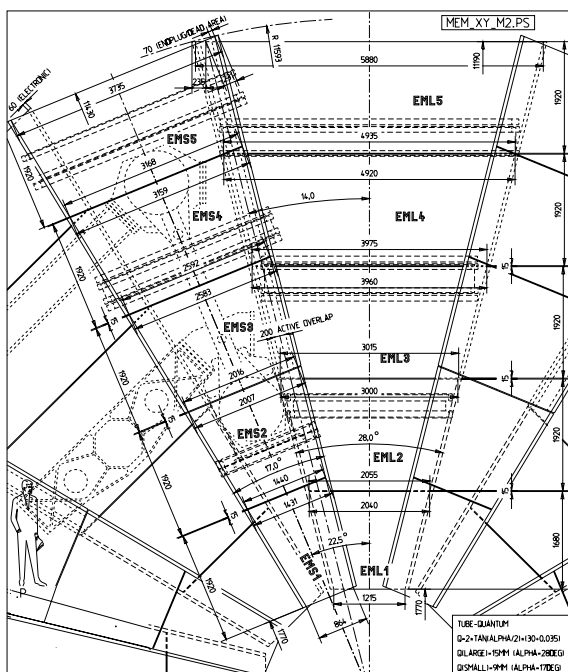
Figure 6-2 Layout of MDTs in the EM plane; shown is the segmentation of the EMS and EML chambers in two neighbouring sectors.
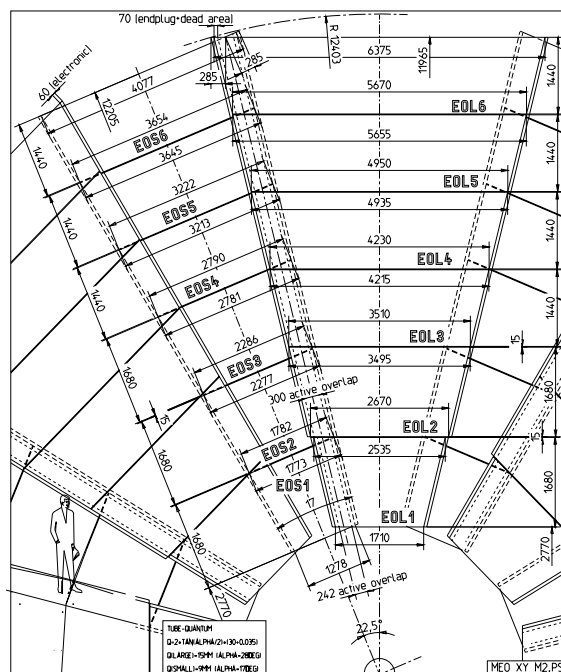
Figure 6-3 Layout of MDTs in the EO plane; shown is the segmentation of the EOS and EOL chambers in two neighbouring sectors.
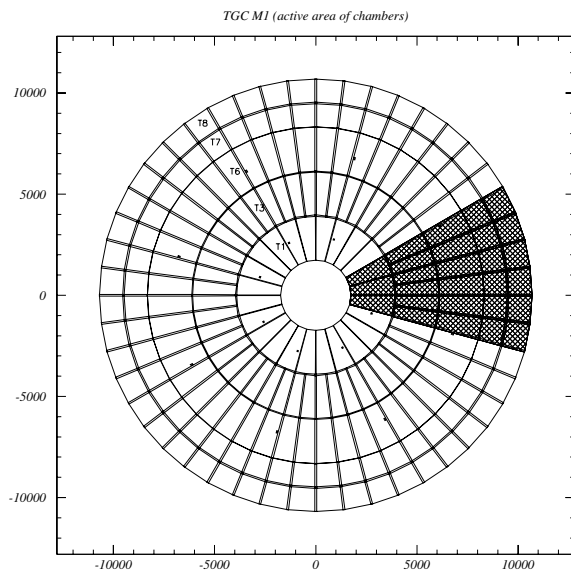
Figure 6-4 Layout of TGCs in the TM1 plane.
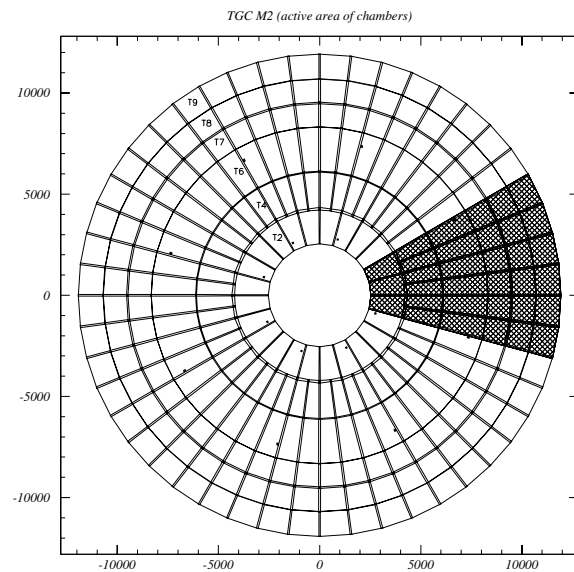
Figure 6-5 Layout of TGCs in the TM2 and TM3 plane; shown is here the TGC2 wheel; the TGC3 chamber layout is almost identical.

6.2 Geometrical acceptance

6.2.1 Monte Carlo simulation

In the Monte Carlo simulation used for acceptance studies, particular care has been taken in describing the different technologies of the Muon System: MDTs, CSCs, RPCs and TGCs are all simulated in detail from the geometrical point of view but are all treated as generic detectors decomposing the physical volume of each chamber into sensitive and non sensitive regions. Different layers of sensitive regions are interleaved with layers of passive material following in detail the layout of the Muon System. In the simulation of the various subdetectors one layer of tubes, or of strips or wires is defined as a sensitive plane.

Unless otherwise stated, all results presented in this section refer to infinite-momentum muons generated at the nominal *pp* interaction point with no interaction with matter. Detector hits are recorded for each individual sensitive element traversed by the particle. Additional studies, which are not reported here, were carried out to study the acceptance of the apparatus for low momentum particles, while Higgs studies (from the acceptance point of view) are reported in a subsequent subsection.

This simulation also includes the finite length of the interaction region, the electromagnetic and hadronic calorimeters, the magnet structures, and the magnetic fields, in order to correctly account for magnetic bending, multiple scattering, and all energy loss processes when necessary.

6.2.2 Precision chambers

The precision chamber acceptance is computed on the basis of so-called 'superpoints'. A superpoint is a coincidence of at least six hits in six different sensitive planes in one chamber. Such a hit multiplicity requirement fully exploits the tracking resolution in most chambers, and ensures local vector measurement capability. A 'half-superpoint' is a coincidence of at least three hits in the adjacent layers that form a multi-layer; it allows for momentum measurement, albeit with slightly degraded resolution.
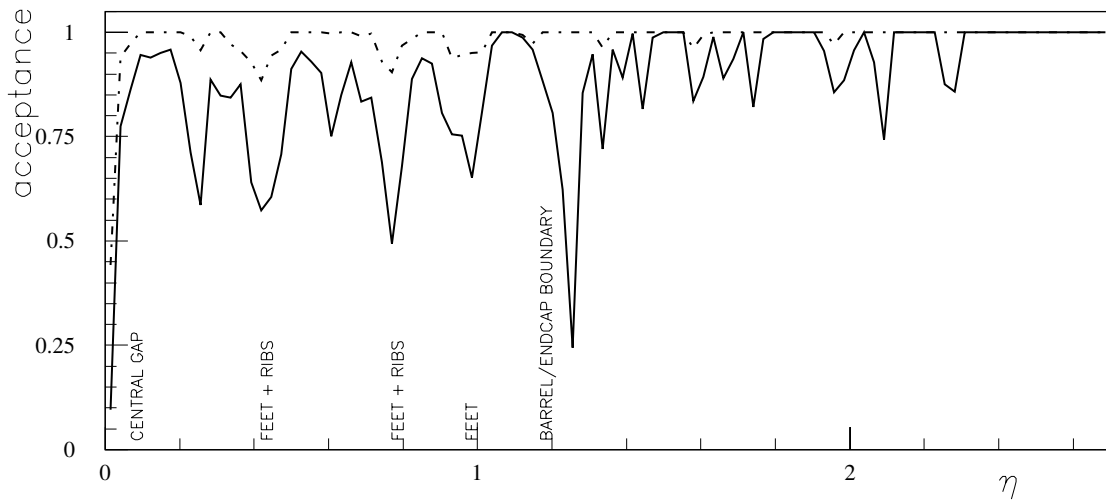
Figure 6-6 Acceptance for the requirements of one superpoint (dash-dotted line) and three superpoints (solid line) in the three stations of the precision chamber system, as a function of pseudorapidity and averaged over azimuthal angle. The acceptance for a coincidence of two superpoints is nearly indistinguishable from that for one superpoint, and is not shown in the figure.
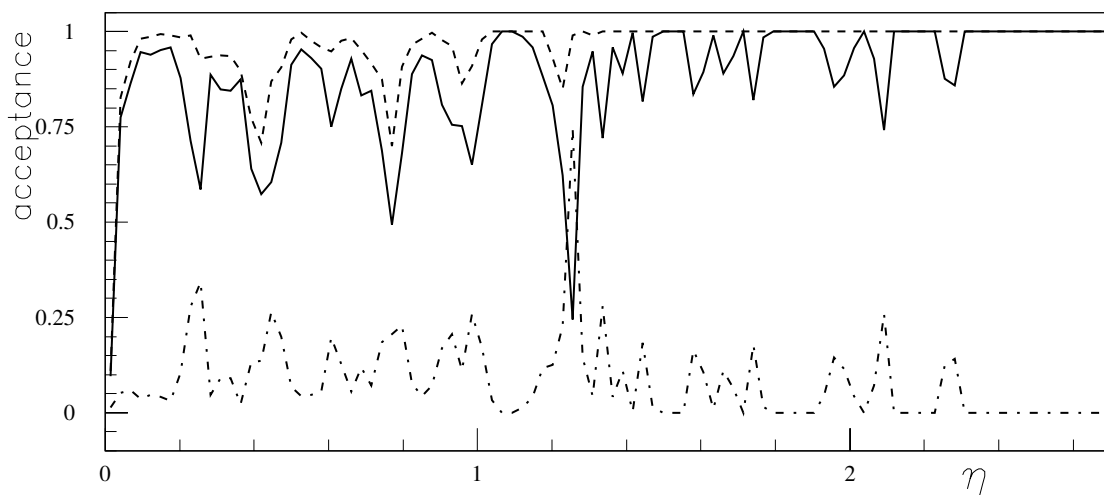
Figure 6-7 Comparison of acceptance for three superpoints (solid line) and three half-superpoints (dashed line) in the precision chamber system, as a function of pseudorapidity and averaged over azimuthal angle. The dash-dotted line shows the difference between the two categories.

Acceptance for different combinations of superpoint requirements, averaged over azimuth, are shown in Figures 6-6 and 6-7. Figure 6-6 compares the acceptance for three superpoints, providing optimal track and momentum reconstruction, to the acceptance for one superpoint, which provides limited muon identification at low occupancy levels. Acceptance losses due to the mechanical structures of the barrel magnet, in the intermediate region between barrel and end-cap or generated by cracks between adjacent rings of end-cap chambers, are visible for tight multiplicity requirements.

Figure 6-7 shows the acceptance for three superpoints in comparison to the acceptance for three half-superpoints as a function of η averaged over the azimuthal angle. The average acceptance increases from ~0.90 to ~0.96 on relaxing the multiplicity requirement from three to three-half superpoints.

Figure 6-8 shows the acceptance for three superpoints as a function of azimuth, integrated over $|\eta| < 2.7$. In this view, acceptance losses are mostly due to the magnet feet centred at 247.5° and 292.5°. The eightfold detector modularity is clearly seen from the acceptance loss near the sector boundaries. Precision chamber acceptance for the different categories, averaged over η and ϕ, are shown in Table 6-1.
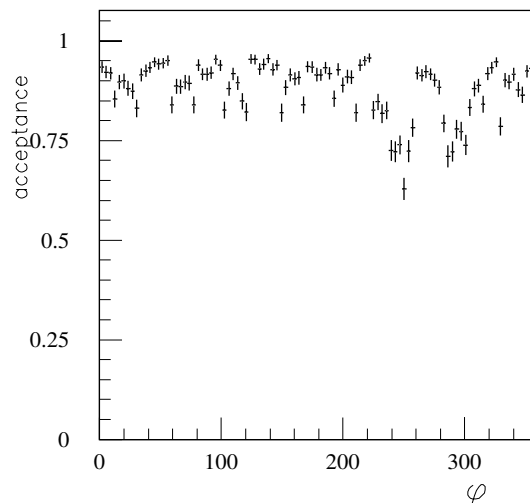
Figure 6-8 Precision chamber acceptance as a function of azimuthal angle, requiring three superpoints, averaged over pseudorapidity.

Table 6-1 Geometrical acceptance of the precision chamber system (averaged over $|\eta| < 2.7$), for different coincidence requirements discussed in the text. The precision chamber acceptance is averaged over $0° < \phi < 360°$.

Precision chamber acceptance category	Average acceptance
1 superpoint	0.997
2 half-superpoints	0.994
2 superpoints	0.989
3 half-superpoints	0.961
3 superpoints	0.896

6.2.3 Trigger chambers

The trigger system in ATLAS is composed of the RPCs ($|\eta| < 1.05$) and the TGCs ($1.05 < |\eta| < 2.4$). The trigger chamber acceptance has been evaluated and discussed in the LVL1 Trigger TDR [6-4] and in the Trigger Performance Report [6-5].

In the RPC system, a low p_T coincidence is defined by those tracks that have hits in at least three of the four inner trigger planes. A high p_T coincidence is the logical 'AND' of a low p_T coincidence and at least one hit in the two planes of the outer stations. A similar algorithm is used in the case of the TGCs [6-4]. Here a low p_T coincidence is a combination of three out of four hits in the outer trigger station (two doublet chambers); a high p_T coincidence is the 'AND' of a low p_T coincidence and at least two hits in the three planes in the inner trigger station (triplet chambers).

The geometrical acceptance is shown in Table 6-2 for the barrel and end-cap independently and for the combined system. Acceptance loss in the range $0 < |\eta| < 2.4$ averaged over full azimuth is ~0.06 and ~0.065 for the low p_T and high p_T coincidences, respectively. No windowing effect in the LVL1 muon trigger and no contributions from the alignment corridors are considered in this study.

Table 6-2 Average acceptance for the trigger chambers system.

Trigger chambers	Barrel	End-cap	Combined system
low p_T coincidence	0.91	0.98	0.94
high p_T coincidence	0.88	0.97	0.93

6.2.4 Acceptance study of $H \rightarrow ZZ^* \rightarrow \mu\mu\mu\mu$

The Higgs boson decay to four muons is a benchmark process for muon detectors at the LHC. In order to evaluate in detail the effects of the muon trigger system acceptance on the Higgs detection capabilities, a sample of Standard Model Higgs decays to four muons through the process $H \rightarrow ZZ^* \rightarrow \mu\mu\mu\mu$ was investigated.

Samples of Higgs events in the mass range 120–180 GeV have been studied in order to evaluate the geometrical acceptance of the precision chamber system and of the trigger system for multi-muon event detection. The acceptance of the trigger system, normalised to the precision chamber acceptance, for two muons is very close to 1, for three muons is about 0.96 and for four muons is about 0.69, independent of the Higgs mass. Details of this analysis can be found in [6-4].

6.3 Single muon performance

6.3.1 Pattern recognition and reconstruction

Compared to most spectrometers in high energy physics experiments to date, the ATLAS muon spectrometer is unique in several aspects. It was designed to maintain high performance, in terms of detection efficiency, momentum resolution and fake track rejection, in the difficult LHC

environment within a 'reasonable' cost. One of the drawbacks of this performance against cost compromise is that many features of this spectrometer make the pattern recognition and track reconstruction more challenging.

- The 'open' air-core toroid concept leads to a magnetic field which, in addition to being relatively modest in magnitude (0.5 T in average), is very inhomogeneous, so that particle trajectories can be very peculiar (especially at low p_T) and cannot be approximated by simple analytical descriptions.

- The unusually large size of the system (22 m in diameter, 44 m in length) implies large distances between measuring stations which induce significant extrapolation uncertainties.

- Due to the cost constraint limiting the number of detector channels, redundancy is small and the precision chambers measure only one coordinate (approximately the bending direction). Thus, no precise three dimensional information is available and the accuracy in the so-called 'second coordinate' is two orders of magnitude worse (1 cm with respect to 80 μm) than in the principal coordinate accuracy.

- Furthermore, the high background level in the experimental hall enhances most of the problems mentioned above.

These features of the muon spectrometer not only put severe constraints on the software that will exploit its data, but also on its hardware.

- In addition to the sophisticated optical system that will ensure, by means of software corrections, a precision of 30 μm on the alignment of the precision chambers, it is also necessary to be able to mechanically position all these chambers such that, in each octant, their wires are parallel within one (or at most a few) milliradian(s). In absence of such precise alignment the inaccuracy of the second coordinate degrades the first coordinate accuracy.

- The magnetic field reconstruction algorithms have been tested with Monte-Carlo simulation and, recently, on a small test superconducting 'race-track' coil [6-6]. They can provide the intended accuracy (roughly 3 Tm) if and only if unforeseen magnetic masses are completely avoided inside the toroidal magnets and anywhere in its vicinity.

The basic principles and main steps of the pattern recognition software have been described in muon TDR [6-1]. Since that time, a large number of technical improvements have been introduced to this software essentially to improve the reconstruction efficiency at low p_T while keeping the CPU usage at an acceptable level.

To improve the low p_T efficiency without introducing too many fake tracks, it is crucial to take into account as precisely as possible the effects of multiple scattering of muons in the material of the spectrometer. Indeed, in spite of the air-core toroids, the amount of material traversed by a muon in the spectrometer can be relatively large and very unevenly distributed along its trajectory. That is why a very detailed description of the passive material of the Muon System (as well as of the whole experiment) has been introduced, together with the geometry of the active detectors, into the pattern recognition and reconstruction software. This information is retrieved from a muon database [6-7] where the geometry and composition of the ATLAS detector materials are described. As an example of the level of detail of the material considered in the reconstruction software, the Figure 6-i displays a muon track traversing the spectrometer.

6.3.2 Tracking back to the beam and energy loss in the calorimeters

An additional improvement in the reconstruction, made possible by the accurate material description, deals with energy losses in the calorimeters as well as in the Muon System itself. Although energy losses and their distribution along the muon track have a very small impact on muon reconstruction inside the Muon System, they play an important role in tracking back the reconstructed muon to the beam line. During this 'backtracking', the muon momentum can be corrected for using the energy measured in the calorimeter cells it has traversed. This procedure, however, is potentially dangerous and it is justified only for isolated high p_T muons (which have a higher probability of 'catastrophic' energy loss). In most cases, it is safer to correct the muon momentum only for the mean energy loss, estimated from the reconstructed momentum as well as from the amount and the nature of the material traversed by the reconstructed trajectory. This estimated mean energy loss correction is shown in Figure 6-9 as a function of η, for two extreme values of p_T (5 and 500 GeV), and compared to the average 'true' energy loss as simulated event-by-event with GEANT.
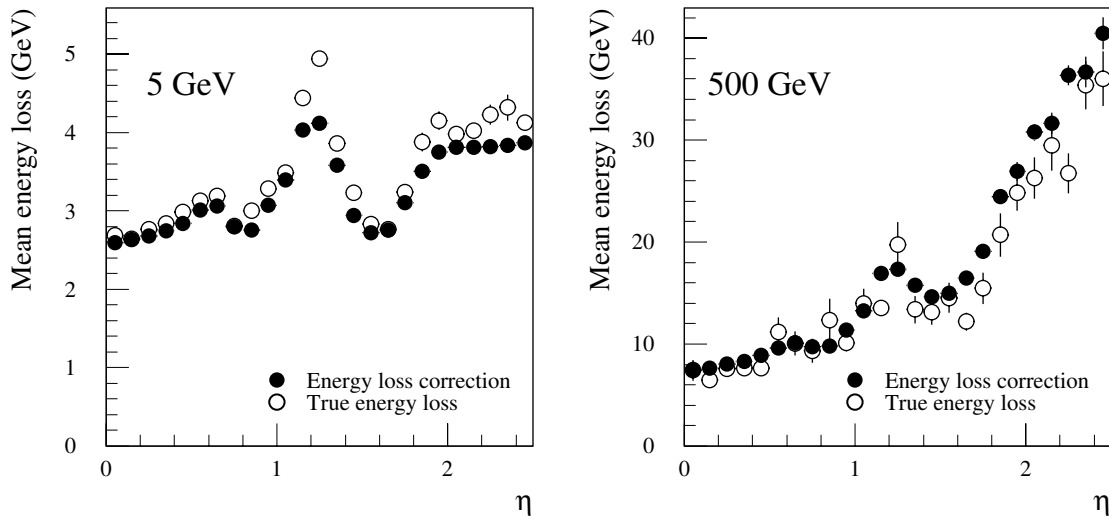
Figure 6-9 Mean energy loss versus η for muons of p_T = 5 GeV (left) and 500 GeV (right). The open circles represent the actual 'true' mean energy loss, as obtained from a GEANT simulation, whereas the filled circles represent the estimated mean energy loss as obtained from the detailed representation of the calorimeters material in the reconstruction program.

Figure 6-9 shows that the reconstruction program is able to predict with good accuracy the energy loss over a wide range of muon momenta. The remaining small discrepancies between the GEANT simulation and the estimated energy loss will be further studied. Since the agreement is satisfactory, however, the backtracking procedure has been included in the muon reconstruction software in addition to methods to compute and to transport the full covariance matrix associated with each reconstructed track. Reconstructed track parameters with their full covariance matrices are provided at three locations:

1. At the entrance to the muon spectrometer, *i.e.* on the cylinder |z|=682 cm, R=425 cm.

2. At the entrance to the calorimeters, *i.e.* on the cylinder |z|=320 cm, R=105 cm.

3. At the perigee of the track.

To illustrate the consistency of these covariance matrices, distributions of the pull of the inverse of the transverse momentum at the perigee of the reconstructed tracks are plotted in Figure 6-10 for four different fixed p_T single muon samples. The pull is defined here as the difference be-
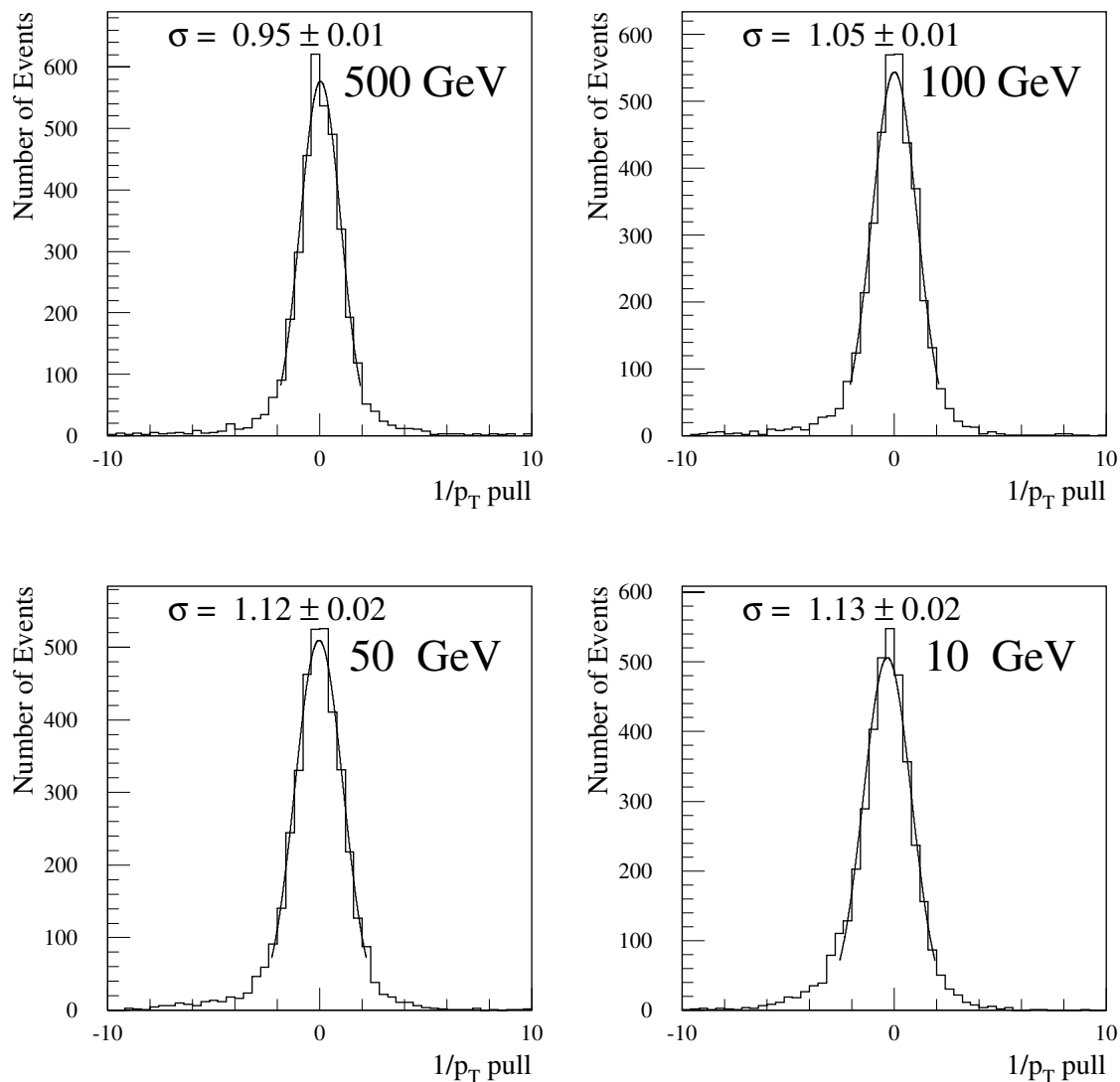
Figure 6-10 Distribution of the pull of the inverse transverse momentum of the muon spectrometer reconstructed tracks propagated down to the vertex.

tween the reconstructed and the true values normalised to the error on the reconstructed value. In spite of a very inhomogeneous momentum resolution (see next paragraph), the fact that these distributions remain roughly compatible with Gaussians of unit width for muons of p_T from 10 GeV up to 500 GeV illustrates the consistency of these covariance matrices.

6.3.3 Momentum resolution

The semi-analytical evaluation of the muon momentum resolution (see Section 12.3.2 of [6-1]) has also benefited from the above mentioned refinements in the material description. The new version of this software performs full 3D tracking for each given set of (p_T, η, φ) and takes into account all the traversed material whereas earlier versions used only the integrated magnetic deflection along a straight line and a simplified parametrised description of the material. Compared to resolution figures obtained in the muon TDR [6-1], the structure of the various spikes in the (η,φ) plane at moderate p_T is more detailed and leads to a degradation of the average resolution. However this small worsening of the resolution is compensated by two other effects:

1. The holes that were foreseen in the EM plane of muon chamber (to allow for the rails supporting the calorimeters and Inner Detector) have disappeared (the rails are now presumed to be dismounted after installation – see Section 6.1.1). This has cured the strong degradation of the φ–averaged resolution that resulted from the absence of measurement inside these holes (around η = 1.6).

2. The value assumed, in the computation of the expected momentum resolution, for the averaged spatial resolution of an MDT multi-layer as well as the value of the averaged global misalignment of the multi-layers were somewhat pessimistic. A more realistic re-evaluation of these quantities (*i.e.* assuming 85 μm averaged resolution for each tube and 35 μm misalignment error on the sagitta) leads to a slightly better expected momentum resolution in those (p_T, η, φ) regions which are not dominated by multiple scattering effects.

6.3.3.1 Standalone muon momentum resolution

As a first check of this analytical evaluation of the muon momentum resolution, results of the full simulation at various p_T values are compared in Figure 6-11 to the results of a model in which the momenta are smeared according to the analytically computed single muon momentum resolution. In order not to blur the result of the resolution evaluation, this comparison is made for the muon momentum at the entrance to the muon spectrometer so that the fluctuations of energy loss in the calorimeters do not contribute to the resolutions. The agreement is reasonable particularly since the resolution is highly inhomogeneous in the (η,φ) plane. In this particular study, chamber misalignment was neglected both for calculated and simulated results.

Figure 6-11 Simulated (points) and calculated (line) p_T dependence of the muon momentum resolution, ignoring energy loss fluctuations and for |η| < 1.5.

These results have proved to be independent of the details of the digitisation scheme assumed in the full simulation, as long as the mean spatial resolution of a single tube is not changed. A realistic MDT response simulation including all the effects discussed in Section 6.3.4 yields the same momentum resolution as the simplified digitisation model described in the

muon TDR. It was also found that the presence of non-Gaussian tails in the tube resolution function does not have any impact. This demonstrates the robustness of the reconstruction algorithm against a few hits with large departures from the track.
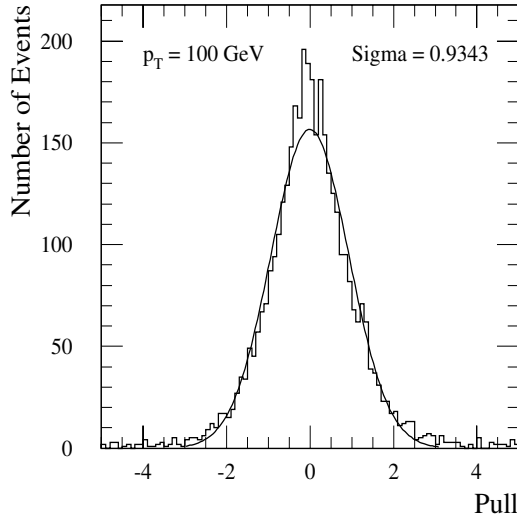
Figure 6-12 Distribution of the momentum pull for p_T = 100 GeV.
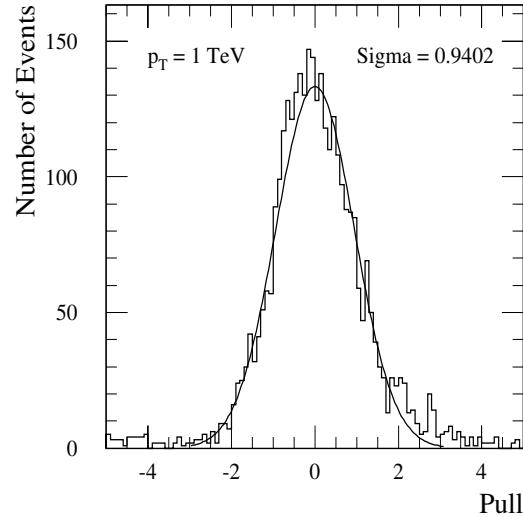
Figure 6-13 Distribution of the momentum pull for p_T = 1 TeV.

The agreement between the full simulation and the analytical calculation is best reflected by the distribution of the pulls. If the theoretical prediction σ_{th} is correct for every track, *i.e.* the measured $\Delta p/p$ follows to a Gaussian distribution with standard deviation σ_{th}, the pull will be distributed according to a normal distribution. Figures 6-12 and 6-13 show example distributions for p_T = 100 GeV and p_T = 1 TeV.

6.3.3.2 Momentum resolution as a function of η and ϕ

The ϕ averaged resolution as a function of η is shown in Figures 6-14 and 6-15 for two values of p_T. In these results, all effects such as chamber misalignment or energy loss fluctuations in the calorimeters are considered. The expected resolutions are slightly better than those quoted in the muon TDR [6-1] for the reasons explained in Section 6.3.3.

The momentum resolution as a function of both η and ϕ is shown in Figure 6-16 for p_T = 100 GeV. Compared to the similar figure in the muon TDR [6-1], the wall-like structure near $\eta = 0$ (corresponding to a region of no measurement due to the gap in the muon chambers) has essentially disappeared. This is explained by the fact that, in this new result, the actual curvature of the tracks is taken into account so that most of the tracks hit at least two stations which is sufficient for a (crude) momentum measurement. However it is already foreseen that the gap in the large chambers near $\eta = 0$ will be increased in order to provide enough space for the passage of services (see Section 6.1.2). Compared to the results presented here, a non-negligible loss of acceptance in the $\eta = 0$ region is then to be expected. The small degradation of the resolution that can be seen in Figure 6-16 in the region $1.7 < \eta < 2.2$ and $20^o < \phi < 25^o$ and that was not present in the corresponding figure of the muon TDR, is due to the material of the 'stay tube' that connects the two flanges of the cryostat of the end cap toroid magnets. The additional mate-
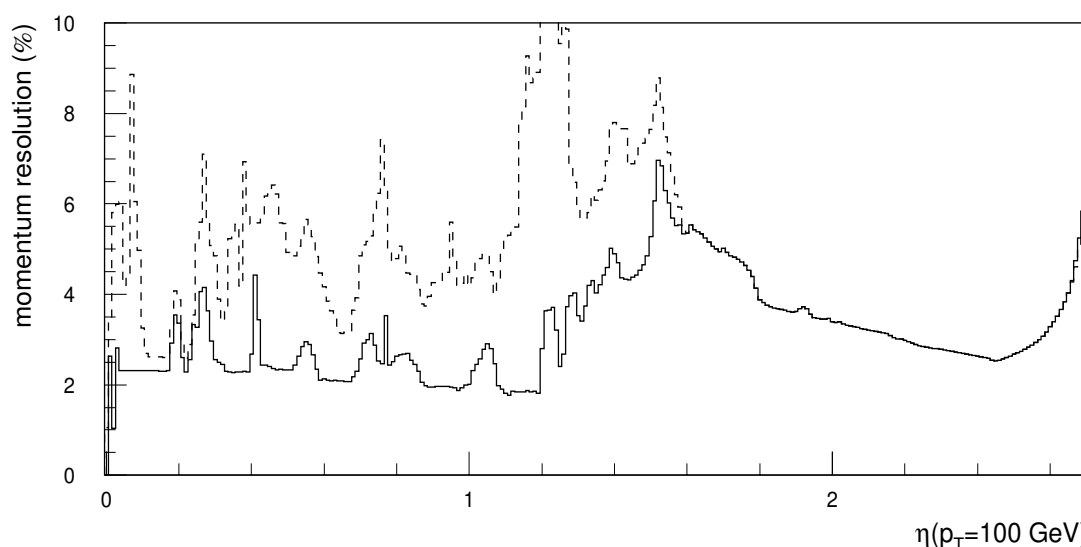
Figure 6-14 Momentum resolution for p_T = 100 GeV, averaged over ϕ in one octant, as a function of the pseudorapidity. The dashed curve corresponds to the two octants that contain the feet.
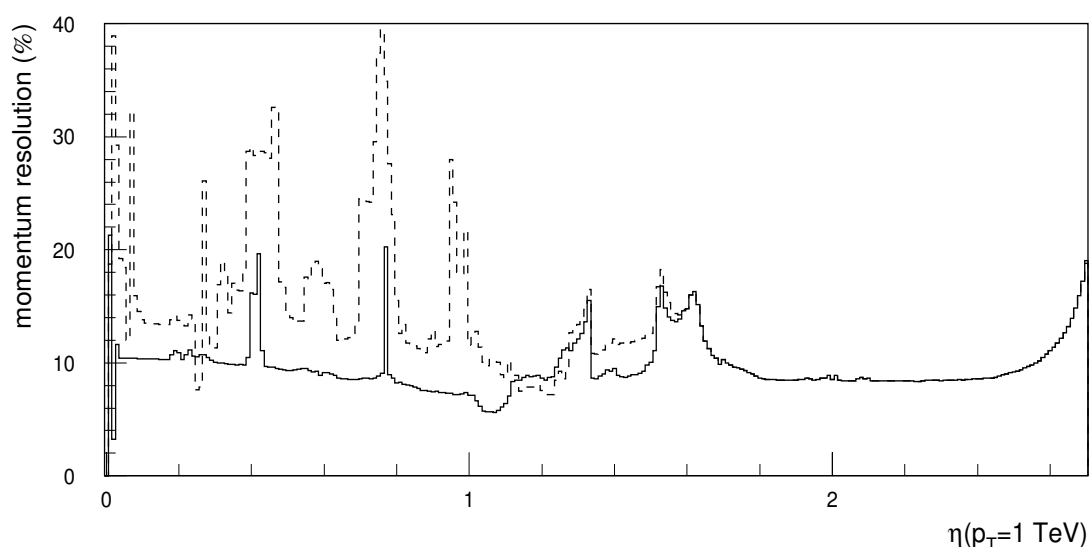
Figure 6-15 As Figure 6-14, for p_T = 1 TeV.

rial traversed by a muon due to this tube is moderate but the averaged location of this matter being just in the middle of the bending of the muon, it has a non-negligible impact on the momentum resolution.
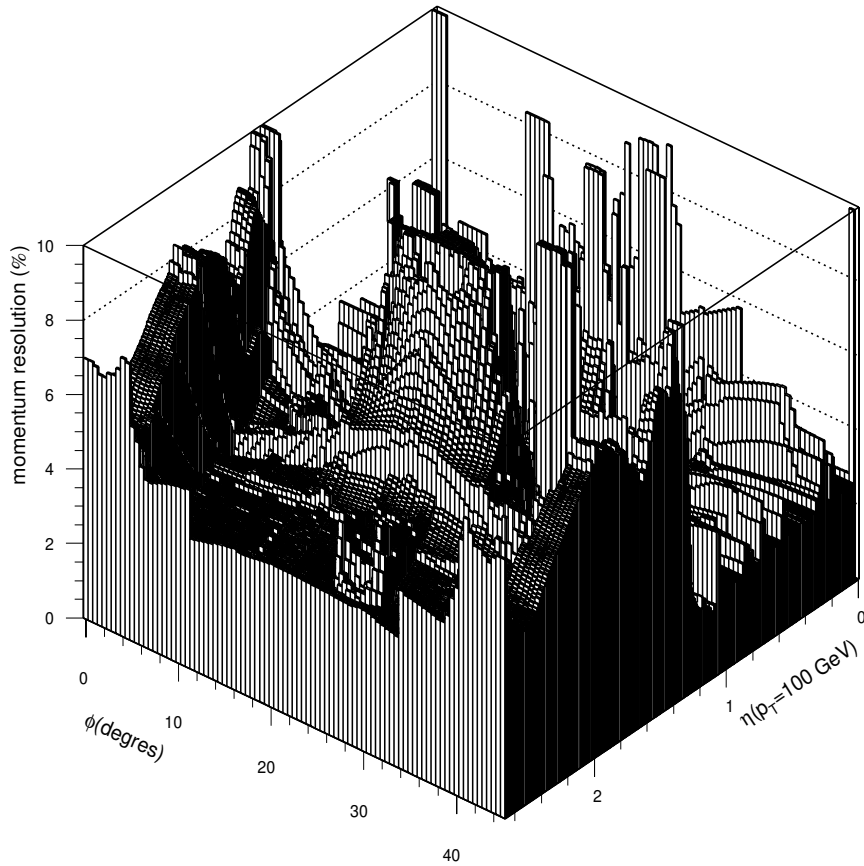
Figure 6-16 Momentum resolution for $p_T = 100$ GeV as a function of η and ϕ.

6.3.3.3 Acceptance versus momentum resolution

A concise way to visualise the performance of the muon spectrometer is to plot, for fixed values of p_T, the fraction of the phase space ($|\eta| < 2.7$) over which the momentum resolution is better than a given value as a function of this value. The momentum resolution results discussed above are presented in such a way in Figure 6-17. Compared to similar plots presented in the muon TDR [6-1], the curves are 'sharper' which means that the resolution is somewhat more homogeneous in the (η, ϕ) phase space. This improvement, which comes mainly from the disappearance of the hole in the EM stations (see above), is welcome because the homogeneity of the resolution may be more important than having a very good resolution in a limited region of the phase space; in a multi-muon event the resolution on the reconstructed mass is dominated by the
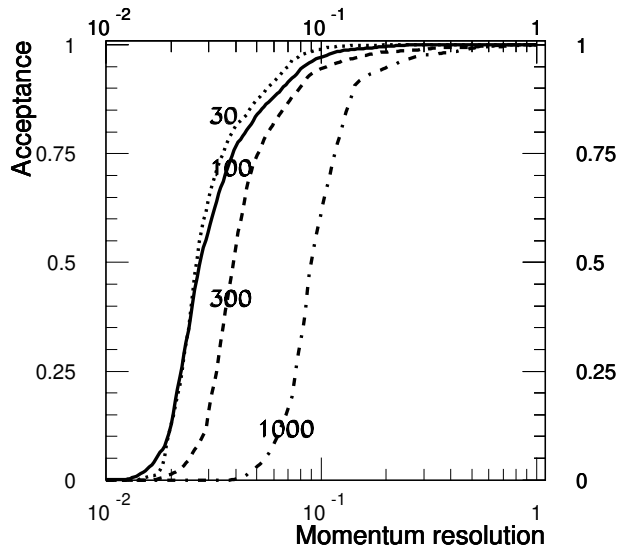
Figure 6-17 Acceptance as a function of momentum resolution for various p_T (see text).

most poorly measured muon. This figure also illustrates the fact that the momentum resolution of the muon spectrometer is better than 5% over 80% of the phase space for a wide range of p_T (roughly from 10 to 300 GeV).

6.3.4 MDT digitisation simulation and impact on reconstruction

First test beams results have allowed the refining of the MDT digitisation simulation relative to that used in the ATLAS muon TDR [6-1]. The impact of this more realistic digitisation on reconstruction efficiency and momentum resolution has been investigated.

For each hit in a drift tube the track radius is converted into a drift time using the *r-t* relationship and smeared according to the time resolution of a single drift tube. For the muon TDR [6-1] a linear *r-t* relationship with a maximum drift time of 500 ns and an *r*-dependent Gaussian resolution with an average of 80 μm (Figure 6-18) were used, which approximates the properties of the gas mixture Ar (91)/N_2 (4)/CH_4 (5). In order to achieve a more realistic description of the MDT response the following effects were added:

- Instead of a linear approximation, the correct *r-t* relationship of the gas Ar (91)/N_2 (4)/CH_4 (5) as measured in a test beam was introduced into the simulation (see Figure 6-19).

- The spatial resolution was changed to that described by the exact time distributions which significantly deviate from the Gaussian shape at drift distances smaller than 2 mm (Figure 6-20)[6-8].

- The description of the Lorentz effect was improved. For the muon TDR a constant deviation angle for the drifting electrons was assumed. In reality, however, this angle depends on the electric field which is inversely proportional to the distance from the wire. Therefore the new parametrisation of this effect which was extracted from the results of test-beam measurements (Figure 6-21) [6-9], differs considerably from the old model.
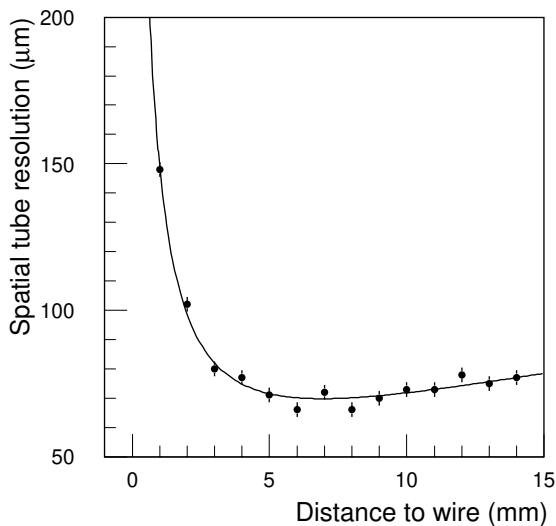
Figure 6-18 Spatial resolution of a single drift tube as a function of the track distance from the wire.
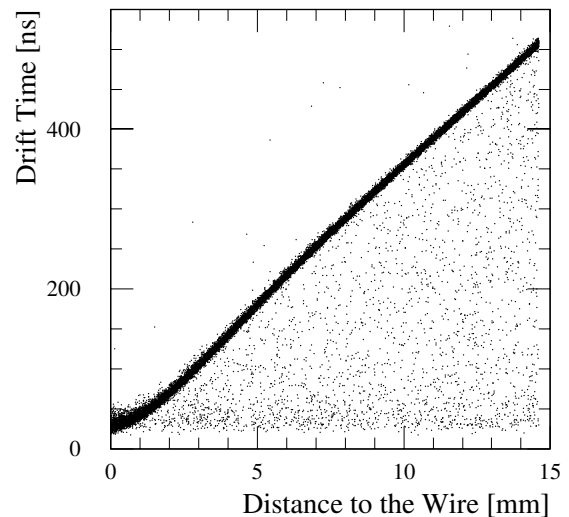
Figure 6-19 r-t relationship for the gas mixture Ar (91)/N_2 (4)/CH_4 (5). The background below the main band is due to Delta rays.
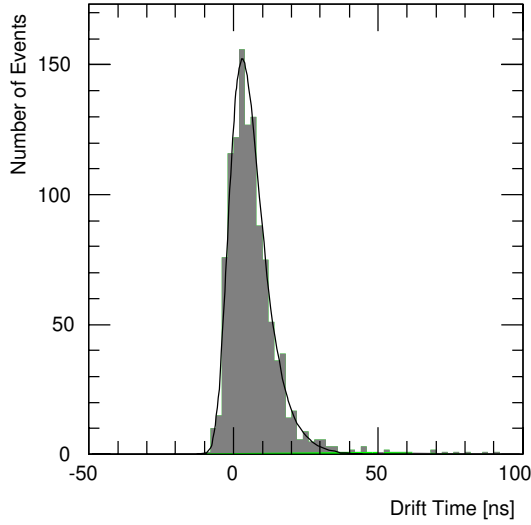
Figure 6-20 Non-Gaussian drift time distribution for 0.25 mm < r < 0.3 mm.
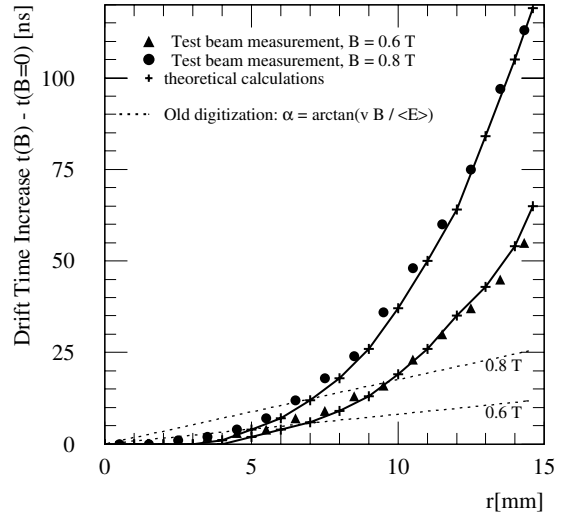
Figure 6-21 Drift time increase due to the Lorentz effect for B = 0.6 T and 0.8 T. The points on the solid curve represent a numerical solution of the equations of motion.

In the reconstruction, the same r-t relationship and resolution as used for the digitisation were employed. Only the non-Gaussian tails in the tube resolution function (see Figure 6-20) cannot be taken into account by a reconstruction algorithm based on χ^2 minimisation. Therefore in the reconstruction a Gaussian approximation was made.

6.3.4.1 Reconstruction efficiency and fake track probability.

Reconstructed tracks are classified according to a hit quality factor, based on Monte Carlo information, and defined as the fraction of hits belonging to the track that were actually produced by the muon.

Fake tracks are defined as those with a hit quality factor lower than 10%. The fake track rate is then the average number of fake tracks per event.

Good tracks are those for which the hit quality factor exceeds 55%, and whose reconstructed momentum p_{rec} is sufficiently close to the true muon momentum p_{true} at the entrance of the muon spectrometer. For this purpose the cut $|\delta| < 4$ was applied to the momentum pull δ defined by:
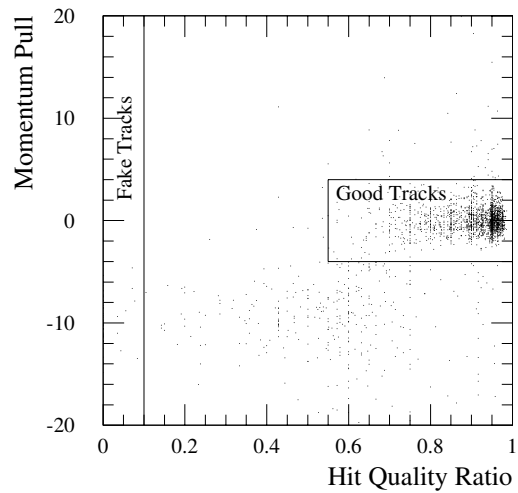
Figure 6-22 Momentum pull versus hit quality ratio (fraction of real muon hits used for the track reconstruction) for p_T =1 TeV.

$$\delta = \frac{(p_{rec} - p_{true})/p_{true}}{\sigma_{th}}$$

Here σ_{th} is the resolution which would be theoretically expected for the generated track taking into account the momentum, direction and position of the muon at the entrance to the spectrometer. Figure 6-22 shows the regions for good and fake tracks in the plane of momentum pull versus hit quality ratio. The reconstruction efficiency is then defined as the fraction of events which contain a good track.

Figure 6-23 shows the dependence of the single muon reconstruction efficiency and the fake track probability on the transverse momentum p_T. As p_T increases, more secondary particles are produced by the muon. Hits from these secondaries can hide the muon hits and thus lead to wrong drift time measurements. They also create hits in tubes which are not traversed by the muon. The consequence is an increasing probability for reconstructing a fake track. In the same way the efficiency for finding good tracks decreases.

Figure 6-23 shows that the reconstruction efficiency does not change significantly if in the digitisation the MDT response description is improved from the old model (triangular markers) to the most realistic parametrisation (circular markers). Switching off the non-Gaussian tails in the tube resolution function has no impact at all (not displayed in the fig-

Figure 6-23 Reconstruction efficiency and fake track probability as a function of p_T for single muons.

ure for reasons of visibility). The fake track probability, however, seems to depend on the MDT response (lower graphs in Figure 6-23). The more realistic and the more complex the description becomes, the less is the chance to build up a fake track from background hits. The details of this mechanism are not understood.

6.4 Reconstruction of quasi-stable charged heavy particles

Heavy long lived particles are predicted in some extensions of the Standard Model. If these particles are charged and are not subject to a strong interaction, they behave as high mass muons. For masses of about 100 GeV, these particles travel at a speed significantly lower than that of light. Therefore they reach the Muon System with a time delay with respect to relativistic particles. For example, a particle with $\beta = 0.5$ reaches the Muon System with a 20 ns delay.

The aim of this study is to evaluate to what extent these particles can be reconstructed in the Muon System, and to estimate the β measurement accuracy. The combination of time and momentum measurement permits the evaluation of the particle mass [6-10]. The results of this study have been applied in Chapter 20 to the study of the supersymmetric partners of the τ lepton in models incorporating Gauge Mediated SUSY breaking (GMSB) [6-11]. In the following, $\tilde{\tau}$ indicates a heavy charged particle. A detailed description of this analysis can be found in [6-12].

6.4.1 Particle tracking and reconstruction

The study was performed for particles with a fixed mass of 101 GeV, as suggested by GMSB; the only relevant parameter is the β of the particle. Table 6-3 shows the list of the generated samples. Each sample consisted of 500 events. Particles at fixed p_T were simulated at $\eta = 0.1$ and $\phi = 2^0$. In addition, a reference sample of 500 GeV muons was generated in the same region as the signal samples.

Table 6-3 Generated samples.

Particle type	p (GeV)	Particle β	η, ϕ
$\tilde{\tau}$	50/76/135/200/500	~0.5, 0.6, 0.7, 0.8, 0.98	0.1, 2^0
muon	500	1.0	0.1, 2^0

All the simulated events were reconstructed accounting, in the pattern recognition program, for the time of flight through the detector. The χ^2 of the reconstructed track was studied as a function of β, determining the value where χ^2 is minimum. This analysis has shown that β can be estimated with an accuracy $\sigma(\beta)/\beta^2 \approx 0.03$; this is consistent with expectation from the muon detector time resolution of about 0.7 ns. The momentum resolution is found to be essentially the same as for muons of the same momentum, except at low energy where it is slightly worse [6-12].

6.4.2 Reconstructed mass

Combining the reconstructed momentum together with the reconstructed β, it is possible to estimate the particle mass. The mass resolution as a function of β and the mass distributions for the event samples are shown in Figures 6-24 and 6-25.

In conclusion, this analysis has shown that ATLAS can measure the mass of heavy stable leptons with an accuracy of 5% for values of β in the range 0.5 to 0.9 for a mass of about 100 GeV. A more detailed investigation needs knowledge of production cross-sections and spectra of the produced heavy particles, and this can only be done by assuming specific theoretical scenarios for the production of these particles.
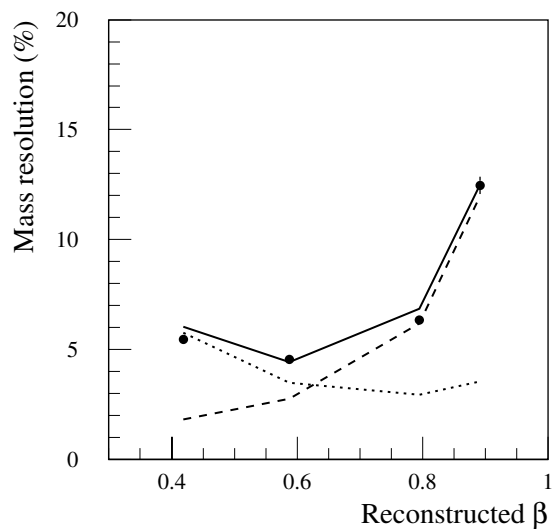
Figure 6-24 Mass resolution as a function of β for the heavy particle samples. The dashed line is the contribution from the β measurement error, the dotted line is the one from momentum.
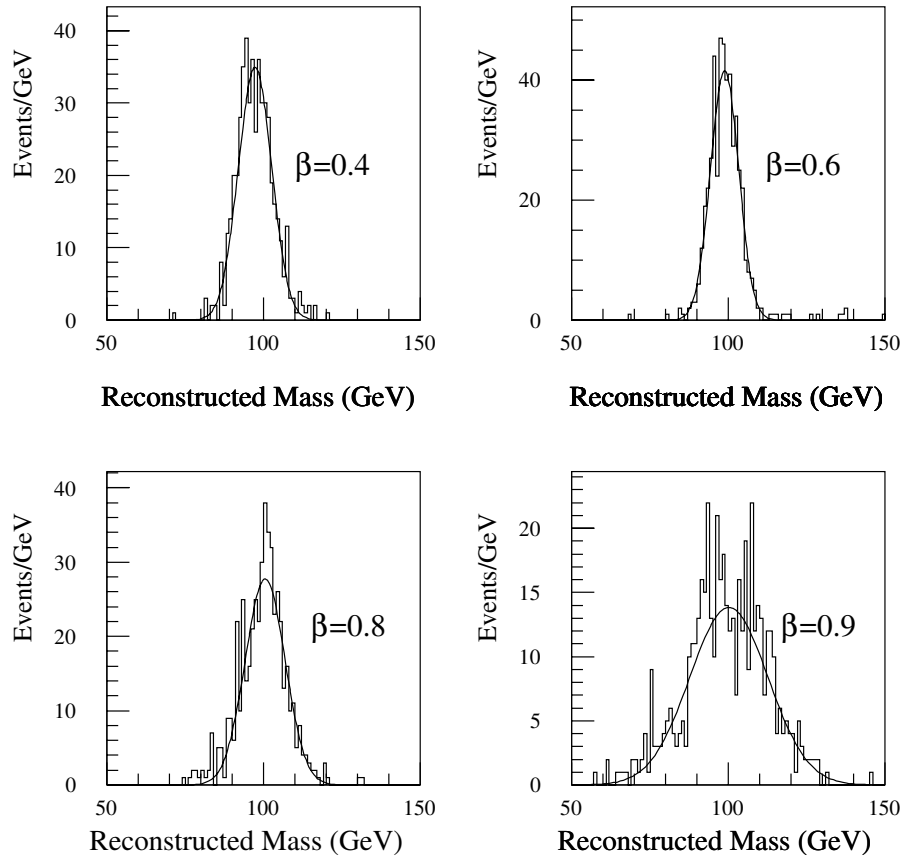
Figure 6-25 Reconstructed mass of the heavy particles with momenta of 50, 76, 135 and 200 GeV.

6.5 References

6-1   ATLAS collaboration, Muon Spectrometer Technical Design Report, CERN/LHCC/97-22 (1997).

6-2   ATLAS Collaboration, Technical Coordination Technical Design Report, CERN/LHCC/99-01 (1999).

6-3   R. von Boehn-Buchholz *et al.*, 'The conceptual design of the ATLAS EM Muon Chamber support structures', ATLAS Internal Note ATL-MUON-98-232 (1998).

6-4   A. Rimoldi, 'Geometrical Acceptance for the Trigger Chamber System and studies of the reaction $H \rightarrow ZZ^* \rightarrow 4\mu$ from the acceptance point of view', ATLAS Internal Note ATL-DAQ-98-119 (1998).

6-5   ATLAS collaboration, ATLAS LVL1 Technical Design Report, CERN/LHCC/98 (1998).

6-6   L. Chevalier *et al.*, 'Test of the magnetic field reconstruction procedure with a racetrack-coil prototype', ATLAS-COM-MUON NOTE-99-012 (1999).

6-7   L. Chevalier *et al.*, 'AMDB_SIMREC: A Structured data base Atlas internal for the ATLAS Spectrometer Simulation Program', ATLAS Internal Note ATL-MUON-97-148 (1997).

6-8   M. Deile *et al.*, 'MDT Track fitting with the Maximum Likelihood Method', ATLAS Internal Note ATL-MUON-98-240 (1998).

6-9   T. Sammer, Autocalibration von Driftrohrkammern fur das ATLAS-Myonenspektrometer, Diplomarbeit, University of Munich, 1997.

6-10   A. Nisati, S. Petrarca and G. Salvini, Rev. of Mod. Phys. Lett. **A12** (1997) 2213.

6-11   I. Hinchliffe and F.E. Paige, 'Measurements in Gauge Mediated SUSY Breaking Models at the LHC', hep-ph/9812233.

6-12   G. Polesello and A. Rimoldi, 'Reconstruction of quasi-stable charged sleptons in the ATLAS Muon Spectrometer', ATLAS Internal Note ATL-COM-MUON-99-008 (1999).

7 Electron and photon identification and measurement

7.1 Introduction

The emphasis of this chapter is a discussion of how the combination of the Inner Detector (ID) and the EM Calorimeter (and to a lesser extent, the Hadronic Calorimeter) can be used to identify and measure electrons and photons. Performance obtained using either the ID or the EM Calorimeter alone is described in the corresponding chapters, namely Chapter 3 or Chapter 4. For example, the electron-pion separation using transition radiation (TR) is described in Section 3.4. In this chapter, strategies for identifying electrons and photons originating from different physical processes in the presence of appropriate backgrounds are discussed. Methods for improving measurements are also presented. In what follows, it is clear that analyses will be improved as a better understanding of the detector is gained and new software is developed. Throughout this chapter, 'low luminosity' will be used to imply no pile-up.

7.2 Electron measurements

7.2.1 Measurements in the Inner Detector

As can be seen from Figure 3-5, there is a significant amount of material in the ID. The total material in the active volume of the ID averaged over $|\eta| < 2.5$ is ~50% X_0, hence there is a sizeable probability for an electron to loose a significant fraction of its energy before leaving the ID. Although much of the bremsstrahlung radiation will be collected by the EM Calorimeter, the track in the ID may be seriously affected causing its p_T to be poorly reconstructed and in some cases, making it difficult to reconstruct the track at all. The probabilities for electrons to radiate a given fraction of their energies are shown in Figures 7-1 and 7-2. For example, 20% of electrons will have lost half of their energy by the time they leave the ID barrel. The distributions are shown for $p_T = 20$ GeV electrons, however, the p_T dependence is small.

7.2.1.1 Bremsstrahlung recovery procedures

The track parameters reconstructed from a set of hits in the ID are not uniquely defined, but depend on the fitting procedure. Adjustments are possible using the ID information alone and further improvements to the track parameters can be made by using the EM cluster centroid as an external point. By allowing for bremsstrahlung on an electron track, it is possible to recover some of the efficiency losses which occur with a simple fit tuned for muons. In the following, the recovery procedures adopted by three of the ID pattern recognition programs (see Section 3.1.2) are discussed.

PixlRec allows for a discreet change of curvature at a fitted radius resulting in a seven parameter fit. For tracks where the fraction of TR hits exceeds 15%, xKalman attempts to recover from the energy loss by bremsstrahlung by incorporating it as an additional noise term in the Kalman Filtering formalism, in a manner akin to the multiple-scattering treatment. The modified track
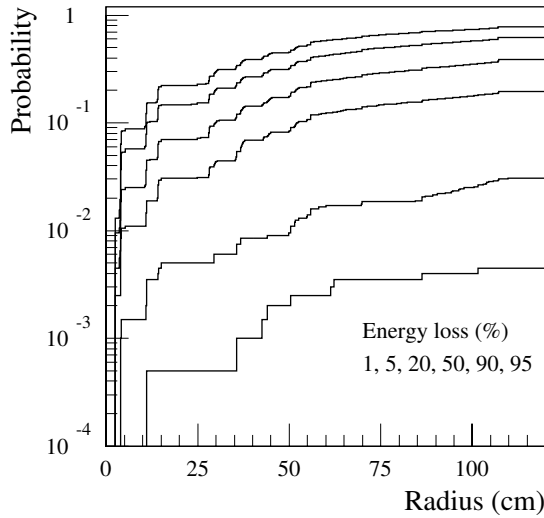
Figure 7-1 Probability that an electron with $|\eta| = 0.3$ (ID barrel) will radiate a given fraction of its energy within a certain radius. (Upper lines correspond to smaller losses.)
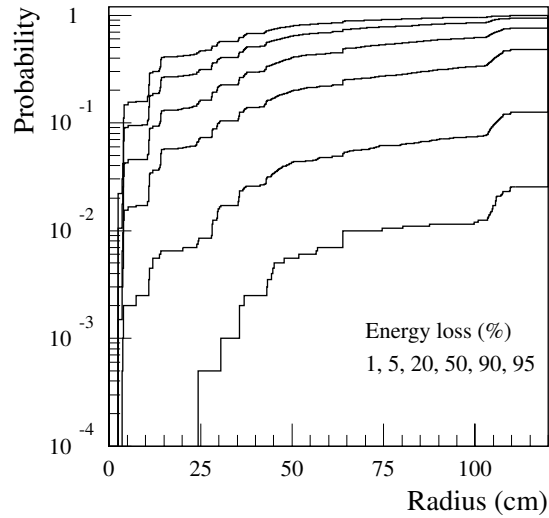
Figure 7-2 Probability that an electron with $|\eta| = 1.3$ (ID barrel/end-cap overlap) will radiate a given fraction of its energy within a certain radius. (Upper lines correspond to smaller losses.)

fit is retained if the track quality, measured by the number of precision hits, is improved (default operation). There exists in iPatRec, the possibility to fit the track in just the first few silicon layers, thereby reducing the sensitivity to the bremsstrahlung. By giving more weight to the earlier part of the track, all of these methods reduce the sensitivity to bremsstrahlung at the cost of reduced p_T resolution.

It can be shown that in the case of a single hard radiation, the energy-weighted barycentre of the impact points of the electron and the photon in the EM Calorimeter lies on the extrapolation of the initial electron trajectory. When the bremsstrahlung photon and the final electron both leave the ID with sufficient energy, these energy deposits merge into a single EM cluster. Hence, in principle, an unbiassed estimate of the original electron energy can be deduced from a helical fit using the track segment before the radiation and including the EM cluster barycentre. xKalman uses this principle to improve the p_T estimate by minimising a χ^2 containing all the fitted track information and the EM cluster position.

7.2.1.2 Momentum measurement in the Inner Detector

Electrons with $p_T = 20$ GeV were reconstructed with iPatRec, and fitted using all the track information (including the TRT) or just the information from the first four or five silicon planes. The ratio of the true p_T to the reconstructed p_T was formed and the core of the distribution was fitted with a Gaussian. The means and sigmas of the fits are shown as a function of pseudorapidity in Figures 7-3 and 7-4 respectively. It can be seen that as the track is truncated, the mean is closer to unity, indicating that there is less sensitivity to bremsstrahlung, but the resolution is degraded. The results of the fit to the complete track are very similar to those obtained with xKalman.

Figures 7-5, 7-6 and 7-7 illustrate different bremsstrahlung recovery procedures implemented in the xKalman program for $p_T = 20$ GeV electrons in the barrel. Gaussian fits were made to the cores ($\pm 1.5\sigma$) of the distributions of the ratio of true p_T to reconstructed p_T. Figure 7-5 shows the ratios obtained using the 'muon-fit', which is appropriate for muons, but makes no allowance for electron bremsstrahlung. The tail corresponding to lower reconstructed p_T is clear. Figure 7-
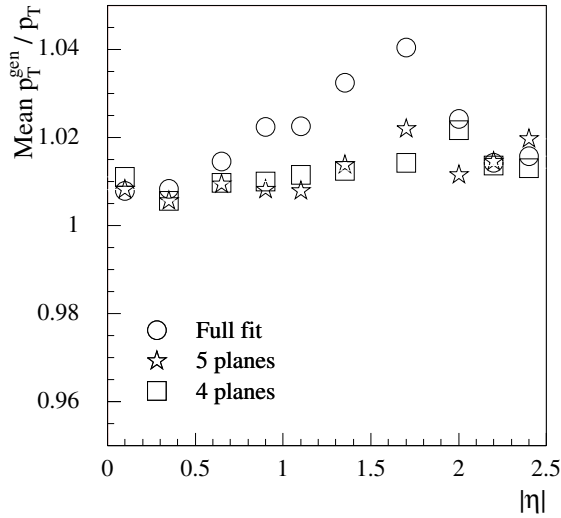
Figure 7-3 Ratio of true p_T to reconstructed p_T for p_T = 20 GeV electrons reconstructed by iPatRec. The means are obtained from Gaussian fits to the cores of the distributions as a function of pseudorapidity. Track fits are made to either the full track or a reduced number of silicon planes.
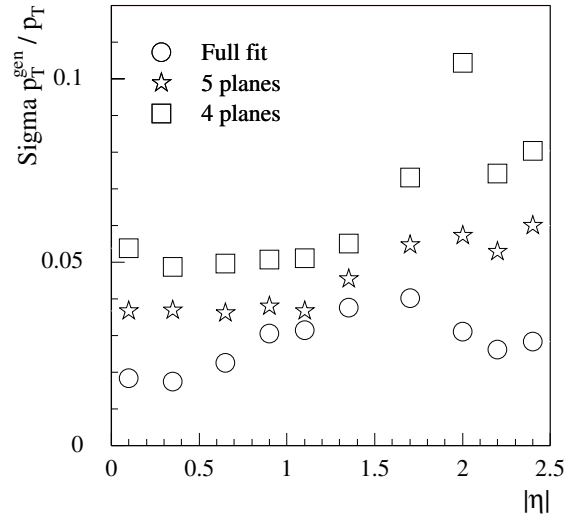
Figure 7-4 Resolution of reconstructed p_T for p_T = 20 GeV electrons reconstructed by iPatRec. The sigmas are obtained from Gaussian fits to the cores of the distributions as a function of pseudorapidity. Track fits are made to either the full track or a reduced number of silicon planes.

6 shows the ratios obtained using the 'electron fit', which does allow for radiation. The distribution is far more Gaussian, but with worse p_T resolution. Figure 7-7 shows the ratios obtained using the muon-fit combined with the EM cluster position. Although there is a tendency to overcompensate for the increased curvature, the tails have been reduced while retaining the resolution of the muon-fit.

The emphasis of the bremsstrahlung recovery algorithms in xKalman is to follow the track through the ID so as to associate as many hits as possible and to reduce the tails in the p_T distribution in order to increase the electron reconstruction efficiency. Figure 7-8 shows the efficiency for the different fitting procedures. The 'combined-fit' is the default fit for identified electrons, as described in the previous section. This corresponds to the combination of the muon and electron-fits, where the muon-fit is retained in most cases, but for the few percent of electrons where the number of precision hits on the track is increased, the electron-fit is kept. The efficiencies were evaluated for electrons passing the extended ID track quality cuts (see Section 3.1.3) and satisfying $0.7 < p_T^{gen}/p_T < 1.4$ (the results are not very sensitive to whether the normalisation is with respect to the true p_T or the E_T measured by the EM Calorimeter). The electron-fit increases the efficiency by ~6% with respect to the muon-fit, although it degrades the p_T resolution by a factor of ~2. The combined-fit increases the efficiency by ~2%, while retaining good resolution. The use of the EM cluster position significantly improves the tails and hence the efficiency at higher p_T. Around 200 GeV, the intrinsic ID resolution starts to dominate the bremsstrahlung tails and causes events to be lost by the cut on p_T^{gen}/p_T.
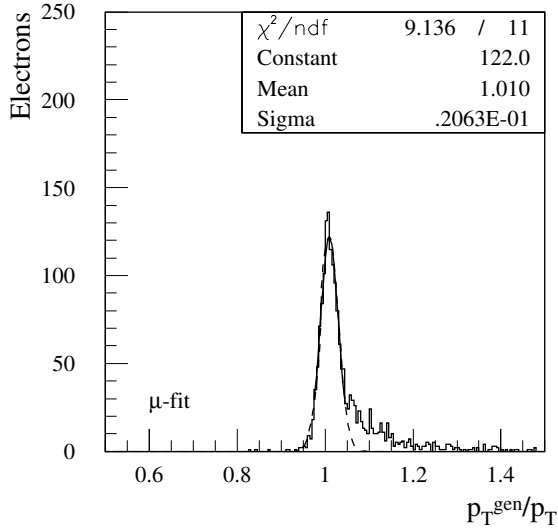
Figure 7-5 Ratio of true to reconstructed p_T from xKalman using the muon-fit for electrons with p_T = 20 GeV and η = 0.3.
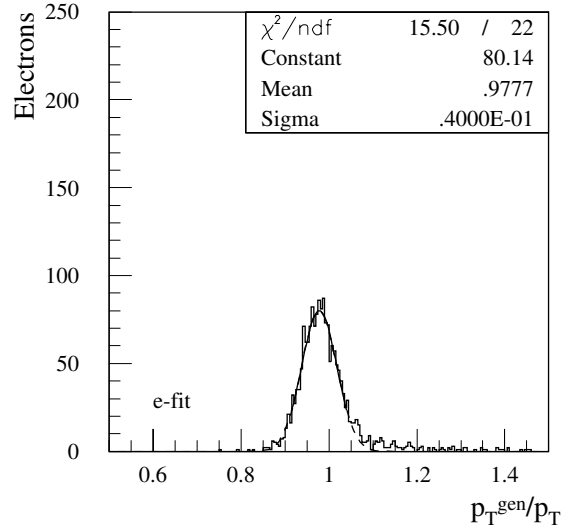
Figure 7-6 Ratio of true to reconstructed p_T from xKalman using the electron-fit for electrons with p_T = 20 GeV and η = 0.3.
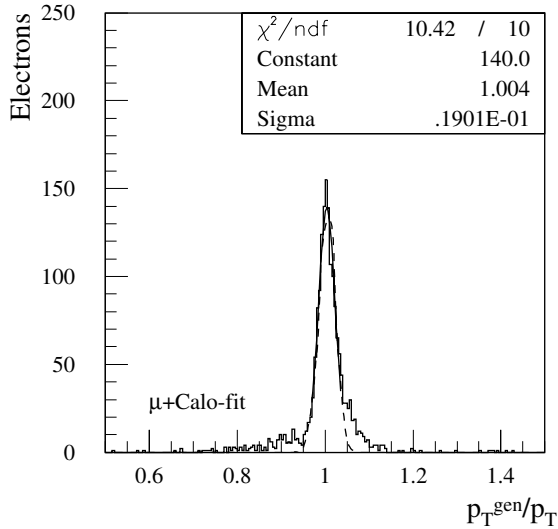
Figure 7-7 Ratio of true to reconstructed p_T from xKalman using the muon-fit along with the EM cluster position for electrons with p_T = 20 GeV and η = 0.3.
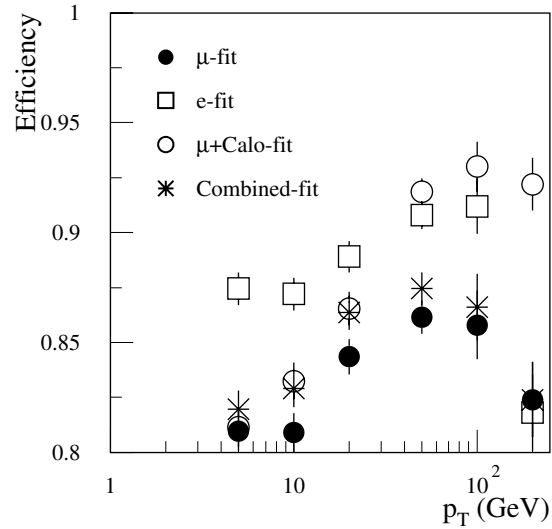
Figure 7-8 Efficiency for reconstructing electrons (η = 0.3) with xKalman using different fits. Electrons are required to satisfy the extended ID quality cuts and $0.7 < p_T^{gen}/p_T < 1.4$.

7.2.2 Matching the Inner Detector and EM Calorimeter

7.2.2.1 *E/p* for electron identification

The comparison between the momentum reconstructed in the ID and the energy measured in the EM Calorimeter is valuable in identifying electrons, as is demonstrated in subsequent sections. It also serves as an important source of calibration for the EM Calorimeter.

Figures 7-9 and 7-10 summarise the shapes of the E/p distributions as a function of pseudorapidity for $p_T = 5$ and 20 GeV electrons respectively. To give the narrowest distributions, full fits were made using all the track information. At $p_T = 20$ GeV, the width of the distributions is ~2.5%.
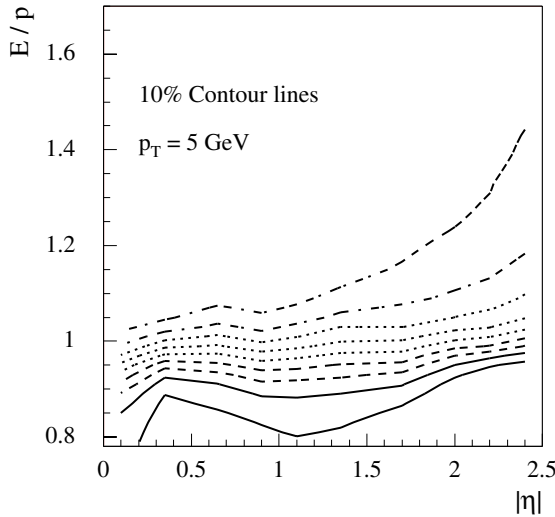
Figure 7-9 Contour plot showing value of E/p below which 10, 20, 30, 40, 50, 60, 70, 80 and 90% of electrons are reconstructed at given values of pseudorapidity. Curves are shown for $p_T = 5$ GeV electrons reconstructed with iPatRec using all the track information.
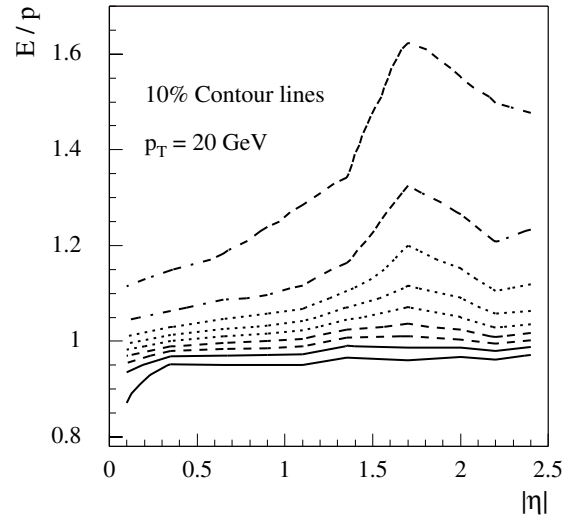
Figure 7-10 Contour plot showing value of E/p below which 10, 20, 30, 40, 50, 60, 70, 80 and 90% of electrons are reconstructed at given values of pseudorapidity. Curves are shown for $p_T = 20$ GeV electrons reconstructed with iPatRec using all the track information.

7.2.2.2 *E/p* for calibration of the EM Calorimeter

The main tool for calibrating the EM Calorimeter will be $Z \rightarrow ee$ events, as described in Chapter 4. The peak of the E/p distribution will provide a valuable cross-check of the calibration. As a precursor to this, it is essential that the momentum scale of the ID is correctly calibrated for muons along the lines discussed in Chapter 12. Subsequently, the calibration for electrons must be made, allowing for dE/dx losses and bremsstrahlung. These corrections will come from Monte Carlo studies like those illustrated in Figure 7-3, and hence will rely on a good model of the detector in the simulation and an accurate description of physical processes by GEANT.

The cores of the E/p distributions for different electron energies were fitted with Gaussians. The means and sigmas of the fits are shown as a function of pseudorapidity in Figures 7-11 and 7-12 respectively. The electrons have been reconstructed by iPatRec using the first four silicon planes to reduce the sensitivity to the bremsstrahlung. The mean values of E/p have a variation with pseudorapidity which comes primarily from the ID p_T (Figure 7-3). However, there are also some effects arising from imperfections in the Monte Carlo calibration of the Calorimeter, for example at $E_T = 20$ GeV, the energy calibration is about $(1 \pm 1)\%$ too low.

The resolution which can be achieved on E/p (Figure 7-12) leads directly to estimates of how many events will be required to check the calibration of the EM Calorimeter. Taking the resolution to be 5%, 400 regions of the EM Calorimeter can be calibrated with a statistical precision of 0.1% with 10^6 electrons. This should not be a problem, since at low luminosity, it is anticipated that 30×10^6 reconstructed $W \rightarrow e\nu$ events will be collected in one year. The 5% resolution comes
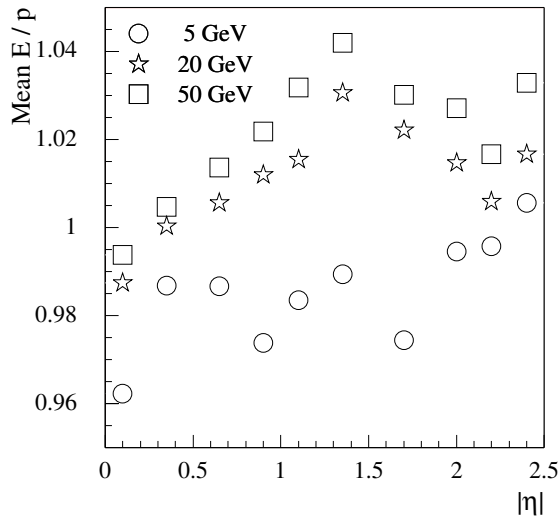
Figure 7-11 Ratio of *E/p* for electrons reconstructed by iPatRec. The means are obtained by fitting to the cores of the distributions as a function of pseudorapidity. Fits are made to the first four silicon planes.
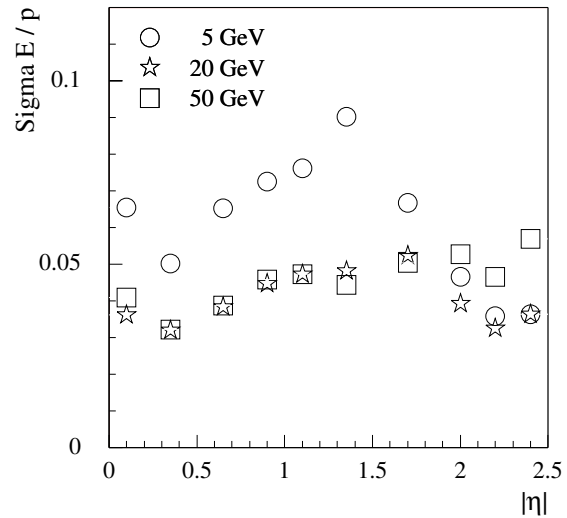
Figure 7-12 Resolution on *E/p* for electrons reconstructed by iPatRec. The sigmas are obtained by fitting to the cores of the distributions as a function of pseudorapidity. Fits are made to the first four silicon planes.

from the track fit to the first four or five silicon planes. If there is sufficient confidence in correcting for the effects of bremsstrahlung so that the full track information can be used, then the same statistical precision will be achieved with a quarter of the number of events.

7.2.2.3 Sensitivity to the material of the Inner Detector

The position of the *E/p* peak depends on the amount of material, especially that located at smaller radii. To test the sensitivity to this in the simulation, the material in the SCT support structures was increased. These structures (cylinders in the barrel and disks in the end-caps) are simulated as simple, uniform surfaces, on which the detectors are mounted. In the barrel, the material increased from 10% to 14.5% X_0. The corresponding change in the *E/p* distribution can be seen in Figure 7-13. There is a small shift in the peak of the distribution and the tail of the distribution has increased, with extra events around *E/p* = 1.3. With the 45% increase in material in the SCT, the peak has shifted by 0.0025, so if it is required to understand this shift at the level of 0.1%, the material of the SCT in the barrel must be understood to better than ~20% of its value - this will be easy. However, should it be desired to understand the shift at the 0.01% level, then the material must be known to ~2% – this will be far more challenging.

To cross-check the EM Calorimeter calibration at the 0.02% level using *E/p* will be possible only if the systematic effects mentioned earlier can be understood. If this can be done, then it will be necessary to determine the SCT material to ~2%. This requirement is likely to be even tighter for the Pixel System, which is located at small radius, and in the end-caps, where there is more material. The requirements for the Pixels will be examined in future studies.

The material in the ID can be estimated from direct calculation, the conversion rates (see Chapter 12) or from the *E/p* distribution itself. Different parts of the *E/p* distribution will be sensitive to bremsstrahlung from different radii. By making a fit to the distribution, which is sensitive to the different components, it should be possible to estimate the ID material by reference to simulation. Using this method, CDF understood the material in their tracker to 10% [7-1]. Clear-

ly, this will rely on having an accurate description of the physical processes associated with tracking electrons by GEANT as well as a good description of the detector. The distributions shown in Figure 7-13 were fitted over a slightly larger range (± 1.5σ) to increase the sensitivity to the effect of extra SCT material. One such fit is shown in Figure 7-14. The difference in the widths of the fitted Gaussians was 0.0052, with an uncertainty on measuring the width of 0.0007. To obtain a precision which is 25 times better would require a determination of the width to 0.0002. The uncertainty on the width was obtained with a sample of 8,800 reconstructed single electrons; to reduce this uncertainty to 0.0002 would require 1.0×10^5 reconstructed electrons. Similar calculations for the end-cap region ($|\eta| = 1.8$), indicate that approximately 2.2×10^5 electrons would be required. With 30×10^6 reconstructed $W \rightarrow e\nu$ events expected for each year of low luminosity running, this should allow a satisfactory determination of the ID material as a function of pseudorapidity. By using an inclusive electron sample (as obtained from the analysis of Section 7.4), larger numbers of electrons could be used. Although it will be more difficult to resolve deviations from the material expected at different radii, sensitivity to the different components should be possible by fitting the *E/p* distribution by functions with more parameters.
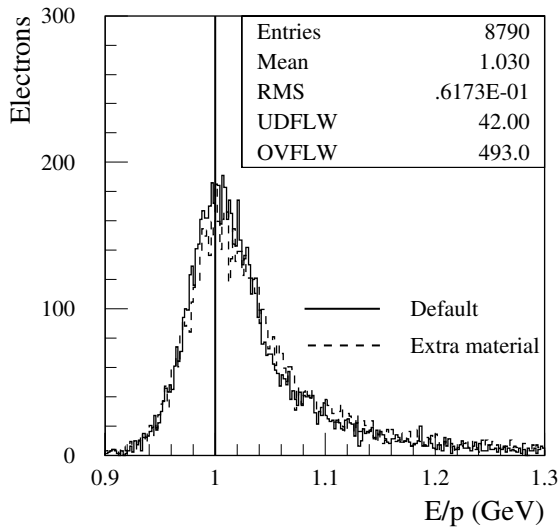
Figure 7-13 *E/p* distribution for single electrons with p_T = 20 GeV and η = 0.3, reconstructed by xKalman. The figure shows the distribution for the default layout as well as for a layout with 45% more material in the SCT.
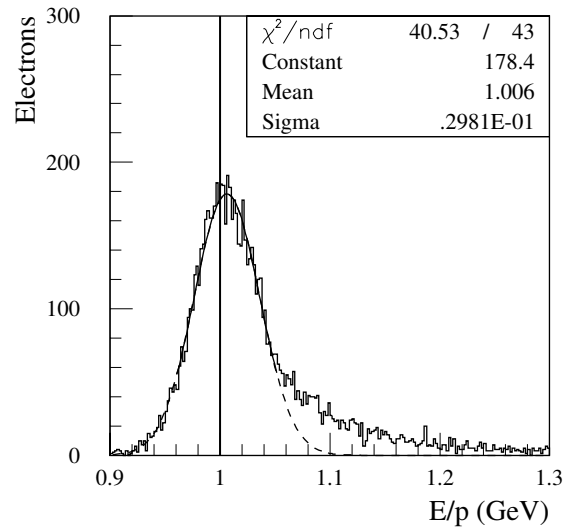
Figure 7-14 *E/p* distribution for single electrons with p_T = 20 GeV and η = 0.3, reconstructed by xKalman, for the default layout. Also shown is a Gaussian fit to ±1.5σ around the peak.

7.2.2.4 Position matching

Tracks and clusters are associated by looking at the matching between the track direction and the corresponding calorimeter quantities. These are evaluated as follows:

- The pseudorapidity is computed from the position measured in the first compartment of the EM Calorimeter, an estimate of the shower depth in this compartment and the *z*-position along the beam line, which is measured by the ID with a negligible error.

- The azimuthal angle is computed from the position measured in the second compartment of the EM Calorimeter and an estimate of the shower depth in this compartment. The measured transverse energy is used to correct for the curvature of the electron trajectory in the magnetic field to give an estimate of the azimuthal direction at the beam line.

Figures 7-15 and 7-16 show the matching in pseudorapidity and azimuth for $p_T = 20$ GeV electrons, without electronic noise or pile-up. The dashed lines indicate the cuts which are used for electron/jet (see Section 7.4.2.3) and photon/electron (see Section 7.7.1) separation. At high luminosity, the probability to find a track from the pile-up with $p_T > 5$ GeV pointing to the $\Delta\eta = \pm0.01$, $\Delta\phi = \pm0.02$ window is about 10^{-4}.
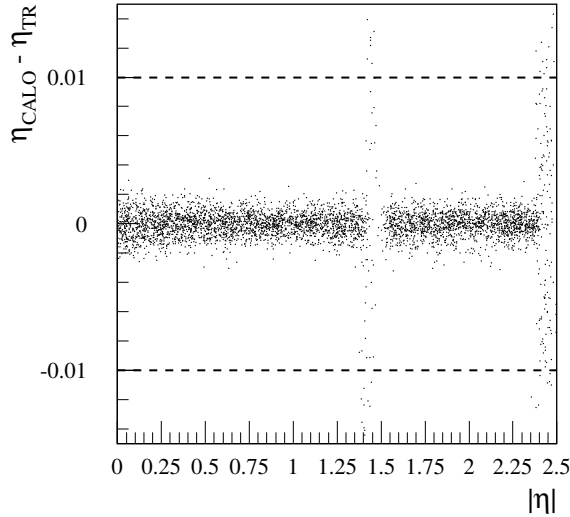
Figure 7-15 Matching in pseudorapidity between the EM Calorimeter and ID for $p_T = 20$ GeV electrons.
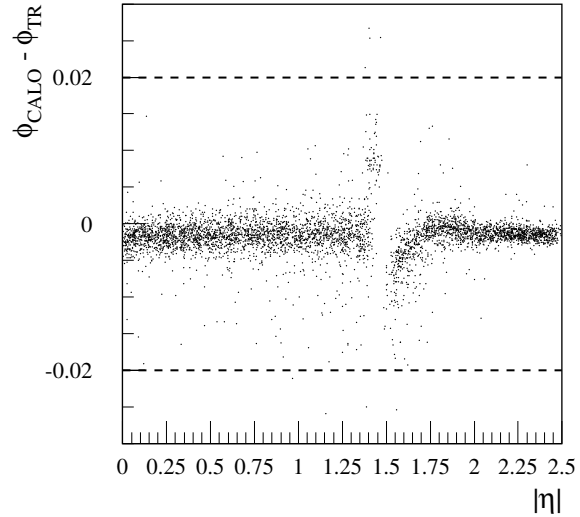
Figure 7-16 Matching in azimuth between the EM Calorimeter and ID for $p_T = 20$ GeV electrons.

7.2.3 Combined energy measurements

The energy measurement of an electron is degraded, both in the ID and in the Calorimeter by bremsstrahlung, leading to significant tails and to a worsening of the energy resolution. Both effects can be reduced by using the following methods, which are illustrated by results for electrons at $|\eta| = 1.1$.

Approximately 50% of electrons at $|\eta| = 1.1$ are accompanied by a conversion since there are a large number of bremsstrahlung photons (for example, on average there are 5.8 photons with $E > 10$ MeV for 20 GeV E_T electrons at $|\eta| = 1.1$). In this case the energy measured in a 3×7 window in the calorimeter is significantly reduced, as shown in Figure 7-17. Conversions can be reconstructed as described in Section 7.5.1, with an efficiency of only 1% for conversions accompanying a 10 GeV E_T electron (at $|\eta| = 1.1$), rising to 21% for a 20 GeV E_T electron and to 33% at 50 GeV. The energy in the 3×7 window when a conversion is reconstructed is also shown in Figure 7-17 – in this case, an appropriate calibration factor can be applied.

The azimuthal width of the shower, measured in the second compartment of the calorimeter, is correlated with the energy loss outside the 3×7 window. When no conversion is reconstructed, the energy in the calorimeter is taken as the energy in the window with a calibration factor depending on the width. Finally, below about 15 GeV E_T, the resolution in the ID is similar or better than in the calorimeter, in which case a weighted average of the two measurements can be made. At 10 GeV E_T and $|\eta| = 1.1$, the resolution of the calorimeter is 3.25%, the resolution of the ID is 2.63% and the combined resolution is 2.32%.

With the methods described above, the amount of the tails, defined as the fraction of events outside the interval $0.95 < E/E^{gen} < 1.05$ is reduced by about 20%, as shown in Figure 7-18.
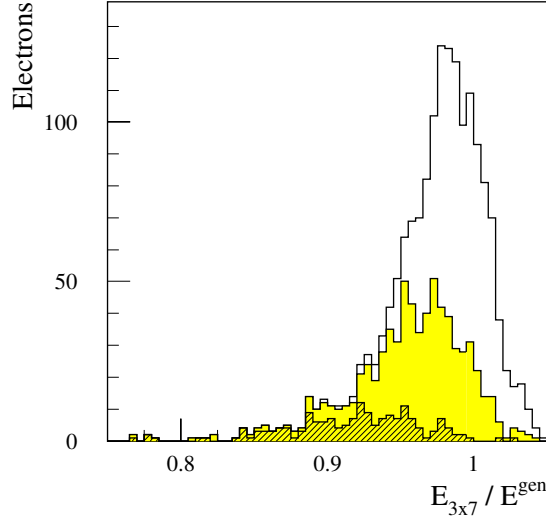
Figure 7-17 Reconstructed energy in the EM Calorimeter divided by the true energy for 20 GeV E_T electrons at $\eta = 1.1$. The histograms correspond to: electrons with reconstructed conversions (hatched), electrons with conversions which are not reconstructed (shaded), electrons without conversions (unshaded).
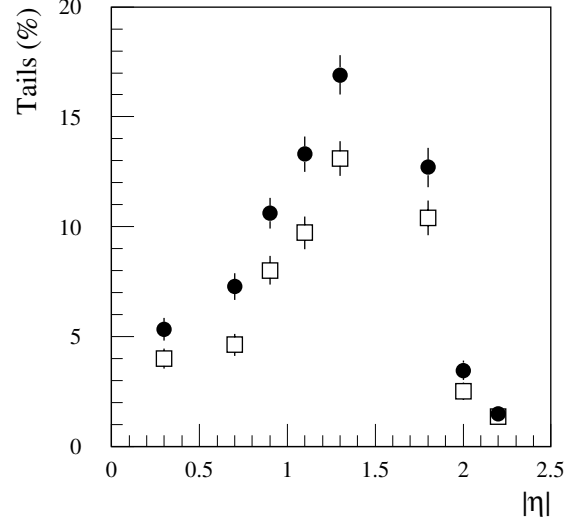
Figure 7-18 Fraction of 20 GeV E_T electrons outside $0.95 < E/E^{gen} < 1.05$ using the raw calorimeter information (black circles) and after the combined energy measurement described in the text (white squares).

7.3 Low energy electrons

7.3.1 Electron/pion separation

For low energy electrons, the trigger will be provided by something other than the electrons (for example a muon with $p_T > 6$ GeV in *B* physics events) and it will not be easy to identify electron candidates by an unguided search of the energy deposits in the EM Calorimeter. Instead the Inner Detector must be used to 'seed' the calorimeter clustering.

A study was made of electrons and pions in the range $1\,\text{GeV} \leq p_T \leq 7\,\text{GeV}$ with $|\eta| \leq 2.4$. The effects of electronic noise in the EM Calorimeter were included. As the response of both subdetectors for low p_T varies quite significantly with p_T and $|\eta|$, the electron/pion separation parameters were calculated for three p_T-ranges:

$$1\,\text{GeV} \leq p_T \leq 2\,\text{GeV}, 2\,\text{GeV} \leq p_T \leq 4\,\text{GeV} \text{ and } 4\,\text{GeV} \leq p_T \leq 7\,\text{GeV}$$

and five $|\eta|$-ranges:

$$0 \leq |\eta| \leq 0.8, 0.8 \leq |\eta| \leq 1.4, 1.4 \leq |\eta| \leq 1.8, 1.8 \leq |\eta| \leq 2.0 \text{ and } 2.0 \leq |\eta| \leq 2.4.$$

The following method was used to identify electrons. After track reconstruction in the ID, loose cuts were applied to all tracks: $p_T \geq 0.5$ GeV, number of precision hits ≥ 8, number of pixel hits ≥ 2, at least one associated hit in the *B*-layer, number of TRT straws ≥ 6, fraction of high-threshold (TR) hits in the TRT > 0.05. For selected tracks, the predicted point of impact was calculated for each of the EM Calorimeter compartments. Based on the information in the surrounding EM Calorimeter cells, the values of the EM Calorimeter and combined ID-Calorimeter separation

variables were calculated. For each of these, the probability of the track being an electron was calculated, with the set of probabilities used being determined by the p_T and pseudorapidity reconstructed in the ID. A discriminating function to distinguish between electrons and hadrons was formed as the product of the above probabilities. Some of the variables used are correlated, and although the method is valid, its treatment of these correlations is not optimal. Alternative approaches, such as neural nets, will be considered in the future. For some values of p_T and pseudorapidity, some of the variables were less discriminating and hence were not used.
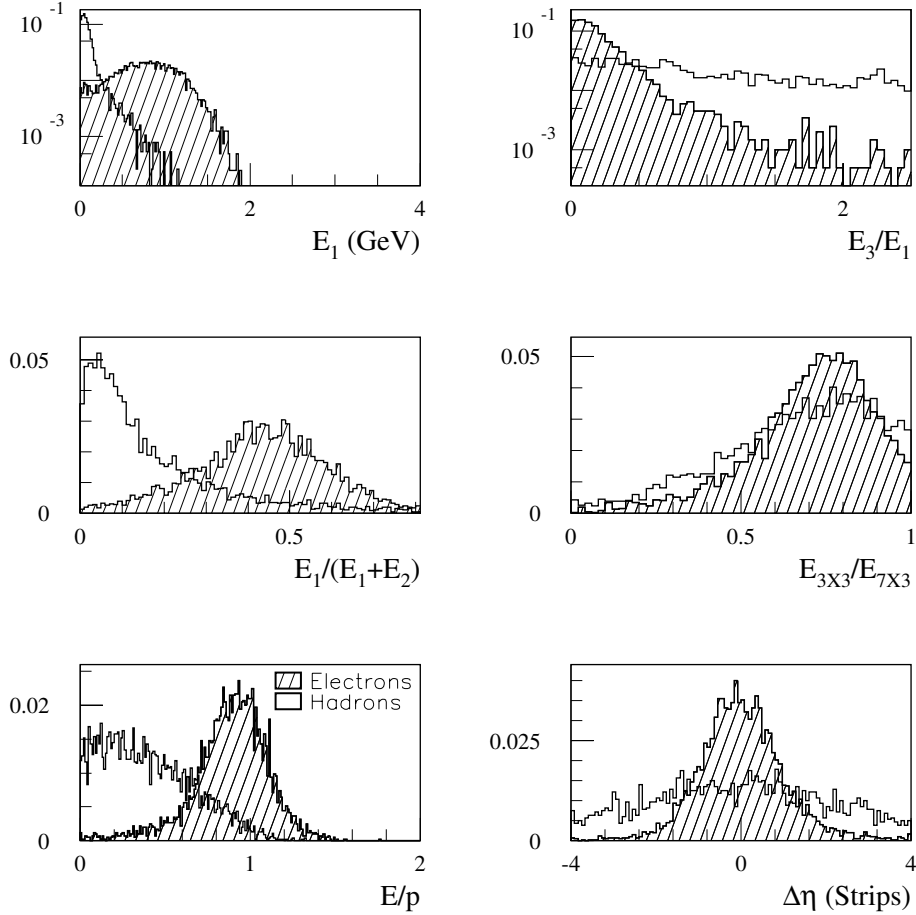
Figure 7-19 Some of the variables used to distinguish soft electrons (hatched) from hadrons (open). The histograms have been normalised to unit area. The distributions correspond to single particles with $2 \text{ GeV} \leq p_T \leq 4 \text{ GeV}$ and $|\eta| < 0.8$. $E_{1,2,3}$ are the energies in the first, second and third longitudinal compartments of the EM Calorimeter.

The variable used in the ID alone was: the fraction of high-threshold (TR) hits in the TRT. The variables formed in the EM Calorimeter alone were: the energy deposited in the first compartment (E_1), the ratio of energies deposited in the third and first compartments (E_3/E_1), the ratio of energies deposited in first compartment to the sum in first and second ($E_1/(E_1+E_2)$), the shower width (in pseudorapidity) in the first compartment, the ratio of energies deposited around the predicted impact point in the calorimeter in 3×3 and 3×7 clusters ($E_{3\times3}/E_{7\times3}$), and the asymmetry in the lateral shower profile measured in the first compartment by the three strips centred on the strip with the largest energy. The cracks between the barrel and the endcaps were excluded. The variables formed using the combination of the ID and the EM Calorim-

eter were: the ratio of energy measured by the EM Calorimeter to the momentum measured by the ID (*E/p*), the difference in pseudorapidity between the point of impact at the first compartment of the EM Calorimeter as predicted by ID extrapolation and as measured by the η-strips ($\Delta\eta$).

An example of the distributions for some of the more discriminating variables are shown for single particles in Figure 7-19. The distributions vary strongly with p_T and pseudorapidity; in particular, *E/p* becomes more discriminating at higher energy, which for a fixed E_T corresponds to higher pseudorapidity.

By cutting at different values of the discriminating function, different electron efficiencies can be obtained, each with a corresponding value of the rejection for single pions. The pion rejection as a function of the electron efficiency is shown in Figure 7-20 for tracks of different p_T.
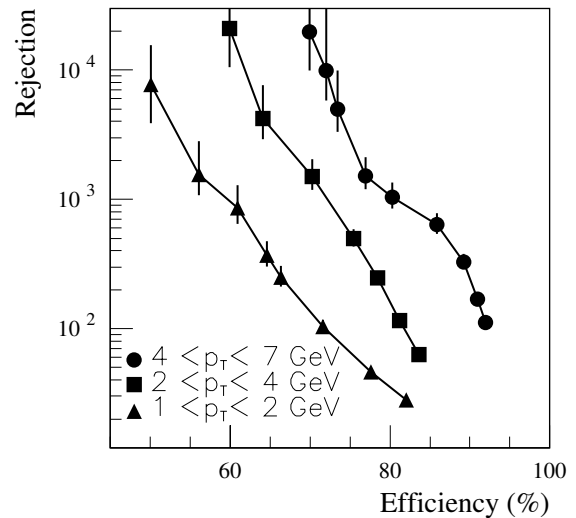
Figure 7-20 Pion rejection vs electron efficiency for single particles of different p_T.

7.3.2 Identification of low energy electrons in physics events

To identify soft electrons in complete events, it is necessary to apply the methods described above to each charged particle reconstructed in the event. In this section, the application to *B* physics events is described; the application to tagging *b*-jets is described in Chapter 10.

For this study, an inclusive $b\bar{b}$ sample was used, with the requirement of a muon with $p_T \geq 6$ GeV for triggering. A subsample of these events containing electrons with $p_T^{gen} \geq 5$ GeV were considered to be signal events, while the remainder were considered to be background. For a given event, the method outlined above was applied to each reconstructed track with $p_T > 4$ GeV and its discriminating variable was formed. For this, new probability functions were obtained from $b\bar{b}$ events.

Figure 7-21 shows the rejection against individual hadrons as a function of the electron efficiency. The electrons mostly originate from heavy flavour or τ decays, however some may come from conversions or Dalitz decays. To identify signal events containing $b \rightarrow e$ decays, the electron identification was applied to each reconstructed track in each event of the inclusive $b\bar{b}$ sample. The discriminating function was found for the best electron candidate in each event. Figure 7-22 shows the rejection of background events compared to the efficiency for identifying signal events, where the points correspond to different cuts on the value of the discriminating

function. The performance is worse than for individual particles since in the background events, there will be several tracks, any of which may be mis-identified as an electron. Further there will be electrons which do not arise from signal processes.
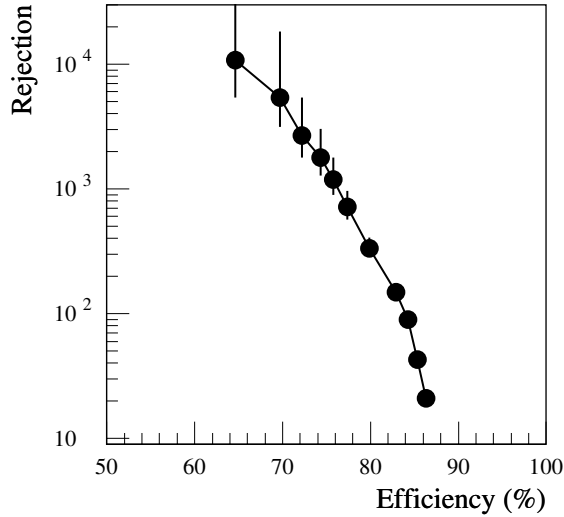
Figure 7-21 Hadron rejection vs electron efficiency for individual particles in $b\bar{b}$ events with p_T > 4 GeV.
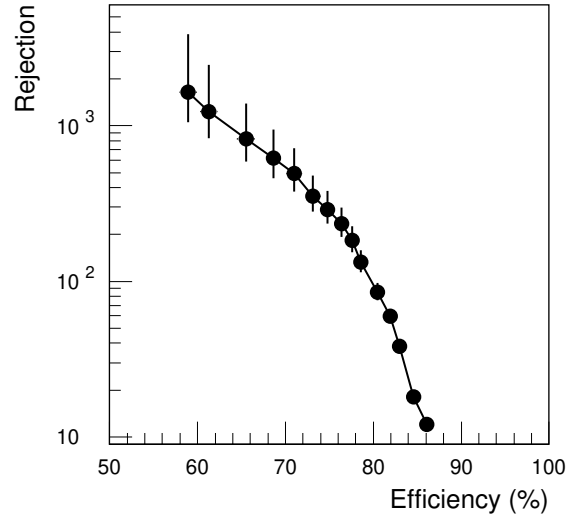
Figure 7-22 Rejection of events without $b \rightarrow e$ vs efficiency for retaining events with $b \rightarrow e$. Electrons have p_T > 5 GeV.

7.4 Electron/jet separation

7.4.1 Introduction

The identification of isolated electrons with $p_T \geq 20$ will be essential for physics at the LHC, including searches for leptonic decays of the Higgs boson, studies of the production and decay of W's and Z's, the extraction of clean samples of $t\bar{t}$ events for the measurement of m_t as well as electrons for E/p calibration. This section describes the inclusive electron selection and the rejection capability against QCD-jets using information from the EM Calorimeter and the Inner Detector. More details can be found in [7-2]. To obtain an inclusive electron signal, a jet rejection O(10^5) is required.

To separate electrons from jets, cuts were developed which maintained reasonable electron efficiency even in the presence of pile-up at high luminosity while removing a high fraction of jet events from an inclusive jet sample. The jet sample was analysed to demonstrate that the signal electrons which it contained could be extracted from the background. In the studies reported in this section and Section 7.6, the jet rejection was normalised to the total number of jets with E_T > 17 GeV, smeared and reconstructed at the particle-level using ATLFAST [7-3]. This is believed to give a better reflection of the rejection which can be achieved by ATLAS and corresponds to the performance which would be observed for physical jets in the detector as opposed to partons. This normalisation results in a rejection which is a factor of three lower than would be obtained were the E_T cut applied at the parton level. The electron efficiencies have been studied for electrons at the nominal trigger thresholds for single isolated EM clusters of 20 and 30 GeV for low and high luminosity respectively.

7.4.1.1 Datasets

A high statistics sample of around 10^6 fully simulated dijet events was used [7-3]. At the parton level, each jet had $p_T > 17$ GeV and was produced within $|\eta| < 2.7$. Initial and final state radiation were simulated. At the same time, other physics processes such as prompt photon production, quark bremsstrahlung, *W*, *Z* and top production were generated with the appropriate cross-sections - the complete set of events is referred to as the 'jet sample'. These events were processed by the LVL1 trigger simulation (see Section 11.3.2) to obtain the 'electron/photon stream'. The jet rejection factor for jets having $E_T > 17$ (25) GeV was approximately 80 (90) for an electron efficiency of about 95% at low (high) luminosity. Only events with showers having a large EM component survived.

For the efficiency studies, samples of single electrons were generated with $|\eta| < 2.5$ and with fixed p_T of 20 and 30 GeV. To study the performance at high luminosity, pile-up was superimposed on the electrons and jets.

7.4.2 Analysis

The electrons and jets were first processed by the LVL1 and LVL2 trigger algorithms to select those events containing electron candidates. The events which passed the trigger were further processed by the offline reconstruction. In the following, the Calorimeter and ID selections of the offline analysis are explained; the trigger algorithms of the LVL2 trigger are explained in Section 11.4.3.

7.4.2.1 Offline calorimeter selection

Significant discrimination between electrons and jets can be achieved by the LVL2 Calorimeter Trigger. Subsequently, the offline calorimeter algorithms can refine the cuts made by the trigger as well as making additional ones.

Only EM clusters with $E_T > 17$ (25) GeV at low (high) luminosity were considered. These values correspond to the E_T threshold cut of the single object electron trigger, which are chosen to be efficient for 20 (30) GeV electrons. Figures 7-23 and 7-24 show the E_T distributions for all clusters found in the EM Calorimeter for electrons of 30 GeV and dijet events at high luminosity. The entries at low E_T correspond to clusters from low energy particles in the minimum bias events (in the case of pile-up) or particles in the jets themselves; the peaks arise from threshold cuts of around 5 GeV. It is clear that clusters from minimum bias events have low E_T and can be completely removed.

The following variables were used to distinguish high-E_T electrons from jets (more details can be found in [7-4]): the ratio of the transverse energy in the first compartment of the Hadronic Calorimeter divided by the transverse energy deposit in the EM Calorimeter, the ratio of the energy deposited in a 3×7 window divided by the energy deposited in a 7×7 window in the second compartment of the EM Calorimeter (see Figure 7-25), the shower width in pseudorapidity in the second compartment of the EM Calorimeter.

To separate the surviving jets from electrons, the very fine granularity in pseudorapidity of the first compartment was exploited by looking for substructures within a shower in pseudorapidity and by analysing the overall shower shape, using a window of $\Delta\eta\times\Delta\phi = 0.125\times0.2$. It was required that the fraction of EM energy in the first compartment exceeded 0.5%. The following
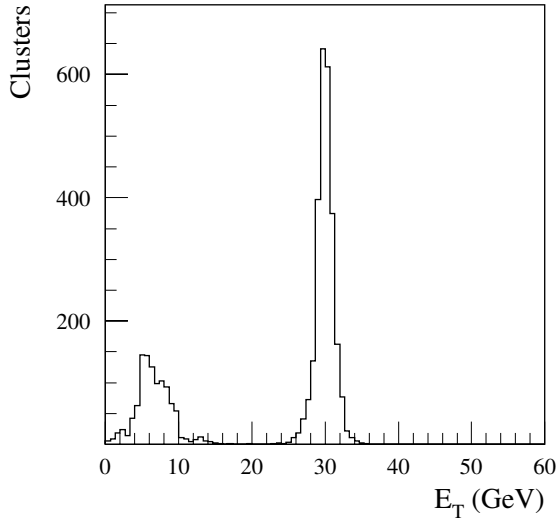
Figure 7-23 E_T distribution of all clusters in each event after LVL1 simulation in the EM Calorimeter for events with E_T = 30 GeV electrons and pile-up corresponding to 10^{34} cm^{-2}s^{-1}.
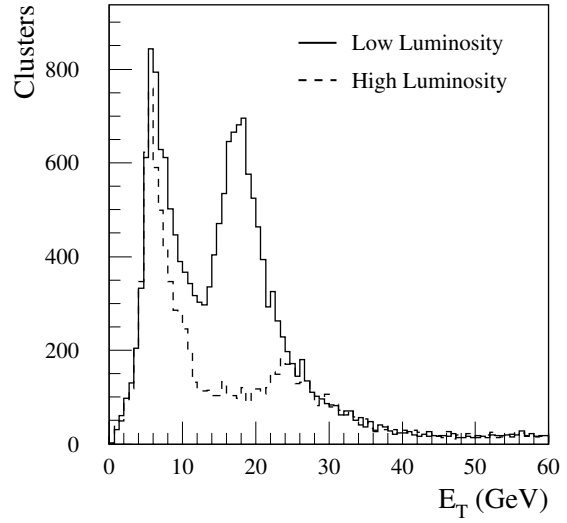
Figure 7-24 E_T distribution of all clusters in each event after LVL1 simulation in the EM Calorimeter for events with jets at both low and high luminosity.
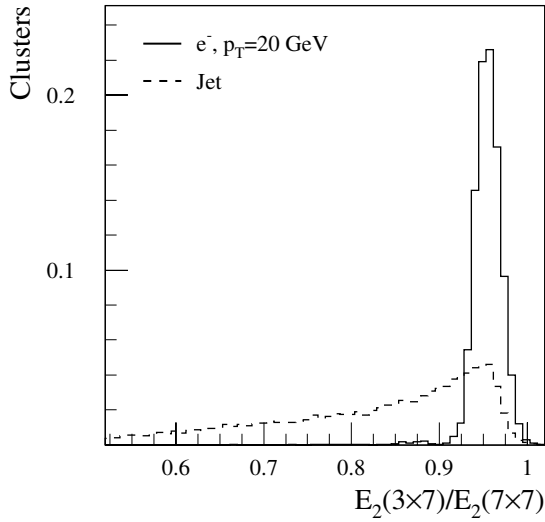
Figure 7-25 Shower shape in the second compartment of the EM Calorimeter for electrons and jets at low luminosity. Only the LVL1 Trigger was applied beforehand. The distributions are normalised to unit area.
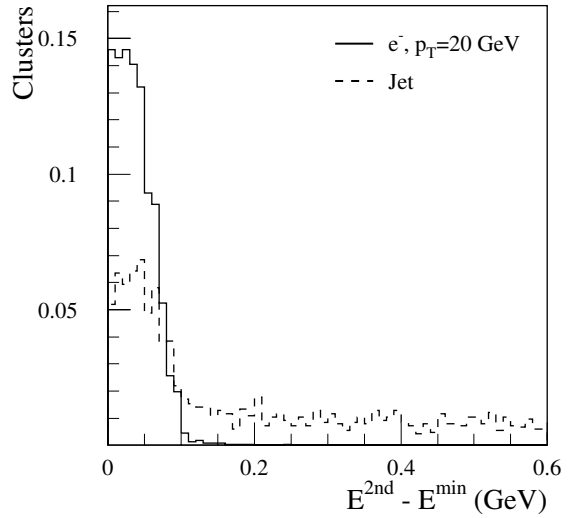
Figure 7-26 Difference between the energy found in the second maximum and the energy found in the strip with minimal value in the first compartment of the EM Calorimeter (before any cuts in first compartment). The distributions are shown for electrons and jets at low luminosity for $|\eta| < 1.37$ and are normalised to unit area.

variable was used: the difference between the energy associated with the second maximum and the energy deposited in the strip with the minimal value between the first and second maxima (see Figure 7-26.). In addition, the energy in the strip in which the second maximum was located had to exceed a value which depended linearly on the E_T of the EM cluster. Additional variables are: the shower width and the fraction of energy outside the three strips in the shower core.

The variables were optimised in several $|\eta|$ intervals to allow for varying granularities, lead thickness and material in front of the calorimeter. The quantities calculated using the first compartment can be used only in the regions $|\eta| \leq 1.37$ and $1.52 \leq |\eta| \leq 2.37$ since there are no strips in $1.4 < |\eta| < 1.5$ nor beyond $|\eta| = 2.4$. The cuts on the variables were tuned in such a way that they were more than 98% efficient for electrons after the LVL1 and LVL2 triggers.

7.4.2.2 Inner Detector selection

After the calorimeter cuts, the contamination of the inclusive signal from charged hadrons was greatly reduced and the remaining background was dominated by background from photon conversions and low multiplicity jets containing high-p_T π^0 mesons. This background was reduced further by requiring the presence of a good ID track pointing to the EM cluster and with a good energy-momentum match.

Tracks were reconstructed with xKalman (see Section 3.1.2) in a cone $\Delta\eta = \pm0.1$, $\Delta\phi = \pm0.1$ around the selected EM clusters, and only tracks with $p_T > 5$ GeV were kept. Where possible, the bremsstrahlung recovery procedures described in Section 7.2.1.1 were used. The reconstructed track with the highest p_T in the cone was required to satisfy the extended ID track quality cuts (see Section 3.1.3). The cuts on the pixels and impact parameter were particularly effective against photon conversions, reducing them by a factor of ~5.

7.4.2.3 Inner Detector and EM Calorimeter matching

The LVL2 trigger tends to ensure that there is an associated charged track to the EM cluster within a cone $\Delta\eta = \pm0.1$, $\Delta\phi = \pm0.1$. Hence the jet rejection which was achieved by the cuts in the ID was quite small, around 1.8. This was significantly improved by ensuring consistency between the EM Calorimeter and ID information. Firstly the angular matching between the track and the EM cluster was checked, allowing for the track curvature and the vertex position (see Section 7.2.2.4). It was required that $|\Delta\eta| < 0.01$ (0.02) at low (high) luminosity and $|\Delta\phi| < 0.02$. Distributions for these two variables are shown in Figure 7-27. The distributions are shown after the LVL2 trigger rather than after the ID cuts so as to increase the statistics in the plots.

Subsequently, the energies measured by the two subdetectors were compared - see Figure 7-28. At low (high) luminosity, it is required that 0.7 $(0.6) < E/p < 1.4$. The tail at low values of E/p for conversion electrons arises when one photon from a π^0 converts and the second photon was included in the EM cluster causing the track fit (incorporating the calorimeter bremsstrahlung recovery procedure) to overestimate the momentum.

7.4.2.4 Use of transition radiation in the TRT

The events which survived the selection procedure described so far consisted mainly of signal electrons. At low luminosity, where the E_T cut is at 17 GeV, 80% of the events came from heavy flavour and 20% from W's and Z's; at high luminosity, the E_T cut rises to 25 GeV and the fractions became 20% and 80% respectively. The contamination of the jet sample arising from the mis-identification of charged hadron backgrounds was 30% (40%) of the jets at low (high) luminosity. The contamination from electrons coming from photon conversions was greatly reduced by the previous cuts.
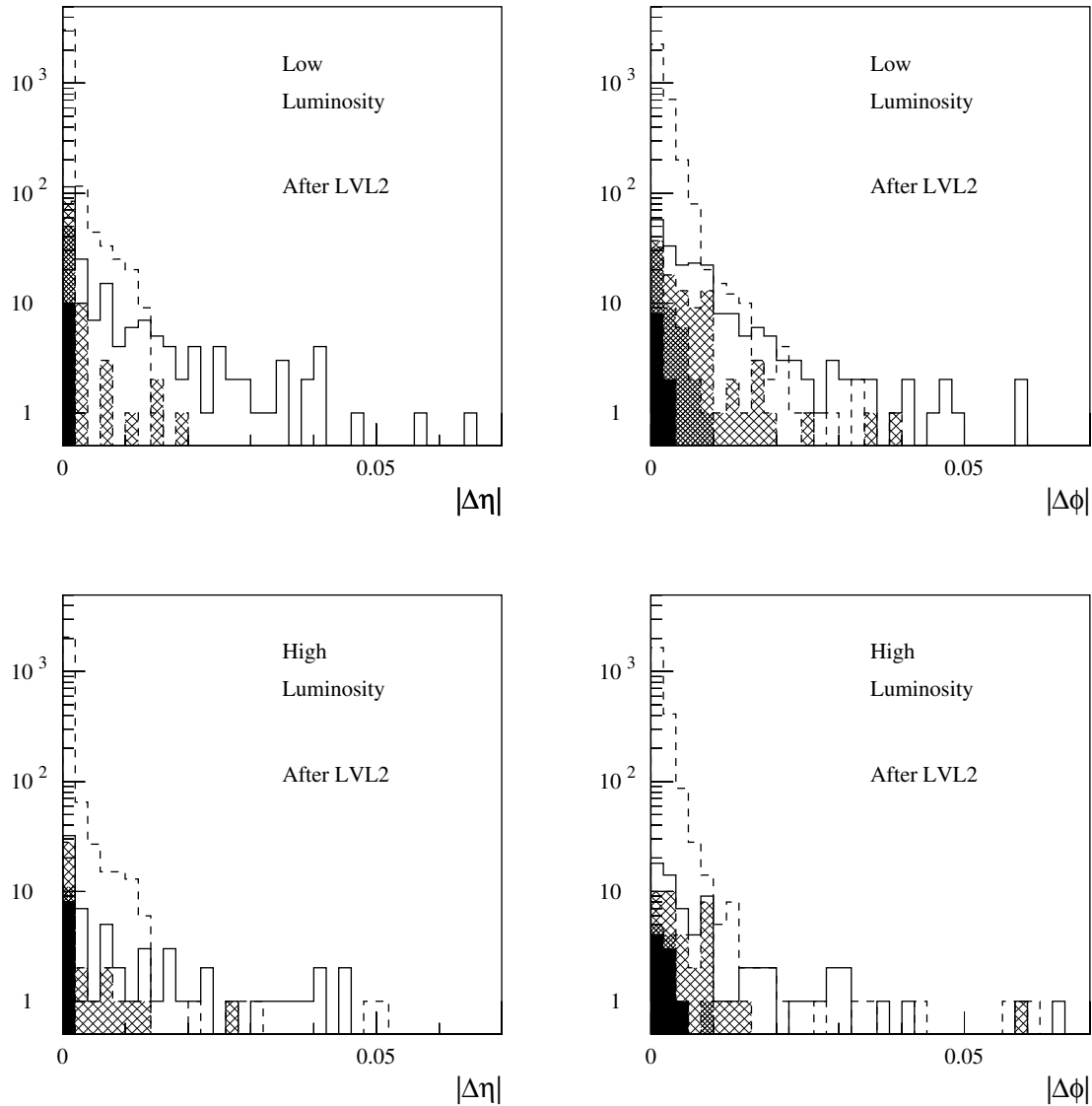
Figure 7-27 Angular matching between charged tracks and EM clusters in pseudorapidity and azimuth for electrons (dashed) and jets. For the 'jet' sample, various components are shown: electrons from *W*'s and *Z*'s (black), electrons from heavy flavour (dense hatch), conversions (light hatch) and hadrons (open). The normalisation between the single electrons and the jet sample is arbitrary.

To reduce further the charged hadron contamination, candidate electrons were required to pass the loose transition radiation cuts described in Section 3.4.1. These cuts retained 90% of the electrons and, with the available jet statistics, reduced the hadrons from 17 (6) events to 0 (1) at low (high) luminosity, consistent with expectations.

7.4.3 Summary of results

Summaries of the electron efficiencies and corresponding jet rejections resulting from the succession of cuts applied and in different pseudorapidity intervals are given in Tables 7-1 and 7-2 respectively. The electron efficiencies are determined from the high-statistics electron samples, while the jet rejection is calculated from the reductions in the jet sample but with the signal electrons explicitly excluded. To normalise the jet rejection, only jets with $E_T > 17$ (25) GeV have
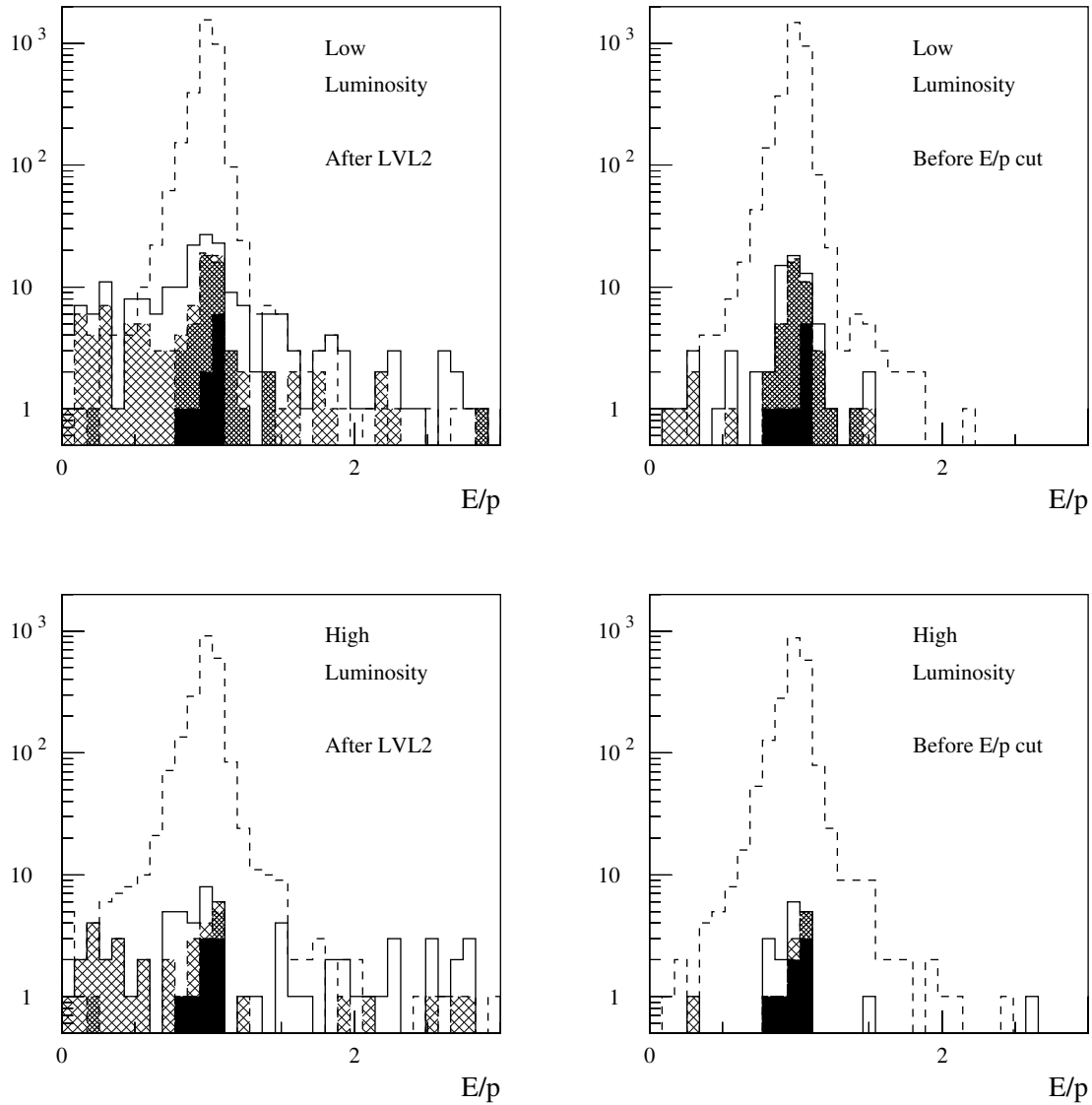
Figure 7-28 Ratio between energy of EM clusters to momentum of reconstructed charged tracks for electrons (dashed) and jets. For the 'jet' sample, various components are shown: electrons from W's and Z's (black), electrons from heavy flavour (dense hatch), conversions (light hatch) and hadrons (open). The normalisation between the single electrons and the jet sample is arbitrary.

been considered at low (high) luminosity. The final jet rejections correspond to 1 (2) events at low (high) luminosity and the values in Table 7-1 correspond to 90% confidence limits calculated according to the prescription in [7-5]. In Figure 7-29, the E_T distributions of candidates in the jet sample are shown at low and high luminosity at various stage of the offline analysis.

With the cuts described in this section, it was possible to achieve an overall electron efficiency for $p_T = 20$ GeV (30 GeV) of 68.6% (72.7%) at low luminosity. The addition of pile-up decreased the efficiency for the 30 GeV electrons down to 67.5%, which is comparable to what was achieved at low luminosity for 20 GeV electrons. A corresponding jet rejection of the order of 10^5 was obtained at both low and high luminosity. For such a large rejection factor, the results will be sensitive to the details of the fragmentation model at a level which is not well tested. Hence there may be considerable systematic uncertainties. Compared to the tabulated results (in particular, Tables 6-2 and 6-4) in the ID TDR [7], the electron efficiency has fallen by 20%

Table 7-1 Effect of different sets of cuts on electron efficiencies (p_T = 20 and 30 GeV) and jet rejections (E_T > 17 GeV and $|\eta|$ < 2.5). The cuts are described in more detail in the text. The numbers shown are the effect of the cumulative cuts, with the relative changes (percent or absolute numbers) shown in brackets.

Cuts	Low luminosity						High luminosity			
	Eff e_{20} (%)		Eff e_{30} (%)		Rej jets (10^3)		Eff e_{30} (%)		Rej jets (10^3)	
LVL1	94.0		99.0		0.08		96.1		0.09	
LVL2 Calo	90.5	(96.3)	96.9	(97.8)	0.39	(4.9)	92.1	(95.6)	0.48	(5.2)
LVL2 ID	82.5	(91.1)	87.9	(90.7)	3.5	(8.9)	82.5	(89.5)	3.7	(7.8)
Offline Calo	80.9	(98.1)	86.8	(98.6)	9.8	(2.8)	81.1	(98.3)	8.4	(2.2)
Offline ID	77.4	(93.8)	83.0	(94.5)	16.8	(1.7)	77.2	(93.6)	22.7	(2.7)
Matching	75.4	(97.5)	79.5	(95.7)	40	(2.4)	75.3	(97.4)	35.8	(1.6)
TR	68.5	(90.8)	72.7	(91.4)	>150		67.5	(89.7)	>45	

mainly because of the explicit application of the transition radiation (TR) cuts (loss of 10%), the simulation of the trigger as well as tighter Inner Detector cuts (number of TRT and pixel hits). The trigger losses can be broken down as follows: 2.3% (5.6%) due to the ID cuts in LVL2, 1.5% (1.5%) due to the calorimeter cuts in LVL2 and 2% (3%) in LVL1 at low (high) luminosity. At the same time, the rejection has increased by a factor 50 mainly because of the TR cuts and the improved calorimeter and ID cuts.

The selection procedure outlined above leads to a signal (inclusive electrons) to background (charged hadrons and conversions) ratio of more than 20 (5) for low (high) luminosity, although large uncertainties remain on the cross-sections for the different processes. The electron efficiency was cross-checked by considering the signal electrons in the inclusive jet sample. However, since the fraction of events with electrons in the sample was very small, the statistical errors are large. For electrons coming from W/Z decays, the efficiency is $(54 \pm 13)\%$ $((60 \pm 15)\%)$ and for those coming from b and c semi-leptonic decays, it is $(14 \pm 2.5)\%$ $((3.4 \pm 2.4)\%)$ for low (high) luminosity - the errors are from Monte Carlo statistics. With the statistics used, it was not meaningful to analyse the background events because there were so few. At low luminosity, all that remained was one conversion; at high luminosity, there was one conversion and one mis-identified hadron.

7.5 Photon measurements

The most demanding requirements for excellent photon measurement and identification arise from the search for a possible Standard Model Higgs boson in the mass range from the LEP limit to 130 GeV. In this mass region, the most promising discovery channel for the Higgs boson is its rare decay to two photons. The signal ($\sigma \sim 50$ fb) has to be observed above large backgrounds and the observed width will be dominated by the energy resolution. Photon reconstruction is mainly based on the information from the EM Calorimeter and is described extensively in Chapter 4. Because of the significant amount of material in front of the calorimeters, many of the photons are converted. Since the $H \rightarrow \gamma\gamma$ signal is small, it is essential to ensure high efficiency, and consequently to recover the conversions. The Inner Detector helps to reconstruct these converted photons and to veto tracks around an EM cluster. The available information can improve the energy measurement as well as the photon identification power.
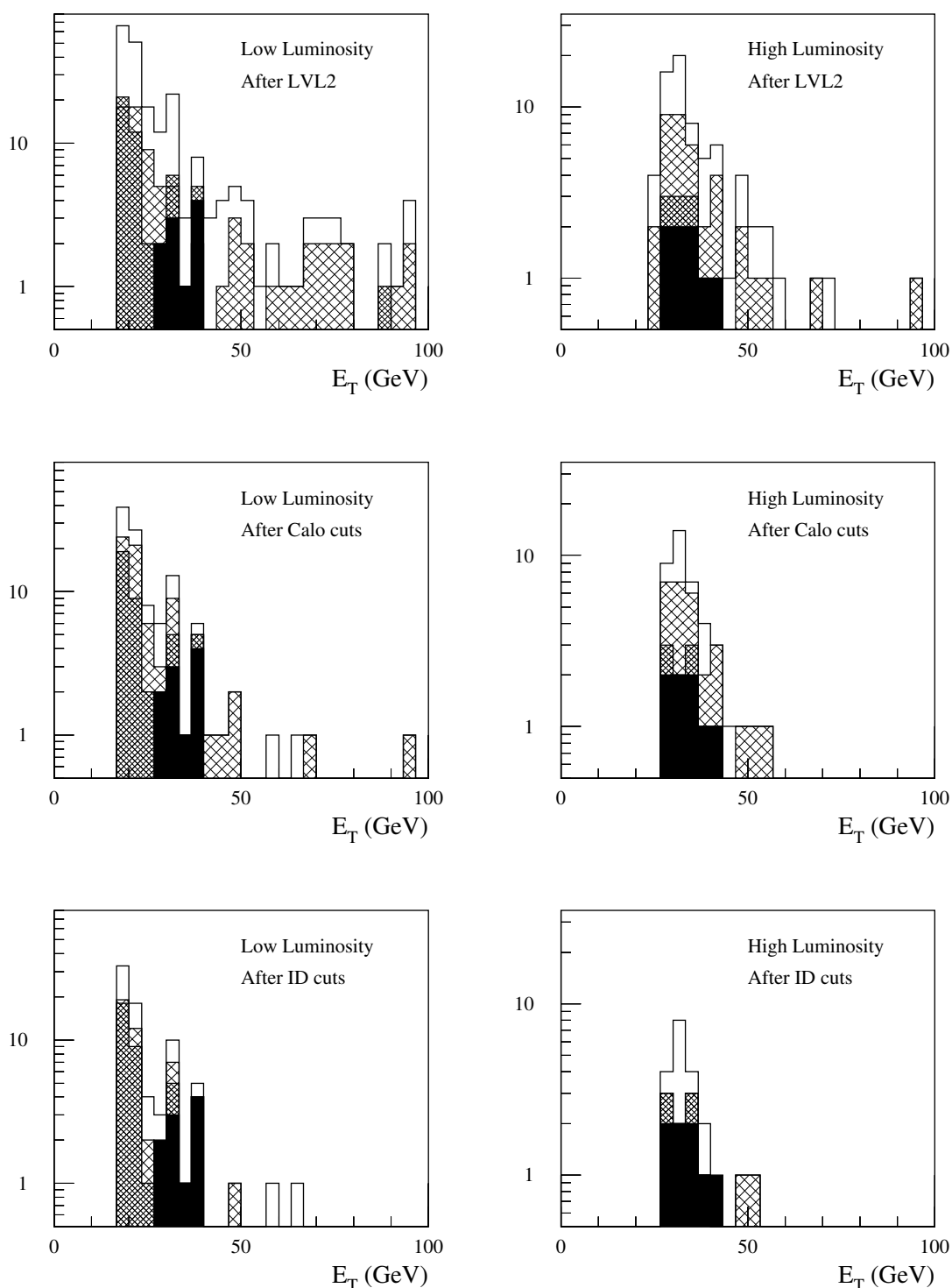
Figure 7-29 E_T distribution for the jet sample at various stages of the analysis both at low and high luminosity. For the 'jet' sample, various components are shown: electrons from W's and Z's (black), electrons from heavy flavour (dark hatch), conversions (light hatch) and hadrons (open).

Table 7-2 Electron efficiencies (p_T = 20 and 30 GeV) after all cuts as a function of pseudorapidity.

Pseudorapidity	Low Luminosity		High Luminosity
	Eff e_{20} (%)	Eff e_{30} (%)	Eff e_{30} (%)
0.0 - 0.7	74.7 ± 1.3	75.0 ± 1.4	70.6 ± 1.6
0.7 - 1.37	68.0 ± 1.4	72.6 ± 1.4	68.4 ± 1.7
1.37 - 1.52	45.3 ± 3.3	49.0 ± 3.4	40.4 ± 3.9
1.52 - 2.0	64.3 ± 1.7	75.2 ± 1.7	65.1 ± 2.1
2.0 - 2.5	71.6 ± 1.6	74.3 ± 1.7	72.8 ± 2.1

Around 30% of all photons convert in the material of the ID cavity (R < 115 cm). Figure 7-30 shows that around 75% of these conversions occur in the volume (R < 80 cm, $|z|$ < 280 cm) in which they can be efficiently identified. Depending on the pseudorapidity, the conversion fraction within this volume varies between 15% and 30%. Conversions occurring outside this region are less harmful because the electrons do not bend much in the azimuthal direction before entering the EM Calorimeter, and hence look more like unconverted photons.
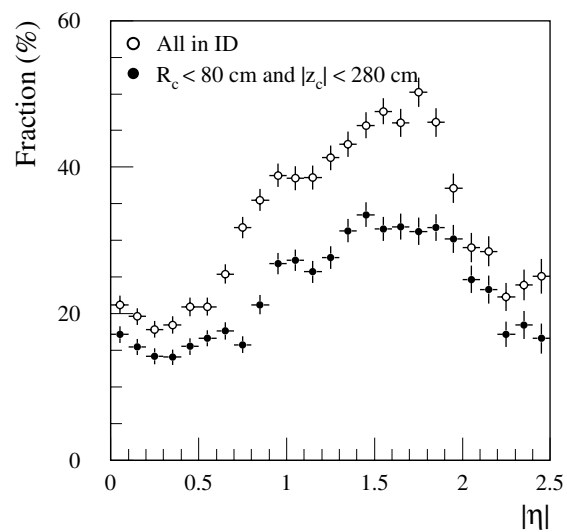
Figure 7-30 Fraction of photons converted in the ID cavity (open symbols) and in the region in which conversions can be efficiently identified (closed symbols) as a function of pseudorapidity.

7.5.1 Conversion reconstruction

7.5.1.1 Methods

Conversions are found by the program xConver which combines pairs of oppositely charged tracks [7-7]. For early conversions (R < 40 cm), both tracks can be reconstructed by xKalman (see Section 3.1.2), provided the minimum number of silicon hits on a track is relaxed to 4 (corresponding to the two outmost SCT layers). For later conversions (R > 40 cm), xKalman fails to reconstruct the tracks because insufficient silicon hits are available and because the histogramming method used to find the TRT track seed fails.

To maintain efficiency for later conversions which take place in the TRT, an algorithm, xHouRec [7-7], was written specifically to find tracks from conversions. This histogramming algorithm generalises the xKalman histogramming by scanning for tracks in the (ϕ, κ, R_c) space (xKalman histogramming assumes R_c = 0), where ϕ is the azimuthal angle at the point of closest approach to x = 0, y = 0; κ is the signed curvature; and R_c is the radius of the conversion. The track candidate is assumed to point to the interaction region from the radius R_c. In the absence of silicon hits, there is no information on the track in pseudorapidity.

A search is made by xConver for pairs of oppositely charged tracks with $p_T > 0.5$ GeV reconstructed from either algorithm (xKalman or xHouRec). A preselection is made on the basis of the separation of the tracks in the bending plane at the radius of their innermost hits. A χ^2 fit is performed using the parameters of the two tracks with the constraints of a common vertex in 3D, a zero opening angle between the tracks, and the pointing of the reconstructed photon to the beam-line.

In case more than one conversion is reconstructed in the search region, the combination with highest photon p_T is chosen. A conversion identified by xHouRec tracks is only considered if no conversion is found using tracks reconstructed by xKalman.

7.5.1.2 Reconstruction efficiency

Figure 7-31 shows that the reconstructed momentum of a converted photon is measured better for those photons which convert early ($R < 40$ cm) as opposed to the later conversions ($R > 40$ cm). The inclusion of hits in the silicon detectors and the larger track length in the magnetic field improve the p_T resolution significantly. The low energy tails in the distribution of p_T/p_T^{gen} are due to instances of hard bremsstrahlung.

The conversion reconstruction was studied for photons from $H \to \gamma\gamma$ decays with $m_H = 100$ GeV. The overall reconstruction efficiency at low luminosity was $(86.4 \pm 0.4)\%$ per photon after the kinematical cuts ($|\eta| < 2.5$, $E_T(\gamma_1) > 40$ GeV, $E_T(\gamma_2) > 25$ GeV). This efficiency was normalised to the number of converted photons with a conversion radius $R_c < 80$ cm and a z-component of $|z_c| < 280$ cm at the generator level. Figure 7-32 demonstrates that the dependence on the conversion radius is small. The figure also shows that at low radii, conversions can be

Figure 7-31 Reconstructed transverse momentum of conversions divided by the true transverse momentum for photons from Higgs events for conversions in which the two tracks are found by xKalman (solid) and by xHouRec (dashed). The distributions are normalised to unit area.

identified by combining xKalman tracks and for higher radii, by combining xHouRec tracks. In total, around 60% of all identified conversions were reconstructed by xHouRec tracks. The reconstruction efficiency was fairly independent of pseudorapidity (see Figure 7-33) with the exception of the transition region between the barrel and end-cap TRT, where xHouRec was inefficient.

At high luminosity, fake conversions arise from combinatorial background. The fake rate is pseudorapidity dependent and below 1% [7-7]. These fake conversions typically have a p_T of 1 or 2 GeV, which is much less than the p_T typical of a converted photon from a signal event and hence, the fakes can be suppressed easily.

Figure 7-32 Efficiency (solid circles) for reconstructing converted photons from Higgs decays as a function of the conversion radius R_c. The contributions of conversions identified by xKalman tracks (early conversions) and by xHouRec tracks (late conversions) are shown separately.
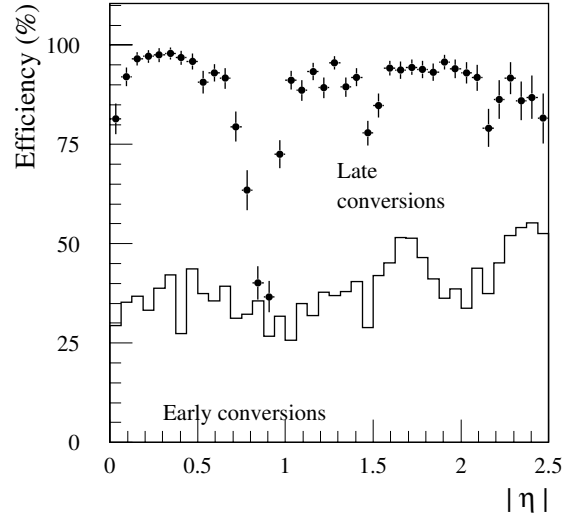
Figure 7-33 Efficiency (solid circles) for reconstructing converted photons from Higgs decays as a function of pseudorapidity. The contributions of conversions identified by xKalman tracks (early conversions - lower band) and by xHouRec tracks (late conversions - upper band) are shown separately.

7.5.2 Combined energy measurement using the EM Calorimeter and ID

Figure 7-34 shows that the energy deposited by a photon in a 3×5 window of the EM Calorimeter exhibits large tails on the low energy side because of conversions occurring in the ID. The size of the tails, defined as the fraction of events outside 0.95–1.05 of the true energy, is shown in Figure 7-35 for 20 GeV E_T photons. For unconverted photons, the tails are at the level of a few percent, apart from the crack regions where the energy resolution degrades. For converted photons, the amount of tails is more than 30% for $|\eta| < 1.8$, decreasing at higher rapidities as the ID material and the integrated magnetic field decrease.

In the Calorimeter Performance TDR [7-8], the tails were reduced by using a 3×7 window for converted photons, with the conversion being identified from the Monte Carlo truth information and corrected by the conversion finding efficiency. In the study presented here, full simulation and reconstruction of the ID and EM Calorimeter were used.

Local energy maxima were searched for in the EM Calorimeter, with $E_T > 2$ GeV. With this energy threshold, ~6×10⁻³ clusters per event due to electronic noise and pile-up in the EM Calorimeter were found in a window of $\Delta\eta \times \Delta\phi = 0.1 \times 0.1$ at high luminosity. The probability to lose a photon was less than 0.1% for $E_T > 10$ GeV and the probability to reconstruct two clusters for a single photon was maximal at $E_T \sim 10$ GeV, $|\eta| = 1.7$, and was about 4%.
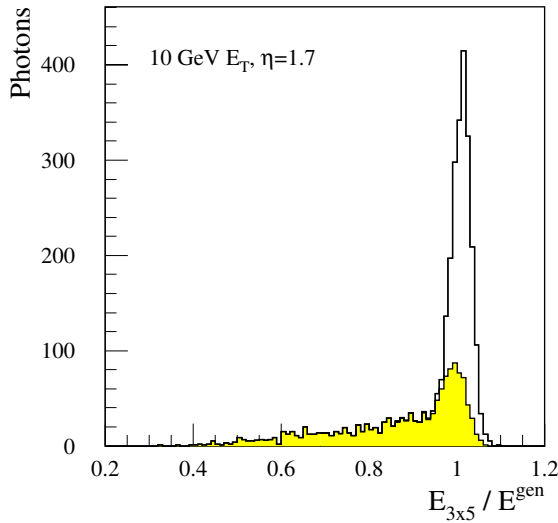
Figure 7-34 Energy in a 3×5 window divided by the true energy for all photons (histogram) and for converted photons (grey histogram).
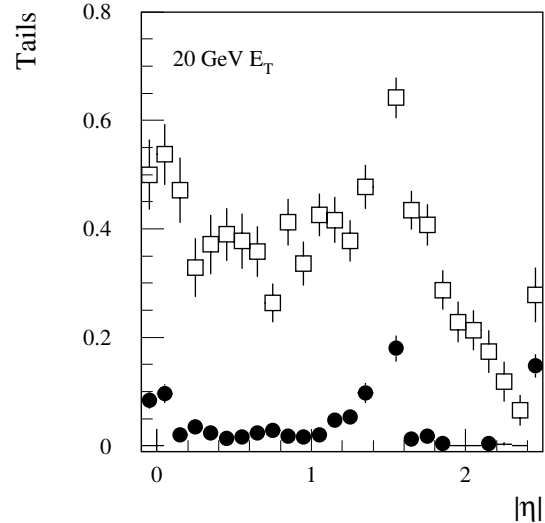
Figure 7-35 Fraction of tails for 20 GeV E_T photons, as a function of pseudorapidity, for non converted photons (black dots) and converted ones (open squares).

When a conversion was found in the ID, a 3×7 window was used in the EM Calorimeter. Figure 7-36 shows the fraction of energy reconstructed in such a window (for converted photons), as a function of the conversion radius and the transverse energy of the photon. A calibration which depends on E_T and R_{conv} was applied (using reconstructed quantities), and which, to first order, was independent of $|\eta|$. In addition, the transverse momentum of the conversion measured in the ID was combined with the corrected calorimeter energy, leading to a reduction in the tails and an improved energy resolution for photons below 20 GeV E_T.
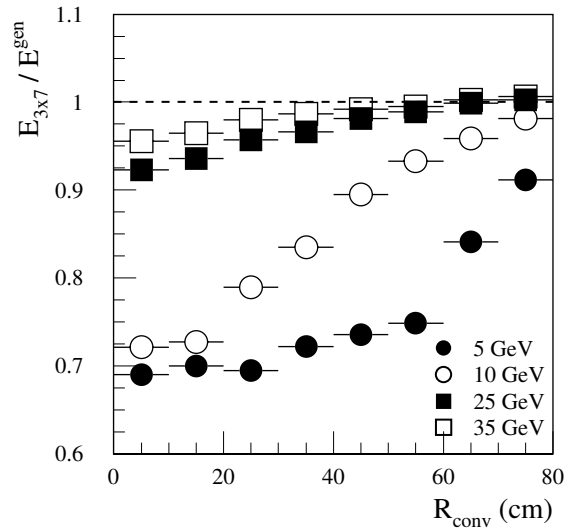
Figure 7-36 Energy in a 3×7 window versus conversion radius, for photons with a reconstructed conversion.

Figure 7-37 shows how the energy distribution was improved for 10 GeV E_T converted photons at $|\eta| = 1.7$ by using this algorithm. The distribution was well centred at 1, and the fraction of events outside 0.95–1.05 was reduced by 20% for $|\eta| < 1.8$ and $E_T < 35$ GeV. As shown in Figure 7-38, the energy resolution is improved by almost a factor two in the absence of electronic noise or pile-up. When they were included, there was still an improvement in the energy resolution, even at low energies, but it was quite small.
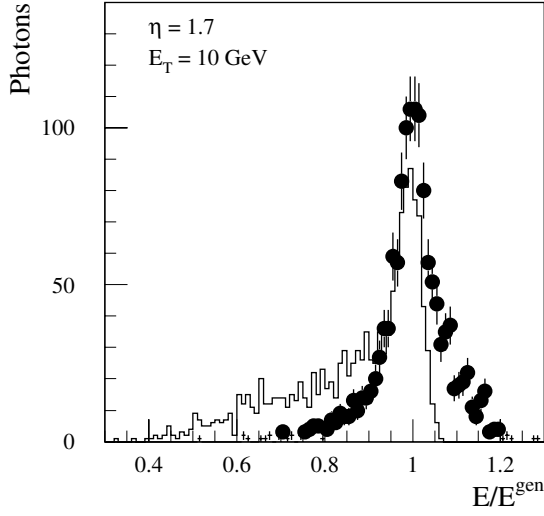
Figure 7-37 Energy distribution for converted photons using a 3×5 window (histogram) and using the EM Calorimeter and ID information (dots).
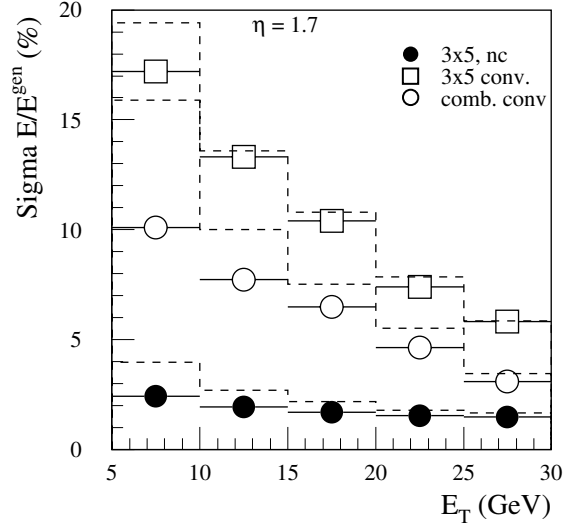
Figure 7-38 Energy resolution for unconverted photons (black dots), converted photons using a 3×5 window (open squares) and converted photons combining the EM Calorimeter and ID information (open circles). The dashed histograms show the values when electronic noise and pile-up in the EM Calorimeter at high luminosity were included.

7.6 Photon/jet separation

7.6.1 Introduction

In this section, the photon/jet separation is presented over the full pseudorapidity range used for precision physics ($|\eta| \leq 1.37$ and $1.52 \leq |\eta| \leq 2.47$) both at low and high luminosity. The separation relies mainly on the analysis of the shower shape in the EM Calorimeter. Some further optimisation can be achieved by reconstructing converted photons in the ID (see Section 7.5.1) and using a track veto. Further information can be found in reference [7-4].

The jet sample ($p_T > 17\,\text{GeV}$) described in Section 7.4.1.1 was used. In addition, a similar jet sample of 10^6 dijet events with parton $p_T > 35\,\text{GeV}$ was used. After the application of the LVL1 trigger simulation, the total jet rejection was approximately 80, while the photon efficiency was nearly 100%. In this study, the performance for single objects (photons or jets) was considered. The LVL1 simulation was based on the EM20I object (see Section 11.7.3) associated with a nominal 20 GeV threshold. At high luminosity, the nominal single isolated EM cluster threshold is 30 GeV. However, $H \rightarrow \gamma\gamma$ events may still be selected with the double cluster trigger 2×EM20I. Hence for both low and high luminosity studies, the nominal 20 GeV threshold was used for LVL1 calorimeter trigger. To determine the photon efficiencies, a sample of 10^4 $H \rightarrow \gamma\gamma$ events ($|\eta| < 2.5$, $E_T(\gamma_1) > 40\,\text{GeV}$, $E_T(\gamma_2) > 25\,\text{GeV}$) was used.

7.6.2 Analysis

Photons can be identified by analysing the leakage of EM showers into the Hadronic Calorimeter and the shower shape seen in the first and second compartments of the EM Calorimeter. This analysis can be performed separately for converted and unconverted photons. In this analysis, the cuts were designed to achieve an 80% photon efficiency, independent of E_T and pseudorapidity.

7.6.2.1 Offline calorimeter selection

The quantities used for photon identification were the same as used for electron identification (see Section 7.4.2.1). Energetic photons tend to shower later than a jet consisting of several photons, where there is a higher chance that one of the photons will initiate an early shower. To be able to use cuts on the shower profile within the first compartment, it was required that the fraction of EM energy in this compartment exceeded 0.005. Clusters failing this cut were classified as photons.

In addition to the variables used for electron/jet separation, the shower shape in the azimuthal direction in the second compartment of the calorimeter helps to distinguish between photons and jets. Figure 7-39 shows the ratio of energy deposited in a 3×3 window divided by the energy deposited in a 3×7 window in the second compartment $E_2(3\times3)/E_2(3\times7)$. The isolation in the azimuthal direction was worse than was seen in pseudorapidity because the electrons from a conversion bend in the magnetic field in the ID volume.

The cuts in the EM Calorimeter used for photon/jet separation were optimised, using the ID information to identify converted photons (see Section 7.5.1). In particular, this led to improvements associated with the cuts on the ratio $E_2(3\times3)/E_2(3\times7)$ measured in the second compartment and on the corrected width in the first compartment using the three central strips.

7.6.2.2 Offline Inner Detector selection

To ensure that reconstructed conversions were consistent with coming from single photons, the momentum of the reconstructed conversion in the ID was compared with the energy measured in the EM Calorimeter. This was particularly useful for removing π^0 decays where one of the photons had converted but the second had not. For reconstructed conversions at low luminosity, it was required that $p/E > 0.6$ (0.4) for early (late) conversions. These cuts were not applied at high luminosity since the proximity to signal photons of low energy background or fake conversions would cause a significant efficiency loss. The p/E distribution is shown in Figure 7-40 for low luminosity. The photons which were lost arose mainly from conversions in which one or both of the electrons underwent bremsstrahlung causing the tracks to be poorly reconstructed. Since events containing these photons tend to end up in the tails of distributions, if they are not removed at this stage, they are likely to removed by subsequent analysis cuts.

To achieve a further improvement in the photon/jet separation, a track veto was applied. In the case where no conversion was identified satisfying the cut on p/E, an EM cluster was retained provided there was no track associated ($|\Delta\eta| < 0.1$, $|\Delta\phi| < 0.2$) which passed the ID quality cuts and had $p_T > 5$ GeV. This p_T threshold ensured that even at high luminosity, a high photon efficiency was maintained.
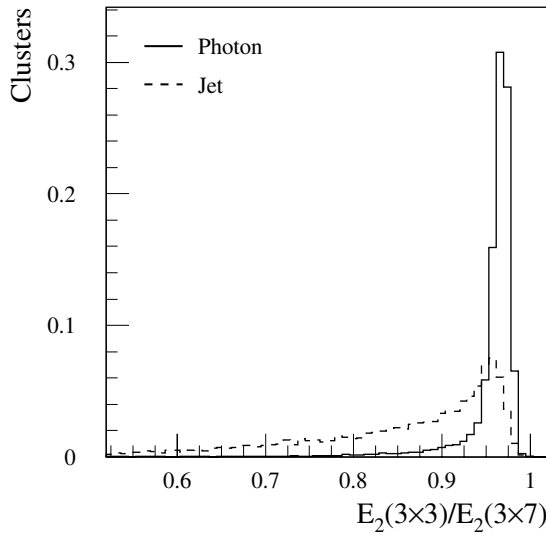
Figure 7-39 Distribution showing the azimuthal shape for photons from $H \to \gamma\gamma$ and jets. The distributions are normalised to unit area.
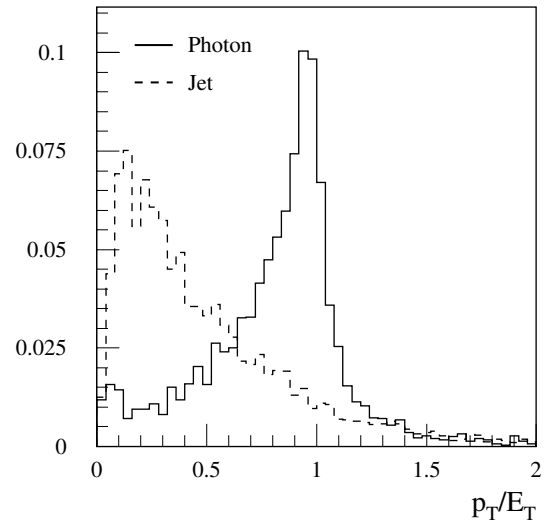
Figure 7-40 Ratio of the p_T of a conversion reconstructed in the ID to the E_T measured in the EM Calorimeter for converted photons from $H \to \gamma\gamma$ and for jets. The distributions are normalised to unit area.

7.6.3 Results

The jet rejection was tuned for an efficiency of ~80% at all E_T's for photons from $H \to \gamma\gamma$ events. Photon identification is based mainly on calorimeter information, hence tighter constraints for the calorimeter quantities were applied than those used for electron/jet separation. As was discussed for the electron/jet separation, these variables are pseudorapidity dependent and were optimised in the same pseudorapidity intervals. The transition region between the barrel and end-cap calorimeters and the region $|\eta| > 2.47$ were excluded (see Section 7.4.2.1).

Table 7-3 Effect of different sets of cuts on photon efficiencies (from $H \to \gamma\gamma$, with $m_H = 100$ GeV, $|\eta| < 2.5$, $E_T(\gamma_1) > 40$ GeV, $E_T(\gamma_2) > 25$ GeV) and jet rejections ($E_T > 17$ GeV and $|\eta| < 2.5$). The cuts are described in more detail in the text. The numbers shown are the effect of the cumulative cuts, with the relative changes (percent or absolute numbers) shown in brackets. The transition between the barrel and the end-cap is excluded.

Cuts	Low luminosity						High luminosity			
	Eff γ (%)		Rej jets $E_T \approx 20$ GeV		Rej jets $E_T \approx 40$ GeV		Eff γ (%)		Rej jets $E_T \approx 20$ GeV	
LVL1	100.0		76		210		99.2		74	
Had Calo	95.7	(95.7)	130	(1.8)	430	(2.0)	94.9	(95.7)	110	(1.5)
2nd Compart.	90.2	(94.3)	390	(2.9)	1220	(2.8)	89.7	(94.5)	300	(2.7)
1st Compart.	85.7	(95.0)	1050	(2.7)	2700	(2.2)	84.0	(93.6)	840	(2.8)
p/E for Conv. γ	84.4	(98.5)	1170	(1.1)	2700	(1.0)				
Track veto	83.0	(98.3)	1270	(1.1)	2900	(1.1)	83.1	(98.9)	910	(1.1)

The jet rejection after the different cuts are shown in Table 7-3 for low and high luminosity. The rejections are normalised to the total number of jets with $E_T > 17$ GeV reconstructed at particle level using the fast simulation program ATLFAST [7-9]. The variables used for the calorimeter cuts are correlated, and hence the actual rejections obtained with each cut depend on the order of the cuts. The jet rejections as a function of the jet E_T are shown in Figure 7-41. A total jet rejection of 1270 ± 80 (910 ± 50) is achieved at low (high) luminosity for jets with E_T around 20 GeV - the errors are from Monte Carlo statistics. For jets with E_T around 40 GeV, the rejection is 2900 ± 300 (3100 ± 800). These rejections are a factor of ~2 less than reported in [7-8] due to the normalisation using ATLFAST - see Section 7.4.1. The corresponding photon efficiencies as a func-

Figure 7-41 Jet rejection after photon selection cuts as a function of jet E_T for low and high luminosity.

tion of rapidity for $H \rightarrow \gamma\gamma$ with $m_H = 100$ GeV are shown in Figures 7-42 and 7-43. The average efficiencies are $(83.0 \pm 0.3)\%$ $((83.1 \pm 0.6)\%)$ at low (high) luminosity. The cuts applied tended to reject more converted than unconverted photons, which is due mainly to the cut on the isolation in azimuth in the second compartment and the corrected width in the first compartment. After all the cuts, the composition of the jet sample was: 55% (31%) photons from π^0, η, η', ω (dominated by isolated π^0's), 18% (33%) photons from quark bremsstrahlung, 6% (5%) from neutral hadrons and 21% (31%) direct photons (which should be considered as a signal) for E_T around 20 GeV (40 GeV). More details of the breakdown after each set of cuts can be found in reference [7-4].

Figure 7-42 Photon efficiencies for photons from $H \rightarrow \gamma\gamma$ with $m_H = 100$ GeV at low luminosity as a function of pseudorapidity. The photon efficiencies are shown for unconverted (dashed line) and converted photons (dotted line). Events in the crack $(1.37 < |\eta| < 1.52)$ are not used.
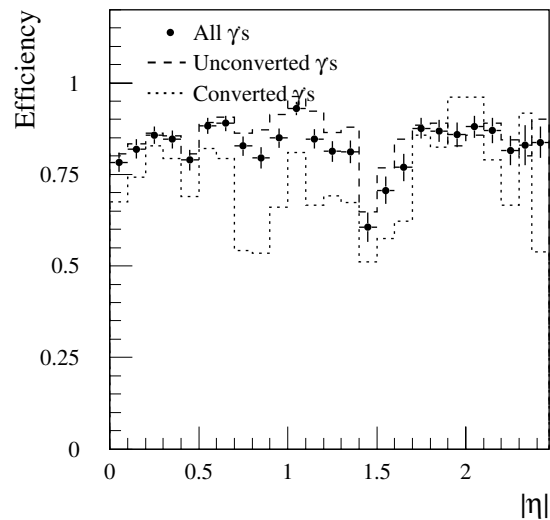
Figure 7-43 Photon efficiencies for photons from $H \rightarrow \gamma\gamma$ with $m_H = 100$ GeV at high luminosity as a function of pseudorapidity. The photon efficiencies are shown for unconverted (dashed line) and converted photons (dotted line). Events in the crack $(1.37 < |\eta| < 1.52)$ are not used.

If the LVL2 photon trigger (see Section 11.4.3) was applied in addition to the offline analysis, only 0.06% (0.3%) of the Higgs events which otherwise would be accepted by the offline analysis were rejected by the trigger at low (high) luminosity. The photon identification variables used in the trigger correspond to a subset of those used in the offline analysis, but with much looser cuts and slightly different definitions for the clusters.

7.7 Photon/electron separation

Photon/electron separation for $E_T \sim 40$ GeV is essential for the $H \rightarrow \gamma\gamma$ search when the Higgs boson mass is close to the Z mass (this is now close to being ruled out for a Standard Model Higgs). If electrons are mis-identified as photons, the large Z cross-section at resonance can result in a significant background to the Higgs boson. To enable the $\gamma\gamma$ signal to be seen, an electron rejection of ≥500 is needed to reduce the background to 10% of the signal. An electron may be mis-identified as a photon if the electron track is not reconstructed because of inefficiencies in the ID or in the case of very hard bremsstrahlung in the first few layers of the ID. For example, 0.8% of 40 GeV electrons have less than 0.5 GeV when entering the TRT. While it is essential to reduce the electron mis-identification, it is important not to lose too much in photon efficiency, since the photons have a significant conversion probability. A photon may be mis-identified as an electron if it converts early in the detector and only one track is seen, or if a fake or unrelated track points by chance to the corresponding EM cluster.

To ensure a high rejection of electrons, an algorithm was developed which used two separate pattern recognition programs in the ID. This enabled the weaknesses of one program to be compensated by the other, and vice versa. The performance of the algorithm was measured on samples of $H \rightarrow \gamma\gamma$ events with and without high luminosity pile-up and a high statistics sample of $Z \rightarrow ee$ events without pile-up. Additional cross-checks were performed on single electrons both with and without pile-up at high luminosity. This study [7-10] was limited to the fiducial region defined in Section 7.6.2 and to the p_T-range of interest: 25 GeV–100 GeV. Photons were required to satisfy the criteria given in Section 7.6.2, but without the track veto.

7.7.1 Calorimeter reconstruction and matching to the ID

The starting point for the analysis was a 3×7 cluster in the EM Calorimeter. Tracks were searched for in a fairly large cone $\Delta\eta = \pm0.1$, $\Delta\phi = \pm0.1$ centred on the direction of the cluster, and the direction of each track found was compared with the position of the cluster. The electron direction measured by the cluster was corrected as described in Section 7.2.2.4. A track was considered as pointing to the cluster if $\Delta\eta < 0.01$ and $\Delta\phi < 0.02$ for a PixlRec track. The window used for xKalman was half the size and for both algorithms it was scaled by a factor $40/E_T$ for E_T less than 40 GeV.

7.7.2 Inner Detector reconstruction

Two complementary pattern recognition programs were used for track reconstruction. Bremsstrahlung recovery was performed in the ID using the ID information alone and not the EM cluster position (see Section 7.2.1.1). The first one, xKalman (see Section 3.1.2) is relatively immune to silicon detector inefficiencies since it is based on TRT hits and is extrapolated to the silicon detectors. However, it is sensitive to hard bremsstrahlung since this is treated as a

continuous noise term in the Kalman Filtering formalism and not as a point-like break in the track curvature. Also xKalman cannot reconstruct tracks which do not reach the TRT or do so but have $p_T < 0.5$ GeV. 2.8% of the electrons are not reconstructed satisfactorily by xKalman. xKalman tracks were selected with $p_T > 1$ GeV, less than 50% missing TRT hits, more than seven silicon hits, and impact parameter multiplied by the sign of the curvature (so that the signed parameter is positive if the beam line and helix axis lie on the same side of the track) between -15σ and $+5\sigma$ were selected.

The second pattern recognition program PixlRec (see Section 3.1.2) builds tracks layer by layer, starting from the *B*-layer. Electrons undergoing hard bremsstrahlung can be recovered, provided they reach the penultimate silicon layer. As the ultimate rejection was provided by PixlRec, less severe requirements were set on PixlRec tracks: $p_T > 1$ GeV, at least two pixel hits and at least seven silicon hits were required.

Tracks found in the search cone associated with the EM cluster were accepted only if they did not form a valid conversion using xConver (see Section 7.5.1.1) with any other opposite charge track. Tight quality cuts were applied on conversions to avoid mis-identifying as photons electrons which had undergone hard bremsstrahlung followed by conversion. xKalman conversions were required to have a χ^2 less than 40 and a p_T in excess of 70% of the E_T of the cluster. PixlRec conversion were required to have a χ^2 less than 10, a p_T between 70% and 120% of the E_T of the cluster; no track associated to a *B*-layer hit if the radius of the conversion is more than 6 cm; and no track with more than 90% of the p_T of the conversion.

7.7.3 Results

The flow of electron and photon events after the calorimeter selection is summarised in Figure 7-44. After xKalman, clusters with one associated track inconsistent with a conversion were classified as electron candidates, otherwise they were passed on to PixlRec. If the events which were passed on were subsequently reconstructed with one associated track inconsistent with a conversion, they were also classified as electron candidates - the remainder being photon candidates.

The acceptance of the algorithm for $Z \rightarrow ee$ at low luminosity was (0.19 ± 0.02)% for electrons (see Figure 7-45), hence reaching a rejection (reciprocal of efficiency) of 500, while maintaining a (96.7 ± 0.2)% photon efficiency. The performance of the algorithm was independent of luminosity for electrons, while the photon efficiency degraded to (94.4 ± 0.5)% at high luminosity (Figure 7-46). 0.02% of the electrons were wrongly assigned to a conversion. A further 0.02% were lost because final state radiation in $Z \rightarrow ee$ displaced the EM cluster away from the track. The rest were not reconstructed by either tracking algorithm, having undergone very hard bremsstrahlung. 0.5% of the photons at high luminosity had clusters which had random tracks from pile-up pointing to them. The majority of the photon efficiency loss arose from failures to tag photon conversions, which increase at high luminosity. The photon efficiency of the algorithm with respect to photons passing the track veto described in Section 7.6.2 was 97.4% at low luminosity and 95.4% at high luminosity.

Lowering the silicon layer inefficiency from the nominal 97% to 90% degraded only slightly the performance of the algorithm. Loosening some of the track quality requirements allowed the same electron rejection to be maintained above 500 while losing a further 1% photon efficiency.
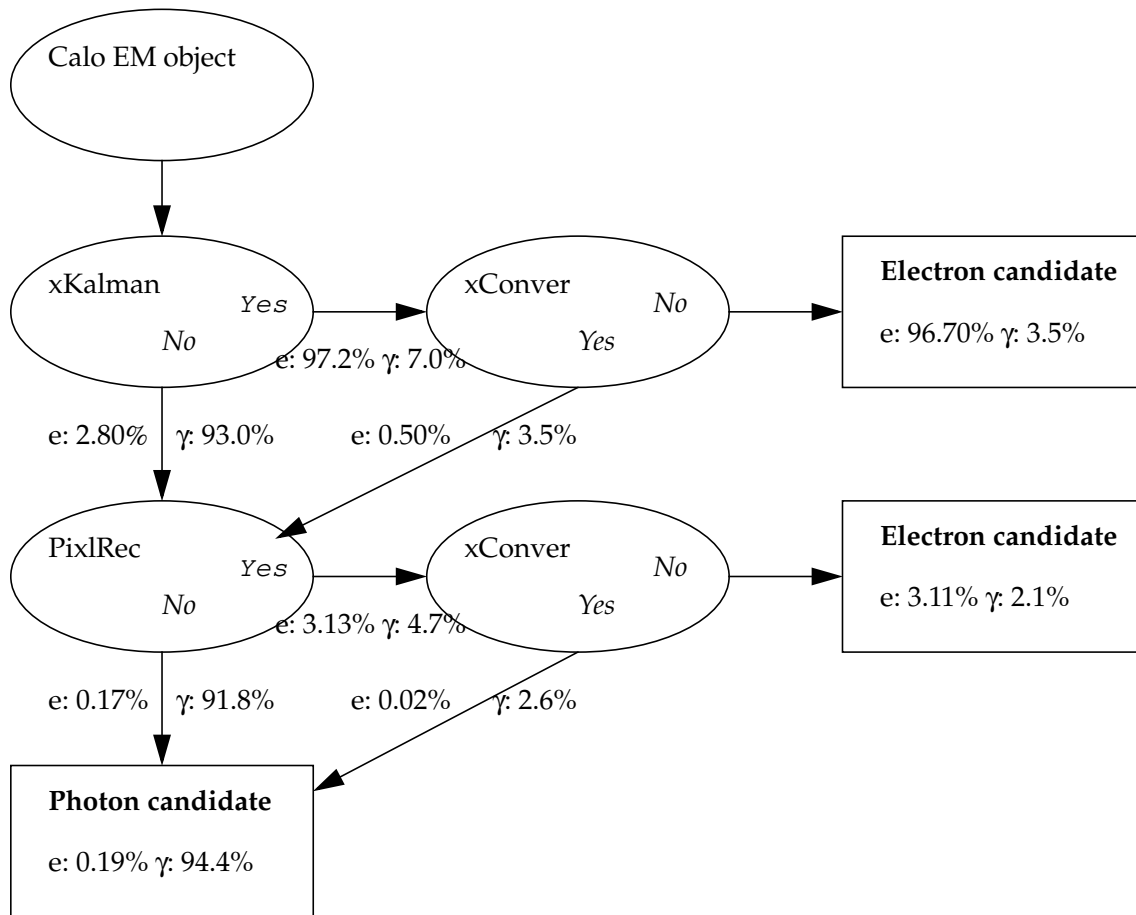
Figure 7-44 Percentages of electrons (e) from $Z \rightarrow ee$ at low luminosity and photons (γ) from $H \rightarrow \gamma\gamma$ at high luminosity which are classified as electron or photon candidates depending on whether tracks have been found ("Yes" or "No") by xKalman and then PixlRec or conversions found ("Yes" or "No") by xConver.
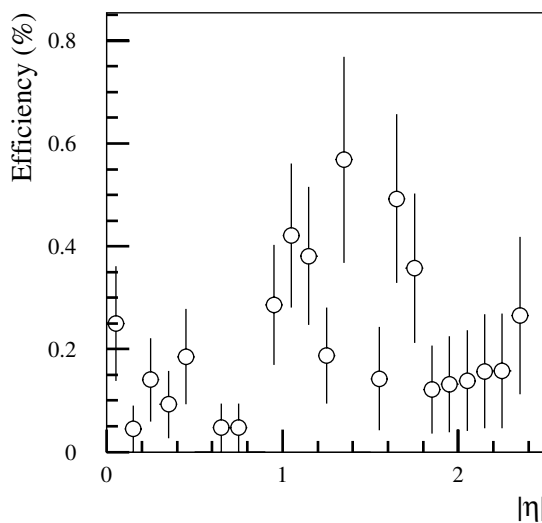
Figure 7-45 Electron efficiency measured on $Z \rightarrow ee$ events. The rejection is the reciprocal of the efficiency.
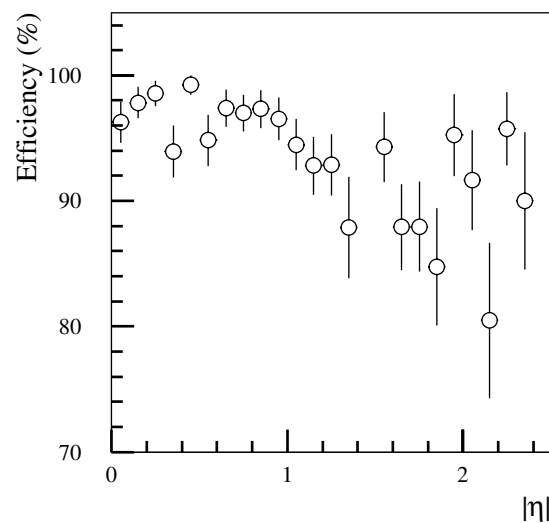
Figure 7-46 Photon efficiency measured on $H \rightarrow \gamma\gamma$ events.

The calorimetric energy of electrons which pass the photon selection is poorly measured since inevitably there is additional energy deposited outside the main EM cluster. The mass resolution of the Z resonance for the mis-identified events is 4.4 GeV (noise and pile-up not included) which is almost four times larger than that of well measured γγ pairs. Although $Z \rightarrow ee$ events misidentified as γγ pairs will form a peak in the invariant mass distribution, because the cuts described in this section reduce this background to ~10% of the signal and lead to a broader distribution, this background should have little effect on the significance of a possible signal from a low-mass Higgs boson (which lies on top of a much bigger irreducible background) (see Section 19.2.2).
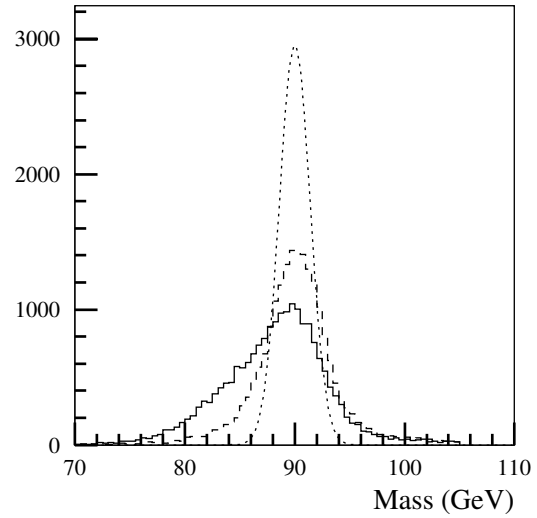
Figure 7-47 $Z \rightarrow ee$ mass resolution for all electrons (dashed), and those electrons mis-identified as photons (solid) compared to the $H \rightarrow \gamma\gamma$ mass resolution (dotted). All histograms are normalised to the same number of events.

7.8 Mass reconstruction

In this section, the mass distributions of important resonances reconstructed through their decays to electrons or photons are presented. The intention is to consider issues associated with the combined reconstruction in the Inner Detector and EM Calorimeter. Of particular concern are the effects of material, noise and their consequences for calibration.

7.8.1 $H \rightarrow \gamma\gamma$

7.8.1.1 Mass resolution

The issues associated with the reconstruction of the $H \rightarrow \gamma\gamma$ channel were discussed in detail in the Calorimeter Performance TDR [7-8]. In this section, an update is given which is based on 10 000 fully simulated $H \rightarrow \gamma\gamma$ events with $m_H = 100$ GeV, and on 10 000 events with $m_H = 130$ GeV.

The event selection required two EM clusters with one having $E_T > 40$ GeV and a second having $E_T > 25$ GeV, both within the pseudorapidity range $|\eta| < 2.4$ (chosen so that the π^0 background could be efficiently reduced). Furthermore, events with one photon pointing to the transition region between the barrel and end-cap EM Calorimeters ($\Delta\eta \sim 0.15$) were rejected. The efficiency of these cuts was 39%. The usual photon identification criteria, corresponding to an overall efficiency of 80% per photon, were then applied as described in Section 7.6.2. This results in an overall acceptance for $H \rightarrow \gamma\gamma$ events of about 25%.

The primary interaction point was reconstructed from the EM Calorimeter alone by a common vertex fit of the two photons, using the constraint provided by the beam-spot: $z = 0$, $\sigma_z = 5.6$ cm. Photon conversions were reconstructed with the xKalman, xHouRec and xConver packages with an efficiency of 80% (see Section 7.5.1.2). Precise vertex position was obtained for 60% of the conversions occurring at a radius less than 45 cm. Figure 7-48 shows the distribution of the reconstructed $\gamma\gamma$ invariant mass. The mass resolution is (1.31 ± 0.05) GeV for $m_H = 100$ GeV. The acceptance in the range of $\pm 1.4\sigma$ around the mass peak is 81% (79%) at low (high) luminosity.

Table 7-4 shows the various contributions to the Higgs mass resolution, including fully simulated pile-up noise. At low luminosity, digital filtering was applied to reduce the electronic noise. The weights are those computed

Figure 7-48   Two-photon invariant mass reconstructed in the EM Calorimeter for $H \rightarrow \gamma\gamma$ events with $m_H = 100$ GeV at high luminosity. The open histogram is for all events; the shaded histogram, for events containing at least one converted photon. The fitted curve is a Gaussian with a width of 1.31 GeV.

in the absence of pile-up, and so are independent of the cluster size [7-12]. At high luminosity, the default (hardware) electronic shaping was assumed.

Table 7-4 Breakdown of various contributions to the mass resolution (in GeV) for $H \rightarrow \gamma\gamma$ with $m_H = 100$ and 130 GeV at low and high luminosity.

	m_H = 100 GeV		m_H = 130 GeV	
	10^{33} cm^{-2}s^{-1}	10^{34} cm^{-2}s^{-1}	10^{33} cm^{-2}s^{-1}	10^{34} cm^{-2}s^{-1}
Sampling term	0.91	0.91	1.07	1.07
Constant term	0.47	0.47	0.65	0.65
Pointing	–	0.47	–	0.57
Pile-up	0.28	0.52	0.23	0.59
Electronic noise	0.19	0.42	0.27	0.42
Total	1.1	1.31	1.3	1.55

At high luminosity, the average pile-up and electronic noise per photon was 930 MeV for $m_H = 100$ GeV. There was a +20% correlation between the two photons which arises from Poisson fluctuations in the number of pile-up events as well as long-range correlations within individual events.

7.8.1.2 Use of the reconstructed primary vertex

To reconstruct the $\gamma\gamma$ mass, it is important to know the position of the primary vertex to obtain the directions of the photons. In principle, greater vertex precision could be achieved by reconstructing the vertex position in the ID when the information is available. The ID information is

fairly unambiguous at low luminosity, but care must be taken not to use the wrong vertex at high luminosity. This possibility was studied by using general assumptions about vertexing. Any vertexing algorithm can be characterised by the efficiency ε_{HV} to find the $H \to \gamma\gamma$ vertex, and by the average number N_{BV} of additional background vertices arising from the pile-up of minimum bias events. This was studied using a simple Monte Carlo simulation whereby vertices were distributed according to ε_{HV} and N_{BV} along the beam line around $z = 0$. The vertex which was closest to the calorimeter prediction was the one chosen as the candidate for the $H \to \gamma\gamma$ vertex and used to recompute the photon directions. The calorimeter pointing information reduces the risk of picking a wrong vertex, but cannot eliminate it. Figure 7-49 shows the change in the statistical significance of a Higgs signal, as a function of both ε_{HV} and N_{BV}, as compared to what would be achieved by using the EM Calorimeter alone. Large values of N_{BV} are equivalent to no ID information at all, because under such circumstances there will always be a vertex very close to the calorimeter prediction. The upper left corner of the figure, $\varepsilon_{HV} \sim 1$ and $N_{BV} \sim 0$, corresponds to the low–luminosity running.

An algorithm to find one or more primary vertices can be implemented in many ways. A very simple algorithm which proceeds in three steps was tested. First, tracks were preselected according to the track quality and a fixed cut on p_T. Then tracks were clustered to form vertices, according to their z impact parameter, until the vertex spread reached 0.5 mm. Finally vertices with less than four tracks were rejected. Figure 7-49 shows the values of ε_{HV} and N_{BV} achieved in this way, as a function of the p_T preselection cut. The results were based on 400 $H \to \gamma\gamma$ events which were fully reconstructed in the presence of pile–up in the Inner Detector. For comparison, results obtained at particle–level, which assume 100% track reconstruction efficiency over $|\eta| < 2.5$, are also shown.

The conclusion from Figure 7-49 is that the angular resolution of the EM Calorimeter is already very good and it will be difficult to enhance the significance of a possible $H \to \gamma\gamma$ signal using the reconstructed primary vertex information - even with a vastly better vertex finder. In principle, it would be possible to tag the $H \to \gamma\gamma$ vertex by using information such as the number of high-p_T tracks associated with the vertex [7-7]. However, such methods are very sensitive to possibly large systematics from the modelling of the minimum bias events and of the p_T spectrum of the Higgs boson.

7.8.2 $H \to eeee$

7.8.2.1 Signal generation and reconstruction

Two samples of fully simulated $H \to eeee$ events with $m_H = 130\,\text{GeV}$ and $m_H = 170\,\text{GeV}$ were studied. The event generation was done using PYTHIA 5.7 and PHOTOS [7-13], in order to take into account the internal bremsstrahlung (also referred to as 'final state radiation') contribution. Full simulation included electronic noise, the effect of the constant term and low or high luminosity pile-up.

Electrons were identified above 7 GeV p_T from EM clusters reconstructed in 3×7 cells associated to charged tracks with loose E/p matching. The average electron efficiency was 91%. The electron 3-momentum was obtained from a combination of track and reconstructed calorimeter information. Angles were obtained from the track, and a first estimate of the energy was obtained from the cluster, digital filtering being applied at low luminosity [7-12]. To improve the electron energy measurement using tracking information without introducing tails, the following proce-
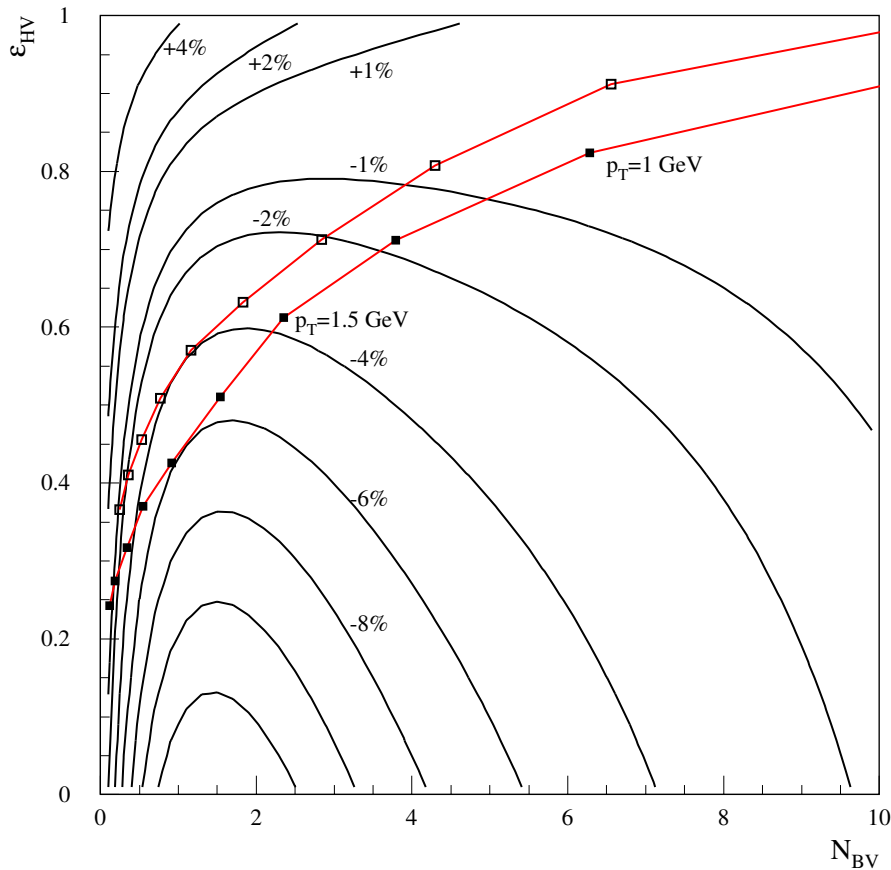
Figure 7-49 Changes in the statistical significance of a possible $H \to \gamma\gamma$ signal (m_H = 100 GeV) which could be obtained by reconstructing the primary vertex in the ID. The efficiency to reconstruct the Higgs vertex, ε_{HV}, is shown versus the number of reconstructed background vertices, N_{BV}. The contours show the change compared to using the EM Calorimeter information alone. Also shown are the results obtained for one particular vertex finding algorithm in the presence of pile-up at high luminosity, obtained with full simulation and reconstruction (black squares) and at particle-level (open squares), where the squares correspond to different p_T threshold applied in the algorithm.

dure was applied. If the track was consistent with coming from the beam-line within 3σ and had a *B*-layer hit, it was refitted using the vertex and cluster position constraint (bremsstrahlung recovery - see Section 7.2.1). If the refit was successful and the refitted p_T uncertainty less than 6%, the track p_T and its uncertainty were rescaled in such a way as to avoid biases in the estimate. If the track and cluster p_T differed by more than 3σ, the uncertainty on the track p_T was increased so that the discrepancy was exactly 3σ. Finally, a weighted mean of the track and cluster p_T was formed. This procedure enabled the p_T resolution of 60% of the electrons to be improved and was particularly effective at high luminosity.

Kinematical cuts were applied as described in Section 19.2.5, mass cuts being optimised as a function of m_H to maintain good acceptance. A Z mass constraint was applied when the mass of an electron pair was within 6 GeV of the Z mass. The constraint was imposed by minimising, as a function of the lepton momenta, a χ^2 involving the measured momenta and their uncertainties, as well as the Z mass and its natural width. This improved the Higgs mass resolution by 10%.

The mass resolution, obtained from a Gaussian fit in a window [–1.5σ,+2.5σ], was 1.54 GeV (1.97 GeV) at low luminosity (see Figures 7-50 and 7-51) and 1.81 GeV (2.17 GeV) at high luminosity for $m_H = 130$ GeV ($m_H = 170$ GeV). The acceptance in the ±2σ mass window was $(83.3 \pm 0.6)\%$ $((84.7 \pm 0.6)\%)$ at low (high) luminosity for $m_H = 130$ GeV. Similar numbers were obtained for $m_H = 170$ GeV. Using the momenta measured in the ID improved the mass resolution by 100 MeV at low luminosity and 200 MeV at high luminosity for both Higgs masses.
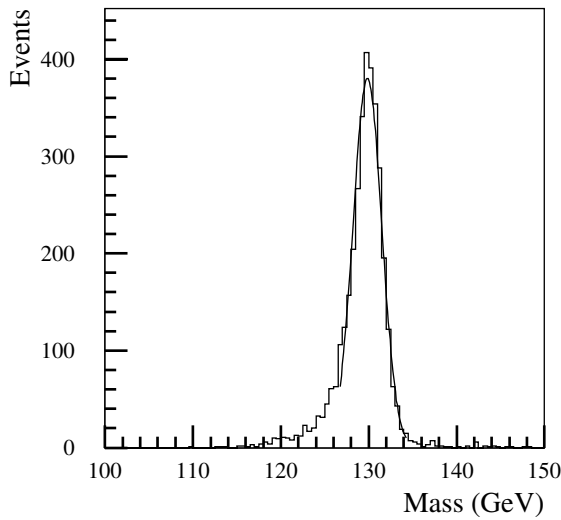
Figure 7-50 Four-electron invariant mass (low luminosity noise and pile-up included) for $m_H = 130$ GeV.
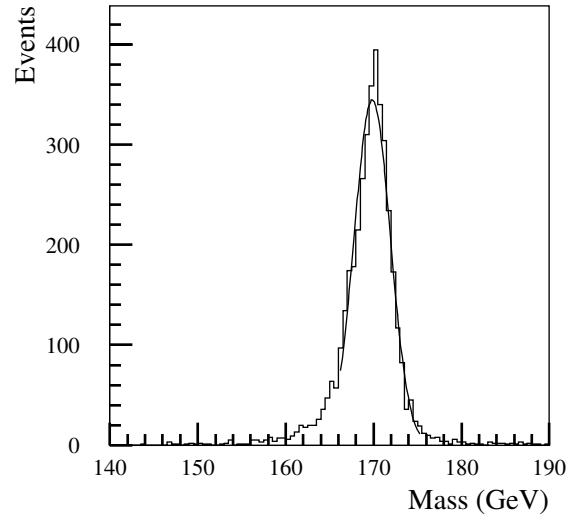
Figure 7-51 Four-electron invariant mass (low luminosity noise and pile-up included) for $m_H = 170$ GeV.

In contrast to the $H \rightarrow \gamma\gamma$ reconstruction, electrons in the crack region were used. These events had lower identification efficiency and somewhat poorer resolution: in the original ±2σ mass window, the acceptance fell by 7% while the mass resolution for these events was 100 MeV worse (see Figure 7-52). Rejecting these events with one electron in the crack would reduce the final yield in the mass window by 16%.
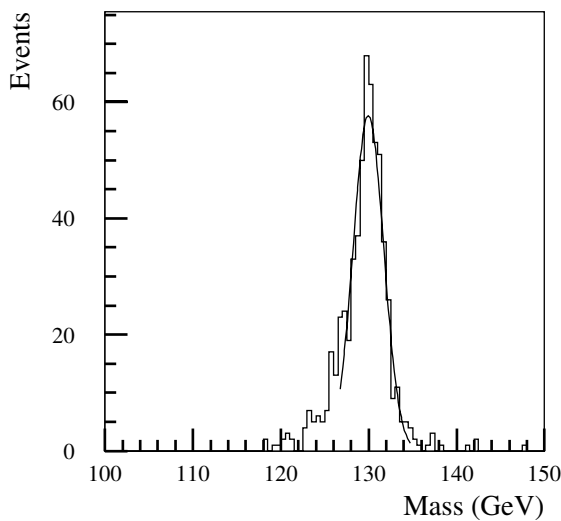
Figure 7-52 Four-electron invariant mass (low luminosity noise and pile-up included) for $m_H = 130$ GeV, at least one electron being in the crack region.
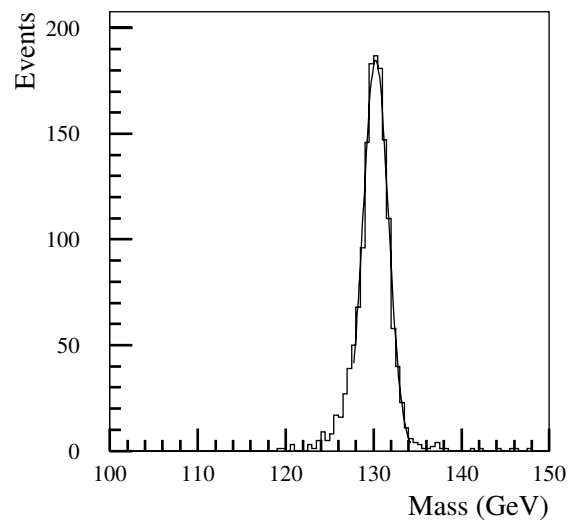
Figure 7-53 Four-electron invariant mass (low luminosity noise and pile-up included) for $m_H = 130$ GeV, without inner bremsstrahlung.

7.8.2.2 Inner bremsstrahlung contribution

When the inner bremsstrahlung contribution was considered, in most cases the emitted photon lay in the same cluster as the electron and hence the photon was taken into account automatically. For hard photons ($E_T > 5$ GeV) which were not contained in an electron cluster, their energy was added to the closest electron in ΔR [7-14] [7-15]. Inner bremsstrahlung degraded the mass resolution by 100 MeV and decreased the fraction of events in $\pm 2\sigma$ by 3%. Figure 7-53 shows the mass spectrum without inner bremsstrahlung, to be compared to Figure 7-50. In addition, the reconstruction efficiency fell by 9%, giving an overall loss of 12% in acceptance, due to the inner bremsstrahlung contribution.

7.8.2.3 Effect of material in front of the EM Calorimeter

The effect of material in front of the EM Calorimeter can be understood from studies which considered layouts where one Pixel layer or one SCT layer was removed [7-16]. These studies cannot be compared directly with the current ones because of different kinematical cuts. The effect on the acceptance in a $\pm 2\sigma$ mass window is shown in Table 7-5 (the same value of σ was used for all three layouts). While the effects of removing a layer in the ID were not huge, it can be seen that the effect of removing a Pixel layer was much more than that of an SCT layer (they are of comparable thickness), indicating that the material at low radius is the most critical.

Table 7-5 Acceptance for $H \rightarrow eeee$ ($m_H = 130$ GeV) in a $\pm 2\sigma$ mass window for the standard ID layout and reduced layouts.

	Acceptance (%)		
	Standard	**Remove SCT layer**	**Remove Pix layer**
No Inner Brem.	86.2 ± 1.5	88.3 ± 2.0	89.0 ± 1.6
All Events	81.0 ± 1.5	82.6 ± 2.0	85.1 ± 1.5

7.8.2.4 Contributions to the mass resolution

The contributions to the four electron invariant mass resolution are shown in Table 7-6. The contributions to the mass resolution are different from the $H \rightarrow \gamma\gamma$ case because of the different p_T spectra of leptons and photons. For $m_H = 130$ GeV, there is one (two) electron with p_T less than 20 GeV in 95% (46%) of the cases, while the photon p_T spectrum starts at 25 GeV in the $H \rightarrow \gamma\gamma$ decays. The acceptance in the $\pm 2\sigma$ mass window departs from the theoretical 95% because of a number of effects. At low luminosity and for $m_H = 130$ GeV, the 12% additional acceptance loss is made up of: 5% from events for which the reconstructed Z mass is more than 6 GeV from the nominal mass causing the Z mass constraint not to be applied, 3% from events with internal bremsstrahlung, 1% from events with one electron in the crack region and 3% from other effects, mainly bremsstrahlung in the Inner Detector.

7.8.3 $J/\psi \rightarrow ee$

In many collider experiments, the decays of the J/ψ and Υ are valuable for calibrating detectors, and in particular electromagnetic calorimeters (see for example [7-1]). For ATLAS, the most important physics requiring precise electron measurement will be in the tens of GeV range. For this, the copious production of $Z \rightarrow ee$ will be more suitable, as described in Chapter 4. Never-

Table 7-6 Contributions to the four electron invariant mass resolution for $H \rightarrow eeee$ ($m_H = 130$ GeV). Inner bremsstrahlung, a Z mass constraint and combined Inner Detector track and calorimeter p_T measurements are used.

Term	Contribution (GeV)	
	Low luminosity	**High luminosity**
Sampling term	1.42 ± 0.05	
Constant term	0.36	
Noise	0.44	0.65
Pile-up	0.10	0.85
Total	1.54 ± 0.06	1.81 ± 0.06

theless, it is important to cross-check the calorimeter calibration and to ensure its linearity. This can be achieved by using the lower energy electrons produced by J/ψ decays. The emphasis of the preliminary study presented in this section is on the calibration; the reconstruction of $J/\psi \rightarrow ee$ decays in the context of B physics is discussed in Section 17.2.2, where it is shown how to obtain the optimal signal using electron reconstruction and vertexing in the Inner Detector.

The $J/\psi \rightarrow ee$ final states originate mainly from $b\bar{b}$ decays, since the semi-muonic decay of the other b-quark, $b \rightarrow \mu X$, is required to fulfil the LVL1 trigger. No such trigger exists for Υ which is produced predominantly by gluon fusion. The cross-section for $pp \rightarrow b\bar{b}$ with a muon of $p_T > 6$ GeV for the LVL1 trigger and $B \rightarrow J/\psi$ with $J/\psi \rightarrow ee$ is estimated to be 2.2×10^{-4} μb [7-11]. This corresponds to a rate of 0.22 Hz at a luminosity of 10^{33} cm^{-2}s^{-1}.

An initial study was made using fully simulated $b\bar{b}$ events at low luminosity in which one B hadron was forced to decay to a muon of $p_T > 6$ GeV and the other B hadron was forced to decay to a J/ψ, which in turn was forced to decay to electrons. The electrons were identified using the method described in Section 7.3. The electron candidates were required to satisfy some basic track quality cuts, have $p_T > 0.5$ GeV and have some minimum value of the discriminating function. The invariant mass of pairs of electrons and positrons was formed using the reconstructed tracks. Candidates were selected in the mass window 2.7 to 3.2 GeV.

In the triggered events, there will be a large combinatorial background from pairs formed from Dalitz decays and conversion electrons as well as misidentified pions. It is not clear what background can be tolerated for calibration purposes. Significant improvements in the rejection will be provided by cuts which are sensitive to the B lifetime in the signal events, as shown in the J/ψ analysis in Section 17.2.2.

The J/ψ mass can be determined from the electron energies and directions. For calibration purposes, the energy will be taken from the EM Calorimeter. The directions could be taken from the more accurate measurements provided by the ID, albeit with a potential problem of biasing the ID track direction by bremsstrahlung. Figure 7-54 shows the reconstructed mass using the ID to provide track directions. The resolution is 450 MeV. Electronic noise has been included in the EM Calorimeter response and degrades the resolution by 110 MeV. Using the EM Calorimeter energy results in a lower reconstructed J/ψ mass due to energy losses, in particular those arising from bremsstrahlung where the radiated photons are not included in the main cluster.
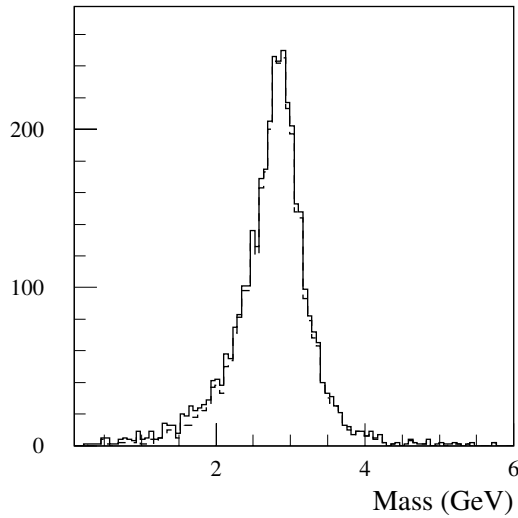
Figure 7-54 Invariant mass of *J/ψ → ee* candidates - the dashed histogram corresponds to real *J/ψ* decays. To form the mass, the energies of the electrons are taken from the EM Calorimeter and the directions from the ID.
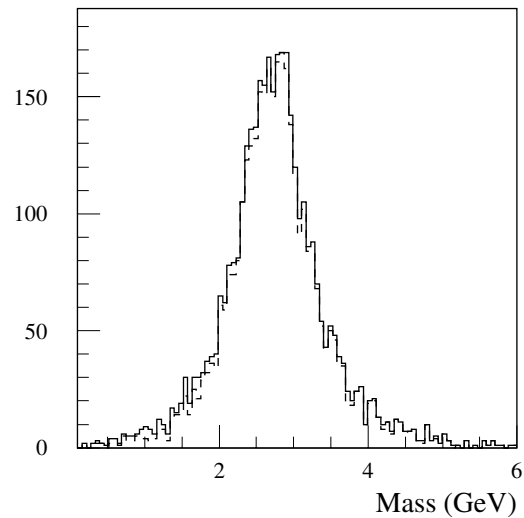
Figure 7-55 Invariant mass *J/ψ → ee* candidates - the dashed histogram corresponds to real *J/ψ* decays. To form the mass, the energies and directions of the electrons are taken from the EM Calorimeter.

One may want to determine the mass purely from the EM Calorimeter to control systematic uncertainties. Figure 7-55 shows the reconstructed mass using the EM Calorimeter only. The resolution is 600 MeV, the electronic noise contributing with 200 MeV. In one year of low luminosity running (10 fb^{-1}), one can expect 4.4×10^5 reconstructed *J/ψ → ee* decays, assuming a 20% reconstruction efficiency. With a mass resolution of ~20%, this allows a calibration of the ~400 motherboard regions ($\Delta\eta \times \Delta\phi = 0.2 \times 0.4$) of the EM Calorimeter at low energy to a statistical precision of 0.6%. Future study is needed to obtain a better understanding of the rejection of the background, the *J/ψ → ee* reconstruction efficiency and the consequences of residual combinatorial background.

7.9 Conclusions

The combination of the Inner Detector and the EM Calorimeter provides the potential to identify and measure the energy of electrons and photons in the presence of the known backgrounds. This will enable ATLAS to achieve the physics goals identified in subsequent chapters.

Electrons and photons are significantly affected by the material in front of the EM Calorimeter. Nevertheless, the effects of bremsstrahlung and conversions can be partially compensated for by a number of methods indicated in this chapter. Using *E/p* from *W → eν* events, it should be possible to calibrate the EM Calorimeter in 400 regions ($\Delta\eta \times \Delta\phi = 0.2 \times 0.4$) to 0.1% after one week of low luminosity running. In the same regions, it should be possible to calibrate at low energy using *J/ψ → ee* to 0.6% after one year, although the background remains to be studied.

Low energy electrons coming from $b \rightarrow eX$ or $J/\psi \rightarrow ee$ can be identified. At higher energies, $E_T > 20$ GeV, an electron efficiency of ~70% can be achieved with a corresponding jet rejection of $\sim 10^5$, resulting in an inclusive electron sample of electrons from W/Z decays and heavy flavour. For a photon efficiency of ~80%, a jet rejection of ~1000 (~3000) can be achieved for $E_T \approx 20$ (40) GeV - the remaining jet sample being dominated by isolated EM particles.

The mass resolution for a light Higgs boson ($m_H = 100$ GeV) decaying to two photons is 1.1 (1.3) GeV at low (high) luminosity, while the mass resolution for the four electron decay ($m_H = 130$ GeV) is 1.5 (1.8) GeV. Electrons from Z decays can be sufficiently well identified so as not to constitute a serious background to a possible nearby Higgs boson signal.

7.10 References

7-1   CDF Collaboration, Phys. Rev. **D52** (1995) 4784.

7-2   P. Pralavorio, 'Electron/Jet Separation with the ATLAS Detector', ATLAS Internal Note ATL-COM-PHYS-99-045 (1999).

7-3   A. Dell'Acqua *et al.*, '1997 ATLAS Jet Production', ATLAS Internal Note PHYS-NO-102 (1997).

7-4   M. Wielers, 'Photon Detection with the ATLAS Detector', ATLAS Internal Note ATL-COM-PHYS-99-011 (1999).

7-5   Particle Data Group, The European Physical Journal **C3** (1998) 1.

7-6   ATLAS Collaboration, Inner Detector Technical Design Report Vol. I, CERN/LHCC 97-16 (1997).

7-7   U. Egede, PhD. Thesis, Lund University LUNFD6/(NFFL-7150) (1997).

7-8   ATLAS Collaboration, Calorimeter Performance Technical Design Report, CERN/LHCC 96-40 (1996).

7-9   E. Richter-Was *et al.*, 'ATLFAST 1.0 A Package for Particle-level Analysis', ATLAS Internal Note PHYS-NO-079 (1996).

7-10   D. Rousseau, 'Electron/Photon Separation', ATLAS Internal Note INDET-NO-198 (1998).

7-11   M. Smizanska *et al.*, 'Overview of Simulations for ATLAS *B* Physics Studies in Period 1996-1999', ATLAS Internal Note ATL-COM-PHYS-99-042.

7-12   S. Simion, 'Pile-up Simulation for ATLAS Calorimeters', ATLAS Internal Note ATL-COM-SOFT-99-001 (1998).

7-13   Z. Was *et al.*, Comput. Phys. Commun. **79** (1994) 291.

7-14   O. Linossier and L. Poggioli, 'Final-state Inner-bremsstrahlung Effects on $H \rightarrow ZZ^* \rightarrow 4l$ with ATLAS', ATLAS Internal Note PHYS-NO-75 (1995).

7-15   O. Linossier and L. Poggioli, '$H \rightarrow ZZ^* \rightarrow 4l$ Channel in ATLAS', ATLAS Internal Note PHYS-NO-101 (1997).

7-16   D. Barberis *et al.*, 'A Comparative Study of Reduced Layouts of the ATLAS Inner Detector', ATLAS Internal Note INDET-NO-188 (1997).

8 Muon identification and measurements

A robust muon identification and high precision momentum measurement is crucial to fully exploit the physics potential of the LHC. The muon energy of physics interest ranges over a large interval from a few GeV, *e.g.* for *B*-physics studies (see Chapter 17), up to a few TeV, where one might expect the presence of new physics (see *e.g.* Chapter 21).

From the point of view of muon detection, the ATLAS apparatus is characterised by two high precision tracking systems, namely the Inner Detector and the Muon System, and a thick calorimeter that ensures safe hadron filtering with high purity for muons of momentum above 3 GeV. In this chapter, the methods for combined reconstruction using these subdetectors and their physics performance are described.

The combination of measurements made in the Muon System with the ones from the Inner Detector improves the momentum resolution in the momentum range 6 GeV $< p_T <$ 100 GeV; this is described in Section 8.1. The matching of the muon track reconstructed independently in the Inner Detector and in the Muon System also allows the rejection of muons from secondary interactions as well as the ones from π/K decays in flight, as described in Section 8.3. The combined reconstruction allows efficient identification of muons inside jets with low hadron misidentification as shown in Section 8.4. Low energy muon identification is possible thanks to the hadron calorimeter; indeed, low rapidity muons with momentum above 3 GeV can be efficiently identified in the outer sampling of the calorimeter; this is described in Section 8.2. The measurement of the activity around the muon track is important to discriminate between processes where isolated muons are produced and background reactions where muons are produced by the semileptonic decay of *b*- and *c*-quarks, as presented in Section 8.5. The excellent momentum resolution and reconstruction efficiency lead to good multi-muon mass reconstruction (see Section 8.6), which in turn allows tight event selection and hence strong background rejection.

8.1 Track measurement combination

In this section the methods to combine tracks from the Inner Detector and the Muon System are described. The combined performance has been evaluated with single muons of fixed transverse momentum. The analysis shows a high reconstruction efficiency for high transverse momenta. Muons with $p_T <$ 6 GeV are difficult to identify in the standalone Muon System, in particular in the barrel. The use of the Tile Calorimeter is mandatory for the identification of low p_T muons produced at small rapidity.

8.1.1 Track combination procedures

In order to combine the tracks reconstructed in the Inner Detector and the Muon System, two complementary strategies were considered. The first strategy is based on the statistical combination of two independent measurements using the parameters of the reconstructed tracks and their covariance matrices. This method is used in the STACO procedure. The second strategy consists in fitting the global muon track using the hits from the two subdetectors which were found and used separately by the standalone reconstructions. This strategy was used in the MUID and COBRA procedures.

8.1.1.1 STACO

The principle of the STACO method is the statistical combination of two independent measurements by means of their covariance matrices. For two tracks on some reference location defined by their parameter vectors, P_1 and P_2, and their covariance matrices, C_1 and C_2, the parameter vector of the combined track, P, is the solution of the equation

$$\left(C_1^{-1} + C_2^{-1} \right) \times P = C_1^{-1} \times P_1 + C_2^{-1} \times P_2.$$

Its covariance matrix, C, is given by

$$C = \left(C_1^{-1} + C_2^{-1} \right)^{-1},$$

and the corresponding χ^2 is given by

$$\chi^2 = (P - P_1)^T \times C_1^{-1} \times (P - P_1) + (P - P_2)^T \times C_2^{-1} \times (P - P_2).$$

In the present implementation of the STACO procedure, the combination is done at closest approach to the beam line in the perigee representation using track measurements performed in the Inner Detector and the Muon System. The track reconstruction in the Inner Detector is performed by the xKalman package [8-1] and the track reconstruction in Muon System is performed by the MUONBOX package [8-2] using the reconstructed track parameters expressed at the Inner Detector exit. The corrections for energy loss in the calorimeters are done in MUON-BOX using a momentum dependent parametrisation and a detailed geometrical description of the detector outside the Inner Detector exit; in addition the effects of multiple scattering and energy losses fluctuations have been taken into account in the covariance matrix propagation. The track is then propagated down to the closest approach to the beam line accounting for multiple scattering effects in the Inner Detector.

Initially, the track combination is tried only for pairs of tracks that show a reasonable matching in the (η,ϕ) plane. Then the track combination is accepted only if the global χ^2 is below a maximal value. When different combinations are possible, a simple algorithm has been applied to solve the ambiguities. The pair giving the best combined χ^2 is retained and the corresponding tracks are removed from the initial samples of the tracks to be combined. The same procedure is then applied until no more combination is possible.

8.1.1.2 MUID

The MUID muon identification package combines Muon System tracks reconstructed by MUONBOX with Inner Detector tracks found using the iPatRec package [8-3]. The principle is to use the hits found in the two subsystems with information from the calorimeters. The purpose of MUID is to identify Inner Detector tracks as muons at all momenta, to obtain improved parameter resolutions at intermediate momenta, and to clip the tails of badly measured high momentum muons (such as those resulting from catastrophic bremsstrahlung and the pattern recognition errors caused by showering in the Muon System).

The first step is to re-express tracks from the Muon System in order to have the same representation as those from the Inner Detector reconstruction. The muons are propagated through the magnetic field with energy loss and multiple scattering contributions included to obtain the pa-

rameters with their covariance at the point of closest approach to the intersection region. This is performed by applying the iPatRec track fitter to a set of scattering planes representing the calorimeter and Muon System material, an energy loss 'measurement' obtained either from the observed calorimeter energy deposition or from parametrisation, and to either the MUONBOX fit parameters given at the entrance of the Muon System or the drift and strip hits assigned by MUONBOX. Currently, the alternative treatments of the Muon System data are essentially equivalent at high energy, whereas at low p_T the error propagation works better in the region of high field gradient. The results presented in this chapter have been obtained using this latter option. It is hoped that the use of the hits will improve the performance in some cases such as badly-measured muon phi-coordinates, and enable an extension to use segments from the first barrel station to improve the low p_T efficiency.

In the next step, tracks are matched by forming a χ^2 with 5 degrees of freedom from the parameter differences and summed covariances. A combined fit is performed to all matches with χ^2 probability above 0.001. When no match satisfies this criterion, a combined fit is attempted for the best match within a road around the muon track. The combined fit is a repeat of the muon fit from the first step with the addition of the Inner Detector hits and scattering planes assigned by iPatRec. Finally all matches to the Inner Detector giving a satisfactory combined fit are retained as identified muons.

For isolated muons the energy loss is taken from the associated calorimeter cells. It is corrected as a function of η and momentum to account for the difference between true and observed energy deposition obtained from the simulation. Typically this correction increases the energy loss correction by about 7%. The benefit of this procedure over parametrisation is to better correct for Landau fluctuations, in particular at intermediate energies where the calorimeter energy loss is significant and the Muon System gives a more precise momentum measurement than the Inner Detector. At low momentum the precision is comparable to that from parametrisation, but here the purpose of the combined fit is to identify the track as a muon rather than to improve the parameters measured by the Inner Detector. Near the threshold for penetration into the Muon System, the calorimeter energy deposition is greater than the remaining track momentum, thus the measured energy provides a valuable consistency check not available from parametrisation. A parametrised correction is used for non-isolated muons. The MUID package is still under development and further improvement in performance can be expected.

8.1.1.3 COBRA

The COmBined Reconstruction for Atlas or COBRA package incorporates the average tracking and error propagation of the GEANE package [8-4]. In doing so, COBRA can access the description of the material and the ATLAS magnetic field as used by the GEANT simulation program, thus allowing for an accurate detector description in the reconstruction phase and preventing any inconsistency with the simulation.

COBRA runs after the Inner Detector and Muon System pattern recognition programs. The tracks identified by the two subsystem reconstruction program are extrapolated to a common point, typically the inner surface of the calorimeter or the vertex, correcting for energy loss and updating the covariance matrix along the trajectory. The global reconstruction is performed by calculating the χ^2 probability of the track parameters at this point that results from the combination of track pairs from the two subsystems. After a successful combination, a global refit follows. The refit is a Billoir-like fit, usually called Kalman filter [8-5].

Encouraging results have been obtained so far with the extrapolation, combination and global refit procedure. Development is still in progress and it was not possible to use the package for the studies presented in this chapter. Final results and performance will be published in a separate report [8-6].

8.1.2 Performance

The performance of the methods described above is studied for single muons samples of fixed transverse momenta p_T. The high p_T and low p_T results are shown separately.

8.1.2.1 High p_T muons

In Figures 8-1 and 8-2, distributions of the pull of the inverse of the transverse momenta of the combined tracks obtained using the STACO and MUID procedures are presented for $p_T > 10$ GeV. The pull is defined here as the difference between the reconstructed and true values normalised to the error on the reconstructed value. The fact that the width of these distributions remains close to unity from $p_T = 10$ GeV up to $p_T = 500$ GeV shows that the combination procedures works well over a large p_T range.
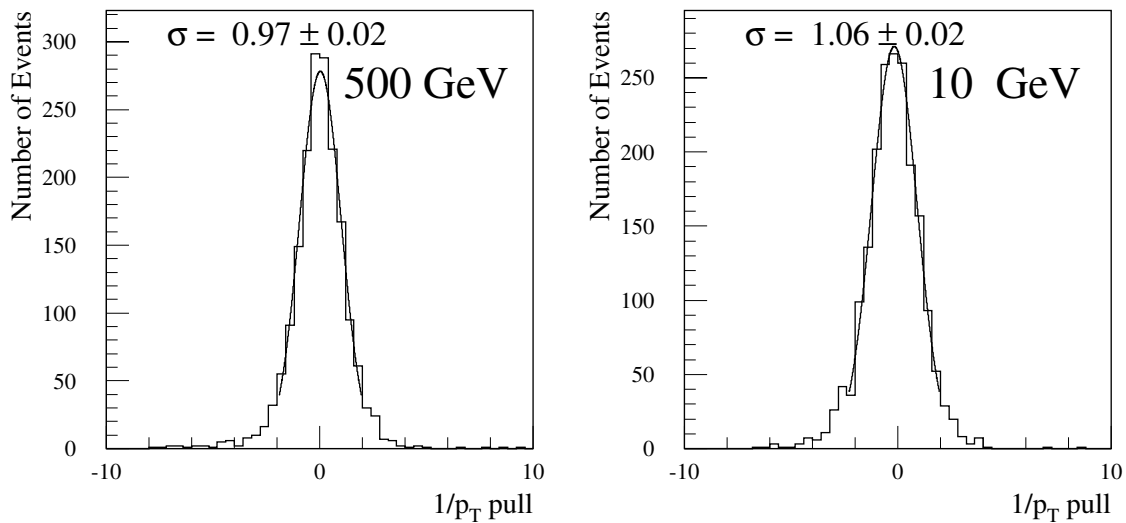
Figure 8-1 Pull distributions of the inverse of the transverse momentum of the combined track using the STACO procedure.

The reconstruction and combination efficiencies and the p_T resolutions are presented in Figures 8-3, 8-4, 8-5 and 8-6 for the full p_T range. The p_T resolutions behave as expected over the whole range: the Inner Detector and the Muon System measurements dominate the combined transverse momentum measurement below 10 GeV and above 100 GeV, respectively. Above 10 GeV, the combination efficiency is high. One notes a slow decrease of this efficiency with increasing p_T from about 97% at 10 GeV down to about 85% at 1 TeV. This decrease, although much less pronounced, is also apparent in the standalone Muon System reconstruction efficiency (from about 98% to about 95%). This behaviour is explained by the increasing (with the muon momentum) probability of occurrence of electromagnetic shower production along the muon track when crossing dense materials. These local showers can create a large number of hits in the Muon System chambers that mask or spoil the genuine muon hits. The lack of meas-
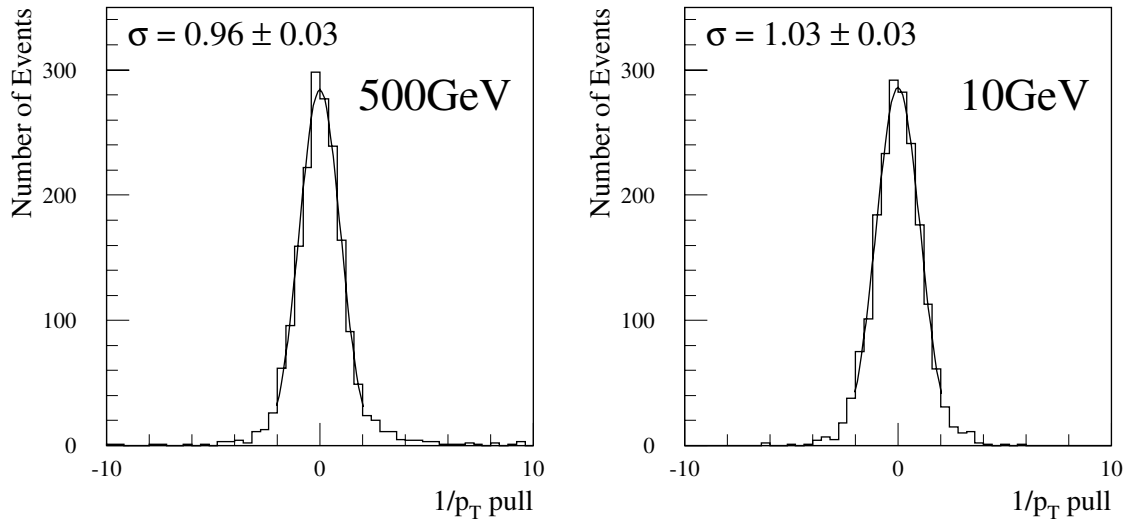
Figure 8-2 Pull distributions of the inverse of the transverse momentum of the combined track using the MUID procedure.

urement redundancy resulting from a cost optimisation (there are only three layers of tubes per multi-layer in the middle and outer stations [8-9]), results in a degradation of the pattern recognition in the Muon System. Some tracks are irretrievably lost leading to an inefficiency of the standalone reconstruction of 5% at 1 TeV. The momentum of some of the reconstructed tracks is spoiled leading to an inefficiency of the combination procedure of order 5% at 1 TeV. This indicates the ultimate reconstruction efficiency of about 90% at 1 TeV.

The remaining 5% needed to account for the observed 85% combination efficiency at 1 TeV comes from pattern recognition errors on transverse position of the reconstructed tracks in the Muon System. It has been shown that a fraction of these tracks have a good momentum measurement but are slightly shifted in the transverse plane. In these cases, the electromagnetic showers have spoiled the hit pattern in the second-coordinates chambers. These tracks could be recovered in the combination procedure by simply increasing the angular errors. The momentum being correctly measured in the Muon System, and the angular measurements being dominated by the Inner Detector measurements, this procedure should be justified; it is under study.

8.1.2.2 Low p_T muons

The reconstruction and combination efficiencies and p_T resolutions for low p_T single muons are presented in Figures 8-7, 8-8, 8-9 and 8-10. As expected, the p_T resolution is completely dominated by the Inner Detector measurements. With respect to high p_T muons, the most important difference concerns the efficiency which decreases very rapidly with decreasing p_T. The combination efficiency follows closely the standalone Muon System reconstruction efficiency and decreases down to about 30% at 3 GeV.

Figures 8-11 and 8-12 illustrate the reasons for this decrease. Accurate tracking of low p_T muons in the highly inhomogenous magnetic field is delicate and requires a dedicated algorithm. Furthermore, the importance of multiple scattering in the Muon System superstructures is enhanced at low p_T and is one of the main reasons for the complexity of the pattern recognition. As p_T decreases, the energy lost by the muons inside the calorimeters becomes comparable to their energy, specially in the barrel region. Therefore, an increasing fraction of the muons exit from the calorimeters with too low energy an to reach the medium or outer muon stations, or do
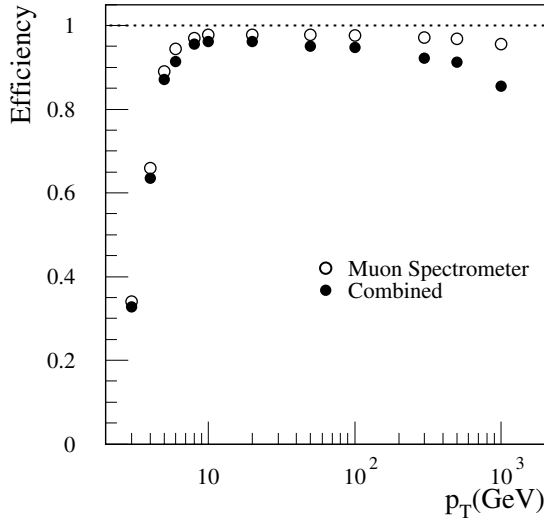
Figure 8-3 Efficiency of tracks reconstruction in the Muon System and of track combination using the STACO procedure as a function of p_T.
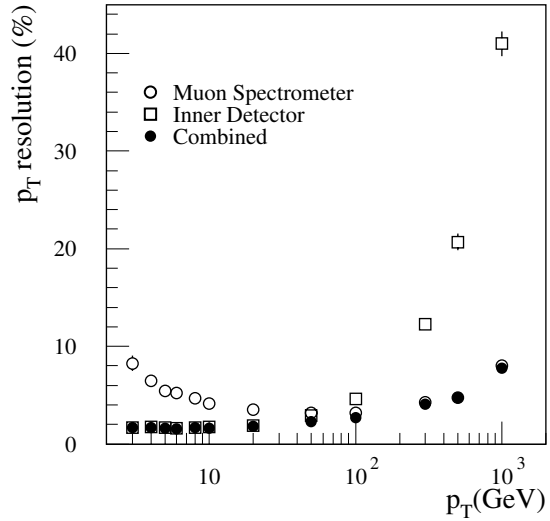
Figure 8-4 p_T resolution of track reconstruction in Muon System, in Inner Detector and of combined tracks using STACO procedure as a function p_T.
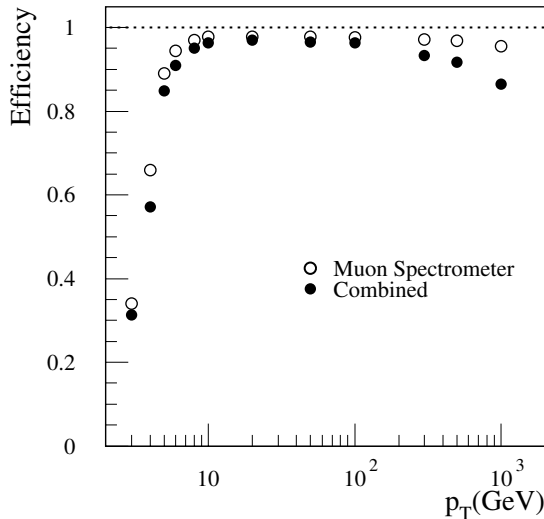
Figure 8-5 Efficiency of track reconstruction in the Muon System and of track combination using the MUID procedure as a function of p_T.
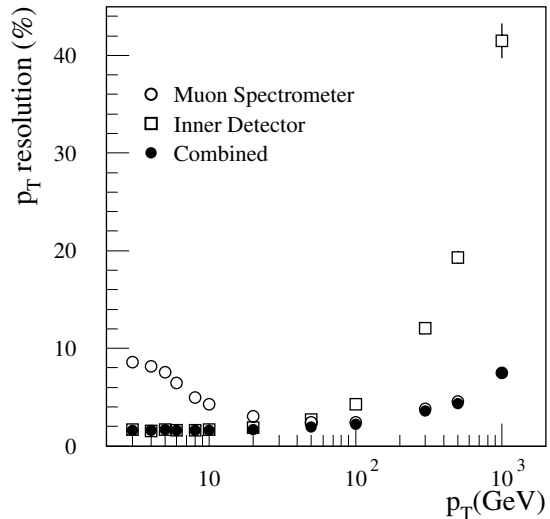
Figure 8-6 p_T resolution of track reconstruction in Muon System (refitted), in Inner Detector and of combined tracks using MUID procedure as a function p_T.

not escape from the calorimeters. Figures 8-11 and 8-12 show that the inefficiency is indeed mainly visible in the barrel region. In the end cap region, even at transverse momentum as low as 3 GeV, the efficiency remains high since the momentum is larger than the 3-4 GeV energy deposited in the calorimeters.

In the absence of a reconstructed track in the Muon System, it is possible to use the straight track segments which can be reconstructed in the inner stations of the Muon System and are made available by the standalone reconstruction program. Figure 8-13 shows the fraction of single muon events with a reconstructed inner station segment as a function of η compared with the standalone reconstruction efficiency. The figure shows that in the high η range, $|\eta| > 1.6$, the
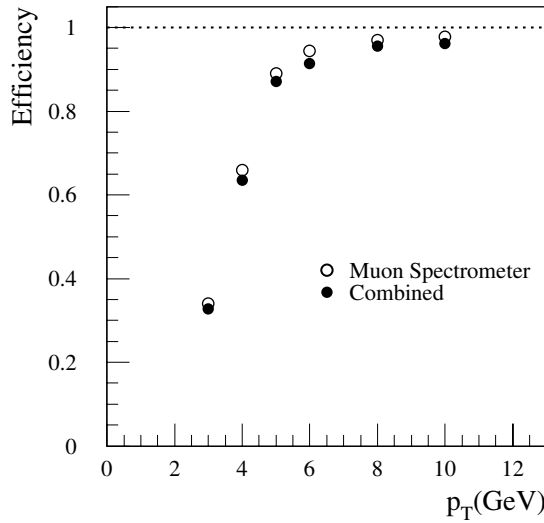
Figure 8-7 Efficiency of track reconstruction in the Muon System and of track combination using the STACO procedure as a function of p_T.
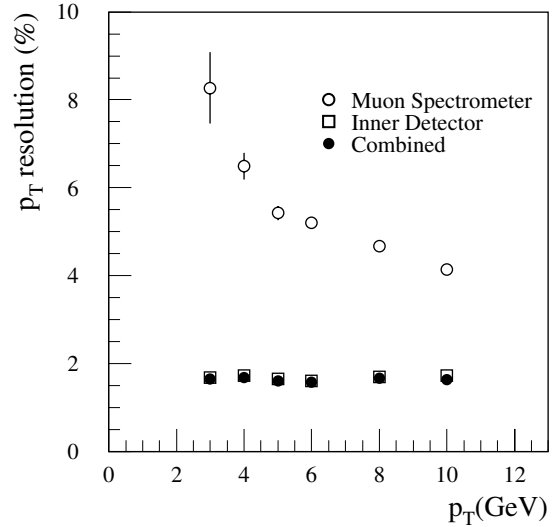
Figure 8-8 p_T resolution of track reconstruction in Muon System, in Inner Detector and of combined tracks using STACO procedure as a function p_T.
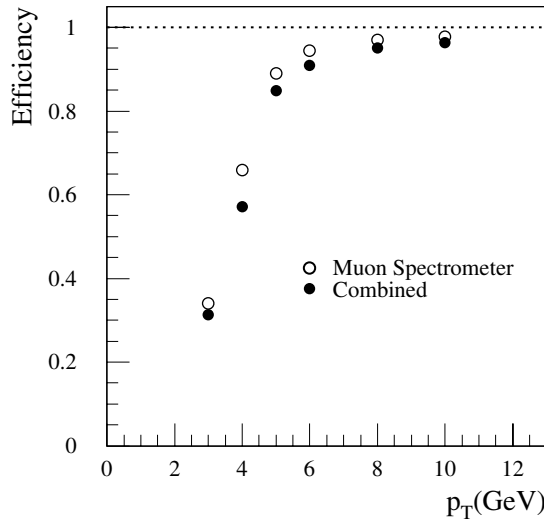
Figure 8-9 Efficiency of track reconstruction in the Muon System and of track combination using the MUID procedure as a function of p_T.
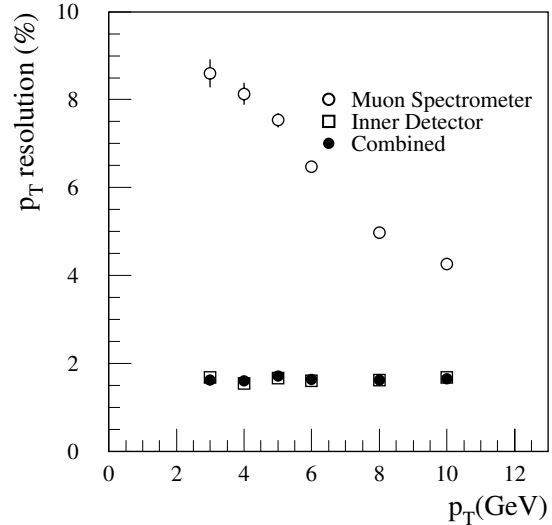
Figure 8-10 p_T resolution of track reconstruction in Muon System (refitted), in Inner Detector and of combined tracks using MUID procedure as a function p_T.

identification efficiency will be marginally increased by using the inner station segments. In the intermediate η range, $1.0 < |\eta| < 1.6$, the use of inner station segments could improve the identification efficiency up to about 90%.

Figure 8-13 seems to indicate that a similar gain can be obtained in the barrel region. In this latter region, the inner stations segments suffer from a very imprecise measurement in the direction along the tubes of the precision chamber because of the absence of second-coordinate chambers in the inner stations. This could lead to a high ambiguity in the association of the inner stations segments to the Inner Detector tracks. An algorithm that uses the inner station seg-
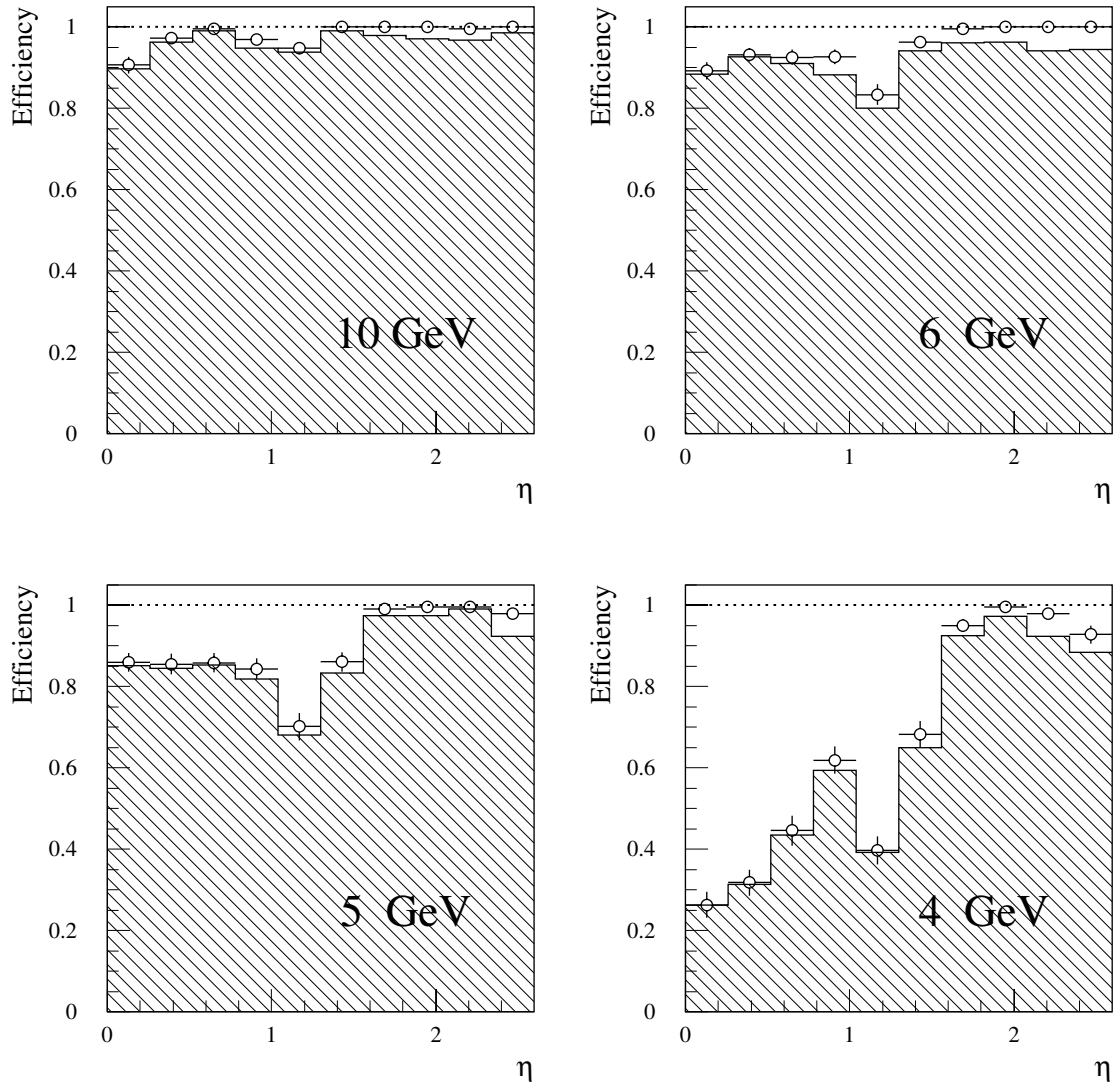
Figure 8-11 Efficiencies of track reconstruction in the Muon System (open circles) and of tracks combination (histogram) using the STACO procedure as a function of η and at different low p_T.

ments together with the Inner Detector and the Tile Calorimeter measurements (in order to have a constraint in the transverse plane) could lead to a good identification efficiency of muons with p_T as low as 3 GeV. This method remains to be studied in detail.

8.2 Identification of low p_T muons using the Tile Calorimeter

Lepton identification in the transverse momentum range from 3 GeV to 10 GeV is essential to perform the *b*-physics studies (see Chapter 17). As already stated in the preceding section, the muon reconstruction efficiency decreases rapidly below 6 GeV specially at low rapidity. In order to efficiently identify low p_T muons, the last sampling of Tile Calorimeter can be used. Muons with energy above 3 GeV reach this sampling and deposit energy of a minimum ionising particle while the inner samplings act as a filter for hadrons which leave very little energy on the last sampling.
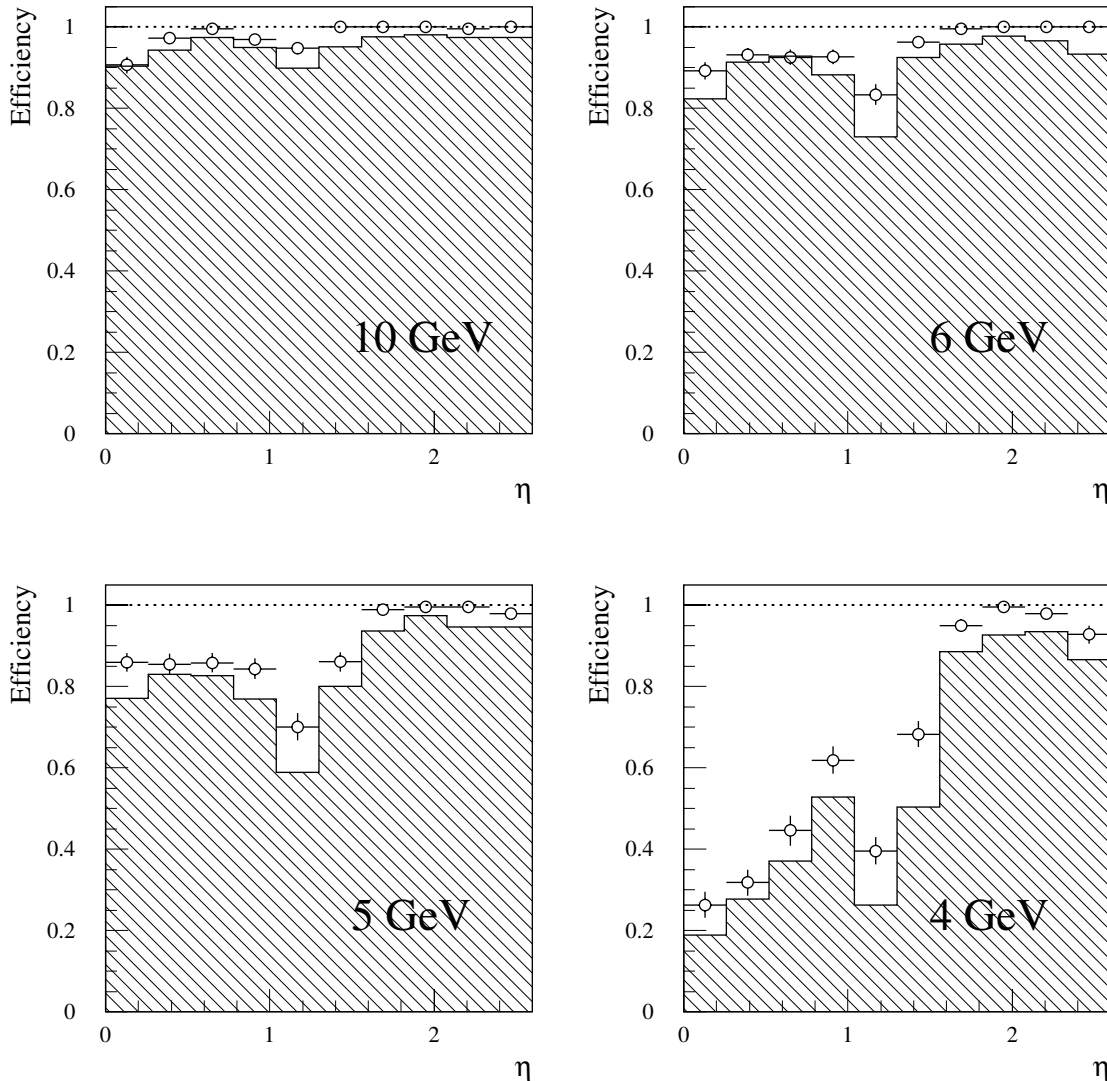
Figure 8-12 Efficiencies of track reconstruction in the Muon System and of tracks combination using the MUID procedure as a function of η and at different low p_T.

Single muons with p_T in the 3-5 GeV range were simulated in the pseudorapidity region $|\eta| < 1.5$ (in the Tile Calorimeter acceptance). Single pions with $p_T = 5$ GeV were also simulated in the same range in order to get a conservative estimate of hadron contamination.

The principle is to reconstruct tracks in the Inner Detector and to propagate those with $3 < p_T < 5$ GeV to the third hadronic sampling. Energy deposition in the calorimeter cells that are hit (on-Road cells) are recorded, as well as energy deposition in the nearest cells (off-Road cells). The most simple criteria is then to analyse the energy deposition in the last hadronic sampling. Figure 8-14 shows the distributions of these energy deposits. Selection of events with energy above 0.3 GeV gives the best results. Such selected cells can then be associated with tracks reconstructed in the Inner Detector. The tracks in a cone of R < 0.4 around the selected cells are tagged as potential muon candidates.

Figure 8-15 shows the muon identification efficiency as a function of η. The drop of efficiency for η around 0.7 is due to the gap between the barrel and extended barrel of the Tile Calorimeter; the efficiency drop at $|\eta| = 1.1$ is due to tracks crossing the extended barrel and depositing
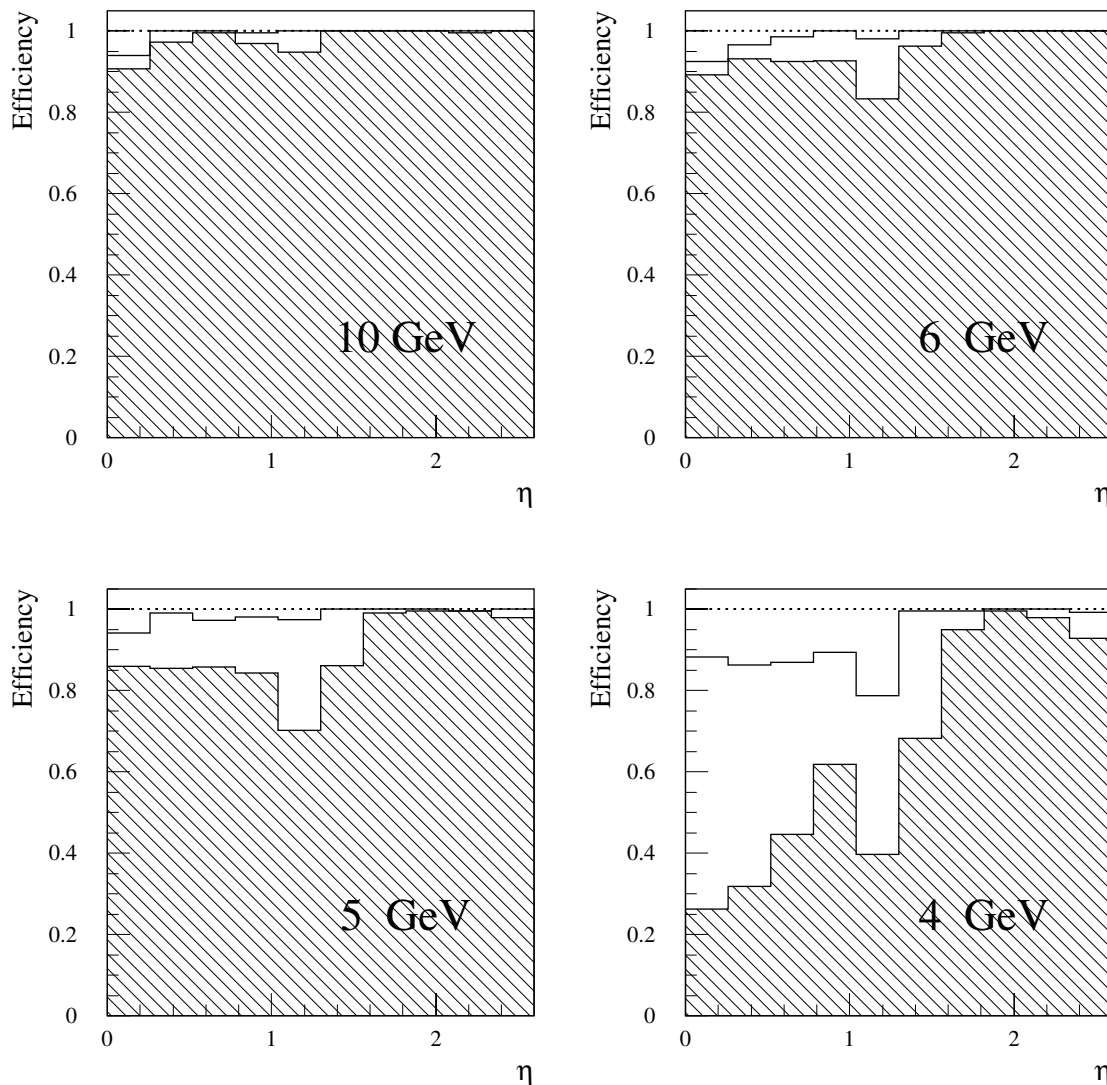
Figure 8-13 Efficiency of track reconstruction in Muon System (hatched histogram) and fraction of events with reconstructed inner stations segments (empty histogram) as a function of η and at different low p_T.

comparable amount of energy in two close cells in the third hadronic sampling. The decrease of efficiency at $\eta = 0$ is due to the large probability of muon absorption in that region. Figure 8-16 shows the probability of hadron misidentification as a function of η. Regions with low rejection occur where the amount of crossed material is minimal.

Muon detection efficiency and hadron rejection could be further improved by using other measurements as the energy deposition in the inner samplings of the Hadron Calorimeter, the energy measurement in the EM Calorimeter and the track reconstruction in the inner most stations of the Muon System
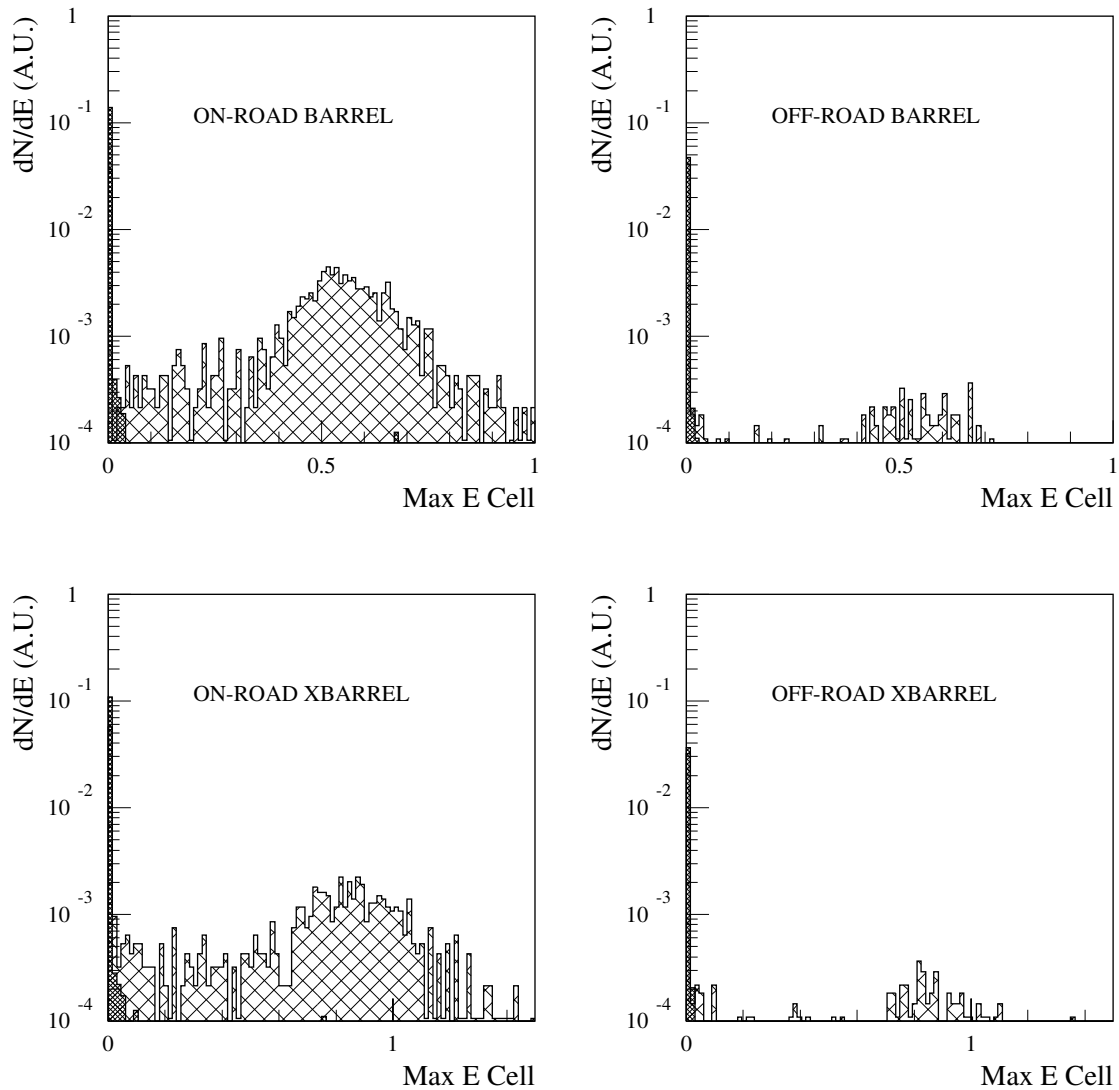
Figure 8-14 Distribution of the energy (in GeV) in on-road and off-road (see text) cells of the third sampling of the barrel Tile calorimeter (barrel and extended barrel) for 5 GeV pions (densely hatched histogram) and for 3 GeV to 5 GeV muons (hatched histogram).

8.3 Muons from π/K decays

For *B*-physics studies, the LVL1 trigger is an inclusive muon trigger with p_T threshold of 6 GeV. At low transverse momenta ($p_T < 8$ GeV) in-flight decays of π and K mesons ($\pi \to \mu\nu$ and $K \to \mu\nu$) are the dominant source of muons and thus of trigger rate in the LVL-1 Muon System. The purpose of the LVL2 muon trigger is the identification of the muon tracks using the Muon System and the extrapolation to the Inner Detector. The comparison of these tracks with those reconstructed in the Inner Detector gives a possibility to reduce the trigger rate by requiring a good match. A muon originating from π/K decay and detected by the Muon System has a momentum lower than the original meson detected in the Inner Detector. In addition, the π–μ or K–μ trajectory shows a kink where the decay occurs; as a consequence the χ^2 of the combined track is spoiled. However, the multiple scattering and energy loss fluctuations (especially in the calorimeters) dilutes this effect.
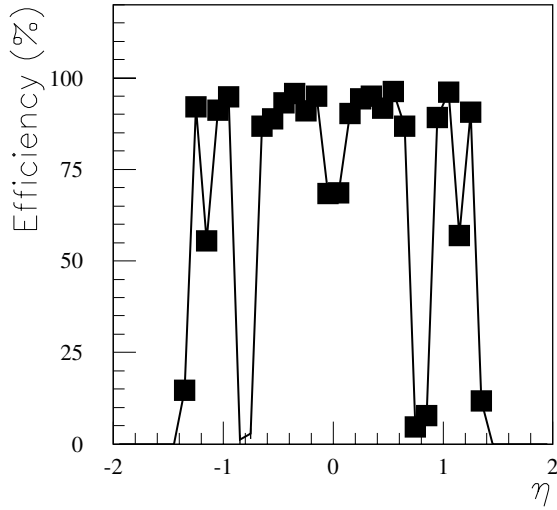
Figure 8-15 Efficiency of selection for 3 GeV to 5 GeV muons.
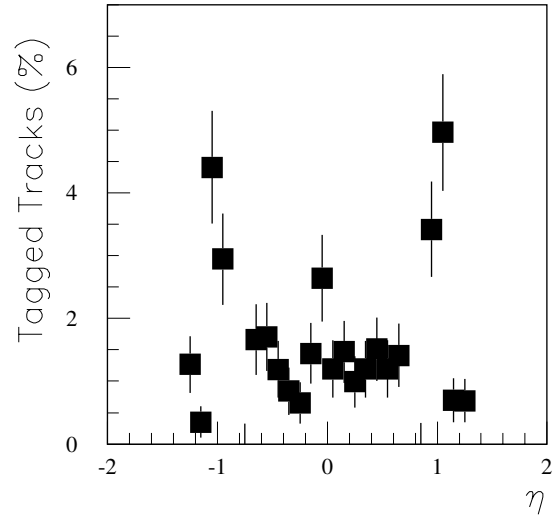
Figure 8-16 Efficiency of selection for 5 GeV pions.

To estimate the rejection, non-prompt muons from π/K decays and prompt muons with fixed p_T between 6 and 12 Gev and $|\eta| < 2.5$, were simulated. The decay of π/K was limited to the maximal radius of 1.40 m. The reconstruction of charged tracks in Inner Detector has been performed using xKalman and in Muon System using MUONBOX. All tracks found in the Muon System were extrapolated to the Inner Detector.

The analysis starts by looping over all tracks reconstructed in the Muon System and it proceeds in three steps. In the first step, only muons with p_T larger than 4.2 GeV are retained. The value of this cut allows high reconstruction efficiency of prompt muons with $p_T > 6$ GeV. Figure 8-17 shows the reconstruction efficiency both for prompt and π/K decay muons. In the second step, a track is accepted if it satisfies the following cuts:

1. Number of precision hits ≥ 9.

2. Number of pixel hits ≥ 2.

3. At least one associated hit in the B-layer.

4. $|d_o| < 1$ mm, were d_o is the transverse impact parameter of the track.

5. χ^2 per degree of freedom of track fit procedure ≤ 2.

6. Number of TRT hits ≥ 20.

The first four cuts correspond to quality cuts which have been developed in the context of *b*-tagging and the last two cuts were added to enhance the rejection of non-prompt muons. Figure 8-18 shows the efficiencies after these cuts.
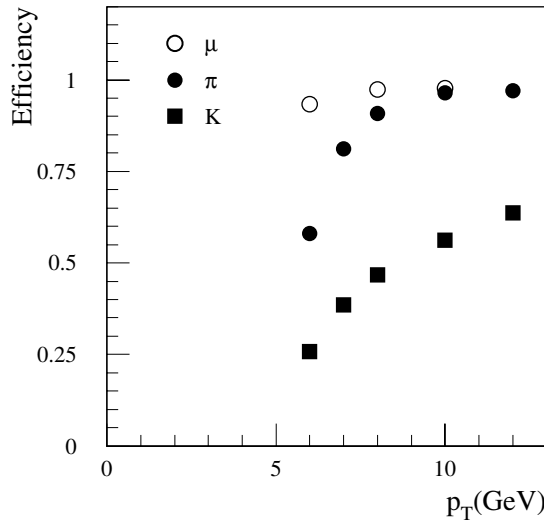
Figure 8-17 Reconstruction efficiency at first selection step (cut on p_T reconstructed the in Muon System) as a function of p_T.
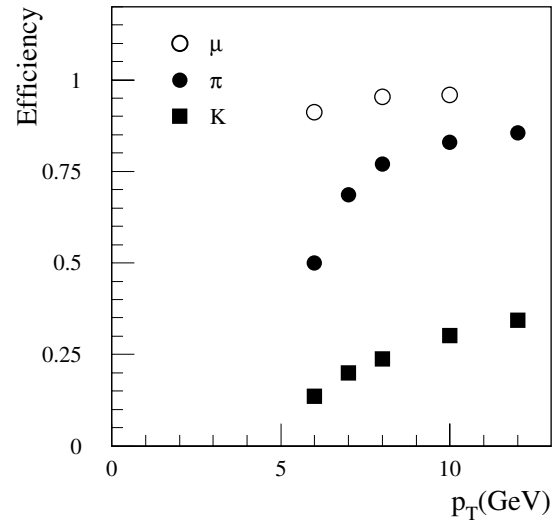
Figure 8-18 Reconstruction efficiency at second selection step (cut on quality of Inner Detector track) as a function of p_T.

Finally, the combination of the reconstructed tracks from the Inner Detector and from the Muon System is performed using the STACO procedure described in Section 8.1. Only combined tracks with χ^2 per degree of freedom less than 6 and $p_T > 5.6$ GeV are accepted.

Figure 8-19 indicates that only 10-15% of muons from K decays and 30-50% of muons from π decays were misidentified as prompt muons and that the efficiency for prompt muons is ~90% in the p_T range 6-10 GeV.

The rejection of non-prompt muons depends strongly on the distance from the beam line where the decay occurs. Figures 8-20 and 8-21 show the reconstruction efficiency of non-prompt muons originating from π/K with $p_T = 8$ Gev as a function of the decay radius after three steps of the selection algorithm.
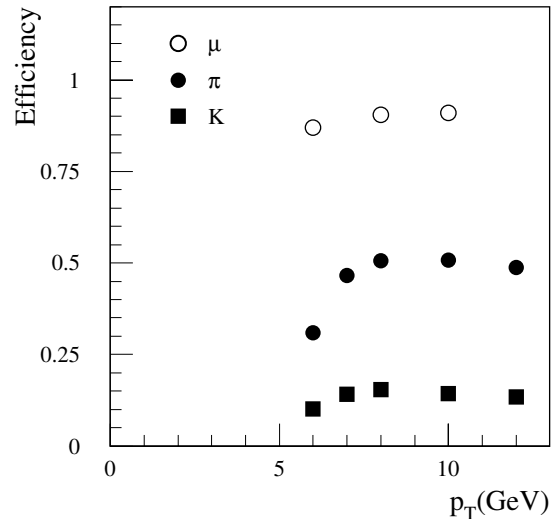
Figure 8-19 Reconstruction efficiency at third selection step (cut on matching quality) as a function of p_T.

The reconstruction efficiency after the first step of the selection does not depend on the radius of the decay. The rejection of non-prompt muons at the second step increases for decay radii between 5 and 50 to 60 cm because of the fine-granularity of the semiconductor tracking detectors. Finally the combination of Muon System and Inner Detector systems in the last selection step partially removes the non-prompt muons from decays at radii above 50 cm.
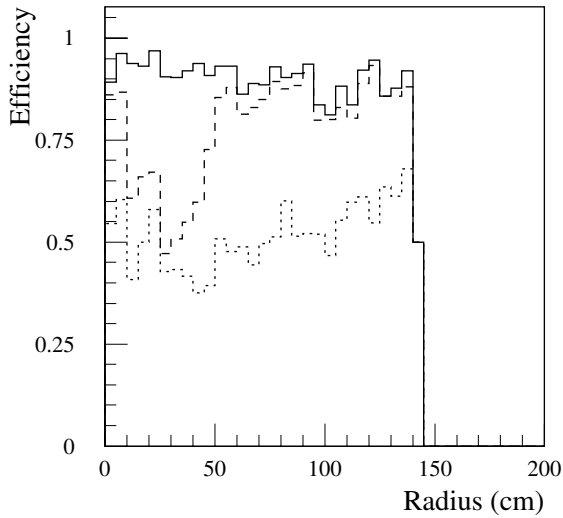
Figure 8-20 Reconstruction efficiency as a function of the radius at which the decay occurs at the different steps of the selection (solid line: first step, dashed line: second step, dotted line: last step) for the π sample.
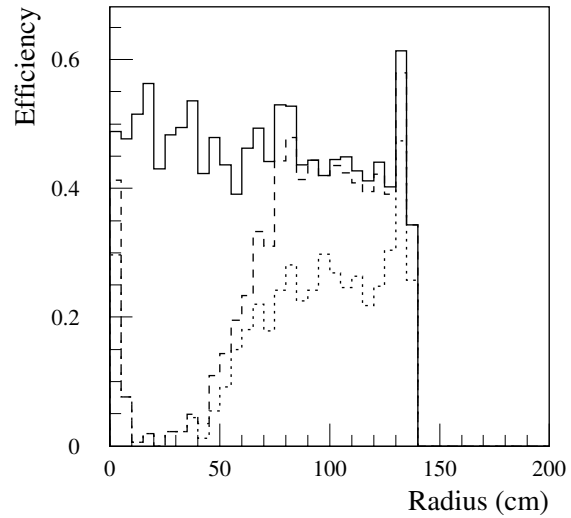
Figure 8-21 Same as Figure 8-20 but for the *K* sample.

8.4 Muons inside jets

Non-isolated muons are predominantly produced by heavy flavour (*b*- and *c*-quarks) decays. For this reason, they can be used to identify jets originating from *b*-quark fragmentation (muon *b*-tag; see Chapter 10). The main ingredients of the muon *b*-tagging are the correct muon identification and a high rejection power for decayed or misidentified hadrons.

For this investigation, muons were studied in *b*-jets produced by Higgs decays, where the Higgs mass was either 100 or 400 GeV. The STACO procedure (see Section 8.1) was used for combining the tracks measured in the Muon System and in the Inner Detector.

The overall reconstruction efficiency of muons with $p_T > 6$ GeV within the Inner Detector acceptance is 90%, which is 5% lower than that for isolated muons. Figure 8-22 shows the reconstruction efficiency as a function of p_T for muons in jets (histogram) and for single muons (triangles). The lower efficiency for non isolated muons can be attributed to the pattern recognition efficiency in the Inner Detector, and to a wrong match between the Muon System track and the Inner Detector track due to the large density of tracks in jets. The latter effect is the dominant.

Hadrons can be tagged as muons. Figure 8-23 shows the hadron misidentification probability for jets which did not contain any primary muon compared to the same probability for jets containing at least one primary muon. In the first case the misidentification is due entirely to decays in flight of pions and kaons; in the latter case the additional contribution arises from muon matching errors.

Muons with $2 < p_T < 6$ GeV and $|\eta| < 1.75$ can be tagged through their energy deposit in the outer segment of the Tile Calorimeter. Figures 8-24 and 8-25 show this energy deposit as a function of pseudorapidity, for muons and for hadrons respectively, with $p_T > 2$ GeV. Selecting only cases where the energy in the last segment was in the band limited by the dotted lines, it is possible to achieve an efficiency of 75% (85% for $|\eta| < 1.25$) with a hadron rejection factor of ~10.
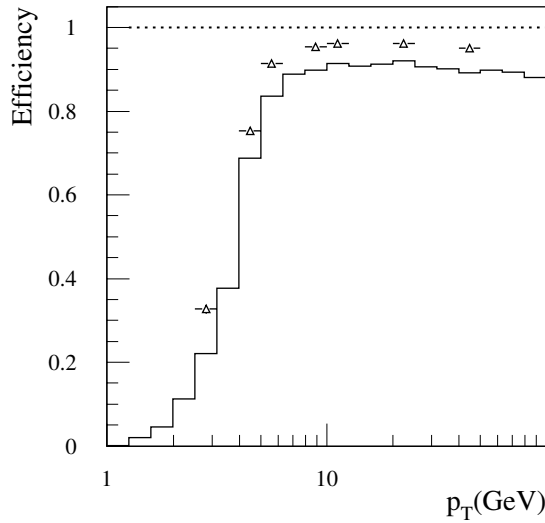
Figure 8-22 Muon reconstruction and identification efficiency as a function of p_T. The histogram is for muons in jets from Higgs decays, the open triangles are for single muons.
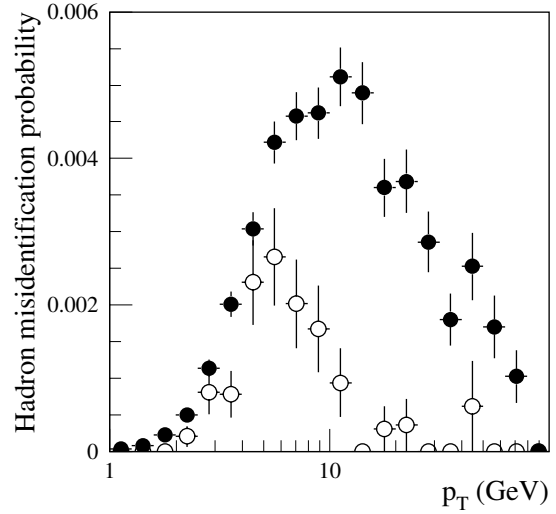
Figure 8-23 Hadron misidentification probability as a function of p_T. Full circles: hadrons in jets containing at least one primary muon. Open circles: hadrons in jets not containing primary muons.

Figure 8-26 shows the muon identification efficiency and hadron misidentification rate as a function of p_T for particles with $|\eta| < 1.75$. Figure 8-27 shows the muon identification efficiency and hadron misidentification rate as a function of pseudorapidity for particles in the range $2 < p_T < 8$ GeV.
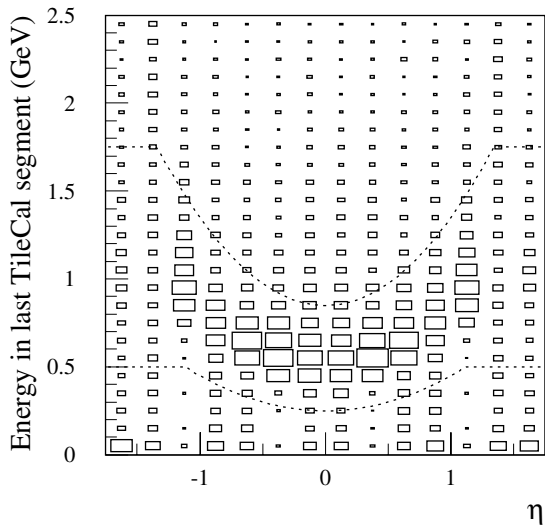
Figure 8-24 Energy deposited in the outer Tile Calorimeter segment by muons in jets as a function of pseudorapidity.
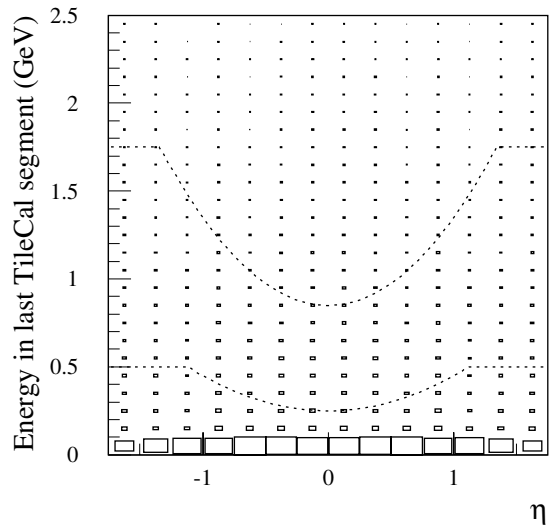
Figure 8-25 Energy deposited in the outer Tile Calorimeter segment by hadrons in jets as a function of pseudorapidity.
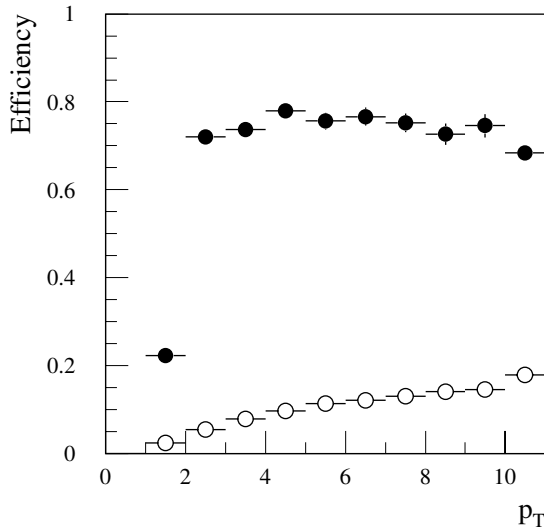
Figure 8-26 Tile Calorimeter muon identification efficiency (full circles) and fraction of misidentified hadrons (open circles) as a function of p_T for particles in jets with $|\eta| < 1.75$.
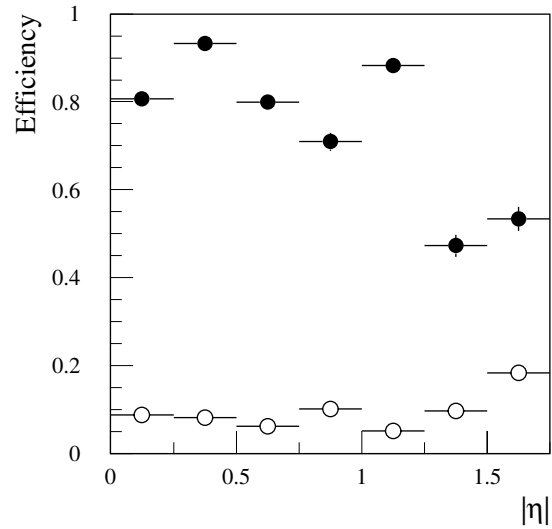
Figure 8-27 Tile Calorimeter muon identification efficiency (full circles) and fraction of misidentified hadrons (open circles) as a function of $|\eta|$ for particles in jets with $2 < p_T < 8$ GeV.

Since the cells of the last sampling are large ($\Delta\eta = 0.2$, $\Delta\phi = 0.1$), the energy entering in Figure 8-25 is not deposited by a single hadron but by several. Thus the probability for a jet to induce a muon signature cannot be simply deduced from the hadron probability shown in Figure 8-27 and the hadron multiplicity in the jet but depends on the jet topology. This method of identifying muons is also used to tag b-jets (see Chapter 10).

8.5 Muon isolation

The dominant background to the $H \rightarrow ZZ^* \rightarrow \mu\mu\mu\mu$ signal consists of four-lepton events from $t\bar{t}$ and $Zb\bar{b}$ production. In these backgrounds, at least two of the muons come from direct or cascade b-decay. Therefore they are non-isolated and one can reject them on the basis of energy deposited in the calorimeters.

For this study, muon candidates reconstructed in the Muon System have been selected. A sample of 1 500 single muons of fixed $p_T = 20$ GeV and a sample of 1 100 events $pp \rightarrow b\bar{b}X \rightarrow \mu X$, where the muon coming from the b decay is required to have a transverse momentum greater than 20 GeV, have been simulated in the detector. Electronic noise was included and pile-up was simulated by adding 2.3 (23) minimum bias events for low (high) luminosity.

Figure 8-28 shows the distribution of the transverse energy collected in the electromagnetic calorimeters cells lying in a cone of radius $R = 0.3$ around the muon direction. The energy deposit in the calorimeters around the muon direction allows to separate isolated from non-isolated muons. Figure 8-29 shows the mean value of the transverse energy collected in a cone around the reconstructed muon direction as a function of cone radius for low and high luminosity and for isolated and non-isolated muons. This plot suggests the value R = 0.3. This value is a good compromise between a large value needed to fully contain the energy from hadrons associated with non-isolated muons and a small value needed to reduce the effect of pile-up and electronics noise.
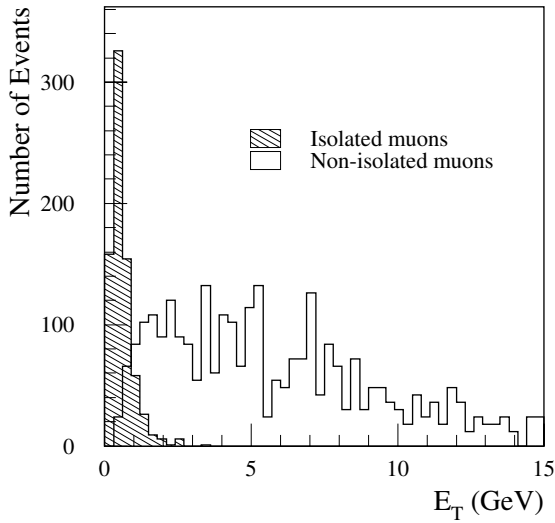
Figure 8-28 Transverse EM-energy distribution in cone of radius 0.3 around muon direction for isolated and non-isolated muons.
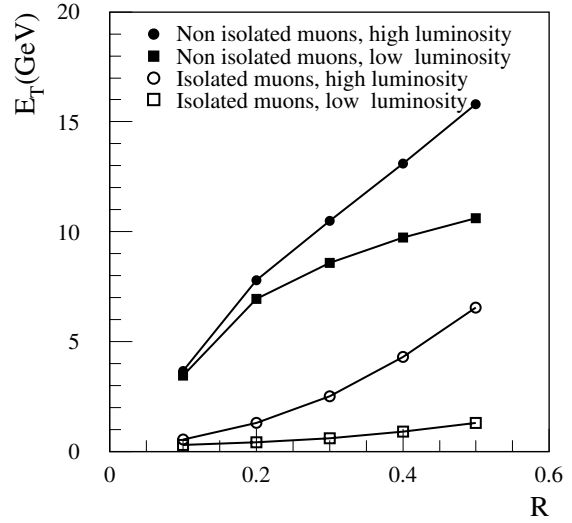
Figure 8-29 Mean value of transverse EM-energy in a cone around muon direction as a function of the cone radius R.

The contribution from pile-up, which increases with the luminosity, introduces also a pseudorapidity dependence of the transverse energy deposited in the calorimeters. This is illustrated in Figure 8-30 where the mean values of the transverse energy is plotted as a function of η. The dependence shown on this latter figure has been removed by using a weight factor in order to get a η corrected transverse energy independent of η.

A cut on the transverse energy collected in the EM Calorimeter cells in the isolation cone is applied to select the isolated muons. At high luminosity, is preferable to cut on η corrected transverse energy. Figures 8-31 and 8-32 show the selection efficiency for isolated and non-isolated muons as a function of the threshold energy for low and high luminosity. One notes that the selection efficiency for non-isolated muons depends on the luminosity and, to some extent, on the muon momentum.
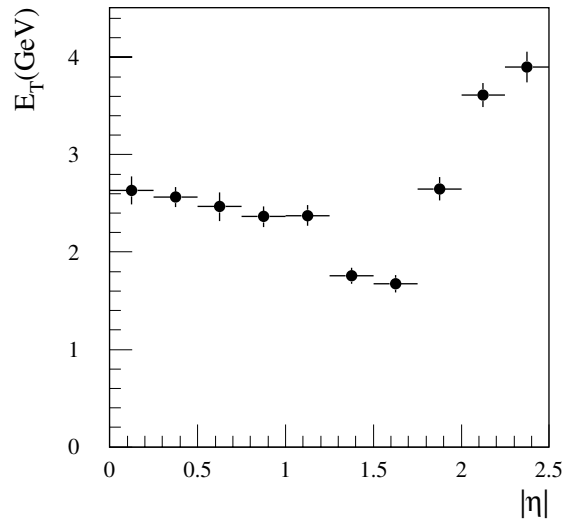
Figure 8-30 Mean value of transverse energy in a cone of radius 0.3 around the muon direction as a function of pseudorapidity for high luminosity.
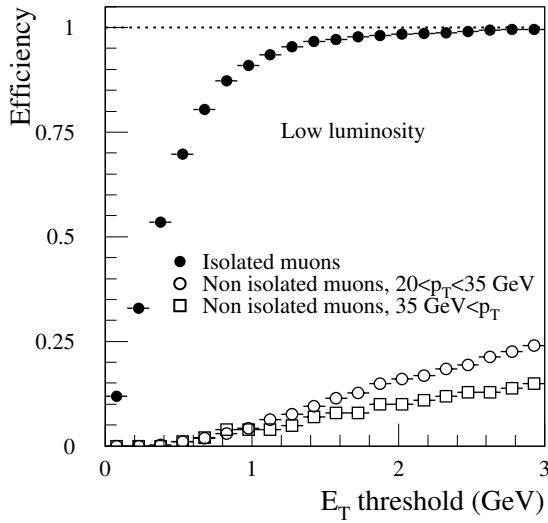
Figure 8-31 Muon selection efficiency as a function of the transverse energy threshold at low luminosity.
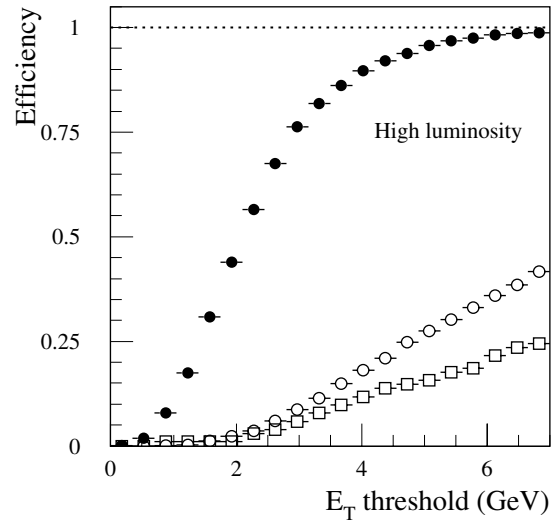
Figure 8-32 Muon selection efficiency as a function of the transverse energy threshold at high luminosity.

8.6 Mass and charge reconstruction

8.6.1 Reconstruction of $Z \rightarrow \mu\mu$

The process $Z \rightarrow \mu\mu$ is a high-statistics control sample which will be used for detector calibration and monitoring of the detector performance. A sample of events has been generated with PYTHIA 5.7 [8-7] and PHOTOS 2.0 [8-8] in order to include inner bremsstrahlung. Figure 8-33 shows the reconstructed Z mass using MUONBOX. A Gaussian fit (within a 2σ window) gives $\sigma = 3.0$ GeV, of which about 1.9 GeV comes from the natural width; the measurement accuracy contributes with an error of 2.0 GeV.

The mass resolution can be improved by combining the measurements from the Muon System and from the Inner Detector. The combined reconstruction has been performed using the STACO procedure. The combined reconstructed mass is shown in Figure 8-34. A Gaussian fit gives $\sigma = 2.5$ GeV.

8.6.2 Dimuon final state

If the MSSM parameter $\tan\beta$ is large enough, the process $H/A \rightarrow \mu\mu$ becomes detectable (see Section 19.3.2.6). The most critical issue in the detection of such a particle in the few hundred GeV mass range is the suppression of the very large dimuon background. There are two main sources of opposite-sign dimuons, namely the Drell-Yan processes and $t\bar{t}$ production. It has been shown that this background is very high and therefore the mass resolution is crucial to isolate the signal [8-11].

A sample of $A \rightarrow \mu\mu$ have been simulated for two higgs masses: 150 GeV and 300 GeV. The event reconstruction has been performed using the MUID procedure described in Section 8.1.
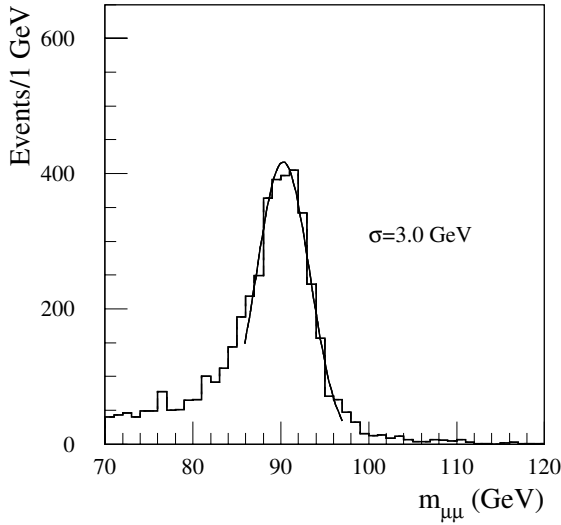
Figure 8-33 Distribution of the reconstructed *Z* mass using the standalone Muon System.
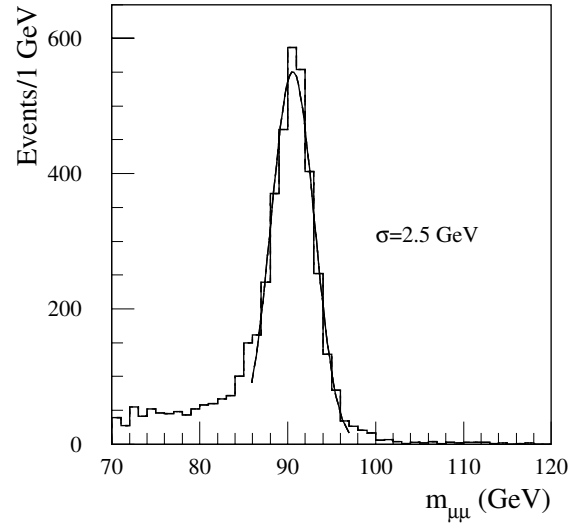
Figure 8-34 Distribution of the reconstructed *Z* mass using the combined information from the Muon System and the Inner Detector.
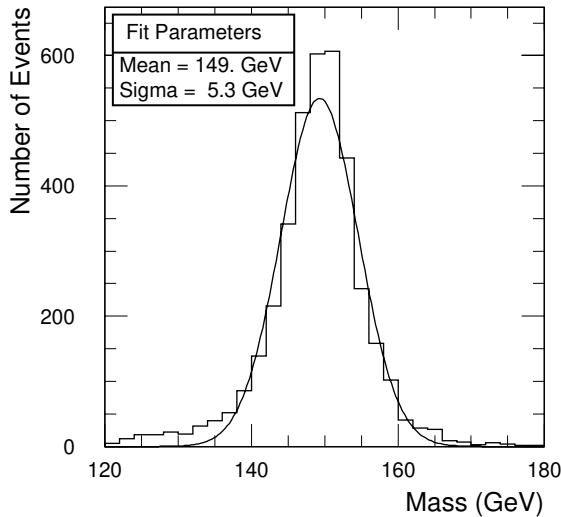
Figure 8-35 Distribution of the reconstructed dimuon invariant mass for an *A* with a mass of 150 GeV using the Inner Detector only.
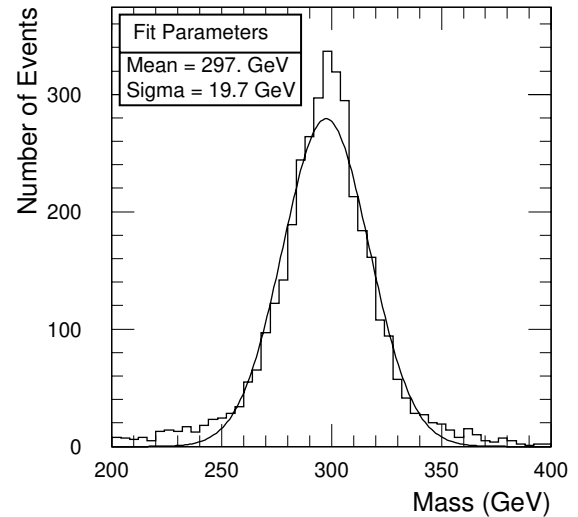
Figure 8-36 Distribution of the reconstructed dimuon invariant mass for an *A* with a mass of 300 GeV using the Inner Detector only.

The reconstructed invariant mass is shown in Figures 8-35, 8-36, 8-37 and 8-38 when the Muon System and the Inner Detector are used separately. The low mass tails in these mass distributions come from inner bremsstrahlung. The result of combined muon reconstruction is shown in Figures 8-39 and 8-40; with respect to the standalone Muon System reconstruction, the mass resolution is improved by about 25% at low mass and 10% at high mass. The dependence on the mass of this improvement reflects the higher p_T of the decay muons. The signal-to-background ratio achievable with this mass resolution is presented in Section 19.3.2.6.

The dimuon mass resolution is also of interest at high mass, where new neutral heavy bosons are possible. A study of the 3 Tev Z' decaying to two muons yields a mass resolution of 8% [8-11].
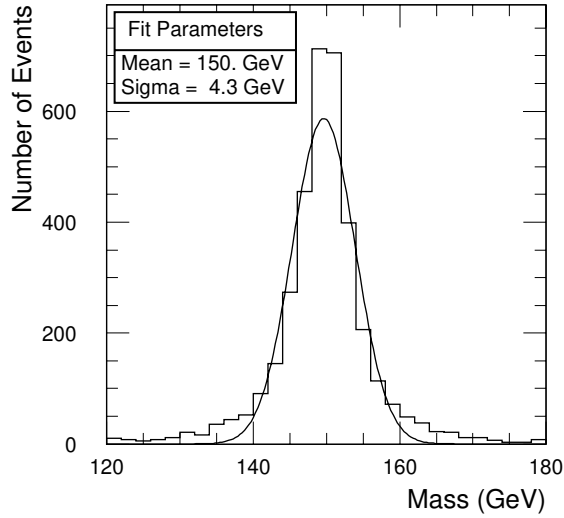
Figure 8-37 Distribution of the reconstructed dimuon invariant mass for an *A* with a mass of 150 GeV using the Muon System only.
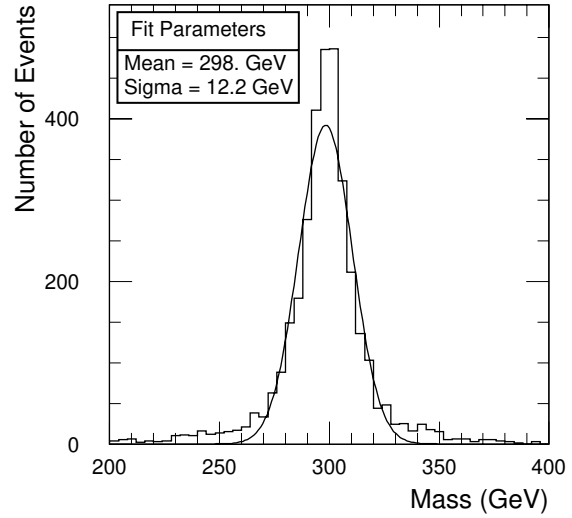
Figure 8-38 Distribution of the reconstructed dimuon invariant mass for an *A* with a mass of 300 GeV using the Muon System only.
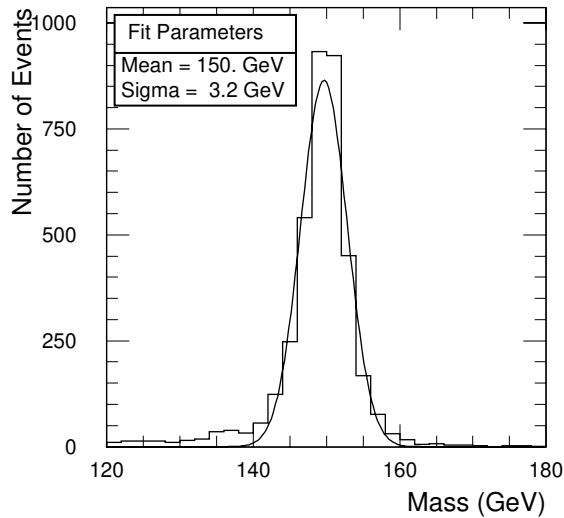
Figure 8-39 Dimuon invariant mass distribution for 150 GeV *A* using combined reconstruction.
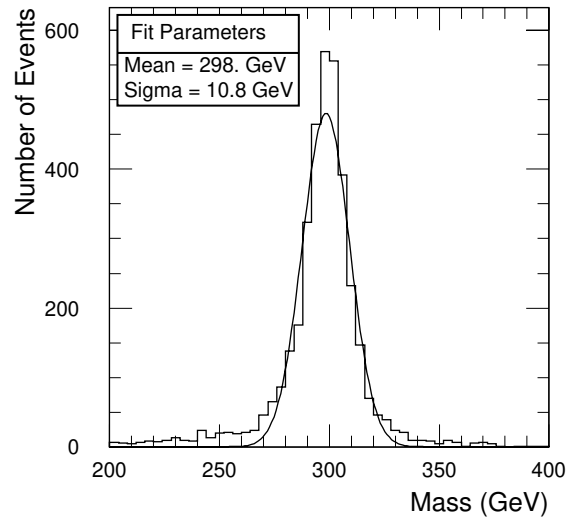
Figure 8-40 Dimuon invariant mass distribution for 300 GeV *A* using combined reconstruction.

8.6.3 Four-muon final state

The SM Higgs decay $H \rightarrow ZZ^* \rightarrow \mu\mu\mu\mu$ has been studied extensively. Details of the event selection can be found in Section 19.2.5. The typical reconstruction efficiency of these events using the Muon System is ~85% for masses greater than 130 GeV (see Table 8-1). This and the following reconstruction efficiencies are normalised to the number of events with all decay muons in the η region $|\eta| < 2.5$. Table 8-1 shows the four-muon mass resolution as a function of the simulated Higgs mass. When only the Muon System is used for the event reconstruction, the measurement accuracy ranges from 2.7 GeV to 4.7 GeV for the mass range from 130 to 200 GeV. This result is obtained with a Gaussian fit in a 2σ interval centred on the peak of the distribution. Table 8-1 shows also the fraction of events that are reconstructed within this interval.

The combination of the Muon System and Inner Detector measurements improves the mass measurement. Figure 8-41 shows the reconstructed mass distribution for 130 GeV Higgs decays using the standalone Muon System, the Inner Detector and combining the two systems. The study has been performed using the STACO procedure. Table 8-1 shows that the mass resolution is improved by about 30-40% and that the non-Gaussian tails are reduced; therefore the detection sensitivity is increased.

Table 8-1 Reconstruction efficiency, mass resolution without/with the *Z* mass constraint and size of tails for different Higgs masses using the combined information and standalone measurement including bremsstrahlung.

Higgs mass (GeV)	Reconstruction efficiency in %	σ Muon System (GeV)	σ Inner Detector (GeV)	σ Combined (GeV)	% of tails Combined
130	83.6	2.7/2.1	1.8/1.6	1.6/1.4	17.5
170	84.7	3.6/3.1	2.4/2.1	2.1/2.0	16.8
200	85.3	4.7/4.0	3.5/3.0	3.1/2.9	20.2

In the Higgs search, the kinematic constraint of the Z mass improves the mass resolution. The Z mass constraint was applied when the mass of muon pair was within 6 GeV of the Z mass. Figure 8-41 shows the reconstructed mass distribution for m_H = 130 GeV after constraining one muon pair to the Z mass. Table 8-1 shows that the improvement is of about 20%, when the mass resolution is dominated by the instrumental precision. If the resolution is close to the natural Z width, the improvement becomes less than 20%. The breakdown of the about 17% of tails at m_H = 130 GeV is, in addition to the expected 5% in the Gaussian case, 5% from events for which the reconstructed Z mass is more than 6 GeV from the nominal Z mass, 4% from events with bremsstrahlung and 3% from muon reconstruction tails.

Table 8-2 Same as Table 8-1 but without bremsstrahlung.

Higgs mass (GeV)	Reconstruction efficiency in %	σ Muon System (GeV)	σ Inner Detector (GeV)	σ Combined (GeV)	% of tails Combined
130	83.7	2.6/2.0	1.7/1.5	1.4/1.3	14.0
170	84.7	3.4/2.9	2.2/2.0	2.0/1.8	14.4
200	85.3	4.5/3.7	3.2/2.7	2.8/2.4	18.9

Table 8-2 shows again the reconstruction efficiency, the mass resolution and the size of tails for event without taking into account the contribution of the bremsstrahlung as it has been done for the Muon TDR [8-9] and in [8-10]. The present results are consistent with those presented in these documents.

8.6.4 Muon charge identification

Charge identification is essential for a wide range of physics topics. Examples are the measurement of CP violation using the charge of the muon to tag the B^0 or $\overline{B}^0$ production; search for strongly interacting Higgs by detecting the same-sign *W*-pairs; search for supersymmetric particles by looking for same-sign dileptons, and charge asymmetry measurement to determine the property of new gauge boson couplings. The Muon System provides excellent charge identification covering the full range of the muon momenta for the above physics processes.
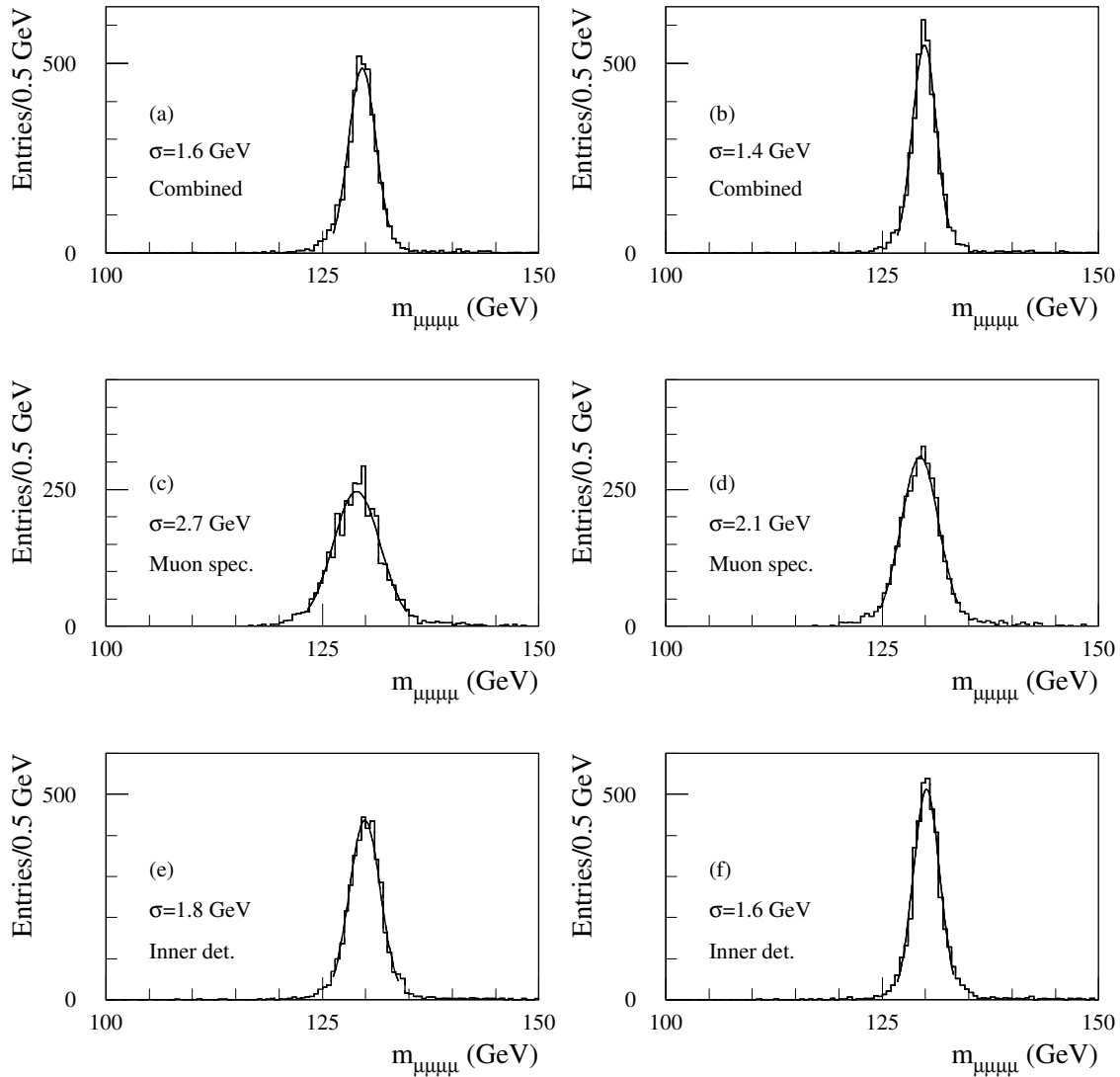
Figure 8-41 Reconstructed mass distribution for the Higgs decay $H^0 \rightarrow ZZ \rightarrow \mu^+\mu^-\mu^+\mu$ (130 GeV) using the combined information (a), standalone Muon System (c), and Inner Detector (e) without applying a Z constraint and with applying a Z constraint (b), (d), and (f). Inner bremsstrahlung has been taken into account.

As an example, $W' \rightarrow \mu\nu$ events simulated and reconstructed with the Muon System reconstruction program have been studied [8-11]. The probability of charge misidentification is determined by the ratio of the reconstructed muon events with the wrong charge determination to the total numbers of reconstructed events. The charge misidentification probability as a function of the W' mass is shown in Figure 8-42. The probability of charge misidentification for a W' of 1 TeV mass is in the range of 0.2% to 0.9%. Even at a W' mass of 6 TeV, the charge misidentification probability is below 4%.
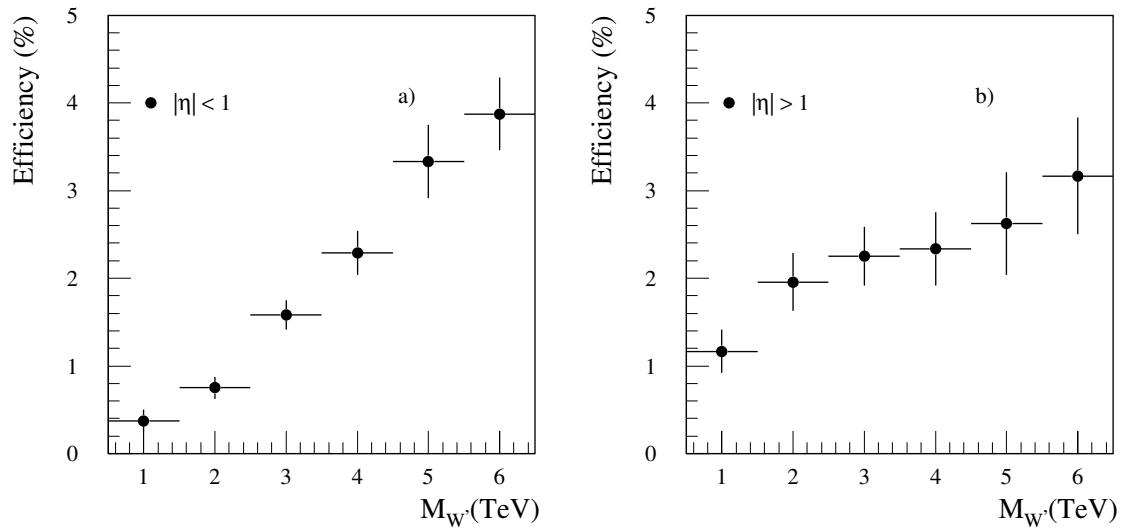
Figure 8-42 Charge misidentification probability for barrel a) and end-cap regions b).

8.7 Conclusion

The ATLAS combined muon measurements provide a highly performant muon reconstruction in a very large momentum range. The global reconstruction based on information from the Inner Detector and the Muon System allows the reconstruction of high energy muons with p_T from 6 GeV up to the limit of the muon spectrometer ($p_T \sim 2$ TeV); the reconstruction efficiency is better than 85%. The correct matching of Muon Spectrometer and Inner Detector tracks allows rejection of background muons, such as those produced in π/K decays, and allows identifying muons correctly in heavy-flavoured jets. Muons with p_T below 6 GeV can be efficiently identified and measured combining the Inner Detector track reconstruction with the energy clusters available in the Tile Calorimeter, using the last compartment to recognise muon tracks.

The accurate momentum reconstruction in a large energy range permits a precise invariant mass measurement of multi-muon final states. The Z-boson mass is reconstructed with a resolution of 2.5 GeV, comparable with the intrinsic width; Higgs decays to four muons are reconstructed with a mass resolution of about 1.1% for Higgs masses below 200 GeV.

8.8 References

8-1   I. Gavrilenko, 'Description of Global Pattern Recognition Program (xKalman)', ATLAS Internal Note, ATL-INDET-97-165 (1997).

8-2   M. Virchaux *et al.*, 'MUONBOX: a full 3D tracking program for Muon reconstruction in the ATLAS Muon Spectrometer', ATLAS Internal Note, ATL-MUON-97-198 (1997).

8-3   R. Clifft and A. Poppleton, 'iPatRec: Inner Detector pattern-recognition and track-fitting', ATLAS Internal Note, ATL-SOFT-94-009 (1994).

8-4   CERN Program Library W5013-E, July 1991.

8-5   V. Innocente and E. Nagy, Nucl. Instr. and Meth. **A324**, (1993) 297.

8-6   W. Lavrijsen, PhD Thesis, to be published.

8-7   T. Sjostrand, PYTHIA 5.7 and JETSET 7.4, CERN-TH.7112/93.

8-8   E. Barberio and Z. Was, CERN TH 7033/93.

8-9   ATLAS collaboration, Muon Spectrometer Technical Design Report, ATLAS TDR 10, CERN/LHCC/97-22 (1997).

8-10   L. Poggioli *et al.*, 'Detection sensitivity for intermediate mass Higgs through muon final state with the ATLAS detector', ATL-PHYS-98-116 (1998).

8-11   J. Shank *et al.*, 'Studies on A^o, Z' and W' with ATLAS Muon Detector', ATLAS Internal Note, ATL-MUON-97-161 (1997).

8-12   CDF II Detector Technical Design Report, Fermilab-Pub-96/390-E.

9 Jet, E_T^{miss}, and mass reconstruction

In this chapter, the reconstruction of the physics quantities relevant to the overall calorimetry is reviewed. There are three main sections. The measurement of jets is discussed in Section 9.1: experimental aspects of jet energy reconstruction and performance of various jet finding algorithms are reviewed, low-p_T jet measurements and forward jet tagging are discussed, finally the special case of τ-jet identification and measurement is studied. Section 9.2 describes the measurement of missing transverse energy. Finally, in Section 9.3, the reconstruction of the mass of objects decaying to jets is discussed: the cases considered include light quark jets, $b\bar{b}$ and ττ jet final states.

9.1 Jet measurement

Jets will be widely used in the analysis of many physics channels at the LHC. Various factors play a role in the chain that goes from the initial parton produced in the hard-scattering process to the reconstructed jet in the calorimeter. Physics effects such as fragmentation, initial and final state radiation, and the co-existence of the underlying event or additional minimum-bias events are intrinsic properties of the events. Detector effects, on the other hand, such as different calorimeter response to charged and neutral hadrons, non-linearities, magnetic field, effects of dead material, cracks between calorimeters, longitudinal leakage, lateral shower size and granularity, and electronic noise, relate to the performance of the detector, which can be optimised.

In the study of physics channels, jets are used in many different ways, for example: in the reconstruction of resonances such as $W \rightarrow jj$, $Z \rightarrow b\bar{b}$ or $t \rightarrow bW$, in measuring jet multiplicity and total jet energy in SUSY searches, for jet vetoes in the central region down to low-p_T's of ~15 GeV for background rejection, for jet tagging in the forward region, and in QCD studies. Specific physics analyses may put emphasis on different requirements such as controlling the energy scale rather than achieving the best efficiency or the best resolution. Minimum-bias events at high luminosity will restrict the area of the calorimeter over which the jet energy can be integrated, hence the optimum 'cone' size will be different for different luminosity conditions. Physics effects such as final state radiation or colour recombination in fragmentation are channel dependent. Hence, there is no unique optimum strategy for jet reconstruction, and the efficiency and calibration will depend on the algorithm, the level of minimum-bias events and the physics channel. In this chapter, the different ingredients to the problem are reviewed in order to disentangle the detector effects from the physics effects. Section 9.1.1 reviews the detector aspects of jet energy reconstruction: calorimeter response, effect of dead material or 'cracks' using a classical 'cone' algorithm as well as the determination of the jet energy. Section 9.1.2 introduces various jet algorithms and discusses some of their basic properties. Section 9.1.3 treats the question of low-p_T jet reconstruction and Section 9.1.4 of forward jet tagging. Section 9.1.5 reviews all the aspects of τ-jet reconstruction and identification. The question of the absolute jet energy scale calibration is treated more specifically in Section 12.5.1.

9.1.1 Experimental aspects of jet energy reconstruction

In this section, aspects of jet reconstruction related to detector performance are reviewed. The sample of jets used are back-to-back $q\bar{q}$ di-jet events generated with PYTHIA 5.7 / JET-SET 7.4. The energy deposited in the sensitive parts of the various calorimeter compartments is first converted to total energy using the electromagnetic (EM) scale. The various calorimeters have different degrees of non-compensation and hence a different response to the charged hadrons jet component. Any reconstruction algorithm will have to apply additional weights to take that effect into account. In addition, the energy loss as a function of η is different for the neutral and charged hadron components of the jets (see Figure 5-25). The energy loss for jets is shown in Figure 9-1. Due to the width of the jets, the impact of the dead material in the vertical crack at $|\eta| \approx 1$ and of the corners of the cryo-

Figure 9-1 Fractional energy loss of 200 GeV jets in dead material as a function of pseudorapidity.

stat walls at $|\eta| \approx 1.45$ are merged and affect a broader region than in the case of single particles (see Figure 5-25).

9.1.1.1 Performance for jet energy reconstruction with the 'Benchmark procedure'
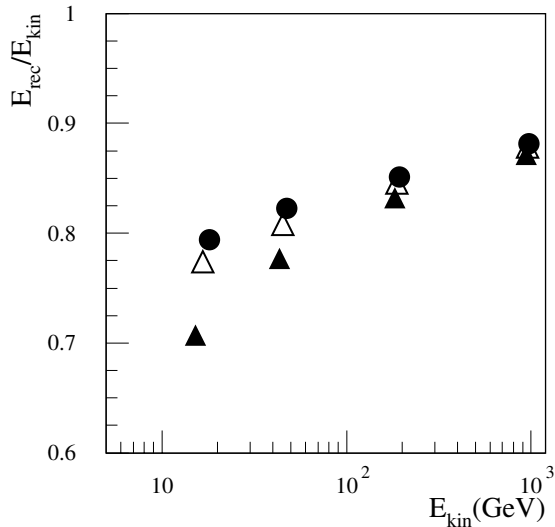
Figure 9-2 Average ratio of the reconstructed jet energy E_{rec} over the particle level jet energy E_{kin} as a function of E_{kin} for di-jet events at $|\eta| = 0.3$ for three cone sizes $\Delta R = 0.4$ (black triangles), $\Delta R = 0.7$ (open triangles) and $\Delta R = 1.5$ (black dots). The calorimeters are calibrated at the EM scale. No correction for energy loss in the dead material is applied.

In the 'Benchmark procedure' for jet energy reconstruction, a standard fixed-cone jet algorithm is applied. Transverse energies in towers are projected in a matrix of (0.1×0.1) granularity in $(\Delta\eta \times \Delta\phi)$ with tower energies calibrated at the EM scale. The highest E_T tower, above a cut, is selected as a jet seed and a cone is created, centred on the seed. Two cone sizes have been considered: $\Delta R = 0.4$ and $\Delta R = 0.7$. In order to disentangle the effect of fragmentation and of calorimeter response, the reconstructed energy in the calorimeter inside the cone (E_{rec}) is normalised to the sum of the momenta of the generated particles inside the cone (E_{kin}), taking into account the effect of the magnetic field. Figure 9-2 shows an example of the mean ratio of (E_{rec}/E_{kin}). No correction for energy loss in the dead material is applied. This ratio is typically of the order of 0.8 and varies as a function of the parton energy and the cone size. This results from the fact that the energy spectrum of the particles contained in the cone depends on the parton energy, and the

e/π ratio varies with the hadron energy. Out-of-cone losses due to lateral hadronic shower size are larger for a smaller cone. A procedure that minimises $\sum (E_{rec} - E_{kin})^2 + \beta \times \sum (E_{rec} - E_{kin})$ is then applied to adjust the calibration coefficients for each parton energy and for each cone size. This 'Benchmark procedure' includes weights for each calorimeter compartment, the presampler, the EM and hadronic calorimeters. Correction terms for the energy loss in the dead material between the EM and hadronic compartments of the central barrel and extended barrels are added. Special weights for the two intermediate tile calorimeters in the vertical gaps and the scintillators covering part of the end-cap cryostat front wall are adjusted to compensate for the energy loss in the dead material located in the cracks (see Section 5.3.2.1 and Figure 5-i) [9-1][9-2][9-3].

Energy scan

Jet energy scans were performed at various values of pseudorapidity. The coefficients used in the jet energy reconstruction algorithm were fitted at every energy point (see Section 9.1.1.2 for a discussion of their energy dependence). In the central region, the range of energies considered was 20 GeV to 1 TeV, while in the end-cap region, the energies relevant for the physics start at about 100 GeV. No electronic noise or pile-up was included at this level. The performance of the barrel and end-cap calorimeters are shown in Figure 9-3 and Figure 9-4, respectively.
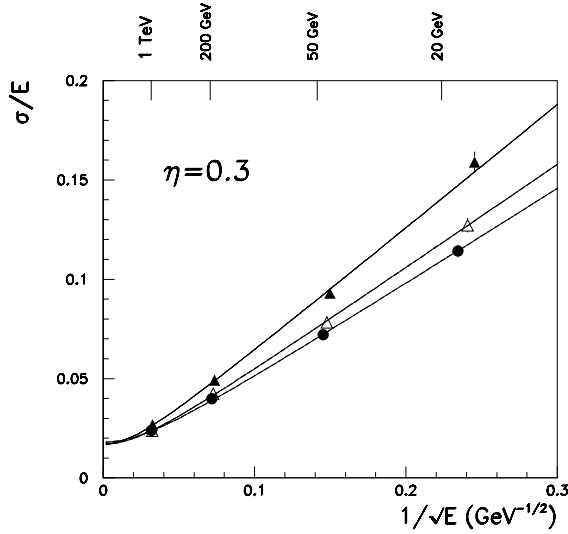
Figure 9-3 Energy resolution in the range from 20 GeV to 1 TeV at $|\eta| = 0.3$. Black circles are obtained using energies summed in cone size of $\Delta R = 1.5$; open triangles for cone size $\Delta R = 0.7$ and black triangles for cone size $\Delta R = 0.4$.
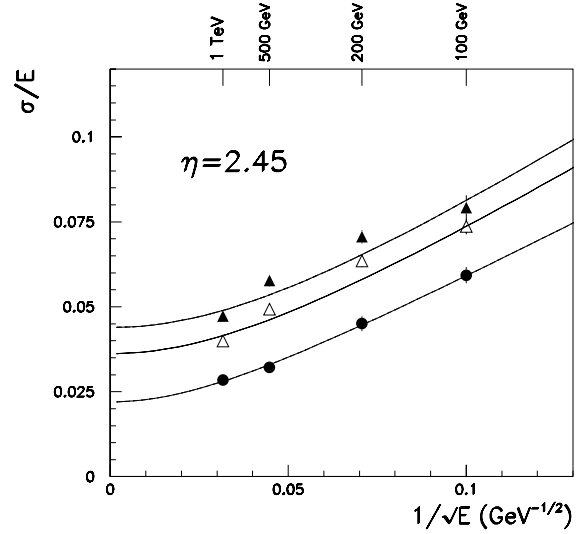
Figure 9-4 Energy resolution in the range 100 GeV to 1 TeV at $|\eta| = 2.45$. Black circles are obtained using the total energy in the calorimeter; open triangles for cone size $\Delta R = 0.7$ and black triangles for cone size $\Delta R = 0.4$.

The results are shown for the total sum of energies in the calorimeter and for two cone sizes $\Delta R = 0.7$ and $\Delta R = 0.4$. The resolution was fitted with the expression $\sigma/E = a/\sqrt{E} \oplus b$. As the cone size becomes smaller, there is a deterioration of the resolution. In the barrel region, the effect is confined to the sampling term which suffers from the fluctuations of the out-of-cone losses from the fragmentation and magnetic field effects. The high energy jets are only slightly affected, since, due the boost, the particles in the jet are more collimated and well contained in

Table 9-1 Coefficients of the jet energy resolution fitted by the expression $\sigma/E = a/\sqrt{E} \oplus b$.

	Barrel region $\eta=0.3$		End-cap region $\eta=2.45$	
	a (%GeV$^{1/2}$)	b (%)	a (%GeV$^{1/2}$)	b (%)
Full calorimeter	48.2 ± 0.9	1.8 ± 0.1	55.0 ± 2.5	2.2 ± 0.2
Cone $\Delta R=0.7$	52.3 ± 1.1	1.7 ± 0.1	64.2 ± 2.4	3.6 ± 0.2
Cone $\Delta R=0.4$	62.4 ± 1.4	1.7 ± 0.2	68.4 ± 3.4	4.4 ± 0.2
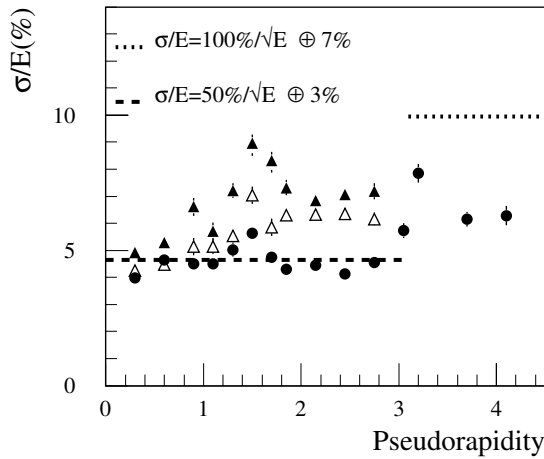
Figure 9-5 Energy resolution for jets of constant energy (200 GeV) across the full pseudorapidity coverage of the calorimeter. Black dots are for total energy in the calorimeter; open triangles for cone size $\Delta R = 0.7$ and black triangles for cone size $\Delta R = 0.4$.
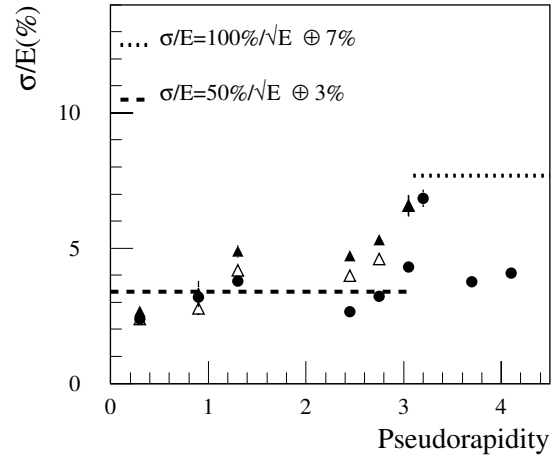
Figure 9-6 Energy resolution for jets of constant energy (1 TeV) across the full pseudorapidity coverage of the calorimeter. Black dots are for total energy in the calorimeter; open triangles for cone size $\Delta R = 0.7$ and black triangles for cone size $\Delta R = 0.4$. Jets of 1 TeV have been simulated at fewer pseudorapidity values than 200 GeV jets.

the cone. In the end-cap, at $|\eta| = 2.45$, both the statistical and the constant terms are affected, because the hadronic shower size becomes non-negligible with respect to the cone size and energy is lost out of the cone even for high-energy jets.

Scan across pseudorapidity

As shown in Figure 9-1, there are non-uniformities in the calorimeter. In the transition region between the barrel and the end-cap, the larger amount of dead material affects jets with pseudorapidity from 1.0 to about 1.8. In the transition region between the end-cap and the forward calorimeters, the region affected extends roughly from $|\eta| = 3.0$ to 3.5. Scans across pseudorapidity were carried out with jets of various energies. Figure 9-5 shows the resolution obtained for jets with a constant energy of 200 GeV, and Figure 9-6 for 1 TeV jets. Values are compared to the target resolution of $\sigma/E = 50\%/\sqrt{E} \oplus 3\%$ for precision jet energy measurement in the central pseudorapidity region, and the target resolution of $\sigma/E = 100\%/\sqrt{E} \oplus 7\%$ for jet tagging and E_T^{miss} measurements in the forward region. Only a relatively small deterioration of the resolution is observed in the crack region around $|\eta| = 1.5$ when the total energy in the calorimeter is used. The effect is more pronounced when a cone algorithm is applied. The deterioration of

the resolution is also observed in the transition region between the end-cap and the forward calorimeters. In the FCAL region, the resolution is shown only for the total energy in the calorimeter, a more detailed discussion of the reconstruction of jets in the FCAL is given in Section 9.1.4.

The energy dependence of the resolution has been fitted at various points in pseudorapidity with the parametrisation $\sigma / E = a / \sqrt{E} \oplus b$. The resulting statistical term a and constant term b are shown in Figure 9-7 and Figure 9-8. When all calorimeter energy is summed, the constant term deteriorates from 2% to about 3.5% in the crack region around $|\eta| = 1.5$ and increases to 4% as one approaches $|\eta| = 3.2$. In the central region out-of-cone losses due to fluctuations in the fragmentation affect mostly lower energy jets and thus only the statistical term. More energetic jets have more collimated fragmentation products and their corresponding hadronic shower is well contained. But as the pseudorapidity increases, a cone of constant size in $(\Delta\eta \times \Delta\phi)$ decreases in terms of the solid angle sustained. Therefore the hadronic shower size becomes increasingly larger with respect to the cone size. Losses due to hadronic shower leakage affect the more energetic jets, resulting in an increase of the constant term.
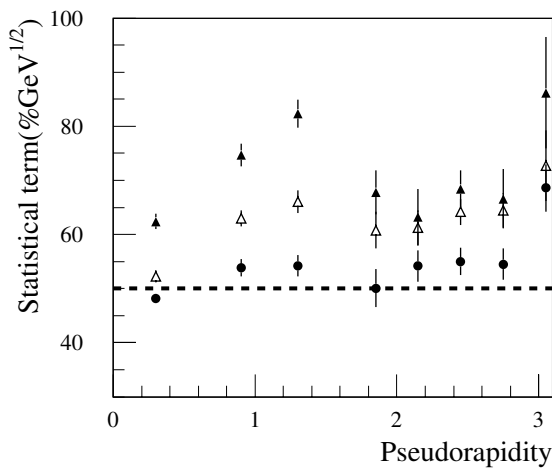
Figure 9-7 Statistical term of the fitted energy resolution for jets as a function of pseudorapidity. Black dots are for total energy in the calorimeter, open triangles for cone size $\Delta R = 0.7$ and black triangles for cone size $\Delta R = 0.4$.
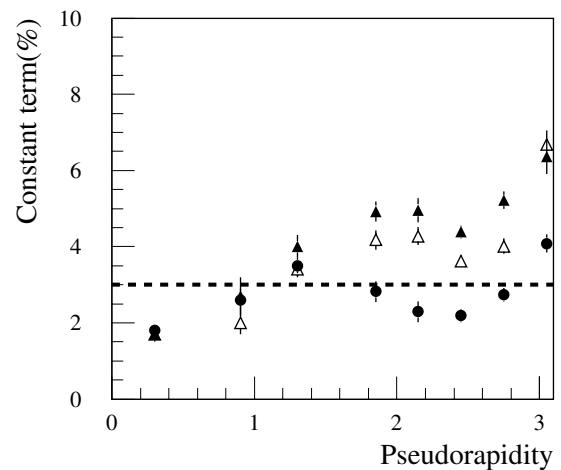
Figure 9-8 Constant term of the fitted energy resolution for jets as a function of pseudorapidity. Black dots are for total energy in the calorimeter, open triangles for cone size $\Delta R = 0.7$ and black triangles for cone size $\Delta R = 0.4$.

Effect of electronic noise and pile-up

The effect of electronic noise was studied in the barrel region at $|\eta| = 0.3$. The noise was simulated applying the digital filtering method. The rms of the noise is of the order of 200 MeV per tower of 0.1×0.1 in $\Delta\eta \times \Delta\phi$, a value estimated for the calorimeter calibrated at the EM scale (Chapter 5). The noise contribution in cones of $\Delta R = 0.4$ and $\Delta R = 0.7$ is 1.4 GeV and 2.5 GeV, respectively. When the jet energy was reconstructed, additional factors were applied to correct for the effect of the non-compensation. Figure 9-2 shows that these factors are of the order of 1.25. The level of noise at the 'hadronic' scale is then equivalent to 1.9 and 3.3 GeV for cone sizes $\Delta R = 0.4$ and $\Delta R = 0.7$, respectively. The data were fitted by the expression $\sigma / E = a / \sqrt{E} \oplus b \oplus c / E$.

The results are given in Table 9-2 and shown in Figure 9-9 for the two cone sizes. The statistical term *a* and noise term *c* are correlated and there are only four energy points available, hence they have large errors. The procedure used was to keep the statistical term *a* and constant term *b* fixed at the values obtained when no electronic noise was added, and, to fit only the noise term *c*. When no cell cut was applied, the noise term found was in good agreement with the estimated contribution. Compatible values were obtained when the three coefficients were fitted simultaneously. Different cell cuts were used and the corresponding noise evaluated. Symmetric thresholds were applied to minimise the bias induced on energy. The scan was done between zero and three times the rms of the noise by steps of 0.5. The optimal cut depends on the energy of the jet and the cone size. The best overall performance was obtained for a 2.5σ cut. The noise contribution was then reduced, the main improvement being found for a cone size $\Delta R = 0.7$ where the noise term decreases from 3 to 2 GeV. The resolution obtained for the two cone sizes, once the electronic noise contribution is included, are similar.

Table 9-2 Coefficients of the jet energy resolution fitted by $\sigma/E = a/\sqrt{E} \oplus b \oplus c/E$ when electronic noise is included. The coefficients *a* and *b* are fixed to the values obtained without noise.

cell cut	a (%GeV$^{1/2}$)	b(%)	c (GeV)
no cut $\Delta R = 0.7$	52.3	1.7	3.0 ± 0.1
2.5σ $\Delta R = 0.7$	52.3	1.7	2.0 ± 0.1
no cut $\Delta R = 0.4$	62.4	1.7	2.0 ± 0.1
2.5σ $\Delta R = 0.4$	62.4	1.7	1.7 ± 0.2

The effect of the pile-up from minimum-bias events was studied in the barrel region at $|\eta| = 0.3$. In addition to the pile-up, electronic noise was added without applying digital filtering (see Section 4.2.4). The contribution of the pile-up and noise in a tower of 0.1×0.1 in $\Delta\eta \times \Delta\phi$ is slightly asymmetric. The mean value is 50 MeV and the rms about 0.5 GeV. In a cone of $\Delta R = 0.4$ ($\Delta R = 0.7$), the pile-up contributes 3.5 GeV (11 GeV). Once the jets are calibrated to the 'hadronic' scale, the equivalent noise term is 4.7 GeV (14 GeV). The resolution obtained for jets reconstructed with cone size $\Delta R = 0.4$ are given in table Table 9-3 and Figure 9-10. No E_T tower cut, nor cell energy cut, were applied to the data.

Table 9-3 Terms of the jet energy resolution fitted by $\sigma/E = a/\sqrt{E} \oplus b \oplus c/E$ when pile-up and electronic noise are included. First row: *a* and *b* fixed to the values obtained without electronic noise. Second row: only *b* fixed to that value.

a (%GeV$^{1/2}$)	b(%)	c (GeV)
62.4 fixed	1.7 fixed	4.7 ± 0.2
81.3 ± 2.9	1.7 fixed	3.9 ± 0.3

9.1.1.2 Determination of the jet energy

In beam tests, several algorithms for reconstructing the energy of pions have been applied [9-4][9-5][9-6][9-7]. The performance of two of them for the determination of the jet energy are presented in this section [9-8]. The algorithms are the Sampling-dependent weighting technique [9-4] with weights applied to the different calorimeter compartments, and the H1 based approach with weights applied directly to the cell energies [9-9]. The data samples used were the fully simulated back-to-back di-jet events with quark energies E_0 equal to 20, 50, 200 and 1000 GeV at $|\eta| = 0.3$, contained in the Barrel Calorimeter. The cell electronic noise contribution to the EM Calorimeter response was simulated applying the digital filtering method. The jets were reconstructed using the fixed-cone jet algorithm [9-10]. The jet seed threshold on the transverse energy in a tower was set to $E_s = 2$ GeV. The cone sizes used in this analysis were $\Delta R = 0.4$ and 0.7. Events in which two, and only two, reconstructed jets have a transverse energy larger than the
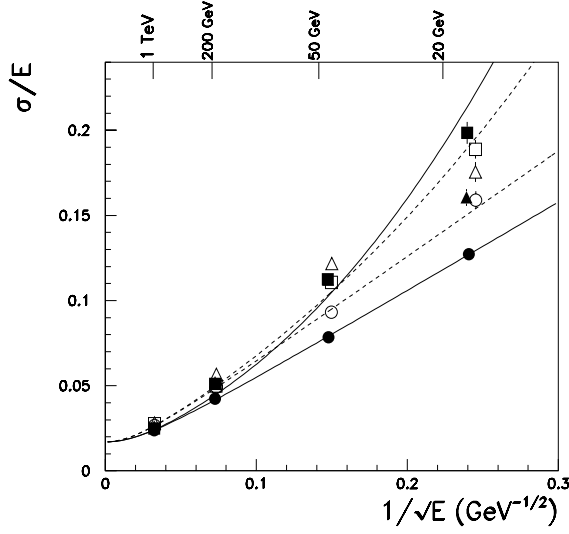
Figure 9-9 Effect of the electronic noise on the jet energy resolution: black dots (open dots) are for cone size $\Delta R = 0.7$ ($\Delta R = 0.4$) when no electronic noise is included; black squares (open squares) are for cone size $\Delta R = 0.7$ ($\Delta R = 0.4$) with electronic noise included; black triangles (open triangles) are for cone size $\Delta R = 0.7$ ($\Delta R = 0.4$) with a cell energy cut at 2.5σ of the noise. The data are fitted with the expression $\sigma/E = a/\sqrt{E} \oplus b \oplus c/E$. The full lines (dashed lines) show the fit to the data with cone $\Delta R = 0.7$ ($\Delta R = 0.4$) without and with noise (no cell cut), see Table 9-2.
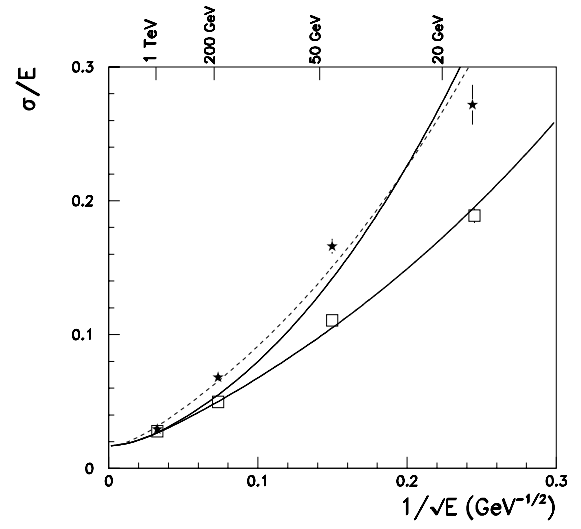
Figure 9-10 Jet energy resolution obtained with electronic noise and pile-up included for cone size $\Delta R = 0.4$: stars are for jets with pile-up and electronic noise, open squares with electronic noise only (digital filtering applied). The data including pile-up are fitted with $\sigma/E = a/\sqrt{E} \oplus b \oplus c/E$. The full lines show the result when a and b are fixed to the values obtained without pile-up or noise and the dashed line when only b is fixed (see Table 9-3).

threshold value $E_T = 5$ GeV for $E_0 = 20$ GeV and $E_T = 20$ GeV for E_0 larger than 20 GeV were retained. To reduce the effect of the electronic noise on the determination of the energy, the absolute values of the cell energies were required to be larger than two times the rms of the electronic noise of the cells and the transverse energy per tower of size 0.1×0.1 in $\Delta\eta \times \Delta\phi$ was required to be larger than 0.2 GeV.

The offline calibration: general procedure

As was shown in the previous section, the ATLAS calorimeters are not compensating and a calibration procedure has to be applied to determine the jet energy and to improve the resolution. In a general form, the reconstructed energy of a jet k can be expressed as a parametric function of the cell energy $\overline{\varepsilon_{i,j}}$ as

$$E^k = \sum_l f(a_l; \overline{\varepsilon_{i,j}}) \qquad \text{9-1}$$

where i defines the calorimeter sampling to which the cell belongs, j is its position in pseudorapidity, and l runs from one to the total number of parameters used. Here, and in the following, the symbol overline on top of an energy indicates that these values were obtained using the EM scale calibration. For each parton energy, the values of the parameters a_l minimise the quantity

$$\sum_{k=1}^{K} (E^k - E^k_{kin})^2 + \beta \sum_{k=1}^{K} (E^k - E^k_{kin}) \qquad 9\text{-}2$$

This function is minimised simultaneously with respect to the Lagrange multiplier β that forces the reconstructed energy in the cone to reproduce the reference energy E^k_{kin}, the particle level energy inside the cone. In the real experiment, the particle level energy of a jet is unknown. Therefore the parameters a_l were parametrised in turn as a function of E_{kin} using smooth functions

$$a_l = g_l(b_n; E_{kin}). \qquad 9\text{-}3$$

The values of the parameters b_n were determined by fitting Equation 9-3 to the values a_l obtained using the knowledge of the energy of the particles associated with the jet. The correlations between the parameters were not taken into account. The following iteration procedure was then applied: a) define a starting value for the reconstructed energy, here the value obtained applying the EM scale calibration was used; b) determine the parameters a_l using Equation 9-3 and reconstruct the energy using Equation 9-1; c) recompute the weights using the energy reconstructed in b); d) iterate the procedure until the change in the energy is smaller than 1 MeV. Typically, less than ten iterations are needed.

First example of the offline calibration: the Sampling method

The energy of the jet k, E^k, is expressed as a linear combination of the energies $\overline{E^k_i}$ deposited in the presampler, in the EM Calorimeter, and in the Hadronic Tile Calorimeter ($i = 1, 2$ and 3 respectively):

$$E^k = a_1 \overline{E^k_1} + a_2 \overline{E^k_2} + a_3 \overline{E^k_3} + a_4 \overline{E^k_4}.$$

The fourth term in the equation describes the deposited energy in the cryostat. The quantity $\overline{E^k_4}$ was parametrised according to :

$$\overline{E^k_4} = \sqrt{\overline{E^k_{em3}} \cdot \overline{E^k_{had1}}},$$

where $\overline{E^k_{em3}}$ and $\overline{E^k_{had1}}$ are the electromagnetic scale energies deposited in the third compartment ('sampling') of the EM Calorimeter and in the first compartment of the Hadronic Tile Calorimeter respectively. This is the 'Benchmark method' applied in the previous section. Using eight parameters instead of four, that is one for each longitudinal calorimeter compartment plus the cryostat term, did not improve the results significantly; therefore, the simpler approach was selected.

Second example of the offline calibration: the H1 method

The H1 method is based on the study of the energy deposited by the particles of the jet in the individual cells of the calorimeters. The parametrisation chosen for the reconstructed energy of a jet inside the cone was

$$E^k = \overline{E^k_1} + \sum_j \alpha_2(\overline{\varepsilon_{2,j}}) \times \overline{\varepsilon_{2,j}} + \sum_j \alpha_3(\overline{\varepsilon_{3,j}}) \times \overline{\varepsilon_{3,j}} + \alpha_4 \overline{E^k_4} \qquad 9\text{-}4$$
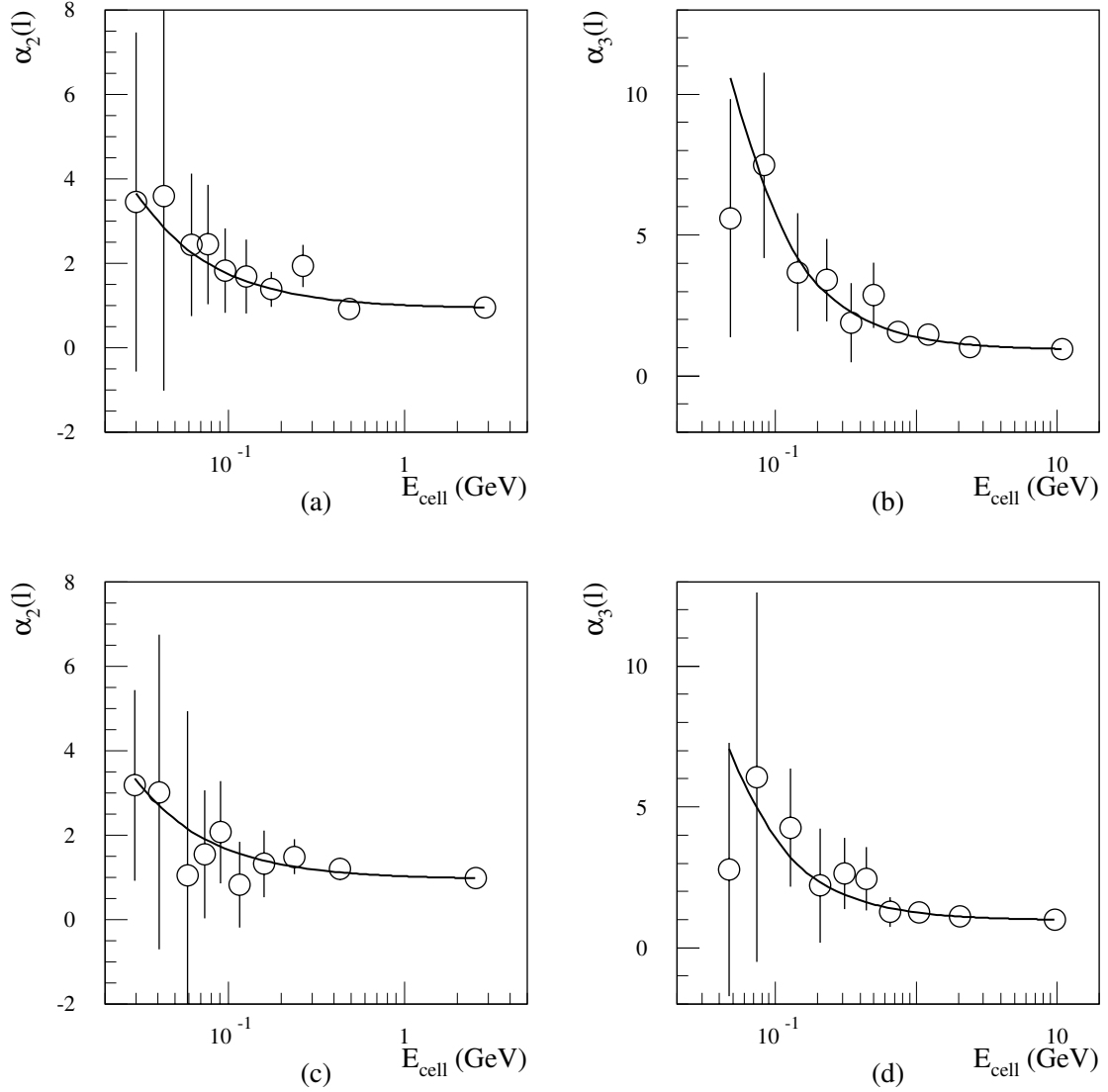
Figure 9-11 H1 method: dependence of the parameters $\alpha_i(l)$ (i = 2, 3) on the cell energy for E_0 = 200 GeV, a) EM Calorimeter with ΔR = 0.4, b) Hadronic Tile Calorimeter with ΔR = 0.4, c) EM Calorimeter with ΔR = 0.7, d) Hadronic Tile Calorimeter with ΔR = 0.7.

where the first term is the total energy deposited in the presampler, the second and third terms are the sums of the energies of all the cells in the EM and hadronic calorimeters, and the fourth term is the cryostat correction defined as before. The $\alpha_i(\overline{\varepsilon_{i,j}})$'s are coefficients that multiply the energy in the cells in the EM Calorimeter (α_2) and the hadronic calorimeter (α_3). They are parametrised by functions that depend on two parameters:

$$\alpha_2(\varepsilon) = a_1 + \frac{a_2}{|\varepsilon|}, \; \alpha_3(\varepsilon) = a_3 + \frac{a_4}{|\varepsilon|} \text{ and } \alpha_4 = a_5. \qquad 9\text{-}5$$

The response of a cell with a small signal is corrected upwards to make its response equal to that of cells with large (typically electromagnetic) deposited energy. Introducing a parametric function of the same type that multiplies the energy deposited in the presampler cells did not improve the reconstruction of the jet energies significantly and therefore was not used.

To determine the functions $\alpha_i(\overline{\varepsilon_{i,\,j}})$ of Equation 9-4, the distributions of the energies deposited in the cells belonging to the EM and Hadronic Tile Calorimeters were divided into ten bins of equal statistics. In this case, the functions $\alpha_i(\overline{\varepsilon_{i,\,j}})$ are represented by two vectors of dimension 10: $\alpha_i(\overline{\varepsilon_{i,\,j}}) = \alpha_i(l)$ ($i = 2, 3$; $l = 1, 10$), where l defines the interval in the cell energy. The minimisation of Equation 9-2 produced the values of the vectors $\alpha_i(l)$ shown in Figure 9-11. The errors in the figure are the rms values of five independent determinations of the parameters obtained by breaking the data samples at each energy into five separate sets of equal statistics and solving the minimisation equation for each set. The fits of the function given in Equation 9-5 have a good χ^2 and the corresponding curves are also shown. The results obtained for resolution and linearity with the simple parametrisation of Equation 9-5 are very close to the results obtained using ten parameters for each calorimeter.

Parametrisation of the a_l's as a function of the beam energy

As an example, Figure 9-12 shows the parametrisation with the particle level jet energy of the a_l's obtained using the Sampling method. Also the values of the parameters resulting from the fits are shown in the figures. Similar smooth shapes were obtained with the H1 method. The results for resolution and linearity obtained without prior knowledge of the energy, applying an iterative process based on these parametrisations, are very close to the results obtained using the knowledge of E_{kin}^k.

Results

The jet fractional energy resolutions and linearities are given in Table 9-4 and Table 9-5 respectively. All the results were obtained fitting a Gaussian function to the data using the full lineshape. As in the previous section, the jet fractional energy resolution was calculated as the width of the distributions of $E^k - E_{kin}^k$ divided by the mean value of the reconstructed energy. The normalised response is given by $\mu = \langle E^k / E_{kin}^k \rangle$. The H1 method gives better resolutions than the Sampling method. Enlarging the cone size does not improve significantly the energy resolution due to the increase of the electronic noise, except for the low energy 20 GeV point. The residual non-linearities are smaller than 2% and 3% using the H1 and the Sampling method respectively.

Table 9-4 Jet energy resolutions obtained with the Sampling and the H1 methods ($|\eta| = 0.3$).

E_0 [GeV]	Sampling method: σ/E [%]		H1 method: σ/E [%]	
	$\triangle R = 0.4$	$\triangle R = 0.7$	$\triangle R = 0.4$	$\triangle R = 0.7$
20	15.7 ± 0.7	13.7 ± 0.6	14.5 ± 0.7	12.5 ± 0.5
50	10.2 ± 0.3	9.8 ± 0.3	8.5 ± 0.3	8.0 ± 0.2
200	5.3 ± 0.2	4.7 ± 0.1	4.0 ± 0.1	4.0 ± 0.1
1000	2.4 ± 0.1	2.4 ± 0.1	2.2 ± 0.1	2.3 ± 0.1
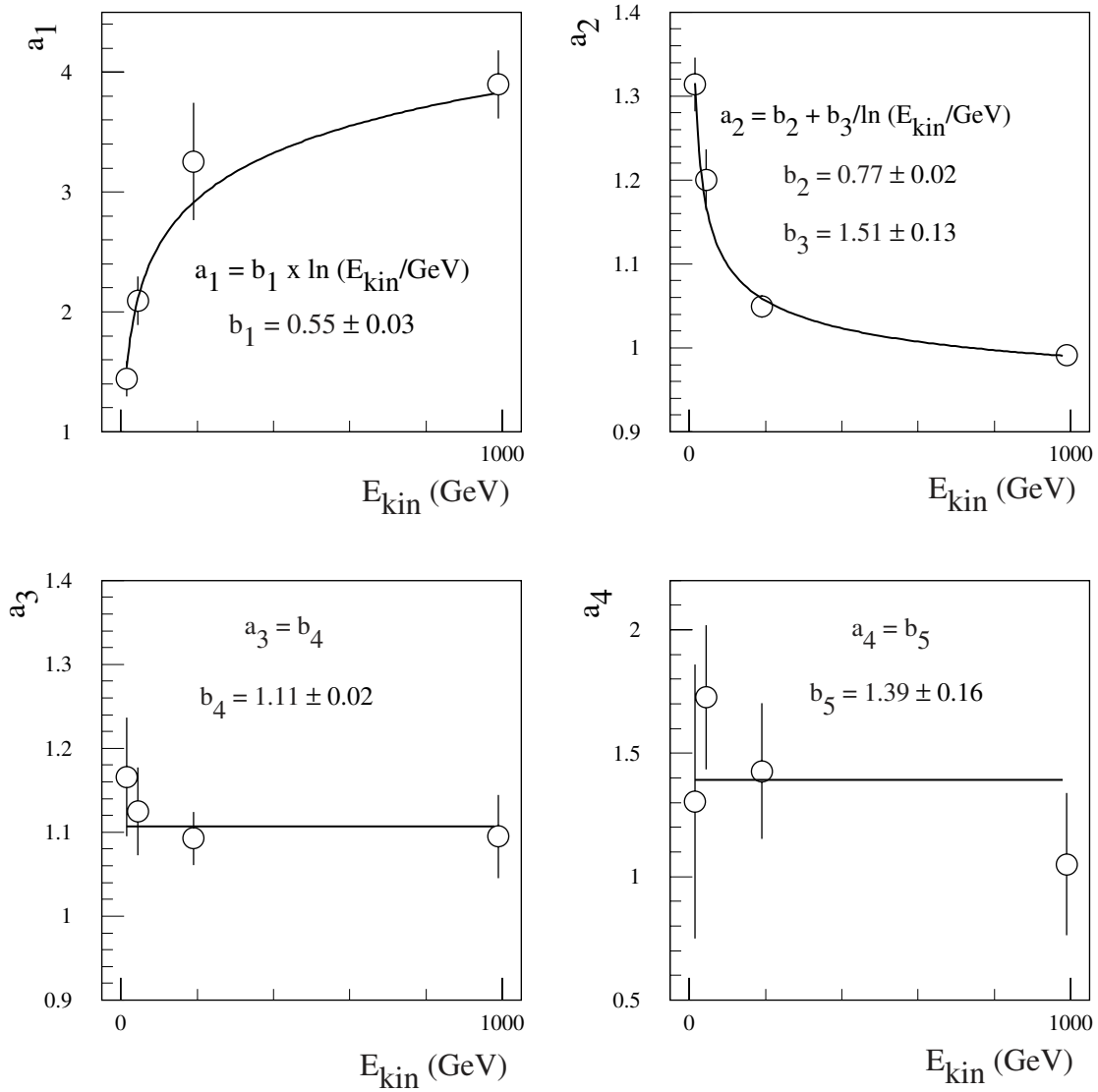
Figure 9-12 parametrisation of the a_i's obtained using the Sampling method with $\Delta R = 0.7$, as a function of the particle level jet energy.

Table 9-5 Residual jet energy non-linearities (see text): $(1-\mu)$ in percent ($|\eta| = 0.3$).

	Sampling Method		H1 Method	
E_0 [GeV]	$\Delta R = 0.4$	$\Delta R = 0.7$	$\Delta R = 0.4$	$\Delta R = 0.7$
20	0.1 ± 0.9	-0.2 ± 0.7	1.1 ± 0.8	2.1 ± 0.6
50	-2.5 ± 0.4	-2.9 ± 0.3	1.3 ± 0.3	-1.5 ± 0.3
200	0.1 ± 0.2	0.2 ± 0.2	-0.3 ± 0.2	-1.4 ± 0.1
1000	2.4 ± 0.2	2.5 ± 0.1	1.7 ± 0.1	2.1 ± 0.1

The energy resolutions have been parametrised according to:

$$\sigma/E \;=\; a/\sqrt{E} \oplus b\,.$$

The results obtained for the two cone sizes and the two calibration methods are shown in Figure 9-13 and summarised in Table 9-6. The results obtained with the Sampling method can be compared to the values shown in Figure 9-9 obtained with the 'Benchmark procedure' after applying a 2.5σ symmetric cut on the noise. They show consistent results except for the 20 GeV point which shows a better resolution in this analysis, as a result of the tighter selection cuts applied. The method presented here could be improved by taking into account the correlations existing between the a_l's when parametrising them as a function of the energy.
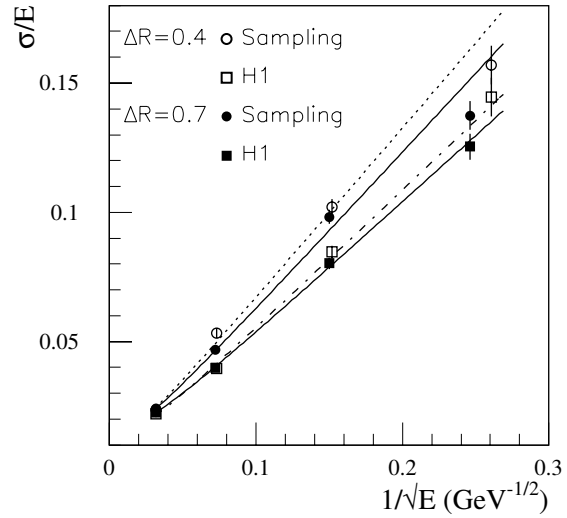
Figure 9-13 Jet energy resolutions obtained with the sampling and H1 methods for the two cone sizes: the full lines represents the fitted resolution for cone size $\Delta R = 0.7$ and the dashed lined for cone size $\Delta R = 0.4$.

In summary, it is found that the jet energy can be determined reliably without prior knowledge of the particle level energy of the jet by using simple smooth functions to describe the energy dependence of the calibration coefficients. The results have been obtained in the central barrel region, at $|\eta| = 0.3$. A total of five parameters are used for the Sampling method and six for the H1 method. Essentially the same performance for the energy resolution and linearity is obtained as when the particle level jet energy is known. The H1 method gives better performance both in resolution and residual non-linearities.

Table 9-6 Parameter values obtained fitting the energy dependence of the jet energy resolution ($|\eta| = 0.3$).

	Sampling Method		H1 Method	
	$\Delta R = 0.4$	$\Delta R = 0.7$	$\Delta R = 0.4$	$\Delta R = 0.7$
a (%GeV$^{1/2}$)	66.0 ± 1.5	61.2 ± 1.3	53.9 ± 1.3	51.5 ± 1.1
b (%)	1.2 ± 0.3	1.4 ± 0.2	1.3 ± 0.2	2.5 ± 0.2
χ^2 prob. (%)	1.6	0.8	27.3	66.7

9.1.1.3 High-p_T jet energy calibration

Physics processes involving known processes such as Z+jet events or $W \rightarrow jj$ decays from top events will provide *in situ* jet energy calibration up to about 500 GeV (see Chapter 12). It will be necessary to extrapolate the jet energy calibration up to the highest jet energies that will be reached at the LHC.

A test was made with the parametrisation of the energy dependence of the calibration coefficients discussed in the previous section. The parameters of the energy dependence, the b_n parameters of Equation 9-3, were fitted using the jets produced by 20, 50 and 200 GeV quarks.

Afterwards the 1 TeV jets were reconstructed using the extrapolated coefficients. Using the H1 method with a $\Delta R = 0.7$ cone, the same resolution was obtained and the non-linearity was $(2.9 \pm 0.1)\%$, about 1% more than when the full energy range was fitted.

Since very high-p_T jets will not be available for *in situ* calibration, the extrapolation of the calibration coefficients can only be checked on jets fully simulated by Monte Carlo. In addition to the uncertainties arising from physics effects such as fragmentation and cone size, the response of the calorimeter to hadrons plays a non-negligible role. It was shown in Chapter 5 that the e/π ratio is larger than one and depends on the hadron energy. The ratio is given by the formula

$$e/\pi = \frac{e/h}{1 + (e/h - 1) \cdot F(\pi^0)} \qquad 9\text{-}6$$

The two ingredients of the hadron response are the intrinsic responses to purely electromagnetic energy (e) and purely hadronic energy (h), and the fraction of π^0's produced in the hadron interaction $F(\pi^0)$. For example, in the barrel calorimeter, typical values of e/π from test beam data are 1.25 (1.10) at 20 GeV (300 GeV). A fit to the test-beam data gives a value for e/h of 1.37 ± 0.01,
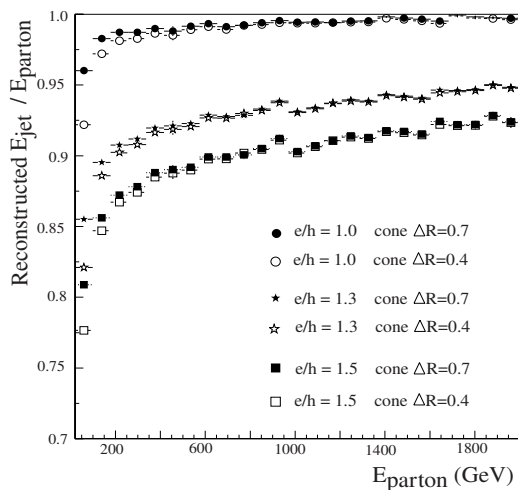
Figure 9-14 Reconstructed jet energy for different levels of non-compensation ($e/h = 1.0$, 1.3, 1.5) and for two cone sizes ($\Delta R = 0.7$ and 0.4).
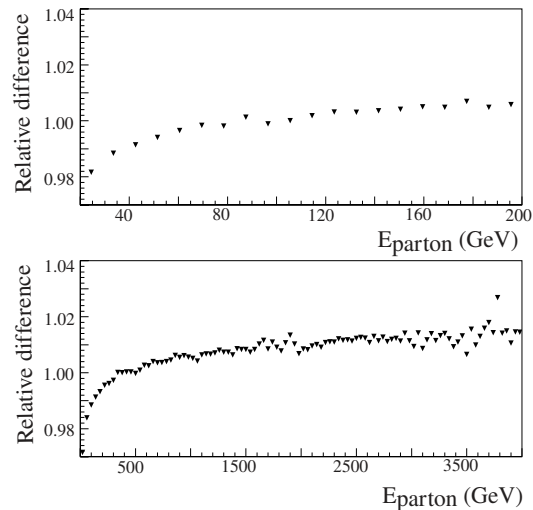
Figure 9-15 Relative difference in the calibration for two degrees of non-compensation ($e/h = 1.3$, 1.5). In the top plot, the responses are equalised at 100 GeV and in the bottom plot at 500 GeV.

while a fit to data simulated with the G-CALOR Monte Carlo results in 1.31 ± 0.01. Different hadronic shower Monte Carlo packages give different predictions for the degree of non-compensation of the calorimeter, with differences of the order of ± 0.2 [9-11]. The failure of the hadronic shower Monte Carlo package to reproduce e/h has been simulated [9-12]. A parametrisation of the hadron response based on Equation 9-6 has been implemented in ATLFAST. The fraction of π^0's in pion and proton induced showers were generated according to the parametrisation given in [9-13]. A sample of QCD di-jet events were generated: one parton was required to be in the central region ($|\eta| < 0.5$) and initial and final state radiation and multiple interactions were not switched on. Figure 9-14 shows the reconstructed jet energy for three values of

e/h: 1.0, 1.3 and 1.5 when the calorimeters were calibrated at the EM scale. At 200 GeV for example, the shift between the parton energy and the reconstructed jet energy is 10% (14%) for *e/h* = 1.3 (1.5), while at 2 TeV the shift reduces to 6% (8%).

Assuming that *in situ* calibration will provide the absolute jet energy scale at least in part of the energy range, it is interesting to look at the residual differences in non-linearity for different values of *e/h*. Figure 9-15 shows that they are of the order of 2 to 3% below 200 GeV and 2% in the range 200 GeV to 4 TeV. The consequence of such an uncorrected non-linearity was studied in the case of the measurement of the inclusive high-p_T jet cross-section. Since the cross-section falls rapidly with p_T, a miscalibration generates an apparent disagreement with the QCD prediction. Figure 9-16 shows the ratio of the measured cross-section and the QCD prediction in the range 500 GeV to 4 TeV in the case where the degree of non-compensation *e/h* is overestimated by 0.2, *i.e.* is equal to 1.5 instead of 1.3. See Chapter 15 and Section 21.5 for a more detailed discussion of the implications for the physics.
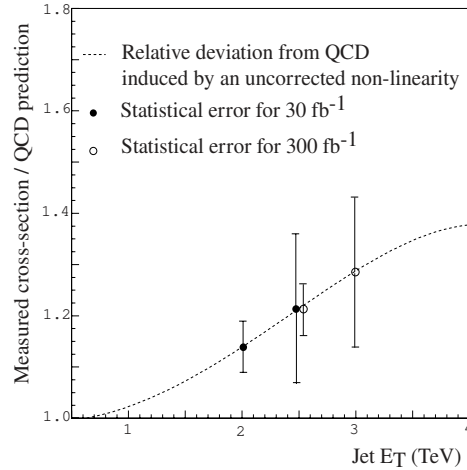
Figure 9-16 Apparent deviation from the QCD cross-section due to the mis-calibration of the calorimeter.

9.1.1.4 Conclusions

The intrinsic calorimeter jet energy resolution is very good across the full pseudorapidity range. The effect of limited cone size in the jet reconstruction on the jet energy resolution increases with pseudorapidity as the hadronic shower size becomes larger. A deterioration of the resolution is observed in the crack regions, the effect being more pronounced when the jet reconstruction is limited to a cone. In the barrel calorimeter, the electronic noise, with digital filtering applied, contributes 3.0 GeV (1.7 GeV) to the jet energy resolution when the jet is reconstructed in a cone of ΔR = 0.7 (ΔR = 0.4). The combined effect of pile-up and electronic noise, for a cone size of ΔR = 0.4, is 4.7 GeV. The performance of two algorithms for jet energy determination have been compared. The 'H1 method' applying weights to individual calorimeter cells provides a better energy resolution than the 'Benchmark method' which applies weights to the calorimeter compartments. The jet energy can be determined without prior knowledge of the particle level energy by using simple smooth functions describing the energy dependence of the calibration coefficients without deterioration of the energy resolution. The residual energy non-linearities in the calibration are smaller than 2% and 3% using the 'H1 method' and the 'Benchmark method', respectively. Effects of the order of few percent, that affect the extrapolation of the calorimeter calibration for very high-p_T jets, beyond the reach of *in situ* calibration, have been discussed.

9.1.2 Jet algorithms

In this section, various types of jet algorithms are introduced and some of their basic properties are discussed in the context of the reconstruction of a sample of medium-p_T W's, for which the two decaying jets are in general well separated. More specific aspects linked to jet overlap or effects of final state radiation are discussed in Section 9.3 (mass reconstruction) and Section 12.5.1 (jet energy scale).

9.1.2.1 Description of a representative set of jet algorithms

There are two basically different approaches used in jet algorithms. The classical 'cone' algorithm which builds a jet around a seed which is representative of the core of the jet and identified usually as the tower with highest E_T. The 'K_T clustering' algorithm [9-14] starts from the full set of final hadrons, approximated by the towers in the calorimeter, and pairs the 'closest' ones, the distance being evaluated typically as $d_{ij} = min(E_{Ti}^2, E_{Tj}^2)((\Delta\eta_{ij})^2 + (\Delta\phi_{ij})^2)$, and progressively merges all 'particles' into jets.

The cone algorithm has several variants. The most basic approach consists of using the tower with the highest E_T as the jet seed and building a cone around that seed. Cells belonging to the cone are not available for subsequent jet finding. The parameters are the E_T^{seed} cut, the cone opening radius and the minimum E_T of the jet. Usually the centroid of the jet is recalculated from the list of towers contained in the cone. This is the baseline algorithm used by ATLFAST. An improvement to this simple approach is obtained by iterating the position of the centroid of the cluster and the corresponding cone. Various strategies for jet energy sharing or jet merging in the case of close jets or hard final state radiation have been considered.

Variants of the K_T clustering algorithm use different merging criteria [9-10], and different ways of ending the merging process, for example applying a cut on the distance or stopping at a certain predefined jet multiplicity. Intrinsically, there is no predefined jet size in this clustering algorithm and the actual size of the jet will vary from event to event adapting to the fragmentation or the presence of final state radiation. This clustering algorithm follows a combinatorial approach that requires looping many times over the towers and therefore is more time consuming than the cone algorithm.

In a third strategy, all towers are classified in order of decreasing E_T. The first tower is assigned to the first cluster, the next tower will be assigned to the same cluster or a new one depending on the distance $\Delta R = \sqrt{(\Delta\eta)^2 + (\Delta\phi)^2}$. One parameter of the algorithm is the 'resolution', the minimum distance between two jets. All towers in the list are sequentially assigned to the closest cluster or a new cluster is started, the cluster centroid being re-evaluated each time a tower is added. This mechanism provides automatically energy sharing, while the shape and size of the cluster are not predefined. Optionally a fixed cone size can be required. This algorithm is described in [9-15] and will be referred to as MGS in the figures.

9.1.2.2 Performance of the jet algorithms

The performance of various algorithms is reviewed in this section. The following cases have been considered: the fixed cone algorithm ($\Delta R = 0.4$ and 0.7), the K_T clustering algorithm with a distance parameter R_{cut} used to stop cell merging set to 0.4, and the MGS algorithm with the two-jet resolution parameter ΔR set to 0.3 (see [9-10] for a more detailed description of the parameters).

The differences arising from the jet algorithms are illustrated here using a sample of W+jet events with $p_T{}^W$ larger than 100 GeV. A minimum E_T of 20 GeV was required for the partons. The range of $E_T{}^{parton}$ studied in this sample extends from 20 to about 200 GeV. Figure 9-17 shows the angular distance ΔR between the two jets.

Results from a particle level study using ATL-FAST at low luminosity are shown in Figure 9-18. The cone algorithm with $\Delta R = 0.7$ shows the best performance in that energy range: the ratio of reconstructed jet energy to parton energy is almost independent of energy and close to 1. The cone algorithm with $\Delta R = 0.4$ shows losses varying from 10% at low E_T to about 3% at 200 GeV. The K_T and the MGS algorithms show a flatter distribution in E_T but with an average loss of about 8%.
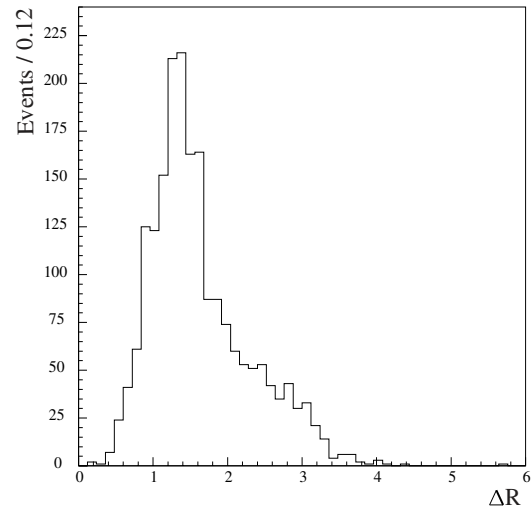
Figure 9-17 Distance in η–ϕ space between the two partons from W decays in W+jet events. The average angular opening between the jets is 1.6.
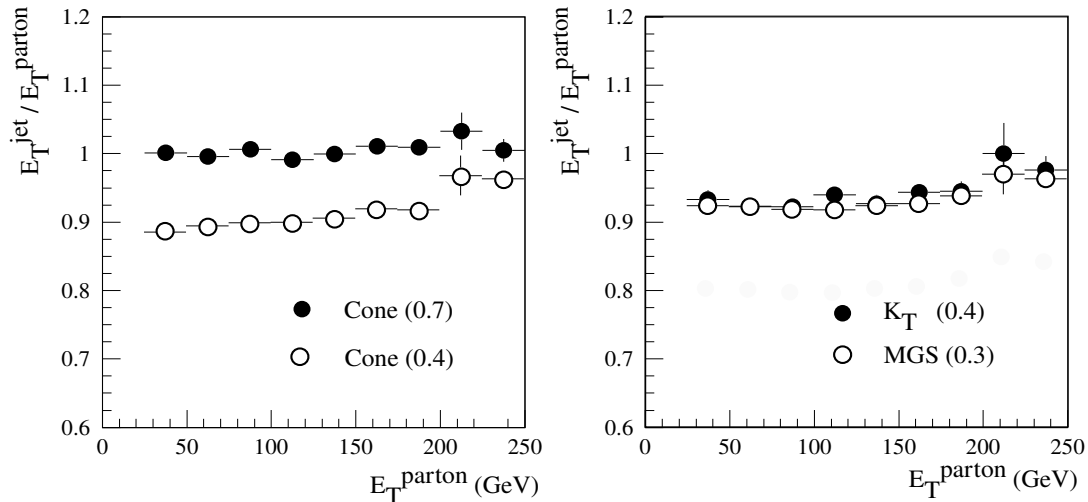
Figure 9-18 Reconstructed E_T of the jet divided by the E_T of the parton for the W+jet sample: the left figure compares the results of the fixed cone algorithm with cone size $\Delta R = 0.7$ and $\Delta R = 0.4$; the right figure shows the results of the K_T algorithm ($R_{cut} = 0.4$) and the MGS algorithm (resolution $\Delta R = 0.3$).

The effect of minimum-bias events has been studied by adding an average of 50 minimum-bias events generated with PYTHIA (with Poisson fluctuations). This number of events corresponds roughly to the effective number of minimum bias events obtained when applying the calorimeter shaping functions. The events were simulated by ATLFAST and added at the level of the projected E_T ($\Delta\eta \times \Delta\phi$) matrix. A p_T cut of 2 GeV per tower was applied. The result is shown in Figure 9-19. The cone algorithm with $\Delta R = 0.7$ suffers most from the effect of pile-up. For a cone size $\Delta R = 0.4$, the shift in the reconstructed jet transverse energy, compared to the case without pile-up, is about 12% at 40 GeV and 2% at 100 GeV. The effect is slightly smaller in the case of the K_T algorithm. The same is true for the MGS algorithm even though it has a variable jet size.
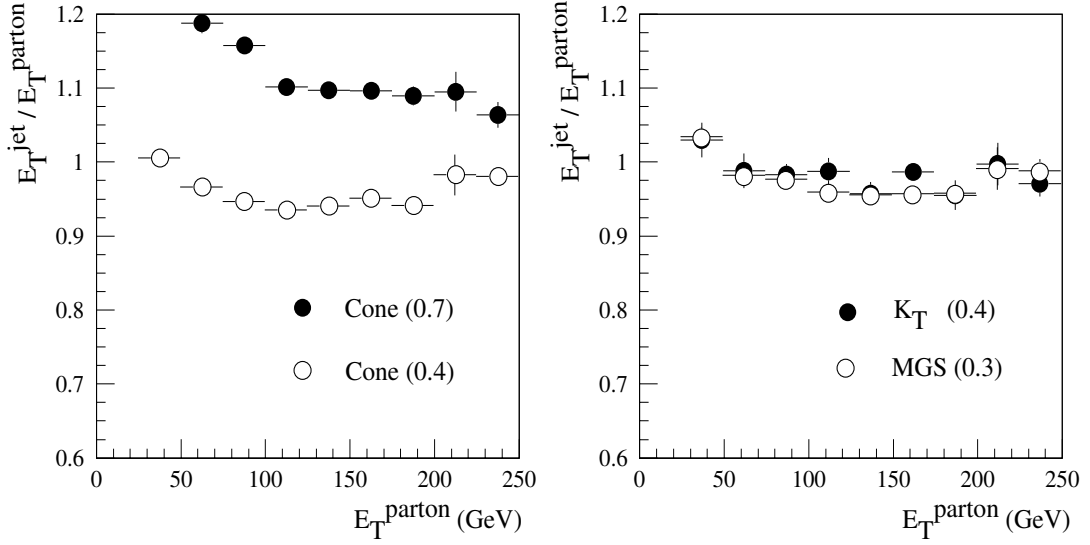
Figure 9-19 Reconstructed E_T of the jet divided by the E_T of the parton for the W+jet sample, with an average of 50 pile-up events added to the events and with an E_T tower cut of 2 GeV: the left figure shows the results of the fixed cone algorithm with cone size $\Delta R = 0.7$ and $\Delta R = 0.4$; the right figure shows the results of the K_T algorithm ($R_{cut} = 0.4$) and the MGS algorithm (resolution $\Delta R = 0.3$).

The figures demonstrate that the conversion from jet energy to parton energy depends on the jet algorithm and on the amount of pile-up. Differences of the order of 10% may arise, the low-E_T end of the spectrum being most affected. In addition, the underlying physics affecting the relation of the jet energy to parton energy, such as the parton shower process and the subsequent hadronisation together with initial state and final state radiation, depends on the physics process and introduces additional differences. The issue of the calibration of the jet energy scale with different physics processes is discussed in Section 12.5.

9.1.3 Low-p_T jet reconstruction

The ability to veto events by detecting the presence of additional low-p_T jets is a powerful tool for the reduction of the background in many physics channels. An example of the power of a jet veto is the case of Z+jet(s) events where the p_T balance between the Z and the jet can be used for *in situ* jet energy calibration, but multi-jet final states have to be vetoed efficiently to avoid biases in the correction. Another example is the rejection of $t\bar{t}$ background that, due to its large cross-section, affects many rarer physics processes. $t\bar{t}$ events tend to have high jet multiplicity and jets with small transverse energy. An efficient detection of these jets down to low-p_T is needed for a good rejection of that background.

A study of the jet veto efficiency in Z+jets was carried out with ATLFAST and full simulation (see Section 12.5.1.3 for more details). The standard fixed cone algorithm with cone size $\Delta R = 0.7$ was used. Figure 9-20 shows the fraction of events where more than one jet is reconstructed as a function of the p_T threshold applied. In the full simulation, jets are reconstructed starting from the projected E_T matrix in ($\Delta\eta \times \Delta\phi$) with the calorimeters being calibrated at the EM scale. Figure 9-2 shows that the reconstructed jet energy is typically of the order of 80% of the particle
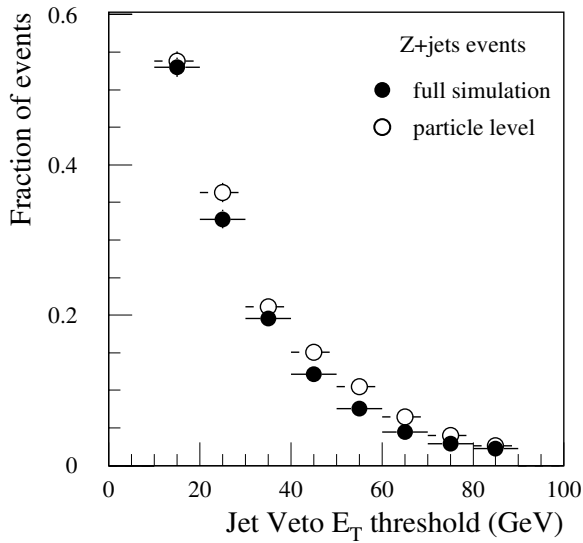
Figure 9-20 Fraction of events from the *Z*+jet(s) sample where more than one jet is reconstructed as a function of the p_T threshold applied. The black circles are for fully simulated events and the open circles are for particle level simulation with ATLFAST.
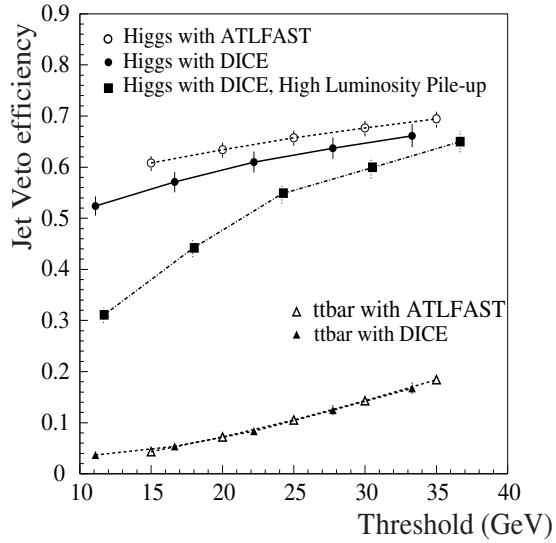
Figure 9-21 Comparison of the jet veto efficiency for the Higgs signal and the $t\bar{t}$ background obtained at particle level (open dots and triangles, respectively) and with full simulation (black dots and triangles) for low luminosity. For the Higgs signal, the black squares show the efficiency at high luminosity.

level jet energy. A good agreement is found between ATLFAST and the full simulation when this factor is taken into account to define the equivalent p_T threshold in the two sets of data, as seen in Figure 9-20.

Particle level and full simulation studies have been carried out in the search for a heavy Higgs signal ([9-16], [9-17], Section 19.2.10.2). The relatively low jet activity in the central region in this case can be used to reject the backgrounds, specifically $t\bar{t}$ events which have two additional jets. The efficiency of a jet veto, applied in the central region ($|\eta| < 2$), has been studied as a function of the jet p_T threshold. The jet veto efficiency, defined as the fraction of events with no additional jet with p_T larger than the threshold, is given in Figure 9-21. At low luminosity, the particle level simulation gives efficiencies that are about 5% higher than the efficiency obtained for the fully simulated Higgs signal. For the background of $t\bar{t}$ events, the agreement between particle level and full simulation is good. At low luminosity the jet veto threshold can be lowered to 15 GeV without losing much efficiency for the signal and while retaining a good rejection of the background. In the presence of high luminosity pile-up, minimum-bias events tend to generate low-p_T jets and the jet veto threshold has to be raised to 25 GeV to avoid a significant loss of efficiency for the signal (see Figure 9-21).

9.1.4 Forward jet tagging

Jet tagging at large pseudorapidities is one of the main tools to reduce backgrounds in the search for a heavy Higgs. For large Higgs masses [9-16][9-17], the dominant production process is vector boson fusion: $q\bar{q} \rightarrow q'\bar{q}'W_LW_L \rightarrow q'\bar{q}'H$. The two accompanying jets are typically detected in the region $2 < |\eta| < 5$. This region is covered by the end-cap and FCAL calorimeters.

The granularity of the End-cap Calorimeter is (0.1×0.1) in ($\Delta\eta\times\Delta\phi$) for $|\eta| < 2.5$, and (0.2×0.2) for larger rapidities. The cells are projective in pseudorapidity and azimuthal angle. This allows the use of fixed transverse energy cuts in the jet finding. On the other hand, the FCAL read-out cells do not have a projective geometry in pseudorapidity and azimuthal angle, but are constructed as cells in x and y, as shown in Figure 9-22. There are two tile sizes in two regions: one from $|\eta| \approx 3.2$ to $|\eta| \approx 4.2$ and the other from $|\eta| \approx 4.2$ to the acceptance limit at $|\eta| \approx 4.9$. Therefore it is not possible to apply a fixed E_T cut on the calorimeter towers since the tile sizes change continuously in

Figure 9-22 Tile read-out scheme in x and y for the FCAL.

pseudorapidity space. It is important to note that even if the towers were projective, the use of fixed E_T cuts would not be optimal. This is due to the fact that in the very forward regions, the lateral spread of the hadronic showers becomes very significant. This can be seen in Figure 9-23 which shows the reconstructed jet p_T inside a cone compared to the total p_T reconstructed in the FCAL. Energy losses at large pseudorapidities are clearly seen. The effect depends on the cone radius; the smaller the cone, the larger the losses due to the lateral shower size. On the other hand, the intrinsic response of the calorimeter is rather linear, as can be seen in Figure 9-24 which shows the total jet signal in the calorimeter calibrated at $|\eta| = 4.1$ with $E = 1000$ GeV jets using one calibration factor for each of the three FCAL compartments. Deviations from non-linearity appear only in the low-energy range: about 10% at 200 GeV and 20% at 100 GeV. Howev-

Figure 9-23 Reconstructed jet p_T inside a cone normalised to the total p_T reconstructed in the FCAL as a function of pseudorapidity and for various cone sizes. The sample of jets used here are back-to-back di-jet events (see Section 9).
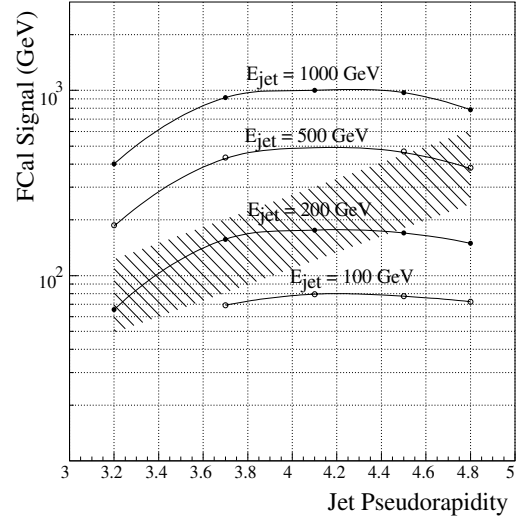
Figure 9-24 Total energy measured in the FCAL for various jet energies at different values of pseudorapidity. The calibration coefficients have been adjusted for $E = 1000$ GeV jets at $|\eta| = 4.1$. The hatched area represents the rms contribution of high luminosity pile-up events in cones of $\Delta R = 0.4$ to $\Delta R = 1.0$.

er, these low energies are not relevant for the FCAL as can be seen from the hatched area in the figure that represents the rms of high luminosity pile-up in jet cones of $\Delta R = 0.4$ to $\Delta R = 1.0$. Cuts based on the significance of the signal in the cells are more appropriate for the FCAL, the significance being defined as the signal divided by the rms of the (high luminosity) pile-up noise collected in a given cell.

The forward tagging efficiency has been studied with fully simulated events in the case of a 1 TeV Higgs produced via vector boson fusion where the two associated quarks are detected typically in the region $2 < |\eta| < 5$ (see [9-17] and Section 19.2.10.2). At lower rapidities $2 < |\eta| < 2.9$, in the End-cap Calorimeter, jets are tagged in the standard way. Each 0.1×0.1 tower in $(\Delta\eta \times \Delta\phi)$ above a 3 GeV E_T threshold was considered as a potential jet seed. This threshold was 6 GeV when pile-up noise was included. The energy of each tower within a radius of $\Delta R = 0.4$ was added to the energy of the jet candidate. An E_T threshold of 1.5 GeV was imposed on the energy in the towers when pile-up was included. The energy of the jet was calibrated without pile-up noise using the known value of the quark energy. The jet energy scale was adjusted to take into account the effect of the cuts and pile-up noise. Finally, a jet had to have a minimum corrected transverse energy of 15 GeV to be 'tagged'.

In the region $2.9 < |\eta| < 4.9$, in the FCAL, the energies deposited in each tube of a given tile were summed to form the cell signal. The pile-up energy rms was calculated for each tile in the three longitudinal segments separately. The jet reconstruction proceeded as follows: tiles having a significance higher than four were considered as potential jet seeds. The significance was defined as the signal divided by the rms of the high luminosity pile-up noise collected in the cell. This cut could go as high as 10 when high luminosity pile-up noise was added (see left plot of Figure 9-25). The energy in a tile was added to the candidate jet energy if its significance was greater than 1.0 and it was within a radius of $\Delta R = 0.4$ of the seed cell. With pile-up noise, a cut was imposed on the significance in a $\Delta R = 0.2$ cone around the seed cell (see right plot of
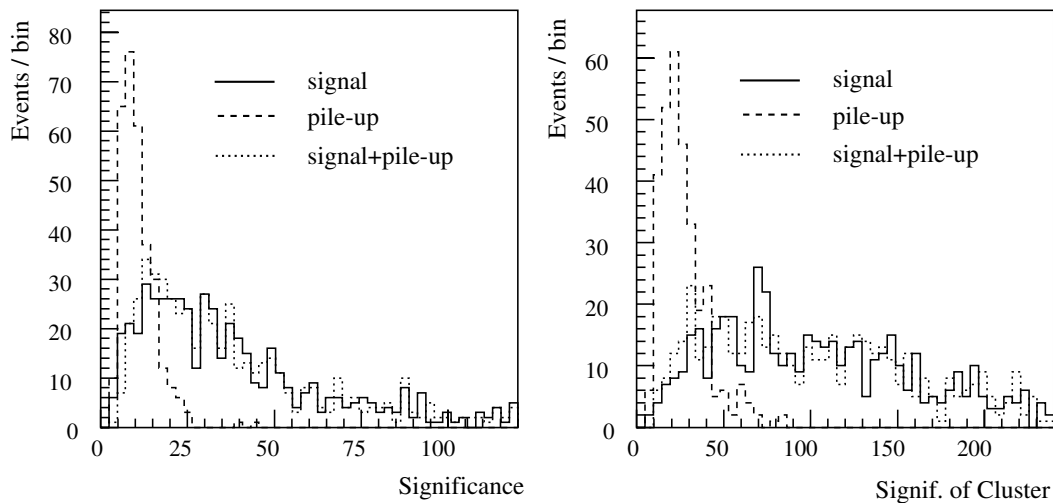
Figure 9-25 The left plot shows the significance of the jet seed cell in the FCAL region. The significance is defined as the signal divided by the rms of the high luminosity pile-up noise collected in the cell. The right plot gives the total significance in a $\Delta R = 0.2$ cone (the sum is linear) around the seed cell.

Figure 9-25). This cut proved to be the most efficient discriminator between pile-up jets and signal jets. Finally, after calibration and the adjustment of the energy scale, which depended on the cuts used, a corrected transverse energy of 15 GeV was required for the jet to be tagged.

The results obtained with this procedure for the case of the 1 TeV Higgs are described below. In the upper plot of Figure 9-26, it is important to note that the average p_T of forward quarks decreases as a function of pseudorapidity and that the tagging efficiency is not only a function of the calorimeter acceptance alone but depends also on the kinematics of the physical process considered. Therefore, the jet tagging efficiencies obtained here are not directly applicable to other physics processes. The lower plot of Figure 9-26 gives a comparison of the jet tagging efficiency without pile-up between the full simulation and ATLFAST. The ATLFAST results show good agreement with the full simulation up to $|\eta| = 4.0$. Beyond this value, the transverse shower development leads to energy losses in the full simulation. The lower plot of Figure 9-26 shows also the forward jet tagging efficiency obtained when high luminosity pile-up is included. The various significance cuts described earlier, as well as an energy cut on the tagged jets in addition to the E_T cut, were tuned to optimise the jet efficiency while keeping the fake jet rate at the level of 10% in the whole $2 < |\eta| < 5$ range. Compared to the low luminosity case the efficiency decreases by less than 10%.
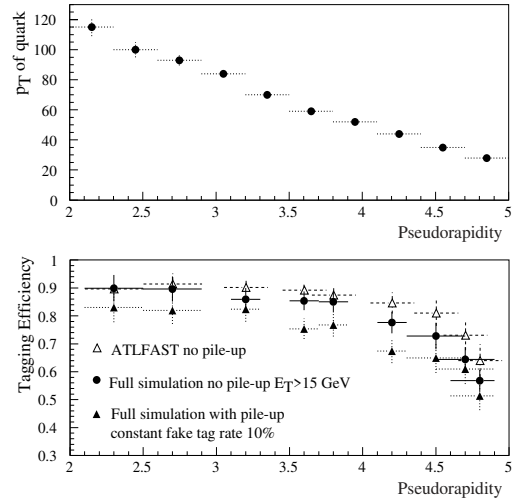
Figure 9-26 The upper plot shows the average p_T of forward quarks produced in association with a 1 TeV Higgs. The lower plot gives the jet tagging efficiency for particle level and full simulation at low luminosity for a 15 GeV E_T threshold. It also shows the jet tagging efficiency obtained with high luminosity pile-up, adjusting selection cuts to maintain a constant fake rate of 10% across pseudorapidity.

9.1.5 τ identification and measurement

Efficient reconstruction and identification of all lepton species are crucial at the LHC. τ-leptons are the most difficult ones in this respect, since they produce neutrinos and hadrons among their decay products. An example of the relevance of τ identification is given by the fact that, over a large region of the MSSM parameter space, the heaviest Higgs bosons can only be observed through their decays to pairs of τ-leptons ($H/A \to \tau\tau$, $H^\pm \to \tau\nu$). The sensitivity to these channels depends strongly on the quality of the τ identification, since backgrounds from jets are potentially very large (see Chapter 19).

The τ identification capability of ATLAS was evaluated by using fully-simulated events containing a Higgs boson A decaying to $\tau\tau$, where one of the τ's decays hadronically and the other leptonically.

The τ identification is based on criteria, such as shower shape in the calorimeters, that can be evaluated realistically only by using a detailed GEANT-based simulation of the detector response. Therefore, high-statistics samples of fully-simulated events were used for this study.

They consisted of ~21 000 $H/A \rightarrow \tau\tau$ signal events (direct A production and $b\bar{b}A$ associated production), corresponding to eight different A masses in the range 100-500 GeV, and of ~11 000 background events ($t\bar{t}$, $b\bar{b}$, W+jets). About 16 000 τ's and 15 000 jets with $E_T > 30$ GeV and $|\eta| < 2.5$ were available in the signal and background samples respectively [9-18][9-19]. In addition, a sample of ~26 000 jets from QCD processes was used. Finally, a sample of 1000 isolated τ's decaying to hadrons, generated at fixed $p_T = 60$ GeV and $\eta = 0.3$ ('single τ's'), was used for some checks. Low-luminosity operation was assumed in most cases, therefore approximately two minimum-bias events were superimposed on the fully simulated events.

9.1.5.1 τ reconstruction

A jet was labelled as a τ-jet if the distance ΔR of the jet barycentre from the barycentre of the hadronic part of the τ decay $(h\tau)$, as computed at particle level, was less than 0.3. By applying this criterion, 98% of τ's from $A \rightarrow \tau\tau$ events with $p_T(h\tau) > 30$ GeV were labelled as τ-jets. The τ-jet energy was reconstructed from the calorimeter cell energies, by applying the same calibration constants as used for the QCD jet reconstruction (Section 9.1). As a consequence, the τ energy was overestimated by ~5% because the electromagnetic content of a τ-jet is on average larger than that of a normal jet. The τ transverse momentum was defined as the p_T of the visible decay products. The τ charge was calculated from the charge of the associated tracks. Using the reconstructed tracks associated to the jet within a cone of size $\Delta R < 0.4$, the weighted jet charge was defined as the sign of $\Sigma_i |p_i| q_i$, where q_i is the charge of a track of momentum p_i. In this way, the sign of the τ charge was determined correctly in 92% of cases.

9.1.5.2 τ identification

Jets from hadronic τ decays and QCD can be distinguished by using the information from the Calorimeters and the Inner Detector. Since hadronic τ decays are characterised by low multiplicity (in 77% of the cases only one charged track is produced), a τ-jet consists in general of a well-collimated calorimeter cluster with a small number of associated charged tracks. The following variables were used to distinguish τ-jets from normal jets:

• R_{em}, the jet radius computed using only the electromagnetic cells contained in the jet. It is defined as

$$R_{em} = \frac{\sum_{i=1}^{n} E_{T_i}\sqrt{(\eta_i - \eta_{cluster})^2 + (\phi_i - \phi_{cluster})^2}}{\sum_{i=1}^{n} E_{T_i}}$$

where i runs over the cells of the EM Calorimeter contained in a cone of size $\Delta R = 0.7$ around the barycentre of the cluster, the coordinates of which are ($\eta_{cluster}$, $\phi_{cluster}$).

• ΔE_T[12], the fraction of transverse energy in the EM and hadronic calorimeters, which is contained in a region defined by $0.1 < \Delta R < 0.2$ around the barycentre of the cluster. This is an isolation criterion.

• N_{tr}, the number of charged tracks with p_T above a given threshold (1, 2 and 5 GeV were used), pointing to the calorimeter cluster within $\Delta R = 0.3$.

The performance for τ/jet separation was studied in two cases, which are discussed below. The first case is for $A \to \tau\tau$ searches, where very stringent τ identification criteria must be adopted, since a large rejection of the potentially large background is crucial. Here the goal was to select a very pure τ sample, with a small contamination of QCD jets. In the second case, the τ efficiency was studied as a function of the jet rejection over a broad range of efficiencies and rejections. This gives rise to τ samples of different purities which can be used in a variety of physics channels according to the specific requirements.

τ / jet separation for $A \to \tau\tau$ searches

A jet with $E_T > 30$ GeV and $|\eta| < 2.5$ was identified as a τ-jet if it satisfied the cuts on R_{em}, ΔE_T^{12} and N_{tr} listed in Table 9-7. This table also shows the cumulative efficiency of these cuts for τ-jets from direct and associated A production, for QCD jets and for the jets contained in typical background events to the $A \to \tau\tau$ channel.

Table 9-7 τ identification criteria used in the search for $A \to \tau\tau$ events and their cumulative efficiency (in percent) for various signal and background samples at low luminosity.

Variable	Cut	$b\bar{b}A \to \tau\tau$	$A \to \tau\tau$	QCD jets	b-jets	$t\bar{t}$	W+jets
$<p_T>$ of τ–jet (GeV)		80	73	44	58	65	52
R_{em}	< 0.07	56 ± 1	45 ± 1	1.1 ± 0.1	1.9 ± 0.4	1.3 ± 0.2	2.9 ± 0.5
ΔE_T^{12}	< 0.1	40 ± 1	32 ± 1	0.6 ± 0.05	0.9 ± 0.2	0.7 ± 0.2	1.8 ± 0.5
$N_{tr}\,(p_T > 2)$	= 1	21 ± 1	17 ± 1	0.09 ± 0.02	< 0.06	0.08 ± 0.06	0.6 ± 0.3
$N_{tr}\,(p_T > 2)$	= 1 or = 3	32 ± 1	25 ± 1	0.19 ± 0.03	0.18 ± 0.1	0.2 ± 0.1	1.1 ± 0.3

The criteria based on the calorimeter information (R_{em} and ΔE_T^{12}) provide a rejection of about 170 against QCD jets for an efficiency of 40% for hadronic τ decays. This performance can be further improved by cutting on the number of tracks associated with the calorimeter cluster. In the Inner Detector, tracks belonging to a low-multiplicity jet are expected to be reconstructed with high efficiency and negligible fake-track rate down to $p_T = 1$ GeV even at the highest luminosities expected at the LHC [9-20]. Therefore, by requiring only one track with $p_T > 2$ GeV associated to the calorimeter cluster, it was possible to improve the rejection against jets by a factor between three and nine, depending on the physics channel. This performance can be further improved by identifying photon conversions, which was not done for the study presented here. On the other hand, requiring one or three tracks associated to the calorimeter cluster increases the τ efficiency by a factor of 1.5, but does not improve the overall sensitivity because the jet background increases by a factor larger than two. These results were obtained by using generated tracks. When tracks reconstructed in the Inner Detector are used, the number of τ's with one associated track increases by 10%, due to inefficiencies in the track reconstruction. For one-prong τ decays, the reconstructed track with the largest p_T is within ±5 GeV of the generated track with the largest p_T in 87% of cases. The impact of varying the track p_T cut was also studied: results are not significantly different for 1, 2 or 5 GeV thresholds [9-19].

The rejection against jets in $t\bar{t}$ events is larger than the rejection against jets in W+jet events, due to the different jet type (quark or gluon) and p_T distribution. The b-jet rejection is larger than the rejection against light-quark or gluon jets.

The results shown in Table 9-7 were obtained by using all clusters with $p_T > 30$ GeV and $|\eta| < 2.5$ reconstructed in the signal and background events. For a fixed set of selection cuts, the τ identification efficiency increases with increasing p_T (from 15 to 130 GeV) and the jet rejection shows a fast increase with p_T up to 20 GeV and a smooth dependence above. The τ efficiency depends also on the pseudorapidity, being higher in the central region of the acceptance [9-19].

According to preliminary studies, additional selection cuts based on the information from the strip section of the EM Calorimeter [9-19] provide no significant improvement on the τ efficiency and jet rejection. This is due to the strong correlation with the criteria discussed above. However, the use of the η-strips for τ identification was not optimised for the study presented here, and it is not excluded that further work may lead to some improvement in the performance.

τ efficiency versus jet rejection

The jet rejection which can be achieved as a function of the τ identification efficiency was studied by applying several different selection criteria, based on the variables R_{em}, ΔE_T^{12} and N_{tr} ($p_T > 2$ GeV), in order to cover values for the τ efficiency in the range 10% to 90%. Samples of τ's from $b\bar{b}A$ events and jets from QCD processes were used.
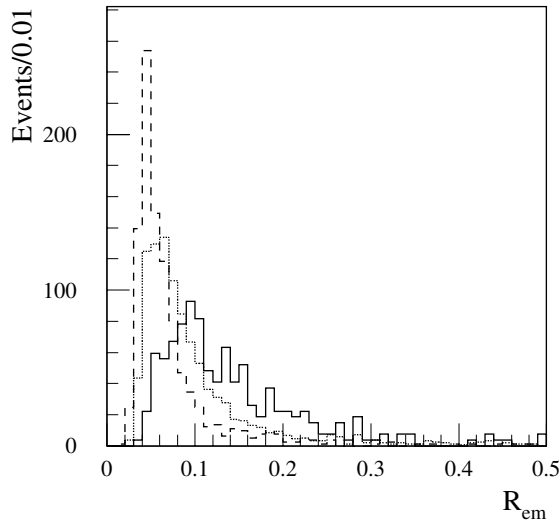
Figure 9-27 R_{em} distribution for τ-jets with different p_T: $15 < p_T < 30$ GeV (full line), $30 < p_T < 70$ GeV (dotted line) and $70 < p_T < 130$ GeV (dashed line). All distributions are normalised to the same number of events.
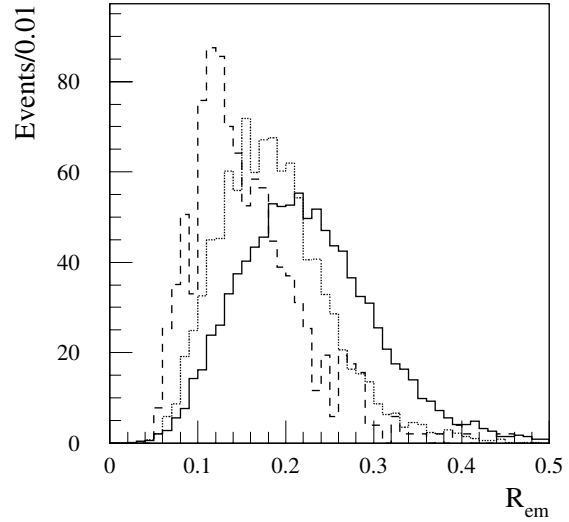
Figure 9-28 As Figure 9-27 but for QCD jets.

Due to the p_T dependence of the τ identification performance, results are given for different p_T ranges. As an example, Figures 9-27 and 9-28 illustrate how the R_{em} distribution changes with the transverse momentum of τ-jets and QCD jets respectively. In both cases, the distribution becomes narrower at high p_T, therefore the τ efficiency increases with p_T whereas the jet rejection decreases. This behaviour can be inferred also from Figures 9-29 and 9-30, in which the τ identification efficiency and the jet rejection are presented as a function of the cut on R_{em} only. The ΔE_T^{12} distribution has little p_T dependence. The N_{tr} distribution for τ's does not depend on p_T, whereas N_{tr} increases with p_T in the case of jets.
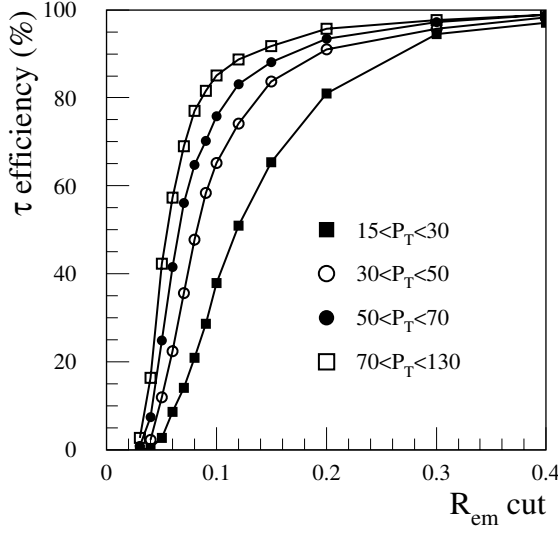
Figure 9-29 τ identification efficiency, as a function of the cut on R_{em}, for various p_T ranges.
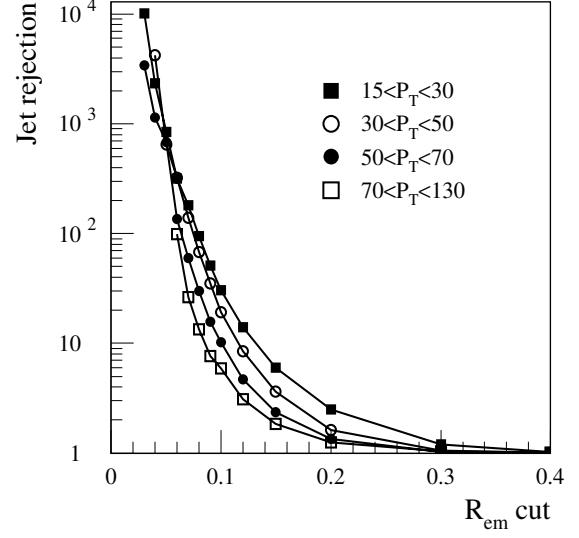
Figure 9-30 Jet rejection, as a function of the cut on R_{em}, for various p_T ranges.

The total jet rejection, obtained in different p_T ranges, is shown in Figure 9-31 as a function of the τ identification efficiency. Straight-line fits are superimposed to each set of points and can be used to parametrise the detector performance [9-21]. As expected, as p_T increases the curves shift towards larger τ efficiencies, for the same jet rejection.

The dependence of the τ efficiency on pseudorapidity was also considered. Whilst the jet rejection does not show any pseudorapidity dependence, the average τ identification efficiency over the full pseudorapidity coverage ($|\eta| < 2.5$) is very similar to the efficiency over the region $0.7 < |\eta| < 1.5$, whereas the efficiency is larger for $|\eta| < 0.7$ and smaller for $|\eta| > 1.5$.

Finally, the efficiency for single τ's is larger than that for τ's from complete physics events. For instance, the R_{em} distribution peaks at larger values for τ's from complete physics events than for single τ's. This is also due to the choice of a relatively large cone ($\Delta R = 0.7$) for the τ-jet reconstruction, so that other particles from the rest of the event contribute to the τ-jet. As a consequence, with the selection criteria used for the $A \rightarrow \tau\tau$ study reported above, the τ identification efficiency for single τ's is a factor ~1.5 larger than for τ's in physics events.
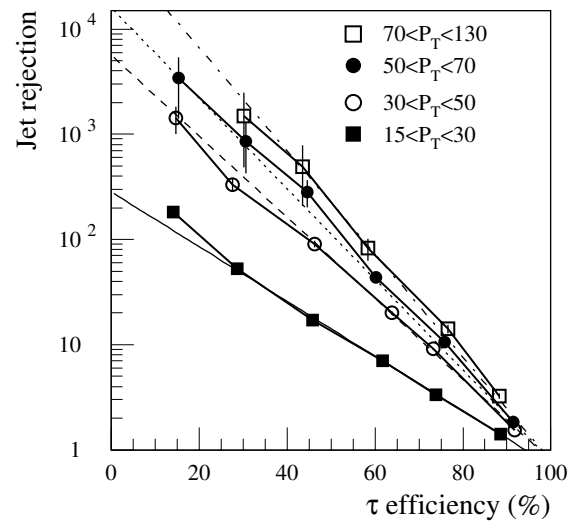
Figure 9-31 Jet rejection as a function of the τ efficiency, as obtained over the region $|\eta| < 2.5$ and in various p_T ranges. Straight-line fits are superimposed.

9.1.5.3 τ veto

The capability of vetoing events containing τ's should be useful for many physics studies at the LHC, for instance to reject backgrounds (*e.g.* $W \to \tau\nu$) to some SUSY channels (Chapter 20).

A study of the τ veto performance was made as a function of p_T, since the difference in the τ identification variables, in particular R_{em}, for τ's and jets decreases with decreasing p_T. The results are shown in Figures 9-32 and 9-33.

By requiring $N_{tr} > 3$ and $R_{em} > 0.08$, a jet efficiency of about 90% was achieved for $p_T > 60$ GeV and for a τ efficiency of only 5%. At lower p_T, a τ efficiency of 5% was obtained with a lower jet efficiency. A jet efficiency of 90% can be reached in this case only with a significant increase of the τ efficiency.
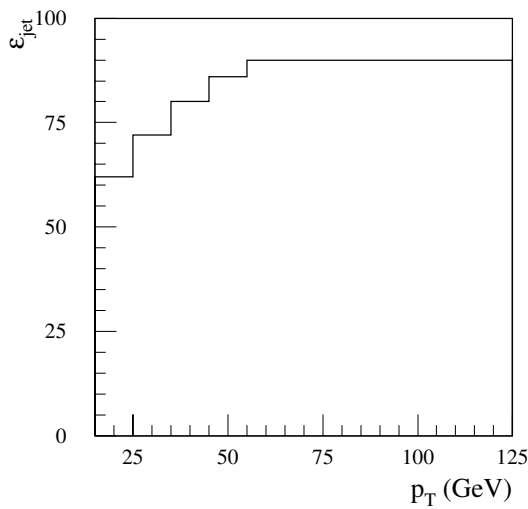
Figure 9-32 Jet identification efficiency, as a function of p_T, for a fixed τ efficiency of 5%.
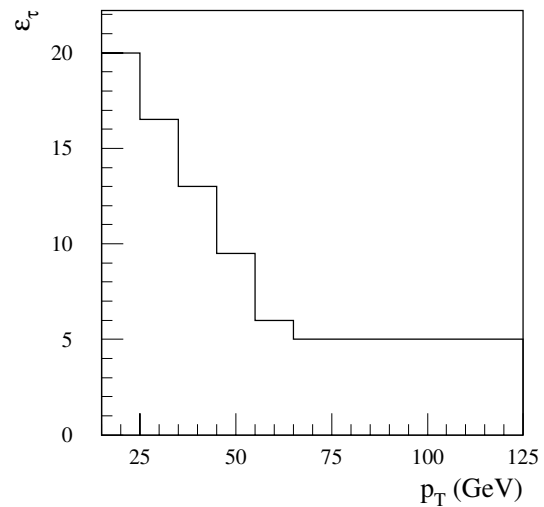
Figure 9-33 τ identification efficiency, as a function of p_T, for a fixed jet efficiency of 90%.

9.1.5.4 Performance at high luminosity

The jet rejection and τ efficiency performance at high luminosity were studied by using $A \to \tau\tau$ events. For this purpose, fully-simulated pile-up events (Chapter 2) were superimposed on the physics events. A threshold of ~2.5σ of the pile-up noise was applied to the energy deposited in the calorimeter towers. Towers were formed in each calorimeter by using the granularity of the longitudinal compartment with the coarsest granularity and by adding longitudinally all cells belonging to that calorimeter.

For the low-luminosity study, the R_{em} and ΔE_T^{12} variables were defined using the cell information in the various compartments, while for the high-luminosity case they were based on the tower information. This latter procedure gives a non-optimal definition of both variables but simplifies the use of energy thresholds. It was also assumed that the number of tracks with $p_T > 2$ GeV is not affected when pile-up is added. After re-optimisation of the τ identification cuts, τ efficiency and jet rejection performances similar to the low-luminosity case were obtained at high luminosity [9-19].

9.1.5.5 Conclusions

Hadronic τ decays can be efficiently reconstructed and identified by using the information from the calorimeters and the Inner Detector. In general, the τ efficiency depends on p_T, pseudorapidity and the physics process. For a τ identification efficiency of ~20%, a rejection factor of 170 to 1 200 can be achieved against jets from W+jets and $t\bar{t}$ production and of about 1 700 against b-jets. This performance, which is similar at low and high luminosity, provides good sensitivity for the $A \rightarrow \tau\tau$ channel in the mass range 100 to 500 GeV (see Chapter 19). It is also possible to veto 95% of the τ's while mainting an efficiency of about 90% for all other jets.

9.2 E_T^{miss} measurement

Good measurement of the missing transverse energy is needed at the LHC for two reasons. Firstly, E_T^{miss} is an important signal for new physics, *e.g.* production and decay of SUSY particles, production and decay of the Higgs boson in the channel $H \rightarrow ZZ \rightarrow ll\nu\nu$. Therefore, minimisation of fake high-E_T^{miss} tails produced by instrumental effects, such as jets badly measured in a calorimeter crack, is mandatory in order to observe events characterised by genuine missing transverse energy. Secondly, in order to reconstruct a narrow invariant mass distribution for new (heavy) particles involving neutrinos among their decay products, good E_T^{miss} resolution is needed. One example is the possible production of an A boson followed by the decay $A \rightarrow \tau\tau$. The most critical experimental issues for a reliable and precise measurement of the event missing transverse energy are related to the performance of the calorimeters: good energy resolution, good response linearity and hermetic coverage are required.

9.2.1 E_T^{miss} resolution

The detector performance in terms of E_T^{miss} resolution was studied by using fully-simulated $H/A \rightarrow \tau\tau$ events in the H/A mass range 100–500 GeV. Typical E_T^{miss} values for these events are in the range 20-100 GeV [9-22].

Events were fully simulated in the pseudorapidity range $|\eta| < 3$. In the forward region $3 < |\eta| < 5$ the contribution of the calorimeter resolution to the accuracy of the E_T^{miss} measurement is small (Section 9.2.1.3) and the CPU needed for full simulation very large. Therefore, the detector response in this region was not fully simulated, but the particle energies were smeared according to the expected resolution. A check with 500 events with $m_A = 150$ GeV, fully simulated up to $|\eta| = 5$, was performed and gave similar results to the case where full simulation is done over $|\eta| < 3$ only. Fully-simulated (over $|\eta| < 5$) samples of minimum-bias events were used also for this study.

9.2.1.1 E_T^{miss} reconstruction

The x and y components of the E_T^{miss} vector (p_x^{miss}, p_y^{miss}) were obtained from the transverse energies deposited in the cells with $|\eta| < 3$, taking into account the additional contribution from the FCAL simulated at particle level as described above.

In the following sections, the most relevant issues for a good E_T^{miss} resolution are discussed one by one. Crucial elements are sufficient pseudorapidity coverage and an accurate calibration of all calorimeters, in particular in the region $|\eta| < 3$ which provides the dominant contribution to the E_T^{miss} resolution. The contribution of low-energy cells, such as cells outside jets, cannot be neglected, and the cell energy cut-off applied in the presence of electronic noise and pile-up has to be carefully tuned.

9.2.1.2 Calorimeter calibration

Particular attention was paid to the accurate calibration of all calorimeters and to the non-linearity of the response at low energy. The calibration accounts also for energy losses in the dead material in front of the calorimeters (*e.g.* cryostats) and at the transition between different calorimeter parts (cracks). The best E_T^{miss} resolution is achieved by using three sets of calibration constants for each calorimeter: one set for electromagnetic clusters, one set for hadronic clusters and one set for cells outside clusters. For the study presented here, however, cells outside clusters were calibrated in the same way as cells inside hadronic clusters. Therefore results are conservative, because the use of specific calibration constants for cells outside clusters, which provide a correction for the non-linearity of the calorimeter response to low-energy particles [9-18], improves the E_T^{miss} resolution by ~5%.

9.2.1.3 Calorimeter coverage

Calorimetric coverage up to $|\eta| = 5$ is essential for a reliable E_T^{miss} measurement [9-22]: the resolution of each component of the E_T^{miss} vector, as calculated at particle level for $A \rightarrow \tau\tau$ events with $m_A = 150$ GeV, degrades from 2.3 GeV to 8.3 GeV if the calorimeter coverage is reduced from $|\eta| < 5$ to $|\eta| < 3$.

On the other hand, the contribution of the forward region to the E_T^{miss} resolution is small, because the particle transverse energy decreases at large rapidity. The resolution of each component of the E_T^{miss} vector, as obtained with full simulation of $A \rightarrow \tau\tau$ events with $m_A = 150$ GeV [9-2], was found to be about 7 GeV (to be compared with 2.3 GeV at particle level), the main contribution coming from the barrel region (about 5 GeV), followed by the end-cap region (about 4 GeV) and the forward region (about 3 GeV).

The dead material in the transition region between the barrel and the end-cap calorimeters has no significant effect on the width of the core of the E_T^{miss} distribution. The impact of these regions on the high-E_T^{miss} tails is discussed in Section 9.2.2.

9.2.1.4 Electronic noise

When the electronic noise in the calorimeter is taken into account (Chapter 4), only cells with an energy larger than 1.5σ are considered for the E_T^{miss} reconstruction. The resulting resolution deteriorates by less than 10% compared to the resolution obtained without noise, the contribution of the noise amounting to about 3 GeV. A study of the optimum cell cut-off was performed. The E_T^{miss} resolution deteriorates by a factor ~1.3 if the cell cut-off is 2.5σ instead of 1.5σ. If cells outside jets, which are more than 50% of the occupied cells, are not included at all, the resolution of the two E_T^{miss} components degrades by a factor ~1.3.

9.2.1.5 Coherent noise

As discussed in [9-2], a coherent noise smaller than 3 MeV per channel (size: $\Delta\eta \times \Delta\phi = 0.025 \times 0.025$) in the EM Calorimeter gives no appreciable deterioration of the E_T^{miss} resolution and of the expected significance of a possible $A \rightarrow \tau\tau$ signal, provided that a reoptimisation of the cell energy cut-off is performed. For larger values of coherent noise, on the other hand, the E_T^{miss} resolution degrades in an unacceptable way. Therefore, a coherent noise of smaller than 3 MeV per channel is one of the requirements for the EM Calorimeter electronics (Chapter 4).

9.2.1.6 Results

The E_T^{miss} resolution was studied with $A \rightarrow \tau\tau$ events, which are characterised by a genuine E_T^{miss} due to the presence of neutrinos, at low luminosity, and with minimum-bias events, which do not contain physical sources of missing energy, at low and high luminosity.

The resolution $\sigma(p_{xy}^{miss})$ of each component of the E_T^{miss} vector is defined as $\sigma(\Delta)$ where

$$\Delta = \sum p_x(p_y)_{gen} - \sum p_x(p_y)_{rec} \qquad \text{9-7}$$

where the first term on the right-hand side is the sum of the x (y) components of the momenta of all generated particles (neutrinos and muons excluded) without any pseudorapidity restriction, and the second term is the sum of the x (y) momenta as reconstructed from the calorimeters.

Figure 9-34 Resolution of the two components of the E_T^{miss} vector, as a function of the total transverse energy in the calorimeters, for $A \rightarrow \tau\tau$ events with $m_A = 150$ GeV at low luminosity.

Figure 9-34 shows the dependence of $\sigma(p_{x,y}^{miss})$ on the total transverse energy measured in the calorimeters ΣE_T for $A \rightarrow \tau\tau$ events. The result obtained using full simulation over $|\eta| < 5$ is compared to the result obtained with full simulation over $|\eta| < 3$ only. No significant difference between the two approaches is observed. The electronic noise of the EM Calorimeter was included, and a low-energy cut-off at 1.5σ was applied to the transverse energy deposited in each cell. The resolution of the E_T^{miss} components varies between about 5 and 10 GeV when m_A varies between 100 and 500 GeV, which allows a good mass resolution from the reconstructed $A \rightarrow \tau\tau$ spectrum (Section 9.3.3.4), and therefore high sensitivity to this channel (see Chapter 19).

The points shown in Figure 9-34 can be fitted with the form

$$\sigma(p_{xy}^{miss}) = 0.46 \times \sqrt{\Sigma E_T}$$

where E_T is expressed in GeV. This result includes the effect of both the energy resolution and the limited coverage of the detector. If the contribution of the limited coverage is unfolded, then the resolution becomes $\sigma(p_{xy}^{miss}) = 0.39 \times \sqrt{\Sigma E_T}$.

Figure 9-35 Resolution of the two components of the E_T^{miss} vector, as a function of the total transverse energy in the calorimeters, for minimum-bias events and $A \to \tau\tau$ events with m_A=150 GeV at low luminosity.
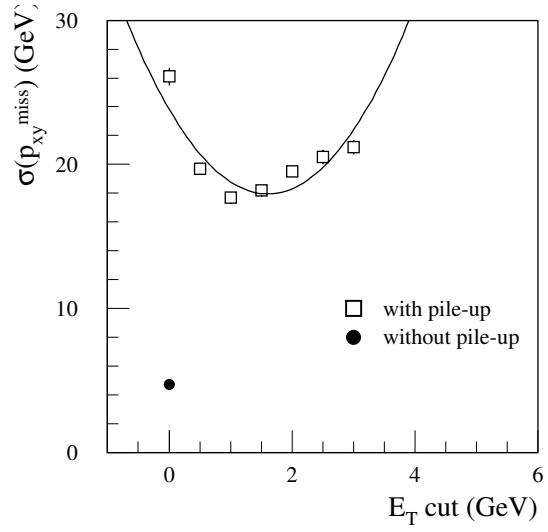
Figure 9-36 Resolution of the two components of the E_T^{miss} vector for $A \to \tau\tau$ events with m_A = 150 GeV at high luminosity, as a function of the tower E_T cut-off.

The dependence of the E_T^{miss} resolution on the total transverse energy measured with the calorimeters was also studied with minimum-bias events fully simulated in the region $|\eta| < 5$. Up to 48 minimum-bias events were combined to obtain a large total transverse energy in the calorimeters. The results obtained in this way are compared to the results from $A \to \tau\tau$ events in Figure 9-35: the agreement is good and the parametrisations obtained for both physics samples are the same. The conclusion of this study is that the E_T^{miss} resolution scales like $\sigma(p_{xy}^{miss}) = k \times \sqrt{\Sigma E_T}$ with $k \sim 0.46$.

When the high-luminosity case was considered, the E_T^{miss} resolution was defined in the same way as in Equation 9-7, with the only difference that the reconstructed E_T^{miss} (second term of the right-hand side of Equation 9-7) was evaluated with the pile-up added in the calorimeters. The contribution of the pile-up in the forward region was neglected, because it is small after a tower energy cut-off is ap-

Figure 9-37 Contribution to $\sigma(p_{xy}^{miss})$ from the pile-up and electronic noise expected at high luminosity (closed symbols). The open symbols show the contribution of the FCAL alone. A cut-off E_T (tower) > 1 GeV was applied in both cases.

plied (see below). From this definition it is clear that the E_T^{miss} resolution is degraded by the presence of pile-up. The impact can be reduced by applying a cut-off on the energy content of the calorimeter towers. Figure 9-36 shows the dependence of $\sigma(p_{xy}^{miss})$ on the cut-off. The reso-

lution is best for a cut-off of ~1 GeV, which corresponds to about 2.5σ of the quadratic sum of the electronic noise and pile-up. Despite the cut-off, the performance is degraded by a factor of larger than two as compared to the low-luminosity case.

Figure 9-37 shows the contribution to $\sigma(p_{xy}{}^{miss})$ coming from the pile-up and electronic noise alone, as obtained by applying the optimum tower cut-off of 1 GeV. The contribution of the pile-up in the FCAL is small if a cut-off is applied, which justifies the choice of simulating the pile-up up to $|\eta| = 3$ only.

9.2.2 $E_T{}^{miss}$ tails

The detection of large $E_T{}^{miss}$ is an important signature in many physics channels. One example is the search for a heavy Standard Model Higgs boson with a mass in the range 500-700 GeV in the decay mode $H \rightarrow ZZ \rightarrow ll\nu\nu$. The decay of one of the Z bosons to two neutrinos generates large $E_T{}^{miss}$ (see Section 19.2.10.1). In that context, one of the potentially dangerous backgrounds comes from Z+jet(s) events, where a badly measured jet could fake large $E_T{}^{miss}$. The rejection factor needed is of the order of 1000 in the region of $E_T{}^{miss}$ larger than 200 GeV.
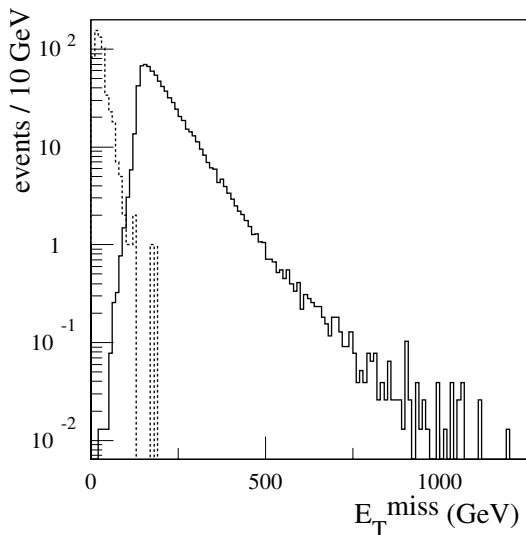
Figure 9-38 $E_T{}^{miss}$ distribution from Z+jet events with $p_T{}^Z > 200$ GeV: the full line is for the case where the jet is undetected and the dashed for the fully simulated jets.
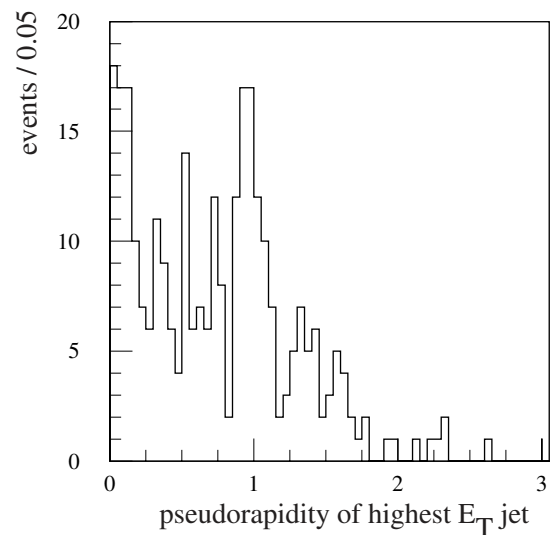
Figure 9-39 Pseudorapidity of the jet with the highest p_T for the events with $E_T{}^{miss}$ larger than 50 GeV.

A sample of 4 667 Z+jet(s) events was fully simulated. A p_T cut of 200 GeV was applied to the Z at the generation level, and the Z was required to decay to two muons. Since the interest is in the impact that the calorimeter cracks and dead material could have on the measurement of $E_T{}^{miss}$, and therefore in using as many events as possible of the sample of fully simulated jets, no additional requirements on the p_T or pseudorapidity of the muons were set and the particle level muon momentum was used in the $E_T{}^{miss}$ calculation. On the other hand, the probability of radiative muon processes is non-negligible for very energetic muons. In that case, the muons deposit energy in the calorimeter affecting the p_T balance. To eliminate radiative muons, events with a jet reconstructed within $\Delta R = 1$ of the direction of the muon were rejected. The particle-

level momentum of the muon was used, correcting simply for the average energy loss in the calorimeter. A sample of 3 826 events passed that selection. The resulting E_T^{miss} distribution is shown in Figure 9-38 as a dotted line. There are only two events with E_T^{miss} above 200 GeV. Those events contain a high-p_T neutrino, hence they contain genuine E_T^{miss}. The full line in the same figure represents the E_T^{miss} reconstructed in the event if the jet balancing the p_T of the Z would go completely undetected. It can be seen that the rejection factor of 1000 needed above 200 GeV is achieved. Figure 9-39 shows the pseudorapidity of the jet with the highest p_T for the events that have a E_T^{miss} larger than 50 GeV. Although the statistics is not large, one sees an accumulation of events around $|\eta| = 1$, the region of the vertical crack between the barrel and extended barrel calorimeters, which results from the deterioration of the jet energy resolution in that region. There is also some accumulation of events around $|\eta| = 0$, where the deterioration of the resolution comes likely from the fact that particles from the jets are parallel to the orientation of the scintillator tiles of the tile barrel calorimeter. In this configuration, the sampling fraction of the calorimeter is less uniform.

The resolution $\sigma(p_{xy}^{miss})$ has been studied as a function of the total sum of transverse energy in the calorimeter (ΣE_T). In addition to the sample of Z+jet(s) events with $p_T^Z > 200$ GeV, a second sample of 4 554 events with $p_T^Z > 40$ GeV has been used. The $\sigma(p_{xy}^{calo})$ is reconstructed in the calorimeter and is compared to $\sigma(p_{x,y}^{\mu})$, the p_T components of the two muons from the Z decay. In this case, the muon momentum is reconstructed in the Muon System and no cut to reject radiative muons has been applied. Since there is no true E_T^{miss} in these events, except for the few events that may contain a neutrino, the two components $p_{x,y}^{calo}$ and $p_{x,y}^{\mu}$ should be equal and opposite and the distribution of their difference can be fitted by a Gaussian whose sigma gives the resolution on the measurement of the components of the E_T^{miss} vector in the event. The values of sigma are shown in Figure 9-40 as a function of the total transverse energy in the calorimeter, taken as the sum of the transverse energy of the reconstructed jets. The resolution is shown for the full simulation and ATLFAST.
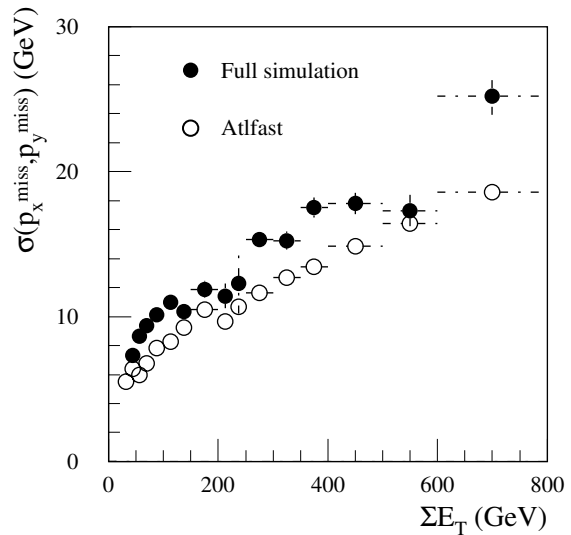
Figure 9-40 $\sigma(p_{xy}^{miss})$ as a function of ΣE_T in the calorimeter for Z+jet(s) events: detector resolution and physics effects are included (see text). Black dots are for full simulation and open dots for ATLFAST.

The full simulation gives a resolution about 20% worse than ATLFAST. The range of energies of the jets that are contributing to this sample is very large: from 20 GeV to about 800 GeV. In the full simulation, the E_T^{miss} is calculated from the sum of the energy of all cells of the calorimeters, applying to each calorimeter a single constant factor that corrects on average for the effect of the non-compensation of the calorimeter. These coefficients have been fitted to minimise the resolution for the overall sample. In ATLFAST, the $p_{x,y}^{calo}$ is calculated from the energy of the reconstructed jets at particle level (cone $\Delta R = 0.4$) smeared with a resolution given by $\sigma/E = 50\%/\sqrt{E} \oplus 3\%$, where cells unused in clusters are also taken into account. As was seen in Section 9.1.1, the best jet energy resolution is obtained when the calibration coefficients de-

pend on the jet energy and pseudorapidity and when correction terms taking into account the energy loss in dead material are added. Therefore the resolution obtained here with the simple algorithm used in this study is not optimum.

The resolution presented in Figure 9-40 is larger than the experimental resolution $\sigma(p_{xy}^{\text{miss}})$ given in Section 9.2.1.6 which is fitted by the form: $\sigma(p_{xy}^{\text{miss}}) = 0.46 \times \sqrt{\Sigma E_T}$. There are various effects that contribute to this difference. The above expression includes the detector energy resolution and the effect of the limited calorimeter coverage, since it is obtained by comparing the reconstructed p_T in the calorimeter to the sum of the p_T of all the particles without restriction in pseudorapidity, but does not include the fluctuation of the fragmentation process that contributes to the overall p_T balance of the event which is shown here. For example, the rms of the sum of the p_T of the particles resulting from the fragmentation of a 200 GeV quark (resp. 1000 GeV) at $|\eta| = 0.3$ is 5.5 GeV (resp. 16 GeV). In addition, in the sample of events considered here, the transverse energy measured in the calorimeter is deposited essentially by a single high-p_T jet. In that case, the contribution of the constant term of the jet energy resolution is important. When an equivalent amount of transverse energy is deposited by various jets, the most common physics case, then the resolution is dominated by the statistical term. This can be illustrated by a simple example: if n jets share equally the total energy E, then the energy resolution of each individual jet is $\sigma_{jet} = 50\% \times \sqrt{E/n} \oplus 3\% \times E/n$ and the total energy resolution is $\sigma_{tot} = 50\% \times \sqrt{E} \oplus 3\% \times E/\sqrt{n}$.

In this section it has been shown that no large E_T^{miss} tail is produced by badly reconstructed jets in the less uniform sections of the hadronic calorimetry. In addition, to obtain the best E_T^{miss} resolution, especially when a large range of jet energies is involved in a process of interest, one should apply an algorithm that adjusts the weights according to the jet energy and pseudorapidity and adds correction terms for energy loss in dead material.

9.3 Mass reconstruction

In this Section, the reconstruction of the mass of objects decaying to jets is discussed: the cases considered are $W \rightarrow jj$, $H \rightarrow b\bar{b}$, $Z \rightarrow \tau\tau$ and $H/A \rightarrow \tau\tau$, and $t\bar{t}$ final states.

9.3.1 *W* → *jj*

The reconstruction of two jets coming from the hadronic decay of *W* bosons will play an important role in many physics signals at the LHC. These signals include: the search for SUSY, the search for a heavy Higgs boson, the measurement of the top quark mass, and QCD studies. The resolution on the reconstructed mass is influenced by physics effects, such as jet fragmentation, jet overlap, final state radiation and minimum-bias events, and detector effects such as calorimeter response, hadronic shower size and electronic noise. The relative importance of the different effects, and hence the best reconstruction strategy, depends on the p_T range of the *W* decays considered, since low-p_T *W* bosons decay to well separated low-energy jets while in the case of high-p_T *W* decays, the two jets tend to overlap.

In this section, a study of the di-jet mass resolution, tails and efficiency for different ranges of p_T of the *W* is presented. The relative merits of different reconstruction algorithms are discussed and the detector effects for different luminosity scenarios are shown. More specific uses of

$W \rightarrow jj$ decays such as the measurement of the top mass or the use of the W mass constraint for *in situ* jet energy-scale calibration are treated separately in the section on the top mass measurement (see Section 18.1.3) and in the section on absolute energy scale (see Section 12.5.1.2).

Three typical ranges of p_T of the W are considered: the very low-p_T range (below 50 GeV), the mid-p_T range (100 to 200 GeV) from W+jet, WZ or top production, and the high-p_T range (200-700 GeV) from heavy Higgs ($m_H = 1$ TeV) decays. Three different methods have been considered:

- Method 1: the mass is calculated from the four-momenta of the two massless jets.

- Method 2: the mass is calculated from the four-momentum of each calorimeter tower ($m_{\text{tower}} = 0$) inside the two jets.

- Method 3: same as Method 2 but the energy is collected in a single cone to treat decays with severe overlap.

9.3.1.1 Low-p_T range

For the decays of low-p_T W's (see [9-23] for details) methods 1 and 2 have been applied using a fixed cone algorithm with $\Delta R = 0.4$. Figure 9-41 shows the reconstructed mass spectrum for W bosons. These events were fully simulated. A simple calibration of the jet energy was done by multiplying the reconstructed energy by the average ratio of the parton energies to the jet energies. This needs to be done on a case-by-case basis, depending on the reconstruction method, the cone size and whether pile-up was included. The two jets in this sample are very well separated. The average angular distance ΔR is 3, and the resolution on the reconstructed W mass is dominated by the jet energy resolution. The resolution, resulting from a $\pm 2\sigma$ Gaussian fit, is 9.5 GeV without pile-up and 13.8 GeV with pile-up (applying a 1 GeV E_T tower cut) for W decays to jets with p_T greater than 25 GeV. The reconstructed mass is compatible with the generated value of $m_W = 80.5$ GeV. The addition of the pile-up did not bias the reconstructed mass for method 1 and shifted it down by about 2 GeV for method 2.

9.3.1.2 Mid-p_T range

W bosons from WZ and W+jet production have been used to study W's with p_T above 100 GeV, with an average value of the order of 120–150 GeV (see [9-23] and [9-15]). The angular distance ΔR between the two partons from W decays in the W+jet events is shown in Figure 9-17. The average jet angular distance of the WZ sample is slightly lower (1.3) than the one of the W+jet sample (1.6).

Methods 1 and 2 (see [9-23]) were applied to the WZ sample using a fixed cone algorithm with $\Delta R = 0.4$. The data were fully simulated and the jet energy calibrated as described in Section 9.3.1.1. The results are shown in Figure 9-42. The two methods show a similar shape for the mass spectrum: there is a Gaussian component but a low-mass tail appears. The Gaussian part comes from the resolution of the jet energy. The tail appears for the events with a small opening angle between the jets, for ΔR between 0.5 and 1. The tail comes from a bias in the angle between the jets. This can be verified by calculating the mass from the reconstructed jet energies but using the true angle between the partons instead of the reconstructed angle. In that case, the low-mass tail disappears but not when the true quark energy is used together with the reconstructed angle. Even though a cone size $\Delta R = 0.4$ was used, energy from one jet is included in the other, inducing a bias in the direction. The average reconstructed mass is (80.7 ± 0.4) GeV for
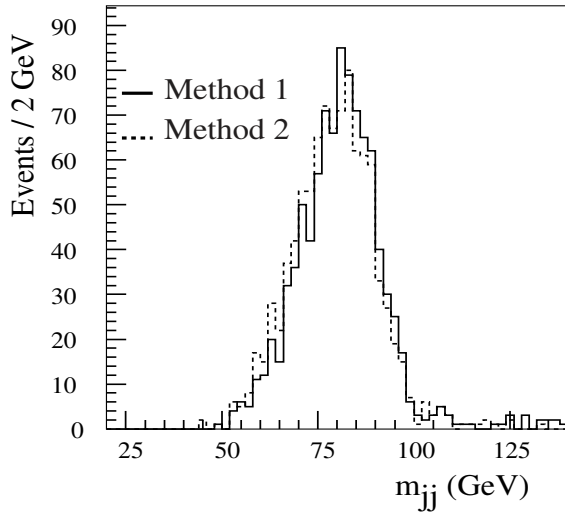
Figure 9-41 Reconstructed mass for low-p_T W's: full line shows method 1 (jet four-vector), and the dashed line shows method 2 (tower four-vector).
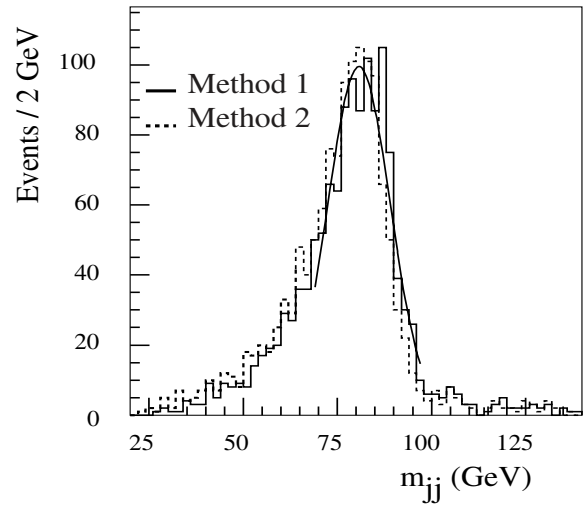
Figure 9-42 Reconstructed mass for mid-p_T W's: full line shows method 1 (jet four-vector), and the dashed line shows method 2 (tower four-vector).

method 1 and (79.5 ± 0.2) GeV for method 2 while the resolution is (7.7 ± 0.3) GeV and (8.3 ± 0.4) GeV, respectively. The addition of pile-up worsens the resolution to (12.9 ± 0.4) GeV even when increasing the cut on the jet transverse energy to 30 GeV.

The performance of method 1 with various jet algorithms has been tested on the sample of *W*+jet events with ATLFAST [9-15]. In this case, the particle-level energy of the reconstructed jet was used (no average calibration factor to the parton energy scale was applied). The comparison was made for the following algorithms: the conventional fixed cone jet algorithm for two cone sizes $\Delta R = 0.7$ and 0.4, the K_T clustering algorithm (with the distance parameter used to stop cell merging set to $R_{cut} = 0.4$ [9-14],[9-10]), the MGS algorithm (with the two-jet separation parameter ΔR set to 0.3 [9-15]).

Figure 9-43 shows the result for the low-luminosity scenario. The cone method with $\Delta R = 0.7$ gives the best performance: the average reconstructed mass is 78 GeV. The K_T and MGS algorithms reconstruct a mass average 3 GeV lower. For the cone method with $\Delta R = 0.4$, the average reconstructed mass is even lower, 72.5 GeV.

Figure 9-44 shows the results for the high-luminosity scenario. The effect of minimum-bias events was simulated by adding an average of 50 minimum bias events generated with PYTHIA (with Poisson fluctuations) and simulated by ATLFAST. The events were added at the level of the projected E_T ($\Delta\eta \times \Delta\phi$) matrix. A cut of 2 GeV E_T was applied to the towers to limit the pile-up effect. In this case, the performance of the cone method with $\Delta R = 0.7$ was seriously deteriorated, while the cone method with $\Delta R = 0.4$, the K_T and MGS algorithms showed similar performance: the addition of pile-up contributed about 10 GeV (in quadrature) to the resolution, as observed also in the fully simulated *WZ* sample. On the other hand, the average reconstructed mass increased by 6.5 GeV for the cone method with $\Delta R = 0.4$, 7 GeV for the K_T algorithm and 6 GeV for the MGS algorithm.
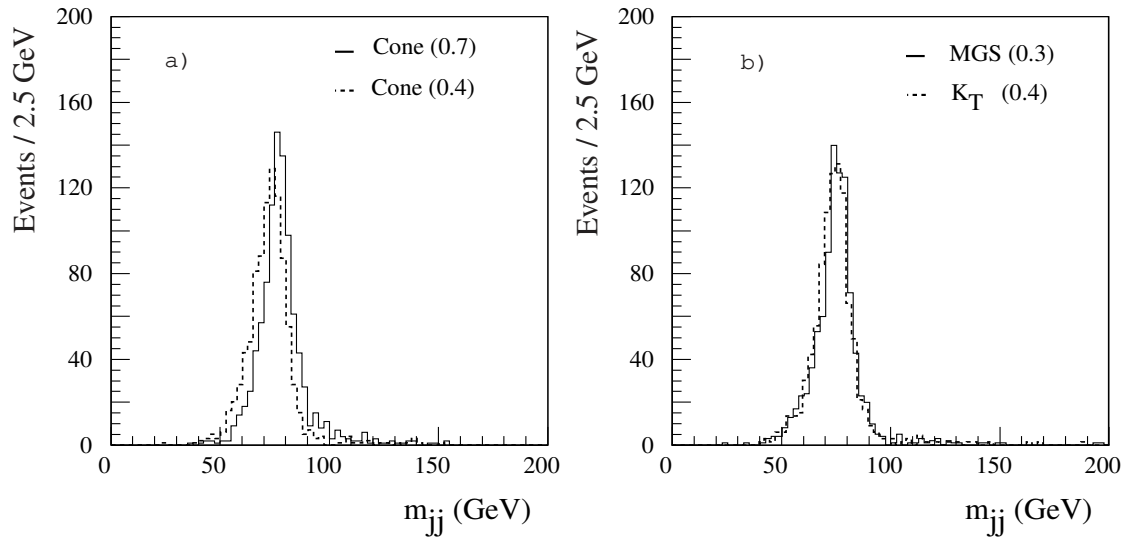
Figure 9-43 Reconstructed W mass without pile-up events for the W+jet sample: a) fixed cone algorithm with cone sizes $\Delta R = 0.7$ (average $m_W = 78$ GeV) and $\Delta R = 0.4$ (average $m_W = 72.5$ GeV); b) the K_T algorithm (average $m_W = 75$ GeV) and the MGS algorithm (average $m_W = 75$ GeV).
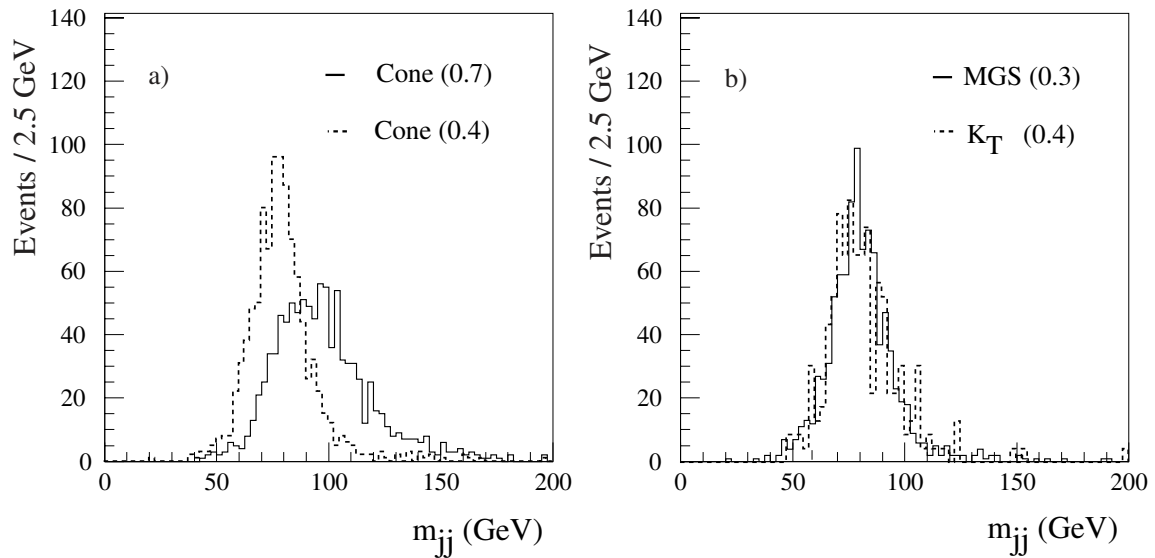
Figure 9-44 Reconstructed W mass with pile-up events added to the W+jet sample and with an E_T tower cut of 2 GeV: a) fixed cone algorithm with cone size $\Delta R = 0.7$ (full line) and fixed cone with $\Delta R = 0.4$ (dashed line); b) MGS algorithm (full line) and K_T algorithm (dashed line).

9.3.1.3 High-p_T range

The search for a heavy Higgs boson ($m_H > 600$ GeV) in the decay channel $H \to WW \to l\nu jj$ is one of the cases where an efficient reconstruction of high-p_T W's will be essential ([9-16],[9-17]). The separation in $\eta \times \phi$ for the case of a 1 TeV Higgs boson, is shown in Figure 9-45. Due to the boost, the two jets can be very close and will overlap. The range of E_T^{parton} studied in this fully simulated sample extends from 20 to about 500 GeV.

In the case of method 1, where the W mass is reconstructed from the four-momenta of the two jets, the fixed cone algorithm has to be applied with a narrow cone in order to be efficient at separating the two jets. In this case the energy inside the cone tends to under-estimate the parton energy and the resolution deteriorates.
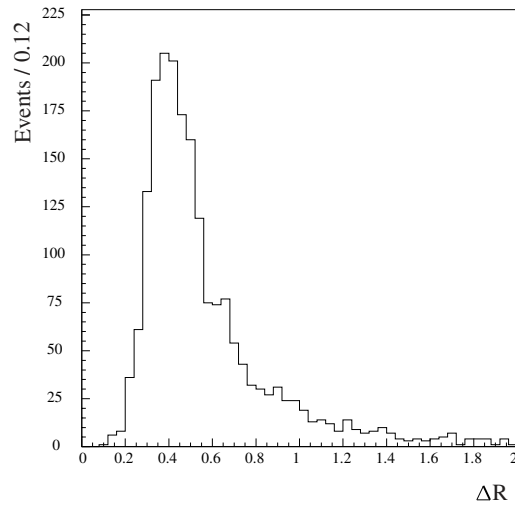
Figure 9-45 Distance ΔR between the two quarks from the *WW* decay of a 1 TeV Higgs.

The results obtained with method 1 for various jet algorithms are shown in Figure 9-46 for the high-luminosity scenario with a 2 GeV cut on the tower E_T. In this particle level study, the energy of the jet is taken from the reconstructed particle-level jet energy. No additional calibration factor to equalise the jet energy to the parton energy was applied. In the case of the standard
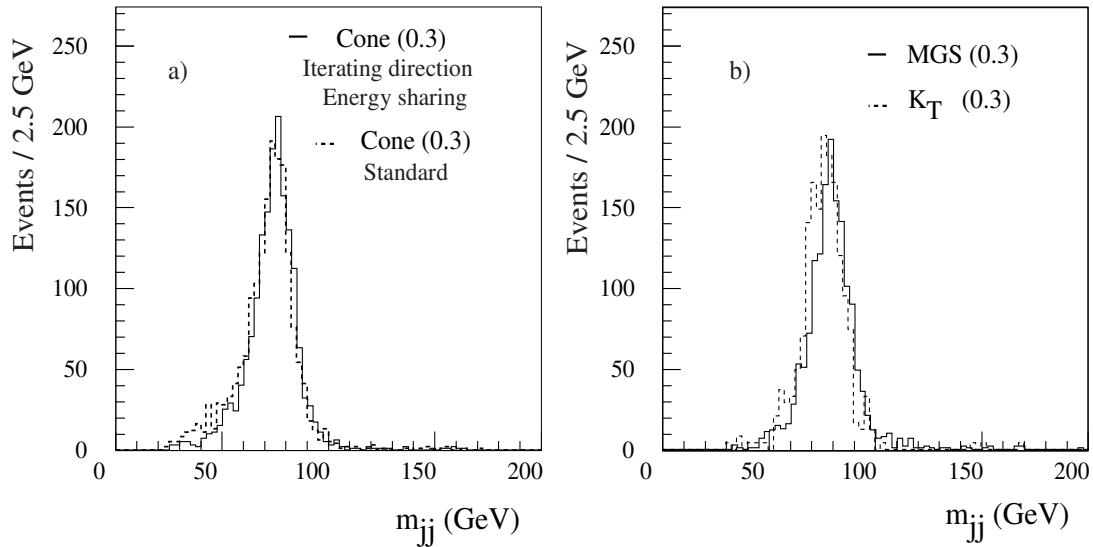
Figure 9-46 Reconstructed *W* mass with pile-up events for the 1 TeV Higgs boson sample, with an E_T tower cut of 2 GeV: a) cone algorithm with cone size $\Delta R = 0.3$ but iterating direction and jet energy sharing (an option of the MGS algorithm (full line), standard fixed cone algorithm with cone size $\Delta R = 0.3$ (dashed line); b) MGS algorithm (resolution = 0.3, full line), K_T algorithm ($R_{cut} = 0.3$, dashed line).

fixed cone algorithm, a low energy tail can be seen, due to the bias in the angle in the case of jet overlap. The tail can be reduced and the resolution improved by iterating the jet direction, resulting in the energy being shared between the two jets without biasing the jet that is reconstructed first, as happens in the standard cone algorithm. The low energy tail is further reduced in the case of the K_T and MGS algorithms with variable jet size but at the cost of some loss of efficiency.

When there is severe overlap between the jets, method 2 and method 3 may be more efficient. This follows since they have the advantage that very narrow initial cones ($\Delta R = 0.2$) can be used to find the jet direction and that no energy sharing is needed, only the list of towers to be considered has to be known.

The performance of methods 1 and 2 has been studied with a sample of fully simulated heavy Higgs events. In this case, the reconstructed jet energies in the calorimeter are calibrated by multiplying by a constant factor taken as the average ratio of the parton energy to the reconstructed jet energy. The mass scale (defined as the ratio of the reconstructed W mass divided by the generated mass) is shown in Figure 9-47 as a function of the p_T of the W. The mass scale is divided, on an event-by-event basis, by the jet energy scale (the ratio of the reconstructed jet energy divided by the

Figure 9-47 The ratio of the mass scale to the jet energy scale as a function of p_T^W for method 1 and method 2 (see text).

parton energy). In the case of method 1, a narrow $\Delta R = 0.2$ cone has been used to determine first the jet barycentres. A cone of $\Delta R = 0.4$ is then used to evaluate the jet energies; jet energy sharing is done by attributing the energy from a cell in the overlap region to the closest jet. The ratio of the mass scale to the jet energy scale is of the order of 0.95 and decreases slightly as a function of the p_T of the W, about 2% between 250 and 700 GeV. When the jets overlap, energy from one

Figure 9-48 Reconstructed W mass using Method 2 after applying a linear correction as a function of the p_T of the W at low luminosity (left) and with high luminosity pile-up included (right)

jet gets included in the other one and result in the centres being too close which lowers the reconstructed mass. For method 2 (the same is true for method 3), the ratio of mass scale to jet energy scale is larger than one and increases significantly with the p_T of the W. This results from the following effect: when a particle points to a tower, it deposits its energy not only in that tower but also in the neighbouring towers because of the lateral shower size. When the mass is calculated, the energy is weighted according to the relative angle of each tower. Instead of all the energy of a particle being assigned to the tower that was hit, part of it is in the neighbouring towers. The overall effect is that the mass gets larger as shower size effects become more important. The W mass spectrum reconstructed with method 2 is shown in Figure 9-48 at low and high luminosity. A linear correction as a function of the p_T of the W has been applied to the mass to correct for the systematic bias mentioned above. The reconstructed mass is 80.5 GeV and the resolution is 5.0 GeV (6.9 GeV) at low (high) luminosity.

9.3.1.4 Conclusions

Jets from low-p_T W boson decays are well separated and the mass resolution is dominated by the jet energy resolution. As the p_T of the W increases, the jets start to overlap and the resulting systematic effects on the reconstructed mass are very dependent on the reconstruction method used.

9.3.2 $H \rightarrow b\bar{b}$

WH production, followed by the decay $H \rightarrow b\bar{b}$, is a promising channel to observe a Higgs boson signal at the LHC, both in the context of the Standard Model and of the MSSM, if the Higgs mass is in the range 80–100 GeV. In addition, $h \rightarrow b\bar{b}$ decays are expected to be a clean signature of SUSY final states, since over a large region of the parameter space squarks and gluinos include the h boson among the products of their cascade decays (Chapter 20). The reconstruction of the Higgs mass in the $b\bar{b}$ channel and the resulting mass resolution were studied by using fully-simulated events at low and high luminosity, and are discussed below. More details about this channel can be found in Section 19.2.4.

9.3.2.1 *WH* generation and selection

A sample of about 900 WH events, with $H \rightarrow b\bar{b}$ and $W \rightarrow l\nu$ ($l = e, \mu$), were generated with PYTHIA 5.7, including initial-state radiation, final-state radiation and hadronisation. The Higgs mass was chosen to be $m_H = 100$ GeV. Events were selected if the b-quarks satisfied $p_T > 15$ GeV and $|\eta| < 2.5$. The sample was then processed with the full-simulation chain.

In the following, a reconstructed jet was defined as a b-jet if its distance from a b-quark with $p_T > 5$ GeV (after final-state radiation) was $\Delta R < 0.2$. No b-tagging in the Inner Detector was required explicitly for the study presented here. This is not expected to bias the Higgs mass reconstruction as obtained from the calorimeters.

9.3.2.2 *WH* reconstruction at low luminosity

Jets were reconstructed with cones of size $\Delta R = 0.7$. The efficiency for reconstructing one or both b's produced in the Higgs boson decay is 83% and 69% respectively, where a b-jet is defined according to the criteria described in the previous section. Figure 9-49 shows the reconstructed in-

variant mass of the two *b*-jets for events where both *b*'s are reconstructed and both have $p_T > 15$ GeV. The jet energies were scaled by the average value of $K_{jet} = p_T^{parton}/p_T^{jet}$, where p_T^{parton} is the transverse momentum (before final state radiation) of the parton which initiated the jet. This correction factor decreases when p_T^{jet} increases and it becomes asymptotically equal to unity for $p_T^{jet} > 50$ GeV [9-24]. Before such a correction was applied, a large down-shift of the peak of the reconstructed two-jet mass was observed, which was mostly due to final-state radiation, hadronisation and the decay of the *b*-quarks: energy leaks outside the jet cone and the presence of neutrinos among the decay products are responsible for the degradation of the mass resolution and the appearance of low-energy tails. As a consequence, only 82% of the events are
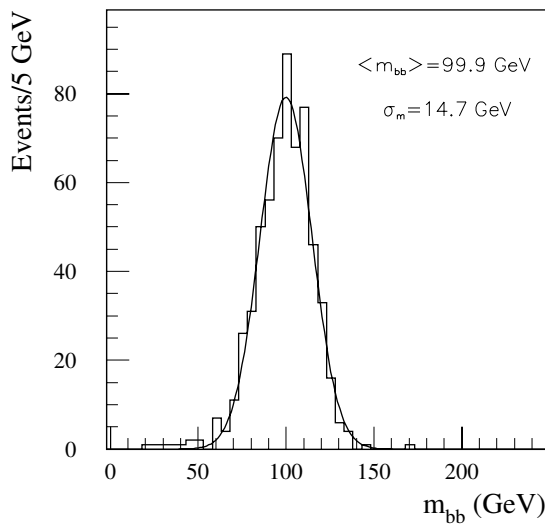
Figure 9-49 Reconstructed invariant mass distribution of the two *b*-jets in the final state for $H \rightarrow b\bar{b}$ events with $m_H = 100$ GeV at low luminosity.
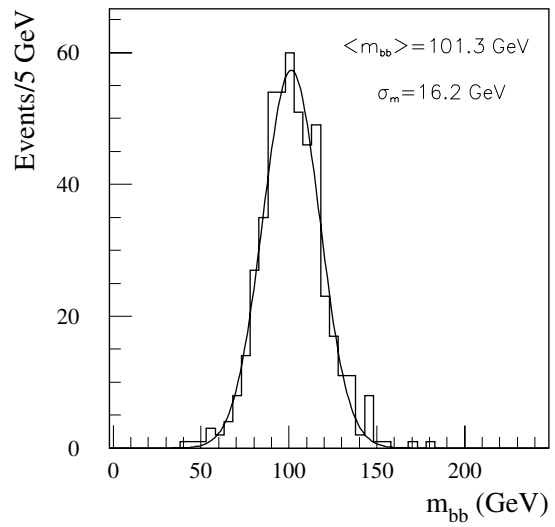
Figure 9-50 Reconstructed invariant mass distribution of the two *b*-jets in the final state for $H \rightarrow b\bar{b}$ events with $m_H = 100$ GeV at high luminosity.

contained inside a window of ±20 GeV around the peak of the distribution. After the calibration of the *b*-jet energy, the reconstructed mass peak is at the expected position, as it can be seen from Figure 9-49, and the mass resolution is ~15 GeV. This can be compared with a mass resolution of 12.8 GeV obtained with ATLFAST [9-24]. It should be noted that the *b*-jet scale will be calibrated *in situ* at the LHC by using for instance *Z*+jet events (see Section 12.5.1.3).

9.3.2.3 *WH* reconstruction at high luminosity

To study the *b*-jet reconstruction and mass resolution at high luminosity, pile-up was added to the signal sample in the way discussed in Chapter 2. Only calorimeter towers with a transverse energy content of larger than 1 GeV were used to reconstruct the jets. A jet cone size of $\Delta R = 0.4$ was chosen in this case in order to minimise the impact of pile-up. The *b*-jets were required to have $p_T > 15$ GeV and the jet energies were calibrated as described above. Figure 9-50 shows the reconstructed invariant mass distribution of the two *b*-jets at high luminosity. The mass resolution is 16 GeV and 80% of the events are contained in a window of ±20 GeV around the mass peak.

9.3.2.4 $H \to hh \to b\bar{b}b\bar{b}$

This channel was studied to assess the capability of reconstructing final states where more than one resonance decaying to jets is produced [9-25]. A high-statistics sample of fully-simulated $H \to hh \to b\bar{b}b\bar{b}$ events with $m_H = 300$ GeV and $m_h = 80$ GeV was used. Pile-up and electronic noise were not included.

Jets were defined as *b*-jets according to the criteria discussed in Section 9.3.2.1. Firstly, both $h \to b\bar{b}$ decays were reconstructed by assuming that the *h* boson has been discovered already and therefore its mass is known. This was used as a constraint to find the optimum combination of the four *b*-jets into two pairs, and therefore to reduce the combinatorial background. The chosen combination was the one which minimised $\chi^2 = (m_{b\bar{b}} - m_h)^2 + (m_{b\bar{b}} - m_h)^2$. The resulting $h \to b\bar{b}$ mass resolution was found to be 11 GeV for $m_h = 80$ GeV, with an event acceptance of 89% inside a mass window of $\pm 2\sigma_m$ around the peak. After selecting events where both $b\bar{b}$ masses are inside the above-mentioned mass window, the *b*-jet four-momenta were recalibrated by applying the constraint $m_{b\bar{b}} = m_h$. Finally, the four *b*-jet mass distribution was reconstructed (Figure 9-51). The resulting *H* mass resolution was about 13 GeV, with ~82% of the events inside a mass window of $\pm 2\sigma_m$.
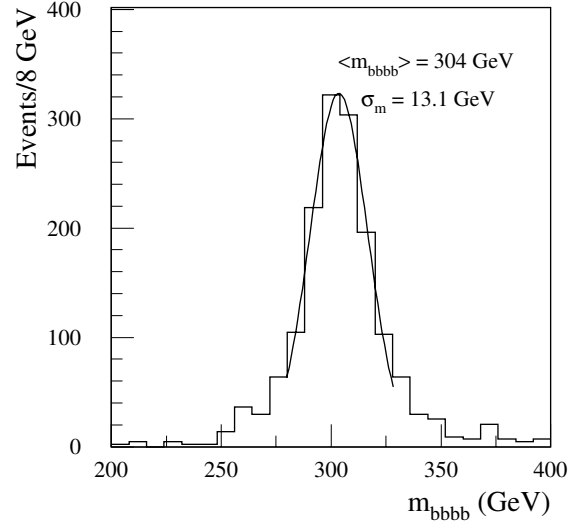
Figure 9-51 Reconstructed four *b*-jet mass spectrum for $H \to hh \to b\bar{b}b\bar{b}$ with $m_H = 300$ GeV.

9.3.3 $\tau\tau$ final states

In this section, the reconstruction of heavy particles decaying into τ pairs, with one τ decaying hadronically and the other one leptonically, is discussed. Such final states are expected for instance from the possible production and decay of the supersymmetric Higgs bosons *A* and *H*. Two methods to reconstruct the $\tau\tau$ invariant mass, one based on all products from τ decays and one on the visible decay products only, are presented.

The section starts with a discussion of $Z \to \tau\tau \to$ jet+lepton events, which could be used as a control sample for $\tau\tau$ final states. Indeed this sample would allow tests of the methods used to reconstruct the $\tau\tau$ invariant mass, and checks of the overall calorimeter calibration since the $\tau\tau$ invariant mass is obtained from several different objects (leptons, hadrons, missing transverse energy). Furthermore, the possibility of using these events for a precise measurements of the τ lifetime is briefly described. Finally, the reconstruction of $H/A \to \tau\tau$ events, and the performance in terms of mass resolution and acceptance in the mass bin, are discussed.

9.3.3.1 $Z \to \tau\tau$ reconstruction from all decay products

Fully-simulated samples of $Z \to \tau\tau \to$ jet+lepton events and of the main backgrounds were used for the study presented here, together with a sample of events simulated with ATLFAST.

The invariant mass of the τ-pair produced in the decay of a Z boson, or of any other particle, in the channel

$$Z \to \tau\tau \to \text{jet } \nu_\tau \, l\nu_l\nu_\tau$$

can be reconstructed under the assumptions that $m_\tau = 0$, that the direction of the neutrino system from each τ decay ($\bar{\nu}_1 = \bar{\nu}_\tau$, $\bar{\nu}_2 = \bar{\nu}_l + \bar{\nu}_\tau$) coincides with that of the detected products of the τ decay, and that the τ decay products are not back-to-back.

The reconstructed mass is then given by

$$m_{\tau\tau} = \sqrt{2(E_1 + E_{\nu1})(E_2 + E_{\nu2})(1 - \cos\theta)}$$

where E_1 and E_2 are the energies of the detected products from the τ decay, $E_{\nu1}$ and $E_{\nu2}$ are the energies of the two neutrino systems, and θ is the angle between the directions of the detected products. $E_{\nu1}$ and $E_{\nu2}$ are obtained by solving the system

$$p_x^{\text{miss}}(p_y^{\text{miss}}) = (E_{\nu1}\bar{u}_1)_{x(y)} + (E_{\nu2}\bar{u}_2)_{x(y)}$$

where $\bar{u}_1$ and $\bar{u}_2$ are the directions of the detected products, and p_x^{miss} and p_y^{miss} are the two components of the E_T^{miss} vector. This system can be solved if the determinant, $\sin\Delta\phi$, is not zero, where $\Delta\phi$ is the azimuthal angle between the jet and the lepton produced in the τ decay. The kinematics of the event, the accuracy in the measurement of p_x^{miss} and p_y^{miss} in the calorimeter, and the assumption made on the particle directions contribute to the width of the reconstructed mass and can result in unphysical negative solutions for $E_{\nu1}$ and $E_{\nu2}$. In this case, the Z mass cannot be reconstructed. The mass resolution obtained in this way is proportional to $\sigma(E_T^{\text{miss}})/|\sin\Delta\phi|$, therefore both the E_T^{miss} resolution and the azimuthal separation between the lepton and the jet are important in the mass reconstruction. The variable $\Delta\phi$ depends on the p_T of the parent particle (*e.g.* a Z), and it is concentrated around π if the p_T is small, as shown in Figure 9-52. The dependence of the reconstructed $\tau\tau$ mass on $\Delta\phi$ is illustrated in Figure 9-53 in the case of Z production and decay; if $\Delta\phi$ is close to π (back-to-back events), the neutrino system yields bad solutions giving rise to tails at high values of the reconstructed mass.

Table 9-8 shows the mean value and the sigma of the $\tau\tau$ invariant mass distribution for $Z \to \tau\tau$ decays, together with the fraction of events lost in the individual selections of the mass reconstruction procedure. All events were used at this level, without applying any cuts, and a 100% τ identification efficiency is assumed. Therefore, event losses were due to cases where the above-mentioned system of equations yielded unphysical solutions for the neutrino energies. Starting from the mass distribution as generated by PYTHIA (first step), four other steps were considered. In the second step, $m_{\tau\tau}$ was reconstructed by using the particle level information, that is using the generated energies and directions. In particular, the components of the E_T^{miss} vector were calculated without any restriction on the pseudorapidity coverage of the detector. At this stage, the event loss and the deterioration of the mass resolution were due to the assumption on the directions of the τ decay products. In the third step, the reconstructed mass was obtained in the same way as in the second step but using a cut $|\eta| < 5$ for the E_T^{miss} reconstruction. The resulting event loss and deterioration of the mass reconstruction were due to the limited pseudorapidity coverage of the detector. In the fourth step, p_x^{miss} and p_y^{miss} as obtained from full simulation were used. The deterioration of the performance was due to the E_T^{miss} experimental resolution. Finally, in the fifth step, the reconstructed energies and directions of the jet and the lepton were used. It can be seen that the event losses and the deterioration of the mass reconstruction and resolution are mainly due to the assumption on the particle directions, to the limited pseudorapidity coverage of the detector and to the E_T^{miss} resolution.
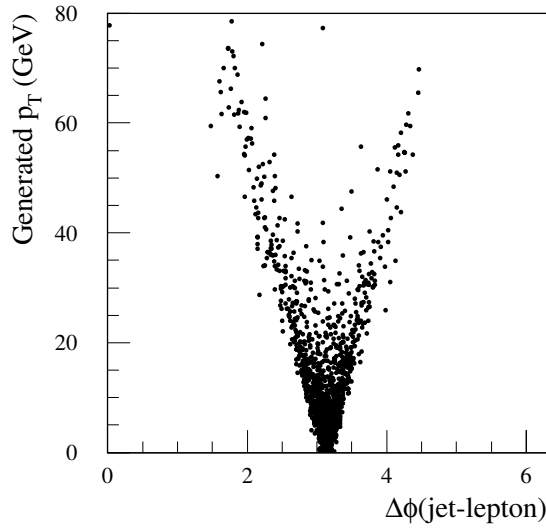
Figure 9-52 The azimuthal angle between the jet and the lepton produced in the decay of the two τ's as a function of the generated p_T of the Z.
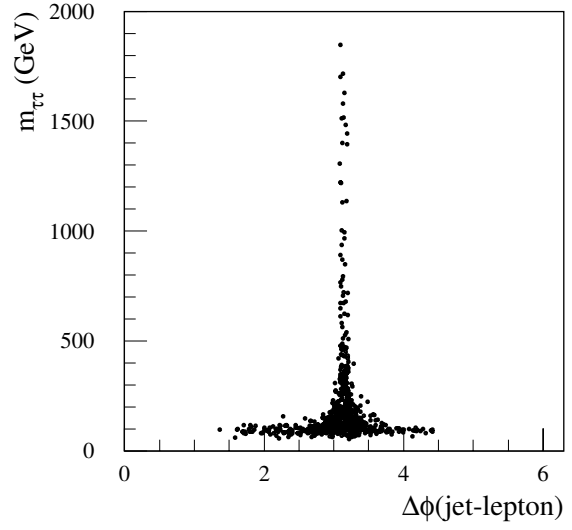
Figure 9-53 The reconstructed $Z \to \tau\tau$ mass as a function of the azimuthal angle between the jet and the lepton produced in the decay of the two τ's.

Table 9-8 For $Z \to \tau\tau$ decays, the mean value and the σ of the reconstructed mass spectrum, and the fraction of events lost, as a function of the selection in the reconstruction procedure (see text).

Selection	$<m_{\tau\tau}>$ (GeV)	$\sigma (m_{\tau\tau})$ (GeV)	Lost events
Generation level	91.2	1.7	0
Particle level	92.0.	7.4	28%
Particle level $|\eta| < 5$	97.0	12.0	46%
E_T^{miss} from full simulation	97.6	15.3	52%
Reconstructed jets and leptons	98.7	15.8	52%

An analysis similar to that used to select final states due to the production and decay of the A boson (Chapter 19) was performed to extract a clean sample of Z events, with a well reconstructed mass, from the main backgrounds (W+jets and $b\bar{b}$ production). The following cuts were used for this purpose:

- The τ-jet should be identified according to the criteria described in Section 9.1.5.

- $p_T^{jet} > 30$ GeV, $|\eta|_{jet} < 2.5$.

- $p_T^{lepton} > 16$ GeV and $|\eta|_{lepton} < 2.5$ for the lepton produced in the leptonic τ decay.

- No tagged b-jet in the event.

- Transverse mass m_T (lepton-E_T^{miss}) < 50 GeV.

- $1.8 < \Delta\phi < 2.7$ or $3.6 < \Delta\phi < 4.5$.

- 66 GeV $< m_{\tau\tau} < 116$ GeV.

Table 9-9 Production cross-section, acceptance and expected number of events with an integrated luminosity of 10 fb^{-1} for the $Z \to \tau\tau$ signal and the main backgrounds.

	$Z \to \tau\tau$	$b\bar{b}$	W+jets
σ (nb)	1.5	19.9 ($p_T^\mu > 16$ GeV)	392 ($p_T^\mu > 16$ GeV)
Acceptance	4.8x10^{-4}	3x10^{-6}	1.3x10^{-6}
Events in 66-116 GeV	3500	270	500

About 3 500 signal events satisfying the above cuts are expected with 10 fb^{-1} of integrated luminosity. The background is about 20% (Table 9-9). The background can be further reduced by applying a more stringent cut on the transverse mass ($m_T < 25$ GeV), which removes W+jet events, and by introducing a cut on the missing transverse momentum ($E_T^{miss} > 18$ GeV), which rejects $b\bar{b}$ final states. With this set of cuts, the background in the mass window is reduced to ~6% and about 1 300 signal events are expected for 10 fb^{-1} of integrated luminosity. The reconstructed Z mass obtained in this way (Figure 9-54) is well centred at the nominal value and has a resolution of about 9 GeV.

It should be noted that the results shown in the last row of Table 9-8 were obtained without applying any cuts. In particular the $\Delta\phi$ cut improves significantly both the mass resolution and the correct reconstruction of the mass peak.
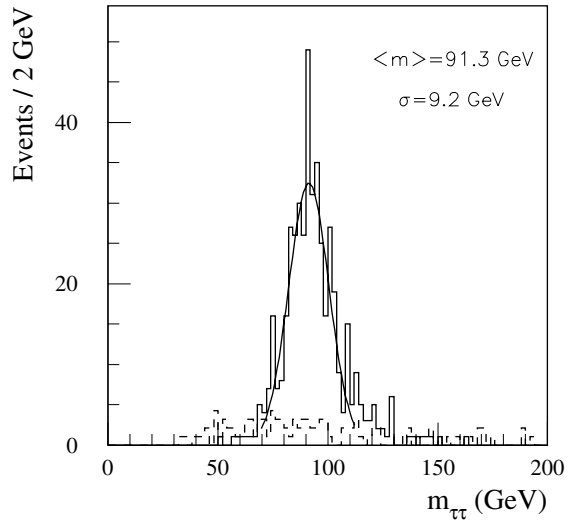
Figure 9-54 Reconstructed $Z \to \tau\tau$ mass spectrum at low luminosity. The dashed line indicates the background.

9.3.3.2 $Z \to \tau\tau$ reconstruction from observed decay products

The reconstruction of the $\tau\tau$ invariant mass shown in the previous section relies on the assumption that the missing transverse energy in the event arises only from the neutrinos emitted in τ decays. There are cases where this is not true and yet the invariant mass of the $\tau\tau$ system is an important quantity. An example is given by the decays of supersymmetric particles in some models (see Chapter 20), where the measurement of the τ momentum and of the $\tau\tau$ invariant mass distribution would provide detailed information regarding the particle masses. In these cases, the $\tau\tau$ invariant mass must be reconstructed from the visible products of the τ decays only [9-26]. Missing transverse momentum and jet activity can be used as a trigger and event selection. The events so selected are rich in τ's, hence the primary background arises from jets in the same event and the τ identification criteria can be relaxed at the cost of lowering the rejection factor against jets. Leptonic τ decays are not useful, since the resulting electron or muon cannot be attributed to a τ decay, given the presence of other leptons in supersymmetry events. Hadronic τ decays must therefore be used.

In order to study how well this can be done, fully-simulated samples of Z+jet events were used. No pile-up was included, therefore the results are limited to the case of low luminosity. Separate samples were generated for different values of the 'Z mass' and for several ranges of transverse momenta. The rejection against jets was studied using the QCD jets in the same events.

Jets were reconstructed using a fixed-cone algorithm with a cone radius $\Delta R = 0.4$. A calorimetric isolation was applied by requiring that 96% of the energy be contained in the core of the jet, *i.e.* within $\Delta R = 0.2$ of the jet's centroid. This retained 74% of the hadronically decaying τ's and 17% of the jets. Additional jet rejection can be obtained by studying the mass of the jet, calculated by assuming that the energy in each calorimeter cell is due to a single massless particle at the centre of the cell. Requiring that this mass be less than 3.6 GeV reduced the acceptance to 65% (6.6%) for τ's (jets). This rejection against jets is sufficient to extract a supersymmetry signal.

In order to make an accurate reconstruction of the τ's, the Inner Detector was used to measure the momentum of charged tracks and the EM Calorimeter to measure the energy and hence the momentum of the photons that arise from π^0 decays. The xKalman package was used to reconstruct tracks in a road defined by the direction of the τ–jet candidate. These tracks were then extrapolated to the EM Calorimeter. Tracks reconstructed in this way can arise from τ decays, γ conversions or particles of the underlying event that happen to be nearby. Tracks of transverse momenta less than 1 GeV were not included to reduce the contamination. To reconstruct the mass of the τ-jet, all EM cells with $E_T > 1$ GeV were combined with the reconstructed charged tracks, which were all assumed to be pions. The Hadronic Calorimeter was not used. If a track deposits energy in a calorimeter cell, care must be taken to avoid overcounting. Assuming that the conversion electrons can be identified, the electromagnetic energy was included and the track dropped. For other tracks, the cell that was hit by the track was not included. The reconstructed jet mass showed the presence of a ρ peak, as expected from τ decay.

In events where two τ-jets were selected, the mass of the di-jet system was measured. This mass distribution showed a broad peak below the Z mass. The peak was sharpened by including only events where the reconstructed τ mass was greater than 0.8 GeV. This biased the sample against single-pion decays and in favour of decays where the energy carried by the neutrino was small. Table 9-10 shows the values of the reconstructed τ-pair mass and resolution obtained as a function of the generated mass. The ratio of the position of the peak to the generated mass is constant within errors and is independent of the transverse momentum of the produced particle (for $p_T < 125$ GeV).

The τ charge was determined as described in Section 9.1.5.1. These results on the efficiency, jet rejection, τ-pair mass resolution and charge identification are parametrised and used in the supersymmetry studies presented in Chapter 20.

9.3.3.3 τ lifetime measurement in $Z \rightarrow \tau\tau$ events

The current world average for the τ lifetime is 290.5 ± 1.0 fs [9-27]. Improvements in this measurement would be welcome in order to provide tests of the universality of the charged current and reduce the error on α_s. In this section, the results of a preliminary study to examine the ATLAS potential in the $Z \rightarrow \tau\tau$ channel are given.

$Z \rightarrow \tau\tau$ events were identified and reconstructed as described in Section 9.3.3.1, where one τ decaying to an electron or muon is used for triggering and the other τ decays hadronically. In order to measure the τ lifetime, three-prong decays were used to reconstruct the decay length ($c\tau = 87$ µm) in the Inner Detector.

Table 9-10 The reconstructed values of the peak of the ττ invariant mass as a function of the generated pair mass 'M_Z'. Also shown are the standard deviation and the ratios of the peak and of the standard deviation to the generated pair mass.

'M_Z' (GeV)	Reconstructed $M(\tau\tau)$ (GeV)	$\sigma(M)$ (GeV)	$M(\tau\tau)/M_Z$	$\sigma(M)/M_Z$
25	18.6	4.9	0.75	0.20
50	36.3	8.9	0.72	0.18
75	50.0	12.4	0.66	0.17
91	63.0	17.5	0.67	0.19
200	131.0	38.0	0.65	0.19

Reconstruction

Fully-simulated $Z \rightarrow \tau\tau \rightarrow$ jet+lepton events were used. To identify the events and reduce the backgrounds, it was required that the lepton should have $p_T > 24$ GeV, the jet $E_T > 30$ GeV and the reconstructed mass should be between 60 and 120 GeV. This resulted in an efficiency of 1.5%.

The direction of the jet was found from the calorimetry and a search was made in the ID in a cone of $\Delta R = 0.4$ around this direction. Jets were required to have at least two reconstructed tracks with $p_T > 2$ GeV satisfying the basic ID quality cuts Section 3.1.3. These tracks were used to reconstruct a secondary vertex using the algorithm described in Section 3.6. It was required that the vertex position should be within 2 cm of the beam spot in both x and y, that the net charge of reconstructed tracks associated with the displaced vertex should be ≤2 and that the invariant mass of these charged particles should be between 0.4 and 1.78 GeV. The efficiency to reconstruct at least two of the tracks was 87%, while the efficiency to reconstruct a vertex satisfying the cuts was 80%. The resolution of the vertex position in the transverse plane was 490 μm, corresponding to a resolution on the proper decay length of 17 μm.

To reconstruct the proper lifetime of the τ, it is necessary to boost back into the τ rest-frame with the Lorentz factor p_τ/m_τ, where p_τ is obtained from the p_T of the system recoiling against the Z, projected along the directions of the τ's. Equivalently, p_τ can be found from the missing energy, as explained in Section 9.3.3.1. A valid solution for the τ momentum was obtained in 52% of cases (see Table 9-8). The uncertainty in the determination of the recoil momentum leads directly to an uncertainty in p_τ and hence in the proper lifetime estimate. The statistical uncertainty on p_τ was typically 15%. It should be possible to control the systematic uncertainty by using $Z \rightarrow ee$ or $Z \rightarrow \mu\mu$ events with similar topologies to $Z \rightarrow \tau\tau$. For these events, the recoil measured by the calorimetry can be compared directly with the p_T of the Z measured by the leptons.

Lifetime estimate

The Inner Detector measures impact parameters of tracks with a resolution which is independent of momentum for particles with more than ~10 GeV. Hence the estimate of the proper decay length (rather than that measured in the laboratory frame) is fairly independent of the τ momentum. The statistical resolution on the proper decay length from the combination of the vertexing and the estimate of the τ momentum is of the order of 21 μm (corresponding to 55 fs). To estimate the statistical uncertainty on the τ lifetime τ_τ which could be achieved with N τ decays, a simple Monte Carlo study was made where the exponential proper lifetime distribution was

smeared with the statistical resolution and the lifetime was obtained using a likelihood method. The effective resolution provided by a single event is the sum of the measurement resolution (55 fs) and the lifetime (291 fs) combined in quadrature. Since the latter is quite a bit larger, it was found to dominate the error with the result that $\sigma(\tau_\tau) \approx \tau_\tau / \sqrt{N}$.

At the LHC, the cross-section for $Z \to \tau\tau$ will be 1.5 nb, with a branching ratio of 11% for a lepton and a three-prong hadronic decay. The reconstruction and selection described above results in an efficiency of 0.54%. If 30 fb^{-1} were collected in the low-luminosity phase, then 26 000 reconstructed τ's could be used, leading to a statistical error on the τ lifetime of 1.8 fs.

For an ATLAS measurement to be competitive, it will be necessary to have higher statistics, since improvements in the vertexing will not help significantly. This may occur from a larger integrated luminosity being delivered or from an increased efficiency. More work is needed to understand how the kinematical cuts could be loosened without increasing the errors resulting from the background. The cuts used in Section 9.3.3.1 give good background rejection but lead to efficiencies which are too small. *W*+jet events will be removed by the mass cuts, and apart from a small amount of gluon splitting to heavy flavour, the jets should not contain significant lifetime information, hence this background should not be a problem. The *B* lifetime is a factor of five larger than that of the τ, hence more care will be required with $b\bar{b}$ events. Nevertheless the background looks tolerable and should be significantly reduced by the kinematical cuts. In addition, further cuts on lepton isolation could be used.

Concerning systematic errors coming from the determination of the decay length in the ID, the average radial position of the detectors in the *B*-layer should be well determined using the constraints of the overlaps [9-28]. The aim is to understand the alignment in $R\phi$ to O(1) μm, which should be compared to the typical impact parameters which will be of the order of $c\tau_\tau = 87$ μm. How this will contribute to the systematics of the lifetime needs to be studied and will depend on the exact nature of the alignment uncertainties; however, it is conceivable that many systematic contributions will cancel for the lifetime estimate.

9.3.3.4 $H/A \to \tau\tau$

The same method for reconstructing the $\tau\tau$ invariant mass as described for $Z \to \tau\tau$ final states in Section 9.3.3.1 was applied to $H/A \to \tau\tau$ decays. The fully-simulated sample of events from direct *A* production described in Section 9.1.5 was used for this study. The resulting τ-pair mass spectrum is shown in Figures 9-55 and 9-56 for $m_A = 150$ GeV and $m_A = 450$ GeV respectively.
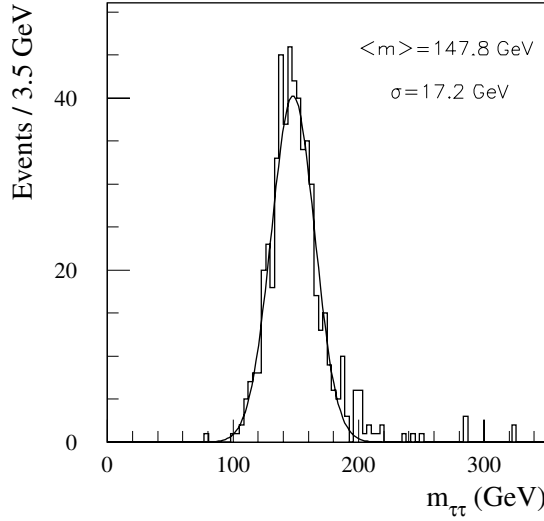
Figure 9-55 Reconstructed $A \to \tau\tau$ mass at low luminosity for m_A = 150 GeV.
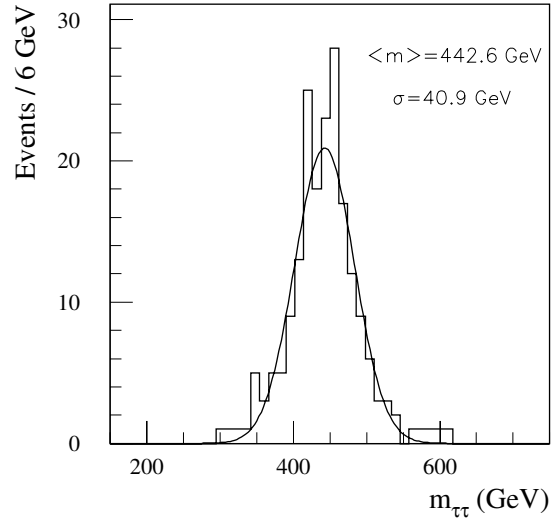
Figure 9-56 Reconstructed $A \to \tau\tau$ mass at low luminosity for m_A = 450 GeV.

Events with $2.9 < \Delta\phi < 3.4$, where $\Delta\phi$ is the azimuthal angle between the lepton and the jet from the τ decays, were rejected in order to improve the quality of the mass reconstruction. As already mentioned when discussing $Z \to \tau\tau$ decays, the reconstructed mass distribution has tails at high values. This is shown in Figure 9-57 for three different A masses. Comparing Figure 9-57 with Figure 9-53, it can be seen that the $\Delta\phi$ distribution is less peaked around π for A events than for Z events. This is due to the fact that the p_T of the A is in general larger than the p_T of the Z. As a consequence, the fraction of events lost because the system of equations giving the neutrino energies yields unphysical solutions is smaller than in the Z case, and decreases with increasing m_A (from ~40% for m_A = 150 GeV to ~25% for m_A = 450 GeV).
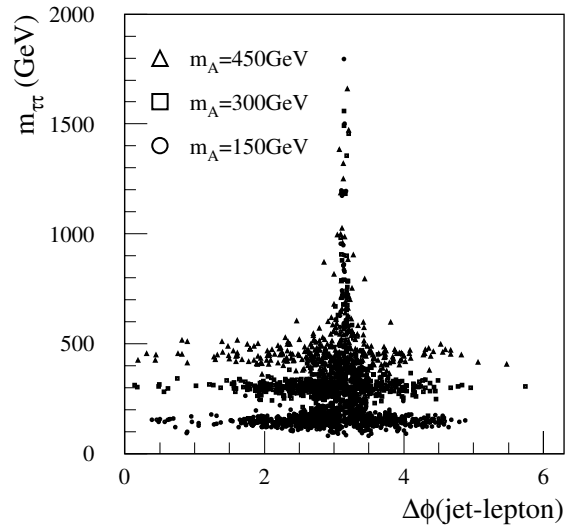
Figure 9-57 Reconstructed $A \to \tau\tau$ mass as a function of $\Delta\phi$ (jet-lepton) for m_A = 150, 300 and 450 GeV.

At low luminosity, a mass resolution in the range 20-40 GeV was obtained for A events with m_A = 150-450 GeV. If only events inside the mass window $m_A \pm 1.5\sigma(m_{\tau\tau})$ are accepted, the signal is reduced by a factor of two while the background by a factor of ten (Chapter 19).

At high luminosity, the pile-up has a large impact on the E_T^{miss} resolution and therefore on the A mass resolution. As mentioned in Section 9.2.1, a cut-off on the minimum transverse energy in each calorimeter tower was applied to improve the E_T^{miss} resolution. This cut affects the energy scale, therefore, prior to the mass reconstruction, the reconstructed τ-jet energy was corrected by a factor obtained by comparing the reconstructed and the generated τ-jet energy. The resulting mass spectrum is shown in Figure 9-58, and can be compared with the low-luminosity result in Figure 9-55. The tower cut-off (~1 GeV) which optimises the E_T^{miss} resolution was applied at high luminosity.

Figure 9-59 shows the ratio of the standard deviations of the reconstructed $\tau\tau$ mass spectrum at high luminosity and low luminosity, as a function of the tower E_T cut-off for m_A=150 GeV. For the optimum cut-off, this ratio is about two, so the selected mass window has to be enlarged at high luminosity to maintain good signal acceptance, at the expenses of a reduced background rejection.

The event acceptances in the mass window $m_A \pm 1.5\,\sigma(m_{\tau\tau})$ at low and high luminosity are compared in Figure 9-60. Although at high luminosity a mass bin twice as large as the mass bin at low luminosity was used, the signal acceptance was 60% of the acceptance at low luminosity. This is due to the fact that in the presence of pile-up, the fraction of events for which the neutrino system has unphysical solutions is larger.

.
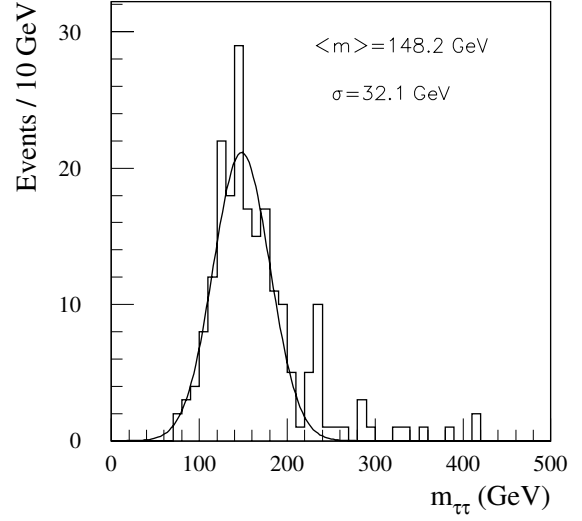
Figure 9-58 Reconstructed $A \to \tau\tau$ mass at high luminosity for $m_A = 150$ GeV and a tower cut-off $E_T > 1$ GeV.
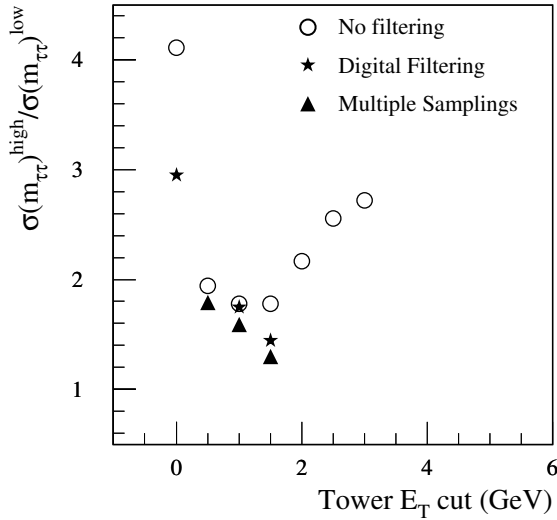
Figure 9-59 Ratio of the $A \to \tau\tau$ mass resolutions at high and low luminosity, for $m_A = 150$ GeV, as a function of the tower cut-off E_T, when no digital filtering is used (open circles), when digital filtering is used (stars), and when multiple sampling techniques are used (triangles).
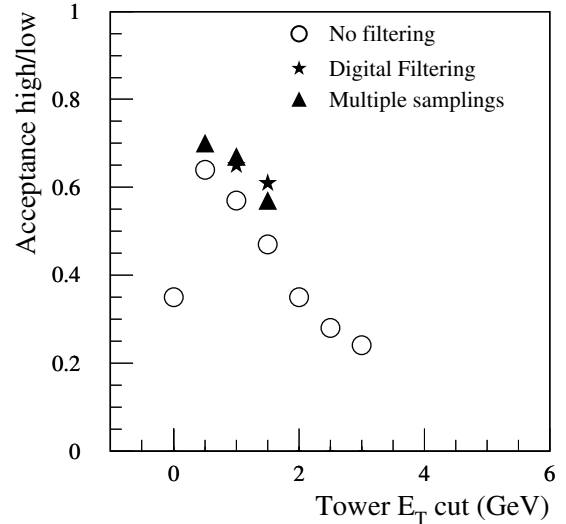
Figure 9-60 Ratio of the event acceptance in a mass window $m_A \pm 1.5\,\sigma(m_{\tau\tau})$ at high and low luminosity, for $m_A = 150$ GeV, as a function of the tower cut-off E_T. The symbols are as in Figure 9-59.

To minimise the effect of the pile-up, multiple-sampling and digital-filtering techniques for the calorimeter signals will be used. Preliminary results obtained by performing digital filtering or simple weighted combinations of multiple samplings look promising and show some improvement in the performance, as can be seen in Figures 9-59 and 9-60.

In conclusion, the impact of pile-up on the physics sensitivity is that the significance of a possible $H/A \to \tau\tau$ signal will most likely be a factor 1.5-2 smaller at high luminosity than it would be naively expected from the increase by a factor of ten in luminosity.

9.3.4 Top-quark final states

Reconstruction of final states containing top quarks is interesting for two reasons. Firstly, inclusive $t\bar{t}$ production will be used at the LHC to measure the top mass with high precision. Second, several channels from new physics (*e.g.* Higgs and SUSY) are expected to contain $t\bar{t}$ pairs produced in association with, or in the decay of, new particles. The reconstruction of events containing top quarks is challenging, because these events are characterised by a high multiplicity of jets, including b-jets, which often translates into a large combinatorial background. Good di-jet and multi-jet mass resolution is needed to reduce this background, and good calorimeter granularity is required to separate nearby jets.

The reconstruction of top final states is discussed here for two cases: the inclusive $t\bar{t}$ sample and the associated production $t\bar{t}H$ with $H \to b\bar{b}$. Both these channels were studied with full simulation and the results are presented in the next two sections. The impact of these results on physics is discussed in the relevant physics chapters (Chapter 18).

9.3.4.1 Inclusive $t\bar{t}$

The gold-plated channel for the measurement of the top mass at the LHC is the inclusive $t\bar{t}$ production, with one top decaying semileptonically ($t \to l\nu b$) and the other one hadronically ($t \to jjb$). In the method presented here, the top mass spectrum is extracted from the invariant mass distribution of the three-jet system arising from the hadronic top decay.

A sample of about 30000 fully-simulated $t\bar{t}$ events from inclusive production and with the above-mentioned decay modes were used for this study. Electronic noise and pile-up were not included. Jets were reconstructed by using the standard fixed-cone jet algorithm with a cone size $\Delta R = 0.4$, and their energies were calibrated by using the method described in Section 9.3.1.1. At least four jets with $p_T > 40$ GeV and $|\eta| < 2.5$ were required, and at least two of the jets were required to be tagged as b-jets (according to the definition given in Section 9.3.2.1). For the accepted events, the decay $W \to jj$ was reconstructed by using those jets which were not tagged as b-jets. The average p_T of the W boson in this event sample was about 130 GeV, which is comparable to the case discussed in Section 9.3.1.2. The jet pair with an invariant mass m_{jj} closest to m_W was selected as the W candidate. The invariant mass distribution of the selected di-jet combinations is shown in Figure 9-61, and has a resolution of about 8 GeV (the resolution obtained with fast simulation was about 7.3 GeV). The event acceptance in a mass window of 20 GeV around m_W was 67%, and the contamination from the combinatorial background of order 10%. Other selection criteria, such as requiring that the highest-p_T jet be part of the combination, did not improve significantly the purity or efficiency, and therefore are not considered in the following. Events with $|m_{jj} - m_W| < 20$ GeV were retained, and the W candidate was then combined with the b-tagged jets to reconstruct $t \to jjb$. If no further restriction is applied, at least two jjb combinations are reconstructed in each event. In this case, the right combination is always selected but the purity of the sample is only 30%. To improve the purity, a variety of criteria were tried, including choosing the jjb combination which gave the highest p_T of the reconstructed top candidate, or using the b-jet which was furthest from the isolated lepton. Similar results were obtained for these various methods. Figure 9-62 presents the reconstructed

m_{jjb} distribution obtained by using the *jjb* combination which gives the highest p_T of the reconstructed top. Fitting the distribution with a Gaussian plus a third-order polynomial yielded a top mass consistent with the generated value of 175 GeV, and a m_{jjb} mass resolution of about 13 GeV. The resolution obtained with fast simulation was 11.4 GeV.

The total acceptance of the selection cuts described above was 5.7%, with a contamination from the combinatorial background from the signal itself of about 20%. These numbers include the event acceptance in the top mass window 175 ± 35 GeV, and are in good agreement with the results found with fast simulation. More details about the top-mass reconstruction, as well as a discussion of the top-mass measurement, can be found in Chapter 18.
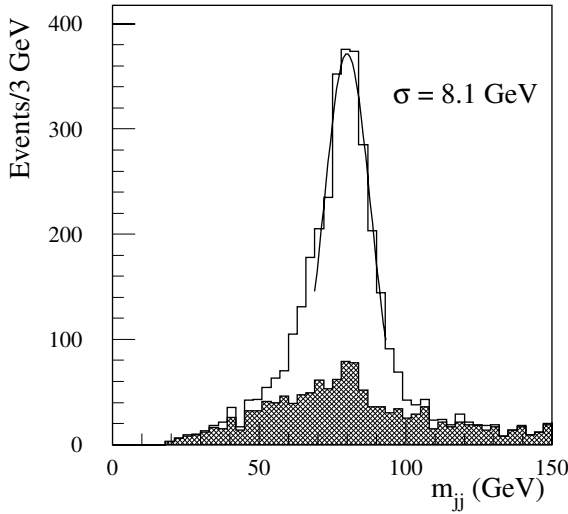
Figure 9-61   Invariant mass distribution of the accepted *jj* pairs from the fully-simulated inclusive $t\bar{t}$ sample (see text). The shaded histogram shows the background from wrong combinations.
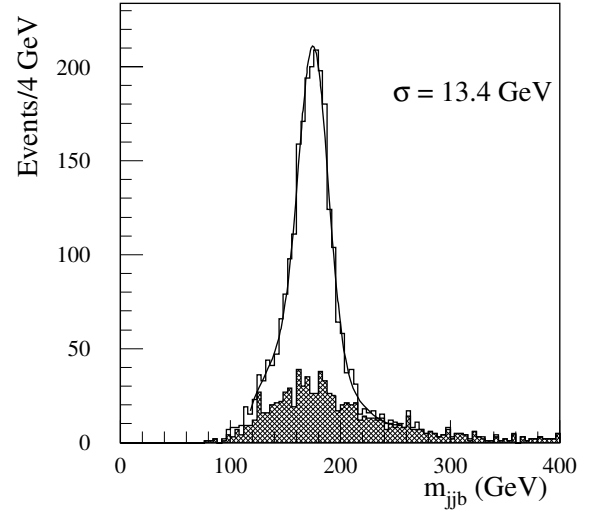
Figure 9-62   Invariant mass distribution of the accepted *jjb* combinations from the fully-simulated inclusive $t\bar{t}$ sample (see text). The shaded histogram shows the background from wrong combinations.

9.3.4.2 $t\bar{t}$ *H* with $H \rightarrow b\bar{b}$

Production of $t\bar{t}H$, followed by $H \rightarrow b\bar{b}$, is a promising channel to search for a Higgs boson decaying hadronically in the mass range around 100 GeV, both in the framework of the Standard Model and of the MSSM (Chapter 19). A high-statistics sample of fully-simulated $t\bar{t}H$ events, with $H \rightarrow b\bar{b}$, was used to assess the capability of reconstructing these final states [9-25]. Electronic noise and pile-up were not included. One top was required to decay semileptonically and the other one hadronically. Since there are four *b*-jets in the final state, combinatorial background from wrong jet pairings is potentially very large in this channel. To overcome this problem, both top quarks were reconstructed. Firstly, only combinations of pairs of light-quark jets which are compatible with coming from $W \rightarrow jj$ decays were selected by requiring $m_{jj} = m_W \pm 25$ GeV. The jet four-momenta were scaled by imposing that the reconstructed *jj* mass be equal to the nominal *W* mass. The lepton momentum and the E_T^{miss} vector where used to reconstruct the decay $W \rightarrow l\nu$ (with a twofold ambiguity on the neutrino longitudinal momentum). Then, the accepted di-jet pairs and the *l*ν pair where combined with *b*-jets and the pairing which minimised $\chi^2 = (m_{jjb} - m_t)^2 + (m_{l\nu b} - m_t)^2$ was chosen. The resulting $t \rightarrow jjb$ mass spectrum is shown in Figure 9-63. The mass resolution is about 12 GeV, and 75% of the events are contained in a $\pm 2\sigma_m$ mass window centred on the peak. After both top quarks were recon-

structed, the invariant mass distribution of the two remaining b-jets showed a peak from $H \rightarrow b\bar{b}$ decays (Figure 9-64). The mass resolution is about 20 GeV and the acceptance in a $\pm 2\sigma_m$ mass window 63%. The fraction of events where both b-jets come from the Higgs decay is about 60% (shaded distribution in Figure 9-64).
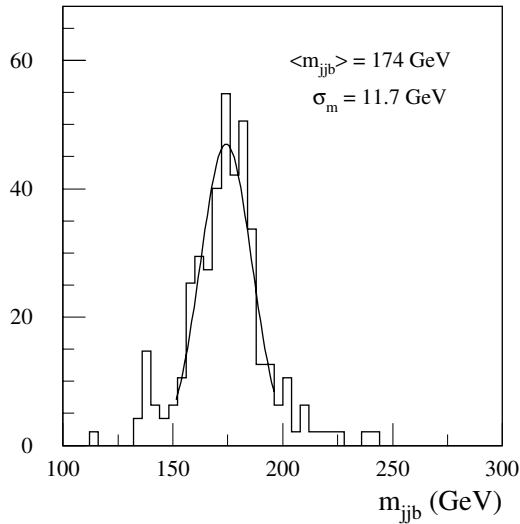
Figure 9-63 Reconstructed top mass from the decay $t \rightarrow jjb$ in $\bar{t}tH$ events.
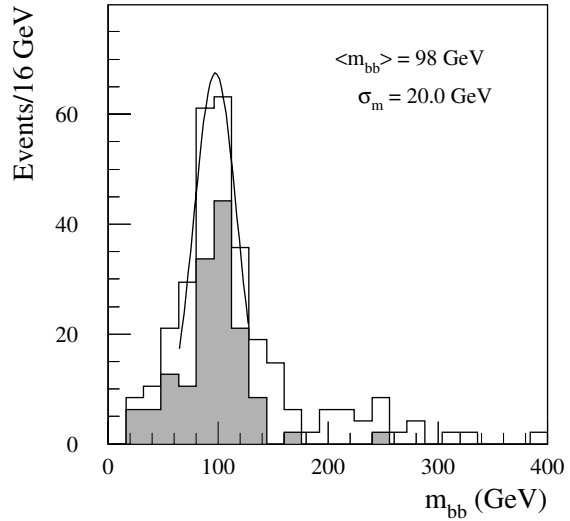
Figure 9-64 Reconstructed $H \rightarrow b\bar{b}$ mass spectrum in $\bar{t}tH$ events, as obtained after reconstructing both top quarks. The shaded distribution is for events where both b-jets come from the Higgs decay.

9.4 Conclusions

The main aspects of the measurement of jets, τ's and missing transverse momentum, as well as the reconstruction of the masses of objects decaying to jets or τ's have been discussed in this chapter. The performance of the ATLAS calorimetry for the reconstruction of jets has been studied. The calorimeters are non-compensating and an algorithm for jet energy reconstruction is applied that corrects for this effect and adds correction terms for the energy loss in the dead material. The intrinsic performance of the detector, in the precision region that extends up to $|\eta| = 3$, is of the order of, or better, than $\sigma/E = 50\%/\sqrt{E} \oplus 3\%$, the target resolution to fulfil the physics goals. The resolution degrades when the jet reconstruction is limited to a cone or when the jet points to a crack region. The coefficients of the energy reconstruction algorithm can be parametrised as smooth functions of the jet energy. Residual non-linearities are of the order of 2 to 3% for jet energies in the range 20 to 1000 GeV. Effects of the order of a few percents that may affect the extrapolation of the calibration to very high-p_T have been briefly discussed. The influence of the jet algorithm and the effect of minimum-bias events on the relation between the reconstructed jet energy and the parton energy has been illustrated in a few physics examples.

Low-p_T jets have been investigated. At low luminosity, the jet veto threshold can be lowered to 15 GeV, while at high luminosity, to maintain a good efficiency for the signal, it has to be raised to 25 GeV. The performance for forward jet tagging in the pseudorapidity range $2 < |\eta| < 5$ has been presented. A tagging efficiency of 90% is obtained up to $|\eta| = 4.0$, then it decreases to about 50% at $|\eta| = 4.8$. At high luminosity, efficiencies of 80% can be obtained with a fake jet rate not higher than 10%.

Hadronic τ decays can be efficiently reconstructed and identified by using the information from the calorimeters and the Inner Detector. For a τ identification efficiency of ~20%, a rejection factor of 170 to 1200 can be achieved against jets from W+jets and $t\bar{t}$ production and of about 1700 against b-jets. This performance, which is similar at low and high luminosity, allows good sensitivity to the $A \rightarrow \tau\tau$ channel in the mass range 100 to 500 GeV (Chapter 19).

The most relevant issues for a good performance in E_T^{miss} measurement have been reviewed: the calorimeter calibration and coverage, and the cuts applied when summing cell energies in presence of electronic noise and pile-up from minimum bias events. At low luminosity, the resolution is well fitted by the form $\sigma(p_{xy}^{\text{miss}}) = 0.46 \times \sqrt{\Sigma E_T}$. At high luminosity, the E_T^{miss} resolution degrades by about a factor two. Tails in the E_T^{miss} distribution have been investigated. No large tails are being produced when a high-p_T jet points to a less uniform region of the calorimeter but some degradation of the resolution is observed.

Various cases of mass reconstruction have been investigated: $W \rightarrow jj$, $H \rightarrow b\bar{b}$, $Z \rightarrow \tau\tau$ and $H/A \rightarrow \tau\tau$, and $t\bar{t}$ final states. The typical mass resolution for W bosons of $p_T = 100$–200 GeV is 8 GeV at low luminosity and 13 GeV at high luminosity. For W bosons of several hundred GeV p_T, systematic effects arise from the overlap between the two jets. The mass resolution for a Higgs boson of mass 100 GeV decaying into $b\bar{b}$ pairs is about 15 GeV both at high and low luminosity, whereas the mass resolution for resonances decaying to τ pairs ($Z/H/A \rightarrow \tau\tau$) is typically 10% at low luminosity. At high luminosity, the degradation of the E_T^{miss} resolution due to the pile-up affects significantly (factor ~2) the width of the reconstructed $\tau\tau$ spectra. Finally, events containing top-quark pairs can be efficiently reconstructed, with a mass resolution for fully hadronic top decays of about 13 GeV. In some cases (*e.g. $t\bar{t}H$* production), the presence of top quarks in the final state can be used to extract a signal from new physics over the background.

9.5 References

9-1   J. Sjölin, 'Jet reconstruction in the ATLAS Barrel Calorimeter', ATLAS Internal Note ATL-COM-TILECAL-99-012 (1999).

9-2   ATLAS Collaboration, Calorimeter Performance Technical Design Report, CERN/LHCC/97-1 (1997).

9-3   A. Kiryunin *et al.*, 'Jet energy measurement in the End-Cap region', ATLAS-HEC-047 (1998).

9-4   M. Cobal *et al.*, 'Analysis results of the first combined test of the LArgon and TILECAL barrel calorimeter prototypes', ATLAS Internal Note ATL-TILECAL-95-067 (1995).

9-5   F. Ariztizabal *et al.*, 'Construction and performance of an iron-scintillator hadron calorimeter with longitudinal tile configuration', Nucl. Instr. Meth. **A349** (1994) 384.

9-6   M.P. Casado and M. Cavalli-Sforza, 'H1-inspired analysis of the 1994 combined test of the Liquid Argon and Tile Calorimeter', ATLAS Internal Note ATL-TILECAL-96-075 (1996).

9-7   M. Cobal *et al.*, 'Analysis results of the April 1996 combined test of the LArgon and TILECAL barrel calorimeter prototypes', ATLAS Internal Note ATL-TILECAL-98-168 (1998).

9-8   R. Lefevre and C. Santoni, 'A study of jet energy reconstruction', ATLAS Internal Note ATL-COM-PHYS-99-041 (1999).

9-9   W. Braunschweig *et al.* (*H1* calorimeter group), Nucl. Instr. Meth. **A265** (1988) 246, DESY 89-022 (1989), and B. Andrieu *et al.* (*H1* calorimeter group), DESY 93-04 (1993).

9-10   M. Bosman *et al.*, 'Jet Finder Library: version 1.0', ATLAS Internal Note ATL-SOFT-98-038 (1998).

9-11   I. Efthymiopoulos, 'Comparison between the ATLAS/Tilecal hadron Barrel Calorimeter prototype test beam data and Hadronic Simulation packages', ATLAS Internal Note ATL-TILECAL-96-092 (1996), Frascati Physics Series Vol. VI (pp.497-507), VI Int. Conf. on Calorimetry in HEP, Frascati, June 8-14 1996.

9-12   M. Bosman *et al.*, 'Conclusions of the workshop on ATLAS requirements on shower models', ATLAS Internal Note ATL-COM-PHYS-99-056 (1999).

9-13   T.A. Gabriel *et al.*, 'Energy dependence of hadronic activity', Nucl. Instr. Meth. **A338** 336 (1994).

9-14   H. Seymour, Z. Phys. **C62** 127 (1993).

9-15   I.C. Park, 'A new Clustering Algorithm: Mulguisin', ATLAS Internal Note ATL-COM-PHYS-99-055 (1999).

9-16   V. Cavasinni *et al.*, 'Search for $H \rightarrow WW \rightarrow l\nu jj$ with the ATLAS Detector (m_H = 300-600 GeV)', ATLAS Internal Note ATL-PHYS-98-127 (1998).

9-17   P. Savard and G. Azuelos, 'The discovery potential of a Heavy Higgs (m_H > 800 GeV) using full GEANT simulation of the ATLAS detector', ATLAS Internal Note ATL-PHYS-98-007 (1998).

9-18   D. Cavalli *et al.*, 'Search for $A/H \rightarrow \tau\tau$ decays', ATLAS Internal Note ATL-PHYS-94-051 (1994).

9-19   D. Cavalli and S. Resconi, 'Tau-jet separation with the ATLAS detector', ATLAS Internal Note ATL-PHYS-98-118 (1998).

9-20   ATLAS Collaboration, Inner Detector Technical Design Report, CERN/LHCC 97-16 (1997).

9-21   E. Richter-Was, D. Froidevaux and L. Poggioli, 'ATLFAST 2.0 a fast simulation package for ATLAS', ATLAS Internal Note ATL-PHYS-98-131 (1998).

9-22   D. Cavalli, 'Missing transverse momentum reconstruction in ATLAS', ATLAS Internal Note ATL-PHYS-96-080 (1996).

9-23   P. Savard, 'The *W* to jet-jet and top mass reconstructions with the ATLAS Detectors', ATLAS Internal Note ATL-CALO-97-092 (1997).

9-24   D. Cavalli and S. Resconi, 'Comparison between full simulation and fast simulation of the ATLAS detector', ATLAS Internal Note ATL-PHYS-97-100 (1997).

9-25   D. Cavalli and M. Sapinski, 'Full and fast simulation and reconstruction of Higgs decay channels with multi-*b*-jets final states', ATLAS Internal Note ATL-PHYS-99-033 (1999).

9-26   Y. Coadou *et al.*, 'Identification of hadronic tau decays in ATLAS', ATLAS Internal Note ATL-PHYS-98-126 (1998).

9-27   S. Wasserbaech, 'Review of tau lifetime measurements', Tau '98, Fifth International Workshop on Tau Lepton Physics, Santander, Spain (1998).

9-28   S. Haywood, 'Offline calibration and alignment of the Inner Detector', ATLAS Internal Note ATL-INDET-99-001 (1999).

10 *b*-tagging performance

10.1 Introduction

Tagging the flavour of *b*-jets is useful for the selection of events containing the top quark, or Standard Model or supersymmetric Higgs bosons, which couple preferentially to heavy objects. This chapter describes the lifetime and leptonic decay methods that can be used for *b*-tagging and the performance that can be achieved, in terms of tagging efficiency and background rejection.

10.1.1 Detector layouts

The simulation of the events needed for the study of the *b*-tagging performance was done with the 97_6 and 98_2 geometries (see Section 2). They are identical as far as the Inner Detector is concerned; differences in the geometry of the cryostat and the calorimeters are taken into account by the reconstruction program and do not affect the performance. The muon identification efficiency was parametrised using an *ad hoc* simulation and then inserted into the global analysis program.

10.1.2 Jets used for *b*-tagging studies

Hadronic decays of Higgs bosons were used extensively as a means of testing pattern recognition within a jet of particles. Further, these decays were used for studies of the *b*-tagging capability of the Inner Detector which can be directly compared with physics requirements. In particular, comparison has been made between the decays $H \rightarrow b\bar{b}$ and backgrounds $H \rightarrow x\bar{x}$ where x is a *u-*, *d-*, *s-*, *c*-quark or gluon. While these background processes actually have negligible rates, the decays are considered representative of actual backgrounds which will be encountered at the LHC, and by generating them from Higgs decays, direct comparisons can be made with background jets having the same kinematics as the *b*-jets. Complete events, $pp \rightarrow WH + X$ and $pp \rightarrow ZH + X$ with $W \rightarrow \mu\nu$ and $Z \rightarrow \mu\mu$ were generated with PYTHIA [10-1].

Previous studies [10-2], [10-3] concentrated on *b*-tagging for a light Higgs (m_H = 80-100 GeV) since this is a plausible method for identifying a Standard Model Higgs in this mass range [10-4]. In these studies, at around 50% *b* efficiency the rejection of gluon jets was found to be limited by gluon splitting to heavy flavours, and no limitations arising from pattern recognition were observed. In the Inner Detector TDR [10-5] and the Pixel Detector TDR [10-6], the emphasis was put on m_H = 400 GeV, which provides a more stringent test of the two-track separation and pattern recognition capability of the Inner Detector. At this mass, the decay to *b*-jets would have a very small branching ratio. Nevertheless, this decay mode was used as a 'factory' for producing high-p_T *b*-jets. Such jets might be seen in the decays of light SUSY Higgs $h \rightarrow b\bar{b}$ which in turn may come from the decays of heavy supersymmetric particles. The current study uses both m_H = 100 and 400 GeV, in order to cover with sufficient statistics the p_T range between ~15 and ~400 GeV and the full pseudorapidity range $|\eta| < 2.5$. The results will be presented as a function of p_T and $|\eta|$. A comparison with the performance calculated using *b*-jets from $t\bar{t}$ events was made and the results found to be the same; this gives confidence in the extrapolation to other sources.

10.1.2.1 Properties of $H \rightarrow b\bar{b}$ events with m_H = 100 and 400 GeV

Figures 10-1 and 10-2 show the transverse momentum and the pseudorapidity distributions of the *b*-jets from Higgs decay, for m_H = 100 and 400 GeV. The distance ΔR of charged particles to the *b*-quark direction in η–ϕ is shown in Figure 10-3. For both m_H = 100 GeV and 400 GeV, 99% of charged particles produced from *b*-quark fragmentation are found in a cone of $\Delta R \leq 0.4$.
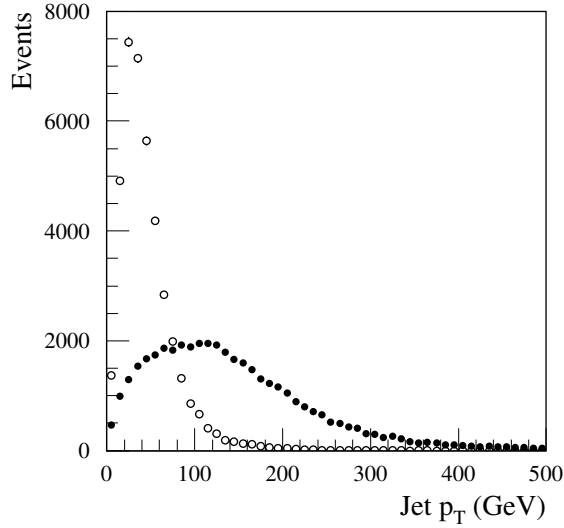
Figure 10-1 Transverse momentum distribution of *b*-jets from $H \rightarrow b\bar{b}$, m_H = 100 GeV (open circles) and 400 GeV (closed circles).
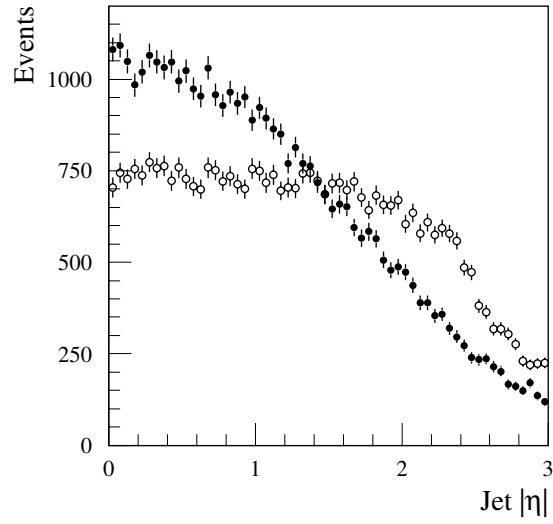
Figure 10-2 Pseudorapidity distribution of *b*-jets from $H \rightarrow b\bar{b}$, m_H = 100 GeV (open circles) and 400 GeV (closed circles).
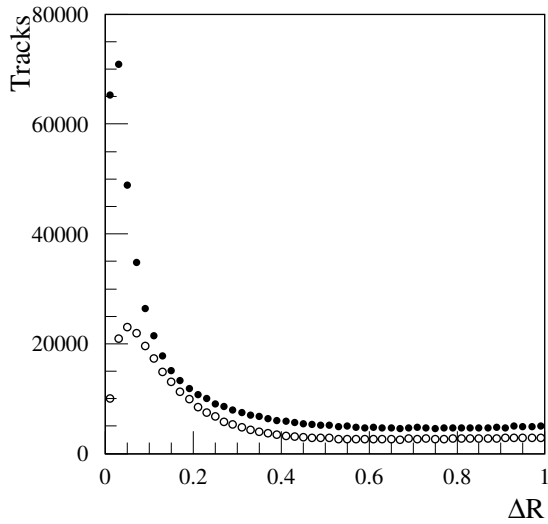
Figure 10-3 Distance ΔR of all charged particles with p_T > 1 GeV to the *b*-quark direction, for m_H = 100 GeV (open circles) and 400 GeV (closed circles).
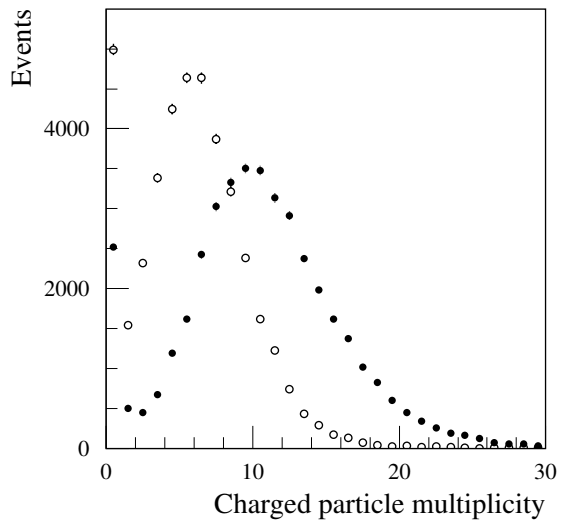
Figure 10-4 Multiplicity of charged particles with p_T > 1 GeV in ΔR < 0.4 around a *b*-jet from $H \rightarrow b\bar{b}$, m_H = 100 GeV (open circles) and 400 GeV (closed circles).
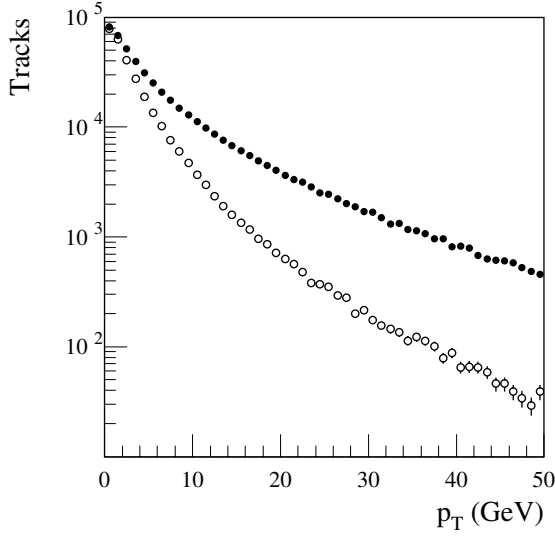
Figure 10-5 Transverse momentum of charged particles in a *b*-jet, $m_H = 100$ GeV (open circles) and 400 GeV (closed circles).
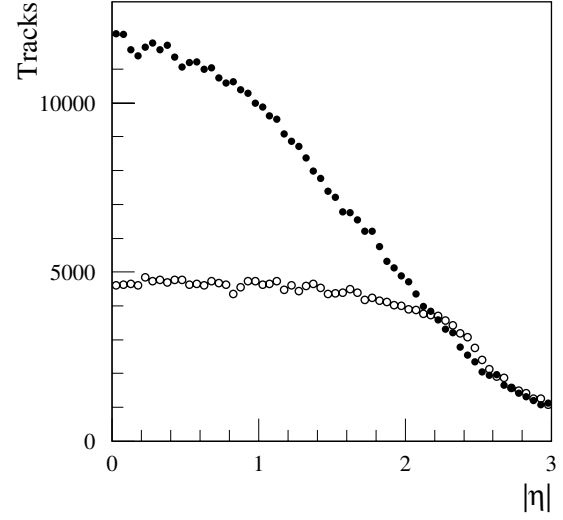
Figure 10-6 Pseudorapidity of charged particles in a *b*-jet, $m_H = 100$ GeV (open circles) and 400 GeV (closed circles).

The charged multiplicity of particles with $p_T > 1$ GeV, in a cone $\Delta R \leq 0.4$ is shown in Figure 10-4. The charged multiplicity in the cone has a mean of 5.5 (10.0) for $m_H = 100$ GeV (400 GeV), 60% (40%) of which come from daughters of the *B*-hadron decay. In 12.5% (6.3%) of the jets, there are no charged particles with $p_T > 1$ GeV in the cone. In a cone $\Delta R \leq 0.4$, the mean number of photons is 10 (18), of which 5 (9.5) have $p_T > 1$ GeV.

The transverse momentum and the pseudorapidity distribution of these particles are shown in Figures 10-5 and 10-6. The average p_T of particles with $p_T > 1$ GeV is 4.9 (8.7) GeV – 70% of particles have p_T less than this. The conclusion is that it is necessary to reconstruct accurately at least four tracks arising from *B*-hadron decays with $p_T < 10$ GeV in a region where multiple scattering dominates the impact parameter resolution.

The *b*-jet direction is not uniquely defined. *b*-quarks in the final state of an interaction or a decay can radiate gluons (Final State Radiation, FSR) and therefore change the direction. As, in practice, the reconstruction of the jet direction and energy is done using the energy deposited in the calorimeters, it is important to check the difference between the jet direction as measured by the calorimeters and the *b*-quark direction. Figure 10-7 shows the distribution of the angular distance ΔR between the *b*-jet axis as reconstructed by the calorimeter and the *b*-quark direction before and after FSR, and
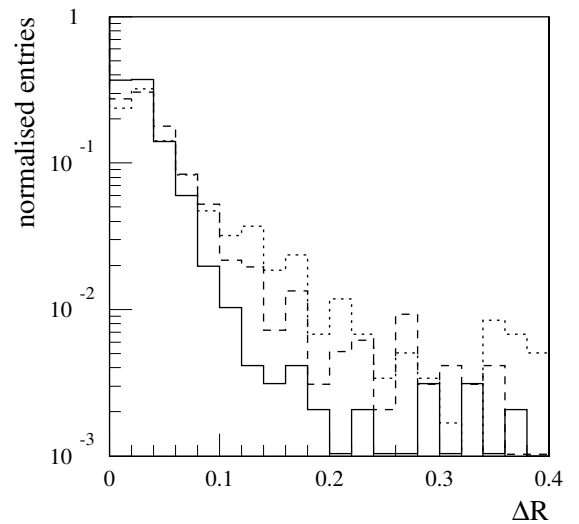
Figure 10-7 Angular distance ΔR between the *b*-jet axis as reconstructed by the calorimeter and the *b*-quark direction before Final State Radiation (dotted), the *b*-quark direction after FSR (dashed) and the *b*-jet axis as reconstructed from charged tracks (solid).

the *b*-jet axis as reconstructed from the centre of gravity of charged tracks. As the resolution of the *b*-jet direction is much better than the standard cone size $\Delta R \leq 0.4$, the use of a finite cone size does not cause significant loss of tracks.

10.1.2.2 Data sets and event reconstruction

The expected rejection factors for non-*b* jets are of the order of 100, at least for most of the allowed ranges of jet transverse momentum and pseudorapidity. In order to have a statistically significant number of events at the end of the selection and analysis procedure, 20 000 events were fully simulated for each of the channels $H \rightarrow b\bar{b}$, $H \rightarrow u\bar{u}$, $H \rightarrow c\bar{c}$, $H \rightarrow gg$ with $m_H = 100$ GeV, and at least 10 000 events for each of the same channels with $m_H = 400$ GeV. Events were selected at the generation level, so that both decay products of the Higgs have $p_T > 15$ GeV and at least one of them is within the pseudorapidity range $|\eta| < 2.5$, before final state radiation.

The reconstruction procedure has to be as realistic as possible, therefore no use was made of the generated event information. First, jets were identified as clusters in the combined electromagnetic and hadronic calorimeters, using a noise threshold of 2σ on each cell and a p_T threshold of 10 GeV for the reconstructed jets. Then the Inner Detector pattern recognition programs xKalman and iPatRec were run, using as seeds the reconstructed jet directions and a road half-width of 0.5; the p_T threshold for reconstructed tracks was set to 0.7 GeV. Finally the xConver algorithm was run in order to identify, and reject, electrons coming from photon conversions.

A jet in the $H \rightarrow b\bar{b}$ events was labelled as a *b*-jet if a *b*-quark from the original hard process pointed, after final state radiation, along the jet within an angular distance of $\Delta R < 0.2$. Similarly, jets were labelled as for *u*-, *c*- and gluon jets for the other data samples.

10.1.3 Minimum bias events

Minimum bias events account for the vast majority of interactions which will result from beam collisions in ATLAS; by implication they do not contain hard-scattering processes. These events are of little interest *per se*, but at the high luminosities at LHC, multiple collisions within one beam-crossing will be inevitable, causing signal events to have several minimum bias events superimposed. The pile-up of these events on top of single particles is essential for realistic studies of pattern recognition.

Minimum bias events were generated individually using PYTHIA 5.7. The processes of interest for tracking studies are the inelastic, non-diffractive *pp* interactions, labelled in PYTHIA as 'QCD high-p_T processes' (the switches set in PYTHIA are: MSEL=1, MSTP(2)=2, MSTP(33)=3, MSTP(81)=1, MSTP(82)=4). The pseudorapidity distribution of charged particles in single minimum bias events is shown in
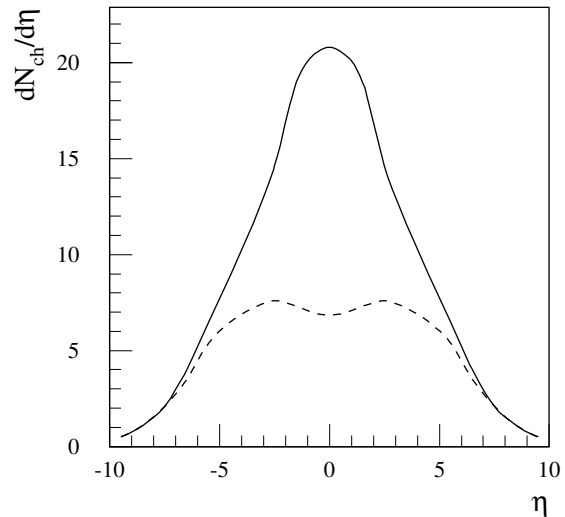
Figure 10-8 Pseudorapidity distribution of charged particles (no p_T cut). The solid line corresponds to all particles in events containing the decay of a 400 GeV Higgs to *b*-jets, the dashed line to all particles in minimum bias events.

Figure 10-8. Comparison is made with the distribution from events containing a hard scatter, namely $H \rightarrow b\bar{b}$ ($m_H = 400$ GeV). The latter is averaged over many events, but is quite different in character due to the high density of particles to be found in the jets and the additional initial state radiation.

The p_T distributions are shown in Figure 10-9, while the integrals of the p_T distributions are shown in Figure 10-10. It can be seen that the average charged particle multiplicity per unit of pseudorapidity, $dN/d\eta$, for a single minimum bias event is 7.5 (no p_T cut), falling to 0.64 for $p_T \geq 1$ GeV and 0.006 for $p_T \geq 5$ GeV. The mean $dN/d\eta$ for neutrals is 9.1, 90% of which are photons, and the mean E_T is 235 MeV [10-7]. Consequently, the number of charged particles with $p_T \geq 1$ GeV from the pile-up of minimum bias events is 1.2 within a cone $\Delta R \leq 0.4$ around a b-quark at a luminosity of 10^{34} cm^{-2}s^{-1}.
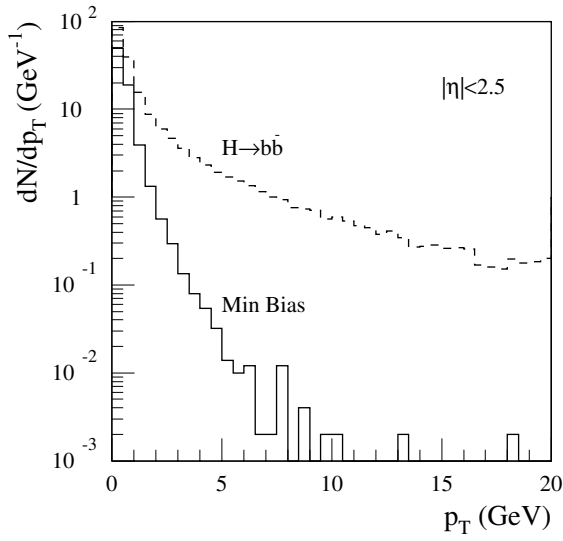
Figure 10-9 p_T distribution of charged particles in minimum bias and $H \rightarrow b\bar{b}$ events.
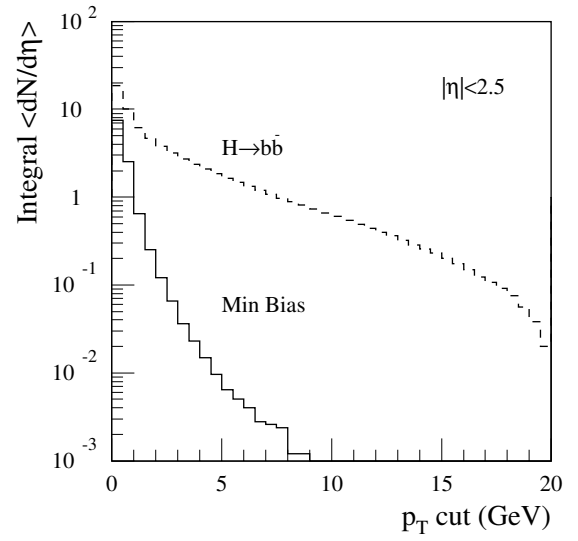
Figure 10-10 Average multiplicity per unit of pseudorapidity ($|\eta| \leq 2.5$) as a function of p_T cut (corresponding to left-hand edge of bin).

10.2 Vertexing algorithm

In this section, the tagging of b-quarks from the decay $H \rightarrow b\bar{b}$ ($m_H = 100$ and 400 GeV) is discussed and compared with the rejection of lighter-quark and gluon decays of the Higgs. The relatively long lifetimes of b-hadrons ($c\tau \approx 470$ μm) give rise to displaced vertices which may be tagged by either explicitly reconstructing the vertex or by examining the impact parameters of the daughters. In the work described in this section, the latter method was used since high b-tagging efficiency (rather than high purity) is required. The rejection of non b-jets is dependent on the fact that for light quarks, most of the stable particles which can be reconstructed in the Inner Detector come from the decays of short-lived objects and hence appear to come from the primary vertex. The extent to which this is true is determined by the impact parameter[1] resolution $\sigma(d_0)$ of the detector, by the rate of conversions and nuclear interactions in the detector ma-

---

1. Unless stated otherwise, impact parameter will refer to the transverse impact parameter d_0, since this is the most relevant one for b-tagging.

terial, and by the frequency of pattern recognition errors. Figure 10-11 shows the impact parameter resolution for primary pions in jets. The rise with $|\eta|$ is mainly due to the increase in material in the forward direction.

What is of interest for *b*-tagging is the signed impact parameter ($sign \times |d_0|$), where the *sign* is positive if the track appears to originate from in front of the primary vertex (*i.e.* the track crosses the jet axis in front of the primary vertex) and negative if it appears to originate from behind. The jet axis is determined accurately from the calorimeter; as explained above, it can also be determined by the charged tracks measured in the ID.

In principle, the primary vertex can be reconstructed from prompt tracks in the event, as described in Section 3.6.1. In practice, since the gain is small, this may not be done in x and y (there is a danger of introducing systematics), and here the impact parameter has been determined with respect to the nominal beam position ($x = 0$, $y = 0$ in this simulation), which is anticipated to be measured with high accuracy as a function of time. Therefore the uncertainty on the impact parameter is the combination of the measurement error $\sigma(d_0)$ and the spread of the beam-spot, 15 μm, taken in quadrature. The effect of this is to increase $\sigma(d_0)$ by about 4 μm.
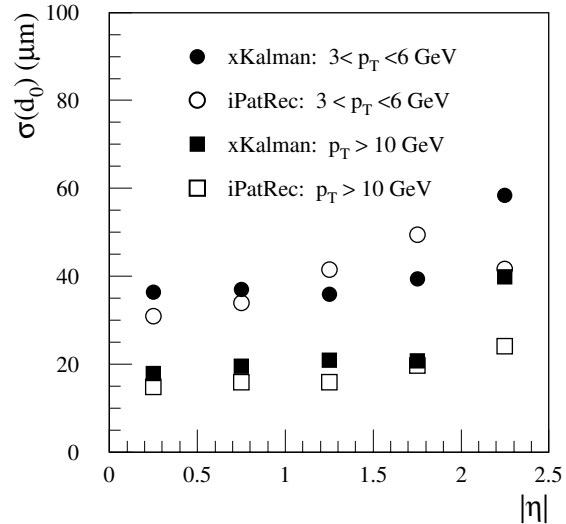
Figure 10-11 Impact parameter *rms.* resolution for tracks found in *b*-jets from $H \rightarrow b\bar{b}$ with $m_H = 100$ GeV.

The z coordinate of the primary interaction point can be reconstructed simply by taking the truncated weighted average of the z_0 coordinates of all well-reconstructed tracks in the event which have a transverse impact parameter $d_0 < 2\sigma(d_0)$. This simple and fast method achieves a resolution ~35 μm for events with at least four reconstructed tracks, which is always the case for Higgs events (see Figure 10-12).

The significance of the impact parameter is defined as the ratio of the signed impact parameter to its total error. This is shown in Figure 10-13 for tracks from *b* and *u*-jets. Both distributions have significant 'cores' which represent correctly reconstructed tracks coming from the primary vertex. These cores can be described by Gaussians of width close to one. The *b*-jets contain tracks with large positive significance, corresponding to genuine lifetime content. By contrast, light quarks and gluon jets have only a small excess of tracks which appear to contain lifetime arising from:

- interactions with material, *e.g.* photons converting to e^+e^- pairs or pions having nuclear interactions;

- daughters of V^0's;

- daughters of heavy quarks formed in the fragmentation (relevant only for gluon jets).

There are tails in the impact parameter distributions which are apparent on the negative side of the significance distribution. For the *b*-jets, these come mainly from an incorrect determination of the sign (corresponding to the uncertainty in determining the *b*-hadron direction) and from decays of charmed states. For the *u*-jets, the tail is dominated by secondaries from interactions.
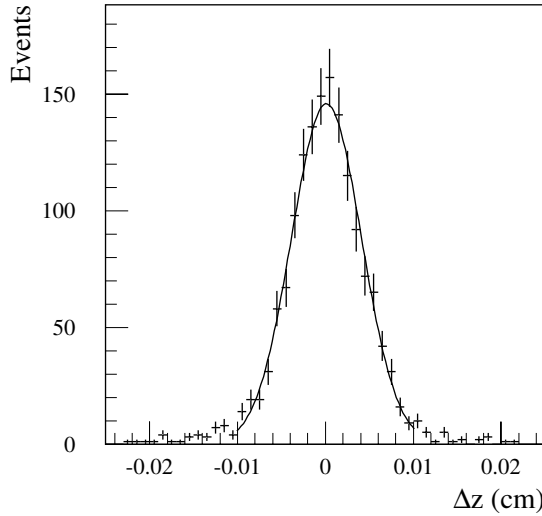
Figure 10-12 *z*-vertex resolution for $H \rightarrow b\bar{b}$ events.
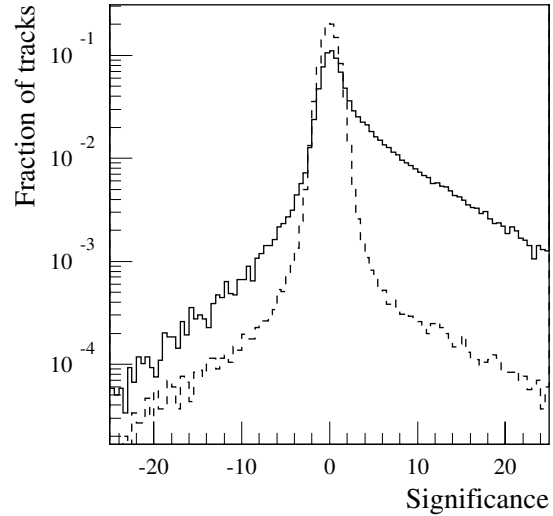
Figure 10-13 Significance distribution: signed impact parameter divided by its error. Curves for *b*-jets (solid) and *u*-jets (dashed) are normalised to the same area.

10.2.1 *b*-tagging methodology

Various *b*-tagging methods have been investigated in the past. The likelihood ratio method appears to offer the best performance, therefore it is the method used for the studies presented here. The emphasis of these studies is on individual jets, rather than complete events. Throughout, the rejection R_j for different background jets is compared with the efficiency ε_b for keeping *b*-jets. The rejection is simply the reciprocal of the efficiency. If there is no discrimination at all, R will behave like $1/\varepsilon_b$.

The method was as follows:

1. For each selected track *i* in a jet, the significance S_i was calculated.

2. The ratio of the values of the significance probability distribution functions for *b*-jets and *u*-jets was computed: $r_i = f_b(S_i)/f_u(S_i)$.

3. A jet weight was constructed from the sum of the logarithms of the ratios: $W = \Sigma \log r_i$.

4. By keeping jets above some value of *W* (a value which can be varied), the efficiency for different jet samples can be obtained.

By using the significance distribution $f_u(S)$ for *u*-jets, the method was optimised for the rejection of *u*-jets. In the case of real data, since the jet type will not be *a priori* known, the rejection will have to be optimised for each specific background under study.

10.2.2 Track selection

Track finding was performed in restricted cones using both xKalman and iPatRec. Only tracks with $p_T > 1$ GeV and in a cone of $\Delta R < 0.4$ around the jet direction were considered. The efficiency for finding any primary charged track in a *b*-jet was 93.9% for xKalman and 92.8% for iPatRec. The following ('standard') cuts were then made:

- number of precision hits ≥ 9 (no explicit TRT requirement was made, although the valid drift-time hits were used for the global track fit);

- number of pixel hits ≥ 2;

- there must be a *B*-layer hit;

- $|d_0| < 1$ mm.
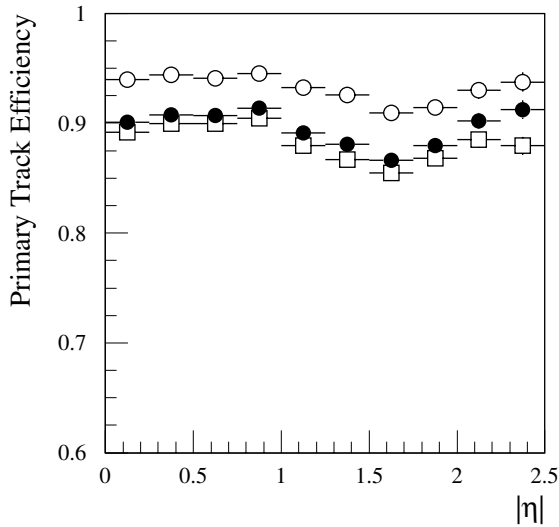
Figure 10-14 Primary track efficiency for xKalman as a function of pseudorapidity without cuts (open circles), after applying standard cuts (closed circles) and after applying quality cuts (open squares).
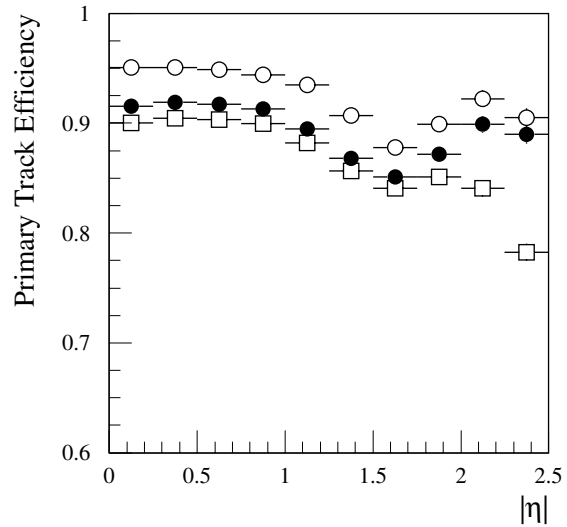
Figure 10-15 Primary track efficiency for iPatRec as a function of pseudorapidity without cuts (open circles), after applying standard cuts (closed circles) and after applying quality cuts (open squares).

After all these cuts, xKalman and iPatRec yielded similar track finding efficiencies of 88.8% and 88.2% respectively for tracks from the primary vertex. The main limitation to the *b*-tagging performance arises from secondary tracks, *i.e.* tracks originating from interactions of primary tracks with detector material. Secondary tracks can only be rejected by applying appropriate cuts on track quality. The additional ('quality') cuts were:

- impact parameter in the *R-z* plane relative to the reconstructed primary interaction point < 1.5 / sin(θ) mm;

- track fit $\chi^2/\text{dof} < 3$;

- at most one hit in the Pixels shared with another reconstructed track;

- at most two hits in the precision detectors (pixel and SCT) shared with another reconstructed track.

Secondaries were now the most important component of the background; 37% of these secondaries were electrons from conversions and these could be removed by direct tagging. The program xConver was used to identify electrons from conversions and remove them from the track sample, as described in Section 7.5.1. Tracks were rejected if they had at least 5% high-threshold hits in the TRT (or no TRT hits at all, which happens in case of hard bremsstrahlung) and formed a good conversion candidate ($\chi^2 < 50$ for the conversion fit and conversion radius > 2 cm) with another track in the same jet. This cut removed 15% of the secondary tracks without affecting the track-finding efficiency for primary tracks.
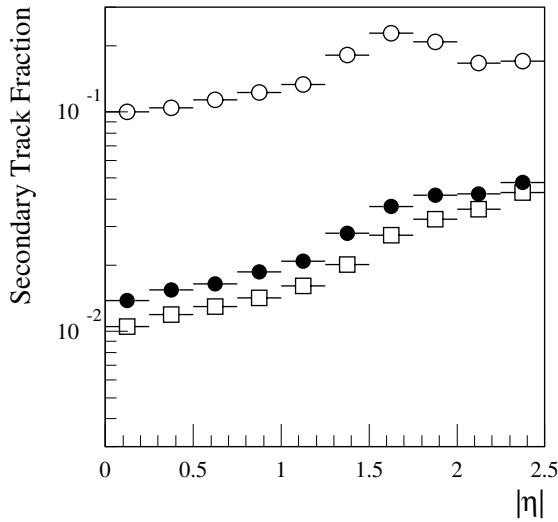
Figure 10-16 Fraction of secondary tracks for xKalman as a function of pseudorapidity without cuts (open circles), after applying standard cuts (closed circles) and after applying quality cuts (open squares).
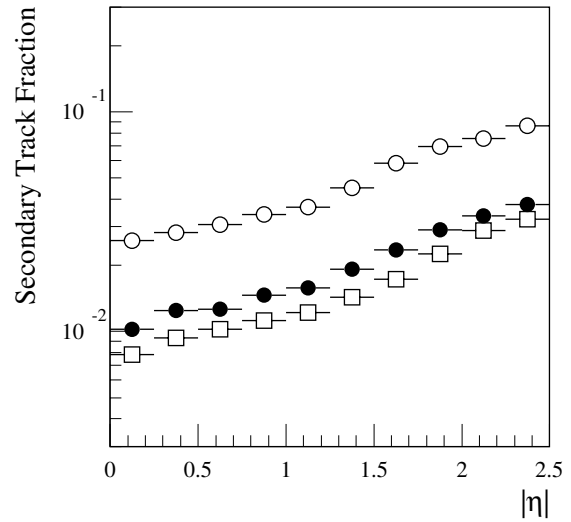
Figure 10-17 Fraction of secondary for iPatRec tracks as a function of pseudorapidity without cuts (open circles), after applying standard cuts (closed circles) and after applying quality cuts (open squares).
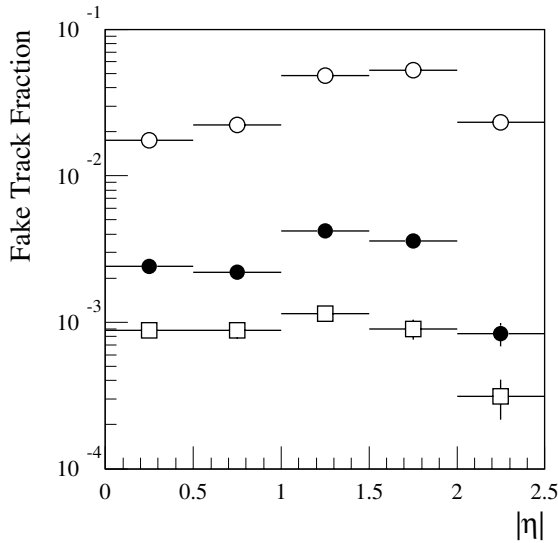
Figure 10-18 Fraction of fake tracks for xKalman as a function of pseudorapidity without cuts (open circles), after applying standard cuts (closed circles) and after applying quality cuts (open squares).
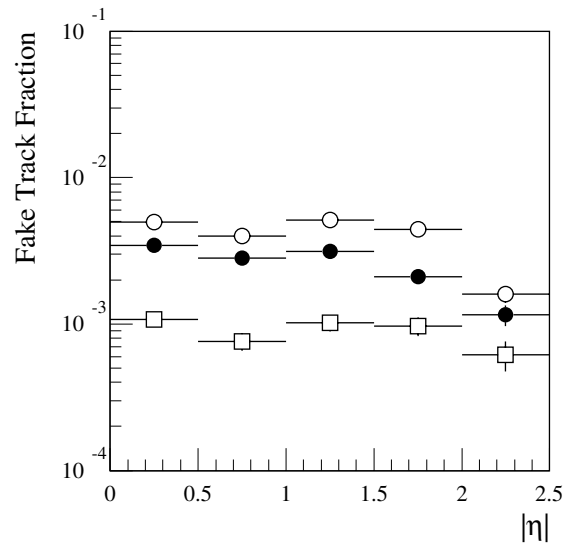
Figure 10-19 Fraction of fake tracks for iPatRec as a function of pseudorapidity without cuts (open circles), after applying standard cuts (closed circles) and after applying quality cuts (open squares).

As an example of the reconstruction performance using these cuts, Figures 10-14 to 10-19 show the primary track finding efficiency and the fraction of secondary and fake tracks in the final track sample.

The quality cuts effectively select a smaller but better-measured sample of tracks. Their net effect is quite different on jets reconstructed with xKalman or iPatRec:

- Even after the standard cuts, xKalman produces a larger fraction of secondary, duplicated and fake tracks, which are efficiently removed by the quality cuts. This is largely due to the sometimes conflicting requirements imposed on xKalman, which is the most widely

used pattern recognition program. These requirements have led to the removal of all or almost all internal quality cuts, *e.g.* to optimise the efficiency to find secondary tracks from long-lived particles. As a consequence, the quality of the reconstructed tracks is entirely determined by the selection cuts described above.

- In contrast, similar cuts to those described above are in some cases already implemented internally in iPatRec, leading to a better track quality after reconstruction.

In the case of iPatRec, the quality cuts described above tend to reduce the track sample, especially for $|\eta| > 2$ (see Figure 10-15), without degrading substantially the *b*-tagging performance, which, as described in Section 10.2.3, is limited much more by the amount of secondaries than that of fakes. Therefore, the results are quoted from now on, for xKalman with quality cuts and for iPatRec with standard cuts. The removal of conversions found by xConver is applied in all cases.

The pattern recognition performance presented in this section is somewhat better than at the time of the ID TDR: after the standard cuts the fraction of secondaries is lower by up to 40% depending on $|\eta|$ and the fraction of fakes is lower by almost a factor of two, for both pattern recognition programs. This can be explained by the continuous improvements and tuning of the pattern recognition and track-following algorithms in both programs.

10.2.3 Basic performance

The jet weights calculated with the likelihood ratio method are shown for *u* and *b*-jets in Figure 10-20. As all the relevant distributions are compatible in the p_T range where the two data sets overlap, in the following analysis the jets from the decay of 100 and 400 GeV Higgs are used together.

The following background compositions can be deduced for xKalman (iPatRec) respectively:

- 31% (21%) of tracks arise from interaction in the material of the detector (53% (32%) of these tracks are electrons from photon conversions, the other particles are products of nuclear interactions).

- 23% (21%) of tracks are produced in the decays of hadrons with significant lifetime (mainly K_s^0); hadrons containing heavy quarks are produced in 1.7% of *u*-jets.

Figure 10-20 Jet weights from likelihood ratio: *u*-jets with standard cuts (dotted line) and with quality cuts and conversion removal (solid line), *b*-jets with standard cuts (dash-dotted line) and with quality cuts and conversion removal (dotted line) (xKalman).

- 46% (58%) of tracks are produced at the primary vertex, with large deflections from multiple scattering or possibly pattern recognition problems.

By varying the cut on the jet weights, it is possible to derive the curves of jet rejections as functions of b-jet efficiency; Figures 10-21 and 10-22 show the rejections obtained for different jet types. The rejections for ε_b = 50% and 60% are shown in Table 10-1. The rejection factors presented here are substantially better than those published in the ID TDR [10-5]. The improvement can be explained by:

- the improvement of the quality of tracks reconstructed by the pattern recognition programs (after the standard cuts only 1.2% (1.7%) of the tracks in jets from 100 (400) GeV Higgs are in the tails of the impact parameter distribution);

- the choice of jet axis: jets produced by very low-p_T quarks (after final state radiation), which are now not reconstructed by the calorimeter, would contain low-momentum particles, whose impact parameter resolution is dominated by multiple scattering.

The rejection of c-jets, R_c, is limited by the lifetime of charmed hadrons: for $D^\pm$, $c\tau$ = 317 μm; for D^0, $c\tau$ = 124 μm. The rejection of gluon jets, R_g, is limited by gluon splitting: $BR(g \to c\bar{c})$ = 6% and $BR(g \to b\bar{b})$ = 4% for m_H = 400 GeV.
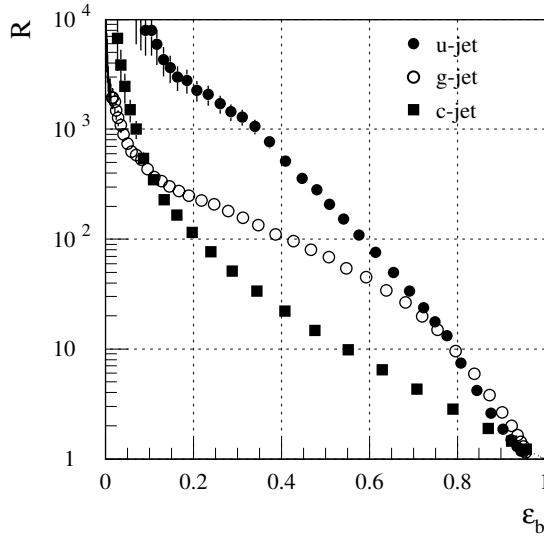
Figure 10-21 Background rejections as a function of b-jet efficiency obtained with xKalman, applying quality cuts and conversion removal.
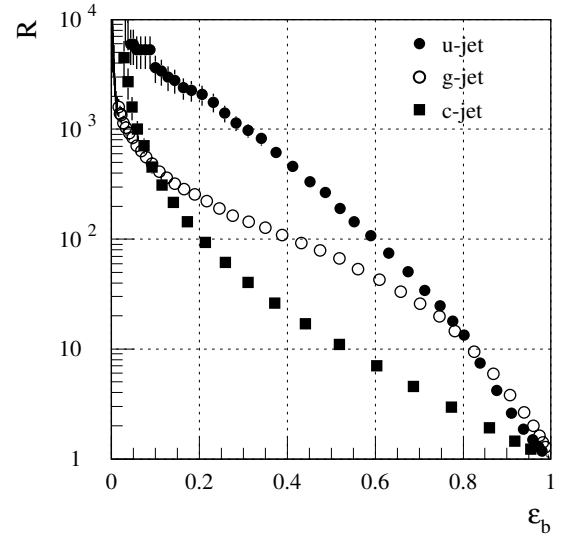
Figure 10-22 Background rejections as a function of b-jet efficiency obtained with iPatRec, applying standard cuts and conversion removal.

Table 10-1 Rejections of various types of background jets.

| | ε_b = 50% | | | | ε_b = 60% | | | |
| | m_H = 100 GeV | | m_H = 400 GeV | | m_H = 100 GeV | | m_H = 400 GeV | |
	xKalman	iPatRec	xKalman	iPatRec	xKalman	iPatRec	xKalman	iPatRec
R_u	326 ± 37	391 ± 49	126 ± 9	183 ± 17	124 ± 9	148 ± 11	65 ± 3	80 ± 5
R_g	135 ± 12	148 ± 14	59 ± 3	58 ± 3	72 ± 4	74 ± 5	38 ± 1	37 ± 1
R_c	13.6 ± 0.4	11.7 ± 0.3	13.3 ± 0.4	13.4 ± 0.4	7.7 ± 0.2	6.9 ± 0.1	8.0 ± 0.2	7.3 ± 0.2

10.2.4 Jet p_T and pseudorapidity dependence

The rejections as a function of $|\eta|$ are shown in Figure 10-23. The drop in rejection observed for $|\eta| > 1.5$ (compared to $\eta \sim 0$) is related to the increase of material in this region.

The dependence on the jet p_T is shown in Figure 10-24. Both xKalman and iPatRec show the same trends: a sharp fall in the rejection at low p_T as p_T tends to 0, and a slow degradation at high p_T as p_T increases.

The sharp fall at low p_T is due to:

- The decrease of charged particle multiplicity in jets. For jet $p_T < 30$ GeV, the charged particle multiplicity after acceptance ($p_T > 1$ GeV) and selection cuts is 2.3 (to be compared with an average of 4.3 for $p_T < 100$ GeV) and 30% of the b-jets have less than two selected tracks (compared with 10% for $p_T < 100$ GeV).

- The worse impact parameter resolution arising from increased multiple scattering of tracks coming from a softer p_T spectrum.
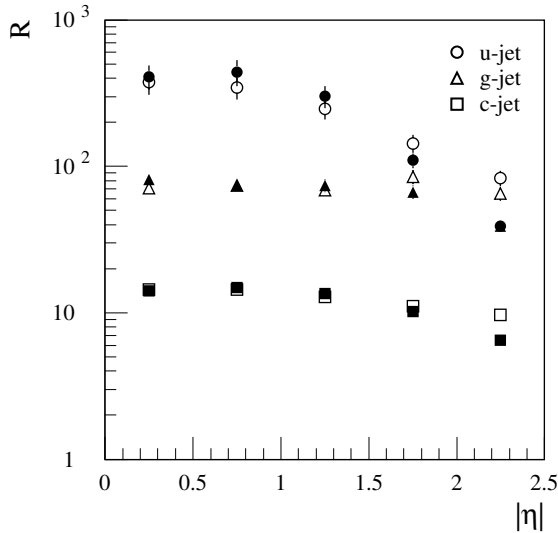
Figure 10-23 Background rejections as a function of jet $|\eta|$ for $\varepsilon_b = 50\%$. xKalman: full symbols; iPatRec: open symbols.
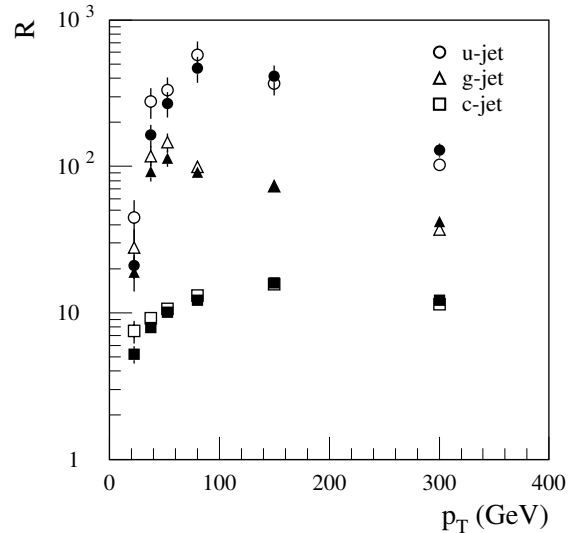
Figure 10-24 Background rejections as a function of jet p_T for $\varepsilon_b = 50\%$. xKalman: full symbols; iPatRec: open symbols.

The slow degradation at high p_T is the consequence of several factors:

- The increase in multiplicity of charged particles from the primary interaction vertex due to the increase of the hadronisation component of the jet. Consequently, the discrimination between b- and u-jets is reduced. For jets with $p_T < 100$ GeV, the number of tracks (after selection cuts) is 4.3 on the average, whereas it is 10.4 for $p_T > 270$ GeV.

- The increase in the fraction of reconstructed secondaries contained in the jet, due to the higher momentum of the interacting particles: 1.3% for jet $p_T < 100$ GeV and 2.2% for $p_T > 270$ GeV.

- The difficulties of pattern recognition in more dense environment at larger jet p_T values result in more tails in the impact parameter distributions. The number of prompt tracks with $|d_0| > 3\sigma(d_0)$ is 1.1% for $p_T < 100$ GeV, and 2.3% for $p_T > 270$ GeV.

In order to study the correlation between the p_T and the pseudorapidity dependence of the non-b jet rejection factor, one can consider the normalised rejection factor R_j^n, *i.e.* the ratio between $R_j(p_T,\eta)$ and the mean value $R_j(p_T)$. R_j^n does not depend much on the actual value of the b-jet tagging efficiency ε_b taken as reference. Figures 10-25 and 10-26 show respectively the normalised u- and c-jet rejection factors as functions of the jet p_T and pseudorapidity. As can be seen, there is little correlation between the p_T and pseudorapidity dependence of R_u, whereas R_c, which is limited by the physics of charm decays, is almost constant. Table 10-2 shows the rejection factor R_u in several bins of $|\eta|$ and p_T.
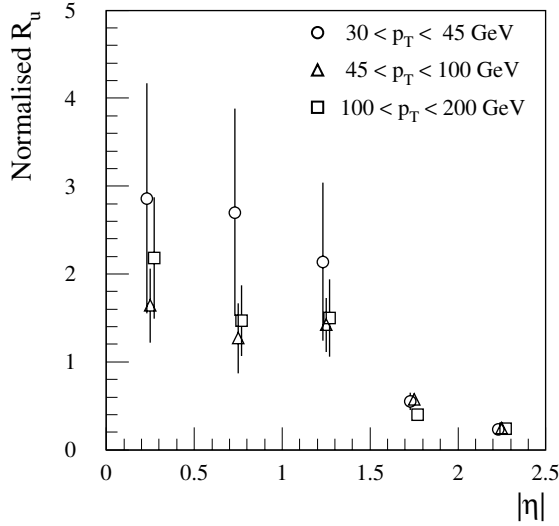
Figure 10-25 *u*-jet rejection factors, normalised to their mean values, as function of pseudorapidity for jets in different p_T ranges.
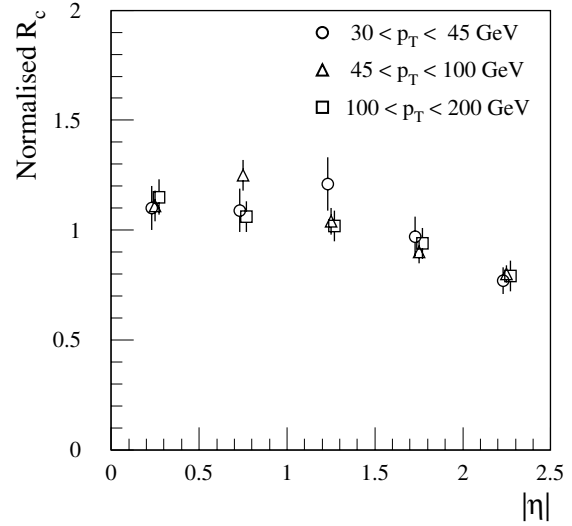
Figure 10-26 *c*-jet rejection factors, normalised to their mean values, as function of pseudorapidity for jets in different p_T ranges.

Table 10-2 *u*-jet rejection for 50% *b*-jet tagging efficiency, for different p_T and $|\eta|$ intervals. In each cell, the first number refers to xKalman and the second to iPatRec. Errors are statistical only.

	all η	**$0 < |\eta| < 0.5$**	**$0.5 < |\eta| < 1$**	**$1 < |\eta| < 1.5$**	**$1.5 < |\eta| < 2$**	**$2 < |\eta| < 2.5$**
all p_T	231 ± 16 237 ± 17	411 ± 76 375 ± 66	442 ± 88 346 ± 60	301 ± 52 246 ± 38	110 ± 13 144 ± 20	39 ± 3 83 ± 10
$15 < p_T < 30$	21 ± 4 45 ± 14	- -	- -	- -	- -	- -
$30 < p_T < 45$	164 ± 29 277 ± 66	267 ± 137 392 ± 200	192 ± 81 301 ± 156	298 ± 134 433 ± 210	153 ± 60 140 ± 47	14 ± 2 54 ± 13
$45 < p_T < 60$	269 ± 54 331 ± 75	369 ± 184 671 ± 384	821 ± 385 519 ± 290	334 ± 150 372 ± 186	153 ± 51 143 ± 50	20 ± 3 110 ± 36
$60 < p_T < 100$	467 ± 95 581 ± 132	646 ± 311 610 ± 295	554 ± 257 432 ± 176	568 ± 277 720 ± 358	311 ± 124 468 ± 230	60 ± 11 398 ± 185
$100 < p_T < 200$	413 ± 74 368 ± 62	889 ± 444 699 ± 310	714 ± 318 633 ± 284	482 ± 200 546 ± 243	184 ± 54 168 ± 47	101 ± 26 111 ± 31
$p_T > 200$	129 ± 14 103 ± 10	188 ± 44 160 ± 34	196 ± 51 127 ± 27	116 ± 26 76 ± 14	61 ± 14 73 ± 18	94 ± 36 80 ± 29

The jet rejections $R_j(p_T,\eta)$ are functions of p_T and $|\eta|$. The same rejections in the relevant bins of p_T and $|\eta|$ were obtained using fully simulated $t\bar{t}$ events. The extrapolation to other processes is therefore justified.

10.3 Soft electrons

The most powerful way to tag b-jets is to look for tracks with significant impact parameter – this is discussed in the previous section. However, the tagging of soft leptons (electrons and muons) will provide a valuable complement to this. In this section, the potential to tag b-jets using electrons from semileptonic decays of b-quarks while rejecting gluon and light-quark jet background is evaluated. Only jets from decays of Higgs bosons with $m_H = 100$ GeV were considered for this study. Only xKalman was used for the pattern recognition in the Inner Detector.

10.3.1 Event characteristics

The branching ratio for the $b \rightarrow e$ decay, $BR(b \rightarrow e)$, is calculated taking into account the direct semileptonic decay of B mesons ($b \rightarrow e$) and the cascade decay of B to D mesons and D semileptonically to e ($b \rightarrow c \rightarrow e$) and normalised to the number of reconstructible b-labelled jets. Only electrons inside b-jets with $|\eta^e| < 2.5$ and b-jets with $|\eta^b| < 2.5$, $p_T{}^b > 15$ GeV were taken into account. For 100 GeV Higgs events, taking a cone around the b-quark direction of half-width $\Delta R < 0.4$, this branching ratio is 15.5% for electrons with $p_T{}^e >1$ GeV and 13.8% for electrons with $p_T{}^e > 2$ GeV.

The signal (irreducible) electrons in b-jets come from the following processes:

- the direct semileptonic decay of B mesons with an electron in the final state ($b \rightarrow e$);

- the cascade decay of b-hadrons to c-hadrons which later decay semi-leptonically with an electron in the final state ($b \rightarrow c \rightarrow e$);

- the leptonic decays of J/ψ's coming from b decays;

- the decays of b-hadrons to τ leptons which later decay into electrons.

These electrons are also expected in the background jets, for example in gluon jets, because of their possible content of heavy quarks. The contamination of the $H \rightarrow u\bar{u}$ sample with heavy flavour quarks from initial state radiation gluon splitting is below 2% for c-quarks and below 0.3% for b-quarks.

The background (reducible) electrons common to all types of jets come from the following processes:

- photon conversions which occur in the detector;

- π^0 Dalitz decays;

- semileptonic decays in the hadronic cascade.

While the signal electrons have very similar kinematic features in the signal and background jets (originating in both cases from the decays of heavy quarks), the kinematics of the background electrons is very different. Another important source of background are hadrons misidentified as electrons.

The fraction of reconstructed jets containing true electron tracks with $p_T > 2\,\text{GeV}$ and within $\Delta R < 0.4$ from the jet axis is given in Table 10-3. Results in the Table are given after the full detector simulation of the events, so they take into account also electrons produced in the interac-

Table 10-3 Fraction of jets containing electrons of a given origin (only electrons with $p_T > 2\,\text{GeV}$ and within $\Delta R < 0.4$ from the jet axis are considered). The numbers are given after the full detector simulation.

Jet type	Fraction of jets containing electrons (%)						
	from γ	from π^0	from B	from D	from other sources	irred. from B and D	reducible
b-jets	3.8	1.8	15.3	10.9	1.1	26.2	6.7
g-jets	3.8	0.7	0.1	0.4	0.1	0.5	4.6
c-jets	3.8	0.9	-	6.1	0.1	6.1	4.8
u-jets	3.8	1.0	-	-	0.1	-	4.9

tions with the detector material. The fraction of jets containing reducible electron tracks is of the order of 5% for the background jets and is dominated by electron tracks from photon conversion (~79%). It increases almost by 50% if the p_T threshold is lowered to 1 GeV. Lowering the threshold, the fraction of b-jets containing irreducible electron tracks increases by at most few percent.

10.3.2 Electron identification

Tracks reconstructed in the Inner Detector were selected applying the same cuts ('standard cuts') as for the vertexing algorithm (see Section 10.2.2), including the removal of electrons from reconstructed conversions. Variables for electron identification were then constructed using information from the Inner Detector and from the EM Calorimeter, as described in Section 7.3 and, in more detail, in Ref. [10-8] and [10-9]. Two additional variables which characterise global features of any track coming from a b-jet were considered, d_0 (the transverse impact parameter) and p_{TJ} (the transverse momentum relative to the jet axis). One expects that the charged tracks from B decays would have significant impact parameter (long lifetime) and also large p_T with respect to the jet axis (decay of a heavy object).

The d_0 and p_{TJ} distributions are shown in Figure 10-27 for signal electron tracks from B and D mesons in b-jets, and for other charged tracks in non-b jets. The rejection power of the d_0 variable is much higher than that of p_{TJ} (notice the logarithmic scale for d_0). One should be aware however that the d_0 variable is effectively the same as the variable used by the vertexing algorithm.

10.3.2.1 Discriminating function

The discriminating function D_{track} is defined for each track as: $D_{track} = \log \dfrac{\Pi_i P_e(x_i)}{\Pi_i P_h(x_i)}$,
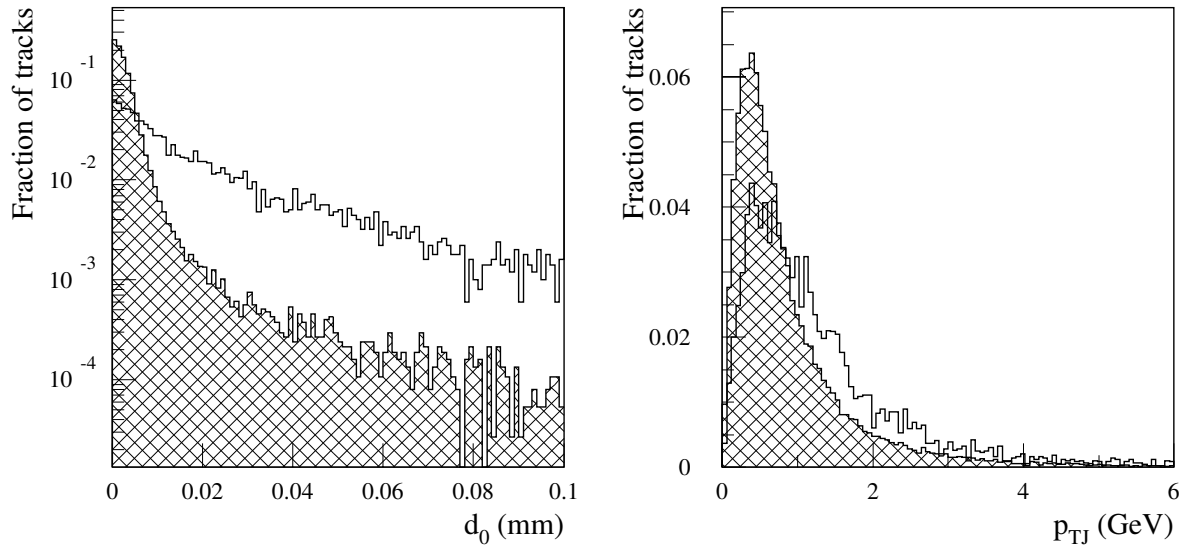
Figure 10-27 Probability density functions of the variables identifying tracks in *b*-jet. Open – signal electron tracks in *b*-jets, shaded – all tracks in non-b jets.

where x_i denotes the value of the *i*-th variable for this track, $P_e(x_i)$ is the probability that the track is a signal electron. $P_h(x_i)$ is the probability that the track is a non-signal hadron. Tracks that fail the track-quality cuts are assigned the value D_{track} = -40.

Higher rejection power can be achieved by the algorithm if, for tracks with transverse momentum below 5 GeV, the value of the discriminating function is rescaled as follows: $D_{track} \rightarrow D_{track} + 1.5 \times p_T$ - 7.5, where p_T is the transverse momentum of the track reconstructed in the Inner Detector. This p_T weighting is effective in rejecting the low-p_T background electron tracks from Dalitz decays and from γ-conversions.

Figure 10-28 shows the distribution of the discriminating function D_{track} for various types of tracks. Applying a threshold on the value of the D_{track} function a good separation of signal electron tracks from *b*-jets and other tracks can be achieved.

Figure 10-28 Distributions of the discriminating function D_{track} for signal electron tracks in *b*-jets from *B* and *D*-meson decays (solid histogram), compared to background electron tracks from γ-conversions or Dalitz decays in non-*b* jets (dotted) and pion tracks from non-*b* jets (dashed).

The identification of a track as a signal electron track is based on the value of D_{track} assigned to a given track. Those for which D_{track} is below threshold (typically D_{track}^{thr} ~ 5-7) are rejected as signal electron track candidates. To quantify the performance of the identification procedure, the following efficiency and rejection factors are defined: the electron identification efficiency ε_e, the pion rejection R_π and the conversion rejection R_{conv}.

Figure 10-29 R_π (left), and R_{conv} (right) rejection factors for tracks in various jet types as a function of the efficiency of identifying signal electron tracks from B and D decays in b-jets. 'e in b-jets', 'e in g-jets', *etc.* denotes electron tracks from γ-conversions or Dalitz decays in b-, g-, u- or c-jets. Only statistical errors are shown.

Figure 10-29 shows the rejections R_π and R_{conv} as functions of the signal electron identification efficiency. As expected the worst rejection factors are obtained for tracks originating from b-jets, both for pions and also for electrons from γ-conversions and from Dalitz decays. While the two rejection factors are almost the same for b-jets, they increase significantly for background jets. This can be explained by the fact that the d_0 variable has no discriminating power in this case as several tracks are in fact originating from B-meson decays.

10.3.3 Jet tagging procedure

The jet tagging procedure is based on the electron track identification procedure. The algorithm is constructed as follows: for each track in the jet the value of the discriminating function D_{track} is calculated, then the track with the highest value of D_{track} is chosen and its value of the discriminating function is assigned as the value of the discriminating function for the jet D_{jet}; jets with $D_{jet} > D_{jet}^{thr}$ are tagged as b-jets.

Figure 10-30 shows the distributions of D_{jet} for signal jets and for background jets: u-, c- and g-jets. The D_{jet} distribution for b-jets is shifted with respect to the distribution for u-, c-, and g-jets. Some fraction of events for each jet type has jets with $D_{jet} = -40$ which corresponds to jets for which none of the tracks passed the quality selection criteria.

10.3.4 *b*-tagging results

In order to improve the rejection power, the probability density distribution functions were calculated separately for several p_T and $|\eta|$ bins. Figure 10-31 shows the jet rejection factors for various types of jets as a function of the efficiency of the b-tagging algorithm. As expected, the highest rejection is obtained for u-jets, intermediate for gluon jets, and the lowest for c-jets.
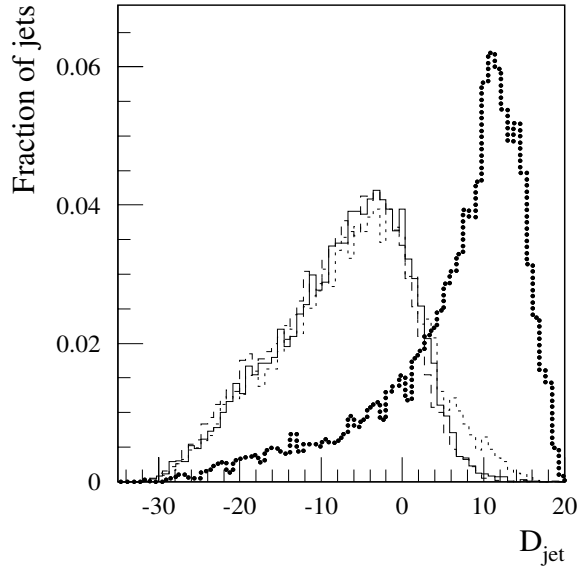
Figure 10-30 Probability density functions of the values of D_{jet} for *b*-jets (bold-dotted), compared to gluon jets (solid), *u*-jets (dashed), *c*-jets (dotted).
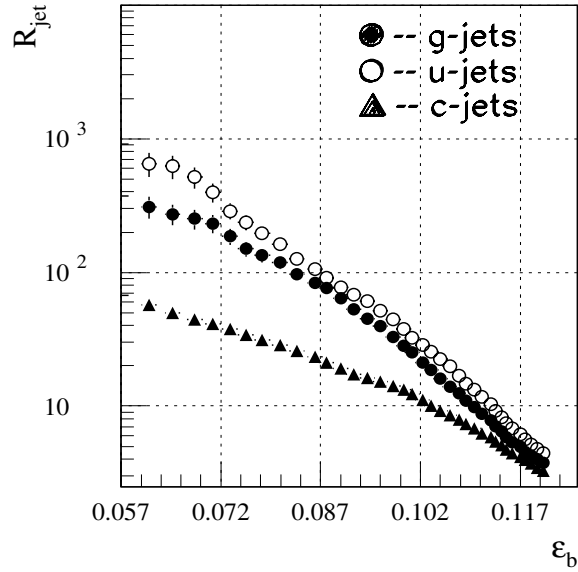
Figure 10-31 Jet rejection factor R_{jet} as a function of the efficiency of the *b*-tagging algorithm for various jet types.

Table 10-4 shows the jet rejection factors for a *b*-tagging efficiency of 7.2%, which corresponds to ~50% efficiency for *b*-jets with an electron. The reason for the lower rejection factors with respect to previous studies [10-8] is mainly the extension of this study to the full rapidity range. As particles at larger $|\eta|$ cross more material, the electron-pion separation power decreases rather rapidly: Figure 10-32 shows the pseudorapidity dependence of the rejection factors. Decreasing the threshold on p_T causes the jet rejection to decrease, as not only the charged track multiplicity, but also the fraction of background jets with true electron tracks in the jet is significantly higher.

Table 10-5 shows the fraction of jets tagged by a given track for $\varepsilon_b = 7.2\%$, which corresponds to a 50% tagging efficiency for *b*-jets with a true electron.

 Most of the jets are tagged by a true electron track, independently of the jet type. This indicates that the electron identification procedure works with high efficiency and good purity. Most of the electron tracks which tag the jets, except for *u*-jets, are signal electron tracks (they come from *B* or *D* decays). For the *b*-jet sample this type of track accounts for 94% of all tagged jets. Noting that in the original sig-
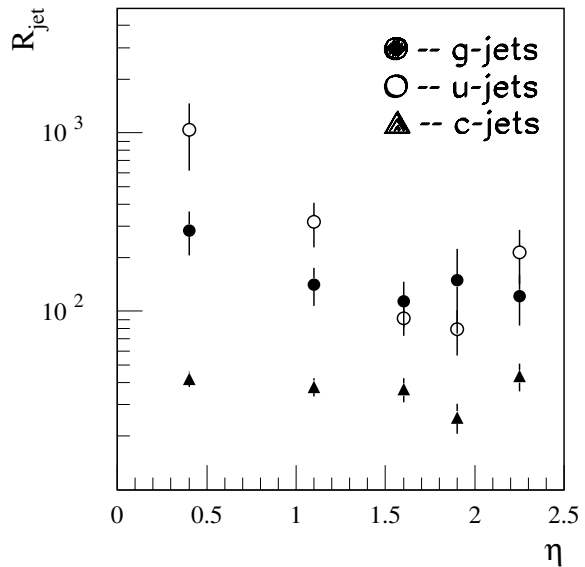
Figure 10-32 Jet rejection factors as a function of pseudorapidity for a fixed (7.2%) *b*-tagging efficiency.

Table 10-4 Jet rejection factors for a fixed (7.2%) *b*-tagging efficiency using XKalman. The p_T threshold is 2 GeV.

R_u	338 ± 50
R_g	202 ± 30
R_c	40 ± 2

nal sample the percentage of jets with such electrons is ~90% (see Table 10-3), then one con-
cludes that the tagging enriches the sample. This effect is even stronger for the g- and c-jets,
where the fraction of jets containing electrons from B and D mesons is greatly increased by the
b-tagging algorithm. The sample of u-jets does not contain electrons from B and D, but these jets
are also tagged mainly (60%) by the electron tracks from γ-conversions and Dalitz decays or
from other sources. In the higher pseudorapidity region ($|\eta| > 1$), pions become a major source
of background.

Table 10-5 Fraction of jets tagged by a specified track for ε_b = 7.2%. Only tracks with p_T > 2 GeV are used. The
'e from γ' column denotes electron tracks from γ-conversions and Dalitz decays.

Jet type	Fraction of jets tagged by a specified track (%)						
	all e's	e from B	e from D	e from γ	other e	π	others
b	99.4	68.7	26.0	1.4	3.3	0.4	0.2
g	82.2	17.8	24.4	37.8	2.2	15.6	2.2
c	91.9	0	86.9	4.6	0.4	5.8	2.3
u	65.2	0	0	65.2	0	26.1	8.7

10.4 Soft muons

In principle, muons are just as good as electrons for the identification of the semileptonic decays
of heavy quarks. In practice, although the efficiency for detecting muons in the Inner Detector is
very high even at very low p_T, they can be identified as such only if they have enough momen-
tum to cross the whole thickness of the calorimeters. The mean energy loss at central rapidity
is ~3 GeV, therefore this is the effective threshold for muon identification in the barrel part of
the Muon System. Muons with p_T > 6 GeV cross the middle muon chamber station and can be
found as tracks in the muon detector; this effective threshold decreases to 2 GeV for muons
crossing the end-cap toroids. The energy deposit in the last segment of the Hadronic Tile Calo-
rimeter can be used to discriminate muons with p_T > 2 GeV in the barrel rapidity range
$|\eta| < 1.7$.

10.4.1 Event characteristics

The branching ratio for the $b \to \mu$ decay, $BR(b \to \mu)$, was calculated taking into account the di-
rect semileptonic decay of B mesons ($b \to \mu$) and the cascade decay of B to D mesons and D sem-
ileptonically to μ ($b \to c \to \mu$) and normalised to the number of reconstructible b-labelled jets. In
both cases only muons inside b-jets with $|\eta^\mu| < 2.5$ and b-jets with $|\eta^b| < 2.5$, $p_T{}^b$ > 15 GeV were
taken into account.

Table 10-6 specifies the branching ratios for two values of the p_T^μ threshold ($p_T^\mu > 3$ GeV and $p_T^\mu > 6$ GeV). As shown in Table 10-6, if muons below the threshold for muon identification in the Muon System can be successfully tagged (using the information from the last segment of the Hadronic Tile Calorimeter), they can add a considerable fraction to the *b*-tagging efficiency for lower-p_T jets.

Table 10-6 The $b \to \mu$ (direct and the cascade decay) branching ratios for $p_T > 3$ and 6 GeV and for $m_H = 100$ and 400 GeV.

	m_H = 100 GeV	m_H = 400 GeV
$p_T^\mu > 3$ GeV	10.0%	15.7%
$p_T^\mu > 6$ GeV	6.5%	13.3%

Signal muons have clearly the same properties as the signal electrons used for the soft electron tagging studies in the previous section. The background consists of:

- muons from π and *K* decays;

- misidentified particles in jets containing real muons, as a result of incorrect matching between the tracks reconstructed in the Inner Detector and the Muon System;

- (for low-p_T muons) particles extrapolated to a region of the Hadronic Tile Calorimeter with an energy deposit compatible with a muon's.

10.4.2 Muon identification

The Muon System performance was parametrised and applied to events which were fully simulated and reconstructed in the Inner Detector and calorimeters, since a full simulation was not possible due to the delayed availability of the Muon System geometry.

The procedure to reconstruct muons in the Muon System and to match them to Inner Detector tracks is described in detail in Section 8.1. Applying this procedure to a sample of *b*-jets where the *B* mesons were forced to decay semileptonically, the muon reconstruction efficiency and hadron misidentification rates were parametrised as functions of $|\eta|$ and p_T as shown in Section 8.4 and in Figures 8-22 and 8-23. Then a muon identification probability was assigned to each track reconstructed in the Inner Detector, depending on the track type and its parameters.

Muons with $p_T > 2$ GeV in the range $|\eta| < 1.7$ can be identified through their energy deposit in the last segment of the Hadronic Tile Calorimeter. If no muon was found in the Muon System and matched to an Inner Detector track for a given jet, the method described in Section 8.4 was used to assign a 'quality factor' to particles in the range $2 < p_T < 6$ GeV which corresponded to an energy deposit in the last Hadronic Tile Calorimeter segment comprised in the band shown in Figures 8-24 and 8-25.

10.4.3 Jet tagging procedure

The jet tagging procedure selected for each jet the muon which had the highest probability of coming from a semileptonic *B* decay. The impact parameter significance, the transverse momentum relative to the jet axis (p_{TJ}) and the muon energy fraction relative to the jet energy (E_{fr}) are all good discriminating variables, and muons from semileptonic *B* decays tend to have larger values of these variables compared to background muons (see the distributions of p_{TJ} and E_{fr} for muons in *b*- and *u*-jets in Figures 10-33 and 10-34). The logarithm of the product of these
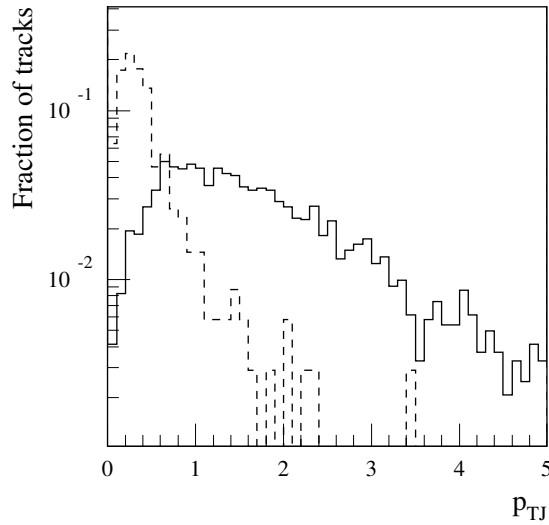
Figure 10-33 Transverse momentum relative to the jet axis for muons from *B* and *D* decays in *b*-jets (solid line) and any muon in *u*-jets (dashed line).
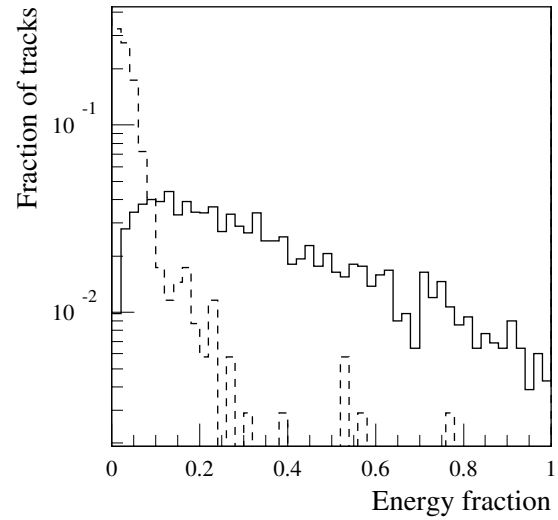
Figure 10-34 Energy fraction relative to the jet energy (as reconstructed by the calorimeters) for muons from *B* and *D* decays in *b*-jets (solid line) and any muon in *u*-jets (dashed line).

three variables was used as the discriminating function D_{track}. The largest value of D_{track} for all tracks in a jet was then used to calculate the jet weights and rejection factors for *u*-, *g*- and *c*-jets. Figure 10-35 shows the jet weights for *b*-jets compared to background jets.

10.4.4 *b*-tagging results

The jet rejection curves as function of the *b*-jet efficiency are shown in Figure 10-36. As can be immediately noted, the much better signal-to-background ratio of the muons in the Muon System sample partially compensates the loss of efficiency for low-p_T central jets; the contribution of the muons recognised in the Hadronic Tile Calorimeter is significant only in the low-p_T range. For the sake of comparison with the soft electron analysis, Table 10-7 shows the jet rejection factors for a fixed (7.2%) *b*-jet efficiency, separately for jets produced in the decays of 100 and 400 GeV Higgs.

Figure 10-37 shows the pseudorapidity dependence of the rejection factors for fixed *b*-jet efficiency. As expected, the lower p_T threshold for muons recognised in the Hadronic Tile Calorimeter contributes to improve the rejection power in the central pseudorapidity region.
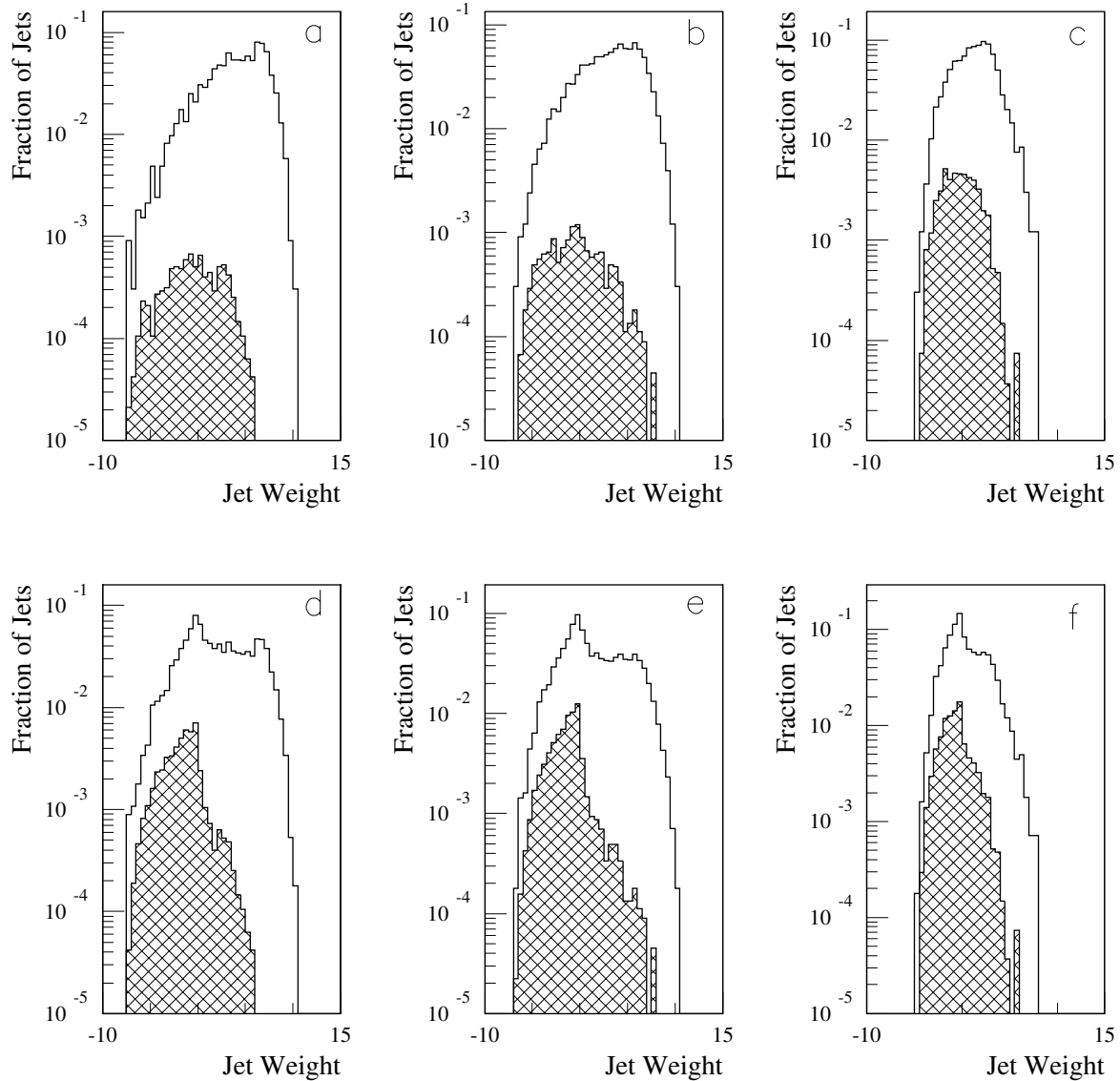
Figure 10-35 Probability distribution functions of jet weights for muon *b*-tagging. Top: muons recognised in the Muon System only, bottom: muons recognised in the Muon System or the Hadronic Tile Calorimeter. Open histograms: *b*-jets, shaded histograms: background jets. a) and d): *b*-jets compared to *u*-jets. b) and e): *b*-jets compared to gluon jets. c) and f): *b*-jets compared to *c*-jets. Jets without muons are taken into account for the normalisation of the histograms.

10.5 Robustness of performance

10.5.1 Effects of high-luminosity pile-up

A large fraction of the Higgs events used for the *b*-tagging studies were processed with the addition of minimum bias events to simulate the high luminosity environment. A random number (on average 24) of minimum bias events were added to all detectors; in addition, on average
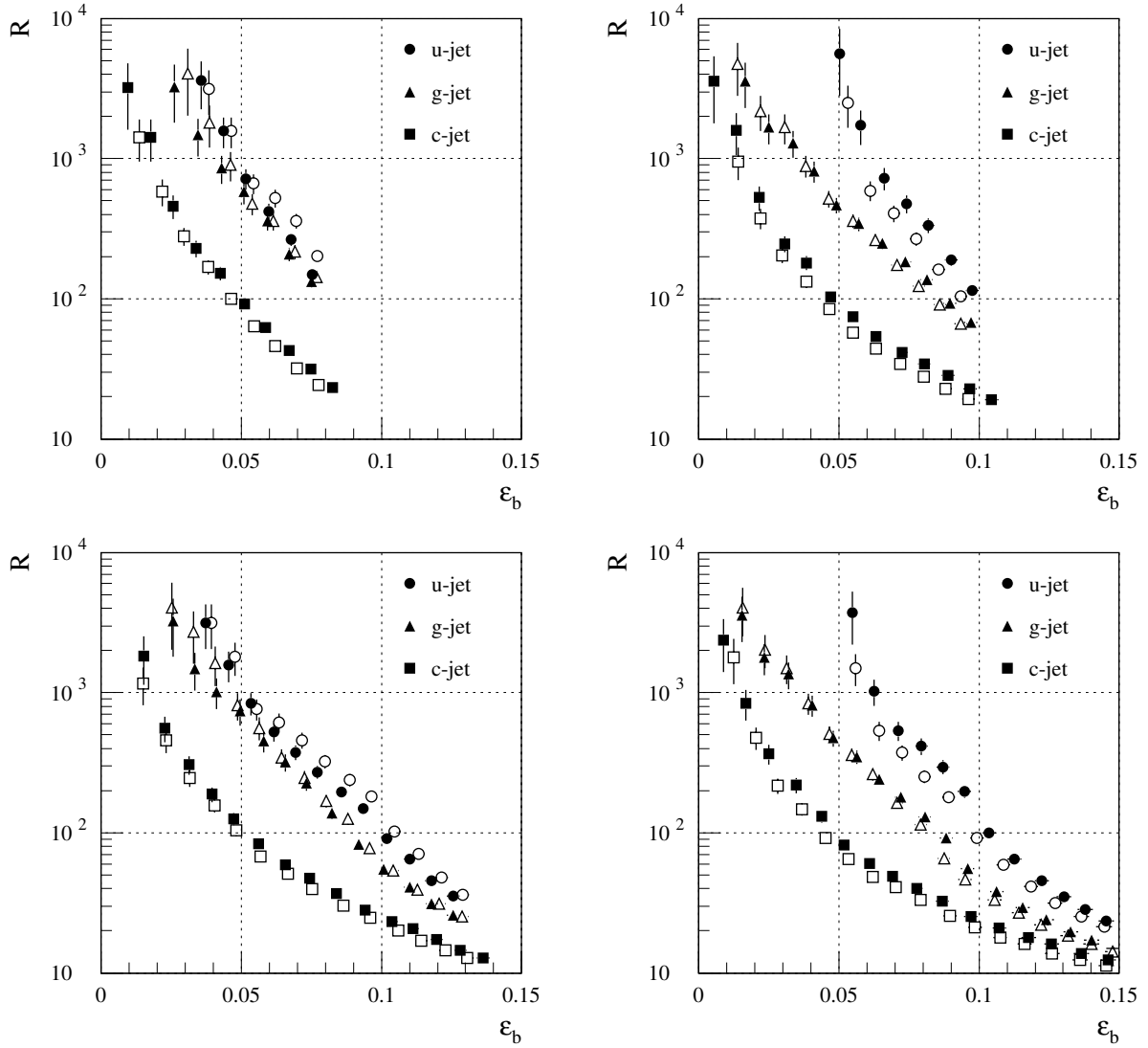
Figure 10-36 Rejection factors as a function of *b*-jet efficiency for the muon tags. Top: only muons recognised in the Muon System. Bottom: all muons recognised in the Muon System or the Hadronic Tile Calorimeter. Left: m_H = 100 GeV. Right: m_H = 400 GeV. Full symbols: xKalman; open symbols: iPatRec.

Table 10-7 Jet rejection factors for a fixed (7.2%) *b*-tagging efficiency.

| | Muon System only | | | | Muon System and Hadronic Tile Calorimeter | | | |
| | m_H = 100 GeV | | m_H = 400 GeV | | m_H = 100 GeV | | m_H = 400 GeV | |
	xKalman	iPatRec	xKalman	iPatRec	xKalman	iPatRec	xKalman	iPatRec
R_u	189 ± 16	299 ± 33	510 ± 77	347 ± 43	334 ± 38	455 ± 61	513 ± 77	379 ± 49
R_g	169 ± 17	182 ± 19	198 ± 16	169 ± 13	250 ± 31	255 ± 32	181 ± 14	159 ± 12
R_c	35 ± 2	30 ± 1	43 ± 2	34 ± 2	50 ± 3	44 ± 3	46 ± 3	40 ± 2

eight events were added to the TRT to simulate its long sensitive time. The pile-up and pulse shaping in the calorimeters was simulated as described in Section 2.3. No pile-up simulation was performed for the Muon System elements as the simulation code was not available in time.
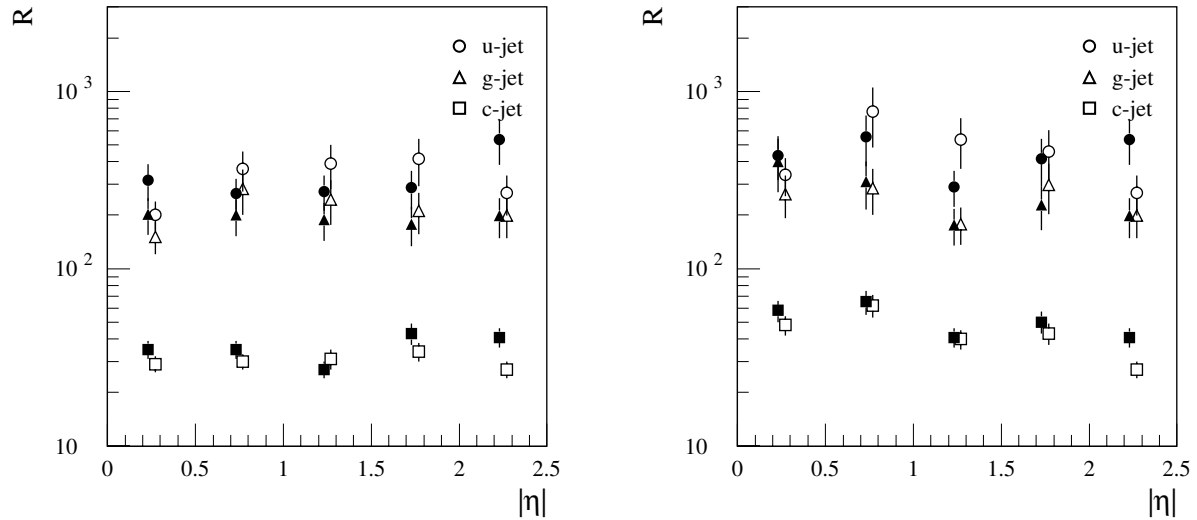
Figure 10-37 Rejection factors as a function of pseudorapidity for 7.2% *b*-jet efficiency for the muon tags (m_H = 100 GeV). Left: only muons recognised in the Muon System. Right: all muons recognised in the Muon System or the Hadronic Tile Calorimeter. Full symbols: xKalman; open symbols: iPatRec.

The same reconstruction and analysis software was run on these events, as for events without pile-up. In order to save running time, and as it was shown by all analyses presented so far that the performance of xKalman and iPatRec for this type of studies are equivalent, only the faster iPatRec algorithm was used. Figures 10-38 to 10-40 show the primary track efficiency and the rates of secondary tracks and fakes for pile-up events.
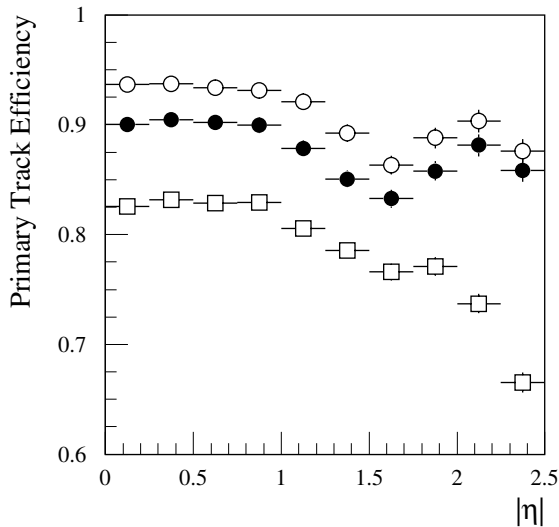
Figure 10-38 Primary track efficiency for iPatRec as a function of pseudorapidity without cuts (open circles), after applying standard cuts (closed circles) and after applying quality cuts (open squares).
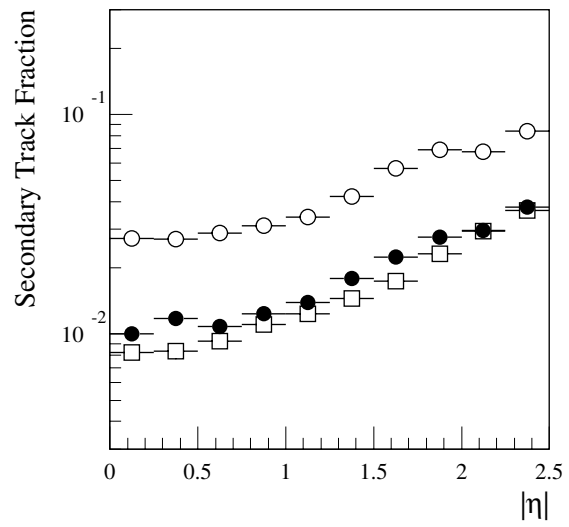
Figure 10-39 Fraction of secondary tracks for iPatRec as a function of pseudorapidity without cuts (open circles), after applying standard cuts (closed circles) and after applying quality cuts (open squares).

It can be noted that for standard cuts the pattern recognition performance is comparable to the performance without pile-up. The quality cuts (especially the cut on the number of shared hits) affect adversely the track-finding efficiency but remove a large fractions of tracks which did not originate from the main Higgs event.
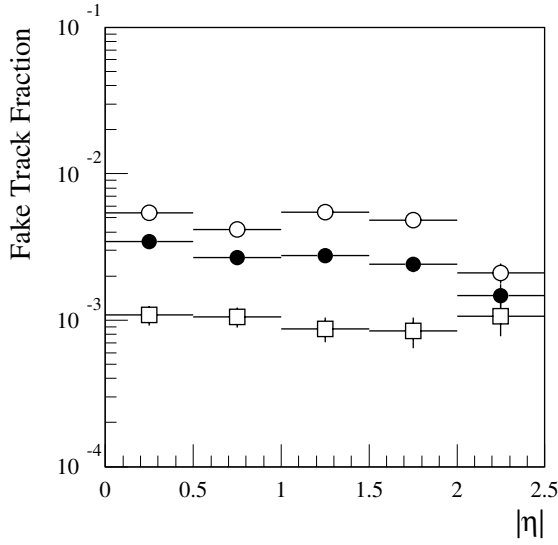
Figure 10-40 Fraction of fake tracks as a function of pseudorapidity without cuts (open circles), after applying standard cuts (closed circles) and after applying quality cuts (open squares) (iPatRec).
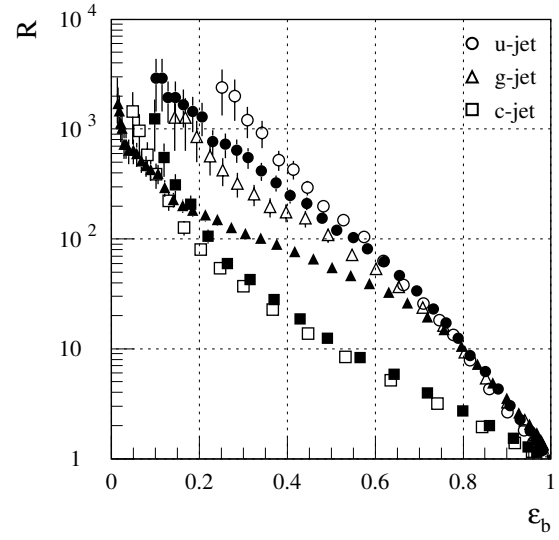
Figure 10-41 Jet rejection factors for the vertex b-tagging method, with high-luminosity pile-up. Open symbols: $m_H = 100$ GeV, full symbols: $m_H = 400$ GeV.

The z position of the primary vertex can be reconstructed with the same resolution (~35 μm) but the fraction of events in the tails of the distribution increases from 9% to 14%.

Table 10-8 Jet rejection factors for different b-tagging methods, with high-luminosity pile-up. Rejections are calculated for ε_b = 50% for the vertex method and 7.2% for the lepton methods.

	R_u		R_g		R_c	
	$m_H = 100$	$m_H = 400$	$m_H = 100$	$m_H = 400$	$m_H = 100$	$m_H = 400$
Vertex	178 ± 22	133 ± 14	104 ± 15	55 ± 4	10.5 ± 0.4	12.1 ± 0.6
Electron	118 ± 11	74 ± 6	115 ± 17	135 ± 16	34 ± 3	31 ± 2
Muon	223 ± 30	284 ± 44	170 ± 31	168 ± 22	32 ± 2	37 ± 3
Muon + Tile	289 ± 45	282 ± 44	157 ± 27	183 ± 24	40 ± 3	46 ± 4
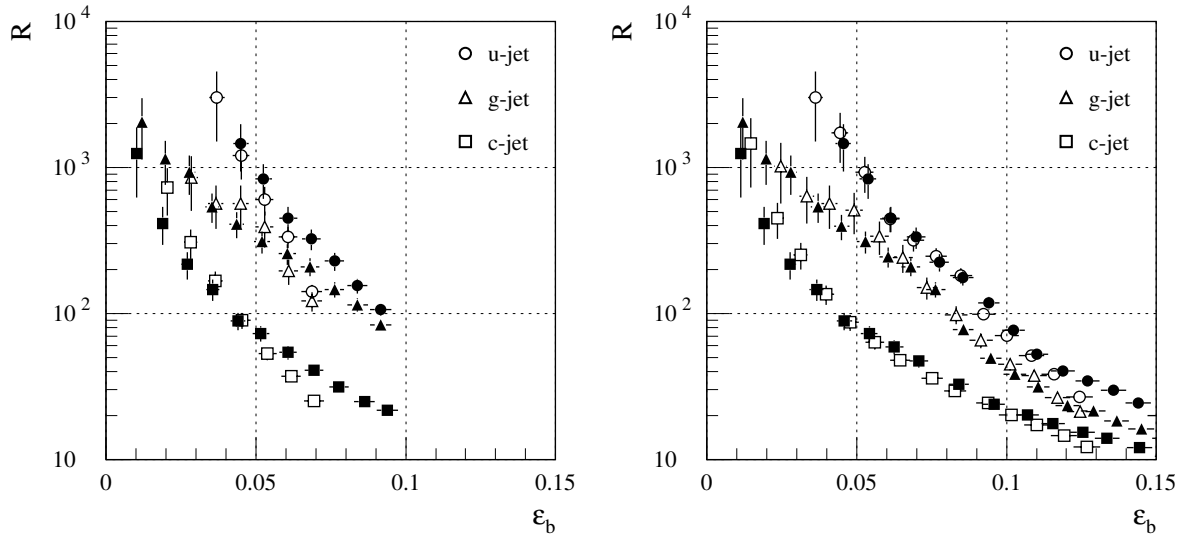
Figure 10-42 Rejection factors as function of *b*-jet efficiency for the muon tags, with high-luminosity pile-up. Left: only muons recognised in the Muon System are used; right: all muons recognised in the Muon System or in the Hadronic Tile Calorimeter are used. Open symbols: $m_H = 100$ GeV, full symbols: $m_H = 400$ GeV.

Table 10-8 and Figures 10-41 to 10-43 present the rejection factors that can be obtained, using the vertex and lepton tags. The rejections are somewhat degraded with respect to the zero-luminosity case (see Tables 10-1, 10-4 and 10-7) but still acceptable and useful.

Figure 10-44 shows the background rejections, for 50% *b*-tagging efficiency, obtained using the vertex method only, as functions of $|\eta|$ and p_T. Comparing to the corresponding Figures 10-23 and 10-24, it can be noted that the loss in overall performance is effectively due to a slower increase of the performance for jets with $p_T < 100$ GeV; above this value the performance is not affected by the presence of pile-up.
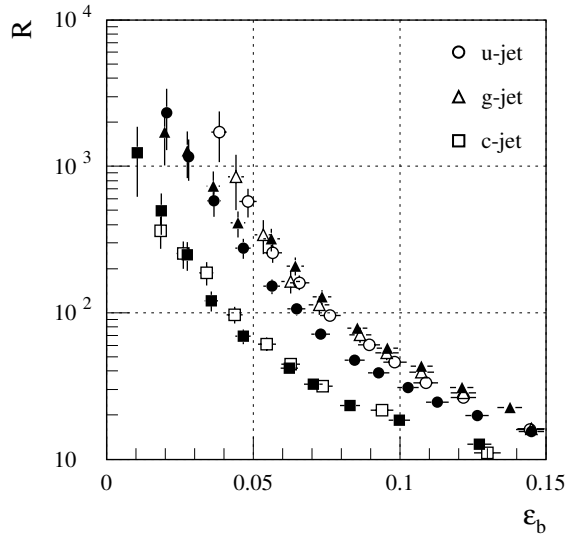
Figure 10-43 Rejection factors as a function of *b*-jet efficiency for the electron tags, with high-luminosity pile-up. Open symbols: $m_H = 100$ GeV, full symbols: $m_H = 400$ GeV.

10.5.2 Effects of reduced detector efficiency and missing detector layers

The effects of reduced detector efficiency and/or of missing detector layers were studied in detail in Ref. [10-10]. Those studies used the same Inner Detector geometry as used for the present study. The reconstruction and analysis software were less developed at that time, which produced a worse *b*-tagging performance than can be achieved now, but it is believed that the relative changes in performance as function of the detector efficiency still apply. Here only the main results are summarised.
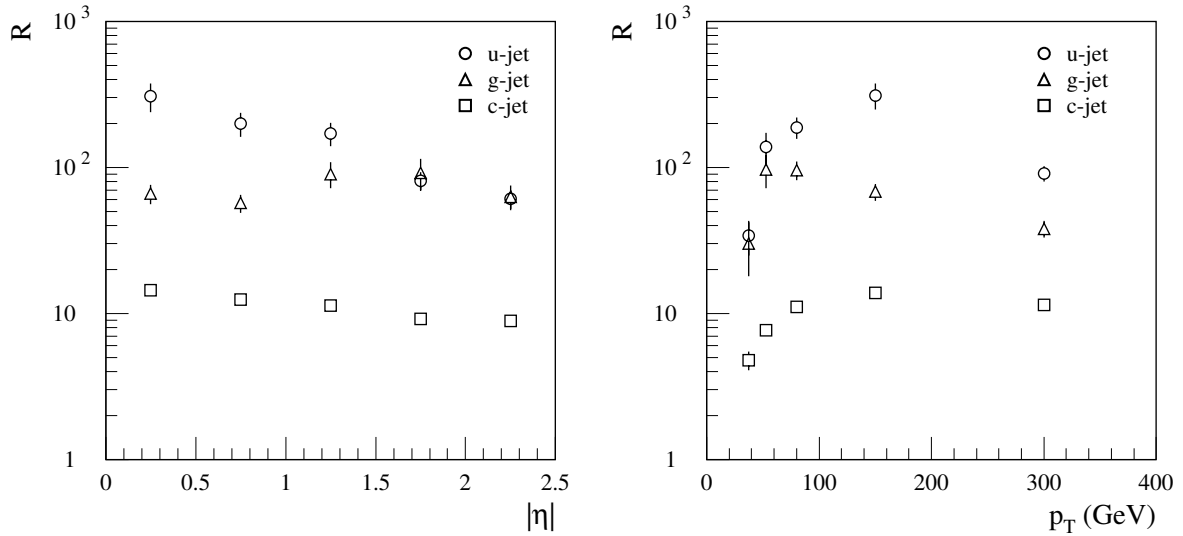
Figure 10-44 Background rejections as a function of jet $|\eta|$ and p_T for $\varepsilon_b = 50\%$, with high-luminosity pile-up. Vertex method only.

Reducing the efficiency of the Pixel and SCT detectors from the default random 97% to 90% reduced the u-jet rejection power to 76% of its original value, independent of the pattern recognition program and of the track selection cuts.

The loss, or removal, of the middle or outer Pixel layer reduced the u-jet rejection power to 70% of its original value, independent of the pattern recognition program and of the track selection cuts. Similarly, the loss, or removal, of an SCT layer reduced the u-jet rejection power to 90% of its original value.

The effect of the loss of the *B*-layer was studied in the Inner Detector TDR: in this case the u-jet rejection power is reduced to 40% of its original value.

10.5.3 Evolution of the Inner Detector layout

The current design of the Inner Detector layout differs in several details from the geometry used for the present studies (see Section 3.2.1). The main impact on the *b*-tagging performance is that of the changes in Pixel Detector geometry: slightly larger *B*-layer radius, slightly smaller outer layer radius, re-arranged disk regions. All these changes result in small degradations of the performance. The cumulative effect is to reduce the u-jet rejection power to 90% of its original value; if hardware constraints forced the adoption of 400 μm long pixels in the *B*-layer, there would be a further 10% performance loss.

10.6 Combined *b*-tagging performance

The algorithms described above for the vertex tagging and the soft lepton tagging all calculate a 'jet weight' which is used as a measure to discriminate *b*-jets from other jets. There is more than one way to combine these weights into a single combined variable. As the rejection power of the vertex method is superior to that of the lepton methods and the lepton tags are efficient only for a few percent of the *b*-jets, the following method was used to select the 'tagged' events: for each

value of the cut on the vertex weight, the cut on the lepton weight is chosen so as to optimise the global performance. The combined performance was then compared to the performance of the vertex method for the same *b*-tagging efficiency or for the same rejection.

Table 10-9 Jet rejection for different combinations of *b*-tagging methods, for 50% *b*-jet efficiency, compared to the vertex method. In each cell, the first column refers to xKalman and the second to iPatRec; the first (second) line is for m_H = 100 (400) GeV.

	R_u	R_g	R_c
Vertex	326 / 391	135 / 148	13.6 / 11.7
only	126 / 183	59 / 58	13.3 / 13.4
Vertex +	329 / 398	148 / 154	13.8 / 12.0
Electron	127 / 185	69 / 58	13.3 / 13.5
Vertex +	326 / 391	135 / 150	13.7 / 11.9
Muon	128 / 187	60 / 58	13.4 / 13.5
Vertex +	326 / 391	135 / 150	13.7 / 11.9
Muon + Tile	128 / 187	60 / 58	13.4 / 13.5

Table 10-9 shows the increase in jet rejection factors, for 50% *b*-tagging efficiency, for different combinations of *b*-tagging methods. For a constant jet rejection factor (corresponding to 50% *b*-tagging efficiency with the vertex method alone), the increase in efficiency is at most 1%. Given the very high rejection achieved with the vertex method, the combination of the vertex method with the lepton methods, which apply only to a small fraction of events, does not produce much improvement in the performance.

The contribution of the lepton methods can become important if the rejection of the vertex method is decreased with respect to the values shown above. If it would be reduced to ~40% of its value (which would be the case if the *B*-layer were not operational), then the lepton tags would add up to 12% to the rejection at 50% efficiency, or up to 2% efficiency for constant rejection. In addition, they make possible a cross-check of results in order to reduce any systematic errors.

10.7 Impact of *b*-tagging performance on the channel *WH*, $H \rightarrow b\bar{b}$

The detailed understanding of the *b*-tagging performance achieved through the studies described in this chapter allowed the implementation of a realistic parametrisation of the *b*-tagging performance into the fast simulation (see Section 2.5.6) used for the study of this signal and backgrounds. This parametrisation was implemented as described below.

The results for m_H = 100 GeV were adapted to account for the different methods used for labelling jet flavour in the full-simulation studies and in the fast simulation program (the latter has to treat many background sources with varying jet multiplicities and flavours). The *b*-tagging performance was parametrised for jets from *u*, *d*, *s*, *g*, which do not contain *c*-quarks nor *b*-quarks in the final parton shower process, and from charm, including the $|\eta|$ and p_T dependence.

Table 10-10 For an integrated luminosity of 30 fb⁻¹ and $m_H = 100$ GeV, expected rates for the signal from Standard Model *WH* associated production followed by $H \to b\bar{b}$ decay and for the various background processes after all selection cuts as a function of the average *b*-tagging efficiency using vertexing; $|\eta|$ and p_T-dependent rejection factors of non-*b* jets are used. The signal-to-background ratio, the ratio $R_{red/irred}$ of reducible to irreducible background and the significance expressed as $S/\sqrt{B}$ are also indicated.

Process	$\varepsilon_b^{vert} = 50\%$ $\varepsilon_c^{vert} = 8.2\%$ $\varepsilon_j^{vert} = 0.43\%$	$\varepsilon_b^{vert} = 60\%$ $\varepsilon_c^{vert} = 14.4\%$ $\varepsilon_j^{vert} = 1.1\%$
$WH,\ H \to b\bar{b}$	294	423
$WZ,\ Z \to b\bar{b}$	422	625
$Wb\bar{b}$	2449	3603
$t\bar{t} \to WWb\bar{b}$	2885	4233
$t\bar{b} \to Wb\bar{b}$	558	755
Wbc	621	1350
$Wc\bar{c}$	698	2045
Wbj	332	1079
Wcj	1082	4796
Wjj	314	2093
$R_{red/irred}$	0.48	1.23
Total bgd (B)	9361	20579
S/B	3.1%	2.1%
$S/\sqrt{B}$	3.04	2.95

The *WH* signal and all the background processes were simulated and reconstructed using the fast simulation, modified to account for the *b*-tagging performance in a statistical way for each reconstructed jet. Table 10-10 shows the expected significance for two values taken from the *b*-tagging efficiency versus rejection curves for an integrated luminosity of 30 fb⁻¹ and for $m_H = 100$ GeV. The background processes can be separated into irreducible background containing real *b*-jets and reducible background (predominantly from *W*+jet events), containing non-*b* jets wrongly tagged as *b*-jets. The ratio $R_{red/irred}$ of the total reducible background to the irreducible background increases from a value of 0.5 for a *b*-tagging efficiency of 50% to a larger value of 1.2 for a *b*-tagging efficiency of 60%. At the same time, the signal-to-background ratio decreases by about 30% from 3.1% to 2.1%. For consistency with previous estimates, the tighter trigger threshold was applied for isolated electrons (30 GeV instead of 20 GeV) in Table 10-10. If the lower threshold is applied, the sensitivity increases by 4% only [10-11].

Clearly this channel remains a difficult challenge at the LHC. The uncertainties on the *b*-tagging performance shown above in terms of possible improvements or degradations do not change the results shown in Table 10-10 by more than 10% for *b*-tagging efficiencies below or around 50%, since the dominant background in this case is the irreducible background. The extraction of the rather broad signal peaks expected for invariant masses involving *b*-jets with a signal-to-background ratio often significantly below unity will obviously require a careful monitoring of the *b*-tagging performance with real data. The most abundant source of events con-

taining *b*-jets which could be used to calibrate the efficiency of the *b*-tagging algorithms is $t\bar{t}$ production, since clean samples can be selected by requiring only one tagged *b*-jet. The second *b*-jet from top-quark decay can then be used for calibration.

10.8 References

10-1   T. Sjostrand, Computer Physics Commun. **82** (1994) 74.

10-2   I. Gavrilenko *et al.*, 'Present status of *b*-tagging studies in ATLAS', ATLAS Internal Note INDET-NO-115 (1995).

10-3   S. Haywood, '*b*-tagging with Atlas Inner Detector using Fast Simulation', ATLAS Internal Note INDET-NO-116 (1995).

10-4   D. Froidevaux and E. Richter-Was, Zeit. Phys. **C67** (1995) 213.

10-5   ATLAS Collaboration, Inner Detector Technical Design Report, Volume I, CERN/LHCC/97-16 (1997).

10-6   ATLAS Collaboration, Pixel Detector Technical Design Report, CERN/LHCC/98-13 (1998).

10-7   ATLAS Collaboration, Calorimeter Performance Technical Design Report, CERN/LHCC/96-40 (1996).

10-8   S. Jagielski, A. Kaczmarska and M. Wolter, 'Tagging *b*-jets using low-p_T electrons', ATLAS Internal Note ATL-PHYS-98-129 (1998), published in Acta Physica Polonica **B30** (1999) 4.

10-9   A. Kaczmarska and M. Seman, 'Identification of low-p_T electrons with the ATLAS detector', ATLAS Communication ATL-COM-PHYS-99-047 (1999).

10-10   D. Barberis *et al.*, 'A Comparative Study of Reduced Layouts of the ATLAS Inner Detector', ATLAS Internal Note INDET-NO-188 (1997).

10-11   B.J. Dick, 'Further work on *WH*, $H \rightarrow b\bar{b}$', ATLAS Communication ATL-COM-PHYS-99-019 (1999).

11 Trigger performance

11.1 Introduction

This chapter presents a summary of the ATLAS level-1 (LVL1) and level-2 (LVL2) triggers and outlines the task of the Event Filter (EF). Details of the algorithms and justification of the proposed selections are explained in [11-1]. Technical details of the LVL1 muon and calorimeter trigger implementation are documented in [11-2]. This chapter is restricted to the presently accepted algorithms, their key selections and resulting efficiencies and rates.

Section 11.2 presents an overview of the ATLAS trigger strategy and summarises the functionality. The next sections present the trigger algorithms and their performance. Section 11.3 is devoted to the LVL1 trigger: the muon trigger and various calorimeter triggers. The trigger objects selected by LVL1 constitute the input to the higher-level triggers, LVL2 and EF. The RoI-guided triggers are summarised in Section 11.4, followed by triggers that do not need RoI guidance, missing-transverse energy (Section 11.5) and the *B*–physics trigger channels (Section 11.6). The resulting sets of trigger objects are input to the global LVL1 and LVL2 decisions, which are driven by lists of hypotheses derived from the list of physics signatures of interest (Section 11.7). The last section presents the task of the Event Filter (Section 11.8).

The present chapter addresses only some of the issues associated with trigger performance. The studies need to be extended and consolidated. The overall optimisation of the trigger implementation, taking into account processing power, data bandwidth and cost requirements, will be a joint task of the LVL2, EF and trigger performance group during the coming years. Especially the work for the EF will need the cooperation of the physics and reconstruction groups to develop the selections and the selection tools.

11.2 Overview of ATLAS trigger strategy

11.2.1 Introduction

The main challenges at the LHC that have an impact on the experiment's trigger system are an unprecedented rate of 10^9 interactions per second, the need to select rare predicted physics processes with high efficiency while rejecting much higher-rate background processes, and large and complex detectors with huge numbers of channels $O(10^7)$. Decisions must be taken every 25 ns; at high luminosity, each bunch crossing contains about 23 interactions. At the end of the decision chain, the event storage rate is limited to approximately 100 Hz, by practical limitations in the offline computing power and storage capacity. The average event size is 1 Mbyte [11-3].

The ATLAS trigger strategy foresees a reduction of the event rate at three levels: LVL1, LVL2 and Event Filter [11-3]. The accepted rates at each level are given in Figure 11-1. The LVL1 trigger receives data at the full LHC bunch-crossing rate of 40 MHz. The output rate is limited by the capabilities of the front-end systems to 75 kHz (upgradable to 100 kHz). The present esti-

Event rate and decision stages
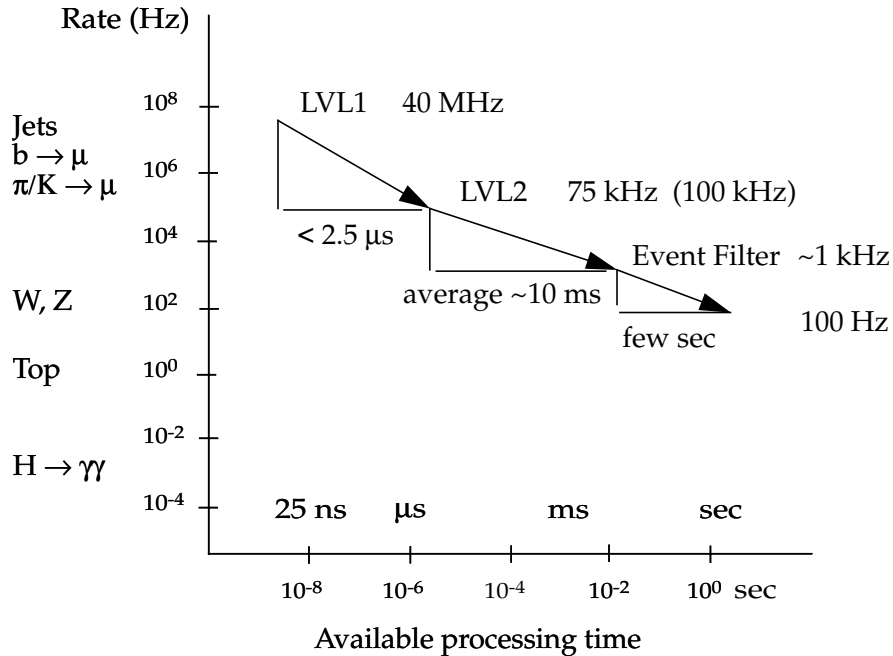
Figure 11-1 The three levels of the ATLAS trigger and their event rates and processing times.

mate of rates, as given in Section 11.7, allows for a safety margin of about a factor of two on the output rate from LVL1. Furthermore, thresholds are deliberately chosen to be lower than strictly necessary for the success of the ATLAS physics programme.

LVL2 and the EF combined will give a reduction factor of order 10^3, where LVL2 is expected to provide a reduction of a factor of about 100 resulting in an input rate to the EF of the order of 1 kHz. The sharing of the selection task between LVL2 and the EF remains to be optimised, so the output rate from the LVL2 trigger is not final. Similarly, there is some flexibility on the output rate from the EF.

The following sections describe the essential steps in the trigger-decision chain and the trigger 'objects' that are used in the selection process. The status and workplan of the LVL2, data acquisition and event filter projects are described in [11-4]. The trigger algorithms at LVL1 must be relatively simple in order to be implemented in very fast custom hardware processors. Much more freedom for algorithm complexity and programmability is available at LVL2 and in the EF. Indeed, both of these high-level triggers may well be implemented using very similar, or even the same, communication and computing structures. They differ only in the way that detector data is accessed and by the framework for software and database access. Simple, fast algorithms are foreseen for LVL2, whereas more offline-like algorithms are applied in the EF. Technology evolution indicates an increase in CPU processing power by an order of magnitude over the next five years and an increase in memory density by a factor of four every two years. A firm division between LVL2 and the EF is therefore premature and even not desirable. The tasks have

to be specified, and their physical location, where they are executed, may shift with time. The allocation depends on the evolution of technology and improved understanding of the tasks. This process of optimisation will continue after data taking begins.

11.2.2 LVL1 trigger and regions of interest

The LVL1 trigger [11-2] identifies the basic signatures of 'interesting' physics with high efficiency. It forms its decision on the basis of multiplicities for the following local trigger objects for various p_T thresholds: muon, EM clusters (where isolation can be required), narrow jets (isolated hadronic τ decays or isolated single hadrons), jets and the global objects: missing transverse energy, total scalar transverse energy.

The muon and calorimeter LVL1 trigger systems use simple algorithms to make fast decisions. Local pattern recognition and transverse-energy evaluation are performed on prompt, relatively coarse-grained information, which is provided by the fast muon trigger chambers and the tower summing electronics of the EM and hadronic Calorimeters.

The LVL1 algorithms are executed by custom electronics, programmed in terms of adjustable parameters. The decision time of ~2 μs includes the transmission of signals between the detector and the trigger electronics. During the LVL1 trigger processing, the data from all detector systems are held in pipeline memories. When LVL1 has accepted an event, the data are read out, formatted and initial preprocessing may be applied (*e.g.* calibration) before they are stored in readout buffers (ROBs) for use by the LVL2 trigger and the EF.

The LVL2 trigger is largely based on the use of regions of interest (RoIs). For each event accepted by LVL1, a small amount of information is passed to LVL2 corresponding to each object identified at LVL1. For local objects, such as muons and EM clusters, the information provided is position (η, ϕ) and p_T threshold range. These RoIs flag the regions that need to be analysed further by higher-level triggers. Also provided by LVL1 are the components of the missing-E_T vector and the total scalar E_T value, as well as information on the criteria that led to the event being selected.

LVL2 processors perform local evaluation of the objects identified at LVL1 using the fine-grained detector data in a window around the position indicated by the RoI. Thus, usually only a small fraction of the event data need to be moved from the ROBs to the designated processor, thereby reducing the required bandwidth and processing power at LVL2.

11.2.3 LVL2 data collection and feature extraction

At LVL2 each RoI is examined in the detector system from which it originated, *i.e.* in the muon or calorimeter system, to see if it is confirmed as a valid object. After the confirmation of the LVL1 RoI, additional features associated with it may be searched for in other detectors, such as the SCT/Pixel and TRT. This is the case for muon, EM cluster and τ RoIs. Jet RoIs are only processed in the calorimeters, with the possible exception of *b*-jet tagging, which requires tracking detectors to evaluate the impact parameters of tracks.

The information from all systems is then combined to form more specialised global trigger objects, which become candidates for muons, electrons, photons, τ's, and jets, as well as generalised missing-E_T and *B*-physics objects. These LVL2 global objects form the input to the LVL2 global decision. An average processing time of ~10 ms per event is currently assumed for the LVL2 trigger.

Processing of *B*-hadron events is different from standard RoI processing. *B*-hadron events are triggered by a low-p_T single muon at LVL1. This muon is then confirmed at LVL2 in the muon spectrometer and the Inner Detector. For events retained after this initial selection, a full track search must then be performed to allow decisions based on semi-exclusive *B*-event hypotheses. The present strategy is to search for tracks in the TRT with very low p_T thresholds. The resulting TRT tracks are used to define additional RoIs (so-called LVL2 RoIs) that guide further track searches in the SCT. The reconstructed SCT tracks, giving information in three dimensions, allow for the calculation of invariant masses; they may be extrapolated into the calorimeter or Muon Systems to confirm low-p_T lepton candidates, in conjunction with the transition–radiation signature from the TRT in the case of electrons.

The RoI information from LVL1 gives the position of the object with a typical resolution ranging from about $\Delta\eta \times \Delta\phi = 0.1 \times 0.1$ (leptons and photons) to about 0.4×0.4 (jets) in pseudorapidity–azimuthal angle space. The area over which the LVL2 algorithms require data is generally larger than this and has to be adapted to the detector system in question and to the algorithms applied at LVL2. For example, for validation of EM clusters in the calorimeters a region of at least about 0.3×0.3 is needed.

11.2.4 Event Filter

The final online selection step is performed by the EF. Here the full event is collected from the different data sources (ROBs) and the EF operates on the complete event using the full-granularity of the detector. The processing time is of the order of seconds. A refined reconstruction is possible using offline-like algorithms, though calibration and alignment constants are not the final ones. Vertex reconstruction and track fitting, including bremsstrahlung recovery for electrons, are examples of algorithms that could be executed at this level. Other examples are operations that require larger RoIs than those used at LVL2, such as γ conversion searches or calculations requiring the complete event data, as is the case for missing E_T. The LVL1 and LVL2 results will guide the EF processing chain, in a mode that is similar to the guidance of LVL2 by LVL1 RoIs. The EF completes the classification of the events, establishes a catalogue of discovery-type events ('express line'), and stores accepted events in the database. Events may be directed to separate output streams, for example if they are needed for calibration or alignment purposes only. Details of the EF are described in [11-4].

11.2.5 Trigger objects and the trigger-decision chain

11.2.5.1 Trigger objects

Through the selection chain from LVL1 to the EF, the trigger objects are progressively refined and made more specific. New trigger objects may be added at LVL2 and in the EF. Trigger objects are combined in 'physics menus': lists of selection criteria which will be described in more detail in Section 11.7. The following sections introduce the essential features of the objects and

describe the global decisions at LVL1 and LVL2. Detailed selection criteria at the level of individual objects are presented in [11-1] and are summarised in Sections 11.3.1 and 11.3.2 for the LVL1 trigger, and in Sections 11.4 to 11.6 for the LVL2 triggers.

LVL1 objects are characterised by a small number of attributes and a set of discrete p_T-threshold values. They are listed in Table 11-1 together with the corresponding pseudorapidity coverage. The number of thresholds is six for the muon trigger; sixteen thresholds are shared between the EM cluster and τ/hadron calorimeter triggers, eight thresholds are used for the E_T^{miss} trigger and four for the total scalar E_T trigger. More precisely, the 'thresholds' of the EM cluster trigger and the τ/hadron trigger each consist of a triplet of thresholds – cluster E_T threshold, and two isolation thresholds for EM and for hadronic E_T depositions. The isolation requirement is relaxed with increasing E_T or for two-cluster triggers; no isolation requirement is made for the highest EM E_T threshold.

LVL1 trigger selections are normally independent of the pseudorapidity, though simple topological requirements can be imposed. For example, jets that pass a given threshold may be required to be produced at central pseudorapidities. A trigger selecting large energy deposition in the forward regions ($|\eta| > 3.2$) is under consideration.

The LVL1 trigger ensures that trigger objects of the same type are not double counted. Overlaps between different trigger categories, however, are not resolved at LVL1. For example, an energetic electron may pass simultaneously as an EM cluster, a τ and a jet trigger. Two muons, if unbalanced in E_T, may give a missing-E_T trigger. Such redundancies are useful for monitoring the trigger. The overlaps are taken into account in the global decision at LVL2. No communication between the systems is available at LVL1. Thus for example, isolation cannot be required for muons.

In addition to the trigger RoIs, LVL1 may indicate other RoIs, typically at lower thresholds. These so-called secondary RoIs do not contribute to the trigger decision at LVL1. They are provided for possible analysis at LVL2 or in the EF and may contribute to the classification of an event.

Table 11-1 LVL1 objects and their attributes in addition to E_T. Tables 11-1 and 11-2 introduce the mnemonics for trigger objects used in the trigger menus, see Section 11.7. A total of 16 thresholds is available for EM and T objects combined.

Object	Number of thresholds	Isolation	$|\eta|$ range	description
MU	6	no	2.4	muon
EM	8 – 16	yes	2.5	EM cluster
T	0 – 8	yes	2.5	$\tau \rightarrow$ hadrons or single hadron
J	8	no	3.2	jet
XE	8	–	4.9	missing-E_T
SE	4	–	4.9	total scalar E_T

LVL2 objects are listed in Table 11-2. Their principal attributes are, as at LVL1, p_T threshold and isolation. The complete list of attributes attached to each trigger object is, however, much richer than at LVL1. For example, the EM cluster is described by its transverse energy in several windows, by its lateral and longitudinal shape and by several parameters that characterise the fine-

Table 11-2 LVL2 objects and attributes in addition to E_T. Additional attributes are discussed in Section 11.4.

Object	Attribute	$|\eta|$ range	Candidate for
μ	isolation	2.4	muon
e	isolation	2.5	electron
γ	isolation	2.5	photon
τ	isolation	2.5	$\tau \rightarrow$ hadrons
h	isolation	2.5	single hadron
j	b-tag ($|\eta| < 2.5$)	3.2	jet
xE	–	4.9	missing-E_T

grained information in the EM preshower compartment. The local features are combined to form global objects, *e.g.* the calorimeter information is combined with the information from the Inner Detector and the quantities that characterise the quality of matching between track and cluster.

The selection criteria may depend on parameters like pseudorapidity. Hence the fine adjustment of parameters in a multi-dimensional space is necessary to achieve optimal background rejection for the highest signal efficiency. Several varieties of electron candidates may be defined, as motivated by the class of physics processes[1]. In practice, simplicity and ease of monitoring are important criteria, which will limit the choice of algorithms, parameters and selection cuts. In Sections 11.4 to 11.6 the trigger algorithms are discussed together with the set of key selection criteria associated with each of these algorithms.

11.2.5.2 Global LVL1 and LVL2 decision

Trigger menus have been derived from the physics requirements. They classify the signatures such that a combination of trigger objects is sufficient to select events. Thresholds and attributes for the trigger objects are optimised to meet the requirements of high efficiencies and acceptable rates. An initial set of trigger menus for low- and high-luminosity running is presented in Section 11.7. Despite the large variety of physics available at the LHC, a short list of inclusive single and multi-object triggers, as well as a small number of combined triggers, are sufficient to cover the expected physics programme. These menus will evolve during the lifetime of the experiment, with improved understanding of the detector, development of technology and shifting physics interest.

The global decision at LVL1 and LVL2 is made by comparing the list of accepted trigger objects to the trigger menus. At LVL1, where the decision must be taken at a rate of 40 MHz, only a small amount of information can be transmitted to the central trigger processor (CTP), which combines the information from the muon and calorimeter triggers. A total of up to 96 menu items are foreseen for the CTP. The triggers are inclusive, and cover physics and detector monitoring, which must run continuously during physics data-taking.

---

1. This is similar to the choice of looser criteria for two-object triggers at LVL1.

The LVL2 strategy for confirming trigger objects is still under study [11-4]. Much effort is going into the development of algorithms and selection criteria to define trigger objects. Once these are defined, the final global decision is straightforward (except for processing of secondary RoIs, which is discussed below). At LVL2, in addition to requiring combinations of trigger objects, the menus may include functional decisions such as invariant-mass cuts, p_T-sum cuts, *etc*. Mass cuts are expected to be used for *B*-physics objects, and they could be applied wherever objects of known masses are part of the hypothesis, *e.g.* for leptonic decays of the Z^0.

Two different trigger objects may originate from the same physical object. For example, if a menu item requires an electron and a τ candidate, then both of these trigger objects could originate from the same high-p_T electron. The menus of Section 11.7 do not at present require such combinations and are hence sufficiently simple to ensure that such cases do not occur. For future extensions of the menus it will be necessary to ensure that such cases either add negligible rates or are correctly resolved. Algorithms will be needed to compare categories of objects and decide whether they have the same physical origin.

The use of secondary RoIs complicates the LVL2 decision logic, but may contribute to the classification of the events. These RoIs require an additional pass in the decision chain after the trigger RoIs have been confirmed. More studies are needed on the use of secondary RoIs at LVL2 or possibly by the EF. This issue is linked to the overall optimisation of LVL2 and the EF.

11.2.6 Specialised triggers

In addition to the triggers that are motivated by the physics programme, the same or specialised triggers at lower thresholds are needed to measure the trigger efficiency, and to monitor the detector and trigger performance. These include triggers for alignment and calibration. The requirements of the detector systems for such triggers are presently being assessed. Lower prescaled thresholds are also needed for certain physics studies, *e.g.* QCD.

11.3 LVL1 trigger

This section summarises the performance of the algorithms chosen for triggering at LVL1, and for delivering regions-of-interest to the LVL2 trigger. The choices of the algorithms and the hardware implementations are justified in [11-2].

11.3.1 LVL1 muon trigger

11.3.1.1 Trigger algorithms

The LVL1 muon trigger is based on the measurement of muon trajectories in three different planes (called stations). The trigger is described in detail in [11-2]. Muons are deflected by the magnetic field generated by the toroids; the angle of deflection depends on their momentum and the field integral along their trajectory. Coulomb scattering in the material traversed, and for low-p_T triggers, the energy-loss fluctuation, are also of importance.
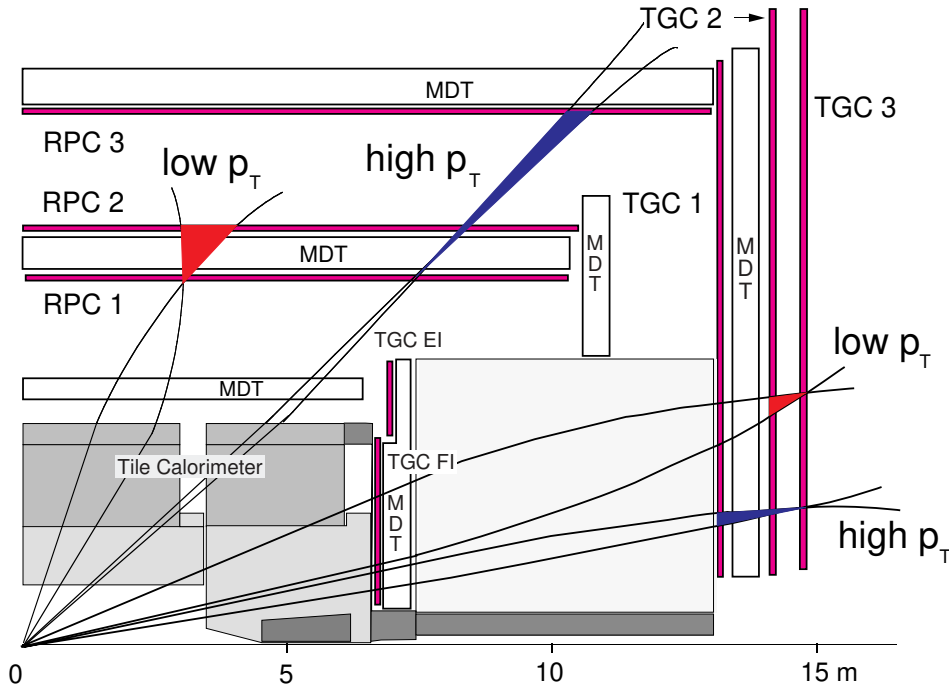
Figure 11-2 The LVL1 muon–trigger scheme.

The differences from a straight-line trajectory of an infinite-momentum track originating at the nominal interaction point are measured using three trigger stations, see Figure 11-2. The trigger plane farthest from the interaction point in the end-cap, and nearest to the interaction point in the barrel, is called the pivot plane. The two different lever arms from the pivot to the other two trigger planes provide two different measurements of the size of the deflection due to the field. The two different lever arms allow trigger thresholds to cover a wide range of transverse momenta with reasonably good resolution: the shorter lever arm (pivot plane and station 2) covers a lower-momentum range and the longer one (pivot plane and station 1 for the end-cap, pivot plane and station 3 for the barrel), a higher-momentum range.

Each hit found in station RPC1 (TGC3) is extrapolated to station RPC2 (TGC2) along a straight line through the nominal interaction point. A coincidence window is then defined around this point, where the window size depends upon the required p_T threshold. The low-p_T trigger condition is then satisfied if, for both projections, there is at least one hit within the coincidence window, and at least one of the two low-p_T stations has hits in both trigger planes satisfying the three-out-of-four logic

A similar procedure is performed for the high-p_T trigger, where the planes of RPC3 (TGC1) together with the pivot plane are used. The high-p_T trigger is satisfied if the track passes the low-p_T criteria, and in the barrel at least one hit in the two trigger planes of RPC3 are in coincidence, and in the end-cap if at least two of the three planes of TGC1 in the η view, and one of the two planes of TGC1 in the r–φ view are within the appropriate coincidence window.

The muon-trigger is divided into regions in η–φ where independent trigger windows can be used. The size of the coincidence window defines the p_T threshold applied in the trigger – the wider the window, the lower the threshold. Windows are defined such that efficiency at threshold is 90%. A tight time coincidence among hits is also required, to identify the bunch crossing.

11.3.1.2 Options to increase trigger robustness

To increase the flexibility of the trigger to cope with higher backgrounds, and in particular to offer additional robustness against backgrounds from the high flux of charged particles of momentum around 100 MeV (see Section 11.3.1.6), the trigger provides additional coincidence options [11-5].

- In both end-cap and barrel triggers the logic of the high-p_T trigger can be adopted for low-p_T thresholds through the use of all three trigger stations. Studies have shown that this is best achieved using the high-p_T planes TGC1 and RPC3 with appropriate window sizes for the low and high-p_T thresholds.

- In the end-cap an additional coincidence can be required in the planes of the inner TGC chambers, the EI and FI stations, see Figure 11-2.

- In the barrel, trigger electronics and logic are being designed such that signals from the Tile Calorimeter can be input to the trigger and used in coincidence with track candidates from the barrel muon trigger chambers. The Tile Calorimeter offers good separation of muons from hadrons, particularly in its outer depth sampling. Studies have demonstrated that a coincidence makes the trigger robust against the most pessimistic estimates of potential background [11-5]. The resulting rates are discussed in Section 11.3.1.6.

11.3.1.3 Trigger efficiency

The lower momentum limit for detecting a muon in the Muon System is set by the energy loss in the calorimeter and corresponds to $p_T \sim 3$ GeV in the barrel, but can be as low as $p_T \sim 1$ GeV in the end-cap. In order to evaluate the level of rejection of muons by the trigger system below a given trigger threshold, single muons over a wide range of momenta were generated in a Monte Carlo program and passed through the detector and trigger simulation programs. The trigger efficiency was evaluated as a function of p_T both for single muons and for muons in physics events, for the combined barrel and end-cap LVL1 trigger system. Since in some regions of the detector (notably in the end-cap) window size and trigger efficiency have some η dependence, the efficiency was evaluated as a function of η (integrated over φ). These calculations were performed for pseudorapidities covering the geometrical acceptance of the trigger system. The total trigger efficiency in the region |η| < 2.4, including geometrical losses, is 79% for 6 GeV muons in the low-p_T trigger with 6 GeV threshold, and 81% for 20 GeV muons in the high-p_T trigger with 20 GeV threshold.

The trigger efficiency was evaluated by simulating the trigger logic using the coincidence windows defined in Section 11.3.1.1. The efficiency, including geometrical acceptance effects, is given by the ratio of the number of triggered muons to the number of generated muons within the η fiducial region. The trigger efficiencies for the combined barrel and end-cap LVL1 system are shown in Figure 11-3 for the 6 GeV low-p_T, and the 20 GeV high-p_T thresholds.

11.3.1.4 Prompt muons and muons from π/*K* meson decays in flight

The rates for the LVL1 muon trigger were calculated by convolving the cross-section for muon production with the efficiency for a muon to trigger at LVL1. Muons from *b* and *c* hadrons, W and *Z* decays and from decays in flight of charged π and *K* mesons were considered. In the end-cap the convolution used four η bins to account for the significant η dependence of the cross-section.
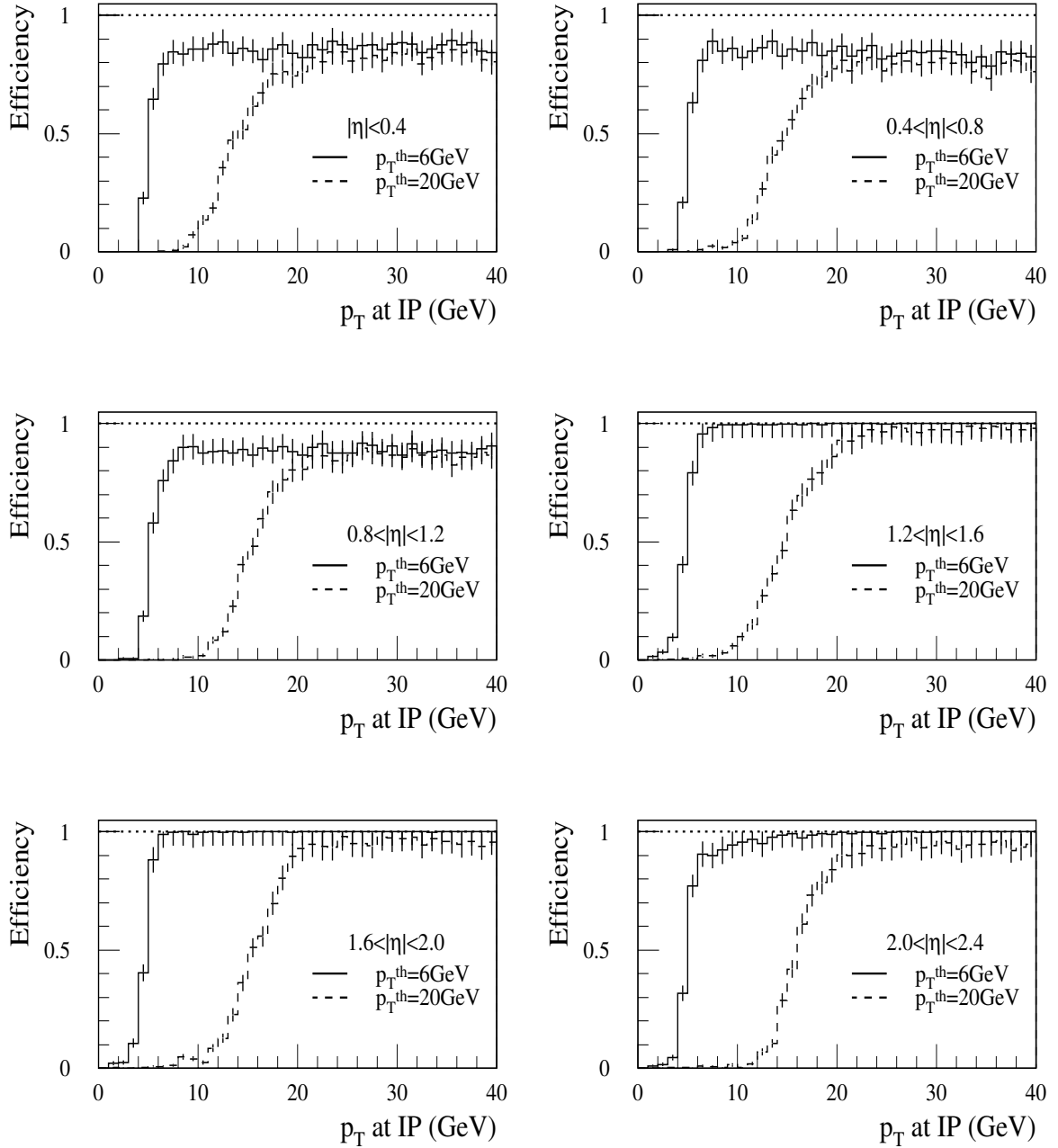
Figure 11-3 The efficiency of the LVL1 muon trigger as a function of p_T and for six pseudorapidity intervals, for the nominal low and high-p_T thresholds of 6 GeV and 20 GeV and the 'TDR trigger scheme' of Section 11.3.1.1. The p_T is given at the interaction point (IP).

The inclusive muon p_T spectrum is dominated, for transverse momenta below 8 GeV, by $\pi/K \rightarrow \mu\nu$ decays. Because of the steeply falling $d\sigma/dp_T$ spectrum, muons with p_T well below threshold still contribute significantly to the trigger rate, despite their low trigger acceptance. At higher p_T, muons from decays of B-hadrons are more abundant, and above 30 GeV $W \rightarrow \mu\nu$ decays dominate [11-6]. These rates were calculated using the PYTHIA Monte Carlo program [11-

7]. Because of the significant contribution of π/K decays to the trigger rate, these were calculated using the Monte Carlo program DPMJET [11-8] and using PYTHIA. The predicted rates were found to agree within 30%. The estimated rates are shown in Table 11-3.

Table 11-3 Trigger rates (kHz) expected in the barrel, end-cap and combined Muon System arising from various physics processes. These rates are calculated by convolving the single muon cross-section from each proton–proton process with the efficiency of the LVL1 trigger for single muons. The low-p_T rates assume a luminosity of 10^{33} cm^{-2}s^{-1} and the high-p_T rates a luminosity of 10^{34} cm^{-2}s^{-1}. The Monte Carlo program DPMJET was used for the rates from π/K decays.

Threshold	Process	Barrel	End-cap	Combined system
Low-p_T (6 GeV)	π / K decays	7.0	9.8	16.8
	b	1.9	2.1	4.0
	c	1.1	1.3	2.4
	W	0.004	0.005	0.009
	Total	**10.0**	**13.2**	**23.2**
High-p_T (20 GeV)	π / K decays	0.3	1.8	2.1
	b	0.4	0.7	1.1
	c	0.2	0.3	0.5
	W	0.035	0.041	0.076
	Total	**1.0**	**2.9**	**3.9**

11.3.1.5 Muons from cosmic rays and beam halo

Despite the significant depth at which the ATLAS experiment is located, cosmic rays contribute to the trigger rate in the Muon System. The ATLAS cavern is located about 75 m underground and access is available through two parallel shafts about 60 m deep, and 9 m and 12.6 m in diameter. The cosmic ray rate arises largely from these access shafts. By normalising the incident cosmic rate to 100 Hz/m² (the approximate rate of the muon component at sea level), a trigger rate in the low-p_T system below 150 Hz was found. The corresponding rate for the high-p_T system is much lower (< 10 Hz). These rates are two orders of magnitude less than those from muon triggers from *pp* collisions, but still sufficient to be useful for the calibration and alignment of the detectors in the barrel region.

A study of muons produced in interactions between the LHC beam and the machine components has been performed for the CMS experiment using a detailed simulation of such processes [11-9]. The differences between the beam conditions in ATLAS and CMS are sufficiently minor that this simulation is also relevant for ATLAS. The interactions modelled are those of a beam of 530 mA at 7 TeV at high luminosity, with all machine components within 1000 m of the interaction point simulated. The particles produced in these beam-machine interactions are passed through the detector and trigger simulation to estimate the resulting trigger rate in the LVL1 end-cap muon trigger [11-10]. The rates from the estimated muon flux are negligible in comparison with the rate from interaction products, and can contribute significantly to the trig-

ger rate only if the halo rate is underestimated by a factor ten; in this instance the rate is still tolerable. The halo rates are, however, sufficient to be useful for the calibration of the end-cap trigger and for timing studies.

11.3.1.6 Fake muon trigger from hadronic debris

A large background flux is expected in the experimental cavern at the LHC due to the interaction of hadrons (produced in *pp* collisions) with the forward elements of the ATLAS detector, the shielding system and machine elements. The particles produced in such secondary interactions and their decay products can induce high counting rates in the muon trigger system. Here the resulting trigger rate is estimated for the trigger scheme presented in Section 11.3.1.1 and [11-2] ('TDR scheme'). The rate reduction achieved for the more robust scheme (Section 11.3.1.2) is discussed in the next section. The background flux seen in the trigger chambers was evaluated using the FLUKA Monte Carlo program [11-11], which provides a better treatment of low-energy particles down to thermal energies, than the standard ATLAS detector simulation.

Particles of low energy (up to 10 MeV) include mainly soft Compton electrons and neutron-induced soft protons. Such particles produce hits in a single trigger counter (*i.e.* no correlation between trigger planes). This incoherent background was shown to produce triggers at rates much below those expected from *pp* collision products [11-2]. The dominant contribution to the fake low-p_T trigger rate in both barrel and end-cap arises from the coincidence of a pair of hits from a penetrating particle in one of the low-p_T stations, with one or more hits deposited by any other particle. The fake high-p_T trigger rate is dominated by a low-p_T trigger in coincidence with any other hits (or track) in the high-p_T station of the barrel or end-cap.

Harder particles (of momenta above 10 MeV) can give rise to hits in more than one plane of trigger detectors, and thus fake a muon trigger. The majority of such triggers are due to muons of momentum around 100 MeV, arising directly or indirectly from the decay of neutral kaons (*e.g.* $K_L^0 \rightarrow \mu\pi\nu$). This background is therefore called the '100 MeV background'. The K_L^0 flux is produced by interactions of secondaries with the material of the detector, and the forward shielding. The probability for the K_L^0 decay particles with momenta ~100 MeV to give a trigger in the LVL1 system, was calculated by simulating the response of the detector and trigger. The particles generated by FLUKA, which impact on the planes of the trigger detectors, were passed through the standard detector and trigger simulation programs. The resulting fake trigger rates are listed in Table 11-4.

Performance of the improved LVL1 muon trigger

The additional options in the muon trigger discussed in Section 11.3.1.2 have been simulated to demonstrate the gain in trigger robustness against charged particles of momentum ~100 MeV in the ATLAS cavern, as modelled by the FLUKA Monte Carlo program.

The use of the full (three station) logic of the trigger for the low-p_T 6 GeV threshold trigger reduces the expected rate in the end-cap by a factor 4, and in the barrel by a factor ~10. This change requires only minor modification of the trigger electronics and adds considerable robustness.

The additional requirement in the end-cap trigger of a coincidence in the TGC chambers of the EI and FI stations prevents any triggers from muons with momentum too low to penetrate the end-cap toroid, and thus removes triggers from ~100 MeV muons. The occupancy in these chambers then determines the expected trigger rate from accidental coincidences. Depending on the exact form of coincidence, preliminary studies suggest that the probability to validate a fake trigger is approximately 0.7% for low luminosity running (6 GeV threshold) and 0.25% at high luminosity (20 GeV threshold). Such probabilities translate to low trigger rates (see Table 11-4).

Table 11-4 Rates expected in the LVL1 muon trigger from 100 MeV muon flux in the cavern, for various trigger schemes. Safety factors are not taken into account.

	Rate (kHz)	
	low-p_T (6 GeV)	high-p_T (20 GeV)
end–cap		
TDR scheme	7.8	6.4
three station logic	1.8	6.4
coincidence with EI/FI	0.05	0.02
barrel		
TDR scheme	6.8	<1.0
three station logic	0.5 – 1.0	<1.0
coincidence with Tile Calorimeter	<0.27	<0.04

In the barrel, a preliminary study of the stand-alone muon identification capability of the Tile Calorimeter indicates that the probability for a hadron to fake a muon signal in the calorimeter is low [11-12]. In an additional study a single muon of 20 GeV was added to pile-up events corresponding to high luminosity. The E_T deposited in a cone ($\Delta\eta \times \Delta\phi = 0.4 \times 0.3$) around the muon and the E_T in a cone not containing the muon was compared for two cases: summation of all samplings in depth or using only the outer sampling. For a muon efficiency of 99% the probability to fake a muon signal was found to be ~1% in both cases (see Section 5.3.3).

The efficiency of the more robust trigger for both low and high-p_T thresholds is comparable to that of [11-2] – the criterion of 90% acceptance of muons at these thresholds is largely maintained. Use of the EI and FI chambers of the TGC in the LVL1 trigger will reduce efficiency below 90% in some regions due to the incomplete ϕ coverage of the forward chambers. The expected rates arising from fake muons in the improved trigger schemes are listed in Table 11-4. These values are tolerable in terms of the maximum rate which the LVL1 and LVL2 triggers can accept, even allowing for safety factors of ~10. Uncertainties in these rates arise largely from assumptions made in the Monte Carlo simulation used to model the backgrounds, and are estimated to be smaller than this safety factor. Additional substantial uncertainties are due to statistical uncertainties arising from the weighting procedure for the Fluka Monte Carlo sample.

In conclusion, if backgrounds are as predicted by the Monte Carlo, it will be sufficient to use only the three-station logic, low-p_T trigger scheme in both barrel and end-cap. The option of including the EI/FI coincidence in the end-cap and the Tile coincidence in the barrel provides a very robust trigger.

11.3.2 LVL1 calorimeter triggers

The input to the calorimeter LVL1 algorithms are a set of 'trigger towers' of granularity 0.1×0.1 in $\Delta\eta\times\Delta\phi$. These are formed by analog summation of calorimeter cells. There are separate sets of trigger towers for EM and hadronic Calorimeters [11-2]. Truncating the digitised values for the tower energies to eight bits effectively applies a 1 GeV threshold to each trigger tower.

11.3.2.1 Electron/photon trigger

The LVL1 electron/photon trigger algorithm is based on a window of 4×4 towers in the electromagnetic and hadronic calorimeters in the region $|\eta| < 2.5$, and consists of four elements:

- a 2×2-tower EM cluster, used to identify the position of candidate RoIs (local E_T maximum);

- a 2×1 or 1×2-tower EM cluster, used to measure the E_T of EM showers – there are four such regions within the RoI cluster, and the most energetic of these is used;

- a ring of 12 electromagnetic towers surrounding the clusters, which is used for isolation tests in the EM Calorimeter;

- the 16 hadronic towers behind the electromagnetic clusters and isolation ring, which are used for isolation tests in the hadronic calorimeters.

The window slides in steps of one trigger tower in both the η and ϕ directions.

It is foreseen that electron/photon candidates may contribute to the LVL1 trigger in three ways: as inclusive triggers, where at least one signal above a given threshold is sufficient to cause an event to be accepted; in electron/photon multiplicity triggers, *e.g.* dielectron/diphoton triggers; and in combination with other trigger inputs, *e.g.* electron and missing-E_T or electron and muon.
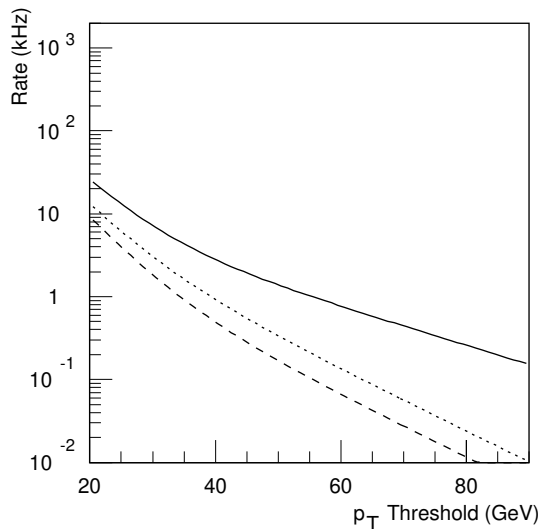
Figure 11-4 Inclusive electron trigger rate for luminosity 10^{33} cm^{-2}s^{-1}, without isolation (solid), requiring only hadronic isolation (dotted) and requiring both electromagnetic and hadronic isolation (dashed).
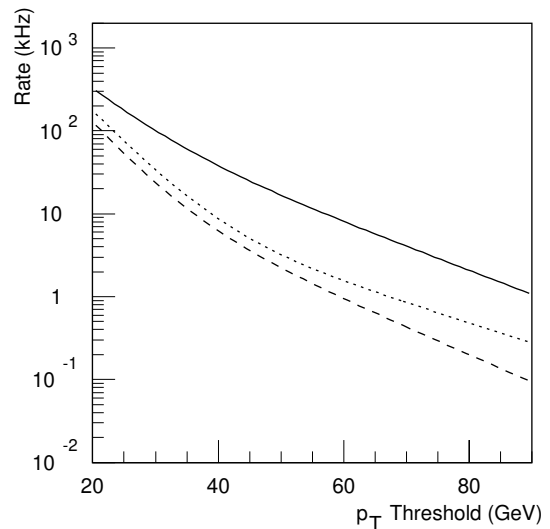
Figure 11-5 Inclusive electron trigger rate for luminosity 10^{34} cm^{-2}s^{-1}, without isolation (solid), requiring only hadronic isolation (dotted) and requiring both electromagnetic and hadronic isolation (dashed).
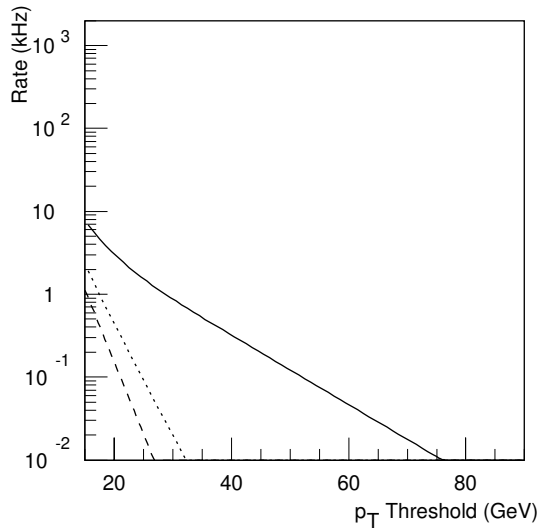
Figure 11-6 Electron/photon pair trigger rate for luminosity 10^{33} cm^{-2}s^{-1}, without isolation (solid), requiring only hadronic isolation (dotted) and requiring both electromagnetic and hadronic isolation (dashed).
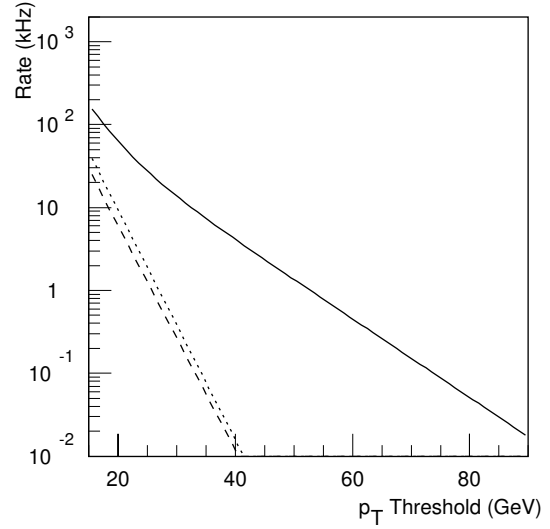
Figure 11-7 Electron/photon pair trigger rate for luminosity 10^{34} cm^{-2}s^{-1}, without isolation (solid), requiring only hadronic isolation (dotted) and requiring both electromagnetic and hadronic isolation (dashed).

Figures 11-4 and 11-5 show the estimated inclusive trigger rates as a function of the actual trigger threshold for 95% electron efficiency at the threshold value, for luminosities of 10^{33} cm^{-2}s^{-1} and 10^{34} cm^{-2}s^{-1}. Each plot shows the rate without isolation, using only hadronic isolation, and using both electromagnetic and hadronic isolation. Figures 11-6 and 11-7 show similar distributions for a dielectron/diphoton trigger. In these, the isolation cuts were chosen to give 95% efficiency for triggering on the pair, rather than a single electron or photon.

There is a dependence of isolation E_T on electron/photon E_T, and so one would not require the same isolation thresholds for different values of cluster E_T. Also, since the trigger rate falls quite rapidly with increasing cluster E_T, there is no need to require stringent isolation for higher-E_T clusters, as the effect on trigger rate is negligible. It is therefore anticipated that the isolation requirements will be progressively loosened with increasing cluster E_T. An example of this is shown in Table 11-5 for low luminosity, and in Table 11-6 for high luminosity.

Table 11-5 An example of how isolation criteria might be progressively loosened with increasing E_T for luminosity 10^{33} cm^{-2}s^{-1}. The total rate is less than the sum of the parts due to overlaps between the different selections. The thresholds listed are those actually applied and are lower than the 'nominal trigger threshold' to guarantee 95% efficiency above the 'nominal threshold'.

Trigger selection	Threshold	Isolation	Rate
≥ 1 electron/photon	$E_T > 17$ GeV	EM + hadronic	11 kHz
≥ 1 electron/photon	$E_T > 35$ GeV	hadronic	1.2 kHz
≥ 1 electron/photon	$E_T > 60$ GeV	none	0.6 kHz
≥ 2 electron/photons	$E_T > 12$ GeV	EM + hadronic	1.4 kHz
≥ 2 electron/photons	$E_T > 20$ GeV	hadronic	0.1 kHz
≥ 2 electron/photons	$E_T > 35$ GeV	none	0.3 kHz
Total trigger rate			**13 kHz**

Table 11-6 An example of how isolation criteria might be progressively loosened with increasing E_T for a luminosity 10^{34} cm^{-2}s^{-1}. The total rate is less than the sum of the parts due to overlaps between the different selections.

Trigger selection	Threshold	Isolation	Rate
≥ 1 electron/photon	$E_T > 26$ GeV	EM + hadronic	21.5 kHz
≥ 1 electron/photon	$E_T > 45$ GeV	hadronic	2.6 kHz
≥ 1 electron/photon	$E_T > 75$ GeV	none	3.0 kHz
≥ 2 electron/photons	$E_T > 15$ GeV	EM + hadronic	5.2 kHz
≥ 2 electron/photons	$E_T > 25$ GeV	hadronic	0.4 kHz
≥ 2 electron/photons	$E_T > 45$ GeV	none	1.5 kHz
Total trigger rate			**29.2 kHz**

11.3.2.2 τ / hadron trigger

The LVL1 τ/hadron trigger can be implemented at relatively little additional cost, using the same input and much of the same logic used for the electron/photon trigger. The algorithm starts from a 4×4 trigger-tower block and requires that the central 2×2 trigger-tower block, summing over EM and hadronic layers, contains more E_T than any of the other eight possible 2×2 tower blocks in the same 4×4 window. This 2×2 block slides by 0.1 in both η and ϕ direction. The core energy is defined as the maximum energy in a 2×1 EM region (within the 2×2 area) plus the 2×2 hadronic block.

For the isolation definition, the 12 trigger towers surrounding the 2×2 core are used, summing the towers in the EM and hadronic Calorimeters separately. The isolation in τ events was compared to that in jet events separately for the EM and hadronic layers. The EM isolation is much more powerful than the hadronic one. The isolation sum in the hadronic layer may also be used, but its discrimination power is not very large.

In order to evaluate the efficiency as a function of E_T, the summed E_T of the hadronic daughters of the τ was used rather than the E_T of the τ itself. The efficiency for the τ events versus this τ hadronic E_T is depicted in Figure 11-8 for a low and a high threshold.

Figure 11-9 shows the absolute trigger rate that would result from using the τ/hadron trigger in a stand-alone way as a function of core-E_T threshold, assuming a luminosity of 10^{33} cm^{-2}s^{-1}. The effect of pile-up has been neglected. The figure shows the rate with and without an electromagnetic isolation cut, where two possibilities are indicated for the dependence of such an isolation cut on the core threshold. The first possibility is no dependence – *i.e.* a fixed cut, while the second possibility is a direct proportionality with the core threshold. The optimal choice probably lies somewhere in between these extremes.

11.3.2.3 Jet trigger

Jet production is expected to be the dominant hard process at the LHC. Unlike the electron/photon and τ/hadron triggers, the main requirement on the jet trigger is therefore not that it should discriminate between two different types of objects, but rather that it should discrimi-
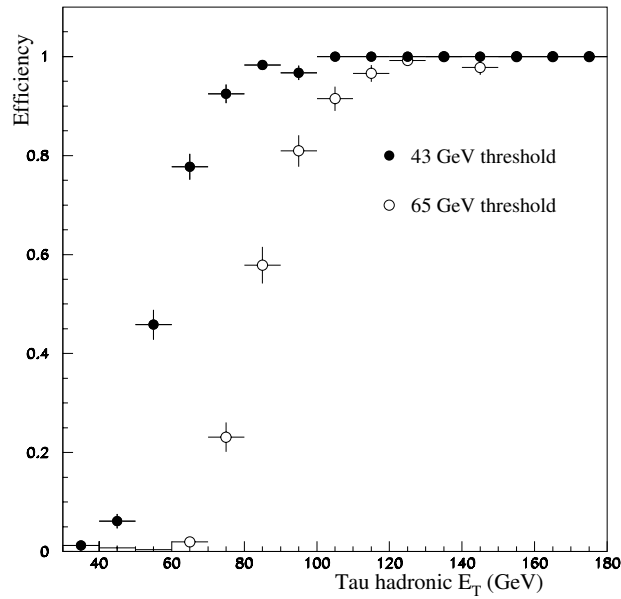
Figure 11-8 Efficiency versus τ hadronic E_T (in GeV) for a low and a high threshold as indicated. No isolation was required.
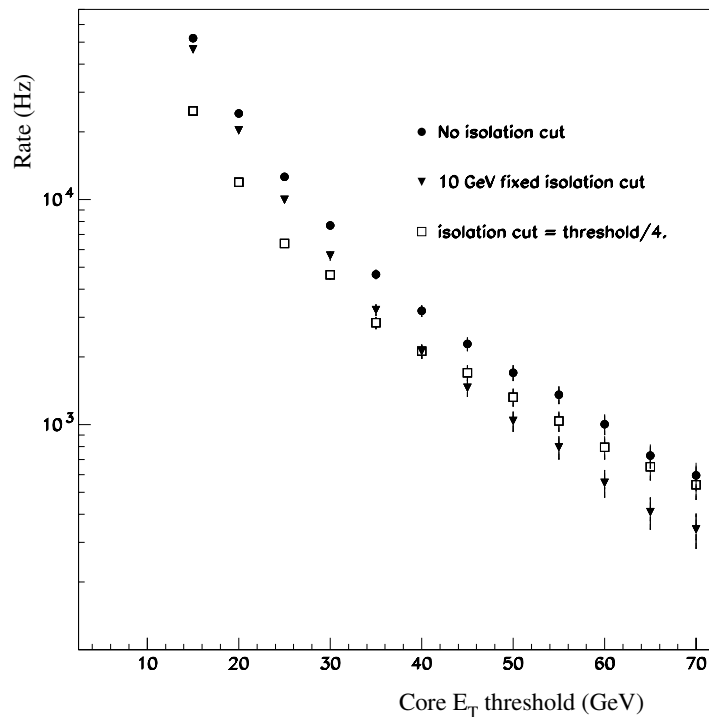
Figure 11-9 Trigger rate vs core-E_T threshold for an inclusive τ trigger, assuming a luminosity of 10^{33} cm^{-2}s^{-1} neglecting pile-up. The effect of using an electromagnetic isolation requirement is indicated.

nate on the basis of the E_T and multiplicity of jets. Only when trying to flag the lowest–E_T jets (20–40 GeV) as secondary RoIs for LVL2, is the question of background from other sources (noise and pile-up) expected to be relevant.

For most of the studies a 'fast' simulation was used. This included a realistic model of the electronics effects, preprocessing and trigger algorithms, but lacked the detailed simulation of the detector and material. This model allowed large, high-E_T datasets to be produced easily. Cross-checks were performed using the full GEANT-based simulation, particularly in the area of low-E_T jet performance, see Section 9.1.

A problem with jet trigger studies is that there is no unique definition of what constitutes a 'jet'. Hence one must use a particular jet-finder as a 'reference' against which the trigger algorithms are compared. Fixed-cone algorithms are widely used, but relying on one of these as a reference carries the risk that it would bias studies of the optimum cluster size. For this reason, both a fixed cone algorithm (with $R = 0.4$) and a k_T algorithm [11-13] were used as references for comparison with the trigger algorithms. The plots shown are for the k_T algorithm, but the results did not significantly depend on which algorithm was used.

The jet trigger algorithm is based on a window of 'jet elements', which have a granularity of 0.2×0.2 in $\Delta\eta \times \Delta\phi$ and are summed in depth between the EM and hadronic Calorimeters. The algorithm has two components, consisting of a 2×2-element cluster, used to identify the position of candidate jet RoIs (local E_T maximum), and a trigger cluster, used to measure the jet E_T. This cluster can be 2×2, 3×3 or 4×4 jet elements (0.4×0.4, 0.6×0.6 or 0.8×0.8 in $\Delta\eta \times \Delta\phi$), where the choice is programmable separately for each threshold setting. The window slides in steps of 0.2 (one element) in both the η and ϕ directions for $|\eta| < 3.2$.

The optimum size of the jet cluster depends on both the jet E_T and the luminosity. The resolution for high-E_T jets at low luminosity is dominated by the containment of the jet E_T within the cluster, favouring a larger cluster. Conversely, when flagging low-E_T jets, especially at high luminosity, the amount of electronic and pile-up noise within the jet cone is the limiting factor in jet trigger performance. For this reason, a flexible system is foreseen, in which different jet cluster sizes may be used simultaneously at different E_T thresholds, allowing optimisation of different jet selections for different purposes. Table 11-7 summarises the jet cluster sizes which are recommended for different jet trigger types; for a detailed discussion see [11-1], Section 6.4.

Table 11-7 Recommended window sizes for different jet trigger types.

Trigger type	Jet cluster size
high-E_T single jet trigger	0.8×0.8
low-E_T single jet trigger	0.4×0.4
multi-jet trigger (≥ 3 jets)	0.4×0.4

Figure 11-10 shows the threshold efficiency curves for 100 GeV E_T jets for different cluster sizes, at a luminosity of 10^{33} cm^{-2}s^{-1}. Such jets are of interest for the inclusive jet trigger at this luminosity. As can be seen, the threshold sharpness for jets of 0.6×0.6 and 0.8×0.8 is very similar, while the smaller 0.4×0.4 cluster produces a much softer threshold. Figure 11-11 shows the dependence between efficiency for these jets and the inclusive trigger rate for the same algorithms. From this it can be seen that the larger clusters produce a lower rate when high efficiency is required. The same quantities are shown in Figures 11-12 and 11-13 for 200 GeV E_T jets at the high luminosity of 10^{34} cm^{-2}s^{-1}. Again, a larger cluster size is favoured.
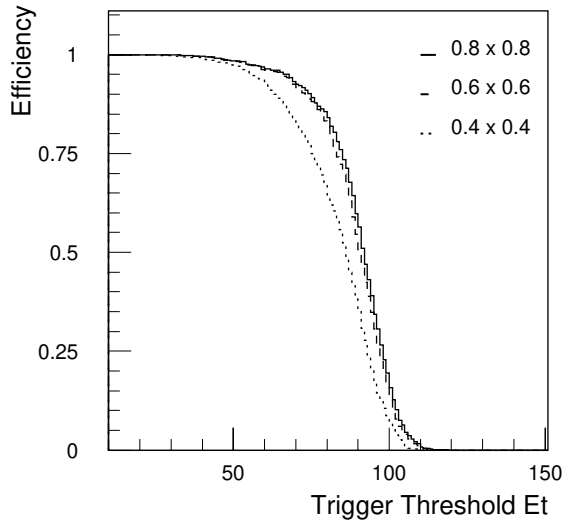
Figure 11-10   Jet trigger efficiency curves for 100 GeV E_T jets, for different cluster sizes, at luminosity 10^{33} cm^{-2}s^{-1}. The efficiency is shown as function of the actual trigger threshold (in GeV).
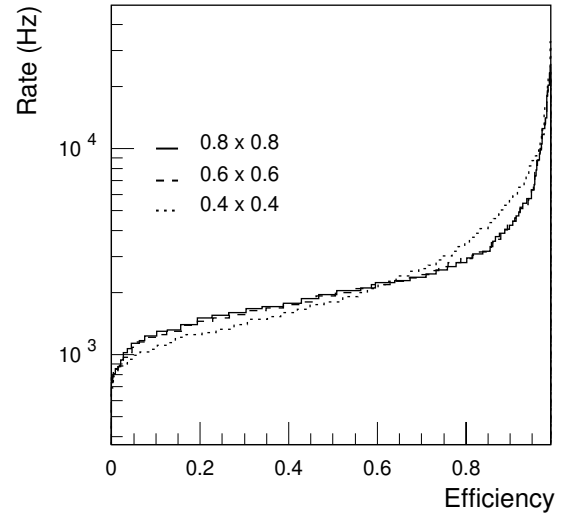
Figure 11-11   Trigger rate versus efficiency for 100 GeV E_T jets, for different cluster sizes, at luminosity 10^{33} cm^{-2}s^{-1}.
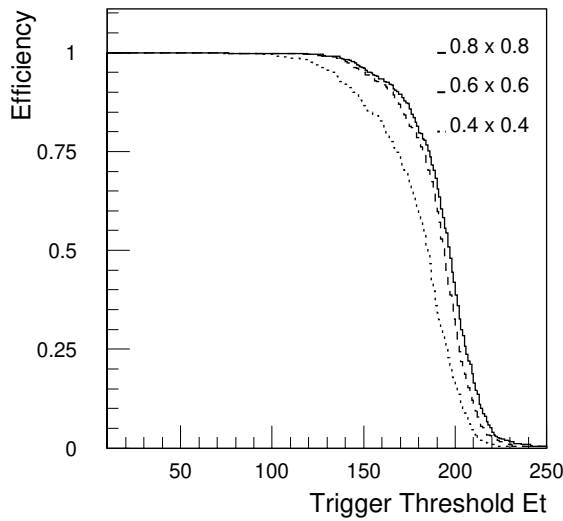
Figure 11-12   Jet trigger efficiency curves for 200 GeV E_T jets, for different cluster sizes, at luminosity 10^{34} cm^{-2}s^{-1}.
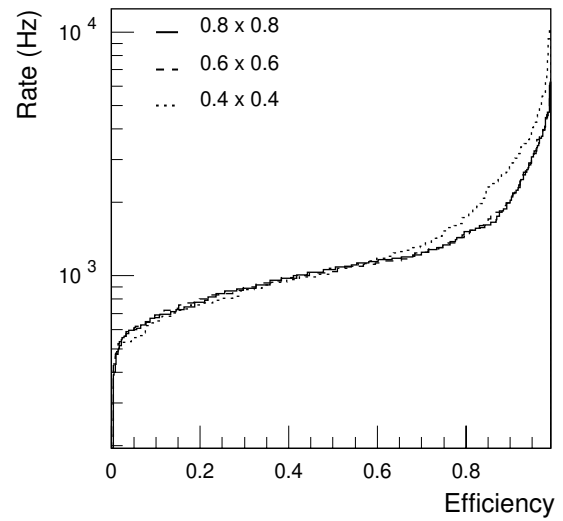
Figure 11-13 Trigger rate vs. efficiency for 200 GeV E_T jets, for different cluster sizes, at luminosity 10^{34} cm^{-2}s^{-1}.

While the resolution for inclusive high-E_T jets depends primarily on the trigger cluster size, the RoI coordinate resolution and the ability to resolve nearby jets depend on the step size and RoI definition. Better resolution is obtained from a smaller RoI cluster. The smaller RoI cluster also results in a higher efficiency to resolve nearby jets. This affects the acceptance of a multi-jet trigger, and the ability to count jets in events with complex topologies.

In addition to providing signals for use in inclusive jet triggers, multi-jet triggers, and combined triggers (such as jet and missing-E_T), the jet trigger system should flag 'secondary jet RoIs' which might be useful for more refined event selections at LVL2. Such jets are of lower E_T. It is important to understand the ability of LVL1 to flag very low-E_T jets. Figure 11-14, shows the efficiency for the trigger to find an RoI matched to a reference jet as a function of jet E_T, for a trig-

ger threshold chosen to give an average RoI multiplicity in electron/photon-triggered events (assumed to dominate in the LVL1 trigger rate over jet triggers) of about three RoIs/event for a luminosity of 10^{33} cm^{-2}s^{-1}. It suggests that efficient identification of 20 GeV jet RoIs might be possible at low luminosity, but lower-E_T jets would be difficult. Figure 11-15 shows similar distributions at 10^{34} cm^{-2}s^{-1}. Here, the use of a smaller cluster (0.4×0.4) is compared to the application of a threshold to the jet-element E_T, both done in order to suppress the contribution from pile-up. It can be seen that these techniques can improve the RoI efficiency at low jet E_T.
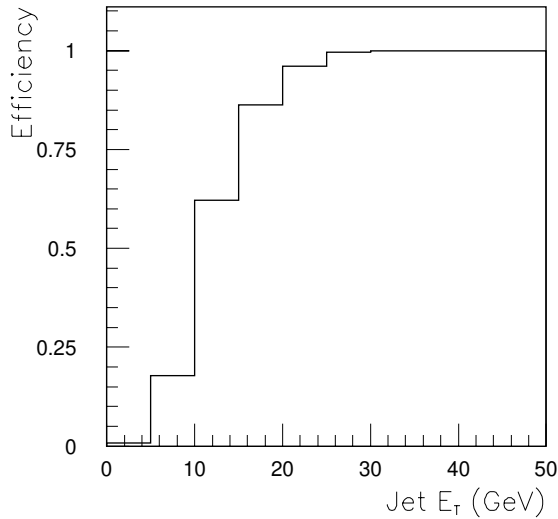
Figure 11-14 Efficiency to flag a jet RoI as a function of jet E_T. The trigger threshold was chosen to give an average RoI multiplicity in electron/photon-triggered events of about three per event. The algorithm used was a cluster of 0.8×0.8, sliding by 0.2 (luminosity 10^{33} cm^{-2}s^{-1}).
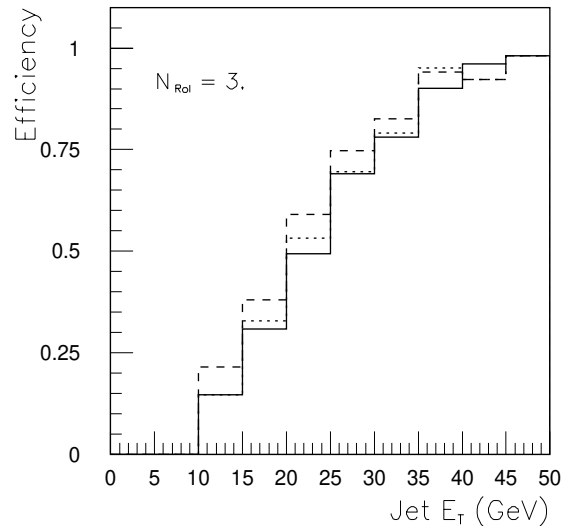
Figure 11-15 Efficiency to flag a jet RoI as a function of jet E_T, at luminosity 10^{34} cm^{-2}s^{-1}. The histograms compare a jet of 0.8×0.8 with no threshold on jet-element E_T (solid), the same cluster but using only elements with $E_T \geq 3$ GeV (dashed), and a jet of 0.4×0.4 (dotted).

The following figures demonstrate the overall performance of the jet trigger. Figure 11-16 shows the estimated inclusive jet trigger rates as a function of trigger threshold for the three window sizes, for luminosity of 10^{33} cm^{-2}s^{-1}. Similarly, the estimated three-jet trigger rates are shown in Figure 11-17. Trigger rates of around 1 kHz can be obtained for inclusive jet thresholds of 100-110 GeV at low luminosity or 190–200 GeV at high luminosity.

In fact, rates substantially lower than this may be required in the LVL1 jet trigger. This is because LVL2 can provide only a modest rejection against LVL1 jets, and so a few kHz LVL1 jet trigger rate would saturate the output of the LVL2 system unless additional criteria are applied at LVL2 to reject events. Allocating 200 Hz rate for each of the inclusive, three-jet and four-jet triggers, the resulting trigger thresholds at low and high luminosity are shown in Table 11-8.

11.3.3 Missing transverse energy and total transverse energy triggers

For the missing transverse energy and total transverse energy triggers the calorimeter energies are summed into a map with a granularity of $\Delta\eta\times\Delta\phi = 0.2\times0.2$, which is the same as for the jet processor for $|\eta| < 3.2$; the map for missing-E_T extends over the largest possible η range,
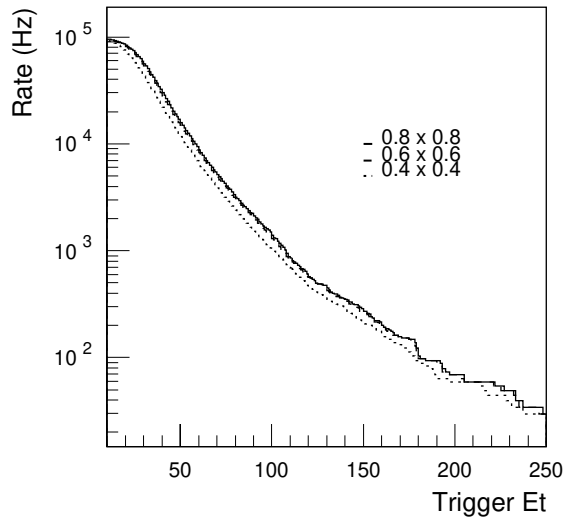
Figure 11-16 Inclusive jet trigger rates versus trigger E_T threshold (in GeV) at $L = 10^{33}$ cm^{-2}s^{-1}. Curves are shown for the three different cluster sizes available to the trigger and as functions of the actual trigger threshold.
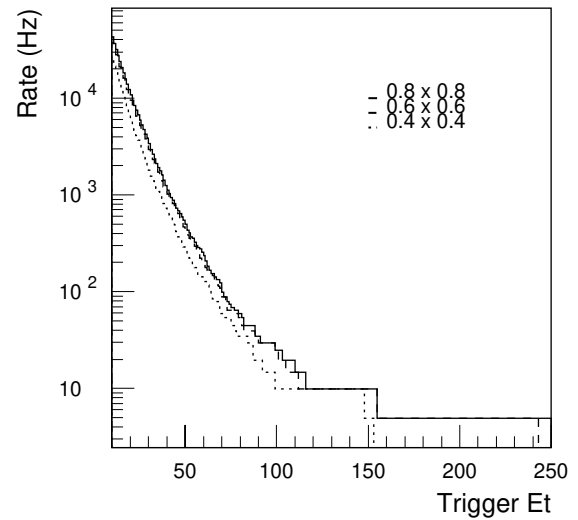
Figure 11-17 Three-jet trigger rates versus trigger E_T threshold at $L = 10^{33}$ cm^{-2}s^{-1}. The rates are shown as functions of the actual trigger threshold. The bins above 150 GeV contain very low statistics.

Table 11-8 Jet E_T thresholds for 200 Hz LVL1 trigger rate, for single, three and four-jet triggers, at low and high luminosity. The E_T threshold is the E_T of the jet for which the trigger is 95% efficient, with a 'jet' being defined as described in the text.

Trigger type	Low luminosity (10^{33} cm^{-2}s^{-1})	High luminosity (10^{34} cm^{-2}s^{-1})
Single-jet	$E_T > 180$ GeV	$E_T > 290$ GeV
Three-jets	$E_T > 75$ GeV	$E_T > 130$ GeV
Four-jets	$E_T > 55$ GeV	$E_T > 90$ GeV

$|\eta| < 4.9$. The total scalar E_T, as well as the components E_x and E_y in the plane transverse to the beam axis, are computed. Although the missing-E_T trigger itself is not included in the basic LVL1 inclusive triggers, its combination with the single-jet, electron/photon, and τ/hadron triggers is important to allow triggering on interesting events with low jet, e/γ or τ/h transverse-energy thresholds.

The missing-E_T resolution is dominated by the calorimeter resolution and response, and by the addition of electronic noise in the tower-builder electronics. The dependence of the resolution, represented by the rms of E_x, on the value of total scalar E_T, is shown in Figure 11-18. Truncating the digitised values for the tower energies to eight bits effectively applies a 1 GeV threshold to each trigger tower, which reduces the noise contribution to the resolution, which is important for low values of scalar E_T. The degradation observed at very high total E_T is due to the limit in dynamical range (256 GeV per trigger element) and has no impact on the physics since such events are selected anyway by other triggers.
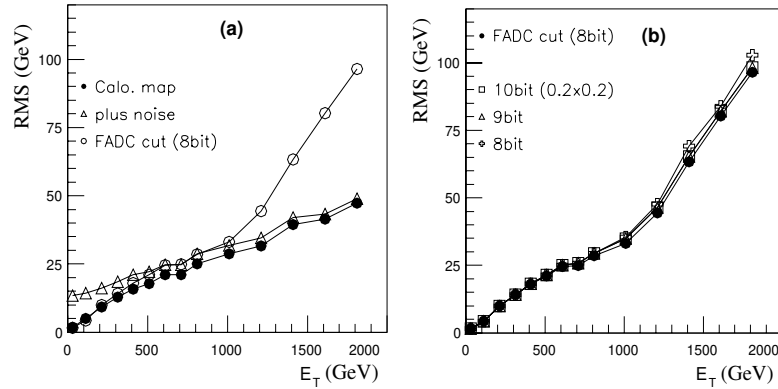
Figure 11-18 Dependence of the resolution of the E_x, E_y components of the total transverse momentum on total E_T. (a) after the trigger preprocessor, in comparison to the resolution obtained at the calorimeter level, using the trigger tower granularity for the E_T calculation; (b) after the transmission of the summed 0.2×0.2 element energies to the Jet/Energy-sum Processor, using 8, 9 (default), or 10 bits.

The inclusive missing-E_T trigger rate is dominated by QCD di-jet events and pile-up. At low luminosity the presence of pile-up (average 2.3 events) increases the trigger rate by about a factor five for $E_T^{miss} < 60$ GeV. Above about 100 GeV, low-luminosity pile-up has no influence. At high luminosity, however, the rate increases by a factor of ~10^3 at $E_T^{miss} \sim 100$ GeV, and by about a factor 10 at 200 GeV [11-14].

For processes with a genuine missing-E_T signature the combination of the E_T^{miss} trigger with the EM cluster and/or jet triggers allows reduction of the EM and/or jet thresholds. High signal efficiency can be retained at low luminosity for $W \rightarrow e\nu$ and $t\bar{t}$ events. For high luminosity the thresholds have to be raised, and rates are manageable only for signal efficiencies of about 50% for W and $t\bar{t}$. A trigger with a moderate E_T^{miss} threshold together with two jets, results in an efficient SUSY trigger, both at low and high luminosity. Details of combined triggers are discussed in [11-14]. Figure 11-19 demonstrates the usefulness of the E_T^{miss} signature for a trigger aimed at SUSY channels (SUGRA point 2 and 3, see Chapter 20) for low and high luminosity, respectively.

11.4 LVL2 RoI-guided triggers

11.4.1 Overview of algorithms

Higher-level triggers must reduce the LVL1 rate of up to 100 kHz to about 100 Hz, where the largest rejection is expected from the LVL2 trigger. The processing steps at LVL2 are as follows. Raw data associated with the RoIs indicated by LVL1 are collected and prepared. Feature extraction (FEX) is performed for each detector system, starting with the confirmation of the LVL1 RoI in the system from which it originated (Muon System or calorimeter), followed by confirmation in other systems, for example the tracking systems. Features from different systems are combined, to form identified LVL2 trigger objects, which are candidates for muons, electrons, photons, τ's, and jets, as well as generalised missing-E_T and B-physics objects. A global decision is taken based on trigger menus, see Section 11.7.3.
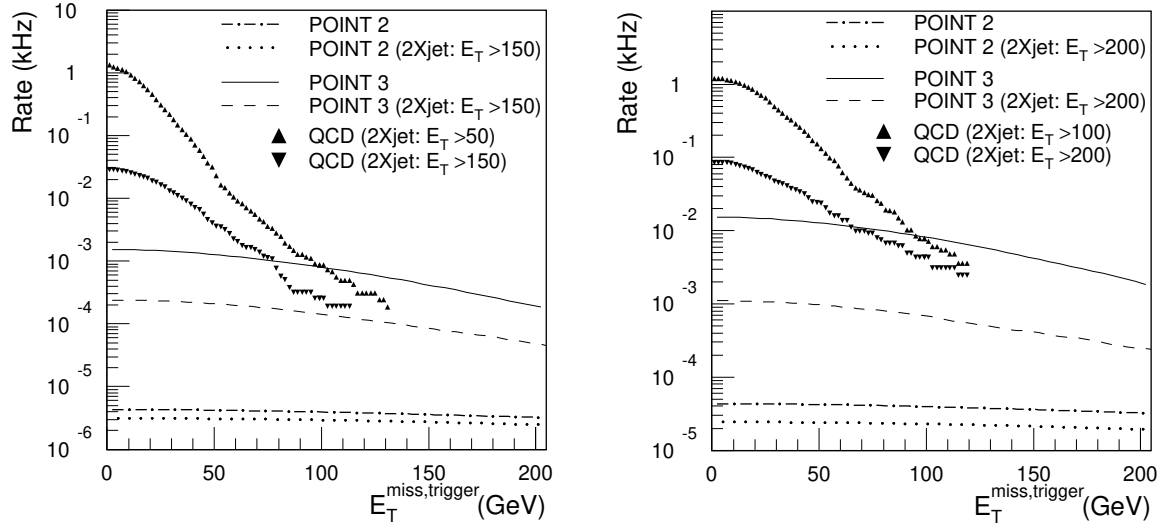
Figure 11-19 LVL1 inclusive E_T^{miss} and combined E_T^{miss}+jet trigger rates for two SUSY points and the QCD background jets. The rates are shown as function of the E_T^{miss} trigger threshold for low (10^{33} cm^{-2}s^{-1}) and high luminosity (10^{34} cm^{-2}s^{-1}) in the left and right figure, respectively.

An average processing time of ~10 ms per event is currently assumed for the LVL2 trigger. The FEX algorithms are at the heart of the LVL2 trigger processing. The performance obtained in efficiency and background-rejection power determines the overall performance of the LVL2 trigger. The data-collection and preprocessing step, which preceeds feature extraction, is important and may be time consuming, but the bulk of the algorithmic complexity lies in the feature extraction. The subsequent object-building step, as well as the global-decision algorithm, is comparatively simple. The special case of *B*-physics triggers is discussed separately in Section 11.6.

The algorithms presented here are prototypes for the ones that will finally be used. They demonstrate the feasibility of obtaining the required trigger performance, while being simple enough to be implemented in the LVL2 trigger. Based on initial timing studies with these algorithms, one can be confident that they are fast enough to be used in the trigger. More work is required, however, to obtain realistic 'benchmark' figures on execution time (in the present software environment there are unnecessary overheads, related for example to diagnostic facilities).

The key requirements common to all algorithms are:

- high efficiency for the signal processes, larger than 95% per RoI relative to the LVL1 selection;

- uniform efficiency in η and constant or increasing efficiency with increasing E_T above threshold, which is difficult to achieve in certain regions of the detector, such as the barrel/end-cap overlap regions or where support structures obstruct the acceptance (these regions may be excluded from this requirement);

- reduction of the background rate. This is achieved by improved object identification and sharper thresholds, and implies good p_T resolution and small rates of fake objects;

- robustness with respect to luminosity;

- robustness with respect to noise, dead channels, imperfections of calibration and alignment constants, within the limits expected for the preliminary values available to the trigger.

The key selection criteria are functions of luminosity, E_T (or p_T), and location in the detector (mainly pseudorapidity), and may vary depending on the trigger menu. For example, looser selections may be applied to electron candidates in di-electron triggers than for single electron triggers. In this multi-dimensional parameter space, the operating point is chosen so as to achieve the required efficiency. Other choices could be the optimisation of the number of correctly reconstructed and tagged events relative to the number of background events. Such studies are part of the overall optimisation of the trigger implementation, taking into account processing power, data bandwidth and cost requirements, which is a joint task of the LVL2, EF, physics and trigger-performance groups. The FEX algorithms and the global algorithms were presented previously in detail in Chapters 8 and 9 of [11-1]. In this document, the FEX and global algorithms are described together, and only summaries of the results are reported here.

In the case of the muon trigger, the techniques to reduce the rate from LVL1 are described in Section 11.4.2 and use data from the muon spectrometer to remove fake LVL1 triggers resulting from noise hits due to radiation in the cavern and will reduce the rate by making a sharper p_T cut. Further rate reduction can be expected from using the Inner Detector to sharpen the p_T cut and to remove some of the background from decays in flight of pions and kaons by requiring a good match between the tracks reconstructed in the Inner Detector and the muon spectrometer. These studies are at an early stage and are at present only available for offline reconstruction, see Chapter 8. A larger rejection factor is expected from requiring isolation of the muon using information from the calorimeters as discussed in Section 11.4.2.2.

The photon trigger (Section 11.4.3.2) uses calorimeter features to reduce the background from jets and preserve high efficiency for $H \rightarrow \gamma\gamma$ events. For the electron trigger, a large background-rejection factor can be obtained by combining the features from the calorimeter and the Inner Detector as discussed in Section 11.4.3.3. Similarly, background to the τ trigger can be reduced by requiring the presence of a track matched to the calorimeter cluster (Section 11.4.4).

Improvement of the jet trigger is possible for low-E_T jets, but is marginal for high-E_T jets (see Section 11.4.5). In Section 11.4.6, a preliminary study of a possible b-jet tag trigger, based on impact-parameter measurements, is presented.

11.4.2 Muon trigger

11.4.2.1 Muon identification in the Muon System

The purpose of the LVL2 muon trigger is the identification of the muon tracks, the accurate calculation of the position and transverse momentum in the muon spectrometer, and the extrapolation to the Inner Detector and calorimeter. The following presents the LVL2 muon algorithm, which was shown to be applicable for low and high thresholds and for both the barrel and endcap system [11-15]. Note that if a muon candidate does not pass the p_T threshold, it may still be of interest as a soft muon candidate, when the event is selected by other triggers.

The Muon System consists of sets of chambers, which are arranged in superlayers (SL, inner, middle, outer). Each chamber has two groups of multi-layers, built from three to four layers of MDT tubes each. The LVL1 trigger function is provided by three layers of RPCs or TGCs. In the

barrel the first two trigger layers are located around the MDT chambers in the middle station and the third layer is located above or below the outer MDT station. In the end-cap a TGC is placed in front of the middle MDT chambers and two TGCs are placed behind them (see Figure 11-2).

The high-background environment in the Muon System requires algorithms with high capability of rejecting background hits due to the activity accompanying the muon track and the soft background in the cavern. Hits from the fast detectors of the LVL1 muon trigger (RPC and TCG), which have very low occupancy, are used to refine the road provided by LVL1. Next, a local track reconstruction is performed to determine a 'superhit' in a given MDT multi-layer. The superhits of the track are assembled to determine the radius of curvature of the candidate track. The momentum is found by matching the reconstructed track with patterns of tracks stored in a fine-grained lookup table. Many tracks, especially in the barrel/end-cap transition region, have complicated chamber hit patterns, which can change rapidly as a function of momentum, η or ϕ. The radius method is a means to use all hit–chamber information in a manner roughly independent of where the super points are actually located.

The first stage of the LVL2 trigger is the refinement of the RoI region. For the barrel the RPC hits bracketing the middle superlayer and the RPC hits in the outer superlayer, if they exist, are used to reconstruct a circular trajectory. This trajectory is used to determine the RoI in the first superlayer and refine the RoI in the middle and outer superlayers. If the outer SL hits do not exist, a rough fit of a circle is performed under the assumption that the muon trajectory in the (R, z) plane is a straight line from the IP up to the first SL. For the end-cap system the refined RoI is determined by a circular fit through the end-cap toroid using TGC hits to fix the tangent line and the IP to determine the position in the first SL. The actual width of the refined RoI is adjusted according to the quality of the fit of the trajectory. For a good quality fit the roads are two to three MDT tubes wide.

The next stage of the LVL2 trigger formation involves the recognition of tracks in a given MDT multi-layer within the refined RoI road. This is accomplished by means of an *ad hoc* quality factor developed from an adjacency test (a type of Hough transformation) and a χ^2 consistency test on all tangent lines of all pairs of hit tubes consistent with broad limits of extrapolation back to the interaction point.

The coordinate along the sense wires (s-coordinate) is determined by the trigger-chamber system. It is assumed that each trigger hit furnishes a space point, *i.e.* that the two planar coordinates are correctly associated at the raw-data level. Each space point is converted to the polar angle ϑ, which is fitted in the end-caps as a function of z (along the beam), or, in the case of the barrel, as a function of x (local coordinate perpendicular to barrel chamber planes). Knowledge of the ϑ-dependence allows the s-coordinate to be estimated by extrapolating to the MDT plane.

Space points are reconstructed from the MDT and trigger planes, although only the MDT information is used to determine the muon trajectory in the bending plane. Given that the trigger planes have a rather coarse segmentation, yielding second-coordinate resolution of 5 to 10 mm, only MDT hits for the same chamber central angle ϕ_0 are used in most cases. All the MDT chamber planes are employed, however, for tracks with fewer than four MDT planes at the same ϕ_0.

The information needed for momentum determination is the curvature of the track and the magnetic-field integral. The momentum at the interaction point is determined by scaling the reconstructed track radius to the radius of the four nearest calibration tracks which are averaged by linear weighting of the three-dimensional distances to the superhit 'match point'. The average radius is then used to determine the trigger momentum by

$$p_T = \frac{r}{r_c} p_c$$

where r is the track radius of curvature, and p_c is the calibration momentum of radius r_c. The charge of the muon is determined by comparison of the sign of the circle centre parameters (x_0, z_0) with those of the calibration file.

The trigger quality is determined by the momentum resolution achieved. In Figures 11-20 and 11-21 the resolution for $p_T = 20$ GeV muons is shown for the barrel and end-caps, respectively, with all associated hits from GEANT processes simulated (delta-rays, bremsstrahlung, *etc.*) and random noise of 10% tube occupancy added. Note that the resolution is in the range 1.3 GeV to 1.8 GeV by Gaussian measure, but there are significant low and high-p_T tails, which will affect the sharpness of the trigger threshold.
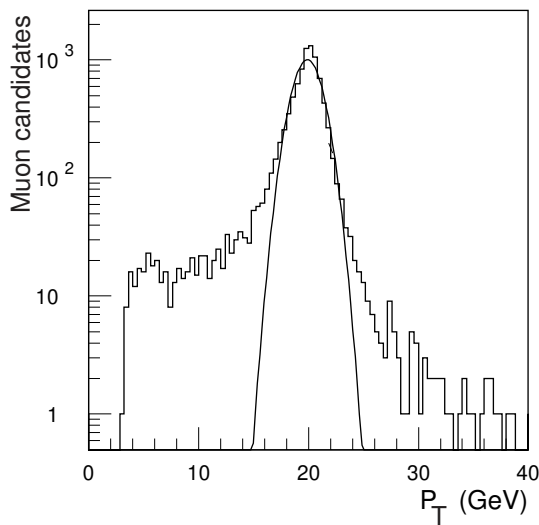
Figure 11-20 Reconstructed p_T for muons generated with $p_T = 20$ GeV in the barrel region $0 < |\eta| < 1$. A random noise of 10% was added.
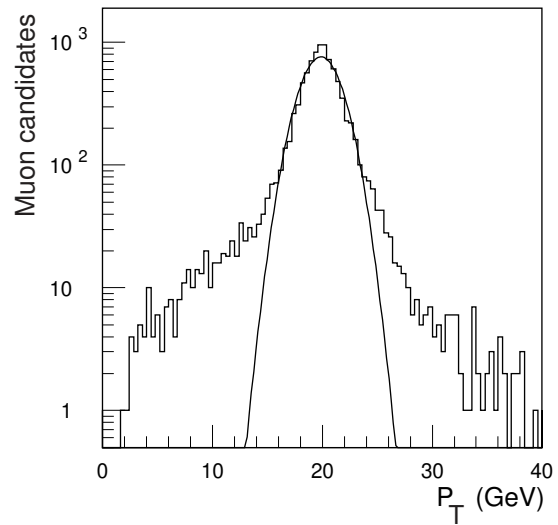
Figure 11-21 Reconstructed p_T for muons generated with $p_T = 20$ GeV in the end-cap region $1 < |\eta| < 2$. A random noise of 10% was added.

Figures 11-22 and 11-23 show the corresponding performance for $p_T = 6$ GeV muons for the barrel and end-cap regions, respectively. As expected, the resolution performance at 6 GeV is degraded from 20 GeV by the energy-loss fluctuations and multiple-scattering effects. At $p_T = 6$ GeV the resolution is typically about 10% by Gaussian measure; here the non-Gaussian tail is mostly on the high side of the peak. In all these figures, no regions were masked so the resolution is an indicator of the average performance over $0 < \phi < \pi/2$, $0 < |\eta| < 1$ for the barrel, and $0 < \phi < \pi/2$, $1 < |\eta| < 2$ for the end-cap.
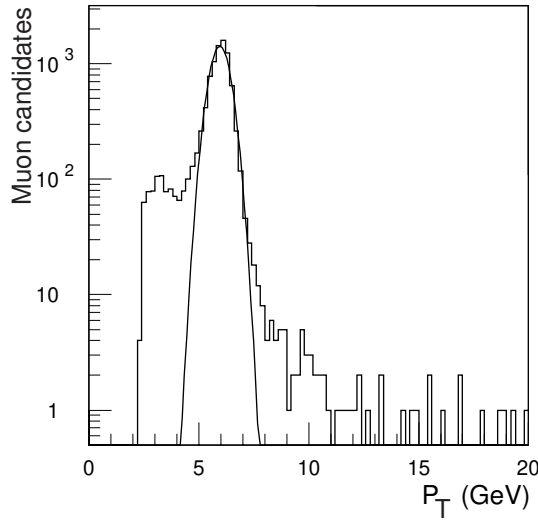
Figure 11-22 Reconstructed p_T for muons generated with p_T = 6 GeV in the barrel region 0 < |η| < 1. A random noise of 10% was added.
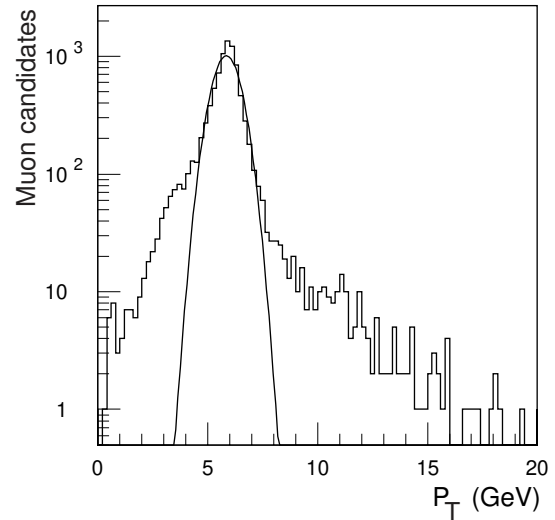
Figure 11-23 Reconstructed p_T for muons generated with p_T = 6 GeV in the end-cap region 1 < |η| < 2. A random noise of 10% was added.

Table 11-9 gives a summary of the performance for p_T = 20 GeV and 6 GeV muons. In the table the efficiency is computed for any reconstruction of the trigger momentum independent of the resultant value and the estimated error; resolutions are computed within the limits of the plots (Figures 11-20 to 11-23). The threshold curves are shown in Figures 11-24 to 11-27 for the barrel

Table 11-9 Summary of reconstruction-efficiency and resolution performance.

p_T (GeV)	Detector region	Efficiency	rms resolution (GeV)	Gaussian resolution (GeV)
20	barrel	99.4 ± 0.1	3.1	1.3
20	end-cap	99.1 ± 0.2	3.1	1.8
6	barrel	99.0 ± 0.4	1.0	0.44
6	end-cap	97.2 ± 0.7	1.3	0.60

and end-cap, and low and high thresholds, respectively. The LVL1 efficiency is not included, which should further suppress the low-p_T events. The efficiency is greater than 95% in the barrel. For triggers in the end-cap it is necessary to apply track-quality cuts to achieve good threshold resolution. Regions where there is negligible bending inevitably degrade the trigger resolution. These regions (|η| = 1.6 ± 0.1, ϕ = 0.4 + m×π/4 ± 0.1, where m = 0, 1, 2 ...) are therefore masked. For the 6 GeV trigger in the end-cap a $χ^2$ cut, which requires a good circle fit, was applied. This introduces some loss of plateau efficiency, but the overall trigger threshold is much sharper than with no quality cut.

The muon spectrum (see Figures 2-3 and 2-4 in [11-1]) is approximately flat in η, and its p_T dependence can be parametrised as

$$\frac{d\sigma}{dp_T d\eta} = \frac{4.4 \times 10^3}{p_T^{4.7}} \frac{\mu b}{\text{GeV}}$$
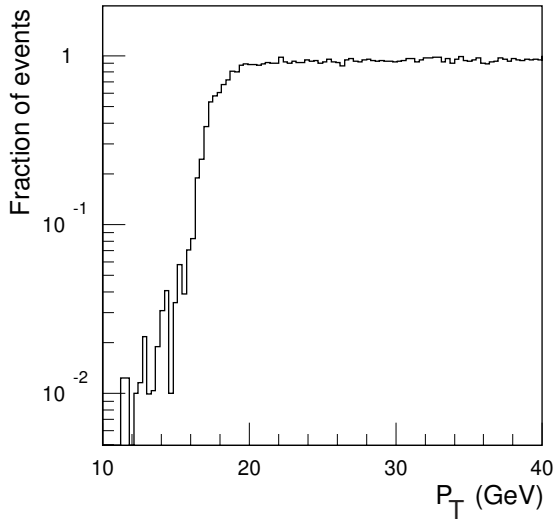
Figure 11-24 Fraction of events that pass the fixed high-p_T LVL2 threshold as function of the generated p_T for the barrel region $0 < |\eta| < 1$. A random noise of 10% was added.
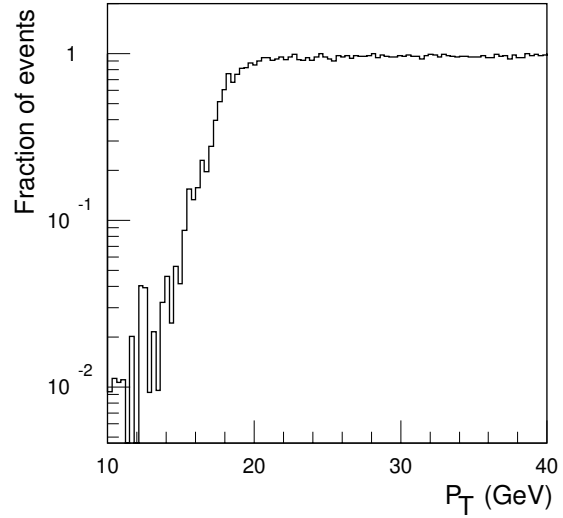
Figure 11-25 As Figure 11-24, but for the end-cap region $1 < |\eta| < 2$.
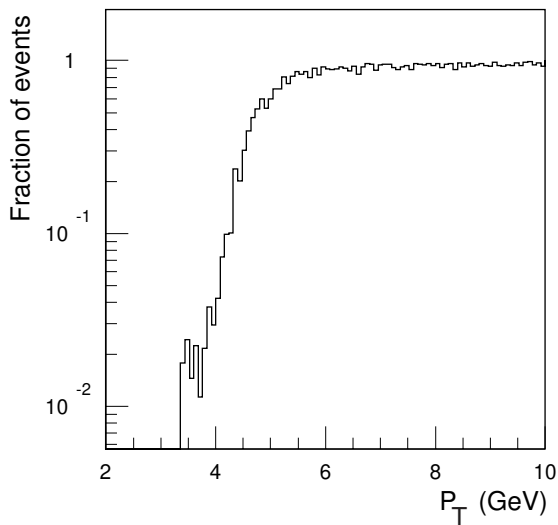
Figure 11-26 Fraction of events that pass the 6 GeV low-p_T LVL2 threshold as function of the generated p_T in the barrel region $0 < |\eta| < 1$. A random noise of 10% was added.
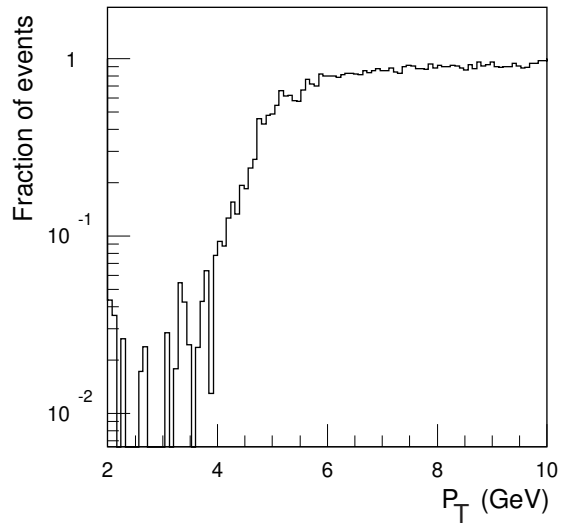
Figure 11-27 As Figure 11-26, but for the end-cap region $1 < |\eta| < 2$. A track-quality cut was imposed in addition.

where p_T is the transverse momentum in GeV at the interaction point. Convolving this spectrum with the efficiency curves, the trigger rates listed in Table 11-10 were deduced for an efficiency (plateau) of 90%.

The rates can be further reduced using information from the Inner Detector. These studies were made for the full reconstruction, but not yet for the trigger algorithms (see Chapter 8).

Table 11-10 LVL2 muon trigger rates for barrel and end-cap system and low and high luminosity thresholds. The rate obtained without quality cuts is indicated in brackets (end-cap, low luminosity). A random noise of 10% is assumed in all cases.

Luminosity	Detector region	Threshold (actual)	Rate (kHz)
low (6 GeV)	barrel	4.6 GeV	3.5
	end-cap	4.7 GeV	2.4 (5.3)
high (20 GeV)	barrel	17.5 GeV	0.29
	end-cap	17.5 GeV	0.30

11.4.2.2 Muon isolation

Muons from π/K decays or c and b semileptonic decays tend to be within jets, whereas muons from heavy objects such as W tend to be isolated. Isolation is therefore relevant for the high-p_T muon trigger and was studied using a sample of fully simulated $W \to \mu\nu$ signal events (muon $p_T > 24$ GeV), and $b\bar{b} \to \mu X$ background events (muon $p_T > 20$ GeV) (see Section 9.1 of [11-1] and [11-16]).

The best results were obtained at both low and high luminosity using information from only the EM Calorimeter. The efficiencies are summarised in Table 11-11. As an example of the selection efficiencies that one might expect, these results are weighted by the muon p_T spectrum from W and $b\bar{b}$ decays for $p_T > 24$ GeV. The results are given in Table 11-12. Note that only the error arising from the statistical uncertainty on the efficiencies is included.

Table 11-11 Signal and background efficiencies, in bins of muon transverse momentum, for a selection based on ECAL information at low and high luminosity. Errors are statistical.

Muon p_T bin	Low luminosity Efficiency (%)		High luminosity Efficiency (%)	
(GeV)	$W \to \mu\nu$	$b\bar{b} \to \mu X$	$W \to \mu\nu$	$b\bar{b} \to \mu X$
24–30	94.6 ± 2.1	10.4 ± 2.2	67.9 ± 4.4	9.7 ± 2.1
30–40	98.2 ± 1.0	8.2 ± 1.8	94.1 ± 1.8	10.8 ± 2.0
40–50	97.8 ± 1.3	7.6 ± 3.3	96.3 ± 1.6	4.5 ± 2.6
> 50	99.1 ± 0.6	10.6 ± 3.3	98.2 ± 0.9	9.4 ± 3.2

Table 11-12 Example of the selection efficiencies for muonic W and $b\bar{b}$ decays, for transverse momenta greater than 24 GeV. Errors arise from the statistical uncertainty on the selection efficiencies.

Process	Low luminosity eff. (%)	High luminosity eff. (%)
$W \to \mu\nu$	97.8 ± 1.1	91.4 ± 1.9
$b\bar{b} \to \mu X$	9.6 ± 2.3	9.6 ± 2.2

11.4.3 Electron and photon trigger

Before photon and electron trigger objects can be identified, the full-granularity information from the electromagnetic and hadronic calorimeters must be used in selecting electromagnetic clusters. The LVL2 electron selection uses additionally information from the TRT and precision tracker (SCT plus pixel system). The parameters of the reconstructed features are compared, and, if consistent, are combined into electron trigger objects.

A common e/γ selection is first made by examining the cluster shower shapes and the E_T deposition in the calorimeters. The next step consists of selecting clusters likely to be due to an isolated electron or photon. The electron hypothesis is accepted if, after examining the TRT and precision tracker within the RoI, the presence of a matching charged-particle track is confirmed. Photon objects are identified by a more detailed analysis of the calorimeter shower shapes. Since the photon trigger does not use the tracking information to identify photon conversions, some clusters will be selected as both an electron and a photon. For photons higher E_T-cuts are applied than for electrons. The identification of photon and electron objects, after all LVL2 cuts, gives a total rejection with respect to LVL1 of 100 (70) for electrons and 75 (50) for photons at low (high) luminosity.

In the following sections a summary of the common e/γ selection, and the photon and electron selections is given and performance results are presented. More details can be found in Refs. [11-17], [11-18] and [11-19].

11.4.3.1 The e/γ selection

This LVL2 e/γ selection takes as input the RoIs selected by the LVL1 EM trigger, see Section 11.3.2.1, and refines the cluster energy and position measurements by using the full calorimeter granularity and an improved energy calibration. This information is then used to build shower-shape variables, which together with the transverse energy, discriminate electrons and photons from jets which passed the LVL1 EM trigger selection.

The trigger quantities used for the e/γ selection are as follows (see Section 8.2.2.4 of [11-1]).

- The transverse energy E_T calculated using the energies of all the electromagnetic-calorimeter layers in a $\Delta\eta\times\Delta\phi = 3\times7$ standard cell area within the LVL1 RoI (standard cells cover an area of $\Delta\eta\times\Delta\phi \sim 0.025\times0.025$).

- The hadronic transverse energy E_T^{had} within the LVL1 RoI.

- The ratio $R_{37} = E_{37}/E_{77}$, of energy contained in a $\Delta\eta\times\Delta\phi = 3\times7$ window to that in a 7×7 window in the second sampling of the EM Calorimeter.

- The fractional difference in energy between the strip with the maximum energy E_1, and the second maximum E_2, in the first sampling of the EM Calorimeter. The fraction is calculated as $R_\eta^{strip} = (E_1 - E_2)/(E_1 + E_2)$. Figure 11-28 shows the different structure seen in the first calorimeter sampling for electrons and jets. The trigger quantity R_η^{strip} is shown in Figure 11-29.

The quantities discussed above were chosen such that they are relatively uncorrelated and simple to implement. The dependence of the quantities on $|\eta|$ and p_T is taken into account in the implementation of the selection cuts. More details can be found in Section 8.2.2.4 of [11-1]. The values of the cuts were optimised so as to give an efficiency of ~95% for 20 (30) GeV p_T electrons passing the LVL1 selection at low (high) luminosity. The corresponding values of the E_T cuts
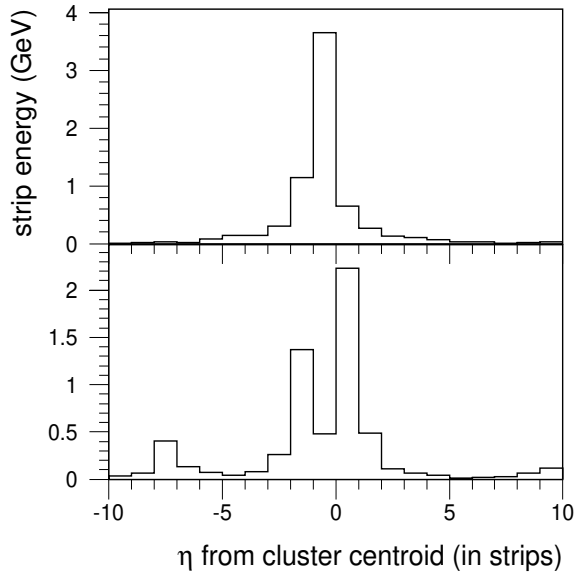
Figure 11-28 Distribution of the signals in η-strips of the first EM Calorimeter sampling for a 30 GeV electron (top) and a jet (bottom). The distributions are centred at the cluster position. The events are chosen to show the typical features after the LVL1 trigger selection at high luminosity.
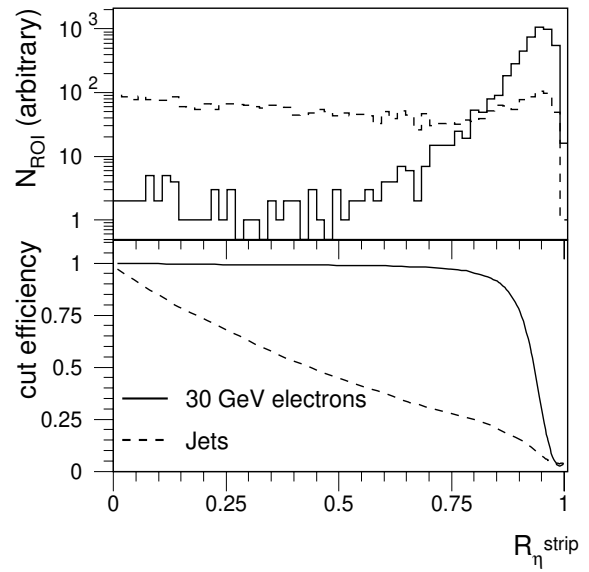
Figure 11-29 Distribution of number of RoIs accepted (top) as function of R_η^{strip} for $E_T = 30$ GeV electrons and jets at high luminosity. Efficiency as a function of a cut on R_η^{strip} (bottom). The distributions are given after the LVL1 trigger selection. No other cuts have been applied.

Table 11-13 Overall cumulative efficiencies of LVL1 and LVL2 e/γ selection for single $p_T = 20$ GeV electrons at low luminosity, and for single $p_T = 30$ GeV electrons at high luminosity. The corresponding trigger rates are also shown.

	Low luminosity		High Luminosity	
Selection requirements	Efficiency (%)	Rate (kHz)	Efficiency (%)	Rate (kHz)
LVL1 CALO	95	7.9	95	25.1
E_T^{em}	93	5.6	94	16.3
E_T^{had}	93	4.1	94	11.6
R_{37}	92	2.3	94	8.5
R_η^{strip}	91	1.0	92	3.9

were 16 GeV (25.5 GeV) for the nominal 20 GeV (30 GeV) thresholds used at low (high) luminosity. The values of the other cuts are listed in Section 8.2.2.5 of [11-1]. With these cuts a rejection of 7.6 (6.4) with respect to the output of the LVL1 trigger for low (high) luminosity is obtained. Table 11-13 shows the efficiencies and rates for the e/γ selection after each step of the selection requirements is applied.

11.4.3.2 The photon trigger

An acceptable photon trigger rate is achieved by applying tighter cuts than in the e/γ selection and by using additional quantities to further reject π^0s and jets [11-19]. Only calorimeter information is used. The additional trigger quantities used to select LVL2 trigger photon objects are:

the energy-weighted shower width in the η-direction, $\omega_\eta = \sqrt{\langle\eta^2\rangle - \langle\eta\rangle^2}$, in the second sampling of the EM Calorimeter, calculated in a $\Delta\eta\times\Delta\phi = 3\times5$ cell window, and the shower shape in the first sampling, R_η^{shape}. This quantity measures the fraction of energy outside the shower core and is calculated from $R_\eta^{shape} = (E_7 - E_3)/E_3$, where E_7 and E_3 are the energies in 7 and 3 strips respectively around the cluster centroid.

Using these quantities, the photon trigger selection is optimised such that converted and unconverted photons have a similar selection efficiency. A more sophisticated analysis using the calorimeter and the Inner Detector information (*e.g.* at the Event Filter or offline level) can reject or select these photons at a later stage, see Chapter 7.

The rates from jets as a function of the sequential LVL2 trigger cuts are shown in Figure 11-30 and Figure 11-31. At low luminosity, raising the E_T threshold by 9 GeV reduces the background rate by a factor of two. At high luminosity, this rate reduction is achieved with a threshold increase of 15 GeV for the single-object trigger. In case the background rate is too high for the dou-
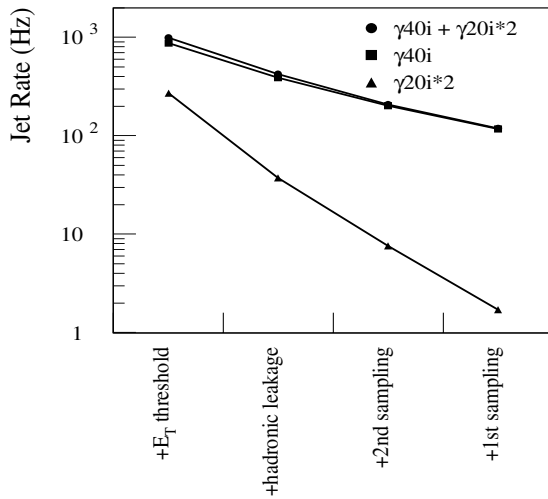
Figure 11-30 Rates from jets at low luminosity for the different LVL2 trigger menu items as a function of the LVL2 trigger cuts in the different parts of the calorimeter. The cuts are applied consecutively and in addition to the LVL1 selection.
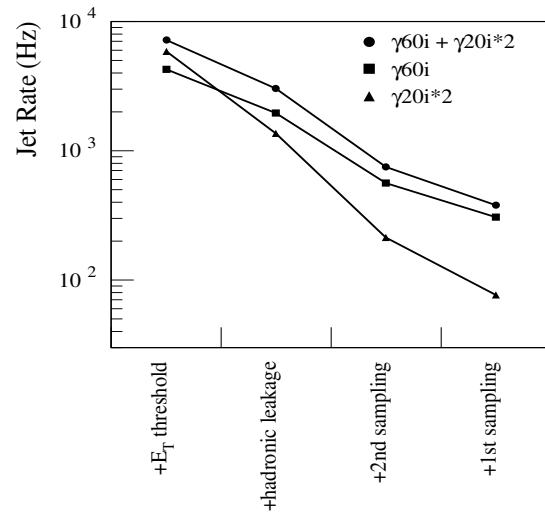
Figure 11-31 As Figure 11-30, but for high luminosity.

ble-object trigger at high luminosity, the rate can be reduced by raising the E_T threshold of the second object. This hardly affects the efficiency for $H \to \gamma\gamma$ events, which is the most important physics process requiring photon identification, see Chapter 19.

Table 11-14 summarises the photon efficiencies at various transverse energies and the corresponding background rates for low and high luminosity. The table also shows the expected efficiencies at low and high luminosities for selecting di-photon final state Higgs events with $m_H = 100$ GeV with the various trigger menu elements. The table includes the photon trigger menu items as defined in Section 11.7.2 and [11-27], *e.g.* $\gamma40i$ is a trigger for isolated photons of $E_T > 40$ GeV.

Table 11-14 Expected efficiencies at threshold and background rates for the LVL2 photon trigger at low and high luminosity. The trigger efficiency for $H \rightarrow \gamma\gamma$ events is also shown for $m_H = 100$ GeV.

Trigger	luminosity	photon efficiency (%)	Higgs efficiency (%)	LVL2 Rate (Hz)
γ40i	low	95.5 ± 0.3	98.3 ± 0.2	117 ± 10
γ20i $\times$ 2	low	81.8 ± 0.4	92.6 ± 0.2	2 ± 1
γ40i OR γ20i $\times$ 2	low		98.3 ± 0.2	119 ± 10
γ60i	high	95.5 ± 0.5	55.0 ± 1.0	304 ± 48
γ20i $\times$ 2	high	81.3 ± 1.0	93.3 ± 0.5	76 ± 24
γ60i OR γ20i $\times$ 2	high		95.3 ± 0.4	380 ± 54

11.4.3.3 The electron trigger

After the LVL2 common e/γ selection described in Section 11.4.3.1 the trigger rates, calculated from the analysis of a sample of simulated di-jet events with and without pile-up, are 1 kHz at low luminosity and 3.9 kHz at high luminosity. A breakdown of the various contributions to these trigger rates is shown as the open histogram in Figure 11-32. For ~90% of events passing the calorimeter e/γ selection, the highest-E_T cluster in the event is due to photons (~60% from the decay of π^0s, the rest from η/ω decays, bremsstrahlung and prompt photons). In the majority of cases the π^0 causes an e/γ trigger because the photons are not well separated and cannot be resolved into separate clusters. In ~20% of all cases it is an electron from a photon conversion which causes the event to trigger. By searching for a track in the Inner Detector and by requiring a match between the measured track parameters and the calorimeter cluster, the trigger rate may be significantly reduced for both cases.
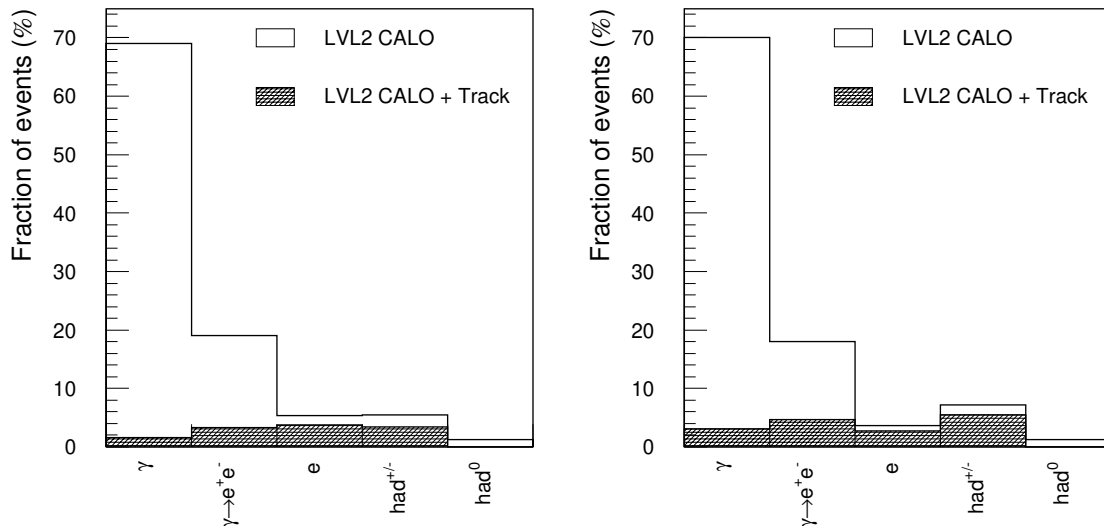
Figure 11-32 The highest p_T particle in events passing the LVL1 and LVL2 calorimeter selections (open histogram) and for those events containing, in addition, tracks in the TRT and precision tracker matched to the calorimeter cluster (hatched). The distributions are shown for jet events without pile-up (left) and with pile-up at high luminosity (right).

A search for track candidates is performed separately in the TRT and precision tracker. The same basic method is used in both cases. This consists of an initial search using a histogramming method to identify sets of hits likely to form a track, followed by a fit to each set of selected hits. In the initial search a histogram is formed of the number of hits along possible track trajectories. For all trajectories with a number of hits above some pre-defined threshold, a fit is performed. The best track candidate is chosen and returned as input to the electron-trigger decision. The TRT uses two readout thresholds. Signals passing the higher threshold are more likely to have been caused by Transition Radiation, characteristic of an electron track. The number of hits on a track passing the higher threshold can, therefore, be used to select track candidates likely to be due to an electron. Details of the algorithms and the process by which the best candidate is selected can be found in References [11-20] and [11-1].
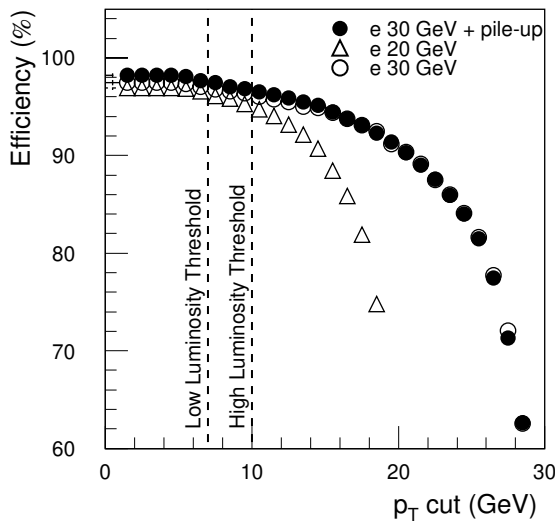
Figure 11-33 Efficiency of the precision tracker as a function of the p_T cut value (GeV) for single-electron events passing the LVL1 and LVL2 calorimeter selection.
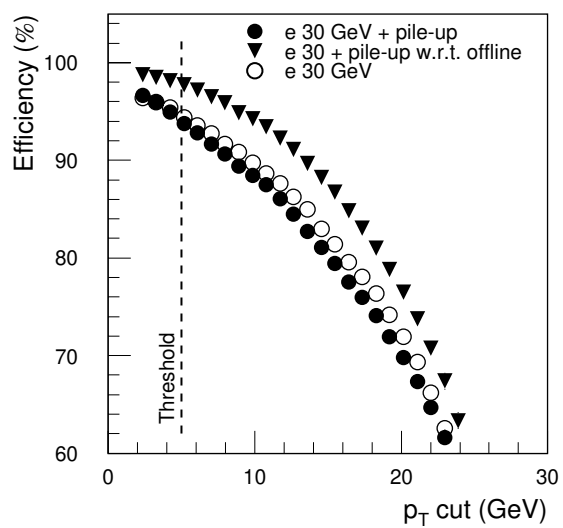
Figure 11-34 Efficiency of the TRT algorithm as a function of p_T cut (GeV). The efficiency is shown relative to events passing the LVL1 and LVL2 calorimeter selections (circles) and relative to those events additionally containing a track found by the offline Inner Detector pattern-recognition software (triangles).

The TRT and precision tracker each return the parameters of a single track candidate found within the LVL1 RoI. The next step in the electron trigger is to apply a p_T cut to these candidates. This discriminates against the predominately low-p_T tracks in jet events. The efficiency of the precision tracker to reconstruct tracks from 20 GeV and 30 GeV p_T electrons is shown as a function of p_T cut in Figure 11-33. Values for the p_T cut of 7 GeV (10 GeV) were chosen for low (high) luminosity respectively so as to give an efficiency of 96% for events passing the LVL2 calorimeter selection. The corresponding distributions of efficiency as a function of the p_T cut are shown for the TRT in Figure 11-34. Since a significant proportion of electrons lose a large fraction of their energy via bremsstrahlung before entering the TRT, the efficiency for reconstructing a track in the TRT rises slowly with decreasing value of the p_T cut. A p_T cut of 5 GeV was applied.

The requirement of a track in both the precision tracker and the TRT, in addition to the e/γ calorimeter selection with a nominal E_T threshold of 20 (30) GeV, gives a rejection with respect to LVL1 of 25 (50) for jets without (with) pile-up at high luminosity. The rates and efficiencies are given in Table 11-15. There is a corresponding loss of efficiency of 9% (7%) for single electrons passing the e/γ selection at low (high) luminosity. In a sizeable fraction of cases the electrons re-

jected have lost a significant amount of p_T via bremsstrahlung. These tracks are also likely to fail an offline selection. A fairly loose set of offline Inner Detector cuts has been defined[1], in order to measure the trigger efficiency for the sub-set of events that would pass an offline physics selection (see Table 11-15). Of the single-electron events at low or high luminosity passing both the LVL2 calorimeter and the offline selections, 96% have tracks found by the trigger algorithms in the TRT and precision tracker.

Table 11-15 Overall combined efficiencies of LVL1 and LVL2 for single p_T = 20 GeV electrons without pile-up (10^{33} cm^{-2}s^{-1}), and for single p_T = 30 GeV electrons with pile-up at high luminosity. Efficiencies are also given relative to events passing both the LVL1 and LVL2 e/γ calorimeter and offline Inner Detector selections. Trigger rates are shown at low and high luminosity determined from samples of jet events without and with pile-up. Details of the Inner Detector track cuts and offline selection are given in [11-1], Section 9.3. In addition, performance results for a tighter set of track cuts are given (bottom row).

Selection requirements	Low luminosity			High Luminosity		
	Effic. (%)	Rate (kHz)	Effic. wrt offline ID (%)	Effic. (%)	Rate (kHz)	Effic. wrt offline ID (%)
LVL1 + LVL2 CALO	91	1.00	–	92	3.9	–
Precision Track	87	0.20	98	89	1.4	98
TRT Track	83	0.39	97	86	1.9	97
Precision and TRT tracks	82	0.19	96	85	1.1	96
Precision track matched to CALO	87	0.14	98	88	0.7	97
TRT track matched to CALO	83	0.31	96	85	1.5	96
Precision and TRT tracks both matched to CALO	82	0.13	95	83	0.6	94
Precision and TRT tracks both matched to CALO (tighter cuts)	77	0.08	91	79	0.4	90

In the majority of jet events passing the e/γ selection, the calorimeter cluster is not caused by a single charged track and hence does not match well in position with the track extrapolated from the Inner Detector. Cuts on the separation in azimuthal angle and pseudorapidity between the extrapolated track and the cluster position thus provide good discrimination against jet events. In addition, the momentum spectrum for tracks in jet events is peaked towards low values. As a result, in jet events, the cluster energy can be much larger than the momentum of any single track. The ratio of the transverse energy of the calorimeter cluster to the p_T of the Inner Detector track, E_T/p_T, therefore provides additional discrimination against jet events. Performance measurements are given in Table 11-15 for a relatively loose set of cuts on these parameters, details of which can be found in [11-1]. With these cuts, rejections with respect to LVL1 of 60 (40) are achieved for jets at low (high) luminosity. A breakdown of the composition of these triggered events is given as the hatched histogram in Figure 11-32. A comparison with the breakdown for events after the e/γ selection alone (open histogram) shows the greatest jet rejection is obtained for clusters due to photons, where the photons do not convert. However a significant rejection is also obtained in the case of conversions.

---

1. The set of offline cuts used is not complete; for example no cut was applied to the ratio E_T/p_T. More details of the offline cuts are given in [11-1].

By varying cut values, some flexibility in the efficiency and rejection may be achieved. As a second example, results obtained with tighter track cuts are given in the bottom row of Table 11-15. With these cuts, rejections of 100 (70) are achieved at low (high) luminosity for an additional 4% loss of efficiency for single electrons.

The algorithms used for the work reported here have been designed to be suitable for an online implementation. Some initial benchmarking results on execution times are available. In addition, work is well advanced to benchmark the algorithms in a realistic trigger environment as part of the LVL2 trigger Pilot Project [11-4]. The work on optimising the association of the information from the Pixels, SCT, TRT and calorimeter in terms of efficiency for electrons and rejection of jet events is ongoing. More details of the programme of work are given in [11-1].

The results presented here indicate that the required trigger rates can be achieved at low and high luminosity with an efficiency of better than 90% for events that would pass an offline selection. Further improvements in the algorithms and selection cuts are being pursued. These include the use of the LVL2 calorimeter information to reduce the region of interest for the track search and the evaluation of more sophisticated but potentially slower algorithms.

11.4.4 τ/hadron trigger

The τ/hadron trigger may be used in coincidence with other triggers, such as a muon or missing-E_T trigger, to improve the efficiency for triggering or to allow the use of lower thresholds. Examples are a trigger for the $Z \to \tau\tau$ decay and the decay of the low-mass $A \to \tau\tau$.

Separation of τ/jet at LVL2 is based on calorimeter and tracking information. The calorimeter selection was described in detail in Section 8.2.3 of [11-1]. The selection based on tracks was presented in Section 9.4 of [11-1]; the preliminary results available at the time used the information of the generated tracks (assuming 90% tracking efficiency).

The signal selection was tuned using events of the type $A \to \tau\tau$ and the rejection of background from jets was optimised using QCD jet samples. The calorimeter selection was performed in two steps. The EM plus hadronic transverse energy contained in a small core of $\Delta\eta \times \Delta\phi = 0.15 \times 0.15$ was required to be above threshold, *e.g.* E_T^{core}(em+h) > 50 GeV. The fraction f_{core} of EM energy in the core was required to be greater than 85%, where the RoI region covers $\Delta\eta \times \Delta\phi = 0.4 \times 0.4$, $f_{core} = E_T^{core}(EM)/E_T^{RoI}(EM) > 0.85$.

Table 11-16 Rates from jets and τ efficiencies for LVL2 τ selections applied sequentially. The columns correspond to different cuts on the LVL2 core E_T. For the first column only the LVL1 cut (E_T > 30 GeV) is applied, for the remaining columns increasing cuts in core E_T are applied, which correspond to jet efficiencies of 40%, 30% and 20% (relative to LVL1). The selections are explained in the text.

Selection	LVL1 Rate Hz	LVL1 Eff$_\tau$ %	E_T > 50 GeV Rate Hz	E_T > 50 GeV Eff$_\tau$ %	E_T > 55 GeV Rate Hz	E_T > 55 GeV Eff$_\tau$ %	E_T > 63 GeV Rate Hz	E_T > 63 GeV Eff$_\tau$ %
E_T^{core}	3110	100.0	966	78.0	719	71.8	418	62.2
+ f_{core} (EM) > 0.85	1090	87.0	316	70.6	245	65.2	158	57.0
+ $1 \leq N_{trk} \leq 3$	670	75.2	158	59.7	110	54.7	63	47.3
+ $N_{trk} = 1$	250	42.9	45	33.3	30	30.2	12	26.7

Table 11-16 shows the evolution of the τ efficiencies and the rates from jets, when these selections are applied. The E_T cut reduces the LVL1 τ trigger rates by a factor of three, and the requirement on core energy fraction gives an additional reduction of more than a factor three, while keeping the τ efficiency close to 70%. Further rejection is obtained by restricting the number N_{trk} of charged tracks associated to the τ RoI, *e.g.* for a threshold of $p_T > 2$ GeV. $1 \leq N_{trk} \leq 3$.

The resulting trigger rate is 160 Hz, and the τ efficiency is close to 60%. Further jet rejection could be obtained by requiring exactly one track; in this case the τ efficiency is reduced to ~30% for one-prong decays.

11.4.5 Jet trigger

The aim of treating jets at LVL2 is to reduce the rate of events containing jets by improving the measurement of the energy and position of the jets. The improvement in the jet measurement is achieved by a refined energy calibration, a jet definition and threshold adjustments. The aim is to achieve an efficiency of 95% with respect to the LVL1 jet, or 90% with respect to the reference jet.

An example of a LVL2 jet algorithm is described in Section 8.2.4 of [11-1]. For a given LVL1 RoI, a window around the RoI direction with a size of 1.0×1.0 was selected. The energy depositions are first summed up into towers of $\Delta\eta \times \Delta\phi = 0.1 \times 0.1$, applying calibrations and thresholds per cell. A threshold per cell is of great importance due to the large number of cells involved. Then a cone algorithm (with radius $R = 0.4$ and E_T threshold on the seed cell of 1 GeV) was run on the trigger towers inside this window. The reference jet was defined with the same algorithm, but using the generated particles before detector simulation (excluding neutrinos and muons and using only particles with $|\eta| < 3.2$).

The achieved (Gaussian) position resolution is $\Delta\eta \sim \Delta\phi \sim 0.03$, but there are significant non-Gaussian tails. The distance $\Delta R = (\Delta\eta^2 + \Delta\phi^2)^{1/2}$ between the reconstructed and the reference jet in the (η, ϕ) plane has a mean of about 0.036, which is an improvement compared to the LVL1 resolution of about 0.2×0.2 described in the Section 11.3.2. This improvement in spatial resolution is important for the separation of nearby jets and the possible calculation of invariant masses of jets. The improved energy measurement allows sharper thresholds, which in turn reduces the rate of accepted events.

Figure 11-35 shows for the case of low luminosity (10^{33} cm^{-2}s^{-1}) the rates for events at LVL2 with at least n jets, where n = 1 to 4. Due to the particle-level filter applied to the data sample used here, it has to be kept in mind that the rate for single inclusive jets is biased. The rate shown can only be taken as a lower limit.

The ratio of the LVL1 and LVL2 rates is displayed in Figure 11-36 as a function of the nominal jet E_T for events with $N_{jet} \geq 1$ to $N_{jet} \geq 4$ jets. One observes a decrease of the ratio with increasing jet energy, indicating that the effect of the 1 GeV threshold per trigger tower at LVL1 becomes less important at larger jet energies. The ratio has a value of about two at a nominal jet energy of 80 GeV for all jet classes. At larger nominal energies, the factor slowly approaches a value close to one. For smaller energies down to 50 GeV the ratio is larger, giving factors between four and six at 50 GeV.
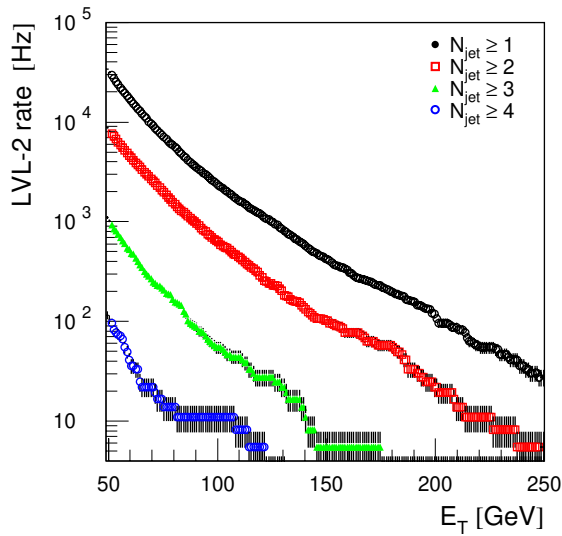
Figure 11-35 Rates for inclusive jet and multi-jet production at low luminosity (10^{33} cm^{-2}s^{-1}) without taking into account the effect of pile-up. The rates shown are given for 90% efficiency of the LVL2 algorithm with respect to the reference jet, see text. Due to the particle-level filter applied to the simulation used, the inclusive single jet rate is underestimated.
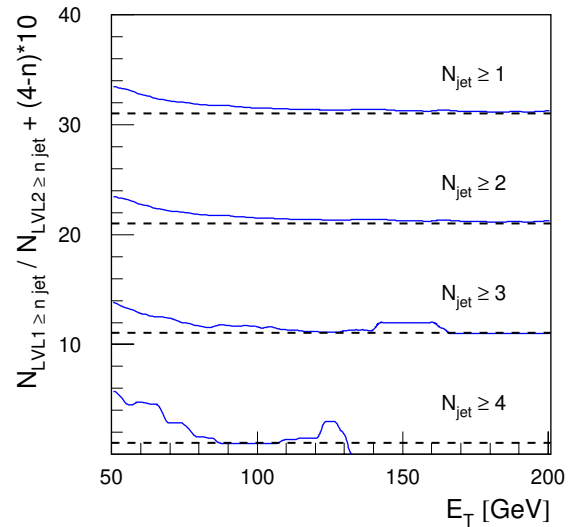
Figure 11-36 Ratio of the rates for inclusive jet and multi-jet production at LVL1 with respect to LVL2, shown for low luminosity (10^{33} cm^{-2}s^{-1}) without taking into account the effect of pile-up. The ratios shown correspond to 90% efficiency for LVL2 and 95% efficiency for LVL1 with respect to the reference jet, see text. For each ratio an offset of $(4 - n) \times 10$ for $\geq$ n jets is added. The dashed line indicates a value of 1 for the ratio.

11.4.6 Tagging of *b*-jets at LVL2

The possibility of implementing a LVL2 *b*-jet tag trigger based on impact-parameter information is under study. Issues to be addressed include the feasibility (beam-position stability, alignment, *etc.*) and comparing the merits of making the selection at LVL2 or in the Event Filter where more complex algorithms and better alignment constants might be available. No strong physics case for this trigger has been established [11-22], but it would add to the flexibility of the trigger.

An algorithm for finding tracks in the barrel pixel detector was studied and presented in [11-1]. Due to the *b*-quark lifetime there is clear distinction between the reconstructed transverse impact parameters (d_0) for *b*- and *u*-quark jets. A simple *b*-tagging algorithm using a likelihood method has been used to distinguish between the different jet types. The performance of this algorithm is illustrated in Figure 11-37, which shows the *u*-quark-jet rejection as a function of the *b*-tagging efficiency for simulated *WH* events ($H \rightarrow b\bar{b}$) without and with pile-up for a Higgs mass of 400 GeV. A rejection factor of 20 can be achieved for a *b*-tagging efficiency of 50% in the presence of pile-up at high luminosity. It should be noted that *WH* events are triggered by the $W \rightarrow e\nu/\mu\nu$ decay, and no *b*-tag is required at the trigger level for this channel.

The trigger and the offline *b*-tagging algorithm (using the xKalman reconstruction program with standard analysis cuts – see Chapter 10) have been compared in order to check their correlation. The two methods have been applied to the same sample of 400 GeV Higgs events. It was found that the correlation between the weights generated by the two methods is sufficient to avoid an excessive degradation of the pure offline performance. To study this further, a trigger
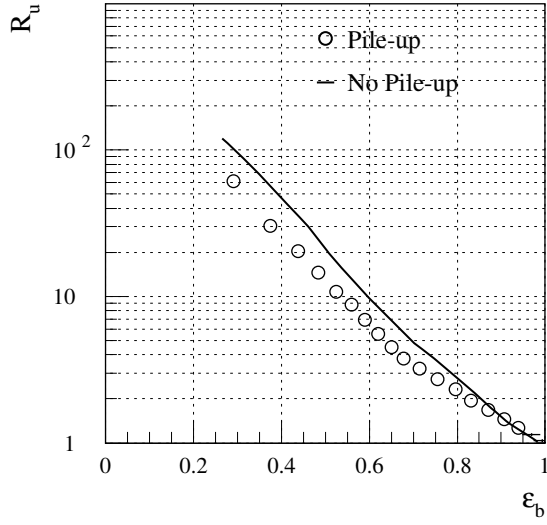
Figure 11-37 *u*-jet rejection as a function of *b*-jet efficiency for 400 GeV Higgs at high luminosity compared to low luminosity in the barrel.
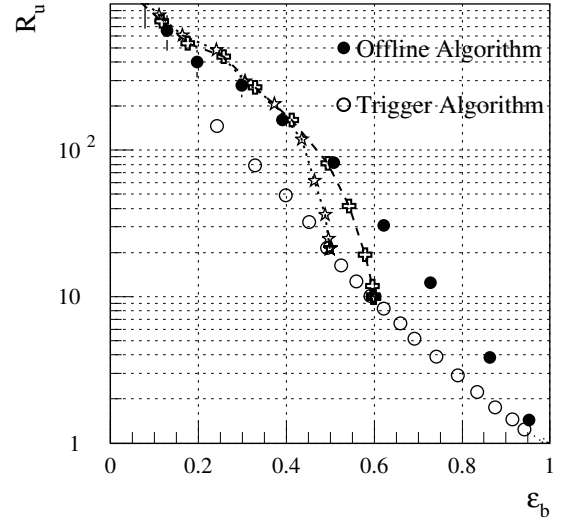
Figure 11-38 *u*-jet rejection as a function of *b*-jet efficiency for 400 GeV Higgs at low luminosity in the barrel for the trigger and offline algorithms. The lines show the offline performance starting from different trigger preselections (stars: $R_u = 10$, crosses: $R_u = 20$).

selection corresponding to $R_u = 10$ (20) and $\varepsilon_b = 60\%$ (50%) has been applied. To this LVL2 trigger selection, offline cuts (corresponding to different ε_b) were applied in order to see whether the pure offline performance could be restored. The results are shown in Figure 11-38. The offline performance is recovered after an offline cut corresponding to a final *b*-tagging efficiency of around $\varepsilon_b = 45\%$ (40%). Further, it can be seen that the same rejection ($R_u \approx 90$) as would be achieved in the absence of any trigger cuts and with $\varepsilon_b = 50\%$ can be obtained with a corresponding loss of *b*-tagging efficiency of about 2% (5%).

It remains to be seen whether improvements in the trigger performance and increased overlap with the offline algorithms can be achieved, and whether more realistic conditions (misalignments, uncertainties in the beam-spot position, degradations in silicon efficiency) would significantly degrade the performance quoted here.

11.5 Missing E_T and total scalar E_T

All calorimeter data have to be transferred to LVL2 for recalculating E_T^{miss} and total scalar E_T. The associated data traffic is of concern. Improvements of E_T^{miss} are however possible without recalculation – *e.g.* the LVL1 E_T^{miss} vector can be corrected for the p_T missed due to energetic muons and for LVL1 ADC saturation. The E_T^{miss} trigger will be used together with other signatures, such as leptons and jets. Events with very large missing-E_T may also indicate new physics.

11.6 Triggers for *B*-physics channels

11.6.1 Introduction and overview

At the LHC the *b*-quark production cross-section is many orders of magnitude higher than for e^+e^- machines and their dedicated *B*-physics experiments. For centrally produced *b*-quarks with $b \rightarrow \mu$ ($p_T^\mu > 6$ GeV) within the acceptance of the ATLAS detector, the Monte Carlo generator PYTHIA predicts a cross-section of ~2.4 μb. The azimuthal angle between the produced *b*-quark and $\bar{b}$-quark extends over the full range of 0–2π. The high particle-multiplicity in *b*-quark events, combined with a typical pile-up of 2.3 minimum-bias events per bunch crossing, at low luminosity of 10^{33} cm^{-2}s^{-1}, gives rise to a large combinatorial background (for reconstructing *B*-hadron decays), which must be rejected at the trigger level.

The *B*-physics programme is discussed in Chapter 17; the *B*-physics trigger has been previously described in [11-1]. All studies, except those of the *B* production mechanism, are based on the reconstruction of exclusive *B*-hadron decays, and in many cases also on the partial identification of the accompanying (anti-) *B*-hadron in order to tag the flavour of the *B*-hadron at production.

The physics channels currently studied may be grouped as follows (see Table 10-1 in [11-1]).

- Hadronic channels, tagged by the decay $b \rightarrow \mu$ of the accompanying *B*-hadron. The hadrons are required to have transverse momentum $p_T > 1.5$ GeV for decays with high multiplicity (*e.g.* $B_s \rightarrow D_s \pi$) or $p_T > 4$ GeV for decays with low multiplicity (*e.g.* $B_d \rightarrow \pi\pi$).

- *B* decays to *J/ψ* with subsequent decay $J/\psi \rightarrow \mu\mu$ or $J/\psi \rightarrow ee$. Tagging may be provided either by the semi-leptonic decay of the accompanying *B*-hadron, by *B*–π correlation or jet-charge measurements.

- Final states with very small branching fractions and containing muons (*e.g.* $B \rightarrow \mu\mu$, $B \rightarrow K^{*0}\mu\mu$).

The key selection criteria at the analysis level are based on particle identification (μ/*e*/hadrons), mass and vertexing cuts. The LVL2 trigger may make use of all these selections, although the use of vertexing or impact-parameter criteria is still under investigation and was not applied in the studies presented here.

The LVL1 trigger selects *b*-events through the muon from the decay of one of the *B*-particles, with $p_T^\mu > 6$ GeV. The LVL2 trigger confirms the trigger muon first in the muon spectrometer and subsequently in the Inner Detector. At this stage the threshold is sharpened and the contribution from π/*K* decays may be reduced. The muon from the decay of a *B*-particle does not indicate the direction of flight of the other *B*-hadron. For further selections, an unguided track search is therefore necessary; this can be achieved by a track search in the full TRT. The TRT tracks are then used as seeds for the track search in the precision tracker. The resulting three-dimensional tracks may be required to originate close to the trigger muon production vertex, thus rejecting tracks from additional minimum-bias events with primary vertices displaced in the *z*-coordinate. Three-dimensional information is also needed for mass cuts and for extrapolation to the calorimeter and Muon Systems to identify additional soft muons and electrons.

The LVL2 trigger addresses specific channels semi-exclusively. The signal is usually only a small fraction of the accepted rate. For example, in events selected with $J/\psi \rightarrow ee$ the rate is dominated by misidentified hadrons and conversion electrons. Similarly, the D_s and $B \rightarrow \pi\pi$ triggers are

dominated by combinatorial backgrounds. The di-muon rate is dominated by muons from decays of *B*-hadrons and from decays in flight of charged pions and kaons. The contributions from charm and direct *J/ψ* production are minor.

Impact-parameter cuts may be applied at LVL2 or in the Event Filter. The use of the precise information from the pixel detector at an early stage of the LVL2 decision chain is currently under study. Secondary-vertex finding can reduce the backgrounds in the offline analysis.

11.6.2 Tools and algorithms for *B*-physics trigger studies

The tools used for *B*-physics studies are described in detail in [11-1], Section 10.2. In this section, only a short account and update on the algorithms and key selections are given.

11.6.2.1 Tracking in the Inner Detector

The trigger algorithms for tracking in the Inner Detector are similar to those used for the RoI-guided LVL2 tracking trigger, but they must be efficient for much lower thresholds; no RoI guidance is available for the TRT algorithm. Typical p_T thresholds are 1.5 GeV for hadron and 0.5 GeV for electron candidates. Fast histogramming methods are used for the track search in the TRT and in the precision tracker. A description of the algorithm steps is given in Refs. [11-1] and [11-23], together with the resolutions achieved for single particles of fixed p_T. For the measurement of execution times, efficiency, fake-track rate, and electron-identification power, fully-simulated events with $B_d^0 \rightarrow J/\psi(ee) K_s^0$ decays with pile-up were used.

Figures 11-39 and 11-40 show the track-finding efficiency for the TRT algorithm as functions of the generated p_T and η for $B \rightarrow \mu X$ with pile-up added for low-luminosity operation.
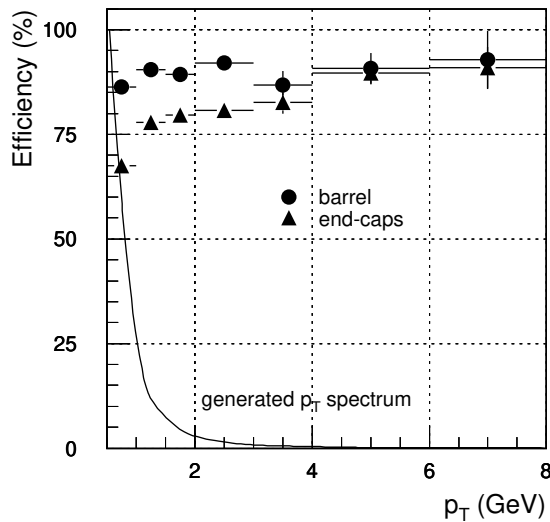
Figure 11-39 Track-reconstruction efficiency for pions with $p_T > 1$ GeV, integrated over $|\eta| < 0.8$ for the barrel and $0.8 < |\eta| < 2.5$ for the end-cap, versus generated p_T. The inlay shows the p_T spectrum of all pions in this η and p_T range.
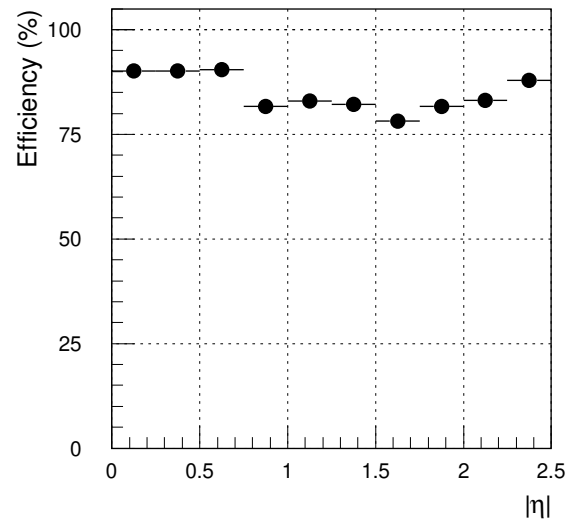
Figure 11-40 Track reconstruction efficiency for pions, integrated over generated $p_T > 1.0$ GeV, versus generated $|\eta|$.

A Kalman filter algorithm [11-24] is presently being studied as a possible alternative trigger algorithm for the precision tracker. The TRT track segments are extrapolated into the SCT. Trajectories within the initial road which contain a sufficient number of hits are retained. Most studies of specific *B*-physics channels were performed with a modified version of the ATLAS offline Kalman filter (xKalman [11-25]), which was adapted for trigger studies. The resulting rates for the different *B*-physics channels are summarised in Section 11.6.3.

All TRT algorithms perform the initial track search without making use of the drift time. Because of the low p_T of the *B* decay products, sufficient momentum resolution can be achieved using only the position of hit straws in the track fit. The studies assume, however, a constant magnetic field of 2 T over the whole tracker volume. The effect of the realistic solenoidal field was studied in [11-26]. Modifications to the TRT algorithms will be needed in the end-cap regions, *e.g.* for $|\eta| > 2$, where the magnetic field drops to 0.6 T.

11.6.2.2 Soft-electron identification

The efficient and clean identification of low-p_T electrons is an important element for *B*-physics triggers. This can be achieved using the combination of the Inner Detector, including the transition-radiation signature in the TRT, and the fine-grained EM Calorimeter. Electron-candidate tracks are extrapolated to the different longitudinal samplings of the EM calorimeter. A cluster of calorimeter cells is formed around each impact point and is used to measure the cluster energy as well as the longitudinal and transverse shape of the cluster. Depending on the set of selections, efficiencies of 80% to 65% are achieved for $b\bar{b} \rightarrow \mu e X$ events, where $p_T^\mu \geq 6$ GeV and $p_T^e \geq 5$ GeV; the corresponding efficiency for background events (excluding electrons from *b* or *c* quarks) is between 3% and 0.2%. The efficiency for this background is ~17% if only the TR function is used, requiring the fraction of transition radiation hits to exceed 0.14. More details are given in Section 10.2.3 of [11-1] and in Chapter 17.

11.6.2.3 Soft-muon identification

The LVL2 trigger for *B*-physics includes a selection on di-muons, with $p_T > 6$ GeV for the first muon, and a lower threshold for the second muon, normally 5 GeV, but thresholds as low as 3 GeV were studied as well. Two methods have been considered for identifying the lower-p_T muons.

- The muon spectrometer may be used if the muon has sufficient momentum to reach it; this is the case for $p_T > 5$ GeV muons in the barrel, and for $p_T > 3$ GeV in the end-caps.

- The identification of muons of 3 GeV $< p_T < 7$ GeV in the barrel, using the energy deposition in the last two layers of the Tile Calorimeter.

Results are reported in [11-1], Section 10.2.4. The muon identification in the Tile Calorimeter can reach high efficiencies > 90% for $p_T > 3$ GeV muons in the region of $|\eta|$ from 0.1 to 0.6 (barrel) and 0.9 to 1.2 (extended barrel). The pion rejection factors are p_T and η dependent and have typical values of 10 to 50, for momenta from 3 to 5 GeV, respectively. The most recent results for offline reconstruction are reported in Chapter 8 and [11-12].

11.6.3 Summary of *B*-physics rates

The rates for *B*-physics channels expected after the LVL1 and LVL2 triggers are summarised in Tables 11-17 and 11-18. Most of the events accepted by LVL1 have a muon with true p_T lower than the nominal 6 GeV threshold, and originate mainly from π/K decays. The rate is reduced to 9000 Hz by requiring that the muon is reconstructed in the Inner Detector with $p_T > 5.9$ GeV. Possible further rejection of $\pi/K \to \mu\nu$ decays by requiring matching of the Inner Detector and muon-spectrometer tracks is under investigation (Chapter 8). The selection of specific *B*-physics channels was discussed in Section 10.3 of [11-1]. Some of the selection criteria are indicated in the summary Table 11-18, and details are described in Section 10.3.3 of [11-1].

Table 11-17 Summary of *B*-physics trigger: rate of events with one muon with p_T threshold 6 GeV after LVL1 and after confirmation at LVL2, represented here by Inner Detector reconstruction only.

	Trigger requirement	Rate (Hz)
LVL1	μ ($p_T > 6$ GeV, $\vert\eta\vert < 2.4$) triggered by the Muon System	23000
LVL2	LVL1 output spectra convolved with reconstruction efficiency in Inner Detector with cut $p_T > 5.9$ GeV	9000 (2300 $b \to \mu$ 1100 $c \to \mu$ 5400 $K/\pi \to \mu$)

Table 11-18 Summary of *B*-physics triggers: rates of events satisfying the LVL2 trigger selections applied to events already containing one muon with p_T threshold 6 GeV identified at LVL1 and confirmed at LVL2.

	Trigger requirements	Selected *B*-channels	Rate (Hz)
Hadron channels	$D_s \to \phi(K^+K^-)\pi$, 3 hadrons $p_T > 1.5$ GeV, loose mass cuts	$B_s \to D_s \pi$, $B_s \to D_s a_1$	190
	2 hadrons $p_T > 4$ GeV, loose mass, angle and Σp_T cuts	$B_d \to \pi\pi$	80
Electron channels	*ee* pair, $p_T > 0.5$ GeV, identification by TRT, 2.0 GeV < m(*ee*) < 3.8 GeV	$b\bar{b} \to \mu B_d(J/\psi(ee)K^0)$	310
	single *e*, $p_T > 5$ GeV, identification in TRT+ECAL of electron reconstructed with $p_T > 4$ GeV in the Inner Detector	$b\bar{b} \to e\, B_d(J/\psi(\mu\mu)K^0)$	93 [51 from true electrons, 42 from wrongly-identified hadrons]
Muon channels	second μ ($p_T > 5$ GeV, $\vert\eta\vert < 2.5$) identification in muon chambers + matching with the Inner Detector	$B_d \to J/\psi(\mu\mu)(K/K^*)$, $B_s \to J/\psi(\mu\mu)\phi$, $B \to \mu\,\mu$, $B \to K^{0*}\mu\mu$, *etc.*, $\Lambda_b \to \Lambda^0 J/\psi(\mu\mu)$, $B_c \to J/\psi(\mu\mu)\,\pi$	170 [80 from *b/c*, 90 from K/π]
Total LVL2 *B*-physics trigger rate			840 Hz

The results presented in this section for the various *B*-physics trigger channels demonstrate that the total *B*-physics rate from LVL2 can be reduced to ~900 Hz (Table 11-18); this is acceptable for input to the Event Filter. The uncertainties in the rates are due mainly to model-dependence in the prediction of cross-sections, which could be as large as a factor four.

11.7 LVL1 and LVL2 global decision

11.7.1 Introduction

This section presents a set of trigger menus that covers the vast majority of main-stream discovery physics; more details are presented in Refs. [11-1] and [11-27]. The menus are split into two groups, a very simple set of menus covering the majority of main-stream discovery physics, and more specialised triggers. The latter are needed to cover standard physics such as jet cross-section measurements and background studies. They also include monitoring and calibration triggers to read out data relating to the trigger and detector subsystems for technical studies. The trigger menus eventually used by ATLAS will be more complex and will include triggers that are not required for any specific physics analysis. Some of these are covered in the second set of menus. The specialised triggers are those that are needed to understand thresholds, pile-up and to take data for studies of known physics processes. They will make use of a range of prescale factors to limit the rate.

11.7.1.1 Rates

The physics-oriented trigger menus are determined by the best compromise between efficiency for physics channels and affordable trigger rate. The LVL1 trigger rate is dominated by background physics processes such as jet events faking isolated $e/\gamma/\tau$, as well as giving high-p_T jet triggers, and muons from $b/c \rightarrow \mu X$, $\pi/K \rightarrow \mu \nu$.

The output target rate for LVL1 is ~40 kHz, which allows a safety factor of almost two, compared to the initial design capability of 75 kHz. The estimated uncertainty on the pp inelastic cross-section is about 30%. The total uncertainty on the main background processes, however, could be as large as a factor of two (inclusive jet production at low p_T) to five ($b, c \rightarrow \mu$ events). No *K*-factor correction has been used. Corrections for biases resulting from η and p_T (hard scatter) cuts applied for reasons of CPU efficiency in the Monte Carlo simulations, are also only approximate. More details on the cross-sections and simulation tools can be found in [11-1] Chapters 2 and 4, respectively.

The output target rate for LVL2 is around 1 to 2 kHz, but it depends on the optimum separation between LVL2 and the Event Filter, which will not be determined for some time. The majority of LVL2 muon triggers will be genuine prompt muons, whereas the LVL2 isolated e/γ rate is still dominated by jet events. The expected rates for inclusive $W \rightarrow e\nu$ and $Z \rightarrow ee$ production with $p_T(e) > 30$ GeV are about 50 Hz and 5 Hz, respectively, at high luminosity (10^{34} cm^{-2}s^{-1}). Detailed references and comments for the quoted rates are available in Chapter 11 of [11-1].

11.7.2 Key to the menus

Figure 11-41 summarises the notation used to formulate the trigger menus and define the trigger objects at the various levels. The notation of Tables 11-1 and 11-2 is used to describe the object type.
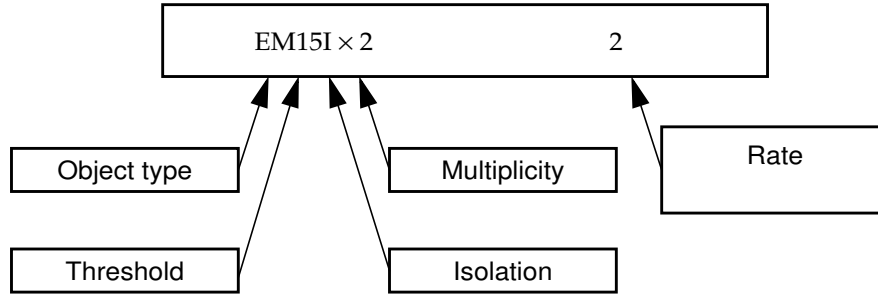
Figure 11-41 Notation used in the menus.

LVL1 trigger objects are shown in capital letters, whereas LVL2 trigger objects start with lower case letters. The E_T threshold and the requirement of isolation are indicated after the object code. The thresholds are generally given at the point where the LVL1 (LVL2) algorithms are 95% (90%) efficient. Exceptions include the E_T^{miss} trigger, where the actual cut is given, and the muon triggers which are given at ~90% efficiency for LVL1. The muon triggers have an additional inefficiency due to the geometric detector acceptance, which is approximately 90%, averaged over the fiducial η coverage.

The isolation thresholds will change with the p_T of the trigger object, becoming looser for higher p_T candidates and being completely removed at very high p_T. At LVL2 the trigger objects may be constrained by additional requirements, like mass cuts. As shown in Table 11-21, more complex objects are used at LVL2 for *B*-physics triggers.

11.7.3 Physics menus

The first set of menus covers the majority of LHC physics studies. They are intended to provide a common focus for physics and trigger-performance studies. They are designed to be simple, inclusive and to satisfy the physics requirements with as short a list of trigger items as possible. The one exception to this is *B*-physics, where selection of particular decay modes must be done in the LVL2 trigger. Where isolation of objects is indicated, it should be understood that the isolation criteria are relaxed as object E_T and multiplicity increase. For very high E_T, isolation is not required. No use is made of veto conditions, though they may be applied at LVL1 and LVL2.

11.7.3.1 LVL1 low luminosity

The LVL1 menu for low luminosity is shown in Table 11-19. The MU6 trigger selects events for *B*-physics studies. The threshold for the two EM object trigger is set as low as possible to maximise the efficiency for $H \rightarrow \gamma\gamma$ and $Z \rightarrow ee$ decays. If possible the threshold will be lowered further to give some acceptance for high-p_T J/ψ and Y decays to *ee*.

The inclusive-jet threshold has been set high to reduce the rate and make more room for other triggers. This is because the additional jet rejection available at LVL2 is small, so the useful LVL1 threshold is effectively limited by LVL2 rate requirements. Multi-jet and jet+E_T^{miss} triggers are given priority when sharing out the rate budget for these types of triggers. The thresholds of the multi-jet triggers are also chosen to give acceptable rates for LVL2. No specific requirements from the physics have been stated which would dictate specific values for these thresholds.

For the J50 + XE50 and T20 + XE30 triggers [11-14], the thresholds and rates should be taken as indicative. These triggers are intended to provide efficient inclusive triggers for SUSY production, and also for calibration via $W \rightarrow \tau\nu$ / $Z \rightarrow \tau\tau$. The additional requirement of missing energy allows lower thresholds than are possible with the jet and τ/hadron inclusive triggers. The aim for these triggers is a missing-E_T threshold of around 30–50 GeV and the lowest possible jet and τ thresholds that give an acceptable rate at both LVL1 and LVL2. It should be noted that there is no direct physics need for the LVL1 τ trigger.

The table entry 'Other triggers' indicates the rate budget which is reserved for specialised, monitoring and calibration triggers that are described later in this document.

Table 11-19 LVL1 low and high-luminosity menus.

Low luminosity		High luminosity	
Trigger	**Rate (kHz)**	**Trigger**	**Rate (kHz)**
MU6	23	MU20	3.9
		MU6 $\times$ 2	1
EM20I	11	EM30I	22
EM15I $\times$ 2	2	EM20I $\times$ 2	5
J180	0.2	J290	0.2
J75 $\times$ 3	0.2	J130 $\times$ 3	0.2
J55 $\times$ 4	0.2	J90 $\times$ 4	0.2
J50 + XE50	0.4	J100 + XE100	0.5
T20 + XE30	2	T60 + XE60	1
		MU10 + EM15I	0.4
Other triggers	5	Other triggers	5
Total	**44**	**Total**	**40**

11.7.3.2 LVL1 high luminosity

The LVL1 high-luminosity menu in Table 11-19 contains mostly the same objects as the low luminosity menu, but with higher thresholds and/or rates. An additional trigger at high luminosity is MU10 + EM15I. Another extra trigger EM20I + XE is being studied. The additional physics that might be caught by these triggers at high luminosity is *e.g.* $W \rightarrow e\nu$ and $Z \rightarrow \tau\tau$ for calibration purposes.

11.7.3.3 LVL2 low luminosity

Most of the menu items in the low-luminosity LVL2 trigger menu, Table 11-20, follow directly from the LVL1 items in Table 11-19. EM triggers can be refined at LVL2 into candidates for electrons and/or photons. It is possible to apply isolation criteria to the muon triggers to help reduce the rate. Events that satisfy the MU6 LVL1 trigger and the LVL2 µ6 preselection are passed to the *B*-physics menu, described in the next section. The inclusive single-muon trigger µ20 does not require isolation. An inclusive di-muon trigger µ6 + µ5 can be found in the *B*-physics menu (Table 11-21). The trigger µ6i + e15i is an example of the use of a secondary RoI (in this case EM15I) which would not in itself constitute a LVL1 trigger.

Table 11-20 LVL2 low- and high-luminosity menus.

Low luminosity		High Luminosity	
Trigger	**Rate (Hz)**	**Trigger**	**Rate (Hz)**
µ20	200	µ20i	200
		µ6 × 2 + m_B	10
		µ10 × 2	80
e20i	100	e30i	600
e15i × 2	~few Hz	e20i × 2	20
γ40i	100	γ60i	400
γ20i × 2	5	γ20i × 2	100
j180	100	j290	120
j75 × 3	80	j130 × 3	80
j55 × 4	40	j90 × 4	80
j50 + xE50	250	j100 + xE100	~few 100
τ20 + xE30	400	τ60 + xE60	~few 100
µ6i + e15i	15	µ10i + e15i	20
B-physics	1150		
Other triggers	100	Other triggers	100
Total	**2400**	**Total**	**2000**

As at LVL1, the additional requirement of missing energy in the SUSY/calibration triggers (j50 + xE50, τ20 + xE30), allows lower thresholds than for the inclusive triggers. It is not necessarily expected that xE will be recalculated at LVL2, but the LVL1 E_T^{miss} value could be refined, for example by including muon E_T and correcting for LVL1 calorimeter trigger ADC saturation. For the rates given here, no LVL2 refinement has been taken into account.

11.7.3.4 LVL2 low luminosity *B*-physics

The low-luminosity *B*-physics trigger menu will only be used if the LVL1 trigger includes a MU6 object, and the LVL2 trigger confirms a µ6 trigger.

Table 11-21 Example of *B*-physics trigger menu.

Trigger Signature	Rate (Hz)	Example Channel
μ6 + additional μ5	170	Inclusive $J/\psi \to \mu^+\mu^-$
μ6 + e0.5 × 2 + m$_{ee}$	310	$b \to \mu X, B \to J/\psi X \to ee$
μ6 + e5	100	$b \to eX, B \to J/\psi X \to \mu\mu$ (second μ not required in trigger)
μ6 + h5 × 2 + m$_B$	80	$b \to \mu X, B_d \to \pi^+\pi^-$
μ6 + h1.5 × 3 + m$_\phi$ + m$_{Ds}$	190	$b \to \mu X, B_s \to D_s(\phi^0(K^+K^-)\pi)X$
μ6 + ...	300	reserved for additional *B* channels
Total	**1150**	

The rates after the LVL2 selection are given in Table 11-21. There is little overlap between the trigger items so the total rate is approximately equal to the sum of the rates for the individual triggers.

11.7.3.5 LVL2 high luminosity

Most menu items in the LVL2 high-luminosity menu, Table 11-20, follow directly from the LVL1 items of Table 11-19. Compared to low luminosity, thresholds have generally been raised and the requirement of isolation has been added to the inclusive muon trigger. The di-muon triggers without isolation requirements are useful for *B*-physics. The rate for the di-electron trigger e20i × 2 is almost a complete subset of γ20i × 2, so the rate is not included in the total.

11.7.4 Menus for specialised triggers

Redundant triggers are needed for cross checks. Inclusive triggers are prescaled with lower thresholds to understand threshold behaviour, collect background samples, and to take low-p_T data. The rates will be controlled by choices of threshold and prescale factors. The rate budgets include 5 kHz at LVL1 and 100 Hz at LVL2 for these triggers. At this stage, the most important aspect is to know the number of thresholds required as this has implications for the design of the LVL1 trigger.

A number of additional inclusive triggers, with high thresholds and low rates without prescaling are foreseen: τ/hadron; E_T^{miss}; ΣE_T, ΣE_T^{jet}. A localised forward-energy trigger is also under consideration.

Prescaled triggers are foreseen with a range of thresholds. Typically, these would have four to six (possibly low) thresholds per trigger, each with a different prescale factor. Prescaled triggers will include: single jet, three jets, four jets; muon, di-muon; electron/photon; τ/hadron; E_T^{miss}; ΣE_T, ΣE_T^{jet}; forward-energy (under consideration).

In addition to the specialised physics triggers listed above, some more technical triggers are foreseen. These include detector-calibration triggers, as well as a random trigger and a trigger on bunch crossings, including a trigger on empty bunch crossings.

11.7.5 Physics coverage of the trigger menus

It is believed that the set of triggers proposed in Tables 11-19 and 11-20 covers most of the physics goals of the experiment. In fact, many processes will be selected through multiple trigger signatures, thus providing optimal efficiency and several means of measuring the trigger efficiency.

Inclusive lepton and di-lepton triggers provide $W \to l\nu$ and $Z \to ll$ selections, where l designates an electron or a muon. They therefore give an unbiased trigger for many Standard Model physics processes and also for many searches for physics beyond the Standard Model. At low luminosity, $W \to l\nu$ and $Z \to ll$ decays are selected by the MU6/EM20I LVL1 triggers and the μ20/e20i LVL2 triggers; $Z \to ll$ decays are also selected by the EM15I × 2 LVL1 triggers and the μ6 + μ5 / e15i × 2 LVL2 triggers.

At high luminosity, the $W \to l\nu$ decays can still be selected by inclusive lepton triggers, although with a somewhat high threshold in the case of electrons (MU20/EM30I at LVL1 and μ20i/e30i at LVL2). A trigger on an isolated electron with a lower threshold and an additional E_T^{miss} requirement is being studied at high luminosity in LVL1 and LVL2 in order to recover efficiency for the inclusive $W \to l\nu$ selection. In contrast the thresholds for the inclusive $Z \to ll$ decays remain comfortably low (MU6 × 2 / EM20I × 2 at LVL1 and μ10 × 2 / e20i × 2 at LVL2).

As mentioned above, many physics processes of interest are covered by the inclusive lepton/di-lepton triggers. Examples include the following.

- Gauge-boson pair production, for the study of anomalous couplings and to investigate the behaviour of the production cross-section at high mass.

- Top-quark production (single top or $t\bar{t}$ pairs), for all cases except $t\bar{t}$ production with fully-hadronic top decays.

- Direct production of SM or MSSM Higgs bosons with $H \to ZZ^{(*)}, WW^{(*)}$ decays, over the full Higgs mass range of interest. Associated production of SM Higgs bosons through $WH/ZH/t\bar{t}H$ processes, with $H \to b\bar{b}$ or $H \to \gamma\gamma$, and $W \to l\nu$ or $Z \to ll$.

- Decays of MSSM Higgs bosons, such as $A \to Zh$, $H/A \to \mu\mu$, $H/A \to t\bar{t}$, and also $H/A \to \tau\tau$ with one leptonic τ decay. Production of $t\bar{t}$ with one top decay to bH, where the other top-quark decay provides the inclusive W trigger.

- Production of new vector gauge bosons (W'/Z'), with W'/Z' decays to leptons. Also, resonance production at the TeV scale (strongly interacting Higgs sector), with resonance decays into gauge-boson pairs.

- Production of supersymmetric particles with final states containing: at least one high-p_T lepton and large E_T^{miss} in the case of R-parity conservation; or at least one high-p_T lepton (*e.g.* from $\chi_2^0 \to ll\chi_1^0$ decay) with or without large E_T^{miss} in the case of R-parity violation with $\chi_1^0 \to 3$ jets, $\chi_1^0 \to l\nu\nu$, or $\chi_1^0 \to ll'\nu$.

- Searches for leptoquarks decaying into electrons or muons; searches for compositeness in the lepton sector through Drell-Yan production.

The remaining physics channels not covered by the inclusive lepton/di-lepton (and electron + E_T^{miss}) triggers discussed above are:

- B-physics, which is covered in a separate menu in Table 11-21. A budget has been foreseen at LVL2 for B decay channels that are not yet part of the studies.

- $H \rightarrow \gamma\gamma$ decays from direct Higgs production, which are covered by EM15I × 2 (EM20I × 2) for LVL1 and by $\gamma20i \times 2$ ($\gamma20i \times 2$) for LVL2 at low (high) luminosity. These triggers also cover possible MSSM Higgs boson decays such as $H \rightarrow hh \rightarrow b\bar{b}\gamma\gamma$.

- Searches for supersymmetry involving high-p_T jets with or without E_T^{miss}. At low luminosity the combination of J50 + xE50, J180, and J75 × 3/J55 × 4 triggers provides excellent coverage for all exclusive final states of interest not containing leptons. In the case of R-parity conservation, final states containing at least two high-p_T jets and large E_T^{miss} (typically two jets with E_T > 150 GeV and E_T^{miss} > 200 GeV) provide a broad inclusive sample for more exclusive searches. In the case of R-parity violation, with χ_1^0 decaying predominantly to three jets. Here the multi-jet triggers will cover most of the exclusive final states of interest. To date the only exclusive final states which have been proven to be observable above the huge potential QCD background are those containing isolated high-p_T leptons.

  At high luminosity, the higher thresholds applied to the various jet triggers and to the jet+E_T^{miss} trigger will be well suited to searches for higher-mass SUSY particles.

- Searches for leptoquarks decaying into a jet and a neutrino that rely on the jet+E_T^{miss} trigger.

- Searches for resonances decaying into jets and for compositeness in the quark structure. These rely largely on the inclusive single-jet trigger (*e.g.* additional vector bosons or technicolour resonances decaying to two jets) or on multi-jet triggers (*e.g.* purely hadronic decays of $t\bar{t}$ pairs), both at low and high luminosity.

A τ+E_T^{miss} trigger may increase the sensitivity to specific SUSY signatures for high values of tan β. It is also expected that the large variety of fairly inclusive triggers presented here would be sensitive to other new physics.

Finally, it is important to emphasise that much of the early large cross-section physics (*e.g.* QCD jets, direct photons, *etc.*) will be studied using more inclusive triggers than the ones quoted explicitly in the menus of Tables 11-19 and 11-20.

11.8 The task of the Event Filter

The task of the Event Filter (EF) is to make the final selection of physics events which will be written to mass storage for subsequent full offline analysis, and to reduce the trigger rates to as close to the real physics rates as possible. This should allow one to reduce the output data rate from LVL2 by an order of magnitude, giving ~100 Hz if the full event data are to be recorded. Event-summary information could be recorded at much higher rates, possibly for certain specific triggers (*e.g.* single-jet or multi-jet triggers for high-statistics QCD studies involving only the calorimeter information) but certainly not for the main-stream trigger items, which make up the bulk of the LVL2 selected events.

After event building, the EF will be able to perform detailed reconstruction using the complex algorithms of the offline code itself. All event data are accessible at the EF level for calculations and selections, though only part of these data will be used by the algorithms. Similar to the LVL2 guidance by LVL1, the EF algorithms will be guided by the LVL2 results and possibly by the LVL1 secondary-RoI information. The processing by the EF must result in efficient and complete tagging of the events to prepare efficient event selection for physics analysis. Depending on the processing time needed by the algorithms, the processing power available, and the sta-

bility of the calibrations and beam position, one may aim at completing in the EF the reconstruction to such a degree that the subsequent analysis steps have only to perform hypothesis-dependent updates of the reconstruction. Thanks to this potential performance, cut adjustments which are not possible at LVL2 will become possible; the exact selection criteria to be used have not yet been chosen.

In contrast to LVL1 and LVL2, some of the EF output rates expected are of the same order of magnitude as the signal itself, as shown below in a few cases for low and high-luminosity operation. Many processes will be selected through multiple trigger signatures, thus providing optimal efficiency and several means of controlling the crucial aspects of the trigger efficiency. Inclusive lepton and di-lepton triggers provide $W \to l\nu$ and $Z \to ll$ selections. They therefore give an unbiased trigger for many Standard Model physics processes and also for many searches for physics beyond the Standard Model, as discussed in the previous section.

The most challenging of these inclusive $W \to l\nu$ or $Z \to ll$ triggers is certainly the $W \to e\nu$ trigger, which has an expected output rate from LVL2 of 600 Hz at high luminosity for $p_T^e > 30$ GeV. Most of this output rate is still due to background from charged hadrons and from photon conversions (see Section 11.4.3). On the other hand, the expected rate for the inclusive $W \to e\nu$ signal events with $p_T^e > 30$ GeV and an additional cut requiring $E_T^{miss} > 25$ GeV is of order 50 Hz.

The above numbers clearly show that one of the main tasks of the EF will be to bring the rate of inclusive $W \to e\nu$ trigger candidates as close as possible to the real physics rate through a combination of tighter electron-identification cuts and of loose E_T^{miss} cuts. Whether the total expected rate of ~50 Hz would be acceptable or not is a matter for further study. More exclusive processes containing $W \to e\nu$ decays are, however, expected to have much lower trigger rates after the Event Filter. For example, the rate for signal events containing a $W \to e\nu$ decay and two jets with $E_T > 30$ GeV and within $|\eta| < 2.5$ is expected to be below a few Hz. This shows that the EF can provide a moderate output rate for all physics searches of the type $WH/ZH/t\bar{t}H$ production with $H \to b\bar{b}$ and $W \to l\nu / Z \to ll$, possibly without processing the event further in the Inner Detector, and without improving the electron identification, which was provided by LVL2. The rate for signal events from top-quark production containing at least one high-p_T electron (or muon) is expected to be of the order of 1 Hz at high luminosity. Again, these events can be selected by the EF in a very inclusive way.

Obviously, the task of the EF in terms of selecting inclusive $W \to \mu\nu$ decays or $Z \to ll$ decays is easier than that of selecting inclusive $W \to e\nu$ decays. This is because the expected LVL2 output rates for the high-p_T single muon trigger and for the isolated high-p_T di-lepton triggers are much lower than for the high-p_T single isolated electron trigger. The expected rate for inclusive $Z \to ll$ signal events is 10 Hz at high luminosity, and the EF will clearly be able to approach that rate by using *e.g.* a mass cut on the lepton pair.

The physics channels not covered by the inclusive lepton/di-lepton (and electron+E_T^{miss}) triggers were listed in the previous section. The area of *B*-physics is another challenging task for the Event Filter, since the expected output rate from LVL2 is of the order of 1 kHz for *B*-physics alone at low luminosity and since most of the candidate events are genuine *B*-events. A complete and accurate reconstruction of the Inner Detector information is necessary in order to further reduce the rate, for example using vertexing cuts. The largest rate from physics channels to be analysed in this field is for inclusive $J/\psi \to \mu\mu$ decays with $p_T^{\mu_1} > 6$ GeV and $p_T^{\mu_2} > 5$ GeV. The total expected rate for signal events is about 5 Hz from direct J/ψ production and about 3 Hz from inclusive $B \to J/\psi$ production. These events are expected to be heavily used in *CP*-violation studies with jet-charge and $B-\pi$ tagging methods applied in addition to the more traditional lepton tagging. To reduce the LVL2 output rates to values close to the physics rates

quoted above, a combination of vertexing cuts on the muon pair and of tighter kinematic cuts, including mass cuts, will have to be performed by the Event Filter. The more exclusive *B*-decays are expected to contribute at much lower levels of typically 0.1 Hz per channel or less.

It is also hoped that the large variety of fairly inclusive triggers presented here would be sensitive to unexpected new physics. Finally, it is important to emphasise that much of the early large cross-section physics (*e.g.* QCD jets, direct photons, *etc.*) will be studied using more inclusive triggers than the ones quoted explicitly in Section 11.7 as well as dedicated algorithms in the Event Filter.

The menus and rates presented in Section 11.7 will be used as basis for menus for more detailed studies of both the LVL2 trigger and the Event Filter, in terms of performance and of implementation. Those trigger items that are considered particularly challenging or critical will be subject to detailed trigger performance studies using fully-simulated data as input and offline reconstruction code as a reference. Wherever possible, the trigger-performance results will be parametrised for use in fast simulations with high-statistics background samples. A complete set of output rates for the EF can only be obtained through a combination of detailed full-simulation studies and of fast-simulation studies, which use parametrised detector performance.

In conclusion, the role of the Event Filter will be very important in determining the scope and breadth of physics channels available to ATLAS to study in detail the physics channels of interest and to constrain as well as possible the background estimates to possible new physics. It is hoped that most of the physics goals, with the notable exception of *B*-physics, can be achieved with RoI-guided processing, *i.e.* avoiding complete processing of the Inner Detector information.

11.9 References

11-1   ATLAS Collaboration, Trigger Performance Status Report, CERN/LHCC 98-15 (1998).

11-2   ATLAS Collaboration, First-Level Trigger Technical Design Report, ATLAS TDR 12,
            CERN/LHCC/98-14 (1998).

11-3   ATLAS Collaboration, Technical Proposal, CERN/LHCC/94-43 (1994).

11-4   ATLAS Collaboration, DAQ, EF, LVL2 and DCS Technical Progress Report,
            CERN/LHCC/98-16 (1998).

11-5   Level-1 muon trigger group, 'Improvements to the level-1 muon trigger giving increased
            robustness against backgrounds', ATLAS Communication ATL-COM-DAQ-99-011 (1999).

11-6   P. Eerola, 'The inclusive muon cross-section in ATLAS', ATLAS Internal Note
            ATL-MUON-98-222 (1998).

11-7   T. Sjostrand, 'PYTHIA 5.7 and JETSET 7.4 Physics and Manual', CERN-TH.7112/93
            (1993).

11-8   J. Ranft, '*DPMJET* version II.3 and II.4: sampling of hadron–hadron, hadron–nucleus and
            nucleus–nucleus interactions at cosmic-ray energies, according to the Dual Parton
            Model', INFN-AE-97-45 (1997).

11-9   A.I. Drozhdin *et al.*, Nucl. Instrum. Methods **A381** (1996) 531.

11-10   S. Robins, 'Level-1 trigger rate from beam-halo muons in the end-cap', ATLAS Internal
            Note ATL-DAQ-98-128 (1998).

11-11   A. Ferrari *et al.*, Z. Phys. **C70** (1996) 413, and FLUKA manual
         http://www.cern.ch/alice/Projects/offline/Simulation/fluka

11-12   D. Costanzo *et al.*, 'Muon trigger with TileCal, a preliminary investigation',
         ATLAS Internal Note ATL-DAQ-99-002 (1999).

11-13   S. Catani *et al.*, Nucl. Phys. **B406** (1993) 187.

11-14   R. Dubitzky *et al.*, 'Level-1 rates for triggers using the missing-E_T signature',
         ATLAS Internal Note ATL-DAQ-98-011 (1998).

11-15   N. Baytch *et al.*, 'A method for a LVL2 muon trigger for ATLAS', ATLAS Internal Note
         ATL-DAQ-99-003 (1999).

11-16   T.G. Shears, 'Studies of muon isolation in the level-2 muon trigger', ATLAS Internal Note
         ATL-DAQ-98-122 (1998).

11-17   S. Gonzalez, T. Hansl-Kozanecka and M. Wielers, 'Selection of high-p_T electromagnetic
         clusters by the Second Level trigger of ATLAS', ATLAS Communication
         ATL-COM-DAQ-99-009 (1999).

11-18   J. Baines *et al.*, 'Identification of high-p_T electrons by the Second Level Trigger of ATLAS',
         ATLAS Communication ATL-COM-DAQ-99-007 (1999).

11-19   M. Wielers, 'Photon Identification with the ATLAS Detector', ATLAS Communication
         ATL-COM-PHYS-99-011 (1999).

11-20   J. Baines, R. Dankers and S. Sivoklokov, 'Performance of a LVL2 trigger feature-extraction
         algorithm for the Precision Tracker', ATLAS Communication ATL-COM-DAQ-99-008
         (1999).

11-21   ATLAS Collaboration, Inner Detector Technical Design Report, ATLAS TDR 4,
         CERN/LHCC/97-16 (1997).

11-22   E. Richter-Was and D. Froidevaux, 'MSSM Higgs searches in multi-*b*-jet final states',
         ATLAS Internal Note ATL-PHYS-97-104 (1997).

11-23   J. Baines *et al.*, 'Global Pattern Recognition in the TRT for *B*-Physics in the ATLAS
         Trigger', ATLAS Communication ATL-COM-DAQ-99-004 (1999).

11-24   R.E. Kalman, Trans. ASME, J. Basic Eng. **82D** (1960) 35.

11-25   I. Gavrilenko, 'Description of global pattern-recognition program (xKalman)',
         ATLAS Internal Note ATL-INDET-97-165 (1997).

11-26   S. Sivoklokov, 'TRT Trigger performance in the solenoidal magnetic field',
         ATLAS Communication ATL-COM-DAQ-99-005 (1999).

11-27   S. George and T. Hansl–Kozanecka (eds), 'ATLAS Trigger Menus', ATLAS Internal Note
         ATL-DAQ-98-121 (1998).

11-28   E. Richter-Was, D. Froidevaux and L. Poggioli, 'ATLFAST 1.0 A package for particle-level
         analysis', ATLAS Internal Notes ATL-PHYS-96-079 (1996) and ATL-PHYS-98-131 (1998).

12 Determination of the mass scale

12.1 Introduction

This chapter describes some of the methods which will be used to understand to the best possible accuracy the absolute measurement scale of the ATLAS detector when the experimental data will be used to extract precise estimates of the masses of known or newly discovered particles.

The need for accurate experimental measurements of particle masses does not require much justification, given the progress made in particle physics over the past decades through such measurements. Nevertheless, a few examples of what might be achieved with ATLAS at the LHC are listed below and described in more detail in the relevant chapters devoted to the physics performance.

An accurate measurement of the Higgs boson mass will provide strong additional constraints on the underlying model. A statistical accuracy of ~0.1% can be achieved over a wide range of Higgs boson masses (see Sections 19.2.12.1 and 19.3.4), and the power of a constraint at this level is clearly demonstrated in the context of the global fits to the parameters of minimal supergravity models, as described in Section 20.2.9.

If supersymmetry were to be discovered at the LHC, it has been demonstrated already a few years ago that ATLAS would be able to perform a wide set of precision measurements of various supersymmetric particle masses (see Chapter 20). The more accurate these measurements will be, the tighter the constraints on the fundamental parameters of the underlying SUSY model will be (see Sections 20.2.9, 20.2.10 and 20.3.5).

Very precise measurements of the masses of the W boson (see Section 16.1) and of the top quark (see Section 18.1.3), beyond those which will be achieved at the Tevatron and at LEP2 in the near future, will provide further additional constraints on the Standard Model. If a Standard Model Higgs boson were also to be discovered at the LHC, the combination of all these measurements would provide overall constraints of the Standard Model an order of magnitude stronger than those available today.

The physics goals described above have led to the following requirements for the knowledge of the absolute scale of energy and momentum measurements in ATLAS:

- In the case of electrons and muons, the scale should be known to an accuracy of ~0.1%. A similar accuracy has already been reached by the CDF [12-1] and D0 [12-2] experiments at the Tevatron. This accuracy should be achievable, given that ATLAS will be able to benefit directly from much larger statistics of vector boson leptonic decays. This will however require considerable work.

  This accuracy will be adequate for almost all the physics goals of ATLAS at the LHC, but will be needed over the full lifetime of the experiment and in particular at the highest luminosities. The one exception is the measurement of the W mass at low luminosity, which requires a much better knowledge of the measurement scale of electrons and muons, namely at the level of 0.02%, as explained in more detail in Section 16.1.4.

- In the case of hadronic jets, the scale should be known to an accuracy of ~1%. In principle, it would be desirable to measure decays involving quarks with a similar accuracy to those

involving leptons. However, it is clear that the fragmentation and hadronisation of the original partons lead to uncertainties in the experimental measurements, which cannot be readily decreased below this level of 1%.

Another aspect linked to the understanding of the absolute scale of measurements performed using the ATLAS detector concerns calorimeter energy measurements at a scale of the order of a TeV or more, which cannot be constrained directly from data taken in test beams during the detector construction. The physics topics of interest in this area are:

- for the EM Calorimeter scale, mass measurements of possible new vector bosons decaying into electrons (see Section 21.6.1);

- for the hadronic calorimetry, QCD physics with high-p_T hadronic jets (see Section 15.5), mass measurements of leptoquarks decaying to a lepton and a jet (see Section 21.4), and quark compositeness studies (see Section 21.5.1).

None of the above physics studies requires an understanding of the absolute scale of the energy measurements to a very high level of accuracy. However, departures of the calorimeter response from linearity may cause serious problems in the searches for quark compositeness using the jet p_T spectrum, and these are discussed in some detail in Sections 9.1.1.3 and 21.5. Therefore this chapter will only discuss issues concerning the overall mass scale in ATLAS.

In order to understand the magnitude of the task set by the physics goals described above, it is important to recall that, when the first LHC collisions will be recorded in the detector, the knowledge of the absolute calibration of the various systems in ATLAS prior to data-taking will be far from that ultimately required:

- the absolute momentum scales for charged particles measured in the Inner Detector and the Muon System will be known to 0.5% or better from the initial magnetic field maps and geometrical surveys;

- the absolute energy scale for electrons and photons will be known to 1-2% from the transfer to the experiment of calibration data taken with electrons in test beam;

- the absolute energy scale for hadronic jets over $|\eta| < 3.2$ will be known to ~5-10% from the transfer to the experiment of calibration data taken with charged pions in test beam and from Monte Carlo simulations of jet fragmentation into hadrons.

There would be clearly little hope to improve this initial knowledge by a factor of ~25 for electrons and muons and by a factor of ~5-10 for hadronic jets, if the large production cross-sections expected for known resonances ($Z \to ee$, $Z \to \mu\mu$ and $W \to jj$) were not to allow very precise and high-statistics *in situ* calibration procedures to be used. The Z line shape will be known to an accuracy of better than 10^{-4} at the LHC, and the W mass will be known to an accuracy of ~5×10^{-4}. These accuracies are significantly better than the ones required to set the absolute scale, respectively for electrons and muons using $Z \to ee$ and $Z \to \mu\mu$ decays and for jets using $W \to jj$ decays.

The abundant production of vector bosons at the LHC will be used to set the absolute scale at the right value to a very high accuracy. Nevertheless, care will have to be taken to extrapolate this scale to masses which most probably will be quite different from the original vector boson mass itself (*e.g.* by a factor of more than two for the top mass measurement). Obviously, decays of other known resonances, such as J/ψ and Y, will provide additional constraints, which will minimise, if needed, the interpolation errors towards lower masses. In this extrapolation proc-

ess from the known vector boson masses to the mass to be measured with high precision, cross-checks between the various systems and disentangling individual contributions to the systematic uncertainty on the absolute scale will be of prime importance to keep it as small as possible.

Based on the above considerations, one can conclude that a precise understanding of the mass scale in ATLAS will require first and foremost an accurate knowledge of the measurement scale in each of the major detector elements, as described below in Section 12.2 for the Inner Detector (electrons and muons), in Section 12.3 for the EM Calorimeter (electrons and photons), in Section 12.4 for the Muon System, and in Section 12.5 for the overall Calorimeter (hadronic jets and E_T^{miss}).

This will not be sufficient, and the best accuracy on the overall mass scale will eventually be achieved by requiring the combination of the information from different detectors and by over-constraining the problem through numerous cross-checks:

- The electron energy measurements will rely mainly on the EM Calorimeter, but the knowledge of the absolute electron energy scale will probably be constrained in an optimal way by combining high-statistics precision measurements in the Inner Detector and the EM Calorimeter.

- The muon momentum measurements will rely on the combination of the measurements in the Muon System and in the Inner Detector on an event-by-event basis, and the knowledge of the absolute muon momentum scale will be constrained in an optimal way again by combining high-statistics precision measurements in both systems.

- The measurements of the energy of hadronic jets will rely on the overall ATLAS calorimetry over the range $|\eta| < 3.2$. In order to constrain to the required accuracy the jet energy scale over this region covered by several very different calorimeter technologies, it is expected that E/p measurements using isolated high-p_T charged hadrons from τ-decay will provide, in a first step, a quite powerful tool to transfer the scale, as known from the test-beam measurements, to the actual detector, to inter-calibrate the various calorimeter technologies, and possibly to constrain the absolute scale of the energy measurements for isolated charged pions (see Section 5.4). The transfer of this absolute scale to that of hadronic jets will require accurate and detailed Monte Carlo tools, as well as an excellent understanding of $W \rightarrow jj$ reconstruction in the hadronic calorimetry.

In the end, there can be only one mass scale for the whole ATLAS experiment and this will be determined by combining the various constraints from the individual systems and from the inter-calibrations between them.

One may expect that the Inner Detector momentum scale will be the most straightforward to calibrate, owing to the proximity of the measurement points to the primary vertex and to the magnetic nature of the measurement. However, systems which are situated further away from the primary vertex and with a rather large amount of material in front of them, such as the EM Calorimeter and the Muon System, will benefit from the very large statistics of $Z \rightarrow ee$ and $Z \rightarrow \mu\mu$ decays expected to be accumulated routinely (about 30 000 events per day at low luminosity) as a part of the inclusive triggers for many new physics searches. In addition, the even larger statistics of $W \rightarrow e\nu$ and $W \rightarrow \mu\nu$ decays, which will also be accumulated with high efficiency, will allow very precise cross-calibrations of these detectors with the Inner Detector.

The following sections present the results of the first attempts at establishing a strategy to achieve the above goals in the various systems composing the ATLAS detector and to combine the individual experimental measurements and scale uncertainties into an overall mass scale and its uncertainty.

12.2 Inner Detector scale

12.2.1 General considerations

As discussed above, the momentum scale in the Inner Detector (ID) should be known to an accuracy of 0.02% to obtain the desired precision on the measurement of the W mass. The implications of these requirements are examined in some detail for the Inner Detector in [12-3] and can be summarised as follows (this assumes that the absolute momentum scale is set using $Z \rightarrow ee$ and $Z \rightarrow \mu\mu$ decays for masses close to m_Z and that residual local effects average out to about 10% of their value over the whole detector):

- the ID alignment must be understood locally to ~1 μm on average in the bending plane;

- the solenoidal magnetic field must be understood locally to better than 0.1% on average;

- the amount of material in the ID must be understood globally to ~1% of its value (this is only required for $W \rightarrow e\nu$ decays);

- The ID p_T resolution must be understood globally to ~1%.

   This latter requirement has not been studied so far, but it seems rather straightforward to constrain the p_T resolution of the ID to the desired accuracy from the measured $Z \rightarrow \mu\mu$ mass distribution and from combined measurements of high-p_T electrons with the EM Calorimeter and of high-p_T muons with the Muon System.

The precise justification for the first three points is not easy to provide, since, as mentioned above and discussed in more detail in several of the following sections, the ultimate calibration of the overall scale will come from the use of the mass constraint in $Z \rightarrow \mu\mu$ decays. Systematics will, however, inevitably arise from not understanding details and hiding them in an all-encompassing calibration. It will therefore be essential to understand as well as possible all the individual components of the momentum determination; otherwise, small but not understood differences between *e.g.* the W and Z bosons will result in uncontrolled systematic uncertainties on m_W.

12.2.2 Alignment

The feasibility of meeting the above alignment requirement is very hard to demonstrate without real experimental data. Nevertheless, such an attempt has been considered in some detail in [12-3]; the main points are summarised below.

The use of reconstructed tracks and, in particular, of module overlaps in the Precision Tracker in the bending (R-ϕ) plane, to perform local alignment to an accuracy close to 1 μm, is described in detail in Section 3.7. Since the p_T of a track reconstructed in the ID alone is not known *a priori*, only certain distortions can be reconstructed through such procedures.

Even though the measurement points in the ID are quite uniformly distributed (in contrast to the Muon System, as discussed in Section 12.4), residual sagitta (or momentum scale) corrections will remain at some level. These cause shifts in the distributions of Q/p_T, where Q represents the charge of the reconstructed particle. Although the measured p_T spectra of oppositely charged particles could in principle be compared directly to correct for such shifts, this method is not precise enough in practice.

On the other hand, if the measured p_T spectra can be normalised by an estimate of p_T, then the uncertainties on the sagitta corrections can be greatly reduced. The estimate of p_T need not even be unbiased: the only condition is that it should not be correlated to the charge of the particle. Given the very large statistics of high-p_T leptons expected to be accumulated by ATLAS, the EM Calorimeter measurements can be used to normalise p_T for electrons, and the Muon System measurements can be used to normalise p_T for muons, although charge-dependent biases will be more of a concern in this case than for the EM Calorimeter.

As discussed in [12-3], there will be enough statistics of $W \rightarrow e\nu$ decays and of LVL1 trigger muons of $p_T > 6$ GeV, to guarantee a statistical error for such measurements below the required accuracy of 0.02% after a few months of LHC operation at low luminosity. What remains to be demonstrated is that the systematic uncertainties associated to the correlation between the EM Calorimeter measurements and the electron charge, which are presumably quite small, and those associated to the correlation between the Muon System measurements and the muon charge, which are potentially much larger (see Section 12.4), can be controlled at the same level of 0.02%.

12.2.3 Magnetic field

Uncertainties arising from the imperfect knowledge of the scale of the magnetic field will feed directly into those on the absolute momentum scale (before calibration). To be confident that the calibration is well understood, it is desirable to reduce the uncertainty coming from the magnetic field to a level such that it does not mask other problems. A goal of better than 0.1% appears to be reasonable as a starting point.

The standard way to map a magnetic field such as that from the ATLAS solenoid is with a machine which scans an array of Hall and nuclear magnetic resonance (NMR) probes over the full ID volume. This will be done after all of the surrounding magnetic materials have been installed and just before the installation of the ID itself. The accuracy required is similar to that which has been achieved in the past (*e.g.* a measurement accuracy of 0.01% was achieved in [12-4] and an accuracy of the magnetic field map of a few parts in 10 000 was achieved in [12-5], although the desired goal was only 0.1%).

The ATLAS solenoid is more difficult to map than other solenoids because of its non-uniform field. NMR probes require uniform fields and hence will only function within ~70 cm from the centre. Therefore, over most of the ID volume, Hall probes will have to be relied upon. Hall probes can be calibrated to better than 0.05% (there is considerable on-going work within ATLAS to produce a large number of calibrated Hall probes to monitor the toroid field [12-6]). The high field gradients expected in the ID volume will require the position of the probes in the mapping machine to be known to ~0.5 mm, which is more precise than was necessary for previous maps. Some understanding of the field can be derived from simulation, but such calculations are typically only accurate to ~0.5%.

In addition to mapping the field at the time of installation, it will be essential to monitor it with the ID in place and during the lifetime of the experiment. The following effects may cause distortions of the field at the 0.1% level:

- Tiny quantities of ferro-magnetic material in the ID, which may be unavoidable, as for example nickel coating on the aluminium power cables, where they join the custom-made connectors on the SCT modules or at the level of the patch-panels.

- The mapping of the solenoid with the barrel toroid (most probably) switched off. Simulations predict that when the toroid is switched on, the solenoid field will decrease slightly because the extra field from the toroids will bring the Tile Calorimeter beams close to saturation and reduce their effectiveness at returning the solenoid field.

Other effects are considered to induce variations much smaller than 0.1%: para-magnetic and dia-magnetic effects due to the other components of the ID, the Earth's magnetic field, variations in the positions of the end-cap Calorimeters relative to the barrel Calorimeter when they are opened and shut, and hysteresis of the iron components.

The first-order effect of ferro-magnetic material (provided that it is uniformly distributed) and of the barrel toroid field, is to change the scale of the solenoid field map without changing its shape. This scale could be measured by building a small number of NMR probes into the SCT Barrel [12-7]. Such a system of probes would also provide a check of the position of the ID relative to the central axis of the magnetic field, which would be useful if the position of the solenoid coil were not absolutely stable.

Rather than simply measuring the field at a set of points in space, it would be preferable to describe it in terms of components satisfying Maxwell's Equations: $\nabla \cdot B = \nabla \times B = 0$. These components could be constrained using the combination of data from: the field map, the monitoring probes and pairs of reconstructed charged particle tracks from the decays of resonances of known mass (J/ψ, Y, Z). One set of functions, suitable for axial symmetry [12-4], are the modified Bessel functions, I_0 and I_1, expressed as a function of radius, R, and of position along the beam, z:

$$B_z = \sum_i a_i \ \cos\frac{iz}{c} \ I_0(\frac{iR}{c})$$

$$B_R = \sum_i a_i \ \sin\frac{iz}{c} \ I_1(\frac{iR}{c}).$$

In practice, the constraint of axial symmetry would probably need to be relaxed for the actual field configuration in the ATLAS ID. As an exercise to test the feasibility of fitting the field, an attempt was made to fit the simulated field. Despite using eight terms, the fit was poor and unstable, suggesting that more terms are needed. Better results were achieved starting from a field corresponding to an ideal solenoid. A scale factor was associated with this field, which was then augmented by two terms from the above power series.

The residuals between the fitted and simulated fields are shown in Figures 12-1 and 12-2, respectively for the axial and radial field components. The comparison is shown at a radius $R = 75$ cm, where the field deviates more strongly from uniformity than along the beam axis. It can be seen that, over most of the length of the coil, the field can be described to better than ±0.02%, corresponding to ±4 Gauss. There are significant deviations at values of $|z|$ larger than 2.6 m (the actual half-length of the solenoid coil is 2.65 m), but these would cause little effect on the momentum determination because they occur at the end of a track.
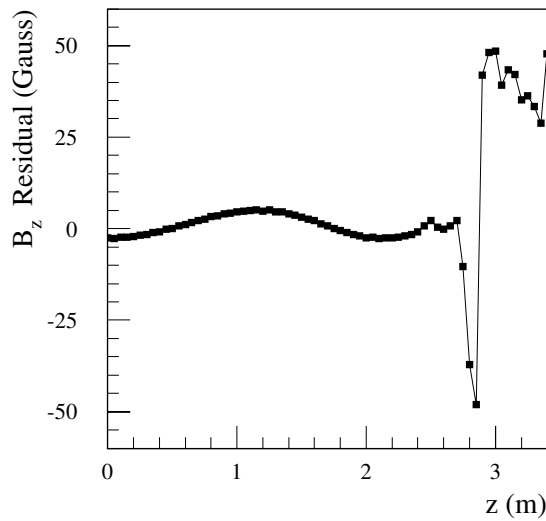
Figure 12-1 Difference between simulated and fitted axial magnetic field (B_z) components of the solenoid at a radius R = 75 cm.
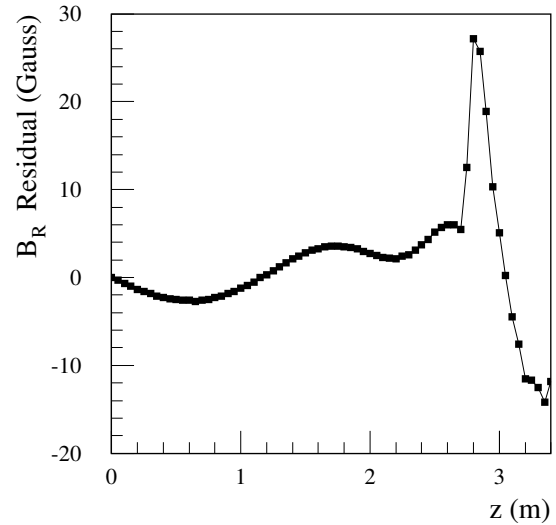
Figure 12-2 Difference between simulated and fitted radial magnetic field (B_R) components of the solenoid at a radius R = 75 cm.

12.2.4 Material in the Inner Detector

Material in the Inner Detector affects directly the momentum reconstruction for electrons, the energy reconstructed in the EM Calorimeter, and the E/p calibration, since the momentum as measured by the Inner Detector is subject to bremsstrahlung effects. Hence, the large amount of material present in the Inner Detector, if not known precisely enough (see also Section 12.3.1.1), might contribute significantly to systematic uncertainties on the knowledge of the absolute scale of the EM Calorimeter.

There are many approaches to determining the amount of material in the ID, all of which will be pursued:

- at the present stage of the detector construction (finalisation of detailed design), the amount of material in the ID is considered to be known to better than 5%, despite inevitable uncertainties in the most difficult areas (exact make-up of hybrids and chips, services and connectors, *etc.*);

- during construction, these estimates will be carefully updated by weighing detector components and assembled units. Valuable reference measurements will be provided in many cases by X-ray sources;

- *E/p* measurements with electrons from $W \rightarrow e\nu$ decay are described in Section 12.2.4.1;

- photon conversions are described in Section 12.2.4.2.

12.2.4.1 Use of *E/p* measurements with electrons from *W → e*ν decays

The combined measurement of *E/p* with isolated high-p_T electrons from $W \rightarrow e\nu$ decays, using the EM Calorimeter and the Inner Detector, will be a key element to ensure a reliable comparison of the absolute momentum scale of the ID and of the absolute energy scale of the EM Calorimeter (see Section 7.2.2.2). This approach will complement the direct calibration of the absolute scale of the EM Calorimeter using $Z \rightarrow ee$ decays (see Sections 4.6 and 12.3).

The use of the shape of the electron *E/p* distribution to determine the amount of material in the Inner Detector is discussed in Section 7.2.2.3. The sensitivity of the peak of the *E/p* distribution, used for these calibrations, is such that, to understand the calibration of the EM Calorimeter to an accuracy of 0.02% will necessitate that the ID material must be understood to an accuracy of ~1% of its total value. This does not mean that every single item in the ID must be known this accurately, but the amount of material in regions of size of a few centimetres must be known to this precision. Like the EM Calorimeter energy measurements, the *E/p* calibration will be most sensitive to material at low radii, which is fortunately also the region where there will be the greatest sensitivity for determining in detail the material distribution.

It is shown in Section 7.2.2.3 that 10^6 reconstructed $W \rightarrow e\nu$ decays constitute a sufficient statistical sample to understand the ID material distribution to the required precision of ~1% of its total value. The available statistics will be about 30 times larger for one year of operation at low luminosity. In addition, high-purity samples of inclusive electrons (see Section 7.4), yet one order of magnitude larger in size than the $W \rightarrow e\nu$ sample, can also be used for such measurements (as shown for example in [12-1]), although only real data will demonstrate whether the required measurement quality and sample purities can indeed be achieved.

12.2.4.2 Use of photon conversions

The most obvious way to determine the amount of material in the Inner Detector is to look at the conversion rates (see Section 7.5.1). To obtain an absolute determination of the amount of material with this method requires a known rate of photons. Although this might be obtained from $Z \rightarrow ee\gamma$ decays, for which the topology is such as to give an easily identifiable photon, there will not be enough events of this type to obtain a map of the ID material to the desired accuracy.

An obvious alternative would be to use photon conversions from much more abundant sources, such as isolated high-p_T photons from direct photon production or even the very large statistics of lower-energy photons (mostly from π^0 decays), which are present in most events. Both these samples can be used for high-statistics relative measurements of the amount of material, as shown in Figures 12-3 and 12-4. Eventually, it is probable that an absolute measurement will be extracted from these samples, but it will require a reference object corresponding to a precisely known position and amount of material.

Figure 12-3 shows the radial positions of photon conversions of $p_T = 50$ GeV, as reconstructed in the barrel part of the ID. The three pixel barrel layers at their respective radii of 4, 11 and 14 cm, a support cylinder at a radius of 25 cm, and the first two SCT barrel layers at their respective radii of 30 and 38 cm can be clearly distinguished above the very small background. The beam pipe and the pixel *B*-layer are barely resolved. The cut-off in Figure 12-3 around the third SCT barrel layer is due to the requirement that a reconstructed track have at least four SCT hits.
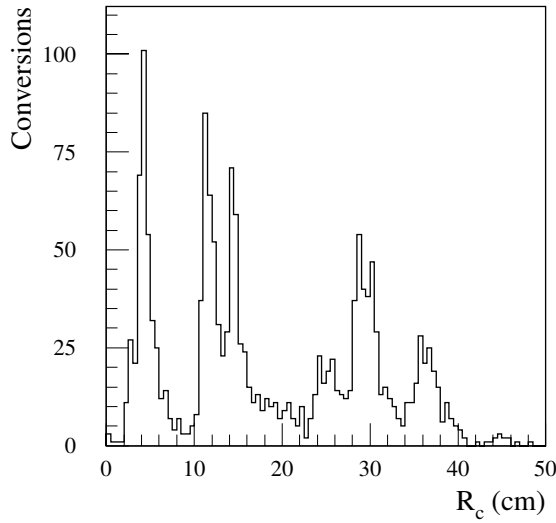
Figure 12-3 Reconstructed radial positions for conversions in the barrel part of the ID.
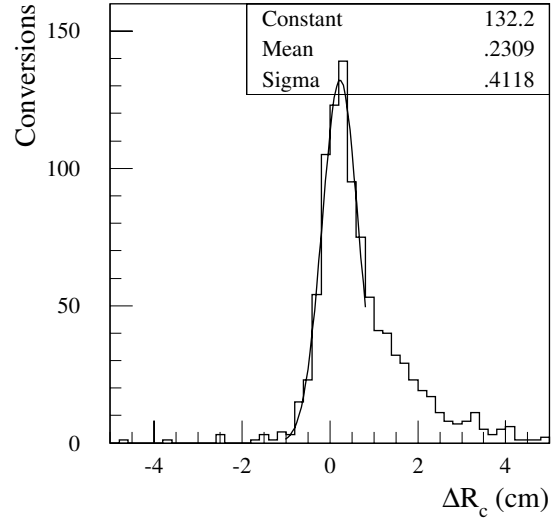
Figure 12-4 Difference between true and reconstructed radial position of conversions arising from $p_T = 50$ GeV photons which convert with $R_c < 20$ cm.

The width of the peaks in Figure 12-3 is dominated by the resolution on the radius of the reconstructed photon conversion, but is also affected by the effects of the azimuthal tilts of the planar detectors. Figure 12-4 shows the radial resolution for conversions in the pixel barrel layers. The resolution is ~4 mm, although there is a significant tail due to bremsstrahlung of the conversion electrons. In the first two barrel layers of the SCT, this resolution degrades somewhat to ~6 mm. Studies of photon conversions in b-jets, where the photon energies are much smaller, indicate that the radial resolution improves at lower p_T, as might be expected from the larger angular separation between the electrons. At very low p_T, the radial resolution is dominated by multiple scattering effects. Photon conversions can be reconstructed at larger radii, up to $R_c \approx 80$ cm, using the TRT alone (see Section 7.5.1), but the radial resolution is significantly degraded.

To determine the material at a given position, it is necessary to compare the number of reconstructed photon conversions at that position with the number reconstructed at the position of some reference object. This necessitates being able to resolve the position of the reference, which may not be trivial, as shown in Figure 12-3, because of the proximity of various layers and the modest radial resolution. Unfortunately, conversions in the beam pipe are not well resolved and may, when originating from π^0 decays, suffer from a significant Dalitz decay background. Although the statistics will be very large, a good understanding of the reconstruction efficiency of photon conversions will be essential, which will require in turn an improved conversion-finding program with higher efficiency.

12.2.5 Calibration with $Z \rightarrow \mu\mu$ and $Z \rightarrow ee$ decays

The general method described in Section 12.4.4 for the Muon System has not yet been applied to evaluate the accuracy with which the Inner Detector momentum scale could be constrained using $Z \rightarrow \mu\mu$ decays. In principle, residual sagitta corrections and the magnetic field components identified in Section 12.2.3 could be determined with this method by performing a global fit of the $Z \rightarrow \mu\mu$ sample, to which the constraint of the Z line-shape is applied. A similar but simpler

technique has been examined for the EM Calorimeter calibration with $Z \rightarrow ee$ decays (see Section 4.6). These techniques provide both an accurate inter-calibration between different parts of the detector, and an accurate estimate of the absolute mass scale at m_Z.

If one scales the statistical precision obtained using $Z \rightarrow ee$ decays over about 400 η–ϕ bins for the study of the EM Calorimeter calibration (see Section 4.6) to the expected statistics of 3×10^6 reconstructed $Z \rightarrow ee$ decays for one year of operation at low luminosity, this leads to a statistical precision of 0.02% in each of these η–ϕ bins. Since the experimental resolution for $Z \rightarrow \mu\mu$ decays reconstructed in the ID ($\sigma(p_T)/p_T \approx 2.1\%$) will be similar to that for $Z \rightarrow ee$ decays reconstructed in the EM Calorimeter ($\sigma(E)/E \approx 1.5\%$), it should be possible to understand the momentum scale in the ID with comparable statistical precision over a similar number of η–ϕ bins. It remains to be studied whether or not such a large number of bins would be needed for a measurement of the W mass to the required accuracy.

12.3 Electromagnetic Calorimeter scale

The EM Calorimeter scale is discussed here in terms of the uncertainty on the absolute energy scale of electrons and photons.

12.3.1 Determination of the electron energy scale with $Z \rightarrow ee$ decays

The use of $Z \rightarrow ee$ decays reconstructed solely in the EM Calorimeter, in particular to reduce the global constant term of the energy resolution, is described in detail in Section 4.6. From the results obtained in Section 4.6, it follows that about four years of data-taking at low luminosity would be needed to achieve an overall statistical accuracy of 0.02% per region of the EM Calorimeter with this method.

In this section, the basic sample of 50 000 fully simulated $Z \rightarrow ee$ decays described in Section 4.6 and a sample of 20 000 $Z \rightarrow ee$ decays, simulated with a modified layout of the Inner Detector, are analysed in terms of the uncertainties on the absolute energy scale of the EM Calorimeter. These uncertainties do not apply at the exact scale of m_Z, since this can be set to an almost arbitrarily good accuracy, but rather when attempting to transfer the absolute calibration at the Z mass to other masses. More specifically, both detector (material of the Inner Detector) and physics effects (inner photon bremsstrahlung, underlying event and pile-up) are examined below.

12.3.1.1 Material in the Inner Detector

The amount of material in front of the EM Calorimeter could affect directly the absolute electron energy scale, with the largest effects arising from external bremsstrahlung in the innermost layers of the Inner Detector. As discussed in Section 12.2.4, the description of the amount of material in the Inner Detector is estimated to be accurate to ~5% at the present stage of the detailed design of all components. This description will be refined during construction and will be carefully cross-checked *in situ*, using E/p measurements and photon conversions.

To evaluate directly the impact of an imperfect knowledge of the Inner Detector material on the calibration of the absolute energy scale of the EM Calorimeter, a sample of 20 000 $Z \rightarrow ee$ decays have been simulated, using a modified layout of the ID. This modified layout corresponds to an increase of the material in the support structures of the barrel and end-cap silicon microstrip detectors, ranging from ~15% in the barrel region to ~30% in the end-cap region. This increase is much larger than the 1% uncertainty, which could be obtained after a modest amount of data taking, using the methods discussed above.

The EM Calorimeter response has been compared to the nominal one, defined using the original sample of 50 000 $Z \rightarrow ee$ decays. As shown in Figure 12-5, the value of the reconstructed Z mass decreases by about 100 MeV.

As summarised in Table 12-1, if the results illustrated in Figure 12-5 were scaled to the estimated overall uncertainty of ~1% on the amount of material in the ID, the corresponding uncertainty on the electron scale should be around 5 MeV at the Z mass. This study has been performed by changing the amount of material in the silicon microstrip detectors. However, there is likely to be greater sensitivity to changes in the amount of material at even lower radii, namely in the pixel detectors. Table 12-1 therefore quotes a more conservative upper limit of 0.01% for the impact of the ID material on the determination of the absolute scale of the EM Calorimeter.
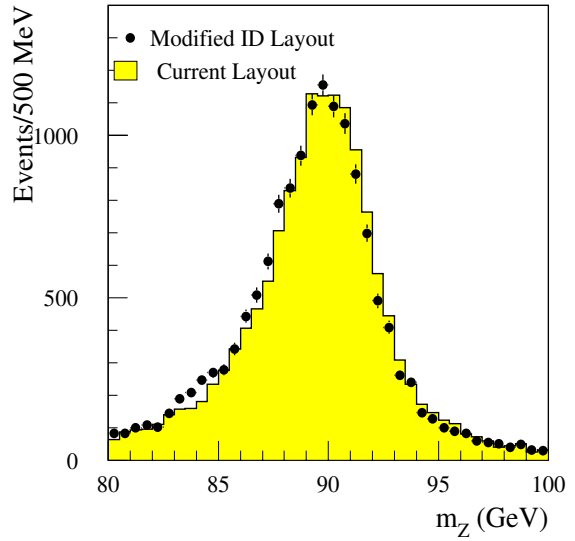
Figure 12-5 *Z*-boson lineshape, as reconstructed directly with the EM Calorimeter for the nominal Inner Detector layout (shaded histogram) and for a modified Inner Detector layout with ~ 20% more material in total (black dots).

Table 12-1 Impact of Inner Detector material on the absolute energy scale of the EM Calorimeter.

Source of uncertainty	Uncertainty on electron energy scale at m_Z
Modified ID layout (material increased by 15-30%)	0.11%
Nominal ID layout (material known to 1%)	< 0.01%

12.3.1.2 Inner bremsstrahlung

The consequences of inner bremsstrahlung in $Z \rightarrow ee$ decays are:

- in a small fraction of events, the production of a high-p_T isolated photon in the final state will significantly distort the reconstructed mass spectrum of the two electrons. These events are easy to identify and to remove from the calibration sample;

- for a much larger fraction of events, the bremsstrahlung photon(s) remains very close to the electron shower, but slightly widens the transverse shower shape, thereby distorting slightly the reconstructed mass spectrum.

The reference sample of 50 000 fully simulated $Z \rightarrow ee$ decays has been generated using PYTHIA interfaced to PHOTOS [12-8], to account for photon emission through inner bremsstrahlung. To evaluate whether the distortions due to inner bremsstrahlung could be significant when compared to the calibration requirements, two additional $Z \rightarrow ee$ samples of 10 000 events each have been fully simulated, reconstructed and analysed, one without inner bremsstrahlung and one with forced photon emission (repeated calls to PHOTOS).

The reconstructed Z masses for these samples were then compared, after a cut on the shower width in the azimuthal plane was applied (see Table 12-2). By making a direct comparison to the sample of $Z \rightarrow ee$ decays, the reconstructed Z mass was found to be decreased by 70 MeV (or 0.08%) due to inner bremsstrahlung. The first-order calculations used at present for the inner bremsstrahlung are accurate to better than 10% (they could be greatly improved with more theoretical input), therefore the uncertainty on the absolute electron energy scale from this source is below 0.01%.

Table 12-2 Impact of inner bremsstrahlung on the absolute scale of the EM Calorimeter.

Sample of $Z \rightarrow ee$ decays and cuts used	Relative shift of reconstructed Z mass
Forced photon emission without cut on shower width	-0.33%
Forced photon emission with cut on shower width	–0.23%
Nominal photon emission with cut on shower width	–0.08%

12.3.1.3 Underlying event

Even though the size of the electromagnetic showers from $Z \rightarrow ee$ decays is quite small, a certain amount of energy from the underlying event is deposited in the calorimeter cells of interest in addition to that of the electrons themselves. The original sample of 20 000 $Z \rightarrow ee$ decays, which was generated with the default underlying event, was analysed a second time after a pre-processing stage, during which each event was superimposed onto itself after a 90° rotation in azimuth. Thus, the contribution of the underlying event to each 3×7 electron cluster in the EM Calorimeter was doubled. This procedure resulted in an increase of the reconstructed Z mass by 30 MeV or 0.03%. Since it will be possible to measure the properties of the underlying event with very large statistics, using the $Z \rightarrow ee$ events themselves, the contribution of this source to the uncertainty on the absolute energy scale for electrons can safely be neglected.

12.3.1.4 Pile–up

The EM Calorimeter readout uses a bipolar shaping and the response, averaged over the entire pulse duration is very close to zero, leading to very small average shifts of the measured energies due to pile-up (normalised to the average energy deposited per pile-up event). The exact values of these averages have been evaluated for every cell of the EM Calorimeter: they range from –1.7% to +2.1% at high luminosity, and from –3.1% to +3.6% at low luminosity (when optimal filtering is applied to reduce the electronic noise). The systematic shift of the absolute energy scale due to pile–up is therefore expected to be smaller than 50% (10%) of the effect of one

minimum–bias event at high (low) luminosity. Thanks to the bipolar shaping, these contributions are significantly smaller than the one from the underlying event, which has an activity typically a factor of two larger than that of a normal minimum-bias event.

12.3.1.5 Conclusions

The contributions of the most prominent sources of uncertainty on the EM Calorimeter scale for electrons are summarised in Table 12-3, which shows that the sum of all contributions can most likely be kept below 0.02%, which is the target set by the precision measurement of the W mass at the LHC (see Section 16.1). It should be noted once again that, at the scale of m_Z, none of the contributions in Table 12-3 matter much. However, they could contribute at some small level, as soon as the mass to be measured would be different from m_Z. In addition, other possible sources of systematic uncertainty, in particular those related to the multi-gain readout electronics of the EM Calorimeter, still remain to be studied and understood.

Table 12-3 Summary of the contributions to the uncertainty on the EM Calorimeter electron energy scale, as determined using $Z \rightarrow ee$ decays.

Source	Requirement	Uncertainty on scale
Material in Inner Detector	Known to 1%	< 0.01%
Inner bremsstrahlung	Known to 10%	< 0.01%
Underlying event	Calibrate and subtract	<< 0.03%
Pile–up at low luminosity	Calibrate and subtract	<< 0.01%
Pile–up at high luminosity	Calibrate and subtract	<< 0.01%

12.3.2 Determination of the photon energy scale using $Z \rightarrow ee\gamma$ decays

It is not clear from first principles that the absolute photon energy scale is identical to the electron energy scale to an accuracy of 0.1%. Additional constraints would be welcome, in particular if a Higgs boson decaying to photon pairs were to be discovered at the LHC. Possibly the only clean source of events which could be used to constrain the photon energy scale consists of $Z \rightarrow ee\gamma$ decays with a high-p_T photon well separated from the electrons. The use of the Z mass constraint could provide a sufficiently precise calibration tool albeit with somewhat marginal statistics.

This is illustrated in Figure 12-6, which shows the reconstructed spectrum of the invariant mass of the two electrons, m_{ee}, for the reference sample of 50 000 $Z \rightarrow ee$ decays, which includes the appropriate proportion of $Z \rightarrow ee\gamma$ decays. Also shown in Figure 12-6 is the distribution of m_{ee} for $Z \rightarrow ee\gamma$ decays with one photon with $p_T > 10$ GeV. It is important to note that more than 90% of the events with $m_{ee} < 70$ GeV are $Z \rightarrow ee\gamma$ decays: this indicates that the non-Gaussian tails from the reconstruction in the EM Calorimeter (events containing electrons in the barrel/endcap transition region have been removed from the sample) and the low-energy tails from the Breit-Wigner line shape of the Z boson are both negligible with respect to the tails due to hard photons from inner bremsstrahlung.

For those events with $m_{ee} <$ 85 GeV and containing a hard photon with $p_T >$ 10 GeV, the measured energies of the photon and of the two electrons were rescaled in order to obtain $m_{ee\gamma} = m_Z$. As a result, the difference between the rescaled and measured photon energies has a resolution of ~0.8 GeV, averaged over all photons with $p_T >$ 10 GeV.

The photons of interest in this section are typically those with $p_T \sim$ 50 GeV from $H \rightarrow \gamma\gamma$ decay for $m_H =$ 100 GeV. The p_T spectrum of inner bremsstrahlung photons in $Z \rightarrow ee\gamma$ decays decreases very rapidly as p_T increases, and only about 0.1% of $Z \rightarrow ee$ decays contain a reconstructed photon with $p_T >$ 30 GeV. This would nevertheless lead to a total sample of 15 000 events for an integrated luminosity of 30 fb^{-1}, which would certainly provide the global statistics needed to be sensitive to a possible difference in scale at the level of ~10^{-3} between photons and electrons.
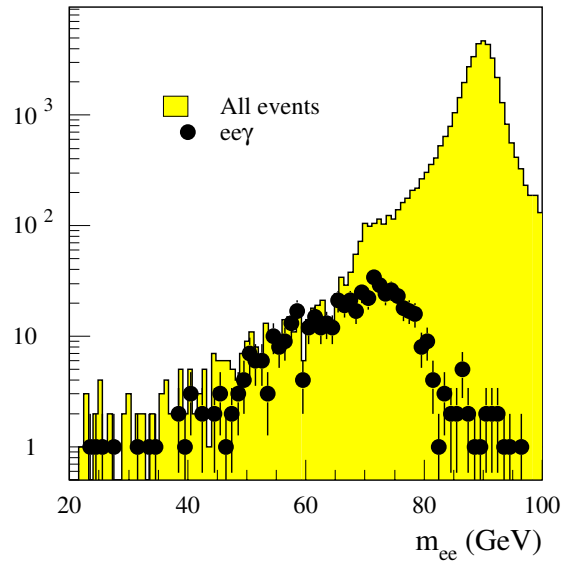
Figure 12-6 Distribution of the invariant mass of the two electrons from $Z \rightarrow ee$ decays reconstructed in the EM Calorimeter. The points with error bars denote events containing a hard photon with $p_T >$ 10 GeV from inner bremsstrahlung. The statistics in the plot correspond to an integrated luminosity of 84 pb^{-1}.

12.4 Muon momentum scale

12.4.1 General considerations

The Muon System will provide high-precision and robust muon momentum measurements, which are almost completely uncorrelated with the Inner Detector measurements, since the magnetic bending occurs in different planes in the two systems. The various procedures involved in the determination of the absolute muon momentum scale and the level of precision that can be achieved are described below. Although the arguments in this section are developed specifically for the Muon System, the discussion on the calibration with $Z \rightarrow \mu\mu$ decays (see Section 12.4.4) applies also to a large extent to the calibration of the momentum scale of the Inner Detector (see also Section 12.2).

The momentum resolution and the absolute calibration of the Muon System measurements depend on the alignment of the precision chambers, the knowledge of the magnetic field, and the knowledge of the muon energy loss in the calorimeters. Since the track curvature measurement in the Muon System is obtained from only three points, the measurements themselves provide no redundancy, and an *in situ* check/recalibration of the Muon System with reconstructed tracks will require some knowledge of the incoming track curvature. This additional information can be provided by three methods:

- special runs without magnetic field (straight tracks to check and calibrate the alignment system), assuming they do not introduce additional uncertainties;

- a comparison with the momentum measured in the Inner Detector;

- the use of $Z \rightarrow \mu\mu$ decays, for which the precisely known Z mass provides strong constraints on the unknown parameters which may affect the measurements of the muon momenta.

Sections 12.4.2 and 12.4.3 respectively discuss the level of accuracy which can be achieved concerning the alignment of the precision chambers and the magnetic field, using special runs with straight tracks and the direct measurements provided by dedicated systems (Hall probes on the chambers and optical alignment system). Section 12.4.4 demonstrates how the calibration of the magnetic field and the energy loss in the calorimeters could be considerably improved by making use of $Z \rightarrow \mu\mu$ decays.

12.4.2 Alignment of the precision chambers

The alignment of the precision chambers is required to be sufficiently accurate, that the alignment contribution to the final measurement error (30 μm sagitta accuracy) remains well below the contribution from the intrinsic chamber measurement error (50 μm sagitta accuracy). The alignment system is based on optical straightness monitors (see [12-9] for an overview). The dominant uncertainty arises from the positioning of the optical sensors on the precision chambers or on carbon-fibre bars, the precision of which has to be better than 20 μm. In principle, the errors in the positioning of the sensors are supposed to be unbiased and randomly distributed over the chambers; therefore, it is hoped that the corresponding systematic error on the sagitta measurement, averaged over the complete system, could be below 2 μm, corresponding to a relative error of 0.02% on the sagitta at 50 GeV.

Alignment with reconstructed tracks will also provide strong constraints on possible residual systematic sagitta errors which would affect the absolute momentum scale. At the start of the experiment and after each major shutdown, it is planned to use straight muon tracks (data taken with the toroidal magnetic field off) to check the alignment systems and eventually to provide effective corrections which should account for errors in the positioning of the sensors on the chambers or on the bars. This may also correct for other spurious effects like local temperature gradients, provided that they are identical for field-off or field-on conditions.

The principle is to select muons with $p_T > 10$ GeV, with the toroids turned off and the solenoid field turned on (for track selection at LVL2 and beyond). In this way, the corrections to the sensor positions can be deduced from a comparison of the apparent track sagitta, as measured with the precision chambers, to the predictions of the optical alignment system. Given that the sensor positions on the chambers will be very stable, this correction map should be applicable to data taken with normal field conditions.

It should be stressed that the residual field from the magnetised iron has to be controlled to ~20% during the field off runs to reach the target resolution. Maintaining any systematic effect on the sagitta correction below 2 μm may require an even better control of these fields. Since the residual field from the iron girders does not extend significantly beyond a radius of 600 cm (in the barrel part of the system), a control of this residual field to 2 Gauss would be good enough to keep the relative effect on the sagitta below 0.02%.

Preliminary simulation studies have shown
that this correction procedure can be imple-
mented easily for the barrel part of the Muon
System, where the alignment rays are almost
purely projective. At low luminosity, enough
statistics are collected in less than an hour to
achieve a precision of 30 μm on the sagitta cor-
rection for sensors positioned up to 1 mm
from their nominal position. For the Muon
System end-caps, the larger departure from
projectivity makes the correction less straight-
forward. Sagitta precisions around 30 μm
seem to be a reasonable target, provided that
the positioning of the sensors is better
than 150 μm.

12.4.3 Magnetic field

In order to measure the field under running
conditions, with all detector components in
place and under the mutual influence of the
different magnets and of magnetic materials
(these are mainly the Tile Calorimeter and the
iron girder serving as return yoke for the sole-
noid flux), the Muon System will be equipped

Figure 12-7 Sketch in two views of the layout of the
mesh of 3D Hall probes mounted on the precision
chambers (BEE, BIL/BIS, BMS, BOS, EES, EMS).

with an array of Hall probes [12-9]. The proposed monitoring and measuring system consists of
an arrangement of about 1500 sensors, accurately mounted on the precision chambers, where
three orthogonal faces are equipped with a Hall probe to measure locally the three field compo-
nents. The readings will be compared with 3D calculations and used for reconstructing the posi-
tion and the shape of the toroid conductors with respect to the chambers (see Figure 12-7). The
Hall probes are mounted directly on the precision chambers, so that they will at any moment
provide the information on the actual position of the conductors with respect to the reference
for the precision measurements, namely the precision chambers themselves.

Preliminary simulation studies using a simplified coil deformation model have shown that the
magnetic field can be determined to a relative accuracy of 0.2% [12-9]. For these studies, the ac-
curacy for positioning the probes was conservatively assumed to be 1 mm and 3 mrad. The ac-
curacy of the absolute calibration of the probes was assumed to be 5 Gauss. This could be
improved by at least a factor of two, if a temperature control at the level of 1 K is achieved.

Limitations coming from the coil deformation model and the imperfect treatment of the iron
contribution to the magnetic field have to be investigated. A successful experimental test of the
field reconstruction method based on the coil shape/position reconstruction has been done
with a small (200x50 cm) prototype of a toroid coil, the so-called 'race-track' coil [12-10]. Further
studies will be done in this direction with the B0 prototype coil.

The relative precision provided by direct measurements of the magnetic field will be limited
most likely to about 0.1%.
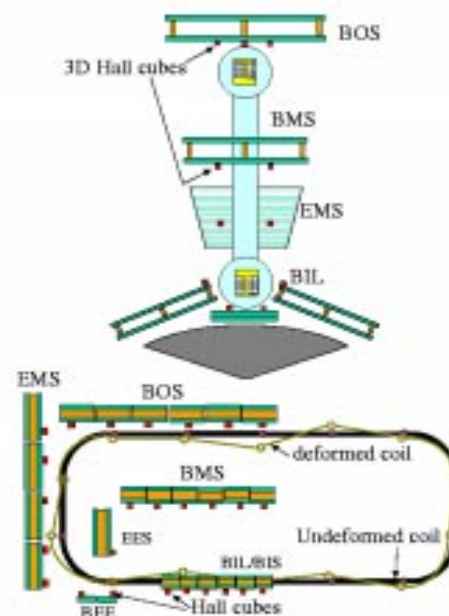
12.4.4 Calibration with $Z \rightarrow \mu\mu$ decays

12.4.4.1 Introduction

As pointed out in Section 12.4.3, a precision better than 0.1% on the absolute muon momentum scale is probably out of reach for the direct magnetic field measurements. In addition, for measurements with the Muon System, the average energy loss in the calorimeters of ~4 GeV would have to be known with an accuracy of 10 MeV to reach the ultimate target of 0.02% for the W mass measurement. Although this may not be totally impossible, it would require dedicated measurements to improve the present knowledge and a very detailed description of the material in the calorimeters.

The only handle to improve the knowledge of the absolute muon momentum scale beyond the level of 0.1% is the abundant rate of $Z \rightarrow \mu\mu$ decays, which provides isolated muon pairs over a wide range of p_T and with a very small background contamination (*e.g.* from $Z \rightarrow \tau\tau$ decays).

The absolute calibration of the Muon System depends on the alignment of the precision chambers, the magnetic field measurements and the muon energy loss in the calorimeters. The muon momentum can be expressed in terms of various calibration parameters, which, for each tower of size $(\Delta\eta, \Delta\phi)$, will control the alignment, the distortions of the magnetic field B and the average energy loss in the calorimeters.

For a muon j traversing the chamber tower i, the measured momentum, p_j^{meas}, can be expressed as:

$$p_j^{meas} = \frac{K_i \alpha_i B_i}{s_j + \delta x_i} + \lambda_i \varepsilon_i(p_j) \qquad \text{12-1}$$

where α_i is a field scale factor, s_j is the true sagitta, δx_i represents the tower misalignment, $\varepsilon_i(p_j)$ is the average energy loss as a function of momentum and λ_i is a scale factor for the average energy loss in tower i.

Equation 12-1 shows that, in principle, by using resonances decaying into muons with a wide momentum spread, the calibration permits the determination of all three effects (alignment, magnetic field and energy loss). In practice, given the limited statistics of the presently available fully simulated events, it will be assumed that the alignment is perfect and the calibration procedure will be restricted to the retrieval of the magnetic field and energy loss scale factors. In addition, Equation 12-1 includes only one unknown parameter per tower to describe the misalignment whereas, in general, six parameters are required.

From the conservation of 4-momentum, the following equations (p_1 and p_2 are the absolute values of the momenta of the two muons) can be obtained:

$$m_{12}^2 = m_Z^2 = 2p_1 p_2 F(\theta_1, \phi_1, \theta_2, \phi_2), \qquad \text{12-2}$$

where ϕ_i and θ_i ($i=1, 2$) are the angles of the muon track at the vertex (these angles are determined by extrapolating the reconstructed muon track back from the muon system through the calorimeters and the Inner Detector to the vertex).
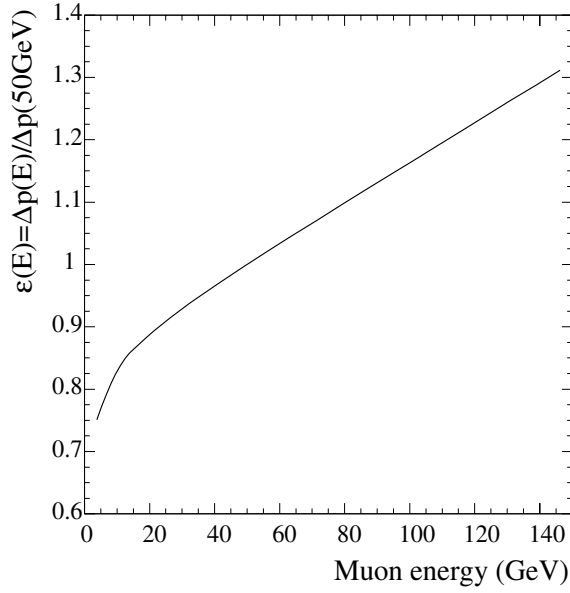
Figure 12-8 Mean energy loss, $\varepsilon(p)$, of muons in iron as a function of the muon momentum p, normalised to the value $\varepsilon(p) = 1$ at a momentum of 50 GeV.
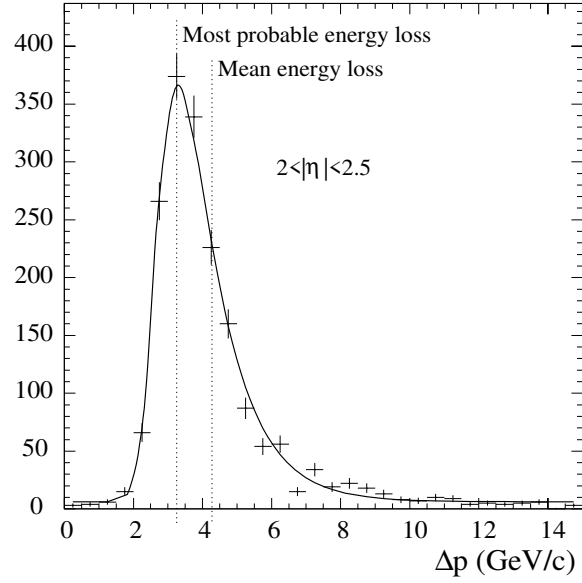
Figure 12-9 Generated energy-loss distribution in the calorimeter for $2 < |\eta| < 2.5$.

12.4.4.2 Energy loss

The energy loss of muons in material is a function of the muon energy. This function was simulated for different materials in [12-11]. Figure 12-8 shows the normalised mean energy loss in iron, $\varepsilon(p)$. Figure 12-9 shows the energy-loss distribution obtained from full simulation for muons in the range $2 < |\eta| < 2.5$, which agrees well with the distribution measured in an earlier hadronic calorimeter prototype [12-12]. In the calibration procedure presented here, only the mean energy loss is taken into account.

In the following, the energy loss of a muon is factorised into the momentum-dependent and the angle-dependent parts:

$$\Delta p(p, \theta) = \varepsilon(p) \cdot \Delta p(\theta)$$

where $\Delta p(\theta)$ is the average energy loss of a 50 GeV muon with polar angle θ. In this study, given the rather low statistics available, the small azimuthal dependence of the average energy loss has been neglected. The calibration algorithm described below would not have to be changed in any major way to introduce an azimuthal dependence of the energy loss.

12.4.4.3 Scale factors for the magnetic field

The roughly toroidal magnetic field in the Muon System will be measured by using about 5000 Hall probes, which will determine the field components locally (see Section 12.4.3). By performing a χ^2 minimisation, the position and shape of the coils can be retrieved. Using this information, supplemented by the calculated contributions from various surrounding magnetic materials, a nominal magnetic field map can be built.

This procedure provides a detailed description of the toroidal magnetic field. However, there is no way to exclude systematic errors due to unforeseen magnetic material or insufficient knowledge of its exact position. Such systematic errors may shift the absolute mass scale of the Muon System. Nevertheless, an effective correction can be done through the introduction of (η, ϕ) dependent scale factors. Since this study was limited to a large extent by statistics, only two scale factors are used, one for $-\pi < \phi < 0$ and one for $0 < \phi < \pi$.

12.4.4.4 Calibration algorithm and results

The algorithm which has been developed [12-13] allows the scale factors and the average energy loss to be obtained by minimising a likelihood function, which accounts for the finite width of the Z boson by the convolution of the Breit-Wigner with the resolution functions. Inner bremsstrahlung effects, which are significant, have not been taken into account in this first simplified approach.
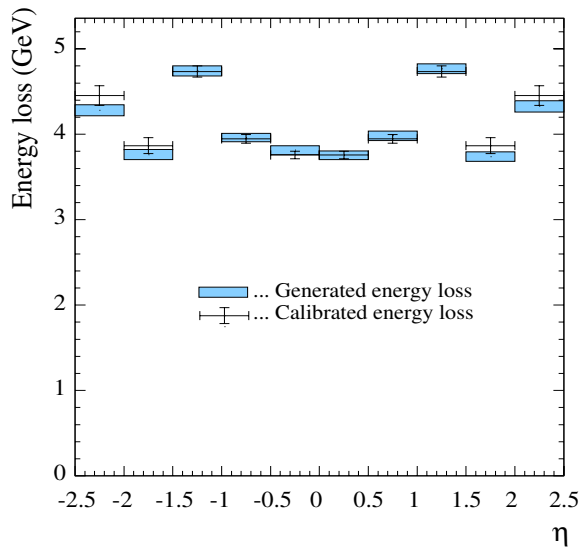
Figure 12-10 Generated and calibrated mean energy loss as a function of η for 50 GeV muons. The variations of the energy loss as a function of η reflect the varying amounts of absorber material in the calorimeters.
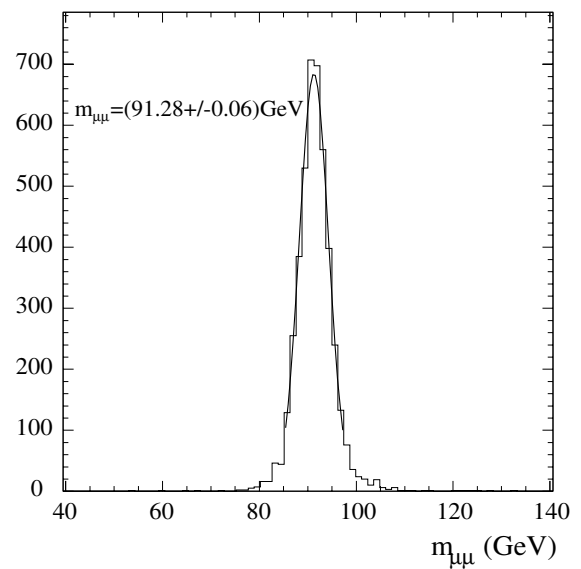
Figure 12-11 Reconstructed dimuon mass using the calibration results from Figure 12-10 and Table 12-4.

A sample of 10 000 $Z \rightarrow \mu\mu$ decays has been fully simulated and reconstructed. The magnetic field was changed by different scale factors α_i for different regions ($B \rightarrow B/\alpha_i$). Applying the method described above, it is possible to retrieve these scale factors with high accuracy and to calibrate the average energy loss as a function of pseudorapidity. The algorithm is reasonably independent of the chosen initial values. For this analysis, the initial values were generated by taking the generated values and smearing them by 10%.

A crucial point is the selection of good reconstructed tracks for the calibration. Since the energy loss obeys a Landau distribution, there are many events which have a huge energy loss and therefore a very small likelihood. Events with a likelihood below a certain cutoff were rejected, and the value of the cutoff was found empirically by minimising the number of iterations needed to converge.

For symmetry reasons, the mean energy loss was calculated as a function of pseudorapidity. The results of the likelihood minimisation procedure are displayed in Figure 12-10, which shows the mean energy loss for 50 GeV muons as a function of pseudorapidity. The calibrated energy loss is compared to the generated energy loss and shows excellent agreement. The accuracy is 45 MeV for small pseudorapidity (barrel region) and about 100 MeV for a pseudorapidity of 2. This accuracy will improve directly with the number of processed events.

Two magnetic field scale factors, $\alpha(\phi<0)$ and $\alpha(\phi>0)$, were fitted simultaneously and are retrieved with an accuracy of 0.1%, as shown in Table 12-4. To obtain the desired accuracy of 10 MeV for the average energy loss and 0.02% for the magnetic field scale factors, the number of events per (η,ϕ) channel (here $2\times5 = 10$ channels) has to be increased by approximately a factor of 40.

Table 12-4 Result of the calibration of the two magnetic field scale factors (the errors are statistical).

Sectors	$\phi < 0$	$\phi > 0$
Generated scale factors	1.01	0.98
Reconstructed scale factors	1.0103 ±0.0009	0.9816 ±0.0013

Figure 12-11 shows the Z mass reconstructed using the results of this calibration. The reconstructed mass is slightly too high, which is due to the fact that the mean energy loss was used (the most probable energy loss is smaller).

12.4.5 Conclusions

In this section, it has been shown that, even with very limited statistics ($10\,000\ Z \rightarrow \mu\mu$ decays) compared to that expected at the LHC, the absolute muon momentum scale can be calibrated to an accuracy of 0.1%. How the final errors scale with the available statistics will depend mainly on the number of (η,ϕ) channels for the magnetic field and energy loss scale factors. This motivates the efforts presently devoted to designing the best possible set of measurements and reconstruction of the magnetic field map in order to reduce the number of magnetic field scale factors.

If the determination of the absolute mass scale proves to be more accurate in the Inner Detector (see Section 12.2), the comparison of the momenta measured independently in the Inner Detector and in the Muon System may improve the calibration of the latter, or at the very least provide a very useful cross-check. The direct comparison is affected by the uncertainty on the average energy loss of the muons in the calorimeters. A comparison at the required level of 0.02% would need a knowledge of this average energy loss with an accuracy of 10 MeV (or 0.25% of the average loss) for a muon of 50 GeV energy. It will be extremely hard to achieve such an accuracy: dedicated energy-loss measurements with the various calorimeter materials would be necessary together with a very detailed knowledge of the materials composing the calorimeters.

A more promising procedure would make use of the difference between the momenta measured in both detectors, averaged over two separate samples of μ^+ and μ^-, selected to have identical distributions for their measured momentum in the Inner Detector. The quantity, $\langle p_{\mu S} - p_{ID}\rangle_+ + \langle p_{\mu S} - p_{ID}\rangle_-$, depends then only upon the average difference in energy loss between μ^+ and μ^-, which can be known to better than 10 MeV. If the Inner Detector is assumed to be perfectly calibrated, this quantity provides a direct estimate of the misalignment and/or of the magnetic field miscalibration in the Muon System.

12.5 Jet and E_T^{miss} scale

In this section, the absolute scale of the overall Calorimeter is discussed, mostly in terms of jet spectroscopy, but also for E_T^{miss} measurements relevant to reconstructed masses containing pairs of τ-leptons. As mentioned in Section 12.1, other Chapters deal with systematic effects possibly affecting the absolute energy scale of high-p_T jets at a scale of ~1 TeV.

12.5.1 Jet spectroscopy

12.5.1.1 General considerations

Many of the precision physics studies foreseen with ATLAS will involve decays of narrow resonances into hadronic jets, and the knowledge of the absolute jet energy scale will be one of the crucial ingredients determining the ultimate accuracy with which such measurements will be performed. This is a rather complex issue, because it is subject to both physics (initial- and final-state radiation, fragmentation, underlying event activity, jet algorithm, *etc.*) and detector (calorimeter response over a wide range of energies and over the full acceptance of the detector, non-linearities at high energies, *e/h* ratio, etc.) effects. All of these have to be understood at the level of a fraction of a percent in terms of systematic uncertainties, if the ATLAS goals for precision measurements in this sector are to be achieved.

As briefly summarised above in Section 12.1 and described in more detail in Chapters 5 and 9, a large fraction of the ATLAS calorimeter modules will have been calibrated in beams of electrons, muons and pions, before installation into ATLAS. *In situ* calibration using high-p_T isolated charged pions from τ-decays would guarantee an accurate and up-to-date inter-calibration between different modules and calorimeters (see Section 5.4). This will be needed over the pseudorapidity range $|\eta| < 3.2$, so the forward calorimeters are considered here only in connection with the knowledge of the absolute E_T^{miss} scale (see Section 12.5.2).

This wealth of calibration data will be one of the key elements in minimising the systematic uncertainties when reconstructing hadronic jets over a wide range of transverse energies and topologies. The next step in the understanding of the performance of the overall calorimetry in terms of jet spectroscopy will be to benefit from the unique features of the data samples which will be available at the LHC to perform an accurate *in situ* calibration of the absolute jet energy scale:

- For the case of light-quark jets, the very large statistics of $W \to jj$ decays from top quark decay will provide the best sample for understanding precisely the interplay between the jet energy scale and the mass scale of resonant jet-jet final states (the *W* mass will be known to an accuracy of ~30 MeV at the start-up of the LHC). It will also provide an almost perfect sample for constraining the top-quark mass when measured from purely hadronic final states (see Section 18.1.3).

- Events containing a *Z* boson decaying to leptons and one high-p_T jet will be very useful to cross-check the calibration of the jet energy scale performed with $W \to jj$ decays, and will also provide constraints on the *b*-jet energy scale, which cannot be obtained directly from top-quark decays. The use of γ+jet events had been considered in [12-14], since this sample could provide much higher statistics than the Z+jet sample, but the systematic uncertainties linked to residual background from hadronic jets misidentified as photons were

estimated to be too difficult to control at the required level and γ+jet events are not considered further here.

12.5.1.2 Use of $W \to jj$ decays

As stated above, the reconstruction of $W \to jj$ decays is the most promising tool for *in situ* calibration of hadron calorimetry at the LHC. The large $t\bar{t}$ cross-section will provide an abundant sample of hadronically decaying W bosons. For example, about 80 000 $t\bar{t}$ events will be produced per day at low luminosity, out of which approximately 1500 $l\nu jj b\bar{b}$ final states can be reconstructed (see Chapter 18). This sample can be cleanly separated from the dominant QCD W+jet and the electroweak WW backgrounds by requiring an isolated lepton with $p_T > 20$ GeV and at least four jets with $p_T > 40$ GeV, two of which are tagged as b-jets.

A sample of 45 000 events would be collected for an integrated luminosity of 10 fb^{-1}. The invariant mass of jets not tagged as b-jets is used to reconstruct the $W \to jj$ decay, as shown in Section 18.1.2 (the combination with the mass closest to the W mass is selected). After these simple kinematic cuts, the background under the peak is small and arises mainly from wrong jet-jet combinations in the signal events themselves. The optimal method to reconstruct the jet-jet mass for $W \to jj$ decays depends quite strongly on the transverse momentum of the W boson and on the physics goals. Several methods and their associated systematics are discussed in some detail in Section 9.3.1 (see also [12-15] for a detailed study). The discussion here limits itself to estimating with fast simulation the size of the systematic uncertainties affecting the absolute jet energy scale, before and after calibrating a high-statistics sample of $W \to jj$ decays to the known value of m_W.

For inclusive $t\bar{t}$ events with a reconstructed $W \to jj$ decay, Figure 12-12 shows, for each reconstructed jet from the $W \to jj$ decay, the ratio of the p_T of the original parton, p_T^{parton}, to the p_T of the reconstructed jet, p_T^{jet}, as a function of p_T^{jet}. The jets are reconstructed using a standard fixed-cone jet algorithm with a cone size $\Delta R = 0.4$ (optimised for high-luminosity operation) and the reconstructed jet-jet mass is required to be within ±15 GeV of the nominal W mass. Figure 12-12 shows the results obtained both with and without including QCD final-state radiation (FSR). Initial-state radiation and underlying event effects are very small. On the other hand, the effect of FSR is quite large for $p_T^{jet} \sim 50$ GeV because out-of-cone losses remain significant, *i.e.* of the order of 10% for these values of p_T^{jet}. For values of p_T^{jet} close to 200 GeV, the ratio p_T^{parton}/p_T^{jet} tends to be smaller than unity. This effect is almost entirely recovered by requiring the opening angle between the two jets to be $\Delta R > 0.8$, indicating that effects related to overlap between the two jets become significant for $p_T^{jet} > 200$ GeV. This corresponds roughly to $p_T^W > 400$ GeV, for which it is well known from heavy Higgs boson searches that the jets from $W \to jj$ decay overlap significantly and therefore require a dedicated algorithm for the reconstruction (see Section 19.2.10).

The 4-vectors of the reconstructed jets from $W \to jj$ decay are then rescaled so that $m_{jj} = m_W$. The result of this procedure is shown in Figure 12-13. For values of $p_T^{jet} > 70$ GeV, this rescaling procedure to the known W mass achieves reasonably well the desired goal of a ±1% overall systematic uncertainty on the absolute jet energy scale. However, for $p_T^{jet} \sim 50$ GeV, residual systematic effects from FSR remain at the level of ~3%. These effects could be further reduced by using a larger cone, *e.g.* of size $\Delta R = 0.7$ at low luminosity, and/or applying a more refined rescaling procedure.
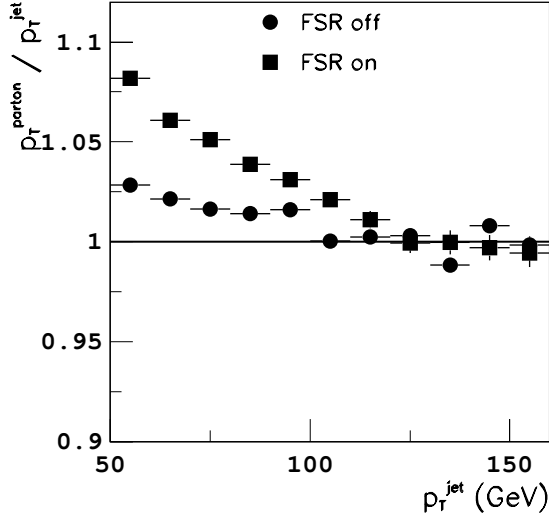
Figure 12-12 Ratio of the original parton p_T, p_T^{parton}, to the p_T of the reconstructed jet, p_T^{jet}, as a function of p_T^{jet}, for $W \to jj$ decays reconstructed in inclusive $t\bar{t}$ events. The black squares correspond to both initial-state and final-state radiation turned on, whereas the black circles are obtained in the case where final-state radiation (FSR) is switched off.
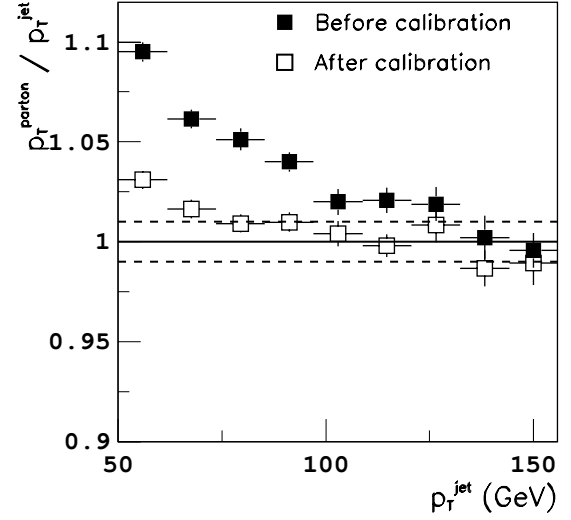
Figure 12-13 Ratio of the original parton p_T, p_T^{parton}, to the p_T of the reconstructed jet, p_T^{jet}, as a function of p_T^{jet}, for $W \to jj$ decays reconstructed in inclusive $t\bar{t}$ events. The black squares correspond to the case without rescaling, whereas the open squares correspond to the result after rescaling the jet 4-vectors to obtain $m_{jj} = m_W$ (see text). The dashed horizontal lines represent the desired goal of a ±1% systematic uncertainty on the absolute jet energy scale.

In conclusion, the high-statistics $W \to jj$ decays reconstructed in inclusive $t\bar{t}$ events should provide an adequate tool to achieve an overall ±1% uncertainty on the absolute jet energy scale, over a range of jet transverse momenta from 50 GeV to several hundred GeV. The lower and upper ends of this range will depend on how well residual systematic effects can be controlled with the data and the Monte Carlo simulation:

- for $p_T^{jet} \sim 50$ GeV, residual effects due to the interplay between final-state radiation and the fraction of the jet energy not collected by the specific algorithm used could be significant with respect to the desired goal;

- for $p_T^{jet} > 200$ GeV, residual effects due to overlap between the two jets from the W decay may also be significant. In addition, the constraints from the data will always be limited by statistics if one attempts to use only well-separated reconstructed jets in this case.

12.5.1.3 Use of *Z*+jet events

It has been shown at the Tevatron [12-16], that Z+jet events, containing $Z \to ee$ or $Z \to \mu\mu$ decays and one high-p_T jet, constitute a useful sample to constrain *in situ* the calibration of the absolute jet energy scale. The method is apparently quite simple and takes advantage of the expected balance in p_T between the precisely measured leptonic Z decay and the highest-p_T jet in the event.

Although the expected rates for this process at the LHC are quite large (see also Section 15.7.4), a clean selection of such events is not straightforward, because initial-state radiation often produces additional high-p_T jets, which degrades the quality of the p_T-balance between the Z boson and the leading jet. This is a source of potentially significant systematic uncertainties in the low-p_T region, where the probability for producing additional jets of comparable p_T is high.

A first step in the study of these Z+jet events is to define selection cuts, which preferentially select topologies with one and only one back-to-back jet produced in association with the Z boson. The impact of these cuts has been assessed using fast simulation by studying the evolution of the average fractional imbalance between the p_T of the Z boson and the p_T of the leading reconstructed jet, $(p_T^Z - p_T)/p_T^Z$, as a function of the cuts applied to the sample. These cuts are the following:

- the difference in azimuth, $\Delta\phi$, between the reconstructed Z boson and the leading jet is required to be $\Delta\phi > 3.06$;

- a loose jet veto requires that no additional jet with $p_T > 40$ GeV and $|\eta| < 3.2$ be reconstructed in the event (this jet veto can also be used at high luminosity), as shown in Section 9.1.3;

- a tight jet veto requires that no additional jet with $p_T > 15$ GeV and $|\eta| < 4.9$ be reconstructed in the event.

Table 12-5 Evolution of the average fractional imbalance between the p_T of the Z boson and the p_T of the leading jet in Z+jet events as a function of the selection cuts applied and of the successive ingredients used in the event generation. The results are shown for jets in the p_T range between 20 and 60 GeV (top line of each cell) and between 60 and 120 GeV (bottom line of each cell). The jets are reconstructed in a cone of size $\Delta R = 0.7$ (the last column shows the effect of increasing the cone size to $\Delta R = 1.0$).

Selection cuts	Hard process	+ underlying event	+ initial-state radiation	+ final-state radiation ($\Delta R = 0.7$)	+ final-state radiation ($\Delta R = 1.0$)
One jet with $p_T > 20$ GeV and $|\eta| < 3.2$	0.026 0.015	0.005 0.002	0.050 0.034	0.097 0.071	0.043 0.030
$\Delta\phi > 3.06$	0.026 0.015	0.005 0.002	0.023 0.014	0.050 0.042	0.020 0.007
$\Delta\phi > 3.06$ and loose jet veto	0.026 0.015	0.005 0.002	0.022 0.013	0.049 0.041	0.019 0.006
$\Delta\phi > 3.06$ and tight jet veto	0.026 0.015	0.005 0.002	0.018 0.011	0.044 0.033	0.014 0.002

The evolution of the average value of the fractional imbalance as a function of the cuts and of the successive ingredients used in the event generation (hard-scattering process, underlying event, initial-state and final-state radiation) is shown in Table 12-5 for Z+jet events with a leading jet with $p_T > 20$ GeV reconstructed in a cone of size $\Delta R = 0.7$. The following observations can be made:

- if no dedicated selection cuts are applied and all ingredients in the event generation are switched on, the average value of the fractional imbalance is about 10% for low-p_T jets in the range from 20 to 60 GeV, and decreases to about 7% for higher-p_T jets in the range from 60 to 120 GeV;

- the cut on $\Delta\phi$ improves the situation considerably, and a further significant but smaller improvement is obtained by applying in addition the tight jet-veto cut. The loose jet-veto cut does not improve the situation much, indicating that the Z+jet calibration method will be more difficult to benefit from at high luminosity;

- the impact of final-state radiation is the largest for the default cone size of $\Delta R = 0.7$, but the impact of initial-state radiation cannot be neglected even after all selection cuts. If a cone size of $\Delta R = 1.0$ were to be used, Table 12-5 shows that the expected average value of the fractional imbalance can be brought down to a level close to or below the desired goal of $\pm 1\%$, even for low-p_T jets.

The distribution of the fractional imbalance is shown in Figures 12-14 and 12-15 for jets reconstructed with $60 < p_T < 120$ GeV, respectively before cuts and after applying the $\Delta\phi$ and tight jet-veto cuts described above. These figures show that the selection cuts not only decrease the average value of the fractional imbalance, but also improve considerably its spread.
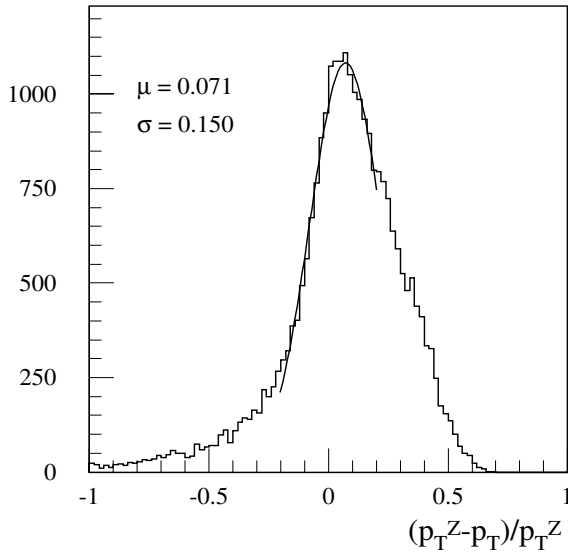
Figure 12-14 Fractional imbalance between the p_T of the Z boson, p_T^Z, and the p_T of the leading jet for Z+jet events with a reconstructed jet in the p_T range from 60 to 120 GeV before any further cuts are applied. A cone of size $\Delta R = 0.7$ is used to collect the jet energy.
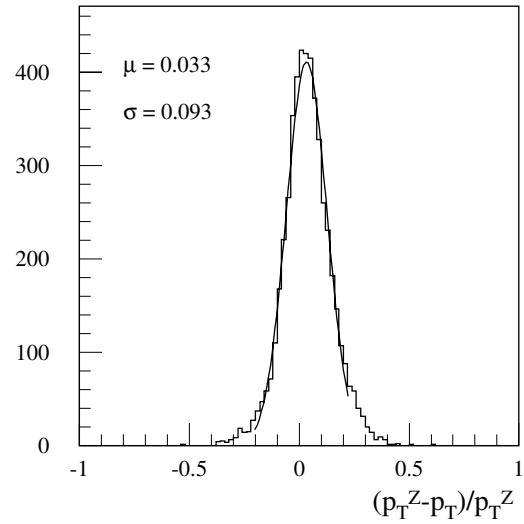
Figure 12-15 Same as Figure 12-14, but after the $\Delta\phi$ and tight jet-veto cuts listed in Table 12-5 have been applied.

The expected rates of Z+jet events passing the $\Delta\phi$ and tight jet-veto cuts of Table 12-5 are shown in Table 12-6 for an integrated luminosity of 10 fb^{-1} and for the various regions of the Calorimeter. These rates are fully adequate to obtain a statistical sensitivity at the required level of $\pm 1\%$ for jets of $p_T < 200$ GeV over the complete coverage, including even the Forward Calorimeter. More integrated luminosity would be needed to measure the response at the same $\pm 1\%$ level of accuracy for jets with $p_T > 200$ GeV. It should be noted that, for obvious reasons linked to the lower expected signal rates and to the lack of precise theoretical predictions, the precision on the absolute mass scale required by physics is not as tight at the scale of 500 GeV to 1 TeV as at the 50-100 GeV scale. Table 12-6 also shows the rates expected for Z+b-jet events, for which the b-jets are assumed to be tagged with an efficiency of 50% (see Chapter 10). The overall Z+jet sample contains a mixture of jet flavours with typically about 28% of gluon jets, 54% of light-

quark jets, 12% of *c*-jets and 6% of *b*-jets. With the *b*-tagging rejections reported in Chapter 10, the *Z+b*-jet samples of Table 12-6 should have a purity close to 90%, hopefully sufficient to constrain independently the absolute energy scale of *b*-jets to the same accuracy of ±1%.

Table 12-6 For an integrated luminosity of 10 fb^{-1}, expected rates for *Z+*jet (top line of each cell) and *Z+b*-jet (bottom line of each cell) events passing the $\Delta\phi$ and tight jet-veto cuts of Table 12-5, for three ranges of jet p_T and for the various regions of the ATLAS hadronic calorimetry. The rates for *Z+b*-jet events assume a *b*-tagging efficiency of 50%.

Region of calorimeter	$20 < p_T < 60$ GeV	$60 < p_T < 120$ GeV	$p_T > 120$ GeV
Barrel ($|\eta| < 1.0$)	190 000	100 000	24 000
	5000	2000	500
Extended barrel ($0.8 < |\eta| < 1.7$)	150 000	80 000	20 000
	3500	1500	500
End-cap ($1.5 < |\eta| < 3.2$)	190 000	90 000	16 000
End-cap ($1.5 < |\eta| < 2.5$)	4500	1500	500
Forward ($3.2 < |\eta| < 4.9$)	30 000	10 000	1000

The use of the *Z+*jet events for an accurate determination of the jet energy scale seems therefore promising, based on the studies with fast simulation reported above. These studies have been complemented by (and cross-checked with) full simulation and reconstruction in the following way [12-17]:

- A sample of *Z+*jet events with $p_T^Z > 40$ GeV was fully simulated and reconstructed in the Calorimeters. This required a careful inter-calibration between the different regions of the calorimetry. Although this sample spanned the pseudorapidity coverage of the Calorimeters over $|\eta| < 3.2$, most of the statistics described here was concentrated in the barrel and extended-barrel regions.

- a very similar but much higher-statistics sample was simulated with fast simulation, essentially reproducing the results of Table 12-5 over a different p_T range.

These samples were then compared in terms of the fractional imbalance between p_T^Z and the jet p_T, as shown in Table 12-7. The agreement between the fast simulation and the full simulation/reconstruction is reasonable, although the jet veto cuts appear to reduce the fractional imbalance more strongly in the fully simulated events. This effect might be due to the difficulty of setting the energy scale accurately for low-p_T jets in the reconstruction.

Figures 12-16 and 12-17 show the distributions of the fractional imbalance before cuts and after the $\Delta\phi$ and tight jet-veto cuts listed in Table 12-7, respectively for the cases of fast and full simulation. These Figures show that the shapes of the distributions are also in good agreement between the fast simulation and the full simulation/reconstruction. Finally, Figure 12-18 shows the variation of the average fractional imbalance as a function of the jet p_T. The results display the progressive decrease of the residual imbalance due to initial-state and final-state radiation as the jet p_T increases.

The next step in assessing the usefulness of the *Z+*jet events for an accurate calibration of the absolute jet energy scale is to compare the reconstructed jet p_T, rescaled to balance the p_T of the *Z* boson, to the original parton p_T. Table 12-8 shows the fractional imbalance, calculated now from the reconstructed jet p_T, rescaled to balance the p_T of the *Z* boson, and from the original parton p_T, as a function of the successive selection cuts and for three ranges of jet p_T. Even after

Table 12-7 Evolution of the average fractional imbalance between the p_T of the Z boson and the p_T of the leading jet in Z+jet events as a function of the selection cuts applied. The results are shown for fast simulation (as in Table 12-5) and for full simulation and reconstruction, both for all jets and for b-jets. The statistical error on the numbers for the fully simulated sample is 0.01, whereas it is negligible for the fast simulation.

	Fast simulation (all jets)	Full simulation (all jets)	Fast simulation (*b*-jets)	Full simulation (*b*-jets)
One jet with $p_T > 40$ GeV and $|\eta| < 3.2$	0.053	0.057	0.106	0.089
$\Delta\phi > 2.99$	0.040	0.037	0.091	
$\Delta\phi > 2.99$ and loose jet veto	0.039	0.027	0.089	
$\Delta\phi > 2.99$ and tight jet veto	0.033	0.024	0.076	0.050
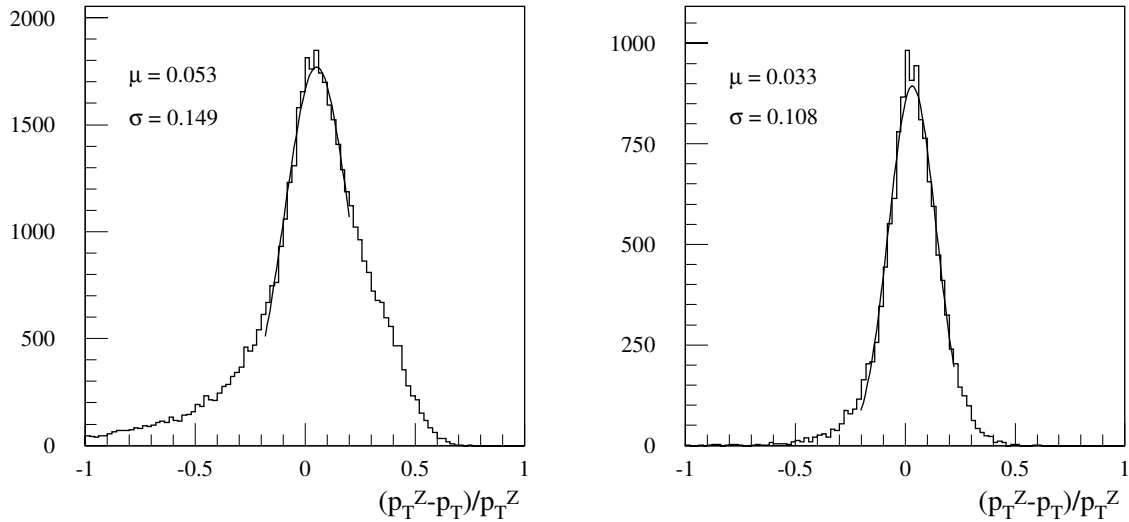
Figure 12-16 After fast simulation, fractional imbalance between the p_T of the Z boson, p_T^Z, and the p_T of the leading jet for Z+jet events containing a reconstructed jet with $p_T > 40$ GeV within $|\eta| < 3.2$, before (left) and after (right) the $\Delta\phi$ and tight jet-veto cuts listed in Table 12-7 are applied. A cone of size $\Delta R = 0.7$ is used to collect the jet energy.

all the selection cuts are applied, the residual fractional imbalance remains significant for jets with $p_T < 60$ GeV. The results shown in Table 12-8 show that the desired goal of an overall systematic uncertainty below ±1% on the absolute jet energy scale may be achieved only for jets with $p_T > 50$ GeV using Z+jet events.
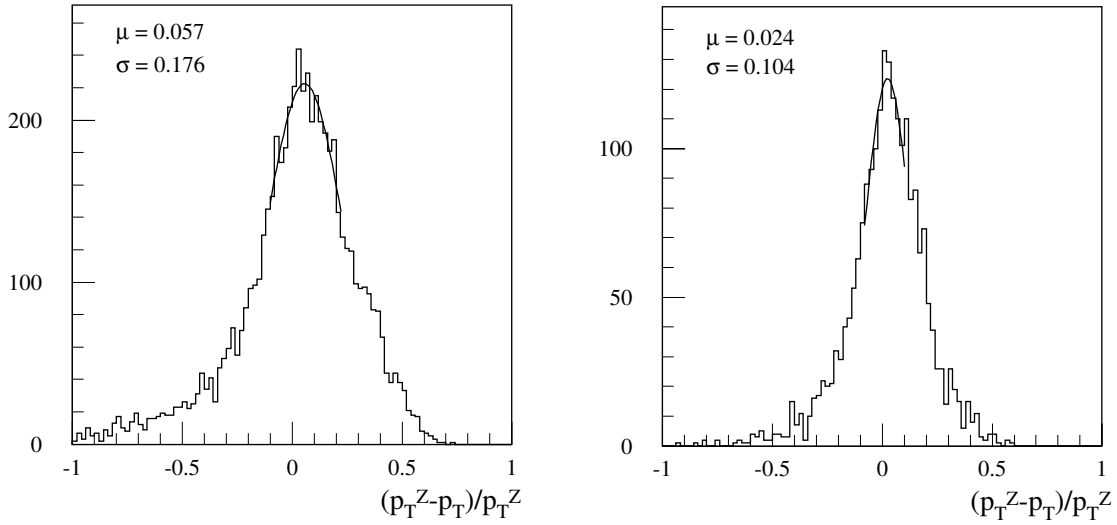
Figure 12-17 Same as Figure 12-16, but for full simulation and reconstruction.

Table 12-8 Evolution of the average fractional imbalance between the p_T of the leading jet in Z+jet events, rescaled to match the p_T of the Z boson, and the original parton p_T, as a function of the selection cuts applied and of the p_T range of the jets.

Jet p_T range (GeV)	20 < p_T < 60 GeV	60 < p_T < 120 GeV	p_T > 120 GeV
No cuts	0.163	0.060	0.011
$\Delta\phi$ > 3.06	0.074	0.030	0.005
$\Delta\phi$ > 3.06 and loose jet veto	0.071	0.026	0.004
$\Delta\phi$ > 3.06 and tight jet veto	0.049	0.015	0.004

As a final step in the present study, the impact of the main sources of systematic uncertainties on the quality of the calibration with Z+jet events was studied. The possible systematic uncertainties arising from the detector response itself are described in Chapter 9 and are not considered here. Other sources of systematic uncertainties which may affect the calibrations using Z+jet events are:

- Uncertainties due to the modelling of initial-state radiation are probably dominant in this particular case. They have been estimated by varying Λ_{QCD} in the event generation by a factor 1.5 in either direction and the resulting variations on the average fractional imbalance, for Z+jet events passing the $\Delta\phi$ and tight jet-veto cuts, are between ±1.5% at low p_T and 0.3% at high p_T.

- Uncertainties arising from the imperfect modelling of the Z+jet events for back-to-back topologies have been estimated by tightening even further the $\Delta\phi$ cut from $\Delta\phi$ > 3.06 to $\Delta\phi$ > 3.12. The effect, in this case, is between -0.7% and -0.1%.

In conclusion, Z+jet events will be a useful high-statistics tool to cross-check the setting of the absolute jet energy scale using $W \rightarrow jj$ decays in $t\bar{t}$ events over a wide range of jet p_T. These events could also be used to set the absolute scale in the forward calorimeter, for which the standard method using $W \rightarrow jj$ decays does not apply. More studies are needed to ascertain better the limitations of the method and possibly to improve it by using the well-known technique of projecting the jet p_T onto privileged axes corresponding to the bisectors of the angle between the transverse momenta of the jet and of the Z boson. In addition, Z+jet events may provide a useful source for calibrating independently the b-jet energy scale, since high-statistics and 90% pure samples of Z+b-jet events should be obtained for an integrated luminosity of 10 fb^{-1}. Finally, Z+jet events may well also be of great importance to check the linearity of the overall Calorimeter as the jet p_T reaches large values in the TeV range.
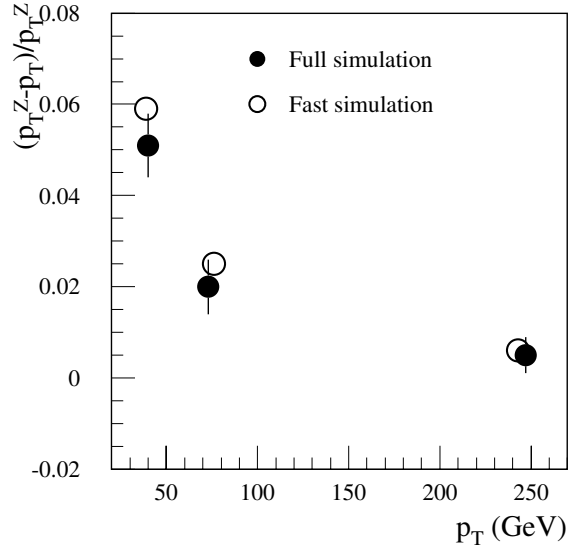
Figure 12-18 Average fractional imbalance between the p_T of the Z boson, $p_T{}^Z$, and the p_T of the leading jet as a function of the jet p_T. The results of fast simulation (open circles) and full simulation and reconstruction (black circles) are shown for Z+jet events containing a reconstructed jet with $p_T > 40$ GeV within $|\eta| < 3.2$ and passing the $\Delta\phi$ and tight jet-veto cuts listed in Table 12-7. A cone of size $\Delta R = 0.7$ is used to collect the jet energy.

12.5.2 $E_T{}^{miss}$ and forward calorimeter scale

Once the absolute energy scale of the ATLAS Hadronic Calorimeter has been set to ±1% over the range $|\eta| < 3.2$, following the methods described in Section 12.5.1, the knowledge of the absolute energy scale over the full pseudorapidity coverage, *i.e.* including the forward calorimeters, is mainly of interest for physics involving an accurate measurement of $E_T{}^{miss}$ (the quality of forward jet tagging, *e.g.* as used in heavy Higgs-boson searches described in Section 19.2.10, depends mostly on an accurate measurement of the jet polar angle). The most prominent examples of such cases are the search for resonances decaying into pairs of τ-leptons (see Section 19.3.2.5) and to a lesser extent precision SUSY studies involving directly the measurement of $E_T{}^{miss}$ (see Section 20.2).

As discussed in detail in Section 9.3.3.1, $Z \rightarrow \tau\tau$ events (with one leptonic τ-decay and one single-prong hadronic τ-decay) can be reconstructed rather accurately for events with $p_T^Z > 15$ GeV, since the expected mass resolution is about 9 GeV at low luminosity. For an integrated luminosity of 30 fb^{-1}, a sample of 3800 $Z \rightarrow \tau\tau$ signal events is expected to be reconstructed above a total background of ~200 events. This would lead to a statistical uncertainty of ~ ± 0.15 GeV on the measured Z mass, and therefore the overall error would be dominated completely by the 1% uncertainty on the absolute jet energy scale, which applies in this case to the high-p_T hadronic jet from τ-decay.

Figure 12-19 shows the sensitivity of the measured Z mass, as obtained from reconstructed $\tau\tau$ pairs, to the absolute E_T^{miss} scale. A variation of $\pm 10\%$ of the E_T^{miss} scale results in a shift of $\pm 2.5\%$ on the measured Z mass. The E_T^{miss} scale can therefore be determined to $\pm 4\%$ for an integrated luminosity of 30 fb^{-1}.
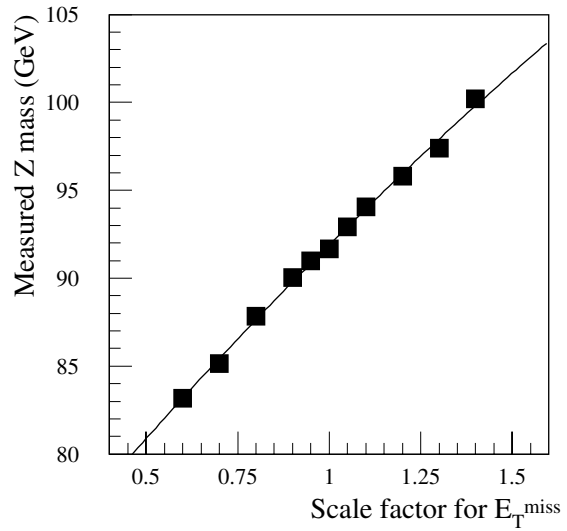
Figure 12-19   Reconstructed Z mass in the $Z \rightarrow \tau\tau$ channel as a function of the uncertainty on the E_T^{miss} scale.

12.6 Conclusions

This Chapter has described some of the prominent methods and event samples, which will be used *in situ* to evaluate the overall ATLAS mass scale to the best possible accuracy. Many of the studies reported here are based on an extrapolation of the techniques pioneered successfully at the Tevatron. Using these techniques, the experiments at the Tevatron have demonstrated that precision physics can be done at hadron colliders, in many cases on a par with that performed at e^+e^- colliders. The overall systematic uncertainties on the absolute mass scale in the Tevatron experiments have been brought to the level of 0.1% for leptons (momentum and energy measurements) and of a few percent for hadronic jet energy measurements.

The experiments at the LHC will have the added advantage of very high statistics of leptonic decays of vector bosons and of hadronic decays of W bosons from top-quark decays. Therefore, it is not unreasonable to hope that the ultimate requirements set by the physics for the systematic uncertainty on the absolute mass scale (0.02% for leptons, 0.1% for photons and 1% for hadronic jets) will be reached with the ATLAS detector.

12.7 References

12-1   CDF Collaboration, Phys. Rev. **D50** (1994) 2966 and Phys. Rev. **D 52** (1995) 4784.

12-2   D0 Collaboration, Phys. Rev. Lett. **77** (1996) 3309.

12-3   S. Haywood, 'Offline alignment and calibration of the Inner Detector',
         ATLAS Communication ATL-COM-INDET-99-001 (1999).

12-4   ALEPH Collaboration, ALEPH Handbook, Vol. 1 (1995).

12-5   D. Newton, H1 Internal Note, H1-8/90-145 (1990).

12-6   ATLAS Collaboration, Barrel Toroid Technical Design Report, ATLAS TDR 7,
         CERN/LHCC 97-19 (1997).

12-7   S. Snow, 'Magnetic field measurement requirements of the Inner Detector',
         ATLAS Internal Note ATL-INDET-97-196 (1997).

12-8   Z. Was *et al.*, Comput. Phys. Commun. **79** (1994) 291.

12-9   ATLAS Collaboration, Muon Spectrometer Technical Design Report, ATLAS TDR 10,
         CERN/LHCC/97-22 (1997).

12-10   L. Chevalier *et al.*, 'Test of the magnetic field reconstruction procedure with the race-track
         coil prototype', ATLAS Communication ATL-COM-MUON-99-012 (1999).

12-11   W. Lohmann *et al.*, 'Energy loss of muons in the energy range 1-10,000 GeV',
         CERN Yellow Report 85-03 (1985).

12-12   A. Henriques *et al.*, 'The muon energy losses in the tile calorimeter', ATLAS Internal Note
         ATL-TILE-95-068 (1995).

12-13   M. Aleksa, 'Absolute mass scale calibration using $Z \rightarrow \mu\mu$ events', ATLAS Internal Note
         ATL-MUON-99-001 (1999).

12-14   ATLAS Collaboration, Calorimeter Performance Technical Design Report, ATLAS TDR 1,
         CERN/LHCC/96-40 (1996).

12-15   P. Savard, 'The W to jet-jet and top quark mass reconstruction with the ATLAS detector',
         ATLAS Internal Note ATL-CAL-97-092 (1997).

12-16   D0 Collaboration, 'Determination of the absolute jet energy scale in the D0 calorimeters',
         Nucl. Instr. Meth. **A424** (1999) 352.

12-17   R. Mehdiyev and I. Vichou, 'Hadronic jet energy scale calibration using Z+jet events',
         ATLAS Communication ATL-COM-PHYS-99-054 (1999).

13 Luminosity measurement

13.1 Introduction

Luminosity L relates the cross-section σ of a given process to the corresponding event rate R:

$$R = L \times \sigma. \tag{13-1}$$

Therefore, luminosity is by definition a process-independent quantity which is completely determined by the properties of colliding beams. Typically a 5–10% precision for the luminosity determination is assumed for measurements in ATLAS, as obtained in previous and existing hadron-collider experiments. However, there may be a few cases which would benefit from a luminosity precision of 1–2%. The possibilities of achieving a precise luminosity determination in ATLAS are therefore also being explored.

Luminosity measurement and monitoring are needed for several purposes with somewhat different requirements. Clearly, for physics analyses, one requires as precise as possible a measurement of the integrated luminosity, used to convert an observed number of events to a cross-section. However, one may need measurements of the instantaneous luminosity, possibly bunch-by-bunch. Such measurements might be needed, for example, when correcting for the effects of pile-up on physics measurements. In addition to following the luminosity evolution for physics-analysis purposes, for which a very fast response time may not be required, information may be needed to give fast feedback for beam tuning.

The collider luminosity can be expressed in terms of the beam parameters. For the LHC [13-1] with a small crossing angle and bunched beams, the formula reads (assuming Gaussian bunch shapes):

$$L = F \frac{f \sum_i N_1^i N_2^i}{4\pi \sigma_x^* \sigma_y^*}, \tag{13-2}$$

where $f = 11$ kHz is the beam-revolution frequency, $F = 0.9$ is a factor which accounts for the non-zero crossing angle, N_1^i and N_2^i are the numbers of protons in the colliding bunches and σ_x^* and σ_y^* are the transverse bunch widths (assumed to be the same for all bunches) at the interaction point (IP).

Even if there are technical means to store high beam currents and to strongly focus beams, the collider luminosity cannot be arbitrarily increased due to the intrinsic beam dynamics, for example due to the defocusing in the electromagnetic field of the opposite beam. The ultimate LHC luminosity is usually parametrised as:

$$L = \xi F \frac{f N k_b \gamma}{r_p \beta^*},$$

where $\xi = 0.0034$ is the so-called beam–beam tune-shift parameter, k_b is the number of (equal) bunches, γ is the beam Lorentz factor, r_p is the proton classical radius, $\beta^* = 0.5$ m is the value at the IP of the amplitude function β. The nominal transverse beam size at the IP is 16 µm and can be calculated from $\sigma = (\varepsilon_n \beta/\gamma)^{1/2}$, where $\varepsilon_n = 3.75$ µm×rad is the normalised transverse beam

emittance. The beam divergence at the IP is given by σ^*/β^* and, for the design LHC parameters [13-1], is equal to 32 µrad. After the first year of LHC operation, 16% of the nominal beam currents should be achieved for $\xi = 0.0021$ (and $\varepsilon_n = 1$ µm×rad) resulting in a peak luminosity of approximately 10^{33} cm^{-2}s^{-1}.

In general, one can distinguish between three types of luminosity measurement. In the first approach the rate for a process with a well known and sizable cross-section is accurately measured and the luminosity is calculated from Equation 13-1. This method is widely used at e^+e^- colliders by measuring QED Bhabha scattering (or at HERA using ep bremsstrahlung) and high precision can be reached. At hadron colliders the QED processes usually have very small cross-sections compared to the hadronic ones and the second method of calculating the luminosity from the beam parameters (using Equation 13-2, for example) is therefore often used. However, the typical precision with this last method is rather poor, about 5–10%.

The third method, utilising the optical theorem in high-energy scattering, is also used at least to calibrate the absolute scale of the luminosity measurement. In this case, the total rate of pp interactions, R_{tot}, as well as the rate of forward elastic scattering, dR_{el}/dt (t = 0), is measured and the luminosity is derived from the relation

$$L\frac{dR_{el}}{dt}\bigg|_{t=0} = R_{tot}^2(1+\rho^2)/(16\pi).$$

13-3

Here ρ is the ratio of the real to imaginary part of the elastic forward amplitude. In this method a dedicated detector of protons which scatter at very small squared-momentum-transfers, t, is required, as well as a high and known efficiency for detection of inelastic pp interactions. Also in this case, the typical precision is only about 5–10%.

One can distinguish between luminosity measurement and monitoring. Measurements via the methods described above give an absolute determination of the luminosity. Other methods may, however, be used to monitor the luminosity and can be calibrated using the absolute methods. Such relative luminosity measurements provide a convenient way to follow the luminosity evolution during a given collider fill and also between different fills. An attractive possibility is to calibrate them under special, favourable beam conditions (*e.g.* low luminosity and high β^*), and then use them to determine the luminosity for normal running (*i.e.* at high luminosity).

13.2 LHC beam diagnostics

For a proper running of the ATLAS luminosity system and also to some extent of the main detector, a number of the LHC parameters should be continuously available and recorded. For example, the parameter list could contain: beam energy, bunch currents, beam orbits near the IP, coil currents for the low-β quadrupoles and nearby correction coils, vacuum conditions, beam-loss monitor data, beam-halo collimation data, and the beam size or transverse emittance. Two aspects of the LHC diagnostics are especially important for the luminosity determination: measurements of the beam currents and the beam orbit near the IP.

13.2.1 LHC bunch structure

The bunch configuration of the LHC beams is determined by the injection and extraction systems in the acceleration chain. According to the present design the bunches are grouped into 'trains' of 81 bunches, which in turn are grouped into 12 batches each containing three bunch trains. Most probably the bunch currents will not be very uniform; one may expect bunch-to-bunch variations of 10% or more. Additionally, some residual currents might be observed in the high-luminosity running in neighbouring RF buckets resulting in the so-called side- (or satellite-) bunches, 2.5 ns apart from the nominal ones.

13.2.2 Beam-line instrumentation

A system of beam-position monitors (BPMs) for the LHC is already well developed [13-2]. The expected BPM performance at full beam current is 10 μm resolution with 100 μm absolute-scale uncertainty in each of the horizontal and vertical directions. The orbit position can be determined separately for each bunch. Non-destructive beam-profile monitors will also be installed.

13.3 Luminosity measurement in ATLAS

In general there are three aspects of luminosity measurement in ATLAS.

- Providing final absolute integrated-luminosity values for use in offline analyses, for the full data sample and for selected periods. Also required are measurements of the average luminosity over a small time interval and for individual bunch crossings.

- Providing fast online luminosity monitoring, as required for efficient beam steering and for optimising the luminosity yield; a statistical precision of about 5% per few seconds and systematic uncertainties below ~20% are desirable.

- Fast checking of running conditions and beam-related backgrounds (also with the main detector in a stand-by mode), such as monitoring the vertex position (in particular its longitudinal coordinate), monitoring the temporal structure of the beams (satellite bunches, de-bunching), and monitoring the level of beam-related backgrounds (possibly including the use of special non-colliding p bunches).

Since there is probably no single experimental technique which can fulfil all of the above requirements, one has to consider a number of complementary measurements.

13.3.1 Absolute luminosity scale with the optical theorem

As discussed in Section 13.1, the luminosity can be obtained using the optical theorem from a simultaneous measurement of the total interaction rate and the rate of forward elastic scattering.

The main challenge of this method lies in the detection of the very forward elastically-scattered protons. The elastic cross-section for small $|t|$ scales as e^{bt} where $b \approx 20\,\text{GeV}^{-2}$ at LHC energies [13-3] (see Figure 13-1). Of course, the protons scattered at zero-angle (or at $t = 0$) cannot be detected, but the degree of extrapolation should be minimised and the smallest possible $|t|$ achieved. Use of so-called Roman pots is a well established technique (proposed for the LHC by the TOTEM collaboration [13-4] for example) for the measurement of the forward protons. The detector sensitive edge can be located very close to the beam centre, only about 15–20 beam widths away. To a good approximation the minimum scattering angle of a detected proton is 15–20 times the beam divergence at the IP. For the design LHC parameters this corresponds to an angle of about 600 µrad, or to a minimum $|t| = (7000\,\text{GeV} \times 0.0006)^2 = 16\,\text{GeV}^2$, and a re-

Figure 13-1 The *b* slopes of the *t* distributions at *pp* and *pp̄* colliders as a function of the center of mass energy.

liable extrapolation down to $t = 0$ is not possible. However, for the low transverse beam emittance expected at the LHC start-up and assuming special running conditions with $\beta^* = 50\,\text{m}$, the minimum angle is 35 µrad and $|t|_{min} = 0.06\,\text{GeV}^2$. This should give extrapolation uncertainties of a few per cent, although running with even higher β^* might also be necessary. Uncertainties in the geometrical acceptance of the detector, as well as of detector inefficiencies, will of course increase the error on the dR_{el}/dt (t = 0) measurement.

In Equation 13-3, the total rate, which is dominated by the inelastic interaction rate, enters squared. In order to avoid large model-dependent corrections the detection efficiency for inelastic events should therefore be very high. The acceptance of the central ATLAS detectors is not sufficient, especially for low-mass diffractive events. Figure 13-2 shows the acceptance loss that results if the detector can only cover a fixed region of rapidity from η_{min} to η_{max}. From this figure, it can be seen that if additional forward detectors were installed, covering the pseudo-rapidity region $3.0 < |\eta| < 7.5$, the overall efficiency would be as high as 98%. Use of these detectors requires low-luminosity running to avoid event pile-up.

Possible locations of the forward-tagging detectors needed for measuring the inelastic rate are at about 5 m and 16 m from the IP, very close to the beam pipe (see Figure 13-3). These forward detectors have to be radiation hard,
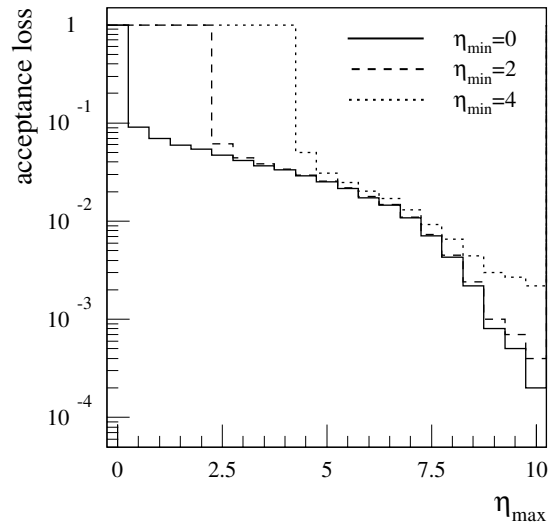
Figure 13-2 The inefficiency of tagging inelastic pp events as a function of pseudo-rapidity coverage. Only geometrical acceptance has been considered without allowing for magnetic field or detector inefficiencies.

but they might be simple, for example in the form of counters with full azimuthal coverage. Installation in the LHC tunnel of more counters, covering very extreme rapidities, will also be considered.

Finally, a measurement of the ρ parameter at the LHC is very difficult [13-4], although the uncertainty on its extrapolation to the LHC energy would result in a relatively small error of the order of 2% on the luminosity determination.
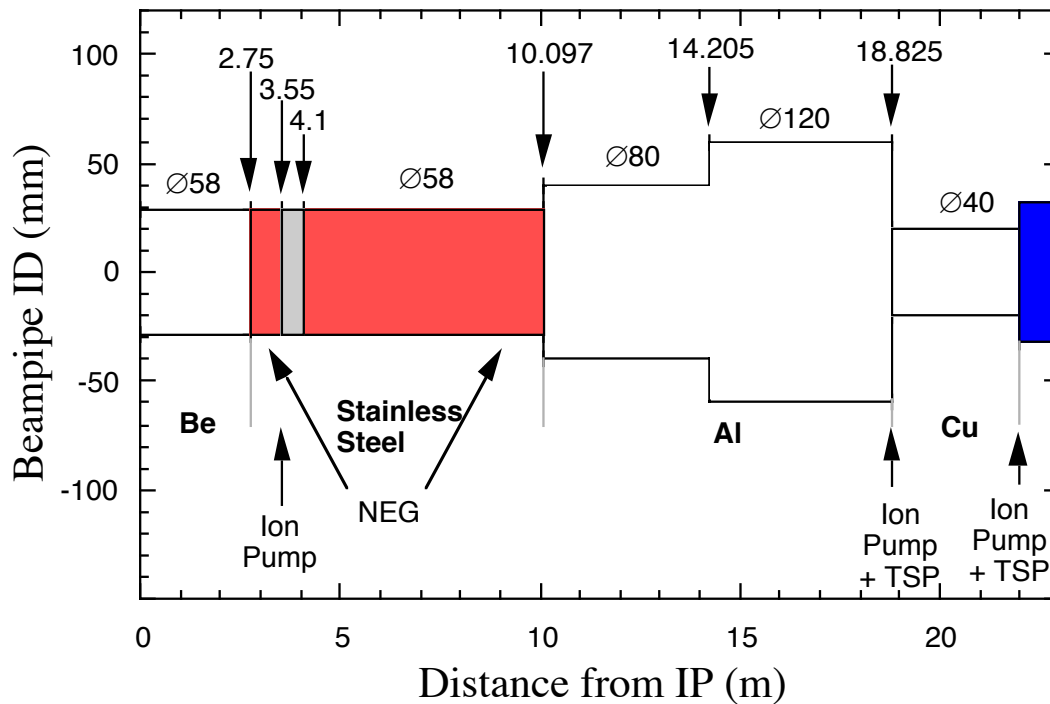
Figure 13-3 Shape of the ATLAS beam pipe showing the beam-pipe inner diameter as a function of the distance from the IP.

In summary, the method using the optical theorem requires additional dedicated detectors and special running conditions at a luminosity less than about 10^{32} cm^{-2}s^{-1} to avoid pile-up, and achieving a precision much better than 5–10% seems difficult unless a very high and well understood efficiency for inelastic events as well as for low $|t|$ elastic scattering can be achieved.

If there were no detector for the elastically-scattered protons in the ATLAS IP, but there were a precise measurement of the total inelastic cross-section, σ_{inel}, from another experiment at the LHC, one can still determine the luminosity from a measurement of the rate of inelastic collisions, R_{inel}, using the relation $L = R_{inel}/\sigma_{inel}$. The precision of such a measurement would be given directly by the uncertainties on σ_{inel} and on the efficiency for counting inelastic events.

ATLAS is studying the option of adding the necessary detector systems. A decision will be made, after the completion of the feasibility study, whether to pursue an engineering study prior to proposing to the LHCC any addition to the ATLAS detector system.

13.3.2 Luminosity determination from the beam parameters

To determine the luminosity from the beam parameters (see Equation 13-2), one needs a good measurement of the lateral beam sizes as well as of the bunch currents. To obtain reliable σ^* values from the beam sizes measured outside the ATLAS IP one has to know precisely the β-function, but typically the uncertainty is up to 10%. This uncertainty could possibly be reduced if the beam divergence at the IP can be measured. In any case, with beam-profile measurements one should be able to verify the assumptions on the Gaussian shapes of the bunches (*i.e.* lack of long tails in the transverse distributions) and on the common width for all bunches.

Another way of measuring beam widths at the IP, which might be potentially more accurate, is the van der Meer method based on transverse beam scans. Originally [13-5], this was done by moving one beam vertically and at the same time recording the relative change of the rate of *pp* interactions. The value of the beam displacement required to decrease the rate to, for example, 50% of its peak value was a direct measure of the beam heights at the IP. The efficiency of counting *pp* interactions should not depend on the beam displacement.

In the case of the LHC, one has to perform scans in both transverse directions and the forward detectors could serve as monitors of the relative rate of *pp* interactions. Such scans are very difficult for low-β^* running since the beam–beam interactions are very strong and may affect the beam sizes while the scans are performed. Additionally, the beam size would be small (16 μm), *i.e.* comparable to the resolutions of the BPMs. Therefore, dedicated runs with large values of β^* (at least 50 m) are required. Another complication is due to the non-zero crossing angle which causes a longitudinal shift of the IP (and hence a change of the beam size since in a straight section $\beta = \beta^* + z^2/\beta$), while one beam is moved transversely. Again the effect is only significant at low-β^* causing, for example, a 4% beam-size increase for a displacement corresponding to two beam widths.

For this method of luminosity measurement, a precise bunch-current measurement is essential. The ultimate precision will depend on the quality of the stored beams, *i.e.* to the level of the current in satellite bunches or in DC beam components (coasting, de-bunched beam). To avoid these effects, running at small beam currents with only a few bunches might be necessary.

In summary, use of the van der Meer method requires dedicated runs at high-β^* and very low luminosity ($< 10^{30}$ cm^{-2}s^{-1}), and a precision of better than 5–10% on the luminosity determination seems difficult. Regular beam scans at high luminosity are unlikely to be feasible.

13.3.3 Luminosity determination from lepton pair production

The production of dilepton pairs via the process $pp \rightarrow ppll$ can be calculated precisely and might be used to measure the luminosity. Two possible methods are explored here: electron pairs produced with low invariant mass and very small p_T, and muon pairs of higher p_T, produced centrally. The former requires additional detector elements, and the latter, while it can be detected with the current ATLAS configuration, has a lower rate. In both cases, the backgrounds are serious and must be carefully studied.

13.3.3.1 Measurement of very forward two-photon production of e^+e^- pairs

The possibility of using two-photon processes for luminosity measurements at hadron colliders was first considered in [13-6]. The cross-section for very forward two-photon production of *ee* pairs can be calculated within QED to an accuracy better than 1%, and at LHC energies the production of high-energy pairs becomes sizeable. The main characteristics of the reaction $pp \rightarrow ppee$ are the very small (of the order of the electron mass) invariant mass and transverse momentum, p_T, of the produced pairs (see Figure 13-4). Inelastic two-photon production of *ee* pairs, where one or both protons break up, has a significantly wider distribution of pair p_T. For hadronic reactions, the typical energy scale is the pion mass or higher.
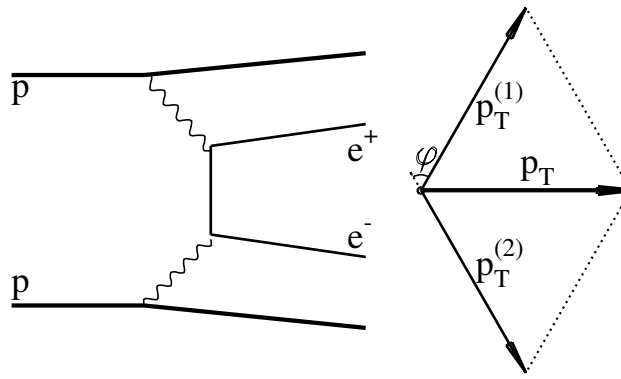
Figure 13-4 Feynman diagram and definition of the kinematical variables for the two-photon $pp \rightarrow ppee$ process.

Since the *ee* pairs are produced at almost zero polar angle, a small additional analysing dipole installed at about 15 m from the IP has been considered [13-7] to deflect the produced electrons and positrons into detectors outside the LHC beam-pipe without disturbing the LHC operation. For example, for a dipole bending power of 0.35 Tm and electron energies in the 5–20 GeV range, the detectors could be located about 20 m from the IP behind the TAS (TDS) shielding of the quadrupole inner triplet and a few centimetres from the beam, as shown in Figure 13-5. Provided the position and energy of the produced electrons can be measured with about 1% precision, resolutions of approximately 1 MeV could be achieved for measurements of the pair p_T and invariant mass. At high electron energies, the p_T resolution is limited by the beam divergence, $\sigma(p_T) = 40$ GeV x 16 μrad ≈ 0.6 MeV. At low energies, the ultimate resolution on the invariant mass of a few MeV results from the deflection of electrons and positrons by the space-charge of the beams.
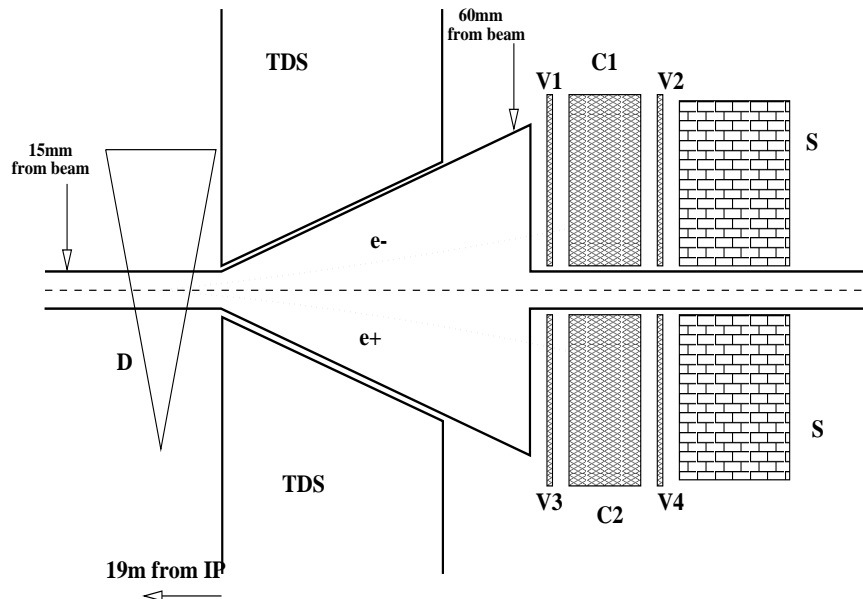
Figure 13-5 Sketch of a possible experimental setup for measuring forward production of *ee* pairs. TDS is the shielding of the inner triplet of quadrupoles, C1 and C2 are calorimeters with position detection, S is an additional shielding, D is a small analysing dipole and V1-V4 are veto counters.

A sizeable cross-section of more than 2 μb is expected for the following selection cuts:

1. electron energies: 5–20 GeV;

2. electron polar angles θ < 0.8 mrad (corresponding to the beam pipe radius at 16 m from the IP);

3. *ee* pair invariant mass < 10 MeV;

4. *ee* pair p_T < 10 MeV;

5. veto on charged particles with |η| < 7.6 (see below).

Note that cut 5 requires the presence of additional detectors to cover the full rapidity range. Cross-section calculations for the kinematic cuts 1–4 were performed using the LPAIR program [13-8]. The dominant physics background is due to pion Dalitz decays and direct pair production in inelastic collisions labelled 'bremsstrahlung' in Table 13-1. The backgrounds were estimated using a modified PYTHIA generator, where direct pair production was simulated using

Table 13-1 Cross-section estimates in μb using analytic calculations for $pp \rightarrow ppee$ and a modified PYTHIA generator for bremsstrahlung pairs and Dalitz decays; The superscript (*) corresponds to the case where an additional cut |φ| < 60° was applied.

Cuts	Signal	Dalitz decays	Bremsstrahlung	Total background
1-4	2.27	2.26	0.90	3.16 (139%)
1-5	2.27	0.011	0.012	0.023 (1.0%)
1-4*	1.08	0.30	0.11	0.41 (38%)
1-5*	1.08	0.0009	0.0010	0.002 (0.2%)

the approximation of classical currents [13-9] and the momenta of the produced charged particles. After the selection cuts 1–4 there is still a significant difference between the two-photon process and the backgrounds in the p_T and acoplanarity-angle (φ) distributions shown in Figure 13-6. Note that the electrons are uncorrelated in φ; this is due to the extremely small transverse momenta (~15 MeV). The lack of correlation can be used either for extracting the signal in a fitting procedure or in making further cuts to suppress the backgrounds. For example, an additional cut on the φ angle can significantly improve the signal-to-background ratio, as shown in Table 13-1.
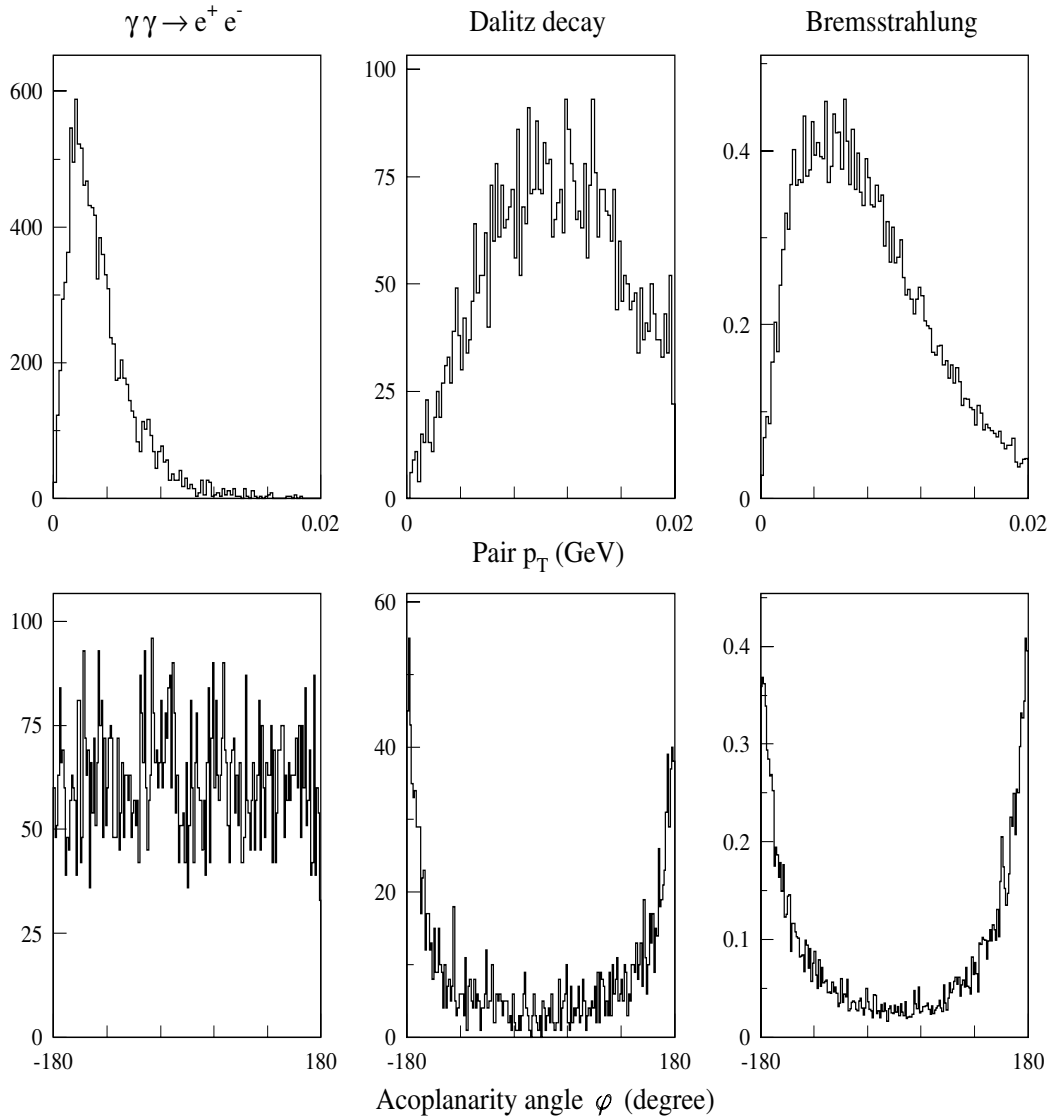
Figure 13-6 Distribution of p_T and acoplanarity angle φ for signal and background events (without detector smearing) after selection cuts 1–4.

At low luminosities the backgrounds can be reduced strongly by requiring no activity in the forward counters, *i.e.* by introducing condition (5), *i.e.* that no charged particles are produced above $|\eta| < 7.6$. One should note, however, that the calculations done so far neglected detector effects such as magnetic field and dead material and possible beam-related backgrounds.

A Monte Carlo simulation using the EGS4 package and a very simple model of electromagnetic-particle showering in ATLAS seems to indicate that the contribution of the secondary particles produced in electromagnetic showers is not very significant. Again, at low luminosities, requiring no activity in other ATLAS detectors would suppress this background even more.

More studies are needed to develop a suitable detection technique, but the potentially clear separation between signal and background makes this method an attractive option both for online and offline luminosity measurements. One should note that the analysing dipoles could become also a very useful tool for various kinds of systematic checks and luminosity-detector calibrations.

ATLAS is studying the option of adding the necessary magnet and detector systems. A decision will be made after the completion of the feasibility study, whether to pursue an engineering study prior to proposing to the LHCC any addition to the ATLAS detector system.

13.3.3.2 Measurement of central two-photon production of $\mu\mu$ pairs

The process $pp \to pp\mu\mu$ (related to the process discussed in Section 13.3.3 above), where the muons are produced at central rapidities, can be recorded using the standard ATLAS trigger and might provide an attractive method of offline integrated-luminosity determination [13-10]. The Feynman diagram of this two-photon process and the notations used are basically the same as for *ee* pair production shown in Figure 13-4. The invariant mass of the selected muon pairs is in the GeV range, but as for the forward *ee* pairs, the total transverse momentum of the pairs is very small. In contrast to the *ee* case, the muons have much larger transverse momenta and consequently are back-to-back in φ. The sharp peak expected in the acoplanarity-angle distribution at $\varphi = 0$ can be used to discriminate against background. Requiring, additionally, low particle multiplicity associated with the muon vertex, all sources of background can be reduced to acceptable levels. Signal extraction is performed by fitting the φ distribution which is not much affected by the detector resolution (unlike the distribution of the pair transverse momentum).

For centrally-produced muons, the elastic two-photon signal process has characteristic transverse momentum and acoplanarity values $p_T^{\mathrm{pair}} \approx 5$ MeV and $\varphi \approx 2$ mrad. The corresponding values for Drell-Yan production are ≈ 300 MeV and ≈ 100 mrad, and those for muon pairs from quark decays are even higher. For all these sources of background, the observable particle multiplicity associated with the event vertex is typically greater than 12–14 particles. In the case of the inelastic two-photon processes $pp \to p^*p^*\mu\mu$, in which at least one proton dissociates, the observed particle multiplicity is low. However, the characteristic acoplanarity value is $\varphi \approx 50$ mrad.

Based on these considerations the following selection criteria were applied:

1. two muon tracks with opposite charges (measured in both the Inner Detector and the muon spectrometer, and triggered by the Muon System), with $p_T > 6$ GeV, and $|\eta| < 2.2$;

2. muon-pair invariant mass < 60 GeV;

3. p_T of the muons is required to be equal within 2.5σ of the p_T measurement uncertainty (typically about 1.5% for low p_T muons);

4. acolinearity angle $\Theta > 1°$, so that the muons are almost back to back;

5. χ^2 probability > 1% for the muon vertex fit;

6. no other reconstructed charged tracks originating from the muon vertex.

Criterion (1) is applied to satisfy the trigger; criterion (2) suppresses the background from Z decays; criterion (3) is related to the requirement that the pair p_T be small, but leaves the acoplanarity angle distribution unchanged for the final background subtraction; criterion (4) suppresses the cosmic-ray background; criterion (5) defines the event vertex and suppresses the background from heavy-quark decays; and finally, criterion (6) strongly suppresses backgrounds with a high particle-multiplicity. Criterion (6) could reduce the detection efficiency for the two-photon process due to pile-up effects. At a luminosity $L = 10^{33}$ cm^{-2}s^{-1} the reduction is 2–3% for the expected longitudinal beam size of the LHC. For $L = 10^{34}$ cm^{-2}s^{-1} criterion (6) should be relaxed such that the reduction should not exceed 10%; this will have to be verified using experimental data.

The signal observability has been investigated using a particle-level Monte Carlo code with the detector properties parametrised according to the ATLAS specifications. The elastic two-photon processes were simulated with an approximate event generator developed for *ee* collisions [13-11]. This was adapted for *pp* scattering according to [13-12]. For the elastic two-photon process, its accuracy is about 1% for the kinematic domain of interest. The proton structure function W_2 used for the inelastic two-photon calculations was extracted from photo- and electro-production data [13-13]. The effect of resonances was taken into account. The predicted inelastic cross-section is greater than that of the LPAIR generator which uses approximate structure functions [13-14]. The event generation includes soft-photon emission which affects the observed distributions of φ and invariant mass.

The signal and background cross-section estimates are presented in Table 13-2 (the detection efficiency was not taken into account). The cross-sections are given for the narrow interval of acoplanarity angle $|\varphi| < 0.005$ containing about 50% of the signal. The background referred to as '2γ strong' is due to strong interaction between the protons in the two-photon process of pair production.

Table 13-2 Observable signal and background cross-sections for the two-photon production of muon pairs; σ_{kinem} and σ_{vertex} correspond to the selection criteria (1–4) and (1–6), respectively (see text).

Process	σ_{kinem} (pb)	σ_{vertex} (pb)
Signal	1.33	1.30
2γ inelastic	0.13	0.13
Drell-Yan process	3.8	0.04
Heavy quark decays	10	0.01
π, K decays	1.8	<0.001
2γ strong	0.04	0.04
Background total	15.8	0.22 (17%)

Figure 13-7 shows various distributions for the elastic two-photon process and dominant background processes, after applying the criteria 1–6, for an integrated luminosity of 10 fb^{-1}. Fitting the acoplanarity would determine the signal rate with a statistical error of 1.6% assuming a detection efficiency of 75%. Even if the background-to-signal ratio were increased by a factor of four to 0.68 the error on the signal would not exceed 2%. Note that the correlation in φ is much sharper for the signal than the background as can be seen from the expanded scale on Figure 13-7. In conclusion, the elastic two-photon production of muon pairs might provide the possibility of offline determination of the integrated-luminosity with a statistical accuracy of about 2% for
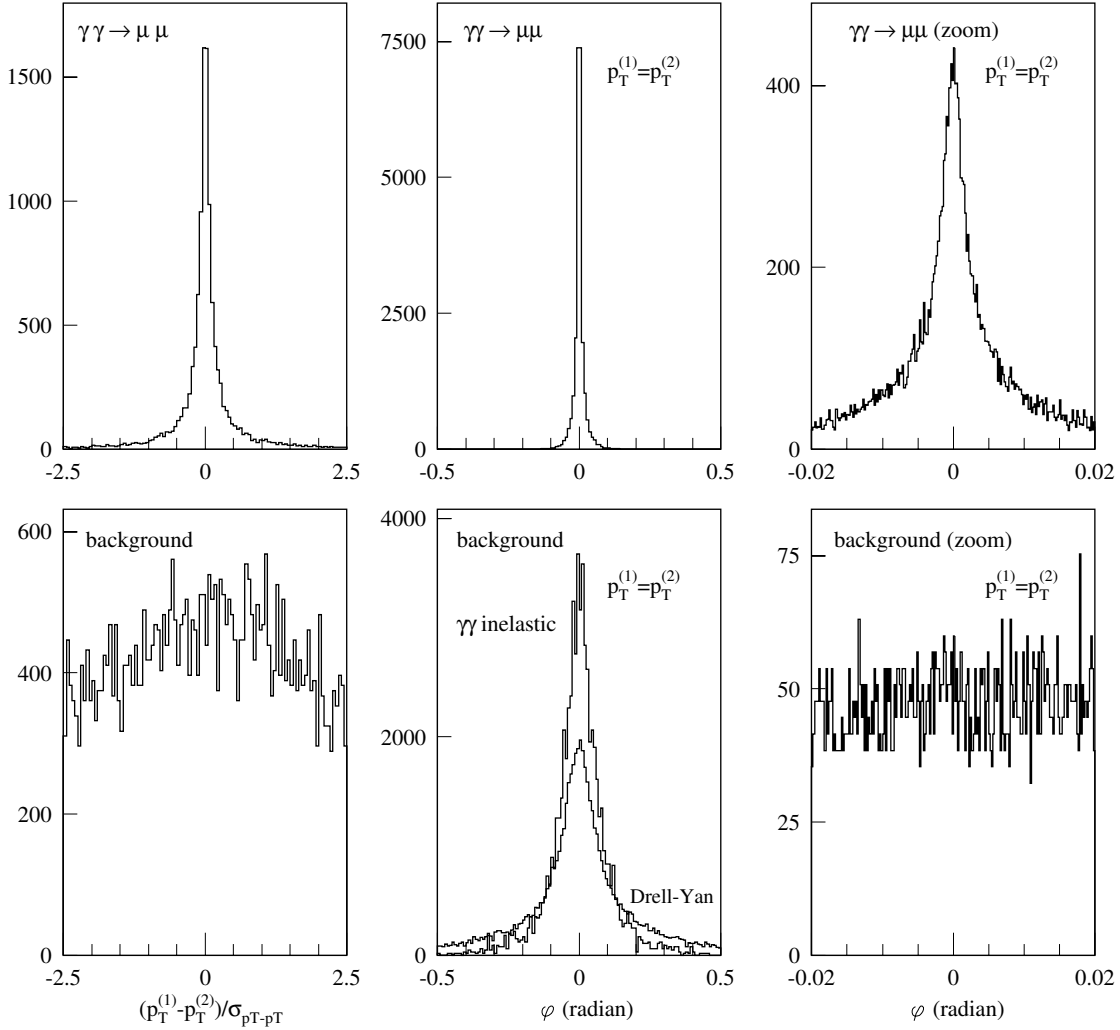
Figure 13-7 The distributions of the transverse momentum difference, normalised to the measurement error, (left) and acoplanarity angle (φ) (middle and right) between the two muons in exclusive two photon production of the muon pairs (top) and the major backgrounds (bottom), for an integrated luminosity of 10 fb^{-1}.

an integrated luminosity of 10 fb^{-1}. The background estimates rely on QCD calculations in regions where they have not been tested. In particular the modelling of the cuts may be deficient. It remains to be proven that the systematic uncertainties associated with these issues can be reduced to the 1% level. Furthermore, at high luminosity, pile-up will limit the effectiveness of the selection criteria.

13.3.4 Relative luminosity measurements

As a primary tool for fast online luminosity monitoring, small-area counters (to avoid event pile-up effects) located at large angles are considered. A possible candidate are the existing intermediate Tile Calorimeter scintillators [13-15] which are finely segmented (128 divisions in azimuthal angle and four in η) and cover $0.8 < |\eta| < 1.6$. The discriminated photomultiplier

signals could be used in coincidence to build simple triggers for monitoring the *pp* interaction rate. The detector signals could also be used in complementary ways, *e.g.* for the measurement of hit rates in the smallest sections of the detector, for the measurement of energy flow in groups of these sections. However, one should note that these counters are not typical hodoscopes since there is a significant amount of dead material in front of them. Therefore, detailed Monte Carlo studies of preshowering effects and detector efficiencies have to be performed before reaching firm conclusions.

The measurement of high-voltage (HV) currents in the liquid Argon [13-16] and Tile [13-15] calorimeters provides another, largely pile-up insensitive, way of monitoring luminosity. For example, in the LAr calorimeter the current will be monitored in η–ϕ regions related to the segmentation of the HV system; there are seven η segments in the barrel, seven in the outer end-cap wheel and two in the inner end-cap wheel of the calorimeter. In azimuthal angle, the segmentation is 32 (128 in the inner wheel), with the two sides of the electrodes monitored independently. The expected current per HV channel at the nominal LHC luminosity varies from about 10 μA at $\eta = 0$ up to 50 μA at $|\eta| = 3.2$. Other sources of current are significantly smaller. A 1% non-linearity of the calorimeter response for high particle fluxes (corresponding to the nominal LHC luminosity) in the end-cap inner wheel was seen with a 2 m prototype tested in a beam. In future tests this effect will also be measured for the HV currents. Changes of the LAr calorimeter response due to temperature and impurity variations with time are expected to be small and slow. A periodic absolute cross-calibration of this method of luminosity measurement should be envisaged.

Last, but not least, measurements using the ATLAS detectors for processes with clear signatures and sizable cross-sections can also be used for relative luminosity measurements. The primary candidate is Z production with a rate for leptonic Z decays above 10 Hz at the nominal LHC luminosity, which corresponds to a 1% statistical uncertainty after about 20 minutes. Uncertainties in the QCD predictions for Z production imply that this method cannot be used for a precise measurement of the absolute luminosity.

13.3.5 Technical aspects

The data acquisition system of the luminosity monitor should be flexible enough to be able to provide the on-line data almost independently of the status of the main ATLAS detector (*e.g.* during beam steering/optimisation when the ATLAS data taking will be in a stand-by mode). It should be capable of storing large sets of calibration data and making fast online calculations.

The read-out and trigger electronics of the luminosity monitoring system (especially for large-angle counters) should allow for building (topologically) different trigger types, with different sensitivity to beam-related backgrounds or event pile-up. For a good control of beam-related backgrounds, special bunch configurations including non-colliding pilot bunches might be very useful. Practically all considered methods are affected to some extent by pile-up effects, therefore storing regularly a number of bunches (*e.g.* two colliding trains of 81 bunches) with 10–20% of the nominal current should be seriously considered. This would allow for both online and offline monitoring of the pile-up effects at high luminosities.

Since one expects significant variations of the luminosity per bunch, an online monitoring of the bunch-to-bunch luminosity is desirable. A possible option is to use the LVL1 Central Trigger Processor scalers [13-17]. These are able to measure the rate for each type of LVL1 trigger independently for each bunch crossing.
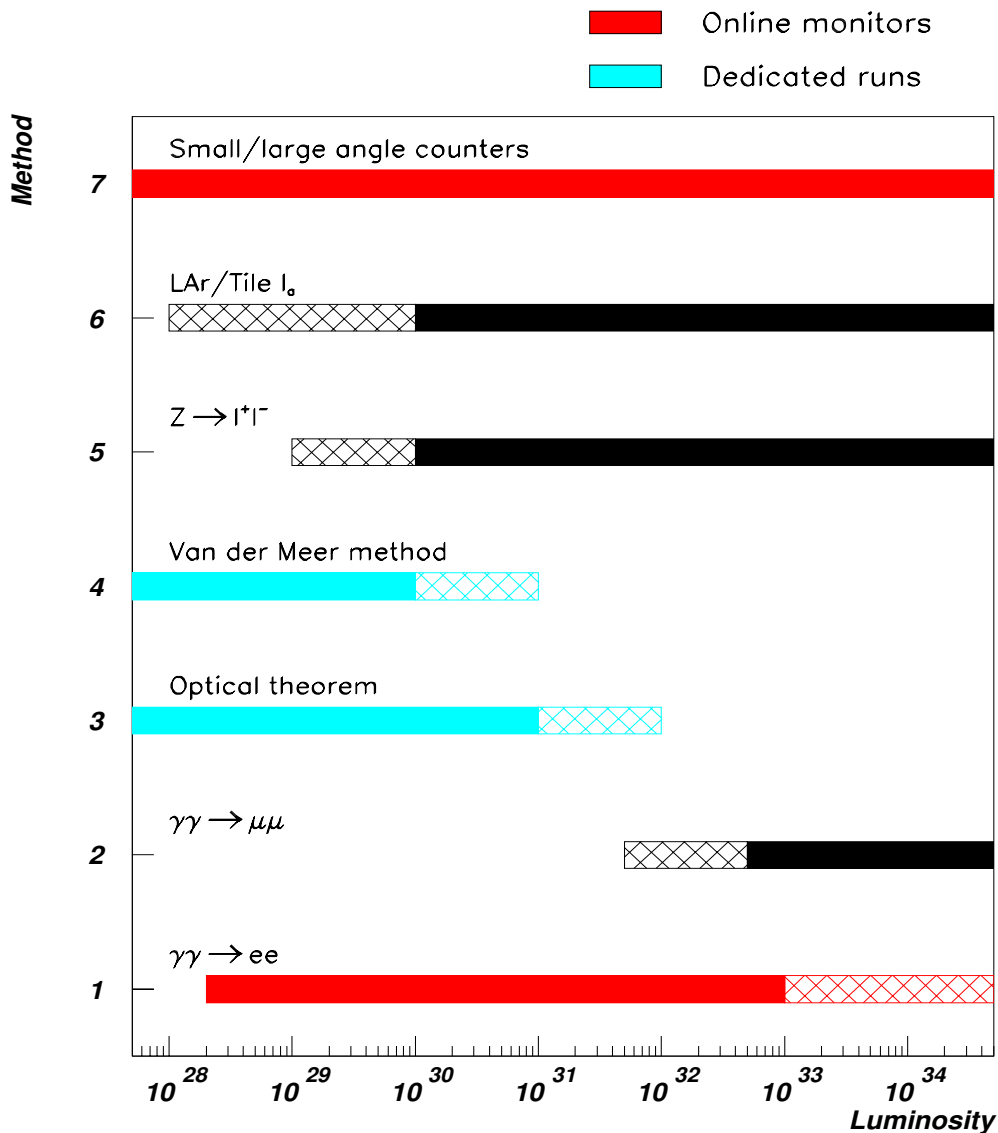
Figure 13-8 Diagram showing the range of applicability of the techniques of luminosity measurement and monitoring in ATLAS; hatched areas indicate luminosity ranges for which precision of a given method will significantly deteriorate. The top three methods are used for relative measurements only. The units are cm^{-2}s^{-1}.

13.4 Summary

To ensure reliable luminosity measurements both for high- and low-luminosity running, a number of complementary methods are needed. Figure 13-8 summarises the applicability of all techniques discussed in this chapter. It shows that, over the relevant range of LHC luminosities, redundant methods of luminosity measurement and monitoring should be possible.

Standard techniques based on the van der Meer method or on the optical theorem and the measurement of elastic and inelastic *pp* scattering, should the additional detector elements become available, are not applicable at the luminosities required for physics runs. Production of

electron or muon pairs through the two-photon process might provide a precision luminosity measurement in ATLAS over the full range of luminosity. However, further studies of systematic effects, background conditions and detector issues are needed before reaching any conclusions. The technique with *ee* pairs would require additional instrumentation in the very forward regions. Measurements using Z decays and monitoring of the currents in the calorimeters will provide precise luminosity monitoring but cannot provide precise measurements of absolute luminosity.To reach a good understanding of systematic effects a number of dedicated runs with high-β^* beam optics and with very low beam currents might be necessary. For good control of beam-related backgrounds, special bunch configurations, including non-colliding pilot bunches might be very useful, as well as storing a number of bunches (e.g. two colliding trains of 81 bunches) with 10–20% of the nominal current for monitoring of the pile-up effects at high luminosity.

13.5 References

13-1   LHC Conceptual Design Report, CERN/AC/95-05 (LHC), (1995)

13-2   C. Bovet, 'Review of Beam Instrumentation and Diagnostics', EST–LEA/085I/KP–lp, 5 (1999).

13-3   M.M. Block, F. Halzen and B. Margolis, Phys. Rev. **D45** (1992) 839.

13-4   W. Kienzle et al. (TOTEM Collaboration), 'Total cross-section, elastic scattering and diffraction dissociation at the LHC, Letter of Intent', CERN-LHCC-97-49; LHCC-I-11 (1997).

13-5   S. van der Meer, 'Calibration of the Effective Beam Height at the ISR', CERN-ISR-PO/68- (1968).

13-6   V.M. Budnev, I.F. Ginzburg, G.V. Meledin and V.G. Serbo, Nucl. Phys. **B63** (1973) 519.

13-7   K. Piotrzkowski, 'Proposal for Luminosity Measurement at LHC', ATLAS Internal Note ATL-PHYS-96-077 (1996).

13-8   J.A.M. Vermaseren, Nucl. Phys. B229 (1983) 347;
        S.P. Baranov *et al.*, 'LPAIR: A Generator for Lepton Pair Production', Proceedings of Physics at HERA Workshop, vol. 3, (1991) 1478.

13-9   A.B. Arbuzov *et al.*, Phys. Atom. Nucl. **60** (1997) 591.

13-10   A. Shamov and V. Telnov, ATLAS Internal Note in preparation.

13-11   A.E. Blinov *et al.*, Z. Phys. **C53** (1992) 33.

13-12   V.M. Budnev *et al.*, Phys. Rep. **15** (1975) 181.

13-13   R.M. Bartel *et al.*, Phys. Rev. **D54** (1996) 1;
        E. Bloom *et al.*, Phys. Rev. Lett. **23** (1969) 930;
        W. Bartel *et al.*, Phys. Lett. **B28** (1968) 148.

13-14   A. Suri and D.R. Yennie, Ann. of Phys. **72** (1972) 243.

13-15   ATLAS Collaboration, Tile Calorimeter TDR, CERN/LHCC 96-42 (1996).

13-16   ATLAS Collaboration, Liquid Argon Calorimeter TDR, CERN/LHCC 96-41 (1996).

13-17   ATLAS Collaboration, Level-1 Trigger TDR, CERN/LHCC 98-14 (1998).

A Members of the ATLAS Collaboration

Armenia

Yerevan Physics Institute, Yerevan
Airapetian A., Grabsky V., Hakopian H., Vartapetian A.

Australia

Research Centre for High Energy Physics, Melbourne University, Melbourne
Dick B., Fares F., Guy L.P., Moorhead G.F., Sevior M.E., Taylor G.N., Tovey S.N.
University of Sydney, Sydney
Hashemi-Nezhad R., Peak L., Saavedra A., Ulrichs J.

Austria

Institut für Experimentalphysik der Leopold-Franzens-Universität Innsbruck, Innsbruck
Epp B., Ghete V. M., Girtler P., Kneringer E., Kuhn D., Nairz A., Rudolph G., Schaller M., Schweiger D.

Azerbaijan Republic

Institute of Physics, Azerbaijan Academy of Science, Baku
Abdinov O.B., Akhmedov A., Akhoundov A., Javadov N., Khalilzade F.T., Mekhdiyev R.R.,
Oussoubov Z., Rzayev H.J.

Republic of Belarus

Institute of Physics, National Academy of Sciences, Minsk
Baturitsky M.A., Bogush A.A., Gazizov A.Z., Gilevsky V.V., Kulchitsky Y., Kuzmin M.V., Levchuk M.I.,
Satsunkevich I.S.
National Centre of Particle and High Energy Physics, Minsk
Kuzhir P., Medvedev V., Pazin A., Prokoshin F., Soroko A., Starovoytov P.

Brazil

Universidade Federal do Rio de Janeiro, COPPE/EE/IF, Rio de Janeiro
Caloba L.P., Dos Anjos A., Gomes R., Maidantchik C.L., Marroquim F., Seixas J.M., Thome Z.D.

Canada

University of Alberta, Edmonton
Armstrong W.W., Burris W., Davis R., Gingrich D. M., Hewlett J.C., Holm L., Macpherson A.L., Mullin S.,
Pinfold J.L., Schaapman J., Soukup J., Wampler L.
Department of Physics, University of British Columbia, Vancouver
Axen D.
University of Carleton/C.R.P.P., Carleton
Armitage J., Dixit M., Estabrooks P., Losty M., Neuheimer E., O'Neil M., Oakham G.
Group of Particle Physics, University of Montreal, Montreal
Azuelos G., Leroy C., Marullo F., Mazini R., Roy P.
Department of Physics, University of Toronto, Toronto
Bailey D.C., Bhadra S., Martin J.F., Mayer J.K., Orr R.S., Sinervo P.K., Stairs G.G., Trischuk W.
TRIUMF, Vancouver
Astbury A., Birney P., Hodges T., Langstaff R., Oram C.
University of Victoria, Victoria
Dobbs M., Fincke-Keeler M., Fortin D., Keeler R., Lefebvre M., O'Neil D., Poffenberger P., Roney M.,
Sobie R.

CERN

European Laboratory for Particle Physics (CERN), Geneva
Aleksa M., Ambrosini G., Anderssen E., Anghinolfi F., Arnaud C., Bachy G., Barberio E., Benincasa G.,
Bergsma F., Bertinelli F., Bjorset L., Bloess D., Bock R., Bogaerts J., Boosten M., Bremer J., Burckhart D.,
Burckhart H.J., Butin F., Cataneo F., Chesi E., Chevalley J.L., Cobal M., Danielsson H., Dauvergne J.P.,
Dell'Acqua A., Dittus F., Dobinson R., Dobson M., Drevermann H., Dudarev A., Dydak F., Ellis N.,
Fabjan C.W., Farthouat P., Fassnacht P., Fernandez A., Flegel W., Francis D., Froidevaux D., Giancomini F.,

Gianotti F., Gildemeister O., Gschwendtner E.M., Hallgren B., Hansen J., Hatch M., Haug F., Hauser R., Hauviller C., Havet C., Heeley R., Henriques A., Hervas L., Hoffmann H.F., Hogbe-Nlend F., Hoimyr N., Jarp S., Jarron P., Jenni P., Jones R., Kantardjian G., Kaplon J., Klioutchnikova T., Knobloch J., Kulseth M., Lacasta C., Lasseur C., Lehraus I., Lemeilleur F., Lichard P., Linde F., Lopez J., Lozano J., Mandl M., Mapelli L., Martin B., Maugain J.-M., McLaren R.A., Meier D., Meinhard H., Mitsou V., Mornacchi G., Myers D., Nessi M., Nicquevert B., Niinikoski T., Onions C., Pailler P., Passardi G., Petersen J., Placci A., Poppleton A., Posch C., Poulard G., Price M., Riedler P., Roe S., Rohrbach F., Rudge A., Schaller M., Schmid P., Schuler G., Schwick C., Shears T., Simion S., Soulhat J., Spiwoks R., Stavrianakou M., Stavropoulos G., Szeless B., Tapprogge S., Tartarelli G.F., Ten Kate H., Teterin V., Tischhauser H., Treichel M., Tremblet L., Tuura L., Turala M., Unel G., Van der Bij H., Vincke H., von Boehn-Bucholz R., Voss R., Vreeswijk M., Vuillemin V., Weilhammer P., Werner P., Witzeling W., Wotschack J.

China

Institute of High Energy Physics, Academia Sinica, Beijing, University of Science and Technology of China, Hefei, University of Nanjing and University of Shandong
Chen C., Chen T-Y., Cheng S., Feng C., Fu Y., Kong F., Li H., Liu T., Lu W.D., Ma J.M., Meng X., Ouyang Q., Qi M., Tong G.L., Wang C., Xie Y.G., Xue L., Xu G.F., Yang B., Yang T., Ye B., Yu X.Q., Zhang B., Zhang N., Zhang Q.J., Zhao J.

Czech Republic

Academy of Sciences of the Czech Republic, Institute of Physics and Institute of Computer Science, Prague
Bohm J., Hakl F., Hrivnac J., Jirina M., Lednicky R., Lokajicek M., Mares J.J., Nemecek S., Rizek S., Sicho P., Simak V., Stastny J., Stedron M., Vanickova M., Vrba V., Weichert J., Zitek K.
Charles University, Faculty of Mathematics and Physics, Prague
Davidek T., Dolejsi J., Dolezal Z., Kucera M., Leitner R., Soustruznik K., Suk M., Tas P., Trka Z., Valkar S., Wilhelm I., Zdrazil M.
Czech Technical University in Prague, Faculty of Nuclear Sciences and Physical Engineering, Faculty of Mechanical Engineering, Prague
Jakubek J., Kubasta J., Ota J., Pospisil S., Sinor M., Sodomka J., Sopko B., Stekl I., Tomiak Z.

Denmark

Niels Bohr Institute, University of Copenhagen, Copenhagen
Dam M., Hansen J.D., Hansen J.R., Hansen P.

Finland

Helsinki Institute of Physics, Helsinki

France

Laboratoire d'Annecy-le-Vieux de Physique des Particules (LAPP), IN2P3-CNRS, Annecy-le-Vieux
Aubert B., Beaugiraud B., Billat C., Boniface J., Cailles M., Chollet-LeFlour F., Colas J., Duchesneau A., Dumont-Dayot N., Girard C., Gouanere M., Jezequel S., Kambara H., Lafaye R., Lesueur J., Masserot A., Massol N., Moynot M., Perrodo P., Perrot G., Prast J., Riccadonna X., Sauvage G., Thion J., Wingerter-Seez I., Zitoun R., Zolnierowski Y.
Université Blaise Pascal, IN2P3-CNRS, Clermont-Ferrand
Biscarat C., Chadelas R., Crouau M., Daudon F., Grenier P., Guicheney Ch., Hebrard C., Lefevre R., Montarou G., Pallin D., Podlyski F., Reinmuth G., Santoni C., Says L.P., Vazeille F.
Institut des Sciences Nucléaires de Grenoble, IN2P3-CNRS-Université Joseph Fourier, Grenoble
Andrieux M.L., Collot J., Dzahini D., Ferrari A., Hostachy J.Y., Martin Ph., Pouxe J., Rabier C., Rey-Campagnolle M., De Saintignon P., Stassi P.
Centre de Physique des Particules de Marseille, IN2P3-CNRS, Marseille
Bee C., Blanquart L., Breugnon P., Calvet D., Clemens J-C., Delpierre P., Dinkespiler B., Djama F., Duval P-Y., Etienne F., Fede E., Hallewell G., Henry-Couannier F., Hinz L., Karst P., Laugier D., Le Van Suu A., Martin L., Martin O., Meessen C., Mirea A., Monnier E., Mouthuy T., Nacasch R., Nagy E., Negroni S., Nicod D., Olivier C., Pralavorio P., Quian Z., Repetti B., Rondot C., Rousseau D., Rozanov A., Sauvage D., Tisserant S., Touchard F., Vacavant L., Valin I., Vigeolas E., Wielers M.

Laboratoire de l'Accélérateur Linéaire, IN2P3-CNRS, Orsay
Arnault C., Auge E., Barrand G., Belot G., Beney J. L., Blaquiere M., Bonivento W., Bourdarios C.,
Breton D., Chollet C., Coulon J-P., Cros Ph., De la Taille C., Delebecque P., Falleau I., Fallou A.,
Fournier D., Grivaz J-F., Imbert P., Jacquier Y., Mace G., Martin-Chassard G., Mencik M., Merkel B.,
Noppe J-M., Parrour G., Perus A., Petroff P., Puzo P., Richer J-P., Schaffer A-C., Seguin-Moreau N.,
Serin L., Tocut V., Vales F., Veillet J-J., Vernay E., Zerwas D.

LPNHE, Universités de Paris VI et VII, IN2P3-CNRS, Paris
Astesan F., Bertoli W., Canton B., David J., Fichet S., Fleuret F., Imbault D., Lacour D., Laforge B.,
Le Dortz O., Martin D., Poggioli L., Rossel F., Schwemling P.

CEA, DSM/DAPNIA, Centre d'Etudes de Saclay, Gif-sur-Yvette
Amadon A., Bauer F., Belorgey J., Berriaud C., Berthier R., Borgeaud P., Bystricky J., Cacaut D., Calvet D.,
Chalifour M., Chevalier L., Cloué O., Daël A., Delagnes E., Desages F., Durand D., Ernwein J.,
Gachelin O., Gallet B., Gastineau B., de Girolamo P., Guyot C., Hansl-Kozanecka T., Hubbard J.R.,
Huet M., Joudon A., Juster F.P., Kiourkos S., Kozanecki W., Laporte J.F., Le Coreller A., Le Dû P.,
Lesmond C., Lugiez F., Machefert F., Mandjavidze I., Mansoulié B., Mayri C., Molinié F., Mur M., Pabot Y.,
Pascual J., Perrin P., Ponsot P., Rey J.M., Rouger M., Schuller J.P., Schune Ph., Schwindling J., Sun Z.,
Taguet J.P., Teiger J., Thooris B., Tirler R., Van Hille H., Virchaux M.

Republic of Georgia
Institute of Physics of the Georgian Academy of Sciences and Tbilisi State University, Tbilisi
Chikovani L., Chiladze B., Djobava T., Gabunia L., Gogiberidze G., Grigalashvili T., Khelashvili A.,
Khorguashvili Z., Khubua J., Kipiani K., Koshtoev V., Liparteliani A., Metreveli Z., Mosidze M.,
Salukvadze R., Sopromadze D., Topchishvili L.

Germany
Physikalisches Institut, Universität Bonn, Bonn
Ackers M., Andre F., Andreazza A., Comes G., Fischer P., Geich-Gimbel C., Klasen V., Keil M., Kobel M.,
Kuhl T., Meuser S., Ockenfels W., Stockmanns T., Treis J., Wermes N.

Institut für Physik, Universität Dortmund, Dortmund
Geiser A., Goessling C., Huegging F., Wuestenfeld J., Wunstorf R.

Fakultät für Physik, Albert-Ludwigs-Universität, Freiburg
Baer Th., Chen J., Ebling D.G., Herten G., Irsigler R., Kollefrath M., Landgraf U., Lauxtermann S.,
Ludwig J., Mohr W., Paschhoff V., Rehmann V., Rolker B., Runge K., Schaefer F., Scherberger G.,
Schmid T., Webel M., Weber C.

Institut für Hochenergiephysik der Universität Heidelberg, Heidelberg
Geweniger C., Hanke P., Kluge E.-E., Mahboubi K., Meier K., Pfeiffer U., Putzer A., Schumacher C.,
Tittel K., Wunsch M.

Institut für Physik, Johannes-Gutenberg Universität Mainz, Mainz
Fuchs K., Geib K.H., Jakobs K., Kleinknecht K., Koepke L., Marschalkowski E., Merle K., Othegraven R.,
Quast G., Renk B., Schaefer U., Walkowiak W., Zeitnitz C.

Lehrstuhl für Informatik V, Universität Mannheim, Mannheim
Kornmesser K., Kugel A., Lay R. , Ludwig J., Maenner R., Noffz K-H., Ruehl S., Sessler M., Simmler H.,
Singpiel H.

Sektion Physik, Ludwig-Maximilian-Universität München, München
Chouridou S., Deile M., Kortner O., Hessey N.P., Schaile D., Staude A., Strohmer R., Trefzger T.

Max-Planck-Institut für Physik, München
Ackermann K., Aderholz M., Andricek L., Blum W., Bratzler U., Brettel H., Dietl H., Dulny B., Fent J.,
Gruhn C., Hauff D., Koffeman E., Kroha H., Lutz G., Manz A., Moser H.-G., Oberlack H., Ostapchuk A.,
Richter R., Richter R.H., Schacht P., Schael S., Soergel V., Stenzel H., Striegel D., Tribanek W.

Fachbereich Physik, Universität Siegen, Siegen
Holder M., Schoefer B., Ziolkowski M.

Fachbereich Physik, Bergische Universität, Wuppertal
Becks K.H., Braun H., Drees J., Gerlach P, Glitza K.W., Gregor I.M., Hamacher K., Kersten S., Lenzen G.,
Linder C., Thadome J., Wahlen H.

Greece

Athens National Technical University, Athens

Dris M., Filippas A., Fokitis E., Gazis E.N., Katsoufis E., Maltezos S., Papadopoulou T.

Athens University, Athens

Fasssouliotis D., Giokaris N., Ioannou P., Kourkoumelis C., Pancheluga V., Petridis A., Tatsis S., Tzanakos G.S., Vassiliou M.

Aristotle University of Thessaloniki, Thessaloniki

Bouzakis C., Chardalas M., Dedoussis S., Efstathiou K., Lagouri Th., Liolios A., Paschalias P., Petridou C., Sampsonidis D., Vichou I., Zamani M.

Israel

Department of Physics, Technion, Haifa

Dado S., Harel A., Landesman H., Lupu N., Robins S., Rozen Y., Tarem S.

Raymond and Beverly Sackler Faculty of Exact Sciences, School of Physics and Astronomy, Tel-Aviv University, Tel-Aviv

Abramowicz H., Alexander G., Bella G., Benary O., Dagan S., Etzion E., Grunhaus J., Oren Y.

Department of Particle Physics, The Weizmann Institute of Science, Rehovot

Breskin A., Chechik R., Duchovni E., Eisenberg Y., Gross E., Hass M., Karshon U., Lellouch D., Levinson L., Mikenberg G.

Italy

Dipartimento di Fisica dell' Università della Calabria e I.N.F.N., Cosenza

Ayad R., Capua M., Lagatta A., La Rotonda L., Schioppa M., Susinno G., Valdata-Nappi M.

Laboratori Nazionali di Frascati dell' I.N.F.N., Frascati

Bilokon H., Cerutti F., Chiarella V., Curatolo M., Dulach B., Esposito B., Ferrer M.L., Maccarrone G., Moccia S., Pace E., Pepe-Altarelli M., Spitalieri M., Zuffranieri F.

Dipartimento di Fisica dell' Università di Genova e I.N.F.N., Genova

Barberis D., Beccherle R., Caso C., Dameri M., Darbo G., Gagliardi G., Gemme C., Morettini P., Musico P., Olcese M., Osculati B., Parodi F., Pozzo A., Ridolfi G., Rossi L., Sette G.

Dipartimento di Fisica dell' Università di Lecce e I.N.F.N., Lecce

Creti P., Gorini E., Grancagnolo F., Palamara O., Petrera S., Primavera M.

Dipartimento di Fisica dell' Università di Milano e I.N.F.N., Milano

Acerbi E., Aleppo M., Alessandria F., Battistoni G., Broggi F., Caccia M., Camin D., Cavalli D., Costa G., Fanti.M., Ferrari A., LaBanca N., Lari T., Mandelli L., Mazzanti M., Meroni C., Perini L., Ragusa F., Resconi S., Rossi L., Sala P., Tartarelli G.F., Troncon C., Vanini S., Vegni G., Volpini G.

Dipartimento di Scienze Fisiche, Università di Napoli 'Federico II' e I.N.F.N., Napoli

Aloisio A., Alviggi M.G., Cevenini F., Chiefari G., De Asmundis R., Merola L., Napolitano M., Patricelli S.

Dipartimento di Fisica Nucleare e Teorica dell' Università di Pavia e I.N.F.N., Pavia

Cambiaghi M., Conta C., Ferrari R., Fraternali M., Lanza A., Livan M., Negri A., Polesello G., Rimoldi A., Vercesi V.

Dipartimento di Fisica dell' Università di Pisa e I.N.F.N., Pisa

Cavasinni V., Cologna S., Costanzo D., Del Prete T., Di Girolamo B., Flaminio V., Lami S., , Marrocchesi P.S., Mazzoni E., Paoletti R., Renzoni G., Roda C., Spano F., Suglia R., Usai G.

Dipartimento di Fisica dell' Università di Roma 'La Sapienza' e I.N.F.N., Roma

Bagnaia P., Bini C., Caloi R., Cardini A., Cavallari A., Ciapetti G., De Zorzi G., DiMattia A., Falciano S., Gauzzi P., Gentile S., Lacava F., Luci C., Luminari L., Marzano F., Mirabelli G., Nisati A., Petrolo E., Pontecorvo L., Veneziano S., Zanello L.

Dipartimento di Fisica dell' Università di Roma 'Tor Vergata' e I.N.F.N., Roma

Aielli G., Baranov S., Camarri P., Cardarelli R., Di Ciaccio A., Liberti B., Paoloni A., Santonico R.

Dipartimento di Fisica dell' Università di Roma 'Roma Tre' e I.N.F.N., Roma

Bacci C., Baroncelli A., Ceradini F., Farilla A., Iodice M., Orestano D., Pastore F., Spiriti E., Stanescu C.

Dipartimento di Fisica dell' Università di Udine, Gruppo collegato di Udine I.N.F.N. Trieste, Udine

Cauz D., D'Auria S., De Angelis A., Pauletta G., Santi L., Scuri B., Waldner F., del Papa C.

Japan

Department of Information Science, Fukui University, Fukui

Tanaka S.

Hiroshima Institute of Technology, Hiroshima
Asai M.
Department of Physics, Hiroshima University, Higashi-Hiroshima
Iwata Y., Ohsugi T.
KEK, National Laboratory for High Energy Physics, Tsukuba
Amako K., Arai Y., Fujii H., Haruyama T., Ikeno M., Iwasaki H., Kanzaki J., Kohriki T., Kondo T.,
Manabe A., Morita Y., Nomachi M., Ohska T.K., Sasaki O., Sasaki T., Terada S., Unno Y., Watase Y.,
Yamamoto A., Yasu Y.
Department of Physics, Faculty of Science, Kobe University, Kobe
Kawagoe K., Kurashige H., Nozaki M., Takeda H.
Department of Physics, Kyoto University, Kyoto
Sakamoto H., Sasao N.
Kyoto University of Education, Kyoto-shi
Takashima R.
Department of Electrical Engineering, Nagasaki Institute of Applied Science, Nagasaki
Nagasaka Y., Tanaka Y.
Naruto University of Education, Naruto-shi
Nagamatsu M., Yoshida H.
Department of Physics, Faculty of Science, Shinshu University, Matsumoto
Takeshita T.
International Centre for Elementary Particle Physics, University of Tokyo, Tokyo
Hasegawa Y., Homma K., Imori M., Kawamoto T., Kobayashi T.
Physics Department, Tokyo Metropolitan University, Tokyo
Fukunaga C., Hamatsu R.
Department of Applied Physics, Tokyo University of Agriculture and Technology, Tokyo
Emura T.

Morocco
Faculté des Sciences Aïn Chock, Université Hassan II, Casablanca, and Université Mohamed V, Rabat
Chakir H., Cherkaoui R., Goujdami D., El Kacimi M., Hoummada A., Saidi H., Sayouty E.

Netherlands
FOM - Institute SAF NIKHEF and University of Amsterdam/NIKHEF, Amsterdam
Bobbink G.J., Bos K., Boterenbrood H., Buis E.J., Dankers R.J., Daum C., Groenstege H., Hartjes F.,
Hendriks P., Heubers W., Kaan B., Kieft G.N.M., Kluit P., Kluit R., Massaro G.G.G., Meddeler G.,
Peeters S., Reichold A., Rewiersma P.A.M., Schuijlenburg H., Spelt J., Vermeulen J.C., Werneke P.,
Woudstra M., van Eijk B., van der Graaf H.
University of Nijmegen/NIKHEF, Nijmegen
Brouwer C., Crijns F.J.G.H., Dijkema J.A., De Jong S.J., Kittel W., Klok P.F., Lavrijsen W.T.L.P., Koenig A.C.,
Metzger W.J., Pols G.-J., Schotanus D.J., Wijnen Th.A.M.

Norway
University of Bergen, Bergen
Eigen G., Frodesen A.G., Klovning A., Stugu B.
University of Oslo, Oslo
Bugge L., Buran T., Dorholt O., Kristiansen H., Madsen R.A., Marshal A., Midttun G., Read A.L.,
Rohne O.M., Stapnes S., Strandlie A., Sundal B.

Poland
Henryk Niewodniczanski Institute of Nuclear Physics, Cracow
Blocki J., Bocian D., Gadomski S., Gornicki E., Godlewski J., Hajduk Z., Iwanski W., Kaczmarska A.,
Kisielewski B., Korcyl K., Madeyski B., Malecki P., Moszczynski A., Olszowska J., Piotrzkowski K.,
Richter-Was E., Sapinski M., Wolter M.
Faculty of Physics and Nuclear Techniques of the Academy of Mining and Metallurgy, Cracow
Dabrowski W., Grybos P., Idzik M., Jagielski S., Jelen K., Kiesilewska D., Koperny S., Kowalski T.,
Rulikowska-Zarebska E.

Portugal

Laboratorio de Instrumentação e Física Experimental de Partículas (University of Lisboa, University of Coimbra, University Católica-Figueira da Foz and University Nova de Lisboa), Lisbon
Amaral P., Amorim A., Carvalho J., Casarejos E., David M., Gomes A., Gomes J., Ivaniouchenkov I., Maio A., Maneira M., Martins J.P., Onofre A., Pinhao J., Santos J., Silva J., Varanda M., Wolters H.

Romania

Institute of Atomic Physics, National Institute of Physics and Nuclear Engineering, Bucharest
Alexa C., Arsenescu R., Badescu E., Boldea V., Caprini I., Caprini M., Constantin F., Constantinescu S., Dita P., Dita S., Micu A., Micu L., Niculescu M., Pantea D., Radu A.

Russia

Institute for Theoretical and Experimental Physics (ITEP), Moscow
Artamonov A., Epchtein V., Gorbunov P., Gurin R., Jemanov V., Khovansky V., Koutchenkov A., Kruchinin S., Maslennikov A., Ryabinin M., Shatalov P., Tsoukerman I., Zaitsev V., Zeldovich S.
P.N. Lebedev Institute of Physics, Moscow
Akimov A., Baranov S., Belov M., Blagov M., Fedorchuk R., Gavrilenko I., Kaioumov F., Komar A., Konovalov S., Kopytine M., Mouraviev S., Popov L., Shikanyan A., Shmeleva A., Snesarev A., Speransky M., Sulin V., Tikhomirov V., Vassilieva L., Yakimenko M.
Moscow Engineering and Physics Institute (MEPhI), Moscow
Bondarenko V., Dolgoshein B., Konstantinov A., Romaniouk A., Semenov S., Smirnov S., Sosnovtzev V.
Moscow State University, Institute of Nuclear Physics, Moscow
Bashindjagian G.L., Basiladze S.G., Berejnoi A., Erasov A.B., Grishkevich Y., Karmanov D.E., Kramarenko V.A., Larichev A.N., Melikhov D.I., Merkin M.M., Nikitin N.V., Rizatdinova F.K., Selikov A.V., Sivoklokov S.Yu., Smirnova L.N., Zverev E.G.
Budker Institute of Nuclear Physics (BINP), Novosibirsk
Batrakov A., Chekhtman A., Fedotov M., Gaponenko I., Klimenko S., Kollegov M., Kozlov V., Kuper E., Merzlyakov Y., Panin V., Shamov A., Telnov V., Tikhonov Y., Velikzhanin Y.
Institute for High Energy Physics (IHEP), Protvino
Amelin D.V., Ammosov V.V., Antipov Yu.M., Batarin V., Bogoliubsky M.Yu., Borissov A.A., Borissov E., Bozko N.I., Bryzgalov V.V., Chekulaev S.V., Denisov S.P., Dushkin A.Yu., Fakhroutdinov R., Fenyuk A.B., Gapienko V.A., Gilitsky Yu.V., Goryatchev V., Gouz Yu.P., Karyukhin A.N., Khokhlov Yu.A., Kirsanov M.M., Kiryunin A.E., Klyukhin V., Kojine A., Kononov A.I., Konstantinov V., Kopikov S.V., Korotkov V.A., Kostrikov M.E., Kostyukhin V.V., Kravtsov V.I., Kulemzin A., Kurchaninov L.L., Lapin V.V., Levitsky M.L., Los S., Maximov V., Miagkov A.G., Mikhailin V.N., Minaenko A.A., Moiseev A.M., Onuchin V.A., Pleskach A.V., Salomatin Yu.I., Senko V.A., Shein I., Soldatov A.P., Solodkov A.A., Solovianov O.V., Starchenko E.A., Sviridov Yu., Sytnik V.V., Tchmil V., Tchountonov A., Tikhonov V.V., Tsyupa Yu., Usenko E., Vorobiev A.P., Vovenko A.S., Zaets V.G., Zaitsev A.M., Zimin S., Zmouchhko V.
Petersburg Nuclear Physics Institute (PNPI), Gatchina, St. Petersburg
Fedin O., Filimonov V., Gavrilov G., Ivochkin V., Khomoutnikov V., Kolos S., Krivchitch A., Lochak I., Maleev V., Nadtochy A., Patritchev S., Prokofiev D., Riabov J., Schegelsky V., Soloviev I., Spiridenkov E., Zalite A.

JINR

Joint Institute for Nuclear Research, Dubna
Alexandrov I., Alexeev G., Alikov B., Anosov V., Astvatsaturov A., Azhgirei L., Backovic M., Baranov S., Boyko I., Budagov J., Chelkov G., Cheplakov A., Chirikov-Zorin I., Chlachidze G., Dedovich D., Dodonov V., Evtukhovich P., Fedorov A., Feshenko A., Flyagin V., Glagolev V., Golikov V., Golubykh S., Gongadze A., Gornushkin Y., Gostkin M., Iamburenko V., Ignatenko M., Juravlev N., Kakurin S., Kallinikov V., Kalinichenko V., Kazarinov M., Kazymov A., Kekelidze G., Khasanov A., Khomenko B., Khovansky N., Kotov S., Kotov V., Kovtun V., Krumstein Z., Kukhtin V., Kuznetsov O., Ladygin E.U., Lazarev A., Lebedev A., Ljablin M., Lomakin Y., Malyshev V., Malyukov S., Manjavidze D., Merekov Y., Minashvili I., Nikolenko M., Nozdrin A., Olshevski A., Peshekhonov V., Pisarev I., Podkladkin S., Pose R., Potrap I., Pukhov O., Romanov V., Rumyantsev V., Russakovich N., Ryabchenko K., Salihagic D., Savin I., Scheltckov A., Sedykh Y., Semenov A., Senchishin V., Shabalin D., Shalyugin A., Shigaev V., Shilov S.,

Simic M., Sissakian A., Snyatkov V., Sorokina J., Tchepournov V., Tkachev L., Tokmenin V., Topilin N., Tskhadadze E., Usov Y., Vertogradov L., Vinogradov V., Vorozhtsov S., Yarygin G., Zhuravlev V.

Slovak Republic
Bratislava University, Bratislava, and Institute of Experimental Physics of the Slovak Academy of Sciences, Kosice
Ban J., Bruncko D., Chochula P., Chytracek R., Dubnicka S., Dubnickova A., Ferencei J., Garabik R., Holik P., Jusko A., Kladiva E., Kocper B., Kubinec P., Kurca T., Luptak M., Masarik J., Povinec P., Rosinsky P., Stanicek J., Stavina P., Strizenec P., Sykora I., Tokar S., Vanko J.

Slovenia
Jozef Stefan Institute and Department of Physics, University of Ljubljana, Ljubljana
Cindro V., Filipcic A., Kramberger G., Mandic I., Mikuz M., Tadel M., Zontar D.

Spain
Institut de Física d'Altes Energies (IFAE), Universidad Autónoma de Barcelona, Bellaterra, Barcelona
Blanch O., Blanchot G., Bosman M., Cavalli-Sforza M., Crespo J.M., Dosil M., Fernandez E., Flix J., Korolkov I., Martinez M., Miralles Ll., Ostankov A., Pacheco A., Pena J.C., Zamora Y.
Physics Department, Universidad Autónoma de Madrid, Madrid
Barreiro F., Del Peso J., Hervas L., Labarga L.
Instituto de Física Corpuscular (IFIC), Universidad de Valencia, CSIC, Burjassot, Valencia and
Instituto de Microelectronica de Barcelona, Campus Universidad Autonoma, Bellaterra, Barcelona
Ballester F., Bernabeu J., Camarena F., Campabadal F., Carrasco R., Castillo M.V., Costa M.J., Ferrer A., Fuster J., Garcia C., Gonzalez V., Gonzalez de la Hoz S., Higon H., Lopez J.M., Martinez C., Modesto P., Moreno A., Lozano M., Roldan J., Romance J.B., Ros E., Salt J., Sanchez J., Sanchis E., Santander J., Ullan M.

Sweden
Fysiska institutionen, Lunds universitet, Lund
Akesson T., Almehed S., Carling H., Danielson H., Eerola P., Egede Anderson U., Hedberg V., Jarlskog G., Korsmo H., Lorstad B., Lundberg B., Mjornmark U.
Royal Institute of Technology (KTH), Stockholm
Akerman D., Carlson P., Clement C., Leven S., Lund-Jensen B., Pearce M., Soderqvist J., Vanyashin A.
University of Stockholm, Stockholm
Berglund S., Bohm C., Engstrom M., Hellman S., Holmgren S-O., Johansson E., Jon-And K., Klereborn J., Sellden B., Silverstein S., Sjolin J., Yamdagni N.
Uppsala University, Department of Radiation Sciences, Uppsala
Bingefors N., Botner O., Brenner R., Bystrom O., Coadou Y., Damet J., Ekelof T., Gustafsson L., Hallgren A., Kullander S., Staaf P.

Switzerland
Laboratory for High Energy Physics, University of Bern, Bern
Beck H.P., Borer K., Hess M., Lehmann G., Mommsen R., Pretzl K.
Section de Physique, Université de Genève, Geneva
Bonino R., Clark A.G., Couyoumtzelis C., Demierre Ph., Efthymiopoulos I., Kowalewski R., La Marra D., Leger A., Perrin E., Vuandel B., Wu X.

Turkey
Department of Physics, Ankara University, Ankara
Atag A., Cakir O., Meric N., Sultansoy S., Turk I., Ulvi Yilmazer A.
Department of Physics, Bogaziçi University, Istanbul
Arik E., Celik O., Cetin S.A., Conka T., Hacinliyan A., Kurtulus O., Mailov A., Nurdan K., Tanoren B.

United Kingdom
School of Physics and Astronomy, The University of Birmingham, Birmingham
Bright-Thomas P., Charlton D.G., Dowell J.D., Garvey J., Hillier S.J., Homer R.J., Jovanovic P., Kenyon I.R., McMahon T.J., O'Neale S.W., Staley R.J., Watkins P.M., Watson A.T., Watson N.K., Wilson J.A.

Cavendish Laboratory, Cambridge University, Cambridge
Batley J.R., Carter J.R., Drage L., Goodrick M.J., Hill J.C., Munday D.J., Parker M.A., Robinson D., Wyllie K.H.

Department of Physics and Astronomy, University of Edinburgh, Edinburgh
Boyle O., Candlin D.J., Candlin E.R.S., Knowles I.G.

Department of Physics and Astronomy, University of Glasgow, Glasgow
Doyle A.T., Flavell A.J., Lynch J.G., Martin D.J., O'Shea V., Raine C., Saxon D.H., Skillicorn I.O., Smith K.M.

Department of Physics, Lancaster University, Lancaster
Brodbeck T.J., Chilingarov A., Henderson R.C.W., Hughes G., Jones R.W.L., Ratoff P.N., Sloan T., Smizanska M.

Department of Physics, Oliver Lodge Laboratory, University of Liverpool, Liverpool
Allport P.P., Booth P.S.L., Carroll L.J., Cooke P.A., Greenall A., Houlden M.A., Jackson J.N., Jones T.J., King B.T., Maxfield S.J., Moreton A., Smith N.A., Sutcliffe P., Turner P.R., Wells D.

Department of Physics, Queen Mary and Westfield College, University of London, London
Beck G.A., Carter A.A., Eisenhandler E.F., Hughes D.M., Kyberd P., Landon M., Lloyd S.L., Newman-Coburn D., Pentney J.M., Pritchard T.W., Thompson G.

Department of Physics, Royal Holloway and Bedford New College, University of London, Egham
Blair G.A., George S., Green B.J., Medcalf T., Strong J.A.

Department of Physics and Astronomy, University College London, London
Anderson B., Attree D., Butterworth J., Charalambous A., Clarke P., Cranfield R., Crone G., Fraser J., Hayes D., Hoare T., Jones T., Lane J., Postranecky M., Sherwood P., Wheeler S.

Department of Physics and Astronomy, University of Manchester, Manchester
Duerdoth I.P., Dunne P.W., Foster J.M., Freestone J., Hughes-Jones R.E., Ibbotson M., Kerr A., Kolya S.D., Loebinger F.K., Marshall R., Mercer D., Pater J., Snow S., Thompson R.J.

Department of Physics, Oxford University, Oxford
Buira-Clarke D., Cashmore R., Coe P., Hawes B.M., Hill J., Holmes A., Howell D., Huffman B.T., Kundu N., Loken J.G., Mitra A., Nickerson R.B., Reichold A.R., Renton P.B., Segar A.M., Wastie R.L., Weidberg A.R.

Rutherford Appleton Laboratory, Chilton, Didcot
Apsimon R.J., Baines J.T., Baynham D.E., Botterill D.R., Clifft R.W., Edwards M., English R.L., Fisher S.M., Gee C.N.P., Gibson M.D., Gillman A.R., Greenfield D., Hart J.C., Hatley R.W., Haywood S.J., Hill D.L., McCubbin N.A., Middleton R.P., Morrissey M.C., Murray W.J., Nichols A., Norton P.R., Payne B.T., Perera V.J.O., Phillips P.W., Pilling A., Saunders B.J., Shah T.P., Tappern G.J., Tyndel M., White D.J., Wickens F.J.

Department of Physics, University of Sheffield, Sheffield
Booth C.N., Buttar C.M., Combley F.H., Dawson I., Grigson C., Lehto M.H.

United States of America
State University of New York at Albany, New York
Alam S., Athar B., Mahmood A., Timm S., Wappler F., Zhichao L.

Argonne National Laboratory, Argonne, Illinois
Berger E.L., Blair R., Dawson J., Drake G., Guarino V., Hill N., May E.N., Nodulman L.J., Price L.E., Proudfoot J., Schlereth J.L., Stanek R., Wagner R.G., Wicklund A.B., Yoshida R.

University of Arizona, Tucson, Arizona
Cheu E., Embry T., Johns K., Loch P., Rutherfoord J., Savine A., Shaver L., Shupe M., Steinberg J., Tompkins D.

Department of Physics, The University of Texas at Arlington, Arlington, Texas
De K., Gallas E., Li J., Sosebee M., Stephens R., White A.

Lawrence Berkeley Laboratory and University of California, Berkeley, California
Barnett M., Bintinger D., Ciocio A., Einsweiler K., Gilchriese M., Haber C., Hinchliffe I., Joshi A., Loken S., Marchesini R., Meddeler G., Milgrome O., Niggli H., Palaio N., Richardson J., Shapiro M., Siegrist J., Spieler H., Trilling G.

Department of Physics, Boston University, Boston, Massachusetts
Ahlen S., Hazen E., Shank J., Simmons E., Whitaker J.S., Zhou B.

Brandeis University, Department of Physics, Waltham, Massachusetts
Behrends S., Bensinger J.R., Blocker C., Hashemi K., Kirsh L.E., Wellenstein H.

Brookhaven National Laboratory (BNL), Upton, New York
Alforque S., Barratt R., Citterio M., Gordeev A., Gordon H., Graf N., Gratchev V., Kandasamy A., Koehler J., Kotcher J., Lissauer D., Ma H., Makowiecki D., Murtagh M.J., Norton S., O'Connor P., Paige F., Polychronakos V., Protopopescu S., Radeka V., Rahm D.C., Rajagopalan S., Rescia S., Smith G., Sondericker J., Stephani D., Stumer I., Takai H., Tcherniatine V., Yu B.

University of Chicago, Enrico Fermi Institute, Chicago, Illinois
Anderson K., Bellerive A., Blucher E., Glenzinsky D., Merritt F., Oreglia M., Pilcher J., Pod E., Sanders H., Shochet M., Tang F., Teuscher R., Wu H.

Nevis Laboratory, Columbia University, Irvington, New York
Cartiglia N., Cunitz H., Dodd J., Gara J., Leltchouk M., Parsons J., Seman M., Shaevitz M., Sippach W., Willis W., Zhang L.

Department of Physics, Duke University, Durham, North Carolina
Ebenstein W.L., Goshaw A.T., Lee A.M., Oh S.H., Robertson W.J., Wang C.H.

Department of Physics, Hampton University, Virginia
Assamagan K.A., Baker O.K., McFarlane W.K.

Department of Physics, Harvard University, Cambridge, Massachusetts
Brandenburg G., Feldman G.J., Felt N., Franklin M.E.B., Huth J., Oliver J., Riegler W.

Indiana University, Bloomington, Indiana
Callahan J., Hanson G., Luehring F., Ogren H., Rust D.R.

University of California, Irvine, California
Fahlund T., Hackett C., Hall R., Lankford A.J., Pier S., Schernau M., Stoker D.

Massachusetts Institute of Technology, Department of Physics, Cambridge, Massachusetts
Haridas P., Osborne L.S., Paradiso J.A., Pless I.A., Taylor F.E., Wadsworth B.F.

University of Michigan, Department of Physics, Ann Arbor, Michigan
Ball R., Campbell M., Chapman J.W., Diehl E., Goldfarb S., Hou S., Kouba D., Levin D., McKee S., Neal H.A., Qian J., Schick H., Tarle G., Thun R., Weaverdyck C., Zhou B.

Michigan State University, Department of Physics and Astronomy, East Lansing, Michigan
Abolins M., Brock R., Bromberg C., Ermoline Y., Huston J., Linnemann J., Miller R., Pineiro B., Pope B.G., Richards R., Weerts H.

University of New Mexico, New Mexico Center for Particle Physics, Albuquerque
Gold M., Gorfine G., Hoeferkamp M., Seidel S.

Physics Department, Northern Illinois University, DeKalb, Illinois
Fortner M., Sirotenko V.I., Willis S.E.

Department of Physics, Ohio State University, Columbus, Ohio
Gan K.K., Honscheid K., Kagan H., Kass R.

Department of Physics and Astronomy, University of Oklahoma
Boyd R., Gutierrez P., McMahon T., Severini H., Skubic P., Snow J., Strauss M.

Department of Physics, University of Pennsylvania, Philadelphia, Pennsylvania
Dressnandt N., Keener P., Newcomer F.M., Van Berg R., Williams H.H.

University of Pittsburgh, Pittsburgh, Pennsylvania
Cleland W.E., Mcdonald J.E., Paolone V., Rabel J., Zuk G.

Department of Physics and Astronomy, University of Rochester, Rochester, New York
England D., Haelen T., Slattery P.

Institute for Particle Physics, University of California, Santa Cruz, California
Dorfan D., Dubbs T., Grillo A., Heusch C., Kashigin S., Litke A., Sadrozinski H., Seiden A., Spencer E., Webster A.

Department of Physics, Southern Methodist University, Dallas, Texas
Chou T.-M., Evans G., Stroynowski R., Ye J.

Department of Physics, High Energy Group, State University of New York at Stony Brook, Stony Brook, New York
Engelmann R., Grannis P., Hobbs J., Jung C.K., McCarthy B., Rijssenbeek M., Schamberger D., Yanagisawa C.

Tufts University, Medford, Massachusetts
Mann A., Milburn R., Napier A., Sliwa K.

High Energy Physics, University of Illinois, Urbana, Illinois
Errede D., Errede S., Haney M.J., Thaler J.
Department of Physics, Department of Mechanical Engineering, University of Washington, Seattle, Washington
Burnett T.H., Cook V., Daly C., Davisson R., Forbush D., Guldenmann H., Lubatti H.J., Mockett P.M., Rothberg J., Zhao T.
Department of Physics, University of Wisconsin, Madison, Wisconsin
Fasching D., Gonzalez S., Jared R.C., Pan Y.B., Scott I.J., Wu S.L., Yamartino J.M., Zobernig G.